19th Aerospace Mechanisms Symposium

Lockheed

NASA

19th Aerospace Mechanisms Symposium

NASA

National Aeronautics
and Space Administration

**Scientific and Technical
Information Branch**

1985

PREFACE

The proceedings of the 19th Aerospace Mechanisms Symposium held at the NASA Ames Research Center on May 1-3, 1985, are in this NASA Conference Publication. The symposium was sponsored by the National Aeronautics and Space Administration, the California Institute of Technology, and Lockheed Missiles and Space Company, Inc.

The purpose of the symposium was to provide a forum for the interchange of information among those active in the field of mechanisms technology. To that end, 25 papers were presented on aeronautics and space flight, with special emphasis on actuators aerospace mechanism applications for ground support equipment, lubricants, latches, connectors, and other mechanisms for large space structures. The papers were prepared by engineers from a broad aerospace background, including the U.S. aerospace industry, NASA, and European and Asian participants.

The efforts of the review committee, session chairmen, and speakers contributing to the technical excellence and professional character of the conference are especially appreciated.

The use of trade names or names of manufacturers in this publication does not constitute an official endorsement of such products or manufacturers, either expressed or implied, by the National Aeronautics and Space Administration.

CONTENTS

THE ORGANIZING COMMITTEE

The papers presented at the Symposium were selected and reviewed by the Organizing Committee. Authors are responsible for the content and the technical accuracy of their respective papers. The committee was composed of the following personnel:

General Chairman
: Charles W. Coale
  Lockheed Missiles & Space Co.

Administrative Chairman
: David F. Welch
  California Institute of Technology

Operations Chairman
: Joseph F. Wilson
  Lockheed Missiles & Space Co.

Host Chairmen
: David F. Engelbert
  Ronald E. Mancini
  NASA Ames Research Center

Committee Members

Richard H. Bentall	European Space Research & Technology Centre
Thomas F. Bonner, Jr.	NASA Johnson Space Center
Kenneth C. Curry	Jet Propulsion Laboratory
Charles R. Darwin	NASA Marshall Space Flight Center
Harvey H. Horiuchi	Jet Propulsion Laboratory
Stuart H. Loewenthal	NASA Lewis Research Center
Allen J. Louviere	NASA Johnson Space Center
Frank T. Martin	NASA Goddard Space Flight Center
Peter A Minderman	NASA Kennedy Space Center
Bowden W. Ward, Jr.	NASA Goddard Space Flight Center
Nathan D. Watson	NASA Langley Research Center

PROGRAM

<u>WEDNESDAY, 1 MAY 1985</u>

10:00-12:00 REGISTRATION AND COFFEE SOCIAL
          Auditorium, Bldg N201, NASA Ames Research Center

12:00 LUNCH

 1:00 AFTERNOON SESSIONS

       INTRODUCTORY REMARKS
           Mr. David F. Engelbert, Host Chairman
             NASA Ames Research Center
           Dr. Charles W. Coale, General Chairman
             Lockheed Missiles & Space Co, Sunnyvale,CA

       WELCOME
           Dr. William F. Ballhaus Jr, Center Director
             NASA Ames Research Center

SESSION I
       Professor Richard K. Pefley, Session Chairman
         University of Santa Clara, Santa Clara, CA

       -The Galileo Spacecraft Magnetometer Boom
             Douglas T. Packard and Max D. Benton
               Jet Propulsion Laboratory, Pasadena, CA

       -Hoop/Column Antenna Deployment Mechanism Overview
             B.B. Allen, Harris Corp, Melbourne, FL
             D.H. Butler, NASA Langley Research Center, Hampton, VA

       -Development of an Energy Absorbing Passenger Seat for a
        Transport Aircraft
             Charles P. Eichelberger and Emilio Alfano-Bou
               NASA Langley Research Center, Hampton, VA
             Edwin L. Fasanella, Kenton Intl, Hampton, VA

       -A Modular Docking Mechanism for In-Orbit Assembly and
        Spacecraft Servicing
             F. Gampe & K. Priesett, Dornier System GmbH
               Friedrichshafen, West Germany
             R. H. Bentall, European Space Research & Technology
               Centre, Noordwijk, The Netherlands

COFFEE BREAK

PRECEDING PAGE BLANK NOT FILMED

SESSION II
     Mr. Lester D. Nichols, Session Chairman
       NASA Lewis Research Center,Cleveland, OH

     -Drag Compensated, Precision-Powered Hinge System
          Georges G. Jacquemin and Stanley J. Rusk
            Lockheed Missiles & Space Co, Sunnyvale, CA

     -Design and Development of a Linear Thermal Actuator
          Gerry Bush and Don Osborne
            Spar Aerospace Ltd, Ste Anne de Bellevue,
            Quebec, Canada

     -The Design and Development of a Constant Speed Solar
      Array Drive
          Howard M. Jones and Neil Roger
            Spar Aerospace Ltd, Toronto, Ontario, Canada

     -Application of Traction Drives as Servo Mechanisms
          Stuart H. Loewenthal, Douglas A. Rohn,
          and Bruce M. Steinetz
            NASA Lewis Research Center, Cleveland, OH

7:30-9:30   EVENING SOCIAL GATHERING
            Piazza Room, Holiday Inn, Palo Alto

THURSDAY, 2 MAY 1985

8:30   MORNING SESSIONS
       Auditorium, Bldg N201, NASA Ames Research Center

SESSION III
     Dr. Horst Klages, Session Chairman
       Dornier System GmbH, Friedrichshafen, West Germany

     -The Properties of Thin-Section Four-Point-Contact Ball
      Bearings in Space
          Robert A. Rowntree
            European Space Tribology Laboratory, Risley, England

     -The Design and Development of a Spacecraft Appendage Tie
      Down Mechanism
          William D. Nygren and Raymond Head
            Martin Marietta Aerospace, Denver, CO

     -The Use of Perfluorether Lubricants in Unprotected Space
      Environments
          Bryan H. Baxter and Barry P. Hall, British Aerospace
            Precision Products Group, Stevenage, England

     -Advances in Sputtered and Ion Plated Solid Film Lubrication
          Talivaldis Spalvins
            NASA Lewis Research Center, Cleveland, OH

COFFEE BREAK

SESSION IV
   Professor Erik K. Antonsson, Session Chairman
      California Institute of Technology, Pasadena, CA

   -Telepresence Work System Concepts
      Lyle M. Jenkins, NASA Johnson Space Center, Houston, TX

   -Dual Arm Master Controller Development
    (Consolidated Fuel Reprocessing Program)
      Daniel P.Kuban, Oak Ridge Natl Laboratory, Oak Ridge TN
      Gerald S. Perkins, Jet Propulsion Laboratory, Pasadena, CA

   -Smart Mechanical Hands for Teleoperation
      Antal K. Bejczy and Bruno M. Jau
         Jet Propulsion Laboratory, Pasadena, CA

   -Man-Vehicle Systems Research Facility
    Advanced Aircraft Flight Simulator Throttle Mechanism
      Seth S. Kurasaki and Wilbur C. Vallotton
         NASA Ames Research Center

12:00 LUNCH

 1:00 AFTERNOON SESSIONS

SESSION V
   Mr. Theron H. Haynie, Session Chairman
      Boeing Aircraft Co., Seattle, WA

   -The Development of Staging Mechanisms for the Japanese
    Satellite Launcher Mu-3SII
      Junjiro Onoda, The Institute of Space Astronautical
         Science, Tokyo, Japan

   -A Rotating Electrical Transfer Device
      Ryan S. Porter, Sperry Flight Systems, Phoenix, AZ

TOUR OF SAN FRANCISCO CABLE CAR BARN FACILITY

   PREVIEW
      "The San Francisco Cable Car System"
         Angelo Giovannetti
            NASA Ames Research Center (Ret)

   TOUR
      Mr Ron Mancini, Tour Chairman
         NASA Ames Research Center

EVENING SOCIAL ACTIVITIES

       Empress of China Roof Garden Resturant
       Chinatown, San Francisco

7:15 Social Hour
8:15 Symposium Banquet
9:00 Awards
9:15 Introduction of Banquet Speaker
           Mr. David F. Engelbert
             NASA Ames Research Center

       BANQUET PRESENTATION

       "Space Station - NASA and Industry's Latest Challenge"
          Mr. Angelo Guastaferro
            Lockheed Missiles & Space Co, Sunnyvale, CA

FRIDAY, 3 MAY 1985

8:30 MORNING SESSIONS
      Auditorium, Bldg 201, NASA Ames Research Center

SESSION VI
      Mr. William G. Smith, Session Chairman
        Aerospace Corp, Los Angeles, CA

      -A Dual Fault Tolerant Aerospace Actuator
         Clete J. Siebert, Martin Marietta Aerospace,Denver, CO

      -Design of a Dual Fault Tolerant Space Shuttle Payload
      Deployment Actuator
         Duane R. Teske, Sundstrand Energy Systems, Rockford,IL

      -Features of the Solar Array Drive Mechanism for the Space
      Telescope
         Raimund G. Hostenkamp
           Dornier System GmbH, Friedrichshafen, West Germany

      -Appendage Deployment Mechanism for the Hubble Space
      Telescope Program
         Herbert T. Greenfield, Lockheed Missiles & Space Co
           Sunnyvale, CA

      -Six Mechanisms Used On the SSM/I Radiometer
         Howard R. Ludwig, Hughes Aircraft Co, El Segundo, CA

COFFEE BREAK

SESSION VII
     Mr. Otto Fedor, Session Chairman
       Lockheed Space Operations Co, Titusville, FL

     -Circulation Control Lift Generation Experiment: Hardware
      Development
          Tina L. Pancntin, NASA Ames Research Center

     -Two-Plane Balance and Slip-Ring Design
          Phil M. Luna, NASA Ames Research Center

     -NASA Ames---A Center Overview
          John W. Boyd, Associate Director
            NASA Ames Research Center

HERZL AWARD
     Presentation of the Dr. George Herzl Award for the best
     symposium paper
          Mr. Alfred L. Rinaldo
            Lockheed Missiles & Space Co (Ret)

CLOSING REMARKS
     Mr. David F. Engelbert, NASA Ames Research Center
     Mr. Joseph F. Wilson, Lockheed Missiles & Space Co

 12:00 LUNCH

  1:00 TOUR OF NASA AMES FACILITIES
          TOUR CHAIRMAN
          Mr Salvador A. Rositano
            Chief, Electrical Systems Branch
            NASA Ames Research Center

THE GALILEO SPACECRAFT
MAGNETOMETER BOOM

Douglas T. Packard and Max D. Benton*

ABSTRACT

The Galileo spacecraft utilizes a deployable lattice boom to position three science instruments at remote distances from the spacecraft body. An improved structure and mechanism to precisely control deployment of the boom, and the unique deployment of an outer protective cover are described.

INTRODUCTION

The Galileo spacecraft contains an 8.2-meter deployable magnetometer boom as shown in Figure 1. The boom consists of two deployable masts, three instrument mounts, and a launch canister. These mechanisms were developed jointly by the Jet Propulsion Laboratory, California Institute of Technology, Pasadena, California and ACE-Able Engineering of Goleta, California.

MAST DESIGN

The masts are coilable, longeron-type, deployable structures. The main structural elements are three continuous (single-piece) longerons which are shear-stiffened when erected. The longerons are elastically deformed (coiled) and the battens buckled in order to stow the boom. They and the shear-stiffening diagonals are made of unidirectional, S-glass epoxy material, and are therefore highly elastic. In effect, the structure is made up of spring members which must be forcibly distorted during initial stowage into the canister. This distortion stores strain energy, which is released to effect deployment. Without some means for controlling the deployment, however, substantial, undesirable accelerations would be imparted to the spacecraft, and the boom itself could be damaged.

The stowed boom is contained in a 0.6-meter-long canister during Galileo launch into earth orbit. The boom then deploys to its full length.

The coilable, longeron-type, deployable structure has been used on previous spacecraft applications, including Voyager, Solar-Max, USAF S-3, and OAST-1. However, the Galileo application is unique with regard to five features:

---

*Jet Propulsion Laboratory, California Institute of Technology, Pasadena, California, U.S.A.; ACE-Able Engineering, Goleta, California, U.S.A.

o   The Galileo boom consists of two independent, deployable sections, an inboard mast and an outboard mast, as shown in Figure 2.

o   As it deploys, the boom is attached to a highly maneuverable, spinning spacecraft, and thus experiences loading due to vehicle spin dynamics such as nutation, wobble, and translational accelerations.

o   Achievement of a stable, spinning-spacecraft attitude requires predictable boom deployment in order to minimize the amount of undesired acceleration to the spacecraft and boom structure during deployment.

o   The Jovian environment requires that the mast structure and electrical cables be protected from electrostatic build-up and micrometeoroids. Protection is provided by the use of a stowable, pop-out cover which totally encloses each mast and provides "first surface" micrometeoroid protection.

o   The protective cover over the masts requires that the launch/stowage canister be mounted around the masts after the masts are stowed.

DEPLOYMENT SEQUENCE CONTROL

The Galileo magnetometer boom contains a deployment-control system which provides a precisely controlled deployment rate and sequence without the use of active or commandable elements. Once released from its canister, the boom automatically deploys in a controlled manner with the erecting sequence proceeding as described below.

The deployment rate is controlled by a rotary, viscous damper located at the base of the inboard mast, as indicated in Figures 2 and 4. A metallic lanyard connects the storage reel to the deployable structure. This arrangement is similar to that of previous applications. However, the method used to attach the end of the lanyard to the deployable structure is unique. The lanyard passes through the center of the mast, from the base of the inboard mast to the outer end of the outboard mast. On previous applications, the lanyard was attached at the outboard support plate, but in this application the lanyard is looped over a pulley at the outboard end and routed back upon itself to the midsection structure, where it is secured. This arrangement produces a mechanical advantage between the lanyard forces produced by the inboard mast on the outboard mast.

As the inboard mast deploys, the elastic energy stored in the erection springs and the masts produces a force of 89 newtons (20 pounds) on the lanyard. That force is transmitted to the rotary damper (rate limiter) as the lanyard pays out in a controlled manner. The 89-newton lanyard force acts around the outboard pulley and back to the midsection structure, thereby producing a force of 178 newtons (40 pounds) across the coiled outboard mast. The 178-newton load holds the outboard mast closed even though it has an 89-newton deployment force of its own.

2

Once deployed, the inboard mast can no longer tension the lanyard. At this time the 89-newton force of the outboard mast and outboard erection springs tensions the lanyard to 44.5 newtons (10 pounds). Now, the outboard mast deploys at a much slower rate than the inboard mast. The rate is slower because the tension in the lanyard is now only half of what it was during inboard-mast deployment, and twice as much lanyard must be deployed for each unit length of mast deployed.

Figure 3 shows that the inboard mast first erects into a rigid structure at its base, and then continues to deploy outward. This controlled erecting sequence minimizes the dynamic loading produced by Coriolis and other forces during deployment.

The inboard end of each mast is caused to erect first by means of a base erecting spring (see Figure 4) at the inboard end of each of the mast longerons. The springs produce a relatively uniform torque through the first 45° of longerons rotation and guarantee that the erecting sequence will begin as shown in Figure 3.

Full deployment of the base of the mast is guaranteed by using batten members with 14% smaller diameters in the first and second batten frames on the inboard end of each mast. This assures that the base of the mast will lock-up into a fully erect structure before the remaining stowed portions of that mast begin to deploy.

Completion of the deployment of a coilable, longeron-type mast results in a large transient load condition resulting from the final release of stored energy as the longerons rapidly rotate into their fully deployed state. This peak load is as much as 20 times greater than the 89-newton deployment force. It is necessary to provide a method for relieving the peak load in order to prevent failure of the lanyard.

Figure 5 shows the method employed for this purpose. The body of the rate limiter is spring-loaded with a negator spring to the base plate of the canister. When the spring preload is exceeded by the peak deployment force, the body of the rate limiter rotates, allowing sufficient additional lanyard to pay out, thereby reducing peak lanyard loads. By using this method, the peak lanyard loads are limited to approximately 200 newtons (45 pounds).

DEPLOYMENT RATE CONTROL

The mechanism to control the magnetometer deployment rate is a "shear-type" rotary damper. The damping force is produced by the fluidshearing action across a gap between the stationary damper housing and the rotor contained within the housing. Figure 5 shows the construction details of that unit.

A similar damper configuration was previously used for boom deployment control on the 3-axis-stabilized Voyager spacecraft (Ref. 1). However, the Voyager boom was smaller in cross section, and the required damping was correspondingly less. Also, deployment from a 3-axis-stabilized platform eliminated much of the need for precise control of the deployment rate.

3

Three specific characteristics of the Voyager damper were unacceptable for the Galileo application:

o   The Voyager deployment force was 38 newtons (8.5 pounds) versus 89 newtons (20 pounds) for Galileo. Therefore, more damping was required.

o   The ambient temperature deployment rate for the Voyager boom varied from 0.26 m/s (10.2 in/s) at the start of deployment to 0.006 m/s (0.25 in/s) at completion of deployment. This large variation in the deployment rate was not acceptable for Galileo applications.

o   Because of the high fluid-shear rate associated with the 0.26-m/s Voyager deployment, a thixotropic loop (See Figure 6) occasionally formed in the damping fluid and this occurrence caused less than expected damping.

DAMPER PERFORMANCE

The performance of the shear-type damper is given by the approximate (but acceptably accurate) equation

$$T = \frac{hD^3}{cC_1}$$

T = Torque

h = Rotor width

   = Dynamic viscosity

   = Rotor speed

D = Mean diameter of the fluid gap

c = Fluid gap width

C_1 = Numerical constant depending on system of units used

This equation can be simplified using the following factors:

h = 1.11 cm (same as Voyager)

   = Kinematic viscosity = 32.11 $(V/C)^{0.5}$lb·s/ft^2 (measured value for 500,000 cSt fluid; see Ref. 2)

c = 0.128 mm (same as Voyager)

V = Velocity across the fluid gap

V_D = Deployment velocity

4

R = Pulley radius

C_2 = Numerical constant depending on system of units used

The damping equation then simplifies to the form:

$$V_D = \frac{F_D^2 \, R^3}{C_2 D^5}$$

This equation identifies the sensitivities of the controlling damping parameters, and shows that D and R greatly affect performance.

This analysis also clearly indicates that the increased deployment force associated with the Galileo boom would result in excessively rapid deployment unless the Voyager damper were redesigned to provide increased damping control. This was accomplished by increasing the mean rotor diameter (D) from the 3.20-cm diameter for Voyager to 7.62 cm for the Galileo damper. Also, the Voyager lanyard pulley allowed a pulley-radius decrease, as the lanyard paid out, from 3.56 cm at deployment initiation to 1.02 cm at deployment completion. This difference of radius (R) allowed the excessive deployment rate variation as previously discussed. For Galileo, the variation of R is minimized by using a larger pulley and a thinner, metallic lanyard with R varying from 3.81 cm at the start of deployment to 3.30 cm at the completion of deployment.

These damper modifications result in the performance indicated in Figures 7 and 8. A fluid viscosity of 50,000 cSt was selected for the Galileo damper, and this resulted in deployment characteristics as shown in Figure 9. The maximum fluid-shear rate which occurred in the Voyager damper was 411/s. But, for Galileo, this maximum value was reduced to 178/s, and, can be seen from the slopes of the damping curves in Figures 7 and 8, the possibility of the formation of a significant thixotropic loop is eliminated.

PROTECTIVE COVER

The magnetometer boom cover provides: (1) a black, nonspecular surface to minimize reflections from the spinning boom back to the science instruments located on the despun section of the spacecraft; (2) a conductive outer surface to prevent build-up of electrostatic charges; and (3) a "first surface" against micrometeoroids in the Jovian environment for protection of the mast structure and the instrument's electrical cables.

The "pop-out" covers (Figure 10) are fabricated from a graphite-coated, Kapton thermal-blanket material. Each cover is spaced from the coilable structures by fiberglass, lenticular-shaped springs (standoffs) (Figure 11) which are attached to the mast at each batten frame. The cover and lattice masts are folded together by manually collapsing all standoffs (Figure 12), and then folding the collapsed cover into the stowed masts (Figure 13).

Figures 3B, 10, and 13 show the cover as being loosely formed and not in the triangular shape shown in Figure 11. The extra material in the cover is to allow for differential thermal shrinkage between the boom and cover. It is desired that the cover be untensioned when cold (approximately -223°C) to prevent it from affecting the mast shape and thus changing the alignment of the instruments.

LAUNCH CANISTER AND RELEASE MECHANISM

The magnetometer outboard support plate and canister are shown in Figure 14. The canister consists of three curved, honeycomb panels joined at three longitudinal joints along the panel edges, and attached to the magnetometer boom base plate by a circumferential bolt pattern on the inboard end of the canister. This structural arrangement is necessary to allow access to the sides of the mast while it is being stowed. Access is required to align the protective cover's "pop-out" brackets and to fold in the deployable protective cover. Once the masts are fully stowed, the canister segments are assembled around them and secured to each other and to the base plate.

Spring-loaded latch pins are located at six places on the canister. These pins engage a set of three slots in the magnetometer boom outer plate and three additional slots in the magnetometer boom midsection structure. Three wire-rope cables (Figure 14) are tensioned to push the spring-loaded pins into the appropriate slots in the magnetometer boom. A single pyrotechnic pin-puller mounted to the side of the canister (Figure 14) releases all of the cables and allows deployment to start.

SUMMARY

The Galileo magnetometer boom development program began in late 1978 and ، ، flight boom was delivered to the Galileo spacecraft in May 1984. Magnetometer boom formal testing included: sine and random vibration, hot and cold deployments, magnetic cleanliness checks, and electrical bonding/grounding checks.

The Galileo magnetometer boom design relied heavily upon the experience gained during the earlier Voyager program. Many potential problems were avoided and the Galileo development effort was mainly problem-free.

For the Galileo magnetometer boom, the use of a larger, less delicate, coilable-mast structure than the one used for Voyager greatly reduced the handling damage which was a continuing problem during the Voyager program. The only significant, unresolved Galileo magnetometer boom problem relates to the complexity of the boom-cover design. Each cycle of operation (deployment/stowage) causes some damage to the cover surface. This damage is repairable after each deployment; however, the cover is definitely life-limited. A total of six deployments is considered to be a reasonable life limit. With the exception of the cover design, and given the same set of design requirements, no design change would be recommended for similar boom applications.

REFERENCES

(1) "The Voyager Magnetometer Boom," David C. Miller, 12th Aerospace Mechanisms Symposium, April 27-28, 1978, Moffett Field, California.

(2) "Mariner-IV Structural Dampers," Peter T. Lyman, 1st Aerospace Mechanisms Symposium, May 19-20, 1966, Santa Clara, California, pp. 37-50.

Figure 1. Galileo Spacecraft

BASE ERECTING
SPRINGS (3)

CANISTER

INBOARD MAST

BATTEN FRAMES

MIDSECTION STRUCTURE

BASE ERECTING
SPRING (3)

OUTBOARD MAST

PULLEY

RATE LIMITER

LANYARD

OUTBOARD SUPPORT
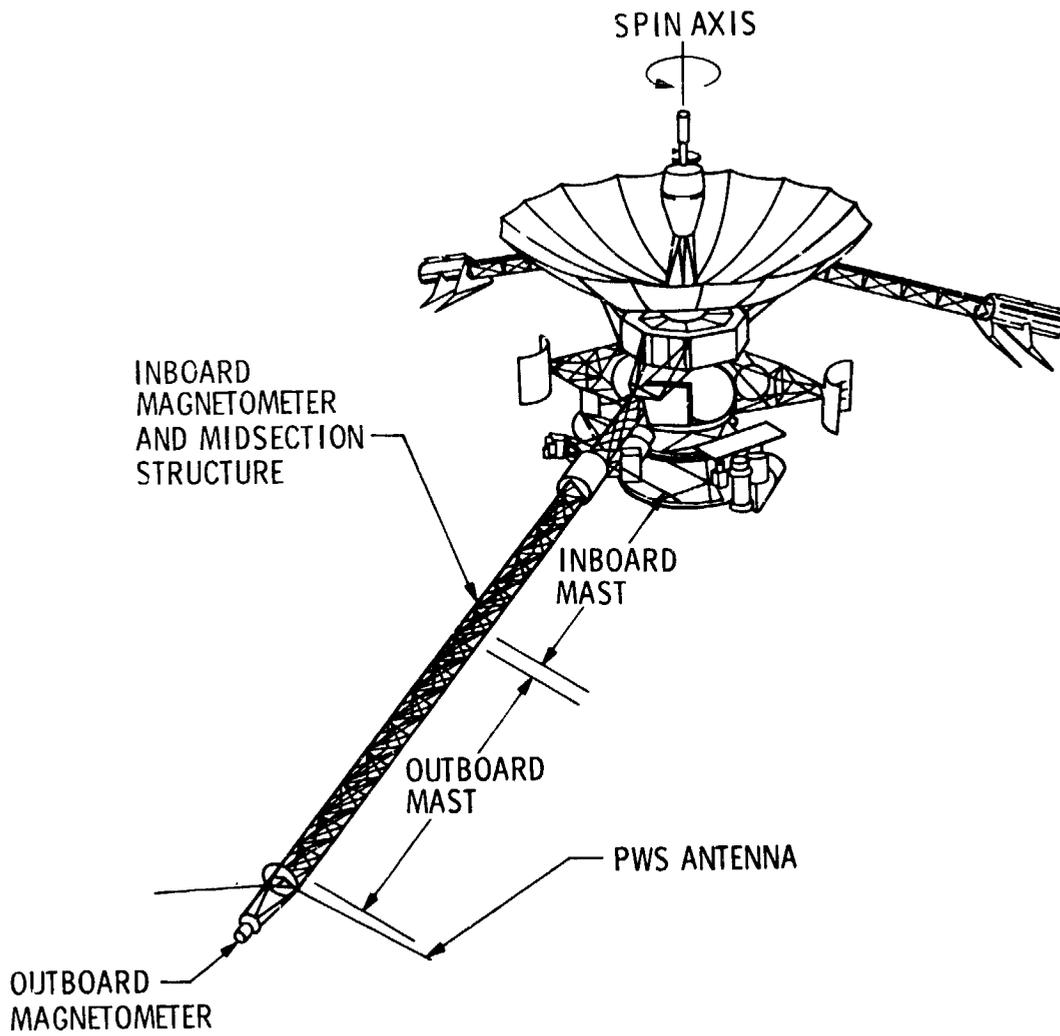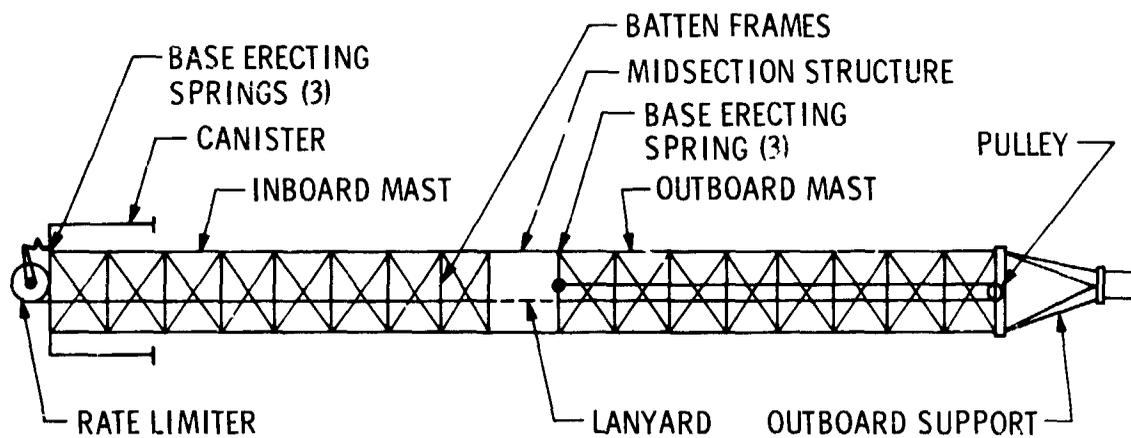
THE BOOM DEPLOYMENT CONTROL SYSTEM
CONSISTS OF THREE FUNCTIONAL ELEMENTS:

1. THE DEPLOYMENT LANYARD.
2. THE DEPLOYMENT RATE LIMITER.
3. THE BASE ERECTING SPRINGS.

Figure 2. Galileo Magnetometer Boom

9

(TRANSITION ZONE MOVES
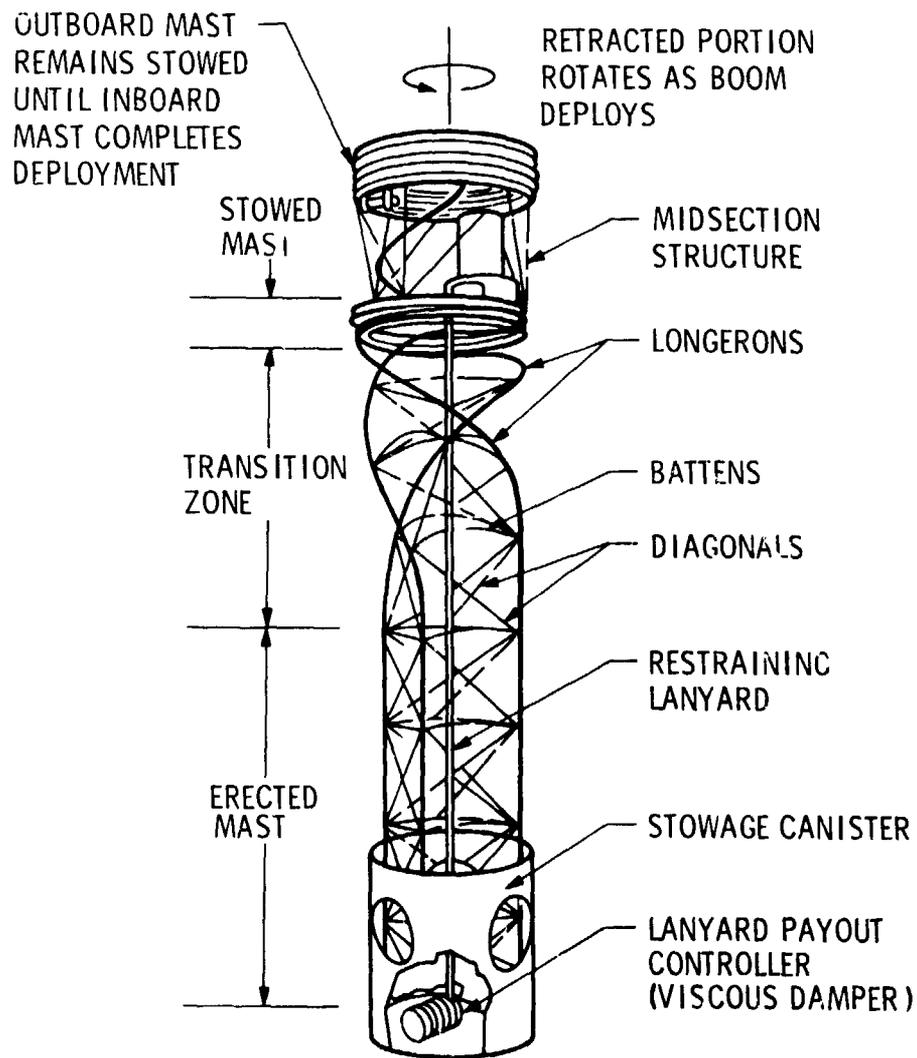OUTWARD AND ERECTED MAST
IS SELF-SUPPORTING)

OUTBOARD MAST
REMAINS STOWED
UNTIL INBOARD
MAST COMPLETES
DEPLOYMENT

RETRACTED PORTION
ROTATES AS BOOM
DEPLOYS

STOWED
MAST

MIDSECTION
STRUCTURE

LONGERONS

TRANSITION
ZONE

BATTENS

DIAGONALS

RESTRAINING
LANYARD

ERECTED
MAST

STOWAGE CANISTER

LANYARD PAYOUT
CONTROLLER
(VISCOUS DAMPER)

Figure 3A.   Erecting Sequence

10
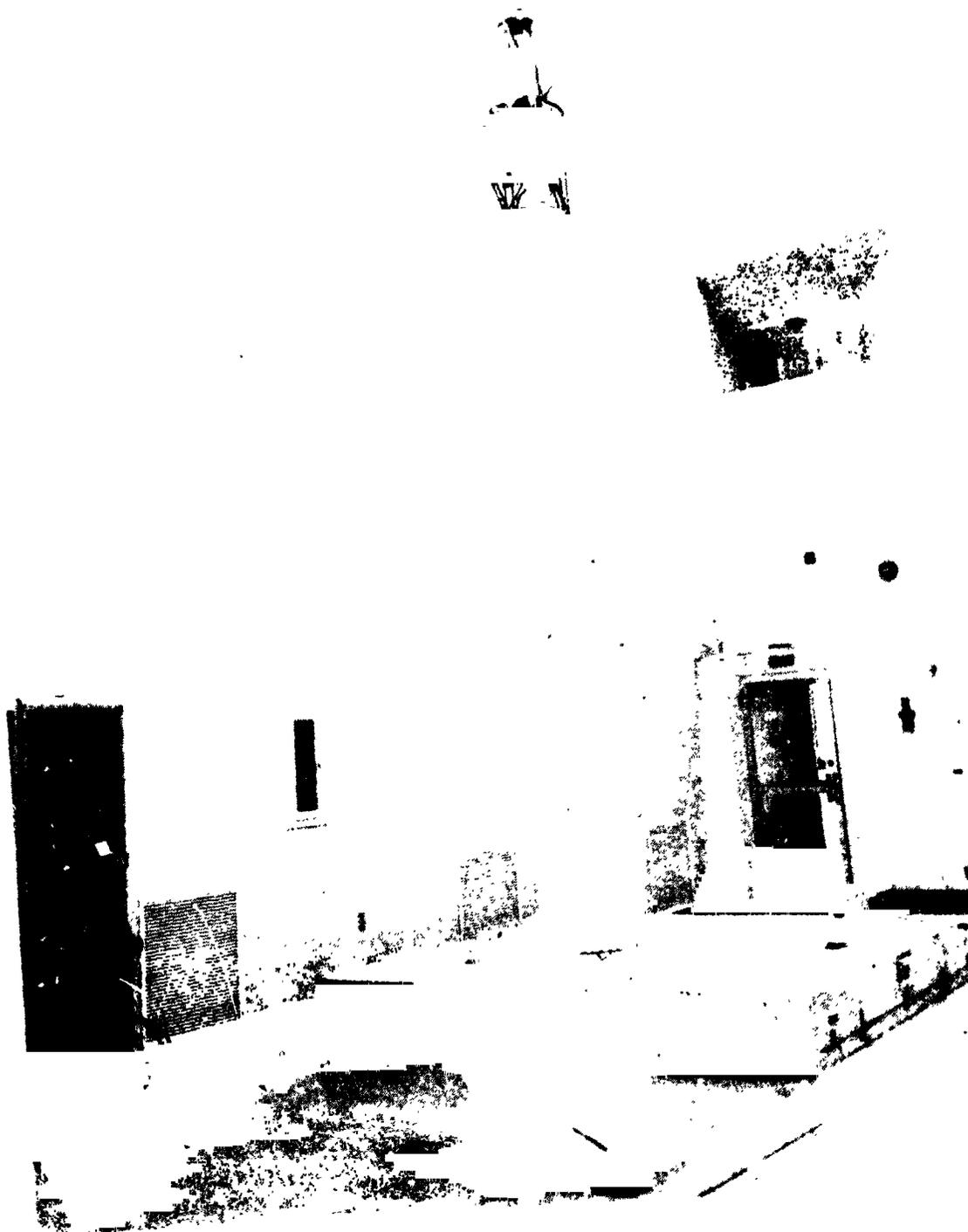
Figure 3B. Galileo Magnetometer Boom at Deployment Midpoint
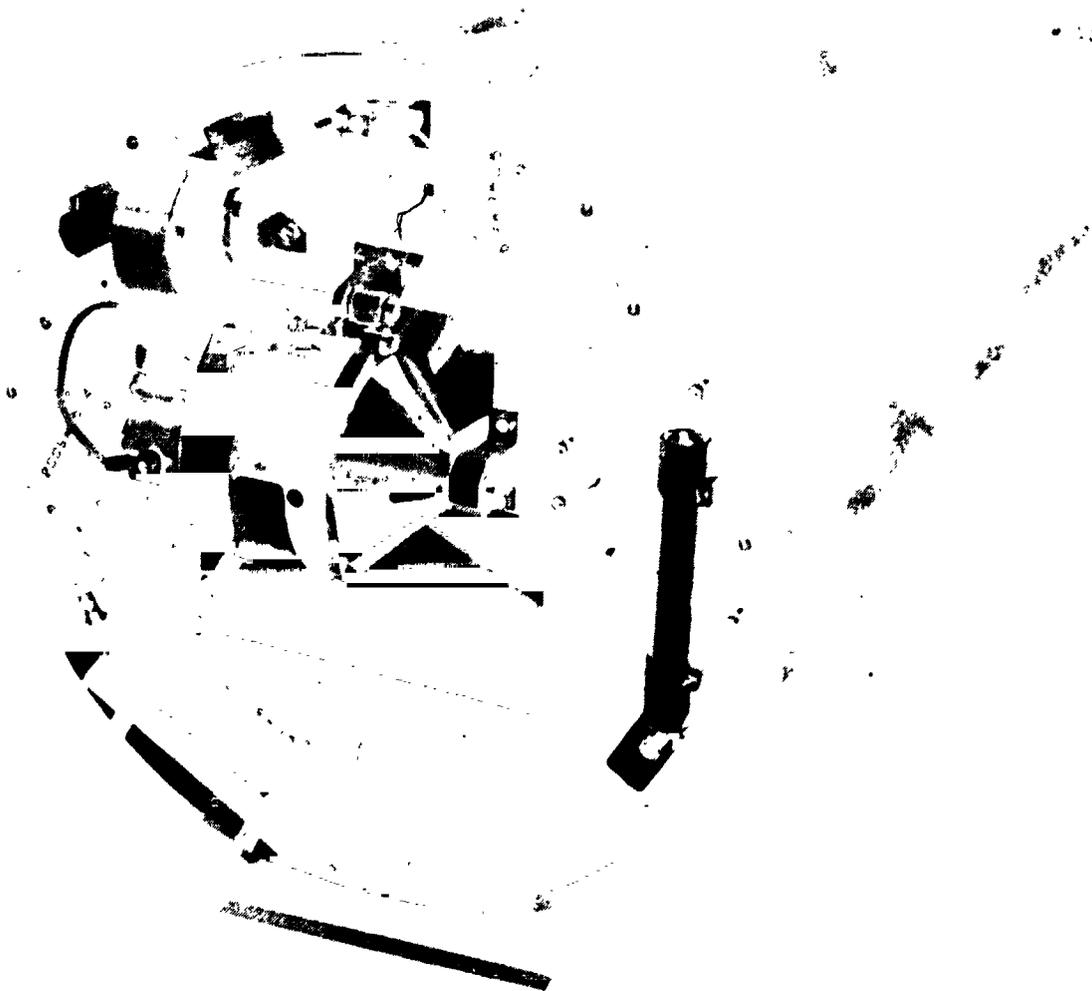
Figure 4. Magnetometer Boom Base Plate
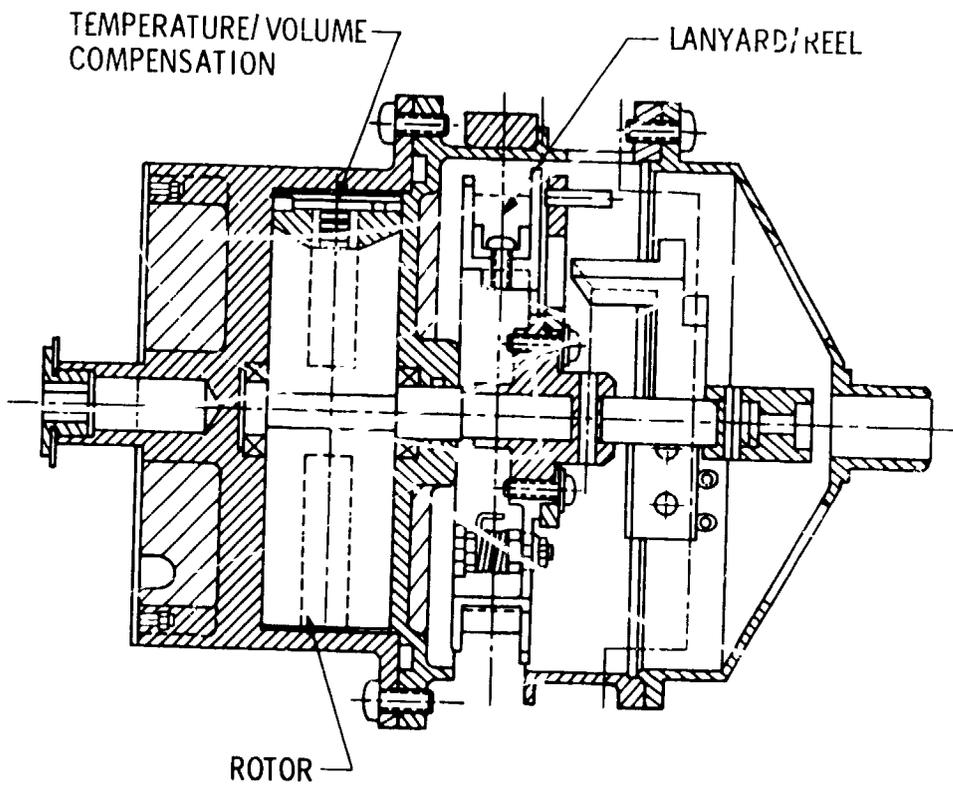
Figure 5. Magnetometer Boom Rate Limiter
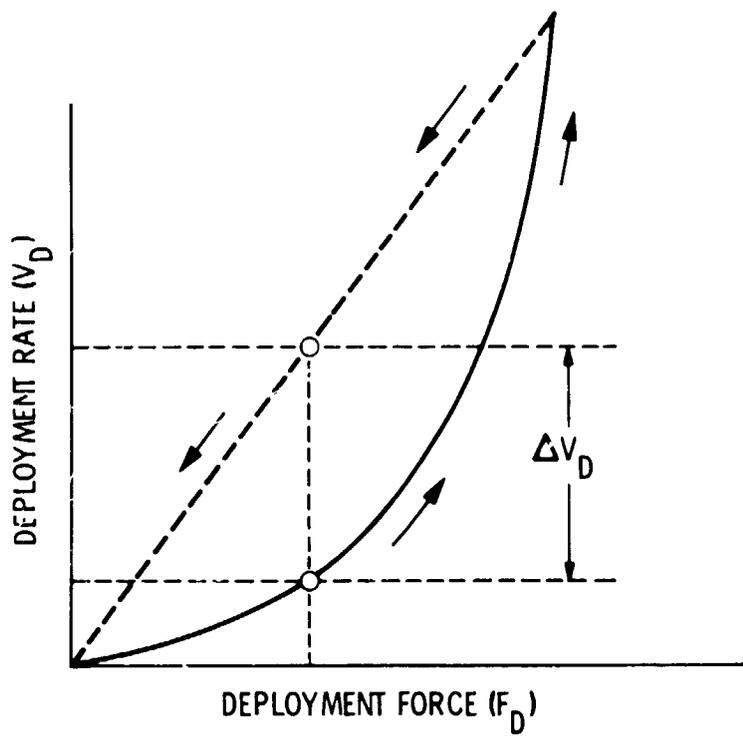
Figure 6. The Thixotropic Loop

14
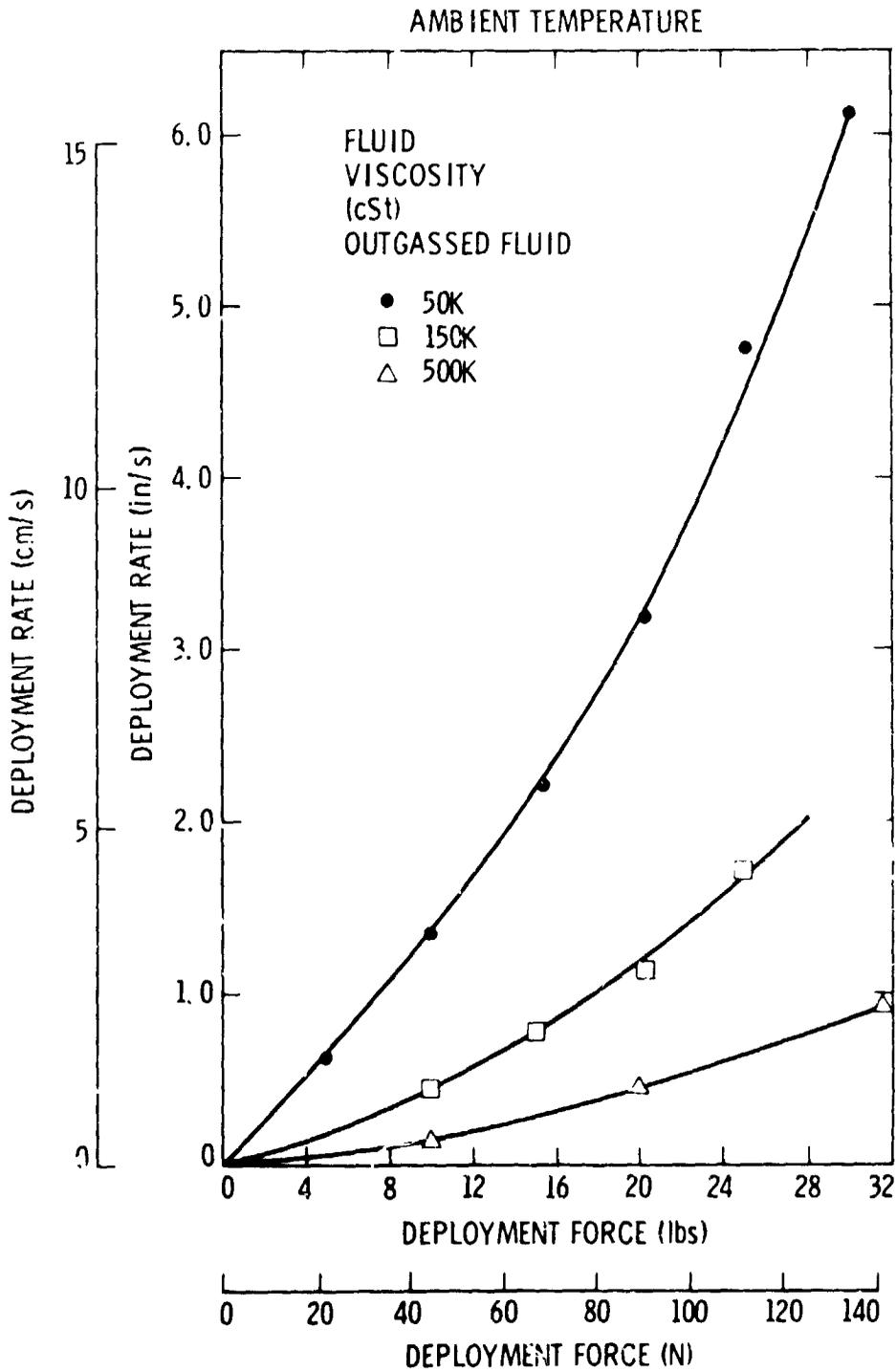
Figure 7. Galileo Magnetometer Boom-Rate-Limiter Damping Characteristics
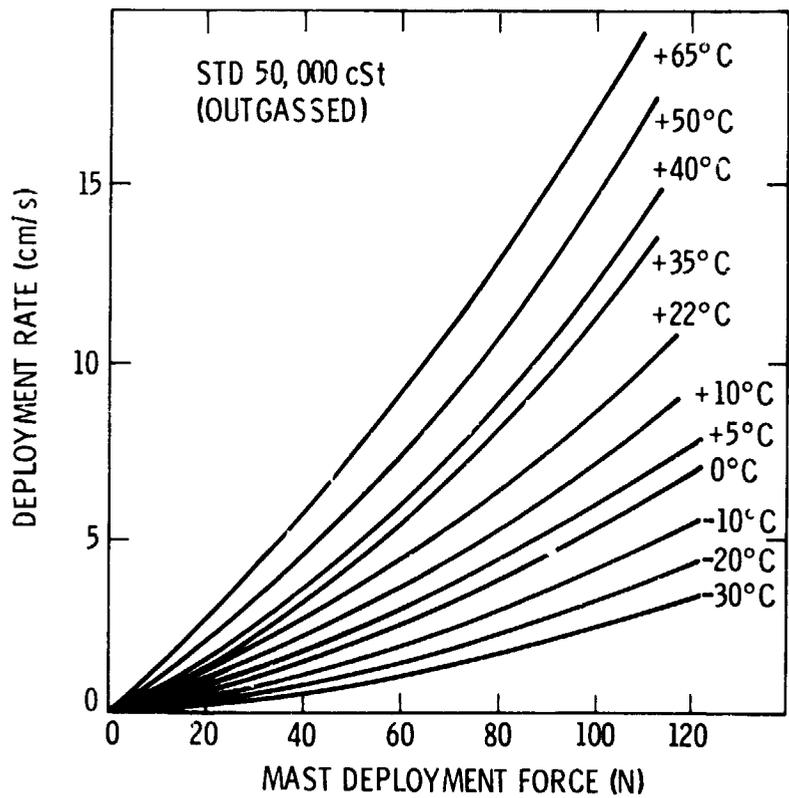
Figure 8. Galileo Magnetometer Boom Rate Limiter Performance at Temperature

Figure 9. Galileo 7-Meter Deployable Mast Deployment Characteristics

Figure 10. Galileo Magnetometer Boom (Fully Deployed)

18

Figure 11.   ESD Cover With Cable Clearance
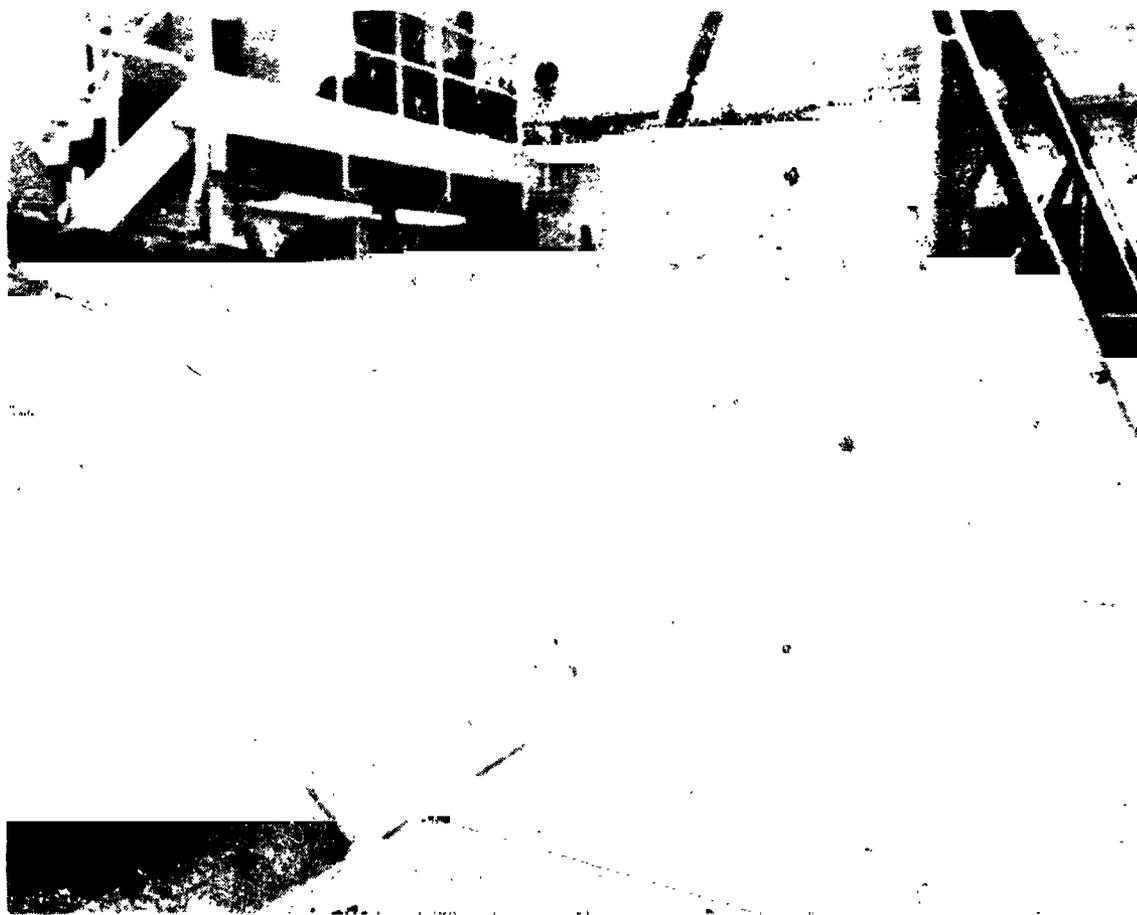
Figure 12. Magnetometer Boom Cover Stowing Procedure

Figure 13. Magnetometer Boom Initial Deployment

Figure 14. Stowed Magnetometer Boom

HOOP/COLUMN ANTENNA DEPLOYMENT MECHANISM OVERVIEW

B. B. Allen* and D. H. Butler**

ABSTRACT

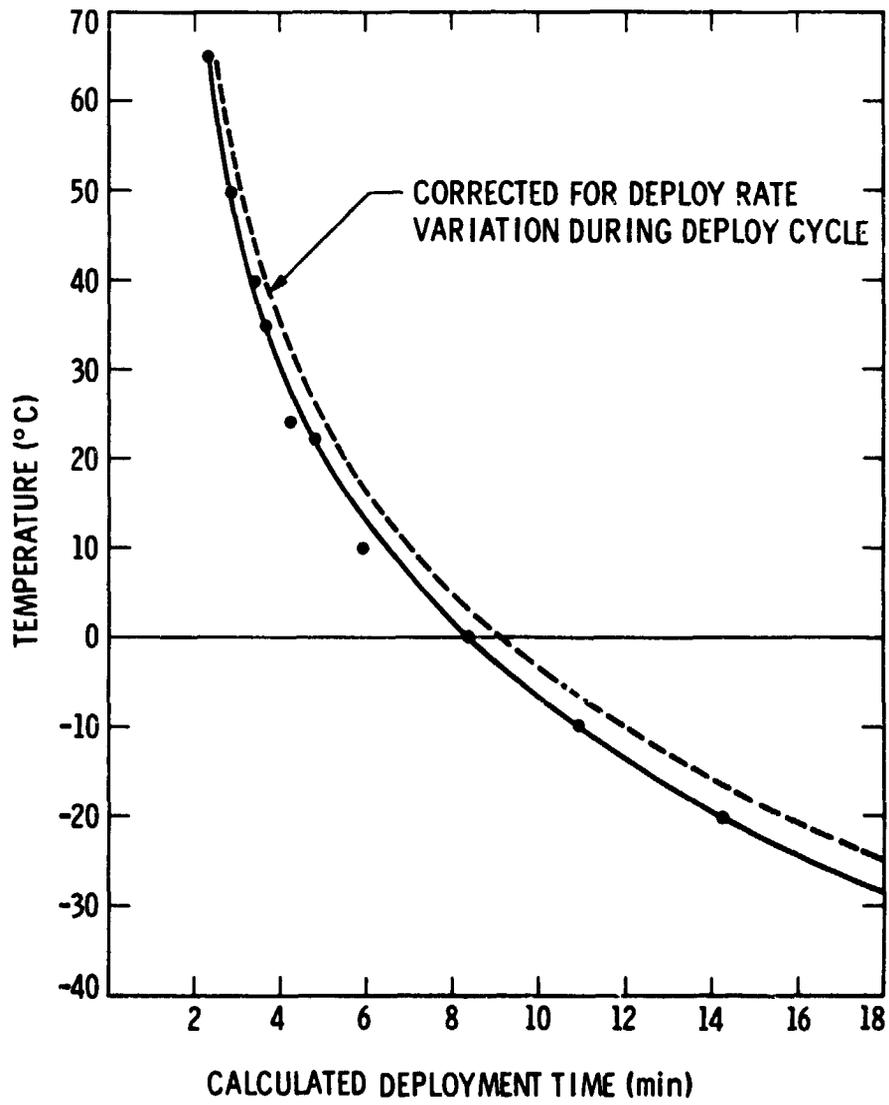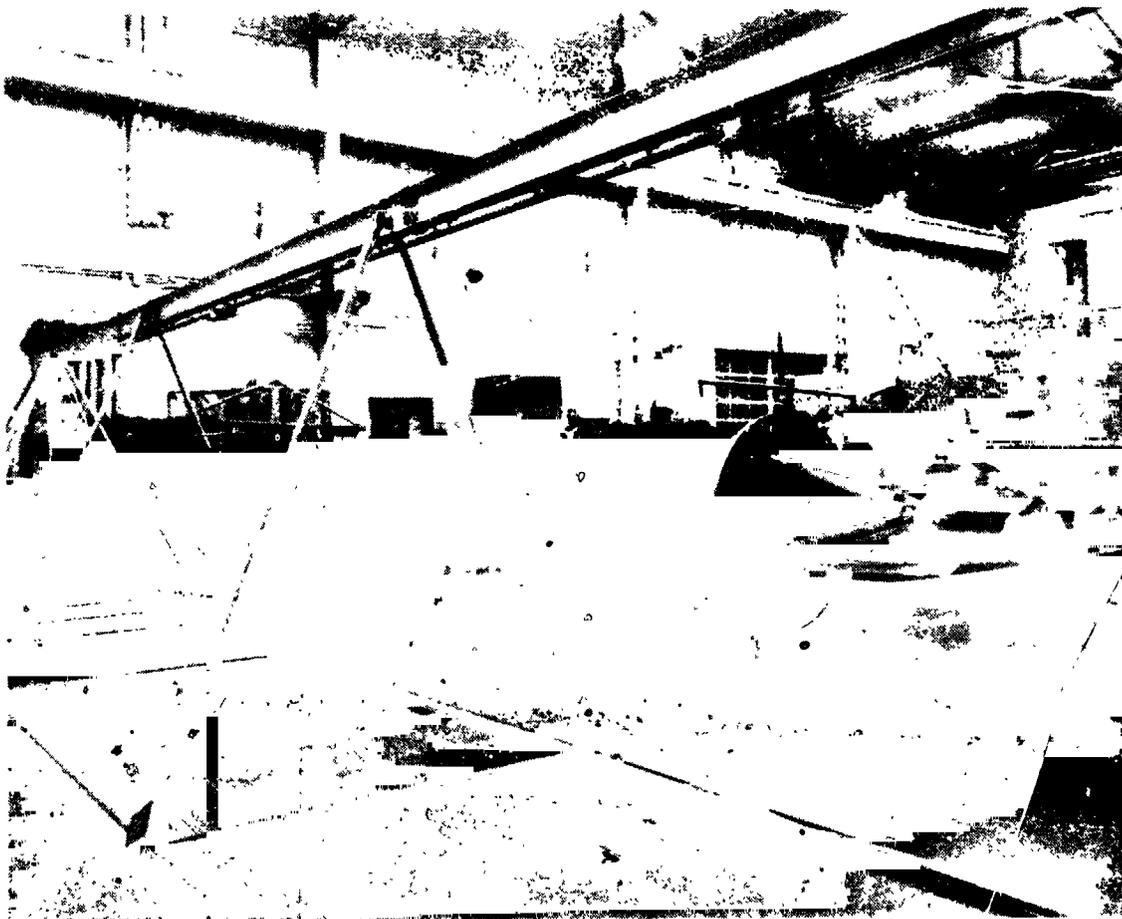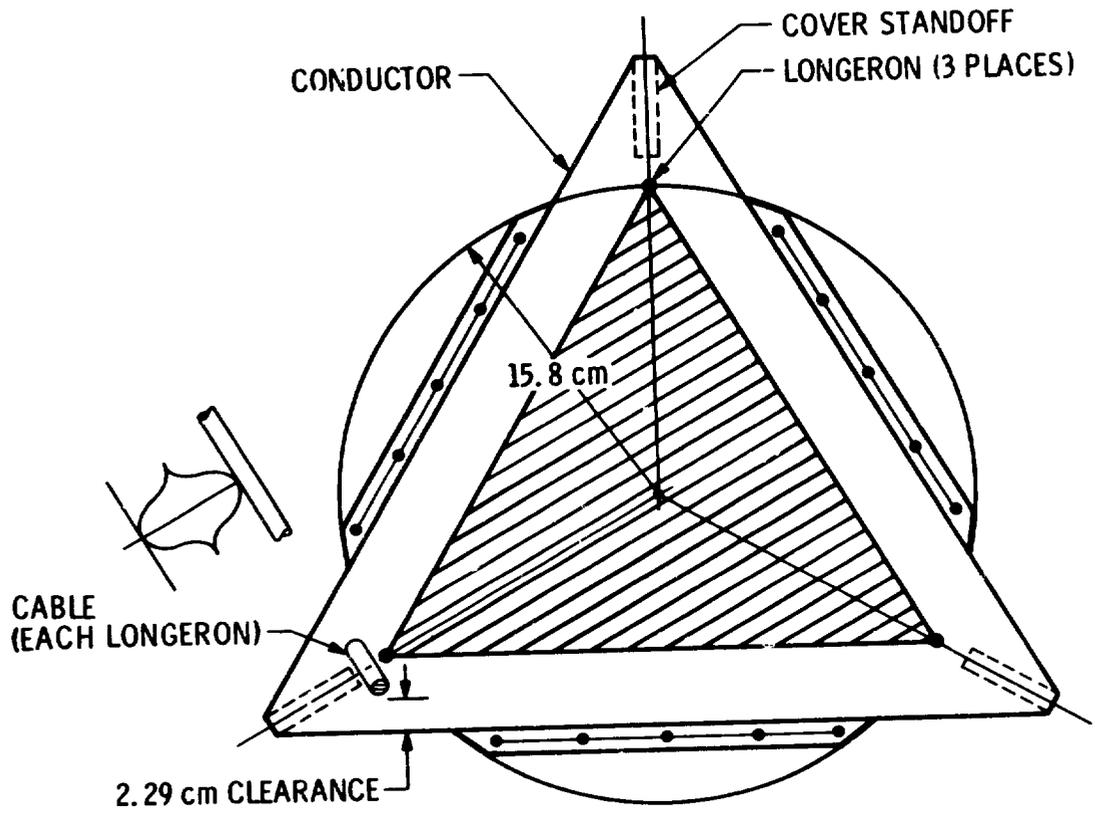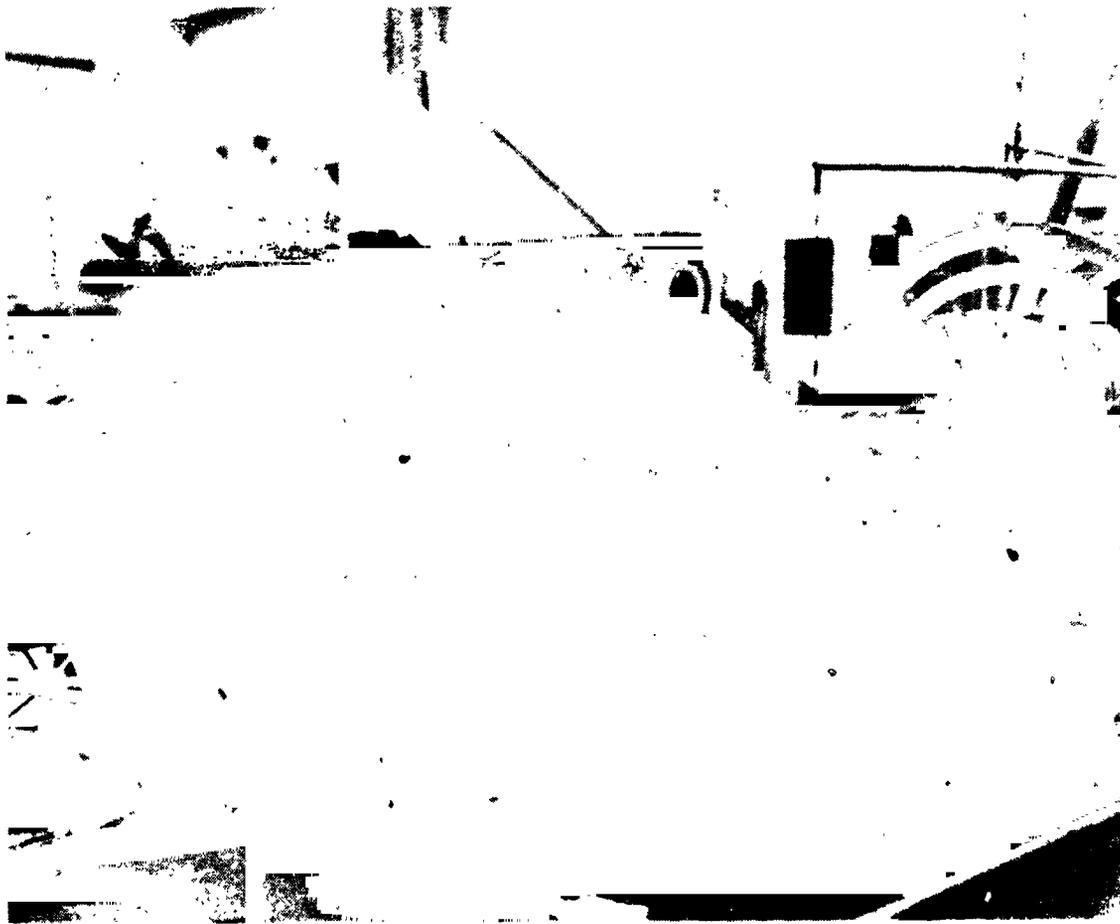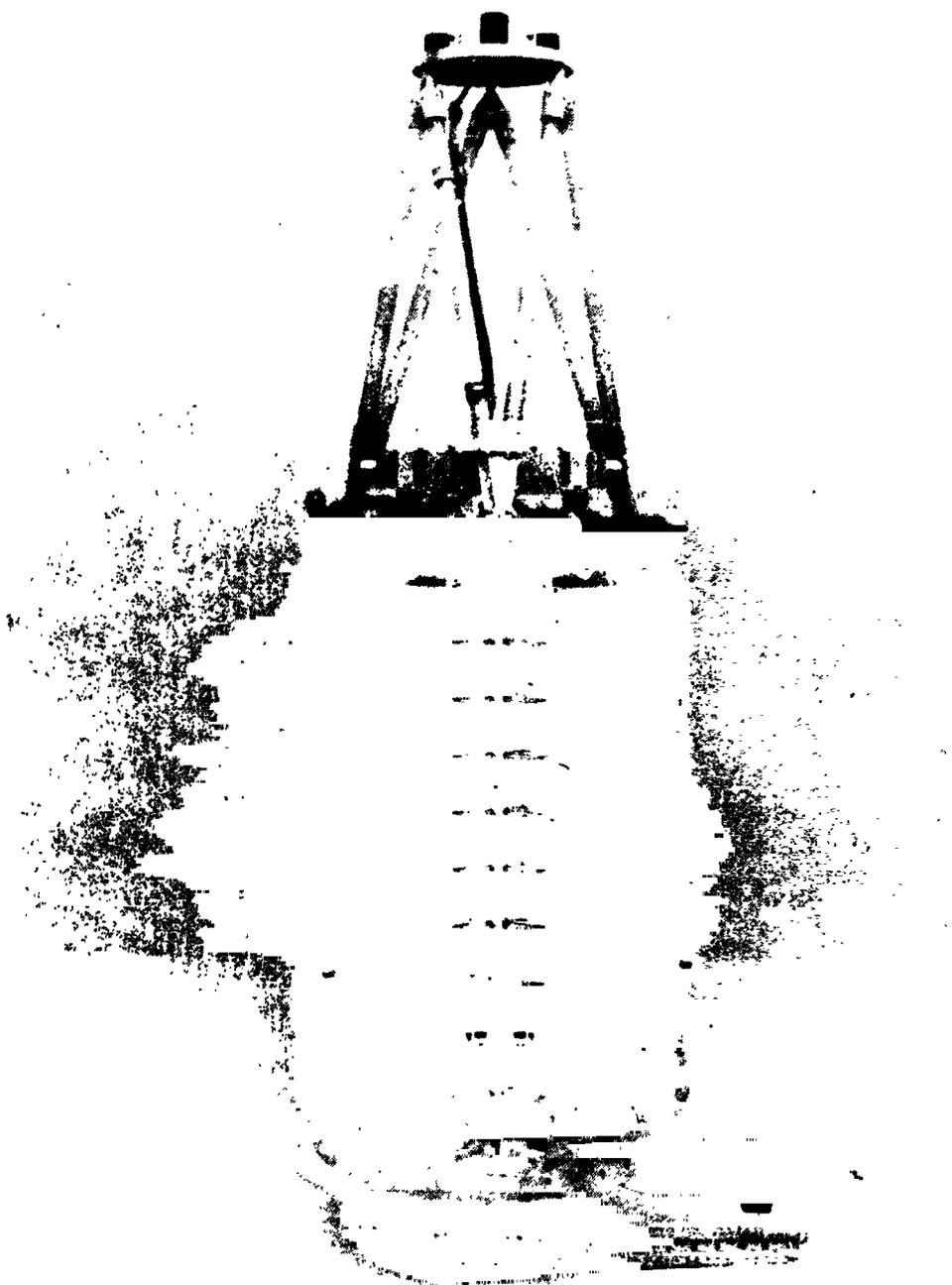The hoop/column antenna program is directed toward the development of a cost-effective, large-area, self-deploying reflector antenna system. Large-surface-area antenna systems (50-300 meters in diameter) are required in future space missions involving improved land communications, Earth resources observation, and the study of intergalactic energy sources. The hoop/column antenna is a concept where a large antenna system can be packaged within the Space Transportation System (Shuttle) payload bay, launched into Earth orbit where it is released either for deployment as an Earth observation or communications antenna, or boosted into deep space as an intergalactic energy probe. Currently, self-deployable antenna concepts are competing with astronaut-erectable concepts as the most efficient means of deploying large-surface-area antenna systems in space.

This paper describes various mechanisms and support structures that are required to deploy the hoop, which is used to support the antenna reflective surface, and the column that is used to position the antenna feeds and the reflector. It also describes a proof-of-concept model (15 meters in diameter) that is currently being ground-tested to determine the adequacy of the deployment mechanisms.

INTRODUCTION

Intergalactic energy probes, land mobile communications, Earth resources observation--these are mission scenarios projected by NASA and the scientific community of the year 2000 and beyond. Large-scale, self-deployable space antennas of diameters ranging from 50 to 300 meters will play an important role in these missions. Large reflectors will one day allow national land mobile communications with transmitter/receiver power levels comparable to today's citizens band radios. Large-aperture radiometers can be used for monitoring global hydrology on a weekly basis to aid agricultural and climate researchers.

The self-deployable hoop/column antenna concept has been under study for several years. The study program is at the proof-of-concept stage where scale-model hardware of the deployment mechanisms and support structure have been built and tested. This paper describes the deployment mechanisms and support structure necessary to launch and deploy an entire large-surface-antenna system with one Shuttle flight. It also describes the scale-model hardware that is currently being ground-tested to determine the deployment characteristics of the hoop/column concept.

*Harris Corporation, Melbourne, Florida
**NASA Langley Research Center, Hampton, Virginia

HOOP/COLUMN DESIGN FEATURES

The elements of the antenna are labeled in Fig. 1-3. Primary structural elements of the hoop/column antenna concept are an extendable column, which deploys from a central hub, and a hoop made of articulating segments that is used as a frame for attaching the peripnery of the reflector surface. The column consists of telescoping segments made of a triangular truss network of structural elements. Hoop position is controlled by a series of cables emanating from both the lower and upper column extremities and attached to each hoop joint. These cables serve to support and locate the hoop. The reflector surface, which is attached to both the hoop and lower hub section, is shaped by a series of catenary cord elements which support and contour the reflective mesh surface. The cord elements are high stiffness/low coefficient of thermal expansion quartz and graphite material which provide a very stable structure to which a gold-plated molybedenum reflective mesh is attached.

The remainder of the paper addresses major features of the 15-meter-diameter scale model of the hoop/column antenna. These features are the same as those of a 100-meter-diameter flight mode. The 15-meter-diameter size for the scale model was chosen so that the model could be tested in existing RF and thermal-vacuum ground test facilities and to minimize the effects of scaling on the deployment characteristics of the antenna.

ANTENNA DEPLOYMENT

Prior to deployment, the scale model antenna is stowed in a package 2.7 m long and 0.9 m in diameter as shown on Fig. 4. Approximately 30 minutes is required for deployment, with the time being divided between visual inspection and mechanism operation. Deployment is accomplished in three basic steps: column extension, hoop/surface deployment, and system preloading, which shapes the surface. Deployment begins with column extension (Fig. 5). The telescoping column is deployed by a cable-driven system that tensions the column during the final phase of deployment. This tensioning process is to allow the column cam lock latches to properly actuate. A feature of the column is the ability to deploy the telescoping sections sequentially, with the sequence being passively controlled by the latches themselves.

The next step is to deploy the hoop and surface (Figs. 6 and 7). The hoop consists of 24 tubular segments that contain double hinge joints at each end which permit rotation but do not allow torsional wrap-up. During deployment, the hoop segments simply rotate from vertical to horizontal orientation about an axis through the center of each member. Eight electrical motors, located at eight different hinge joints, drive worm gears that transmit torque through four bar mechanisms to passive joints. The surface is deployed with the hoop, but not shaped. Shaping of the surface is accomplished by the extension of the lower extremity of the column called the preload segment. Preloading consists of extending the column an additional 0.4 meter by means of a screw to properly pretension the structure and the surface (Fig. 8).

24

COLUMN DEPLOYMENT

The column is a sequentially deployed, cable-driven, telescoping, triangular truss unit with diagonals that resist compressive loads. The column, which is symmetrical about the center hub, extends in both directions from the hub. Longerons, circumferentials, and diagonals are all tubular members laminated from graphite epoxy material. A typical column segment is shown in Fig. 9. Diagonal direction is reversed from bay to bay to minimize column "wind-up" or a rotation relative to the hoop.

COLUMN DRIVE SYSTEM (CDS)

The following is a list of the major CDS requirements:

o   Must be located at the stowed column center
o   Must deploy and stow each column end simultaneously at a uniform rate
o   Must be remotely controlled
o   Must place column in tension during final phase of column deployment.

The column drive system (Figs. 10-13), located at the geometrical center of the column, is responsible for providing the forces necessary to deploy and stow the counterbalanced column system during testing. A tensile load is applied to the column by the CDS at the final stage of deployment to allow proper latching of the telescoping column sections. This tension is relieved upon completion of column deployment The CDS does not pretension the antenna. The structural design for the CDS consists of two large triangular plates separated by beam-column spacer brackets located directly in line with the column longerons.

Deployment of the column is accomplished by retrieving the deployment cables onto a drum (Fig. 11). There are six deployment cable which are threaded through each of the three longerons on each column half. The drum is threaded to ensure that the cables remain in a selected area. Longeron cables are routed from the drum to a single pulley on the spacer brackets which in turn directs the cable through the longerons. When the cable reaches the top of the longeron, a pulley in the striker housing turns the cable 180° and it proceeds (between the longerons) to the bottom of the second longeron. Then it is intercepted by another pulley located in the latch housing of the adjacent telescoping section and turns 180° to proceed up the inside of this longeron to the second striker housing. This path is repeated until the cable has been threaded though all four longerons.

The stow cables are attached to the latch actuation arms on the end telescoping section through a bridle unit. This cable is routed down along the column centerline and through the drum to a pulley attached to the opposite triangular plate. This pulley directs the cable to the beam spacer bracket containing dual pulleys, each turning the cable 90°. This brings the cables to the threaded drum and cam portion of the mechanism. Both stow cables have a small residual tensile load applied during the deployment and stow phases. Hi-lift cams (Fig. 12) relieve the residual tension loads in the stow cables, thereby allowing them to go slack. This feature is necessary for

proper latching of the end sections because the stow cables are attached to the latch pawl (of the end telescoping sections) and latching can't occur while the cables are in tension. The cable drum is suspended between ball bearings attached to the triangular base plates (Fig. 13). Drum rotation is accomplished by a 28-VDC gear motor connected to a pinion and gear system. Drum back-driving is resisted by the gear motor. The motor and pinion assembly is mounted on the upper triangular plate.

The materials used for construction are primarily 6061-T6 aluminum, with 300 and 400 series stainless steel components and cables.

COLUMN LATCH

Primary latch requirements are

o   Latch the column sections into a rigid, predictable structure
o   Withstand a preload of 4000 N
o   Latch and unlatch the column sections remotely
o   Passively provide sequential deployment and stow
o   Provide adjustment capability.

The latch design provides positive latching, passively actuated sequential deployment, reasonably direct load path from longeron to longeron, and a high tolerance for error through adjustment capability. A depiction of the latch delineating the major components is shown in Fig. 14.

The latch is comprised of two assemblies located on the ends of the column longerons. The assembly loaded on the top of the longeron of each telescoping assembly is called the striker housing and contains the pawl striker plate. Active latching elements are contained in a latch housing located on the bottom of the telescoping column sections. The latch provides a continuous load path along the longerons without introducing excessive bending moments into the longerons. Both latch housings contain rollers that guide the deploying sections along the longerons of the previously latched telescoping section. When the column is in the stowed configuration, the latches are all positioned as shown in Fig. 15. When deployment is initiated, the motor, pinion, and gear arrangement rotates the CDS cable drum such that the deployment cable threaded through the longerons are collected on the drum. This in turn translates the inboard column segments upward (Fig. 16), thereby allowing the latching actuation gear to come into contact with the deployment trip roller. All telescoping sections deploy as a unit because the pawl cam does not allow the stowage rollers to advance. The pawl and lever arrangements are overcenter devices and are held in place by the spring/plunger assembly. Deployment continues unchanged until the latch actuation lever contacts the trip roller attached to the striker upward (Fig. 16), thereby allowing the latching actuation gear to come into contact with the deployment housing. The lever tip cannot traverse past the rollers, so the bottom of the pawl begins to move toward the striker housing. Binding is prevented because the spring/plunger assembly allows for length adjustments. Adjacent section release begins when the pawl cam rotates away from the stowage roller. It can be seen that the pawl has total control over the deployment sequence and, also, that no additional mechanisms are required to maintain that control.

26

A unique feature of the pawl is the cam profile (Fig. 17a) on the surface that contacts the striker plate. This feature allows the pawl to seat itself against the striker plate so that the normal force vector at the point of contact results in an opening moment, preventing binding. The cam profile also compensates for possible errors in the striker plate location (Fig. 17b). This design incorporates shims under the striker plate so that the deployed pawl angle can be adjuste. prior to final column assembly. The cam feature allows the pawl to be prestressed to reduce the joint nonlinear motion. Prestressing is accomplished by applying a large tensile force to the deployment cables located inside each longeron (Fig. 17c). The cable tension strains the latch housing and the pawl pivot to increase the distance between the latch/striker housing interface and the pawl pivot. Pawl rotation will continue because the spring/plunger assembly pushes it clockwise. When the cable tension is relieved, friction prevents pawl release (counterclockwise rotation).

Latch housings are plaster mold A355 aluminum castings and the latching components are 17-4 PH stainless steel.

The column latch has demonstrated conformance to the requirements through component and system-level testing.

PRELOAD SEGMENT

Preload segment design requirements are

o   Extend against a load of 3560 N
o   Deploy against rigid stops
o   Be remotely controlled
o   Have a redurlant stop mechanism

The preload segment (Figs. 18 and 19) attaches to the lower end of the column (Fig. 8). The purpose of the preload segment is to extend the column to its design length in order to pretension the hoop and surface control cords. The preload segment travels approximately 0.4 m from its stowed to deployed state.

An axial, motor-driven screw was selected to drive the preload segment from the stowed to the deployed position. Screw loads are carried to the longeron through a triple beam arrangement. The beam brackets are bonded to the inside of the longerons as shown in Fig. 18. This bracket design is not the most desirable, but the outer portions of the longerons were reserved for rollers and guides located on other deployable sections (Fig. 14). Power to drive the screw is provided by a 28-VDC gear motor. Motor torque is transferred to the column nodes through a thin flex plate. The plate is essentially rigid in torsion, but can allow axial displacement to account for manufacturing errors. The screw is 16-mm steel with acme threads. Ball screws were considered and rejected because the coefficient of friction is not adequate to prevent back driving under load without a brake. Preload segment extension is terminated by limited switches and redunjant current sensors.

The preload segment is manufactured from the same structural materials as the column.

HOOP DEPLOYMENT

The primary hoop requirements are to deploy under its own power and against the following loads:

o   One-g catenary load of the mesh
o   A 1500-N compressive load
o   A 20-N-M deployment moment
o   Forces developed by the hoop support and surface control cords.
o   Internal friction
o   Counterbalance system unbalances

The hoop (Fig. 20), when deployed, forms a rigid ring around the column. It is precisely located at each of its 24 joints by the hoop support cords (Fig. 2) and forms a rigid boundary to which the RF reflective surface attaches.

In order to ensure a smooth and symmetrical deployment, each of the 24 joints is kinematically linked to another (Fig. 21). Synchronization rods working in concert with the gears at each of the joints provide the hoop with its kinematic synch. onization. Deployment energy for the hoop is supplied by eight 28-VDC gear motors located 45° apart. (A space-deployed antenna would use four motors at 90°.) The gear motor is directly coupled to a worm which drives mutually interfaced worm gears (Fig. 22). This configuration provides a mechanical advantage of 35 to 1. During deployment the synchronization rods, which are tension members only, maintain the platforms parallel to one another. Passive gears (Fig. 23) transmit the moment necessary to deploy the hoop into the passive segments and synchronization rods. The gear motors are elect. ically connected in parallel to synchronize hoop deployment. Hoop deployment is terminated by limit switches.

Primary materials for the hoop are 6061-T6 aluminum alloy, graphite epoxy, and 416 stainless steel gears.

GROUND TESTING

Ground-based testing that simulates the zero-g space environment presents a great challenge for the 15-meter hoop/column antenna and, for that matter, any other large, deployable, structural system. This is because large, deployable structures are usually not self-supporting in the Earth's gravity field during deployment. Neutralizing the gravity field cannot be accomplished on all elements, such as the reflector surface for example. The 15-meter antenna is self-supporting after deployment, but the structural deformations associated with the 1-g effect require that the surface be designed to include these deformations. This surface would not have the same shape in space.

The counterbalance system shown in Fig. 24 was used to offset the 1-g effects of the structural elements during deployment. The system consists of eight towers supporting a 24-segment, 16-m-diameter ring. Twenty-four radial cables attach the ring segment intersections to a central hub. Trolleys containing a small cable attached to the hoop, and a hoop counterbalance

28

weight, traverse the radial cables during deployment. The counterbalance system central hub is raised or lowered to attempt to cancel the drag induced by friction in the hoop joint worm gears and counterbalance system cable sag. The drag increased near full deployment, requiring full capacity off our four 28-VDC electrical motors. Radial cable tracks were used because of installation/removal requirements for the counterbalance system in various facilities.

The mechanisms utilizing electric gear motors were controlled by a remote console during ground testing. The console contained current sensors that terminated deployment approximately one second after a system current level exceeded predetermined values. This remote console would be replaced with a on-board computer system for a flight antenna.

Test observations were conducted during and after deployment. Gear motor current levels and hoop synchronization sensors were monitored during deployment. After pretensioning, structural element positions and loads were measured and correlated with required values. The antenna mechanisms performed as designed, but the couterbalance system drag on the hoop require' the addition of four active joints (for a total of eight) so that hoop deployment can be implemented when the surface is installed. There was a 3 second delay between deployment termination of the first hoop active joint and the final active joint. This time delay did not appear to affect the hoop geometry.

The geometry of the structural system was within the error budget except for the hoop radial component. The allowable radial deviationwas 1.27 mm rms as compared to the measured value of 4 mm rms. Adjustments will be implemented to attempt to obtain the error budget when the surface is installed.

TEST CONCLUSIONS

All mechanisms performed as designed. The hoop drive system needs to be reevaluated with respect to the friction associated with worm gears in the hoop joints. Ground-test results indicate structural elements of a 15-meter hoop/column antenna can be fabricated and adjusted so that when the reflector is installed a 1.75 mm rms deviation from a true parabola, when referenced to surface nodes, can be expected. Precision measurements of all structural components are needed before assembly to assure compliance with error budgets.

The structural deployment program is considered to have been successful. This leads to the conclusion that large, deployable antennas can be fabricated, ground-tested, and placed in orbit with the expectation of success.

If future programs require a high-quality zero-gravity simulation, design and development of such a facility would be comparable to the antenna or structural system itself.
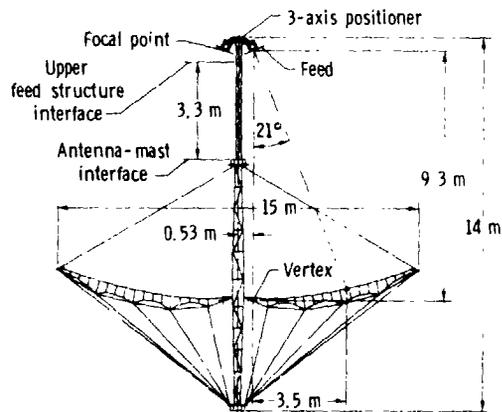
Figure 1.   15-Meter Hoop/Column Antenna
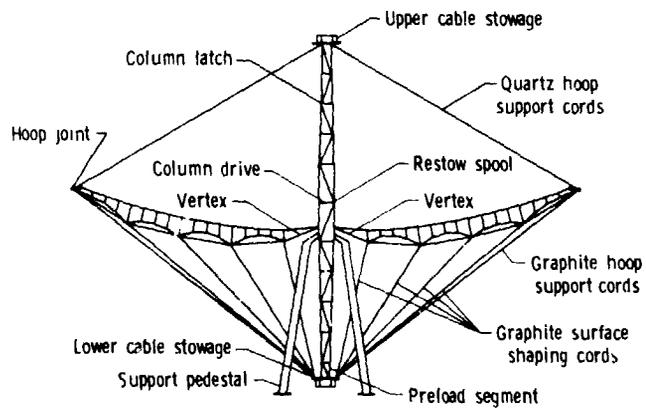
Figure 2.   15-Meter Antenna Structure
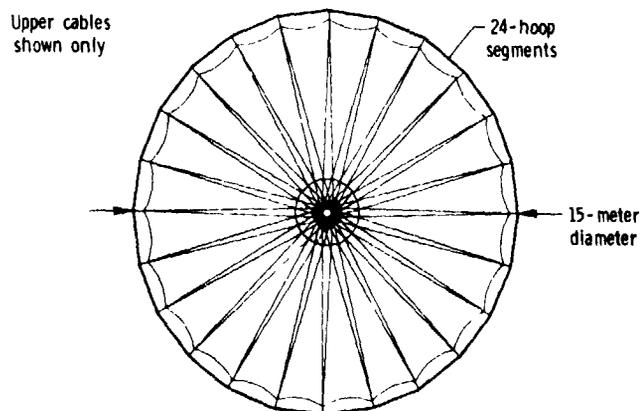
Figure 3.   15-Meter Antenna — Top View
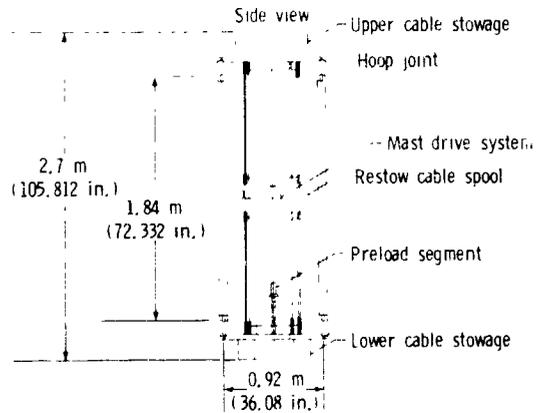
Figure 4. 15 - Meter Antenna — Stowed
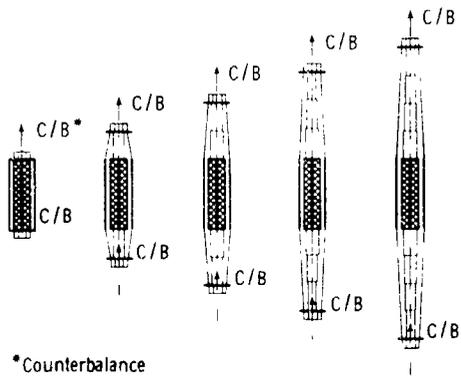
*Counterbalance

Figure 5. Column Deployment
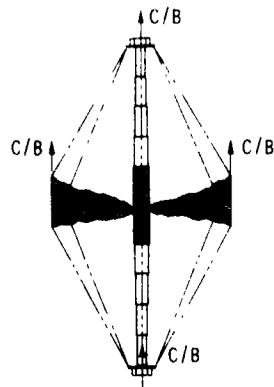
T ~ 8.5 minutes

Figure 6. Partial Hoop Deployment
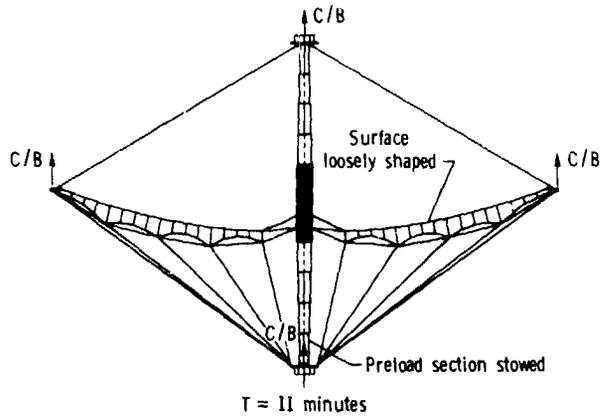
Figure 7. Hoop and Column Deployed
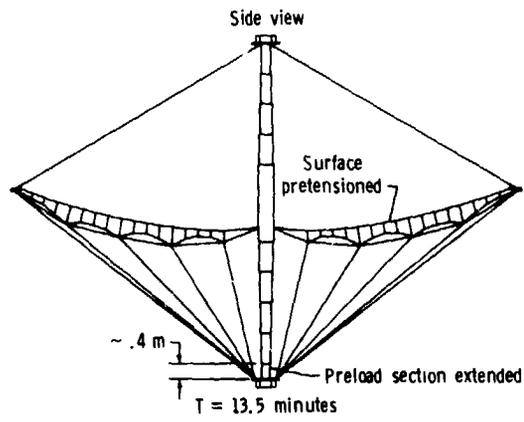
Figure 8. Antenna Fully Deployed
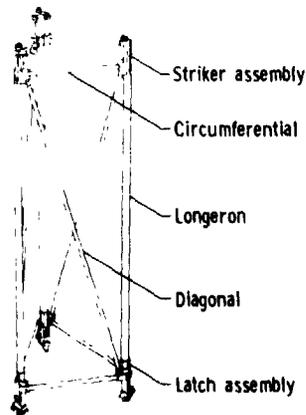
Figure 9. Typical Column Segment

32

1 - Longeron cable
2 - Stow cable
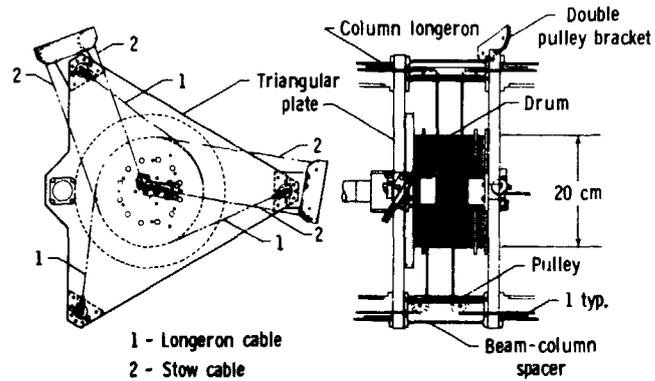
Figure 10. Column Drive System
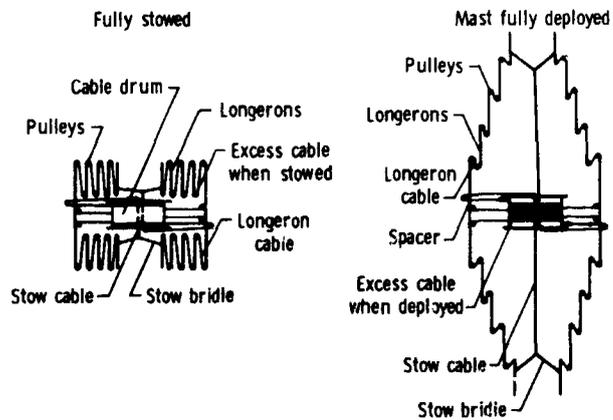
Figure 11. Column Drive System Principle
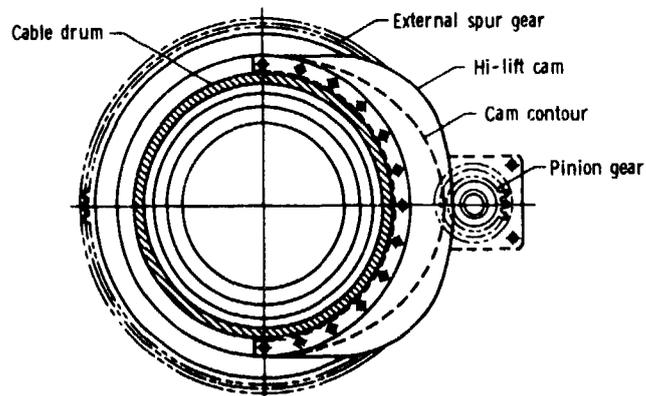
Figure 12. CDS Hi-Lift Cam
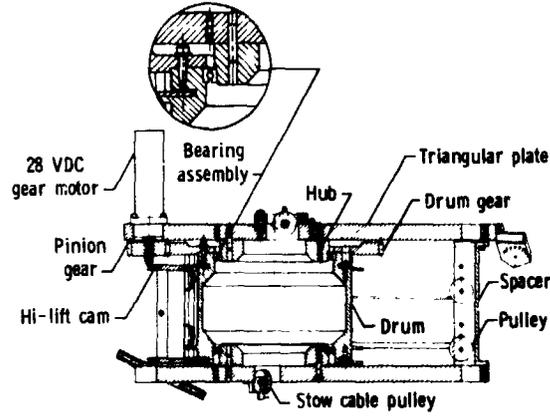
Figure 13. CDS Cross Section
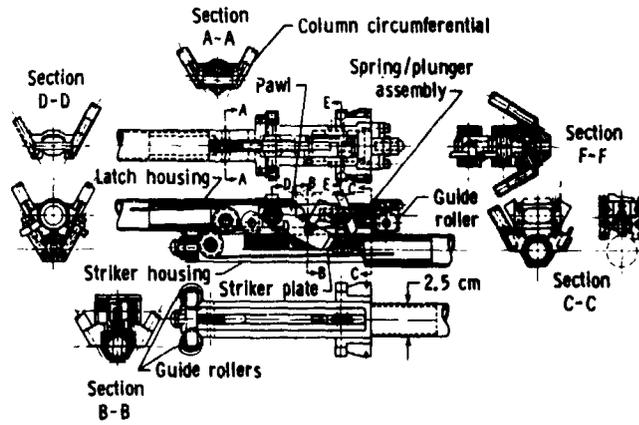
Figure 14. Column Latch Assembly
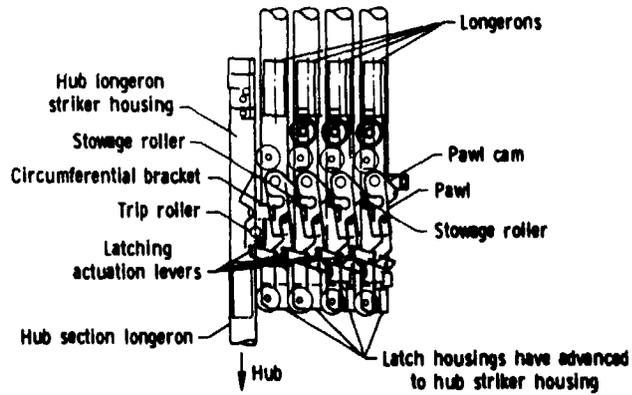
Figure 15. Stowed Column Latches

34
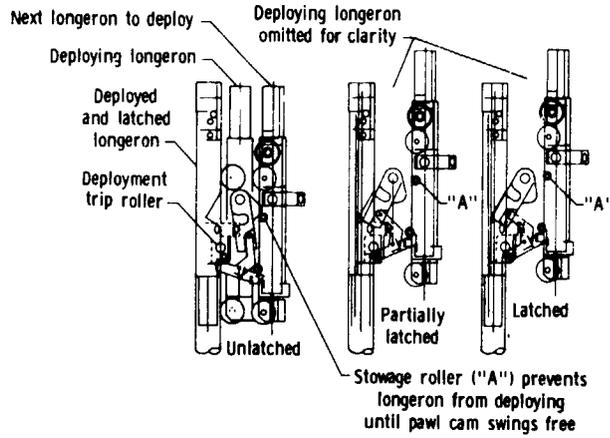
Figure 16. Column Latch Actuation Sequence
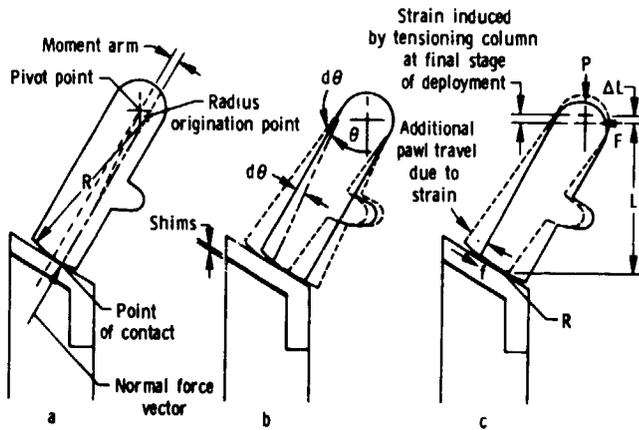
Figure 17. Column Latch Unique Features
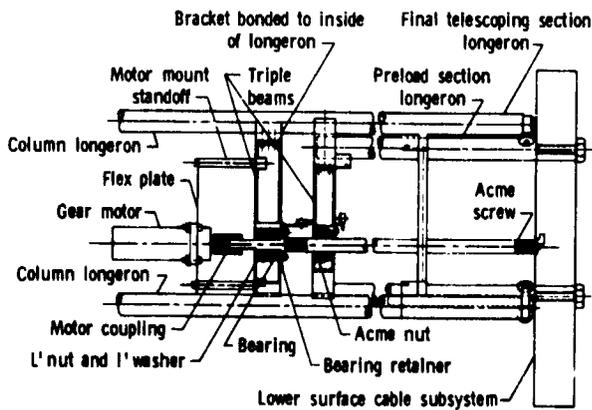
Figure 18. Column Preload Segment

35
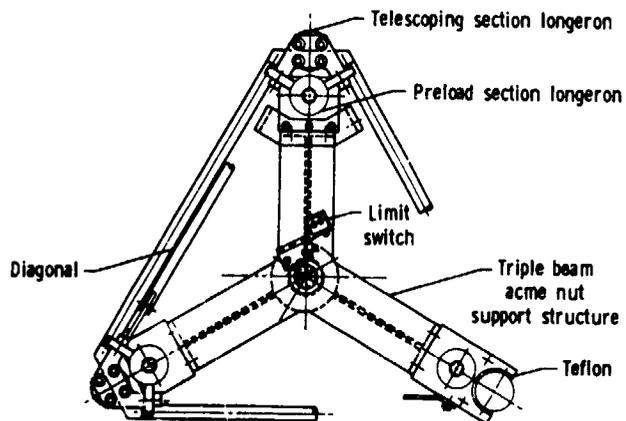
Figure 19. Preload Segment — Top View
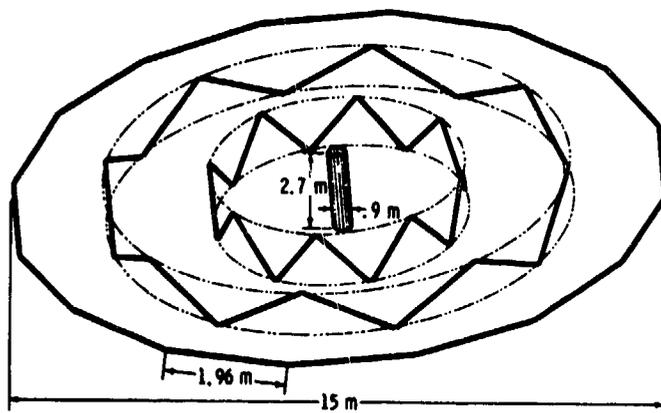
Figure 20. Hoop Deployment Sequence
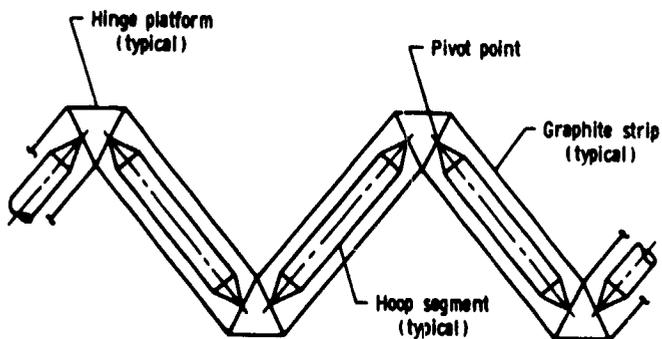
Figure 21. Hoop Synchronization Approach
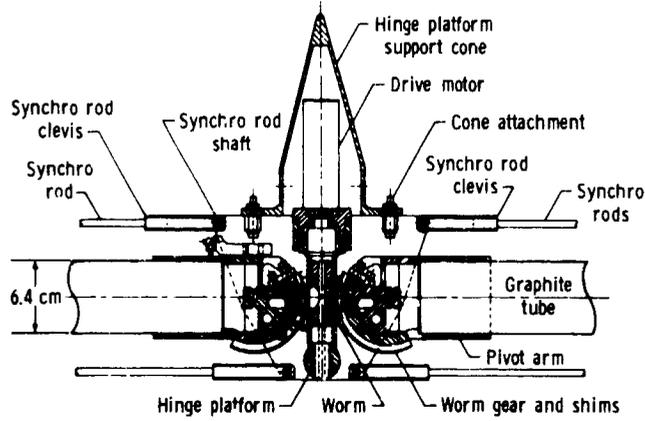
Figure 22. Active Hoop Hinge
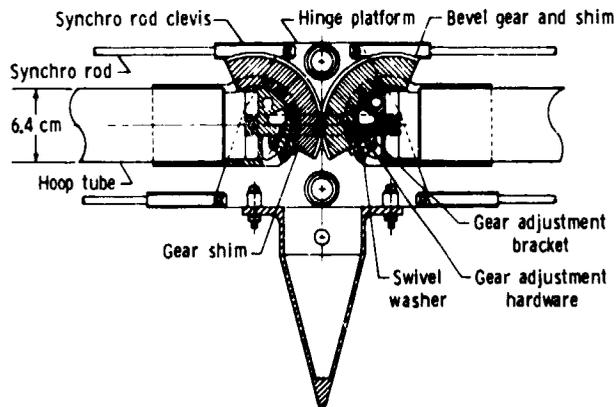
Figure 23. Passive Hoop Hinge
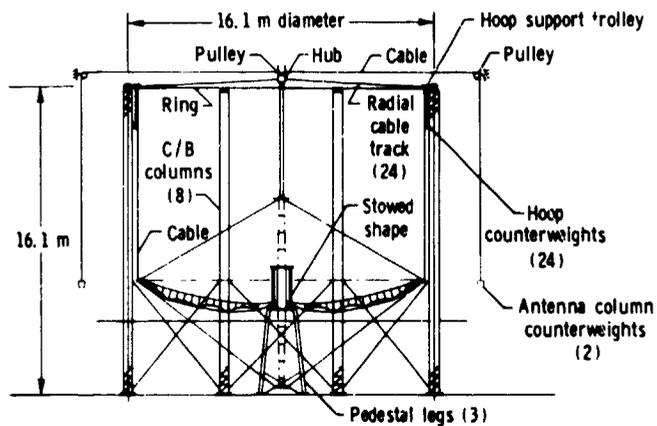
Figure 24. Antenna Counterbalance System

DEVELOPMENT OF AN ENERGY-ABSORBING
PASSENGER SEAT FOR A TRANSPORT AIRCRAFT

Charles P. Eichelberger and Emilio Alfaro-Bou*
Edwin L. Fasanella**

INTRODUCTION

Commercial air transport passenger safety and survivability, in the event of an impact-survivable crash, are subjects receiving increased technical focus/study by the aviation community. One such study was recently initiated by a joint understanding of the Federal Aviation Administration (FAA) and the National Aeronautics and Space Administration (NASA). A B-720 aircraft, highly instrumented, and remotely controlled from the ground by a pilot in a simulated cockpit, was crashed on a specially prepared gravel-covered impact site. The aircraft was impacted under controlled conditions in an air-to-ground gear-up mode, at a nominal speed of 150 knots and 4-1/2° glide slope. The flight test was performed at the NASA Ames Dryden Flight Research Facility at Edwards Air Force Base, California.

Data from a number of on-board, crash-worthiness experiments provided valuable information related to structural loads/failure modes, artimisting kerosene fuel, passenger and attendant restraint systems and energy-absorbing seats. This paper describes the development of an energy-absorbing (EA) seat accomplished through innovative modification of a typical modern-standard, commercial aviation transport, three-passenger seat. Values are given in both S.I. and U.S. Customary units. The EA seat development effort was carried out at the NASA Langley Research Center and tested on the B-720 aircraft used for the FAA/NASA Controlled Impact Demonstration Test.

SEAT SELECTION

The commercial transport passenger seat selected by NASA Langley for modification to an energy-absorbing collapsible seat was a triple passenger seat manufactured by the Fairchild Burns Company, Winston Salem, North Carolina.

The seat (trade name Airest 2000*) was deemed typical of the designs now employed by commercial airlines on modern air transports. The seat's basic structure consists of a rectangular shaped frame fashioned from nominal

---

4.45-cm (1 3/4-in.) outside diameter aluminum tubes. Four forged aluminum legs, bolted to the frame and stabilized by two aluminum diagonal- and base-rail attach members, support the seat and its occupants. Plastics plus lightweight cushions and covers complete the outer appearance. Weighing about 25 kg (55 lb), the seat possesses excellent strength-versus-weight qualities. Figure 1 illustrates a frontal view of the Airest 2000, while Fig. 2 displays the structural features.

DESIGN GOAL

The design goal in the development of an energy-absorbing passenger seat for a transport aircraft was to protect the passengers, simulated by three 75-kg (165 lb) anthropomorphic dummies, against both a vertical and longitudinal velocity change of 6.40 m/sec. (21 ft/sec). Each of the three dummies represents a 50th percentile passenger, defined in reference 1. Figures 3 and 4 present graphic data pertaining to human tolerance acceleration limits for vertical and horizontal motion (reference 2).

SEAT MODIFICATION DESIGN

Several innovative design changes were featured in converting the standard triple passenger seat (Fig. 5) to an EA unit. To limit acceleration the seat was modified (Fig. 6) so that it would rotate forward under high load. To allow seat rotation, split-sleeve-type bearings were affixed to the upper ends of the rear legs and a combination nylon bearing, block-steel yoke unit was installed on the upper ends of the forward legs. All bearings sufficiently encircled the seat frame tubes to allow rotation and yet withstand the impact loads. Conventional aircraft bolts were employed as hingepins to permit pivot rotation of both the forward and rear legs at their lower seat rail attachment. These changes effectively converted the standard seat to a four-bar linkage system. The original flexible membrane seat pan was replaced with a 0.079-mm (1/32-in.) thick aluminum sheet. Both forward and rear legs were inclined parallel to each other at an angle approximately 65° with the horizontal. Two graphite-epoxy, energy-absorbing tubes, installed diagonally between the forward and rear seat legs (Fig. 6), replaced in the original diagonal members to stabilize the seat under normal flight conditions. The tubes progressively crush as axial columns during the aircraft impact. Figure 5 displays a graphic cross section of the unaltered standard seat. Figure 6 depicts the same cross section of the modified seat for comparison. The energy-absorbing, graphite/epoxy tubes, associated tube attachment hardware, and overall seat dimensions are shown. Note that the passenger seat pan height above the aircraft floor level and body posture angle are the same in both standard and modified designs. Figure 7 graphically traces the kinematic stroke of the seat during the energy-absorbing process. The stroke is limited by hardware constraints to a maximum distance of about 16.5 cm (6.5 in.).

ENERGY-ABSORBING TUBE DESIGN

Various design characteristics were considered when selecting the energy-absorber device. The energy absorber should be lightweight, small, and as simple as possible to be cost effective. It should possess long-term

reliability, require minimum maintenance, and be corrosive/environmental resistant, and unaffected by vibration. Most importantly, the device must decelerate the passengers while not exceeding the load limits of human tolerance.

Graphite epoxy crushable tubes were chosen to meet the requirements for the energy-absorbing process. Since the energy absorption is a function of the materials (fiber and matrix) and ply orientation, the tubes could be readily tailored to absorb the dummies' kinetic energy. A series of developmental tests plus the knowledge gained from a recent study (reference 3) resulted in the selection of 10- and 12-ply graphite-epoxy tubes 21.08 cm (8.30 in.) in length to balance the uneven seat weight distribution caused by lack of symmetry between the seat legs and the occupant seating positions. The tubes were fabricated from the prepreg material of Thornel 300 graphite fibers and Narmco 5208 matrix composed of an MY720 epoxide base. Each ply had a nominal 0.0140-cm (0.0055-in.) thickness and a ply orientation of $\pm 60°$. Data from investigations (refernce 3) indicated changes in energy-absorbing values from 90° to 45° ply orientation; thus, 60° was selected for size and strength considerations. A taper and circular notches (Fig. 8) were machined on one end of the tubes to reduce an initial high load spike without affecting the sustained crushing load.

During the development phase of the composite tubes, static and dynamic tests were conducted to determine the crush load-displacement characteristics and the deceleration-time response of the tube. The static tests were conducted on a 533,786-N (120,000-lb) capacity compression-testing machine. During the static tests, a cap was placed on the tapered end of the tube and a plug was inserted in the flat end to simulate the effect of the cap and plug used in th seat mechanism that holds the tube in place. The crush force-displacement curve for a 6-ply composite tube is shown in Fig. 9. Figures 10 and 11 display the static tests results for the 10- and 12-ply tubes used in the seat. Although the proper initial force level was achieved, the 12-ply tube crushing load was found to increase at a high rate after 4 in. of crush (Fig. 11) because the crushed material filled the remaining volume of the tube. A larger-diameter tube with less plies would have been more desirable but would have required making new end caps.

The dynamic tests on the tube were performed on a drop-tower impact-test machine. A weighted head of approximately 77 kg (170 lb), guided by two rails, was dropped vertically on the tube. Deceleration of the head was measured using accelerometers and was recorded on a strip-chart recorder. A typical deceleration-time curve for a 6-ply-tube dynamic test is displayed in Fig. 12. Head-impact velocity was 4.52 m/sec (14.83 ft/sec), resulting from a drop height of 1.04 m (3.42 ft). Pulse time was about 70 ms. Deceleration ranged between 6 and 12 g. Compacted crushed material, filling the remaining volume of the tube during the tube-crushing energy-absorbing process, accounted for the deceleration g buildup. About 21-cm (6.4-in.) length of tube crushed in absorbing the head's kinetic energy.

STATIC AND DYNAMIC SEAT TESTS

Static Seat Test

With the graphite-epoxy tubes in place on the assembled seat, a problem arose during static loading tests conducted to determine maximum stroke distance. A local bending condition at the ends of the graphite-epoxy tubes prevented uniform axial crushing and resulted in tube failure. The problem was solved by the installation of an axial aligning pivot cap and plug attachment at each end of the tube. As the seat stroked downward and forward, the pivot attachment mechanisms caused the tubes to crush uniformly in an axial compressive mode.

The utilization of this mechanism has several possibilities. The energy-absorbing device aligns only in one direction, since the seat had a misalignment problem in only one plane of rotation. A ball joint could be used for multidirection misalignment if necessary. It should provide a useful tool to other designers working with compressively loaded energy absorbers that require the dual characteristics of movable joints and fixed axial alignment conditions. This application is ideal for composite tubes which crush in a brittle mode and are thus difficult to control.

In actual use, the seat is unevenly loaded because of lack of symmetry between the seat legs location and the occupant seating positions. The outboard legs sustain twice the load of the inboard legs because of the offset. However, this effect was nullified during static seat test by locating the hydraulic ram symmetrically between the seat legs. For this symmetrically loaded seat, both composite tubes were 6 ply. Four static tests were performed to check the operation of the seat mechanism. The applied vertical load (hydraulic ram), and the vertical (Z) and horizontal (X) floor reaction forces for a typical test are shown in Fig. 13.

Dynamic Seat Tests

The assembled seat, with installed 10- and 12-ply EA tubes, was dynamically tested at the Langley Research Center's Dynamic Impact Test Facility. A series of dynamic drop tests were conducted to simulate the vertical and forward expected shock pulse characteristics. The drop tests were accomplished by mounting the seat at a 45° tilt angle to the horizontal flat surface of a steel carriage. The carriage structure basically consisted of two horizontally positioned, built-up beam units, connected by steel plate members. The carriage, with the 45° tilted seat containing the three anthropomorphic dummies, was then raised and dropped vertically. Impact pulse was controlled by permitting the falling carriage to strike and deform a series of steel bars at ground level. The dummies were restrained by lap belts and were positioned leaning forward with their head between their legs in a crash preparation body posture. Data acquisition consisted of accelerometers, load cells extensiometers, and high-speed motion picture cameras. This method of dynamic impact testing was based on knowledge and techniques established by many previous experiments performed at the Langley Research Center (see reference 4). Figure 14 illustrates an actual stroked

seat which resulted from these shock tests. About 12.7 cm (5 in.) of each composite tube crushed from the 4.27-m (14-ft) drop height, in absorbing the dummy passenger kinetic energy. Carriage input pulse plotted with the resulting pulse on the seat pan is shown in Fig. 15. Acceleration levels remained within the range of human tolerance levels (see Fig. 1 and 2). Data analysis of the seat from the Boeing 720 crash had not been completed at the time this paper was prepared.

CONCLUSIONS

This investigation applies the concept of an energy-absorbing, axial, tube-crushing unit to commerical aviation passenger transport seats. The investigative effort was limited by the primary schedule of the Controlled Impact Demonstration Project which prevented optimizing the energy absorbers. For optimum seat performance, further development of the energy absorbers is recommended.

Such parameters as belt restraints, varying passenger seat weight loads and their distribution, seat rebound, and economic aspects must be examined.

Preliminary results from the work conducted so far are encouraging. The desired objective of demonstrating the concept/feasibility of converting a standard commercial passenger seat to a axial, tube-crushing, energy-absorbing unit as an additional crash safety feature has been attained.

REFERENCES

1. U.S. Code of Federal Regulations, Title 49, Chapter 5, Part 572: Anthropomorphic Test Dummy. U.S. Government Printing Office, Washington, D.C., (Rev.) 1978.

2. Eiband, A. M.; Human Tolerance to Rapidly Applied Accelerations: NASA Memorandum 5-19-59E, June 1959. Data curves as published in Aircraft Crash Survival Design Guide, Volume II, USARTL-TR-79-22B, January 1980.

3. Farley, Gary L.: Energy Absorption of Composite Materials. NASA TM-84638, March 1983. Also, Journal of Composite Materials, vol. 17, May 1983, pp. 267-279.

4. Alfaro-Bou, Emilio; Williams, M.S.; and Fasanella, E. L.: Determination of Crash Test Pulses and Their Application to Aircraft Seat Analysis: SAE Paper 81061, Business Aircraft eeting and Exposition (Wichita, Kansas), April 7-10, 1981.
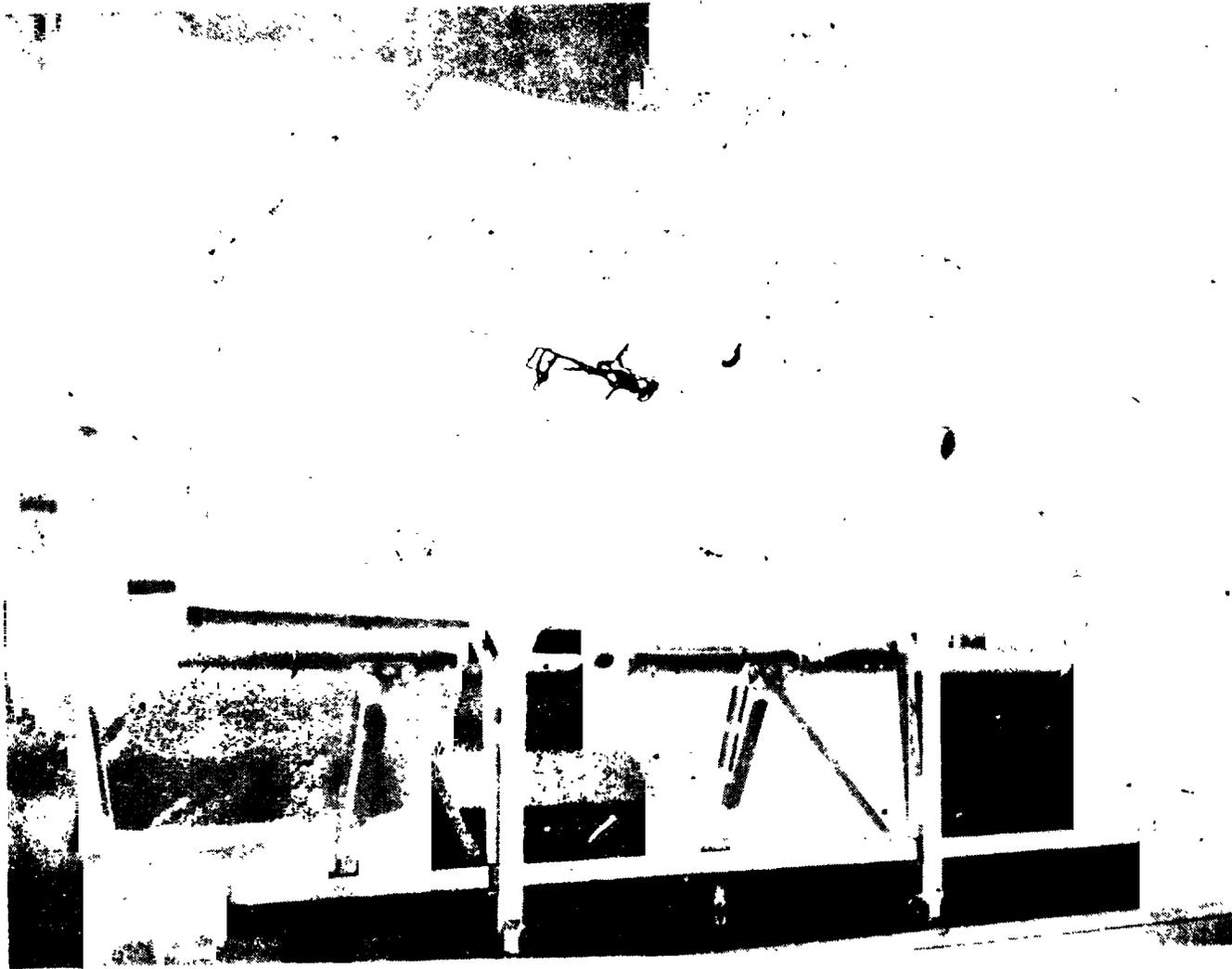
Figure 1. - Airest 2000 Triple Seat

44
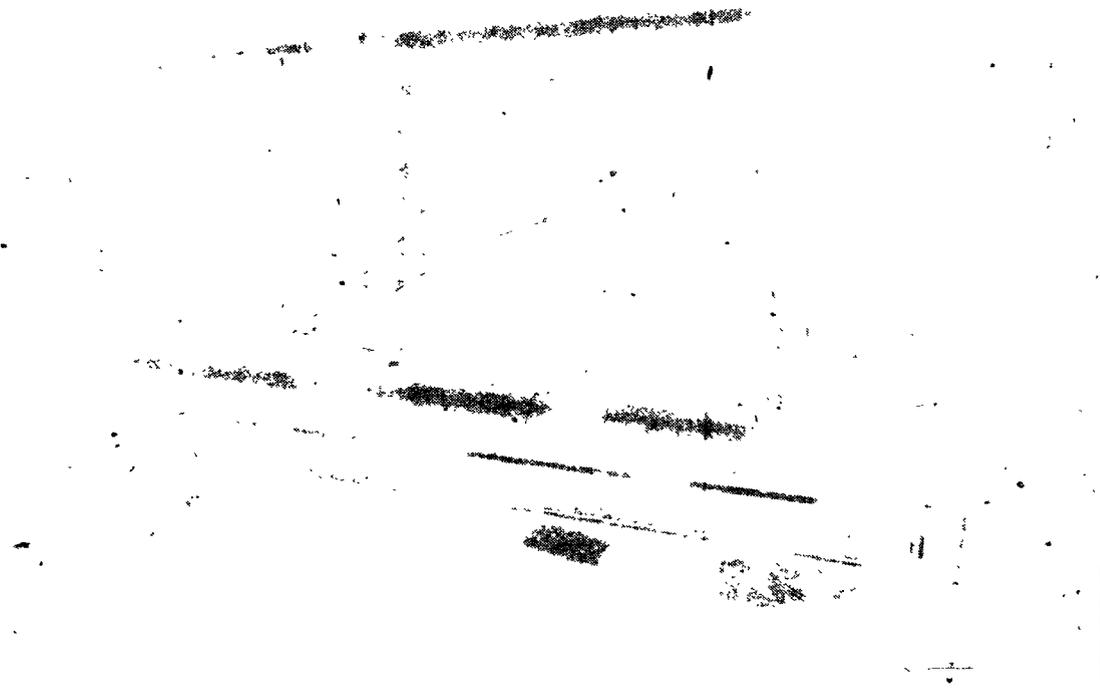
Figure 2. - Airest Seat - Structure View
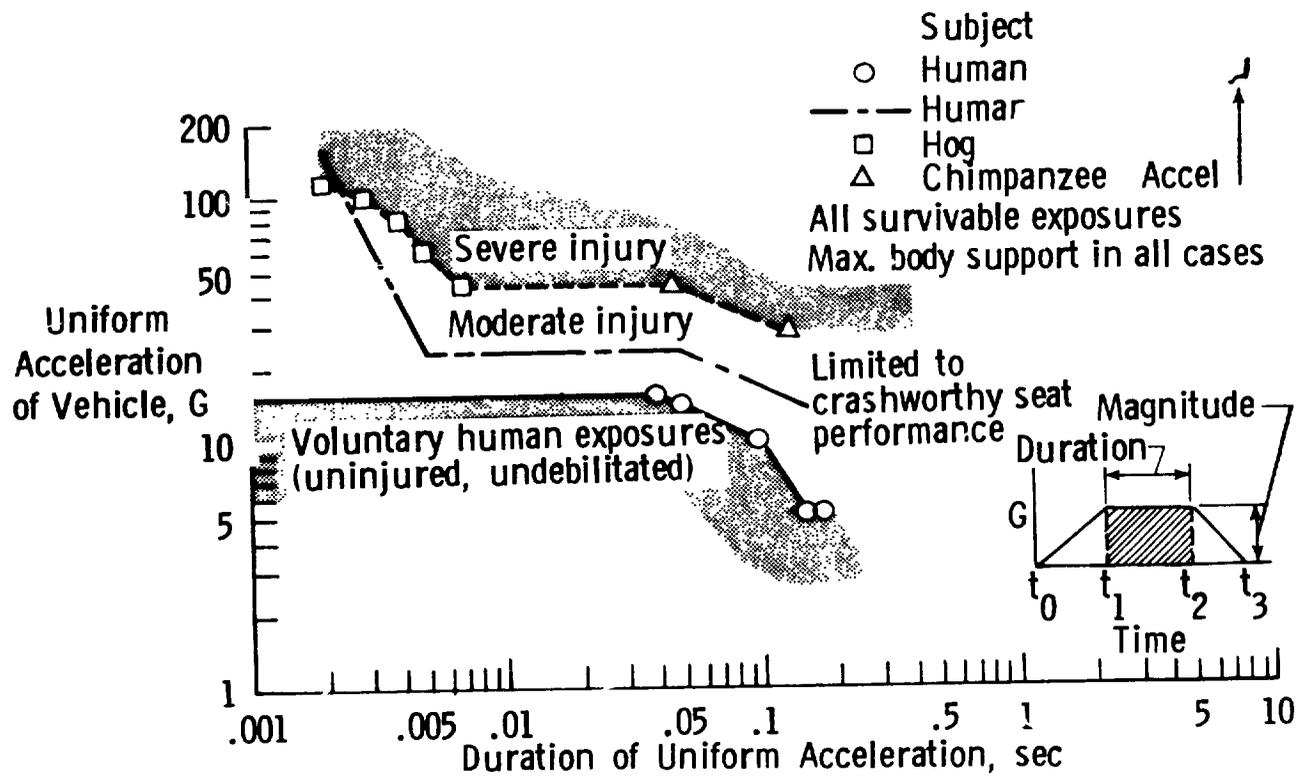
Figure 3. - Duration and Magnitud of Headward Acceleration Endured by
Various Subjects. (Frc Reference 2)

Figure 4. - Duration and Magnitude of Spineward Acceleration Endured by
Various Subjects. (From Reference 2)

31.75 (12.50)

31.45
(12.38)

≈65°

31.45cm
(12.38)

TRACK

45.44 (17.89)
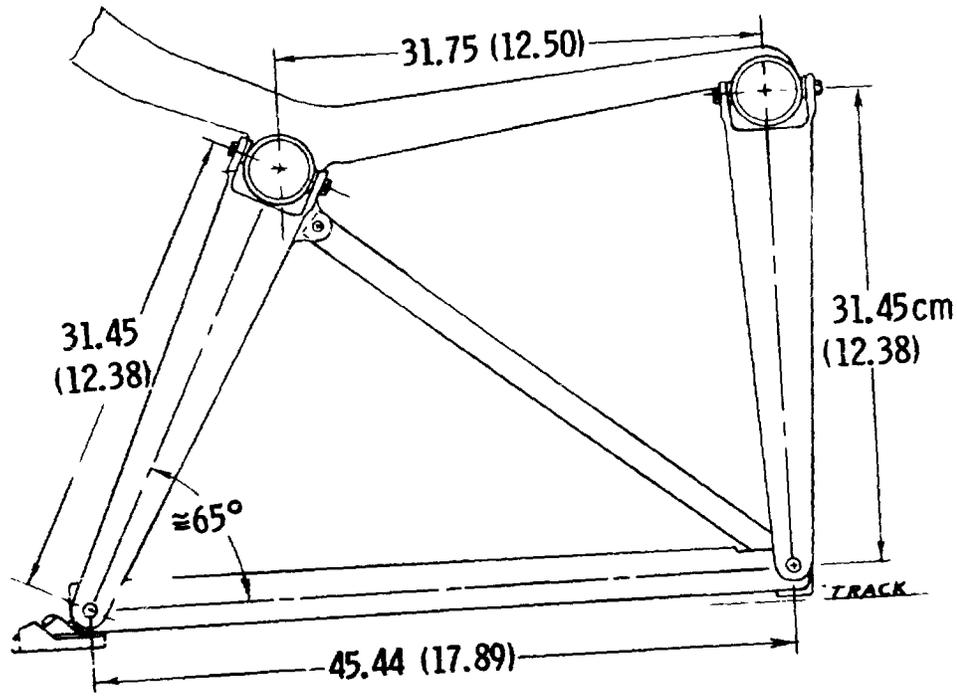
Figure 5. - Airest Seat Cross Section
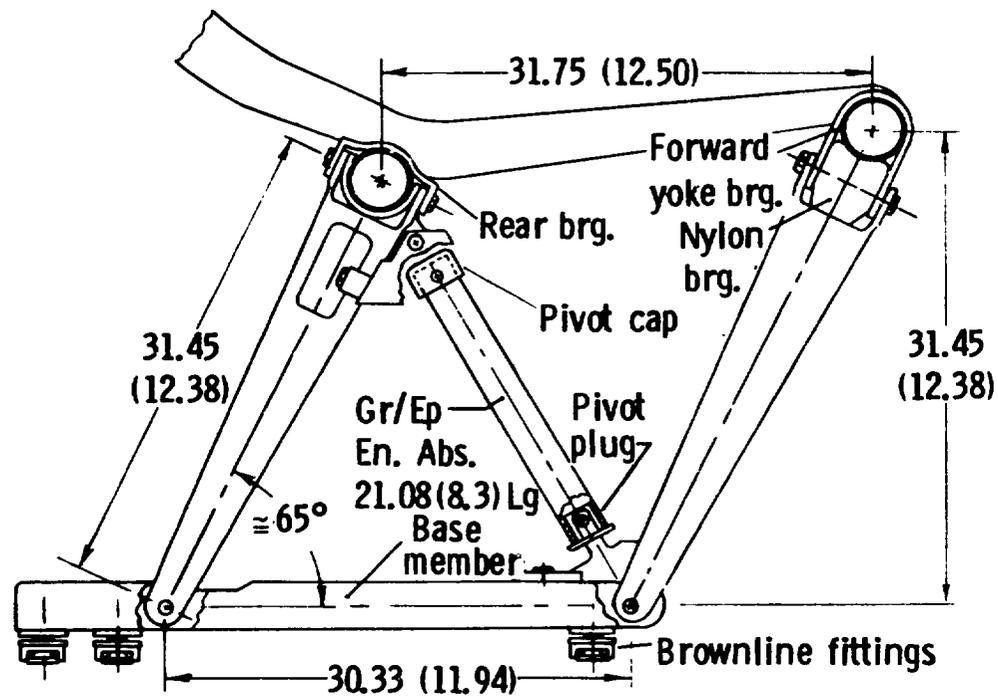
Figure 6. - Modified Seat Cross Section

0cm(in.)
2.54cm(1.0in.)

15.24cm
(6.0in.)

Figure 7. - Seat Kinematic Stroke
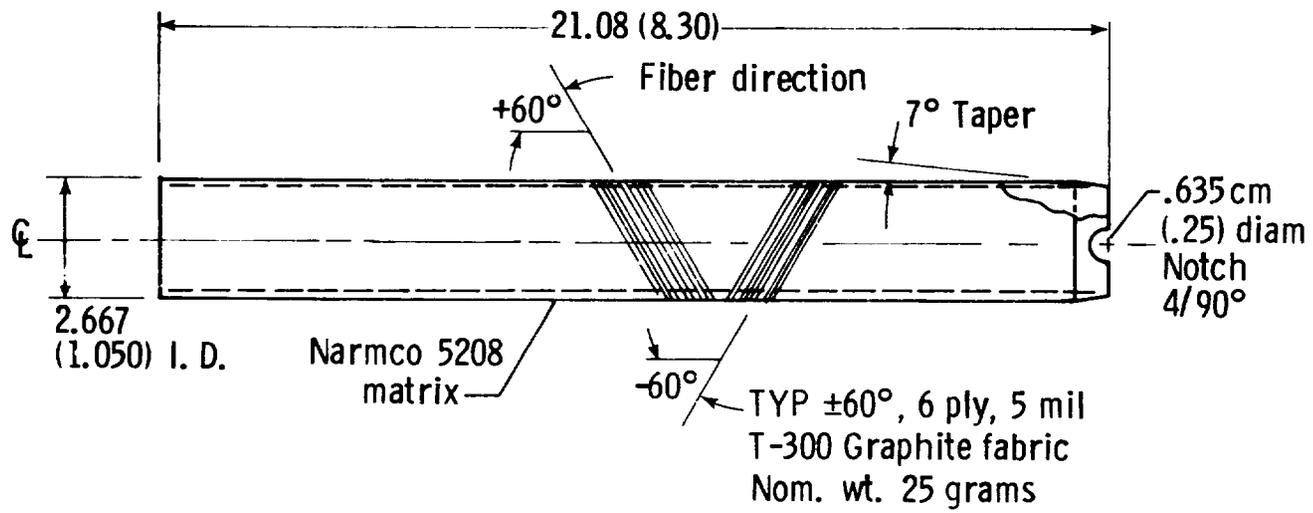
Figure 8. - Typical Energy Absorbing Tube
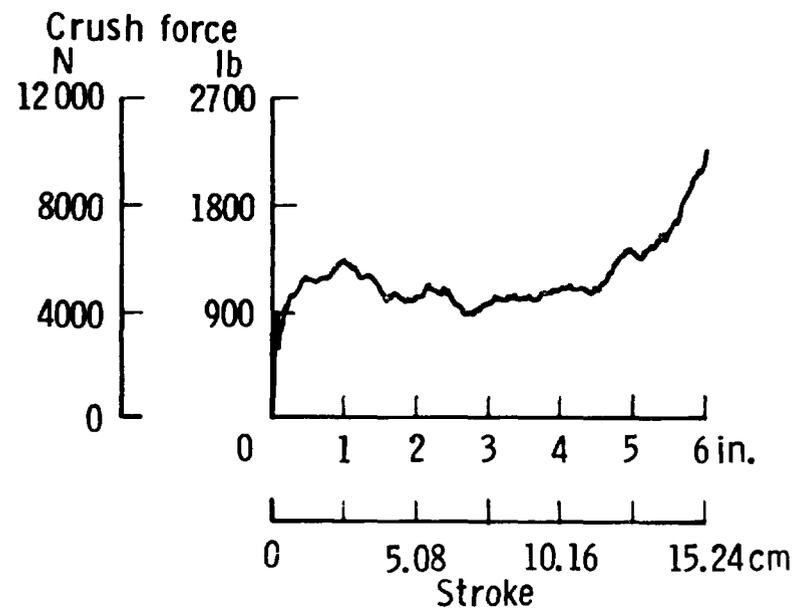
Figure 9. - Static Crush Force VS Displacement, 6 Ply Tube
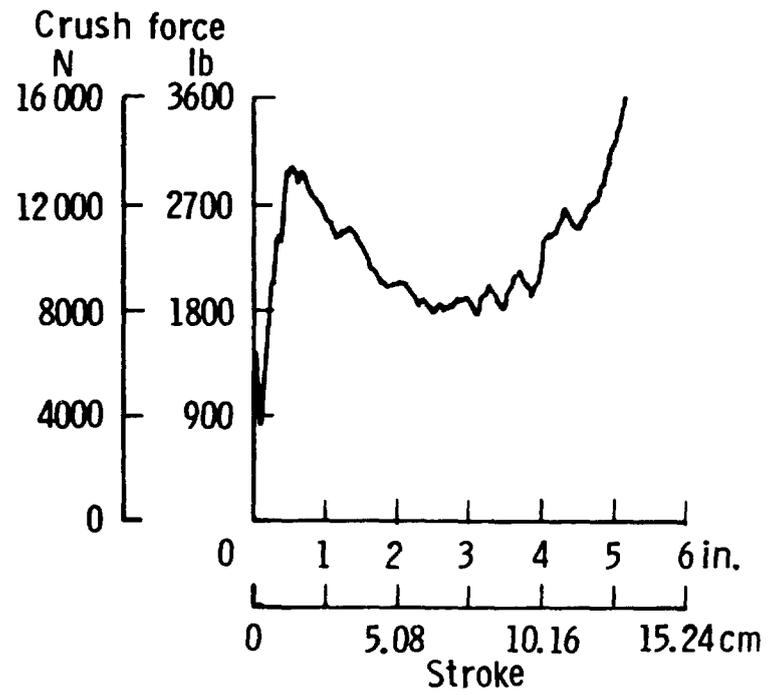
Figure 10. - Static Crush Force VS Displacement, Seat 10 Ply Tube
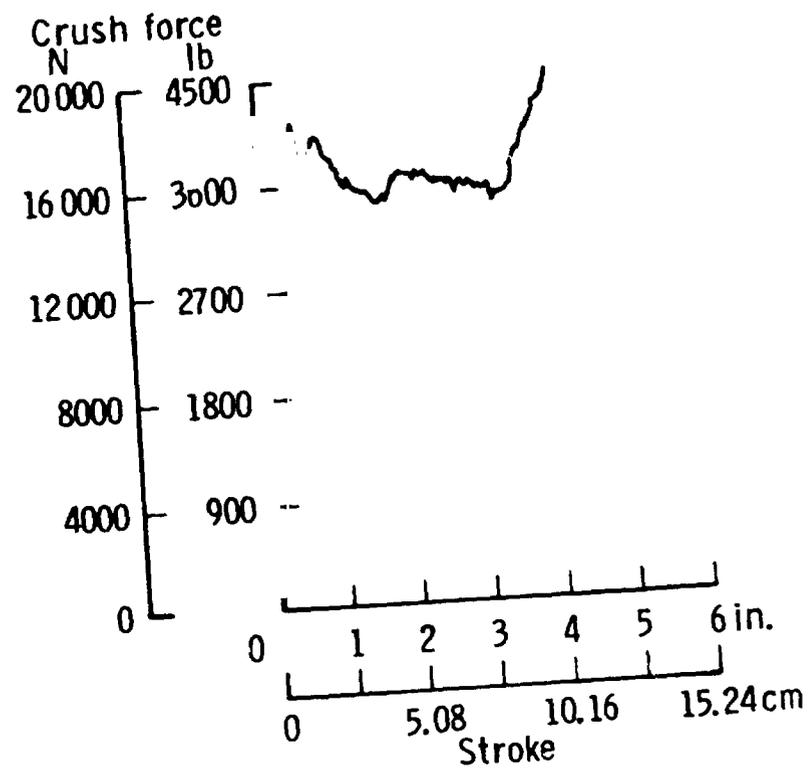
Figure 11. - Static Crush Force VS Displacement, Seat 12 Ply Tube
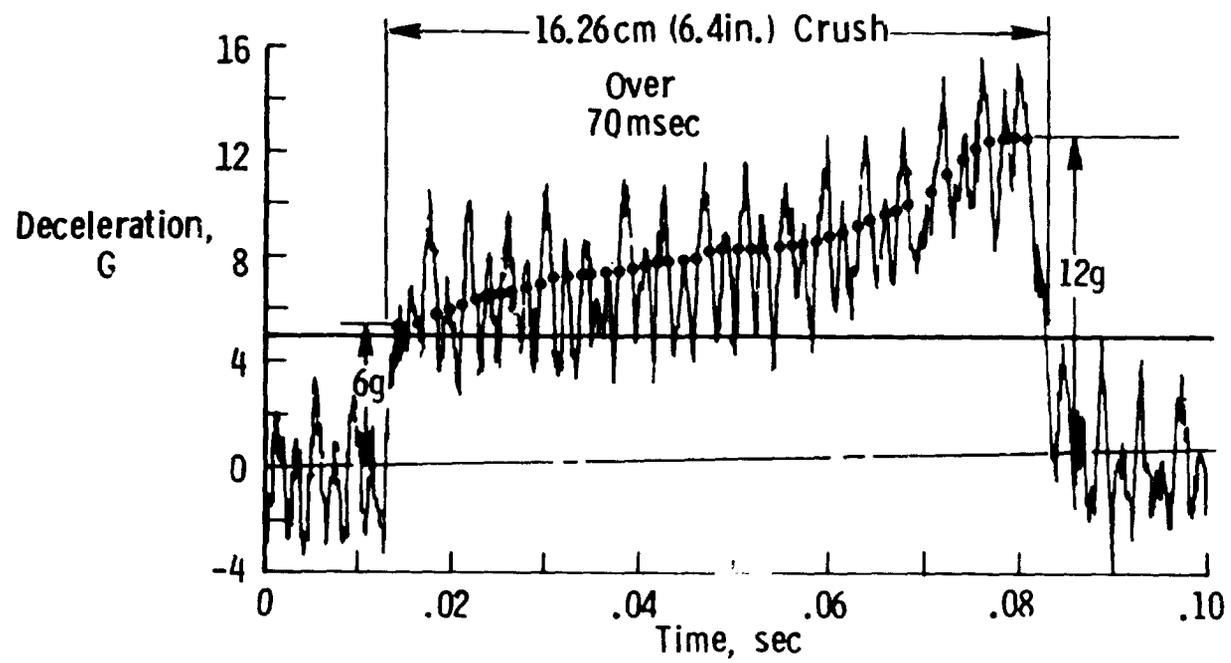
Figure 12. - Typical EA Deceleration Time Curve, 6 Ply Tube
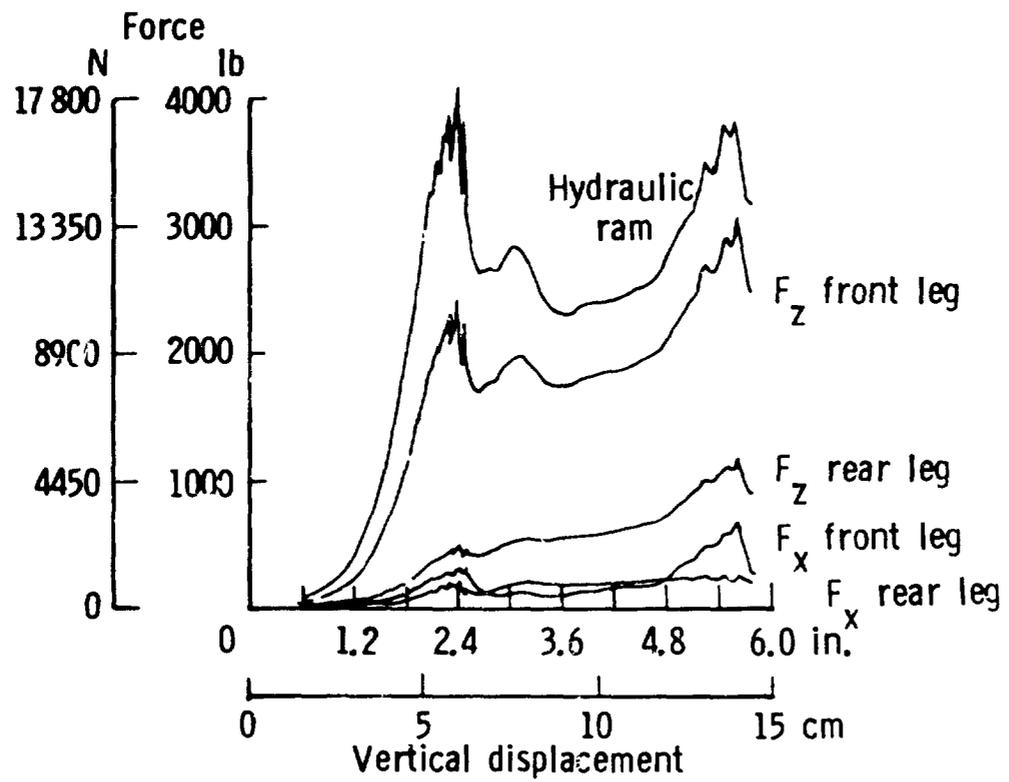
Figure 13. - Static Seat Test, Force VS Vertical Displacement
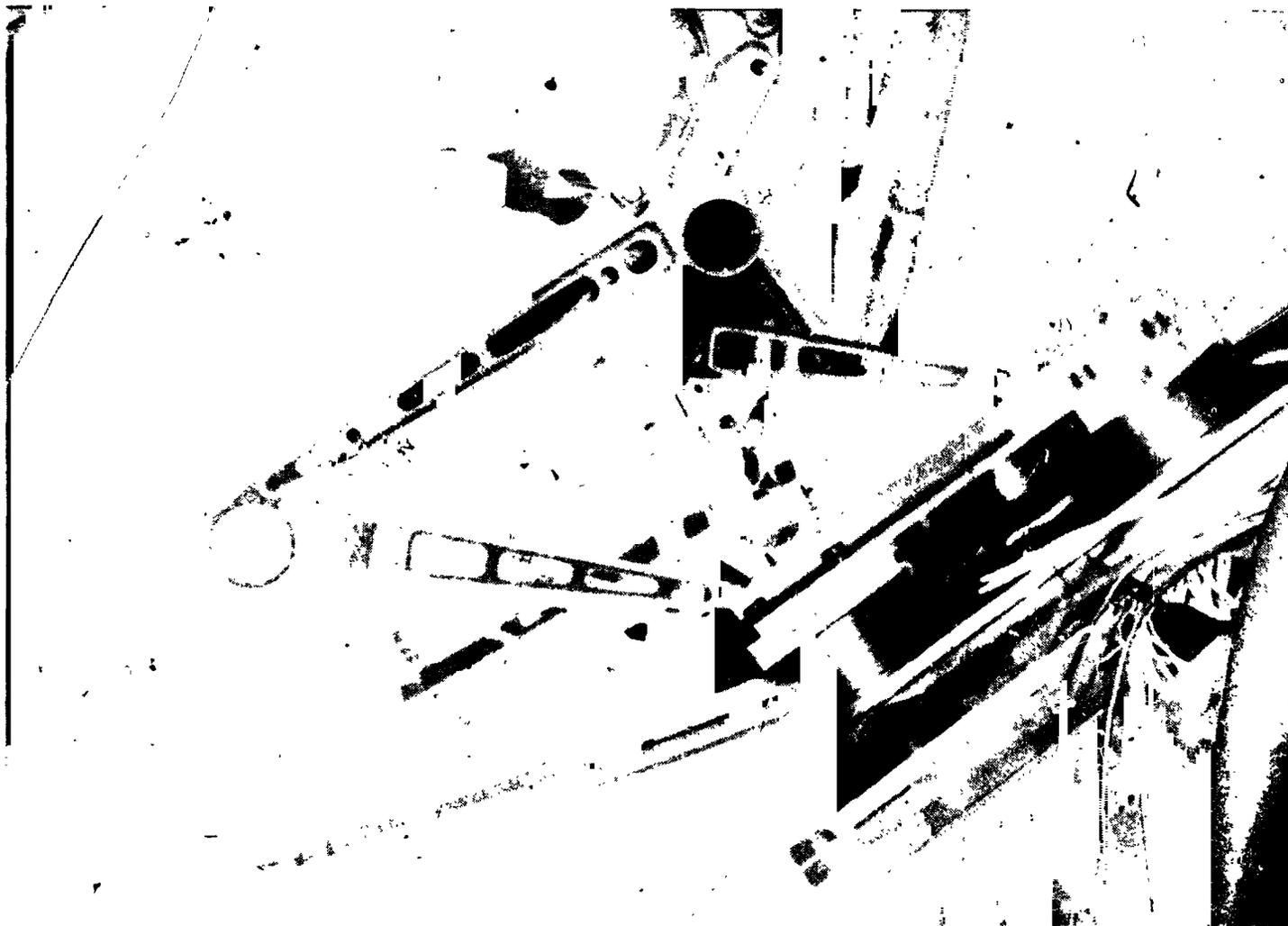
Figure 14. - Dynamic Impact Test - Stroked Seat
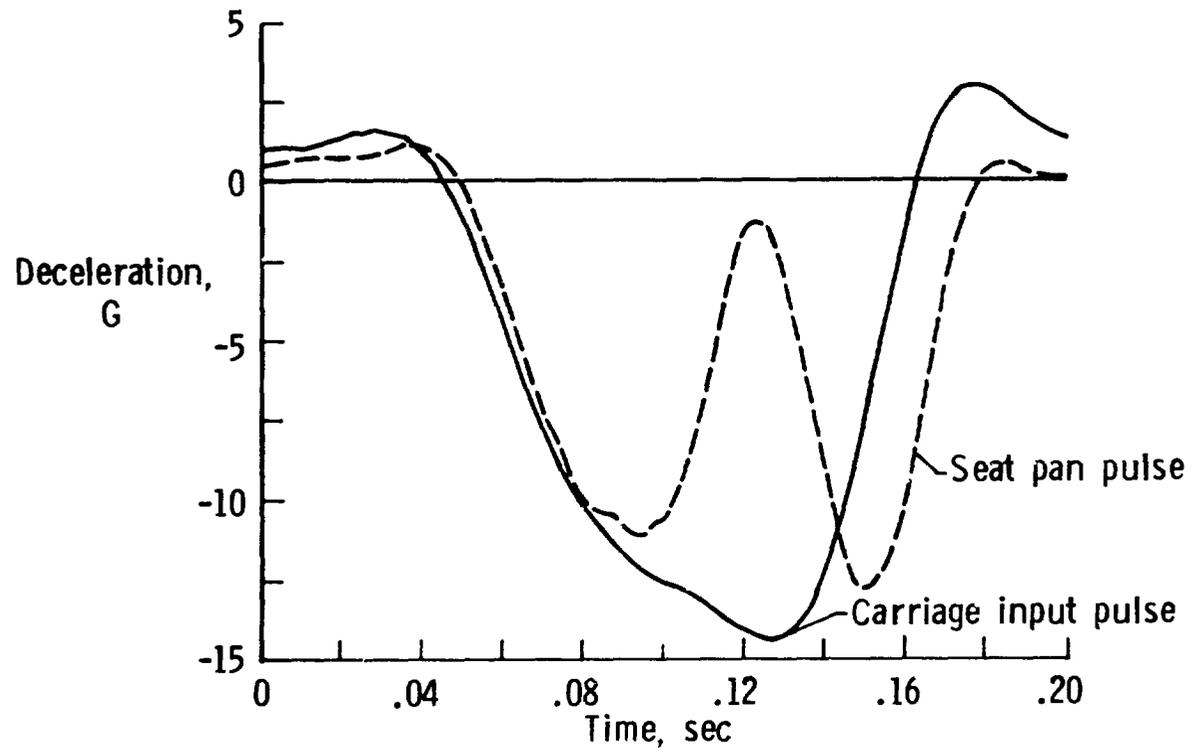
Figure 15. - Dynamic Impact Seat Test, Carriage and Seat Pan Pulse Levels

A MODULAR DOCKING MECHANISM
FOR
IN-ORBIT ASSEMBLY AND SPACECRAFT SERVICING

By: Dipl.-Ing. F. Campe*,
     Dipl.-Ing. K. Priesett*, and Dr. R. H. Bentall+

INTRODUCTION

As space operations become accepted as "normal" business enterprises, two requirements tend to dominate any future technological developments:

   o   systems are required to be reliable over a long period of time, either by their inherent reliability, or by means of scheduled maintenance.

and

   o   future space technology developments need to be cost-effective to warrant their incorporation.

Rendezvous and Docking (RVD) technology, being a prerequisite for advanced space operations, is a typical example of this technology development. Since the RVD process is not only mission critical but also contains the risk of damage to the in-situ space investment, its technology has to be highly reliable. But it must also sat. °y the other criterion, of being available at reasonable cost, so that the l ts of in-orbit assembly and sc vicing can be realized.

The above requirements are passed on to the subsystems comprising the RVD system. This paper is about one of them, the Docking Mechanism Subsystem (DMS) developed during an ESA sponsored contract.

DOCKING MECHANISM CONCEPTS

The various docking mechanism concepts which have flown (e.g., Gemini, Apollo, Soyus/Saljut) were of the "impulse", or "impact", type where the kinetic energy of the active chaser spacecraft was used to trigger, or actuate, the docking mechanism. This was possible because the spacecraft involved were (more or less) rigid and rugged bodies and because their centres of gravity were aligned.

* Dornier System, Friedrichshafen, West Germany
+ ESA, ESTEC, Noordwijk, The Netherlands

For future space missions, however, such as large, flexible, and locally fragile platforms, it is very desirable to adopt non-impact docking techniques to avoid the risk of damage, and to make use of self-actuated, and re-usable, docking mechanisms.

Non-impact docking systems can be sub-divided into two categories where, following the close rendezvous of the two satellites, they are brought together into intimate contact either by means of the Docking Mechanism via an extended probe, or by active control of the AOCS of one of the spacecraft. This bringing together is known as "Closure", and the two means of achieving it are referred to in the following as "DMS controlled closure" (DMS-CC) and "AOCS controlled closure" (AOCS-CC). These two closure techniques differ in the operations which are needed, and in the make-up of their constituent components. Table 1 gives an overview of the operations associated with each category. Figure 1 illustrates the two different docking mechanisms implied.

It is clear that, in principle, AOCS controlled closure can result in a simpler mechanism, in that the boom is not needed, nor are the necessarily complex grapple and actuator mechanisms. However, this is at the expense of a greater demand on the AOCS and the need for short range docking sensors. A very major advantage accrues, however: that is the possibility of using a very simple structural docking interface which is compatible with adoption as a "standard" interface.

REQUIREMENTS

The general requirements for the DMS are based on typical European scenarios for automated RVD missions, where the spacecraft are unmanned and 3-axis-stabilized. These missions require a high flexibility and modularity in the DMS concept. Further, to protect the higher investment in orbit it is desirable to ensure that only passive parts of the DMS are located on the more "permanent" spacecraft.

Safety requirements become, in fact, design drivers, and Table 2 gives typical requirements with which the DMS must comply. Latch performance requirements derived to contain a number of alternative missions are given in Table 3, and the range of satellite parameters is given in Table 4. Finally the DMS is required to support certain operational strategies; these are shown in Table 5.

Notable among these requirements is the requirement that, regardless of the failure, it should be possible to separate the two spacecraft in order not to prejudice a further attempt at RVD. The DMS therefore not only needs to be reversible, it must have back-up systems which ensure complete release.

DOCKING MECHANISM DESIGN

THE LATCH

If the technique of AOCS controlled closure is adopted, the mechanical components needed in the DMS are reduced to latches and connectors and their (passive) interfaces. The design task, for latching, assumes a close maneuver of the Chaser Spacecraft up to the target, to within about 60 mm in the longitudinal axis and about ±40 mm in the lateral axis. The role of the AOCS may thereafter be passive, or it may assist in the docking process.

Although the end result is very simple, considerable thought was given to different latch interfaces. Various forms of interface can be envisaged, which lend themselves to passive guidance at the time of final closure. However, as the geometry of the interface is made more complex, so too are the artificially induced requirements on the latch itself, and the design freedom of the latch designer is inhibited.

The latch interface chosen, termed the "cruciform concept", is shown in Figure 2. The structural interface itself is a round bar, radially stiff, but with some axial compliance and with rotational freedom.

The latch is required to perform three fundamental functions:

o   Capture and alignment of the Handle
o   Absorption and partial storage of residual (small) kinetic energy
o   Provision of structural joint (Table 2)

Elements of the chosen latch design are given as an exploded view in Figure 3, and the method by which it operates is outlined in Figure 4. Should at any time the latch jam, a pyrotechnic device collapses the linkage, enabling the clamp to retract under action of a spring. The structural joint can, however, be maintained by two of the remaining three latches. (The cruciform concept is tolerant to failure of two out of the four latches.)

The selected linkage for the latch is shown in Figure 5. Here points C, D and G are fixed points. Link No. 1 (D-A) represents the crank and α_1 the input crank angle. Link No. 3 (B-E) represents the pretension spring. Link No. 5 (F-G) represents the claw, with α_5 the output claw angle.

61

Based on this layout, with the following dimensions, Figures 6 to 8 give the latch performance parameters, based on the following dimensions:

D-A = 31.50 mm	1 START = 130°
A-B = 32.48 mm	1 END = 76.9°
C-E = 82.10 mm	5 START = 186°
F-G = 30.00 mm	5 END = 60°

LATCH DESIGN TESTING

In order to gain some insight into the latch performance, testing has been performed on a single latch, and Figure 9 shows the test setup used. Two massive blocks (160 kg each) onto which the handle and latch assemblies were mounted, were supported on air bearings and made to approach each other at varying rates and alignments, simulating a constant AOCS thrust. Interactive forces were measured using a piezoelectric transducer mounted between the latch and the base. Figure 10a shows a typical behaviour during such a test with an initial lateral misalignment of 60 mm. Several bounces against the reception element are shown prior to claw engagement. Figure 10b shows a capture with the same approach velocity (15 mm/sec), but with no misalignment.

The results of the testing confirmed in general the performance of the latch, and gave valuable guidance to the modelling of the latch for RVD simulation purposes. Testing also indicated that some detailed improvements were necessary in the configuration of the spring energy absorber – for example, the addition of a damper. This damper could either be a conventional passive damper (velocity proportional), or an active damper where the interactive forces are measured and the claw is controlled appropriately.

THE CONNECTOR MECHANISM

It soon became apparent that the requirement for achieving electrical and fluid connection within the DMS could become a design driver on the latches, not just with the precision of latching required, but also with the forces which the latches should withstand. The forces required to mate and de-mate connectors, particularly for the fluid connectors, were relatively high, and in order to maintain modularity of design, keeping the latch development independent of connector development, it was decided to provide a self-powered, self-reacting mechanism to achieve connection. This mechanism is still undergoing development, and will not be reported here. However Table 6 shows typical connector mechanism requirements.

STANDARD DOCKING INTERFACE

With a growing number of satellites in orbit, and a growing capability of direct intervention by means of vehicles designed to dock with them, it is particularly interesting to develop usable and commercially viable standard docking interfaces.

The latch design described has certainly some attributes to its credit, but it is not the only latch design that can be found which interfaces with the simple handle. Indeed this latch has co-existed with a latch of totally different concept which is also being considered as an alternative design. This possibility arises from the classic simplicity of the handle. The handle is light (0.4 kg) and the design freedom offered to the latch means that it is not therefore necessary to purchase the latch always from the same supplier.

The handle may be in a number of alternative configurations, e.g., 3 instead of 4, and located at different diameters without invalidating the essential of the standard, or the principles of operation of the DMS. Four such "handles" were chosen as the interface for the design presented in this paper, over the more conventional alternative of a 3-handle configuration for kinematic reasons because of the added security against failure during latching. In addition, aided by the inherent self-centering capability of the latch/handle combination, the concept is also suitable for the so-called androgenous DMS, where active parts are placed on both sides of the interface to allow initiation of separation by either satellite. In this configuration the location of the latches is alternated between the spacecraft, i.e., latches 1 and 3 on spacecraft 1 and latches 2 and 4 on spacecraft 2 (see fig. 11). However in this concept the release security is compromised if the command link fails.

CONCLUSION

A Docking Mechanism concept has been described which is suitable for use with autonomous docking systems. The central feature of using simple cylindrical handles on one side and a type of prism seating on the other is offered as a practical method of achieving a standardized structural interface without freezing continued development of the latches, either technically or commercially.

The main emphasis in future Docking Mechanism concepts will probably be in two directions:

o   The first is towards a very simple Docking Mechanism, involving mainly the latch mechanism to achieve a structural link
o   the second is towards a sophisticated Docking Mechanism, where the latch mechanism is designed for non-rigid spacecraft and the achievement of very low dynamic interactions between spacecraft during the docking process.

63

Electrical Connector
Mechanism

Liquid/Gas Connector
Mechanism

Electrical and
Liquid/Gas Connector
Mechanism

Handle

Latch
Mechanism

Close-Up Sensor

Docking
Mechanism
Electronic

Target
(Passive Side)

Docking Mechanism
for
AOCS Controlled Closure

Chaser
(Active Side)

Latch

Camera

Electrical
Connection
Mechanism

Grapple
Mechanism

Boom

Boom
Extension/
Retraction
Mechanism

Liquid
Connection
Mechanism

Camera

Power and Data
Electronics

Docking Mechanism
for DMS Controlled Closure

FIGURE 1: DMS AND AOCS CONTROLLED CLOSURE CONCEPTS

HANDLE   LATCH

CRUCIFORM

TARGET   CHASER

ROTATIONAL   AXIAL
FREEDOM   COMPLIANCE

100 mm   152 mm

BARRELNUT   100 mm
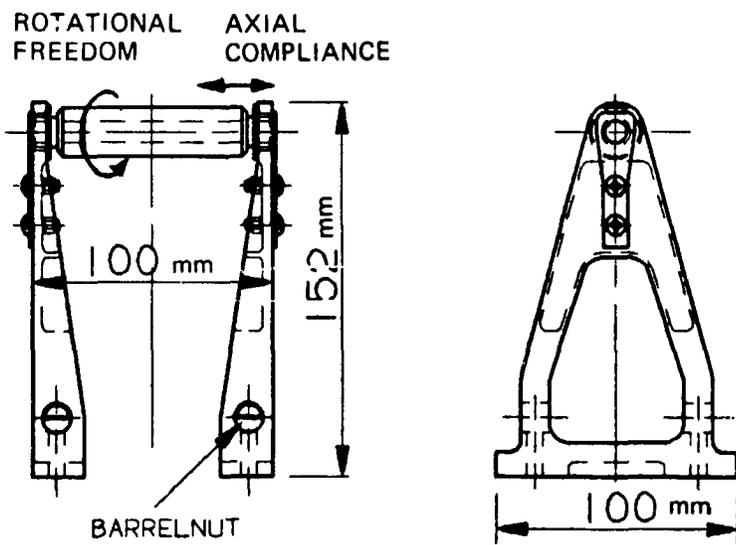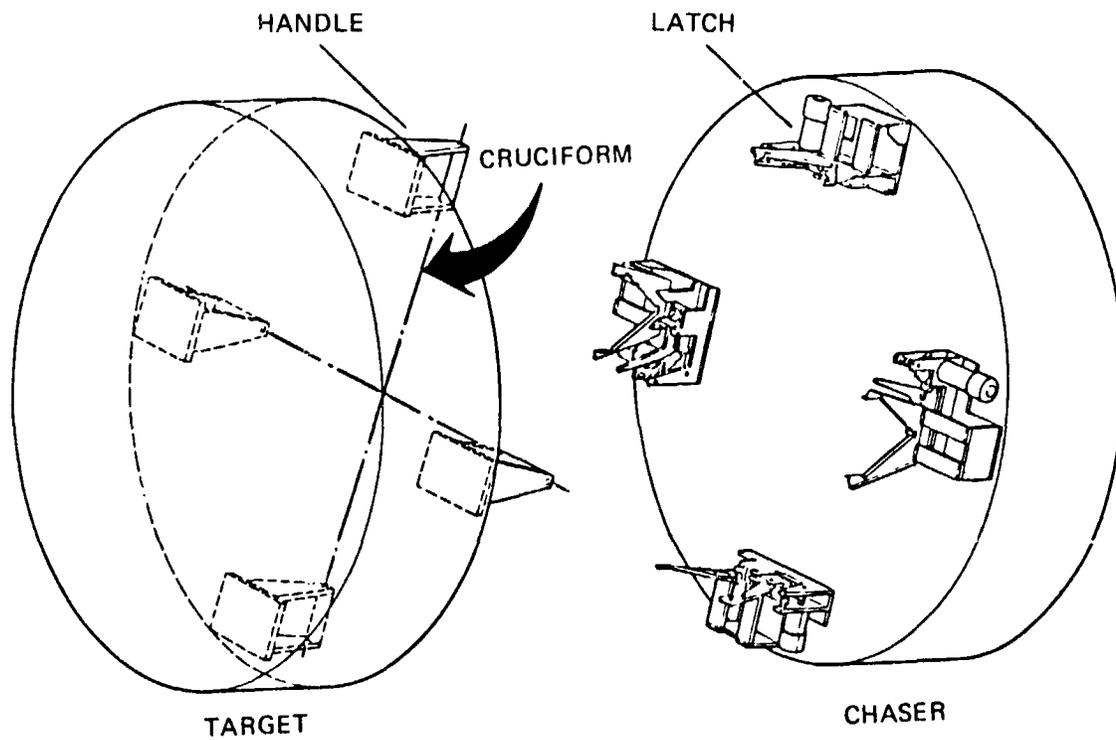
FIGURE 2:   THE CRUCIFORM CONCEPT AND ITS BASIC ELEMENTS

65

CLAW

EMERGENCY
DEVICE

LINKAGE

PRETENSION
SPRING

MOTOR

GEAR

ENCODER

END SWITCH

BASEPLATE

HANDLE SUPPORT

HANDLE BAR

RECEPTION ELEMENT OF
VARIOUS SHAPES

SPRINGS OF VARIOUS
STIFFNESS-CHARACTERISTICS

PRISM SEAT

FORCE/TORQUE SENSOR

DAMPER

EMERGENCY SPRING
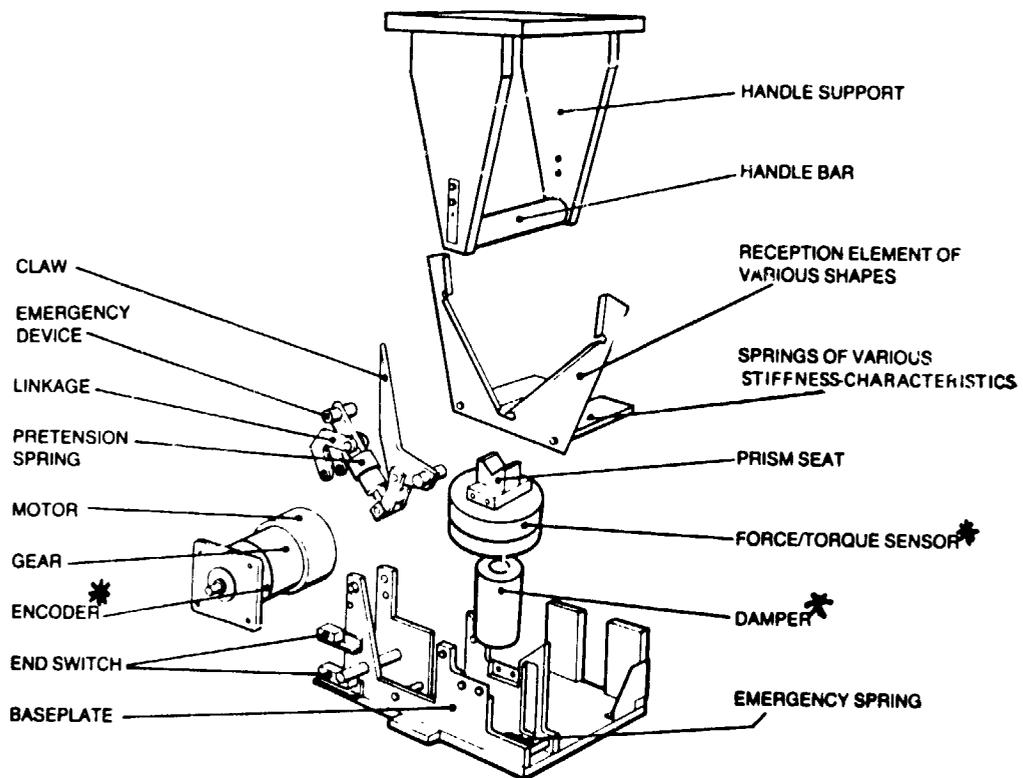
FIGURE 3:   BASIC ELEMENTS AND POSSIBLE ADDITIONAL ELEMENTS* OF THE
            LATCHING MECHANISM

FIGURE 4a shows the reception positons of latch and handle, which do not necessarily involve immediately a real mechanical contact, but which give the final initiation command for the latch actuator.
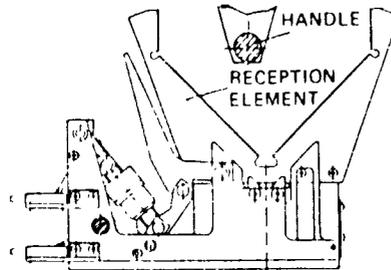
FIGURE 4b shows the first mechanical contact. The handle runs against the reception element, which, fixed to the springs, limits the interactive forces by compliance in the axes. The claw is rotated by the actuator for engagement with the handle.
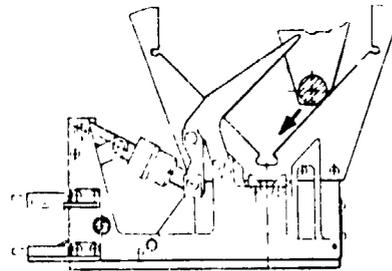
FIGURE 4c shows the handle captured by the claw. The docking process may now be controlled for the minimum dynamic interaction between Chaser and Target. The actuator has to overcome the reaction forces, the spring force and the emergency spring force.
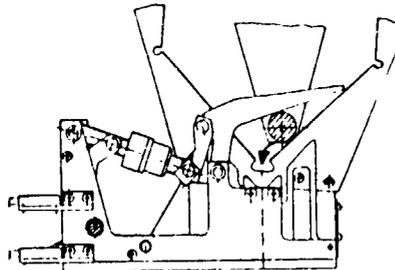
FIGURE 4d shows the final latching position when the handle is forced into the prism seating by the overcenter linkage and loaded pretension spring.
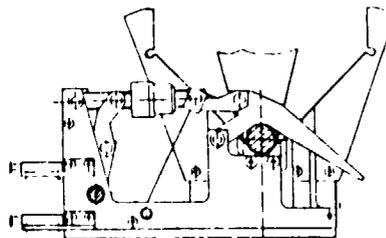
FIGURE 4e shows the emergency undocking when, after disabling a linkage hinge, the chaser is undocked by the spring element.
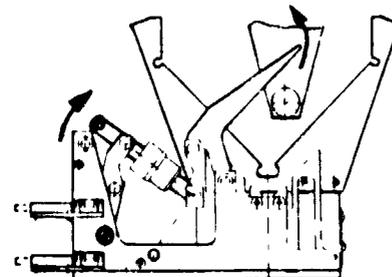
FIGURE 4. OPERATIONAL SEQUENCE OF LATCH FOR DOCKING AND EMERGENCY UNDOCKING

67
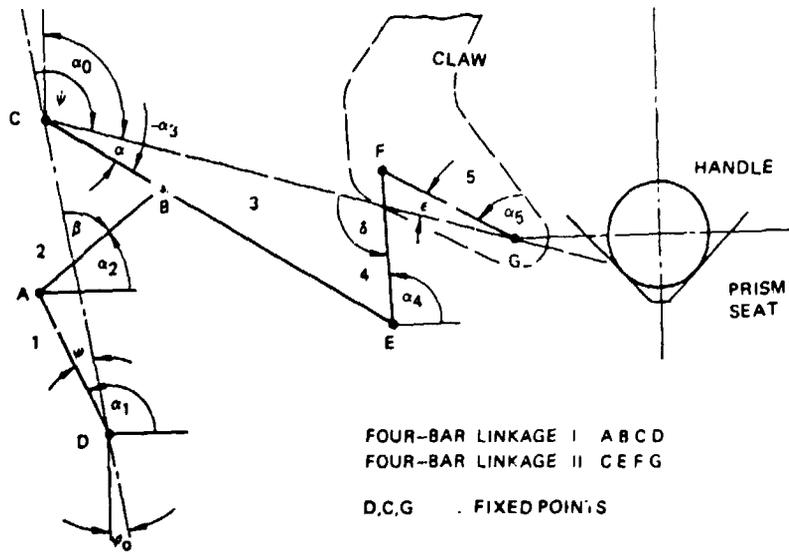
FIGURE 5: LATCH LINKAGE IN 2x4-BAR LINKAGE LAYOUT
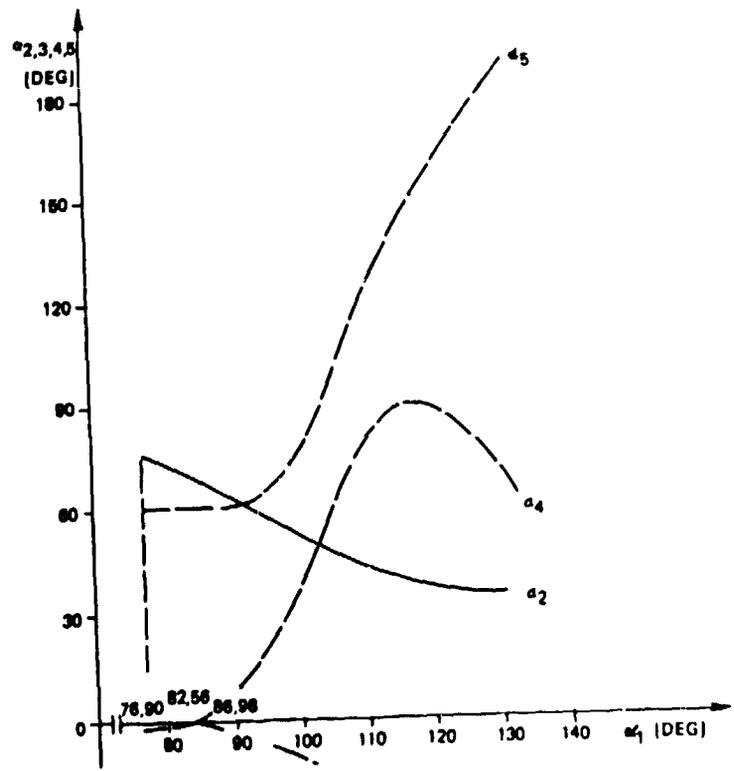
FIGURE 6: INPUT LINKAGE ANGLE (α_1) VERSUS OUTPUT LINKAGE ANGLE (α_5)
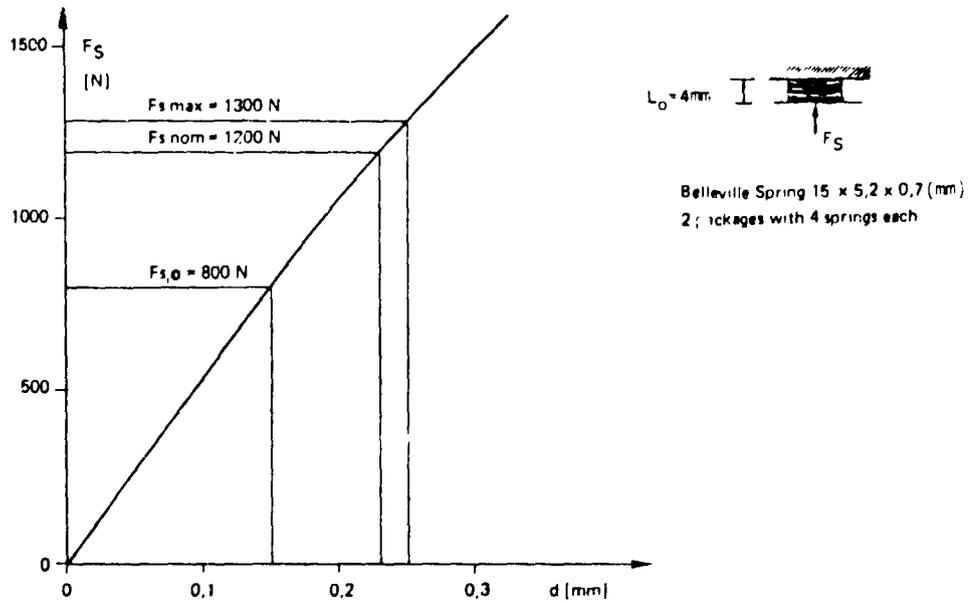
FIGURE 7: CHARACTERISTIC OF PRETENSION SPRING PACKAGE
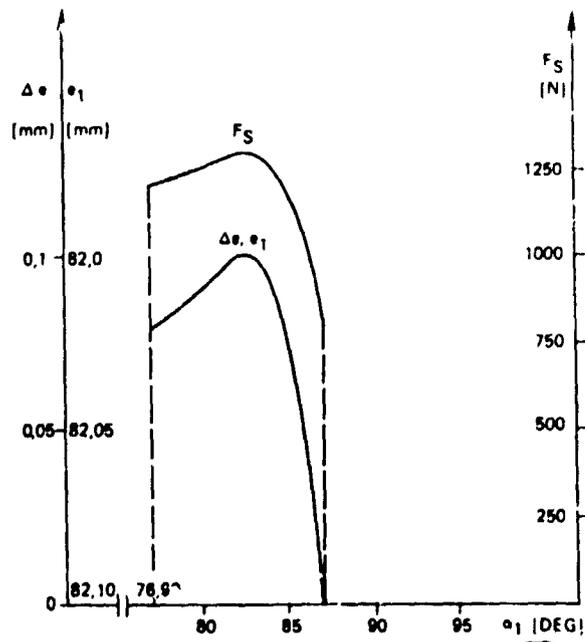
FIGURE 8: LENGTH VARIATION OF LINK 3 AND SPRING FORCE VERSUS
CRANK ANGLE

69
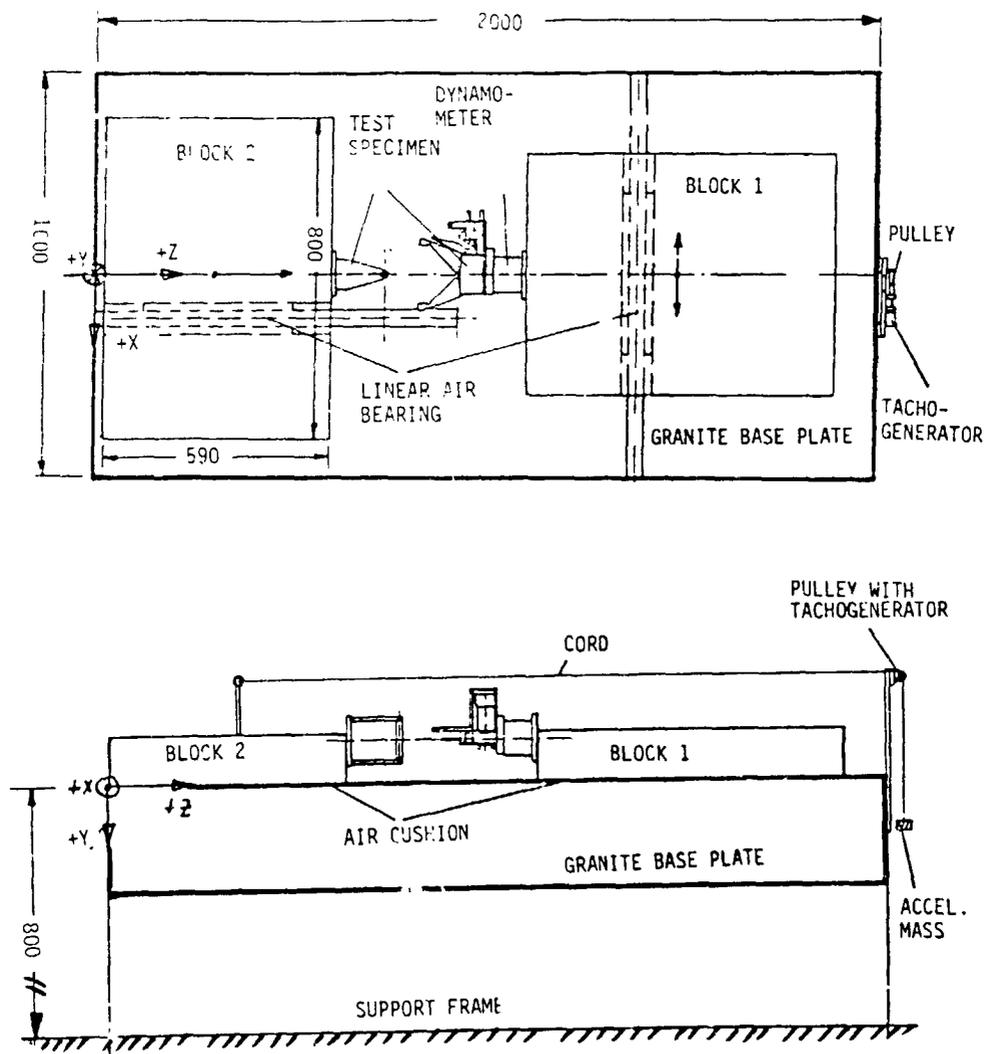
FIGURE 9: AIR BEARING TABLE 'ST SETUP TO TEST DOCKING DYNAMIC
INTERACT?ON WITH ONE LATCH ONLY (ALL CIMENSIONS IN mm)

70
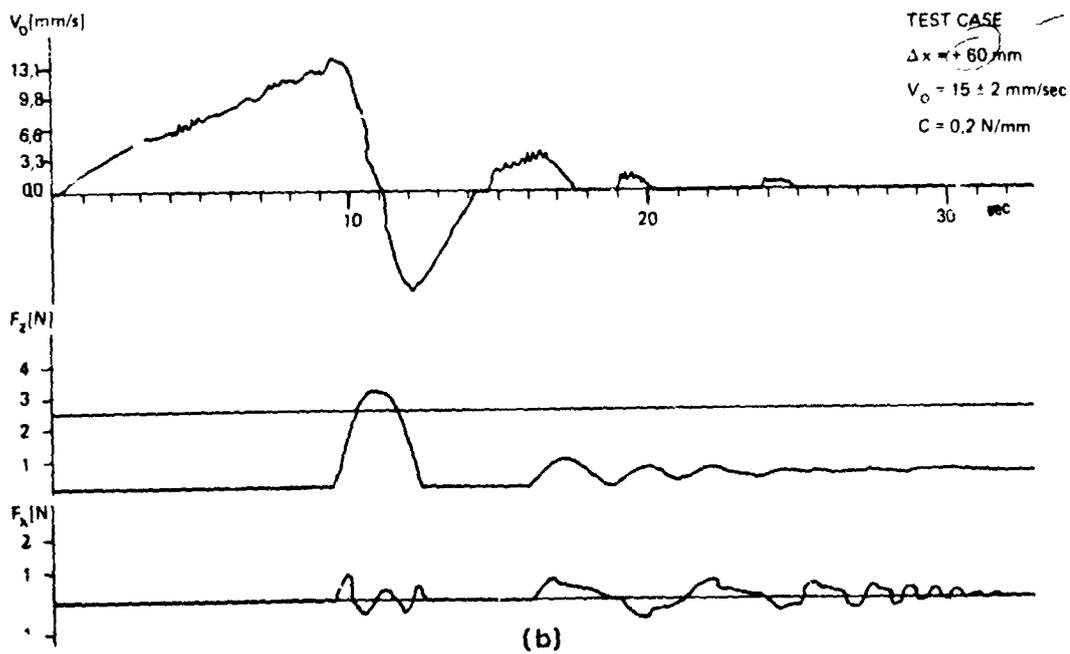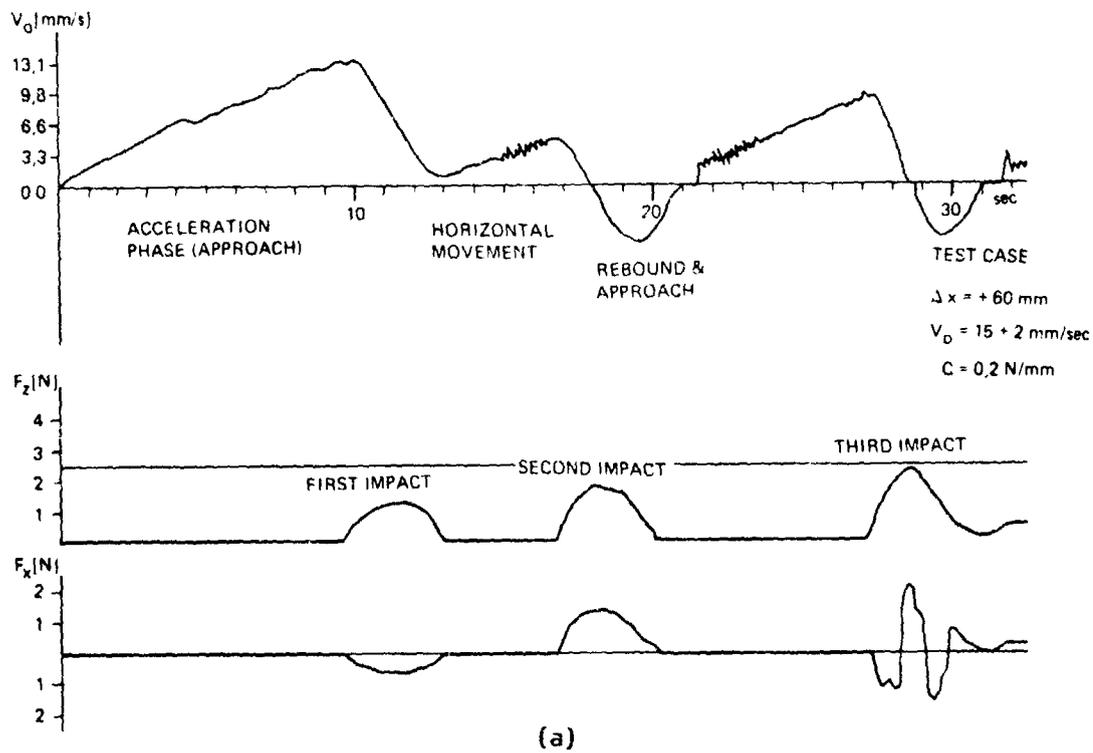
FIGURE 10: DYNAMIC INTERACTION FOR TWO DOCKING CASES WITH
CONSTANT AOCS FORCE

71

```
                        ┌─────────────────┐
                        │  DMS CONCEPTS   │
                        └─────────────────┘
                                 │
               ┌─────────────────┴─────────────────┐
       ┌───────────────┐                    ┌───────────────┐
       │ IMPACT DOCKING│                    │  NON IMPACT   │
       │               │                    │   DOCKING     │
       └───────────────┘                    └───────────────┘
                                                    │
                                   ┌────────────────┴────────────────┐
                           ┌───────────────┐              ┌───────────────┐
                           │     DMS       │              │     AOCS      │
                           │  CONTROLLED   │              │  CONTROLLED   │
                           │   CLOSURE     │              │   CLOSURE     │
                           └───────────────┘              └───────────────┘
```

GRAPPLING DISTANCE < = 1 m	CLOSURE	LATCHING	CONNECTION	RECEPTION DISTANCE < = 0 1 m	LATCHING	CONNECTION
Verify readiness for grappling	Reduce kinetic energy of relative motion	Fine alignment	electrical connections	Verify readiness for latching	Fine alignment	Electrical connections
Move grapple mechanism into position	Align vehicle	Rigid mechanical connection of vehicles	liquid/ Gas connections	Capture	Rigid mechanical connection of vehicles	liquid Gas connections
Close grapple mechanism	Draw vehicles together					

TABLE 1: DOCKING CONCEPTS AND RELATED DOCKING OPERATIONS

General
- The DMS shall not hazard to other equipment or personnel during ground testing.
- The DMS shall have no credible single point failure which results in an unsafe condition for either vehicle
- The DMS shall make available provisions for docking abortion at any time a. d satellite release without damage to either satellite.
- The DMS shall be protected against false commands.
- The DMS shall be designed to a fail-safe, fail-safe standard
- The first point of contact shall be grounded.

During Docking
- No damage shall occur to either satellite during docking, nor shall their operational performance be isolated.
- It shall be possible to abort docking at any point in the sequence.
- The docking operation shall be man supervised.

During Contingency Operations
- It shall be possible, following contingency operations, to re-dock with the same two spacecraft
- The DMS shall provide failsafe means for Contingency operations.

During Emergency Operations
- Emergency Operations shall not impair the docking capability of the Target Satellite.
- There is no necessity for docking with the same Chaser Satellite following Emergency Operations

TABLE 2: SAFETY REQUIREMENTS

72

INITIAL SEPARATION CONDITIONS

Parameter	AOCS Controlled Closure
displacement (mm)	$-55 \leq d_{x,s}, d_{ys} \leq +55$
	$0 \leq d_{zs} \leq +30$
approach velocity (mm/sec)	$-2.0 \leq v_{xs}, v_{ys} \leq +2.0$
	$5 \leq v_{zs} \leq 15$
angular misalignment (deg)	$-0.5 \leq \emptyset_{xs}, \emptyset_{ys}, \emptyset_{zs} \leq +0.5$
rotational speed (deg/sec)	$-0.05 \leq \omega_{xs}, \omega_{ys}, \omega_{zs} \leq +0.05$

LATCHING CHARACTERISTICS

Parameter	Final Conditions at End of Latching
displacement (mm) between both satellites	$-1.0 \leq d_{xe}, d_{ye}, d_{ze} \leq +1.0$
misalignment between both satellites (deg)	$-0.2 \leq \Theta_e, \emptyset_e, \Psi_e \leq 0.2$
Stiffness axial, lateral forces	$K_x = K_y = K_z \geq 2.2 \cdot 10^6$ N/m
bending, torsional	$C_x = C_y = C_z \geq 12 \cdot 10^3$ Nm/deg

The DMS shall maintain these characteristics while transmitting the following loads across the docking interface:

— axial, lateral forces $\quad F_x = F_y = F_z \leq 220$ N

— bending, torsional moments $\quad M_x = M_y = M_z \leq 200$ Nm

TABLE 3: FUNCTIONAL PERFORMANCE REQUIREMENTS

PARAMETER	CHASER			TARGET		
Mass (kg)	200	$\leq$ m	$\leq$ 4000	1200	$\leq m_p$	$\leq$ 15000
Moment of inertia (kg – m²)	100	$\leq J_{XA}$	$\leq$ 11000	5000	$\leq Jx_p$	$\leq$ 250000
	100	$\leq J_{YA}$	$\leq$ 11000	9000	$\leq Jy_p$	$\leq$ 520000
	100	$\leq J_{ZA}$	$\leq$ 8000	12000	$\leq Jz_p$	$\leq$ 600000
Centre of gravity (m) (relative to DMS)	0.05	$\leq X_{CGA}$	$\leq$ 0.25	0.2	$\leq X_{CGP}$	$\leq$ 10.0
	0.05	$\leq Y_{CGA}$	$\leq$ 0.25	0.2	$\leq Y_{CPG}$	$\leq$ 4.8
	0.75	$\leq Z_{CGA}$	$\leq$ 2.00	0.2	$\leq Z_{CPG}$	$\leq$ 2.5
Eigenfrequencies (Hz)	f1	$\leq$ 10 Hz		0.9	$\leq f_{7p}$	$\leq$ 2.0
	f2	$\leq$ 35 Hz		1.20	$\leq f_{8p}$	$\leq$ 2.0
				1.25	$\leq f_{9p}$	$\leq$ 2.0
Flexible appendages and moving parts	TBS			TFS		

TABLE 4: PHYSICAL PROPERTIES OF CHASE AND TARGET

Operational Principles: man involvement shall be limited to:

- Supervision of DMS operation
- Interpretation of housekeeping data
- Specially assigned stop/go commands
- Contingency and Emergency control

Operational Modes:

- Permanent docking
- Episodical docking

Nominal Operations Task Structure:

- The DMS shall be checked for docking readiness prior to the initiation of docking
- Nominal operations shall be based on a predetermined operational sequence
- Prior to each sequence and after each sequence go-ahead checks shall assess the status of the docking process and the DMS itself
- The DMS shall provide automatic correction and switch-over commands and/or control of those functions from the ground, according to the mission requirements.

Contingency Operations Task Structure:

- Contingency and Emergency operations shall be initiated when any system of either spacecraft is endangered and safety is no longer guaranteed
- Contingency and Emergency operation shall be initiated by the DMS and/or from the ground, according to the mission requirements

<div align="center">

TABLE 5: OPERATIONAL REQUIREMENTS

</div>

TRANSFER CAPABILITIES

ELECTRIC		LIQUID/GAS	
		• High Pressure Gas	— 80 kg total at 100 DM³/H
• 2 kW at 50 V			— 280 bar initial pressure
• 1 kW at 28 V			
• Low Rate Signal:	100 lines	• Low Pressure Gas:	— 100 DM³ total at 100 DM³/H
• High Rate Signal:	100 mb/sec		— 1 bar
• Only Parasitic Loads to DMS latches			
• Plate Travel ≤ 30 mm		• Liquid Connectors:	
• Emergency Separation Capability		— 100 kg of freon 21, 45 bar, 350 K, 360 kg/h, Δ_p = 6 bar	
• Separation of Electrical from Liquid/Gas		— 500 kg bipropellant, 20 kg/h	

<div align="center">

TABLE 6: REQUIREMENTS FOR CONNECTING MECHANISM (TYPICAL)

74

</div>

DRAG-COMPENSATED, PRECISION-POWERED HINGE SYSTEM

By G. G. Jacquemin* and S. J. Rusk*

SUMMARY

The design of a high-precision powered hinge is complicated by the
unavoidable presence of parasitic drag torque resulting mainly from friction
and transfer of power, signals, and fluids across the hinge. Regardless of
the type of drive system selected, it is impossible to completely eliminate
all parasitic drag. However, the mechanism described here comes very close
to providing a drag-free system. All sources of parasitic drag torque are
collected on a shaft which is powered by an electric motor independent of the
main hinge drive. Under control of a sensor, the electric motor applies a
compensating torque equal to that of the parasitic drag torque, allowing the
main hinge drive to operate in a practically drag-free environment with very
high positioning precision.

INTRODUCTION

In the design of robotic arms, precision pointing systems and other
mechanisms which require very accurate angular positioning, it is necessary
to find methods for minimizing or eliminating the parasitic drag torque. The
presence of parasitic drag torque introduces step functions into the torque-
vs.-displacement curve, the nonlinearity of which is further aggravated by
the effect of static friction. The parasitic drag is difficult to predict.
It is known to vary with angular position, velocity, load, temperature, and
other variables, especially if wire bundles and flex hoses are routed around
the hinge. If the hinge drive mechanism design includes a gearbox gear
backlash introduces deadbands in which positioning cannot be controlled.

The powered hinge mechanism presented in this paper eliminates gearing and
its associated problems by using direct-drive motors, and reduces parasitic
drag torque to that of one lightly loaded ball bearing.

POWERED HINGES - GENERALITIES

Powered hinges can be classed into two broad categories:

1. Deployables (nonretractable)
2. Remotely controlled continuously adjustable

The deployable systems of category 1 are usually spring-driven with
deployment rates controlled by adjustable dampers. Precision positioning in
the deployed position is provided by the lockup mechanism. This type of
powered hinge is of no interest in the following discussion.

The remotely controlled systems of category 2 cover an array of devices
adapted to various degrees of positioning precision, ranging from simple
powered door actuators to robotic arm hinges and high-precision pointing
systems. If high-precision pointing is not a requirement, relatively simple

*Lockheed Missiles & Space Company, Sunnyvale, California

devices can be designed using gear-train reduction drives. Such mechanisms can sometimes be tolerant of significant parasitic drag torque so that transfer of power and electric signals can be performed externally by means of wire bundles or slip rings and fluids via flexhoses. However, the design of a hinge system with the high pointing precision of a fraction of an arc sec. presents difficult problems which cannot be resolved by simple conventional mechanisms. To meet such requirements, it is necessary to use more complex electromechanisms.

GENERAL REQUIREMENTS

The high-precision powered hinge system discussed in this paper was designed to meet the following specifications:

1. Maneuver an 8000-lb payload at the end of a 75-in. arm in a vacuum/ zero-g environment.
2. Achieve fine pointing with a 0.50 arc sec. resolution and within ± 2 arc sec. of the specified value.
3. Ensure that the jitter does not exceed:

Freq., Hz.	Max. jitter, arc sec.
0 to 5	0.60
5 to 20	0.50
20	0.20

4. Provide fcr electrical power transfer across the hinge (two lines).
5. Provide for signal transfer across the hinge (40 channels).
6. Provide for fluid line transfer across the hinge (four lines) or into the hinge systems, if cooling is required.

The pointing precision requirements are not too meaningful when expressed in terms of arc sec. In order to give a better appreciation of their severity, they are expressed below in inches at 1 mile from the hinge point.

pointing:	± 2 arc sec.	=	$\pm$ 0.62 in. at 1 mile
resolution:	0.50 arc sec.	=	0.16 in. at 1 mile
jitter:	0.60 arc sec.	=	0.19 in. at 1 mile
	0.50 arc sec.	=	0.16 in. at 1 mile
	0.20 arc sec.	=	0.06 in. at 1 mile

BASIC CONCEPT

To provide a mechanism which will perform with the high precision consistent with the above specifications, it is necessary to neutralize the parasitic d. ag torque such that the drive motor effectively operates a drag-free system. It is also necessary to use DC torque motors in direct drive to eliminate difficulties inherent with reduction drives and/or stepper motors.

The neutralization of the parasitic torque drag is provided by means of a drag torque eliminator system (DTES). The DTES senses the presence of drag torque and applies additional power independently from the main drive motor in such a manner that the drag torque is balanced out without disturbing the main drive.

The main drive is provided by a DC torque motor controlled by an electronic feedback control system which ensures the appropriate pointing precision.

The transfer of electric power is performed by means of rotary transforme using AC current. Similarly, the transfer of all electrical signals is provided via rotary capacitive couplers. Advantage is therefore taken of the property of both rotary transformers and capacitive couplers which perform their functions through air (or vacuum) gaps without physical contact, i.e., without parasitic drag torque.

BASIC HINGE MECHANISM

Figure 1 shows the hinge mechanism's major components as designed for a development prototype. To clarify the basic components of the system, Fig. 2 presents a schematic of the mechanism. It s ould be noted that since this device was primarily intended for space use, all electric motors are provided with identical backups for use in case of primary motor failure.

The system is supported by two large self-aligning spherical roller bearings inserted in two pillow blocks. These roller bearings are mounted on stub shafts over conic sleeves which are forced under the inner races. This expands the inner races radially to eliminate all internal clearance and apply controlled radial preloads needed to meet launch requirements. As a result of the preloads, these bearings exhibit a significant drag torque which, together with the fluid coupler O-ring friction, provide the major contributions to the system parasitic drag torque. The two stub shafts are connected through a large cy.indrical shell as shown in Fig. 1. Supported by flexure bearings, the stub shaft assembly can rotate through small angles with respect to the main hinge shaft. These flexures allow a total differential displacement of only $\pm 2°$ with a stiffness of 100-400 in-lb/rad depending on the thickness of the flexure blades.

The differential angular displacement between the stub shaft assembly and the hinge shaft is detected and measured by a sensor as shown in Fig. 2. This sensor controls the operation of a twist motor which adds sufficient torque to the stub shaft assembly to counteract all parasitic torque drag collected by the stub shafts. Thus, the primary hinge drive motor operates in a torque-free environment, thereby ensuring the desired hinge positioning accuracy.

The misalignment coupling in Fig. 2 is intended to provide enough compliance to accommodate manufacturing tolerances in shaft alignment at that point. This coupling allows for bending and for axial and lateral mismatching. However, its torsional compliance is not significant.

PARTIAL ANALYTICAL MODEL

In order to more clearly describe the operation of the powered hinge, it was found convenient to develop a simplified analytical model in which the masses, inertias, and details of the electronic loops were left out. This model is shown in Fig. 3.

It is shown in this system that a displacement provided by the drive motor acts directly upon the output branch and indirectly upon a parallel branch

which, by means of a detector and a feedback control system, provides power to cancel out all parasitic drag torque.

An examination of the mechanism in Fig. 1 shows that some parasitic torque drag must necessarily exist in both branches of the system. However, by careful design, only one small ball bearing is left in the output branch to ensure proper alignment of the encoder wheel. In zero gravity, the torque drag of this bearing is expected to be at or near the noise level of the branch. All other sources of parasitic drag torque are collected on the other branch to be sensed by the drag torque eliminator system. These sources of parasitic torque include that of the main roller bearings, the smaller ball bearings, and any external torque drag (such as that of the rotating fluid couplings).

In operation, the position sensor detects an angular displacement $\Delta\theta$ and sends a signal to the twist motor. This signal closes the loop mechanically by rotating the stub shafts to cancel the displacement, thereby eliminating the drag torque.

The response characteristics of this control system are not addressed in this paper; however, the system is designed to function much faster than the primary drive system to ensure a very small lag angle $\Delta\theta$ and the intended drag-free operation of the powered hinge.

ACTIVE FLEXURE

The operation of the flexure is shown in Fig. 4, which illustrates one cycle of motion. The flexure consists of two concentric hollow shafts held together by thin flexible blades mounted as shown in Fig. 4-1. The two shafts have a small radial clearance such that large lift-off and landing radial and axial loads transmitted from the inner main shaft to the outer stub shaft can be taken by direct contact of the two shafts. The radial clearance between the two shafts is small enough that the flexure blades are not unduly stressed during static load. This clearance is also selected to ensure that no contact is made between shafts in the normal zero-g operation.

As can be seen in Fig. 4-1, the main shaft (output) is inside the stub shaft (drag eliminator system). The main shaft is connected to the main motor; the stub shaft is connected to the twist motor and runs with the drag-producing roller bearing.

When the main motor is activated, the main shaft rotates. Fig. 4-2 shows the small rotation θ, which brings the flexures almost in contact with the edges of the main shaft windows. The sensor, upon detecting this misalignment, energizes the twist motor, which rotates the stub shaft and restores a null position at the displacement angle θ, thereby driving the roller bearing and any other drag-producing components which may be connected to the stub shaft.

In a practical application, the angle θ is made as small as possible; in this instance, 1 arc sec   The lag of the stub shaft over the main shaft is not perceptible.

EFFECT OF PARASITIC DRAG TORQUE ON SYSTEM RESPONSE

In order for this system to perform with the expected efficiency, the torque required to deflect the flexures must be as low as possible. This requirement implies a combination of low spring rate and small angular displacement. Bottoming out of the flexure is highly undesirable. Figure 5 shows a representation of a typical torque-vs.-displacement curve for a flexure where the bottoming angle is $\pm 2°$. In a well-designed system, the sensor must be capable of detecting a displacement of 1 arc sec. so that the flexures remain virtually undeflected with no parasitic torque being produced.

The residual torque along the output branch (see Fig. 3) must be very small, since it will not be eliminated.

All other sources of internal and external drag torque are applied to the "Eliminating" branch (Fig. 3) to avoid disturbing the output branch. The disturbance introduced by parasitic drag torque is shown in Fig. 6, which compares the displacement under the same torque of a one-degree-of-freedom system with and without friction drag. This plot shows how troublesome the effect of static friction is. In order to obtain a displacement, it is necessary to apply a torque at least equal to that produced by the static friction. However, as soon as the torque corresponding to the static friction is reached, the motion starts and the friction coefficient drops to the lower value corresponding to the dynamic condition. The system then jumps to a position of equilibrium, such as θ_1. By comparison, a friction-free linear system with the same stiffness and under the same torque would reach its equilibrium position at θ_2, going in a controlled manner through all intermediate angles as shown by the straight line passing through the origin.

Since friction is the major contributor to the parasitic torque drag, it is clear that a high-precision hinge cannot be designed unless it can be operated in a friction-free manner.

SOURCES OF PARASITIC DRAG TORQUE

In the general hinge system, sources of parasitic drag torque are to be found in the following components:

1. Main bearings (rollers or ball bearings)
2. Auxiliary motors bearings (ball bearings)
3. Encoder bearing (ball bearing)
4. Power line transfer system
5. Signals transfer system
6. Fluid lines transfer system

In the powered hinge discussed here, only Item 3, the encoder bearing, remains effective as a minor source of parasitic drag torque. Items 4 and 5 are transmitted by induction and capacitive coupling through   r gaps (or vacuum gaps) while the remaining three, Items 1, 2, and 6,   eliminated by the twist motor feedback loop.

CONCLUDING REMARKS

A full-size model of this powered hinge has been designed and built for test purposes. This model (Fig. 7) meets the requirements specified in this paper. It has been successfully subjected to qualitative running tests of the main drive motors without any drag relief.

Precision pointing tests have not been carried out at this stage because of delays in the design of the electronic feedback systems. However, analytical simulation techniques have shown that excellent controlled performance could be achieved at any selected angle. It should be noted that the hinge rotation angle is not limited, it can be a fraction or any number of revolutions.

In its present configuration, this precision powered hinge is a large device adapted to perform the functions represented by its specifications. Its large size was convenient for prototype fabrication, development, and testing. Application to smaller devices will require changes in its configuration to accommodate more severe space restrictions.

In addition to obvious aerospace applications, the principles of this mechanism should be adaptable in miniaturized form to robotics systems and other devices.
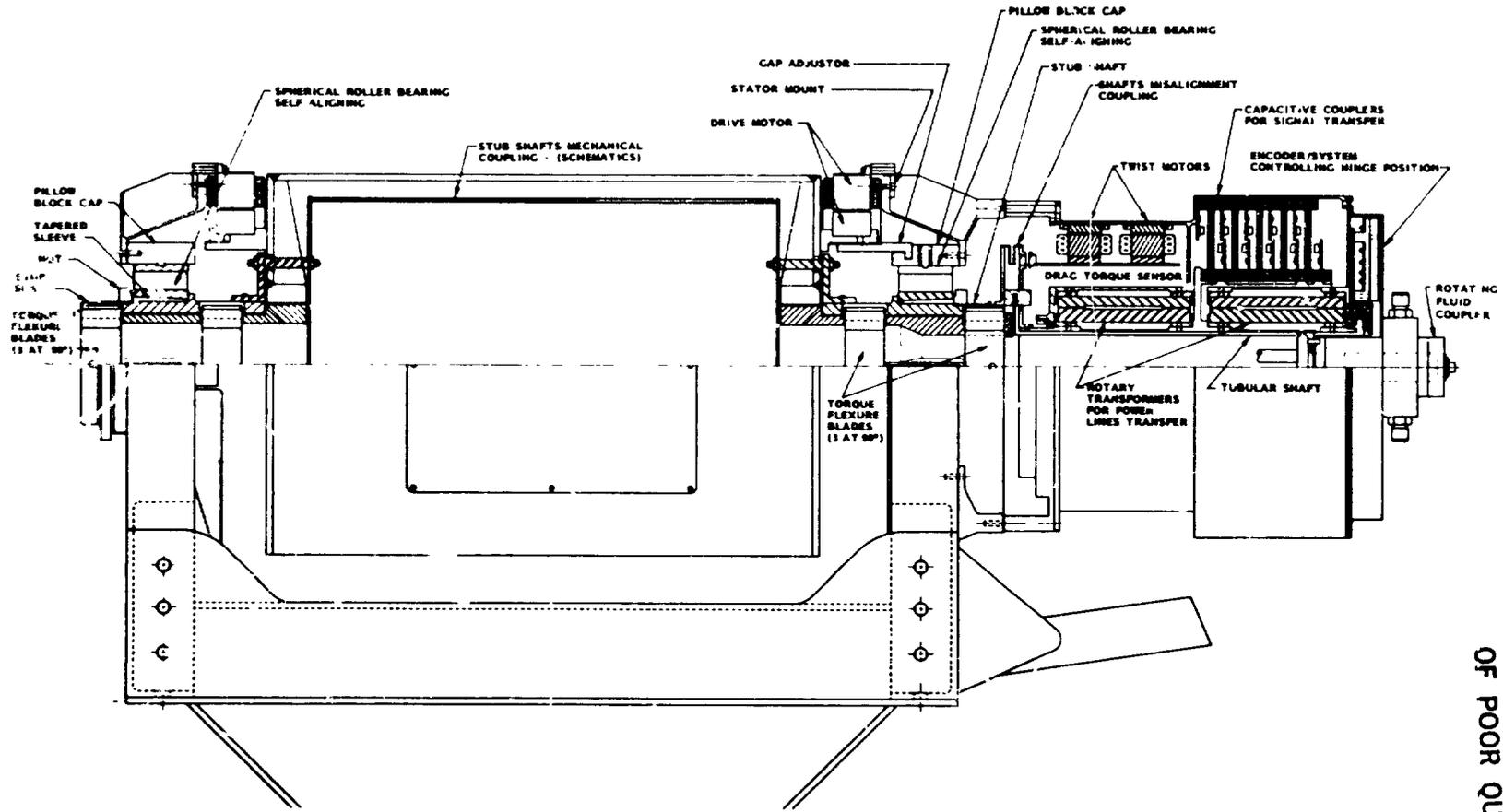
Fig. 1   Precision Hinge Mechanism
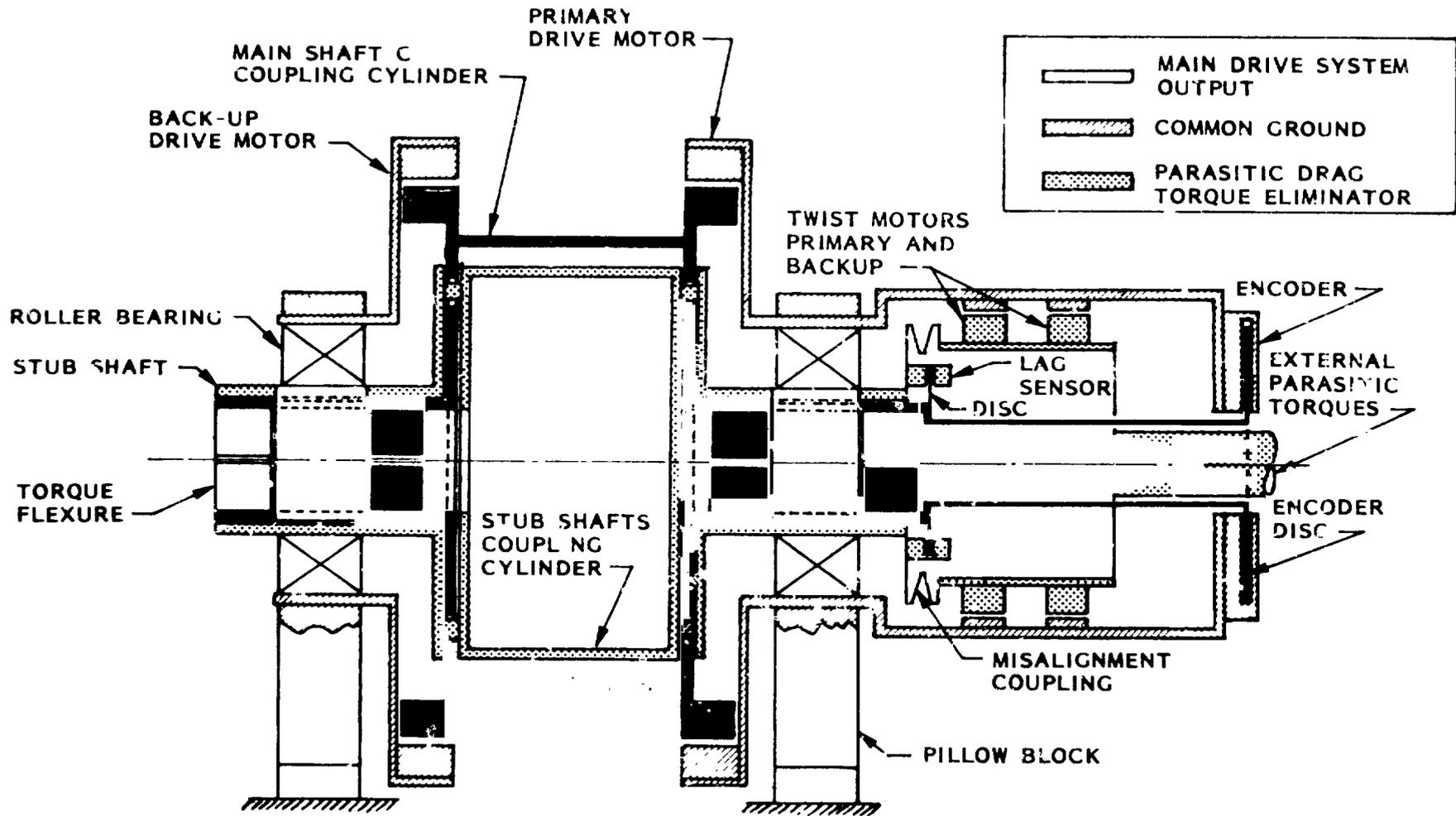
Fig. 2 Schematics of Basic Hinge Mechanism
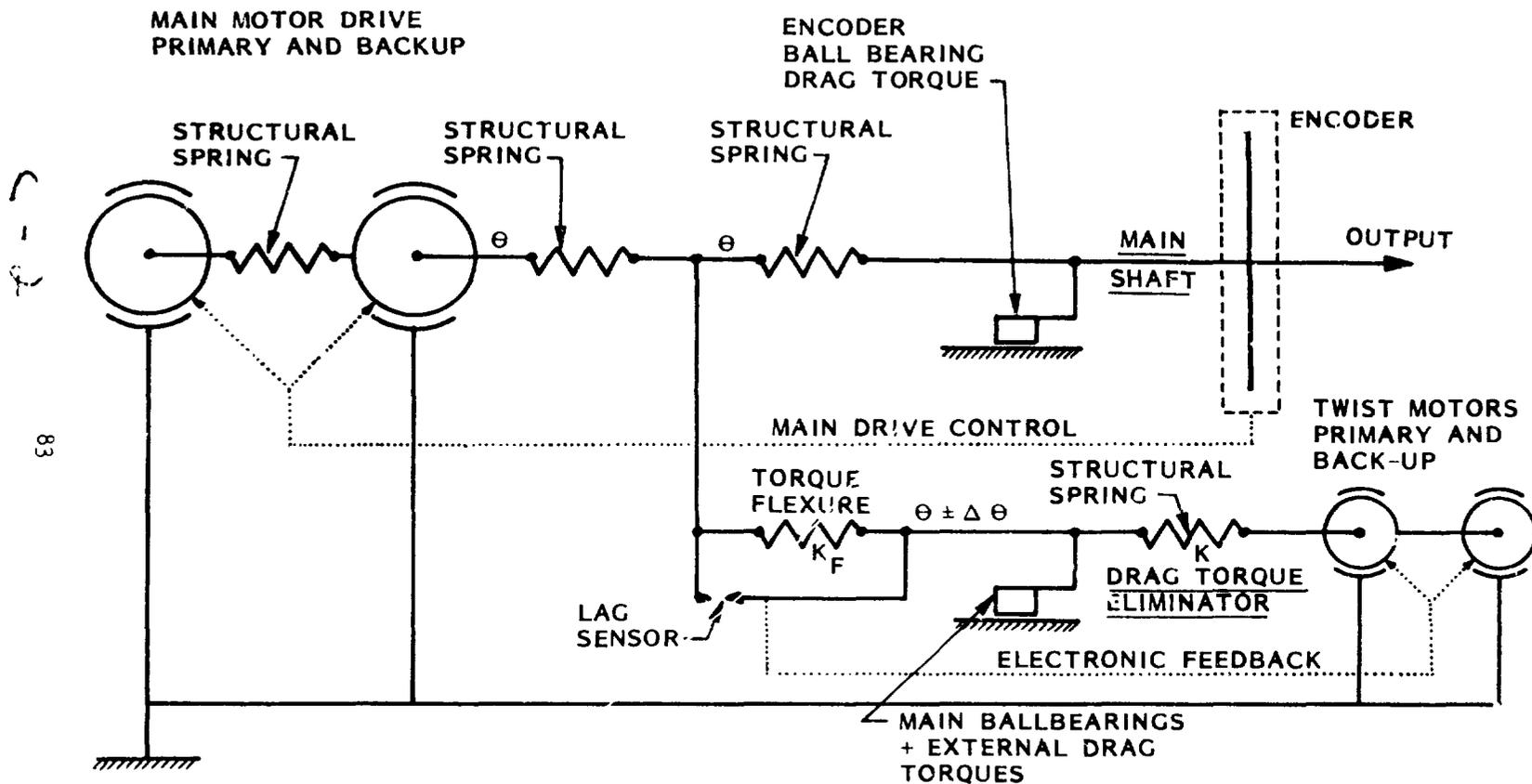
Fig. 3   Partial Analytical Model of Precision-Powered Hinge
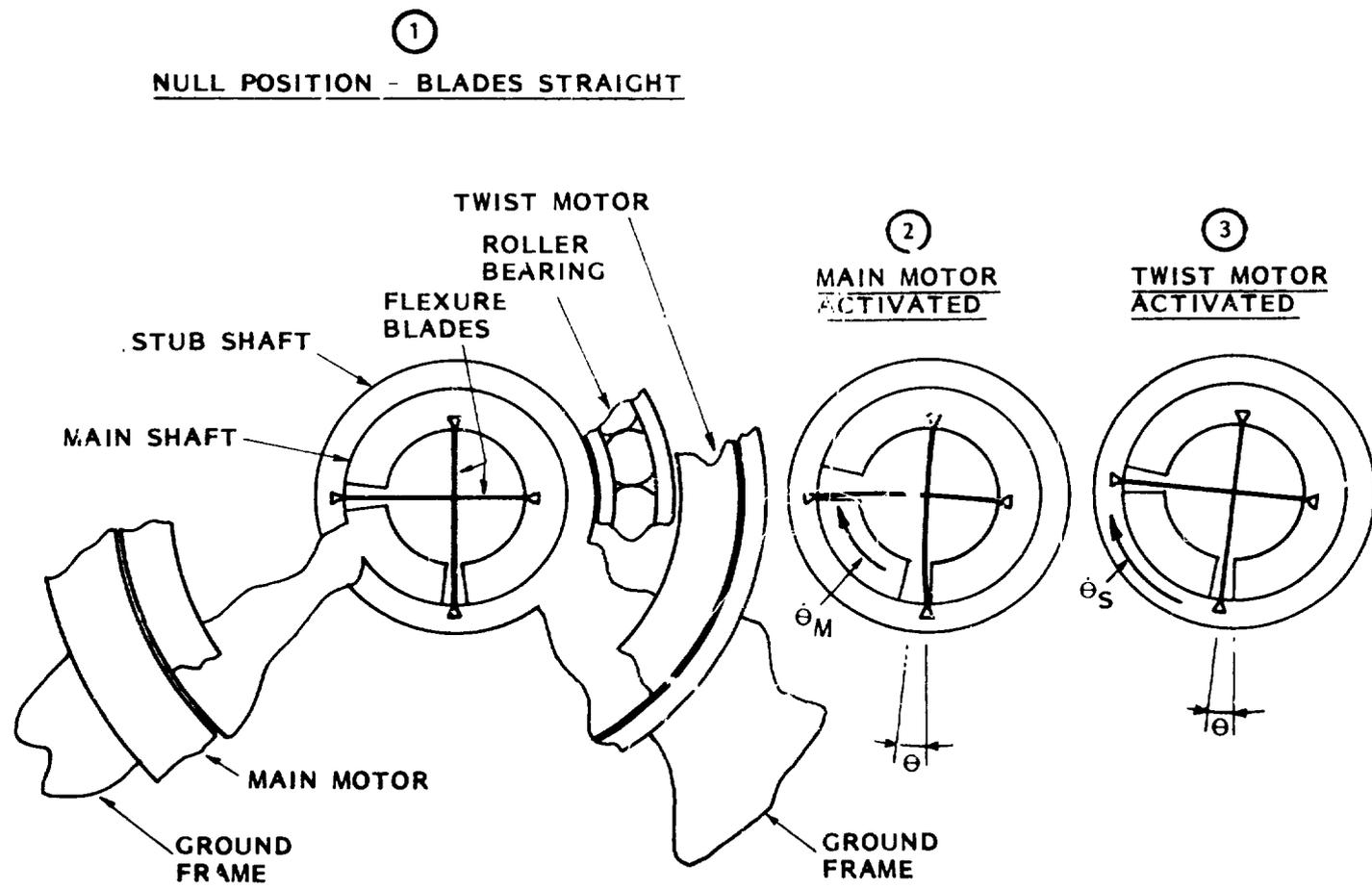
Fig. 4 Active Flexure Operation
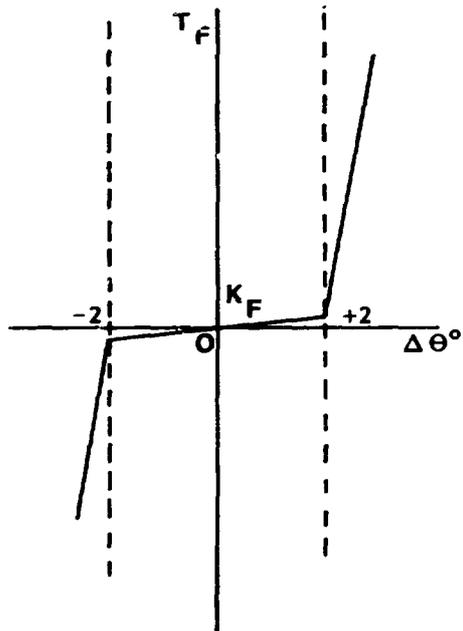
Fig. 5 Flexure Stiffness

DTES = DRAG TORQUE
ELIMINATOR SYSTEM
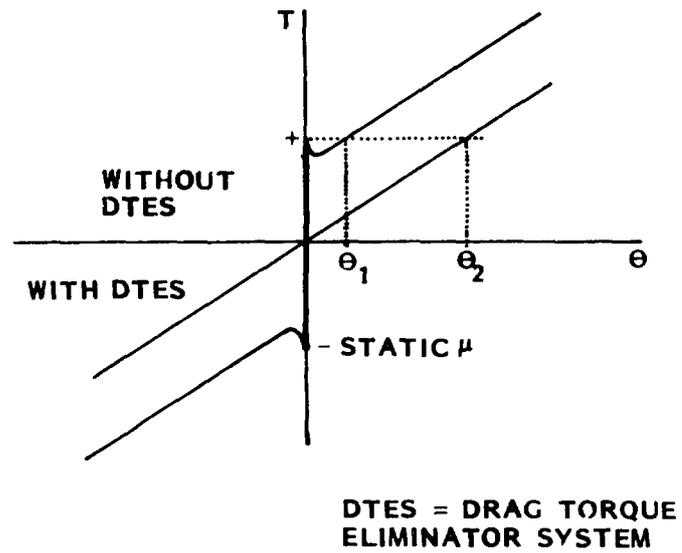
Fig. 6 Typical Torque-Displacement Curves With and Without Drag
Eliminator System For a Simple One-Degree-of-Freedom Device
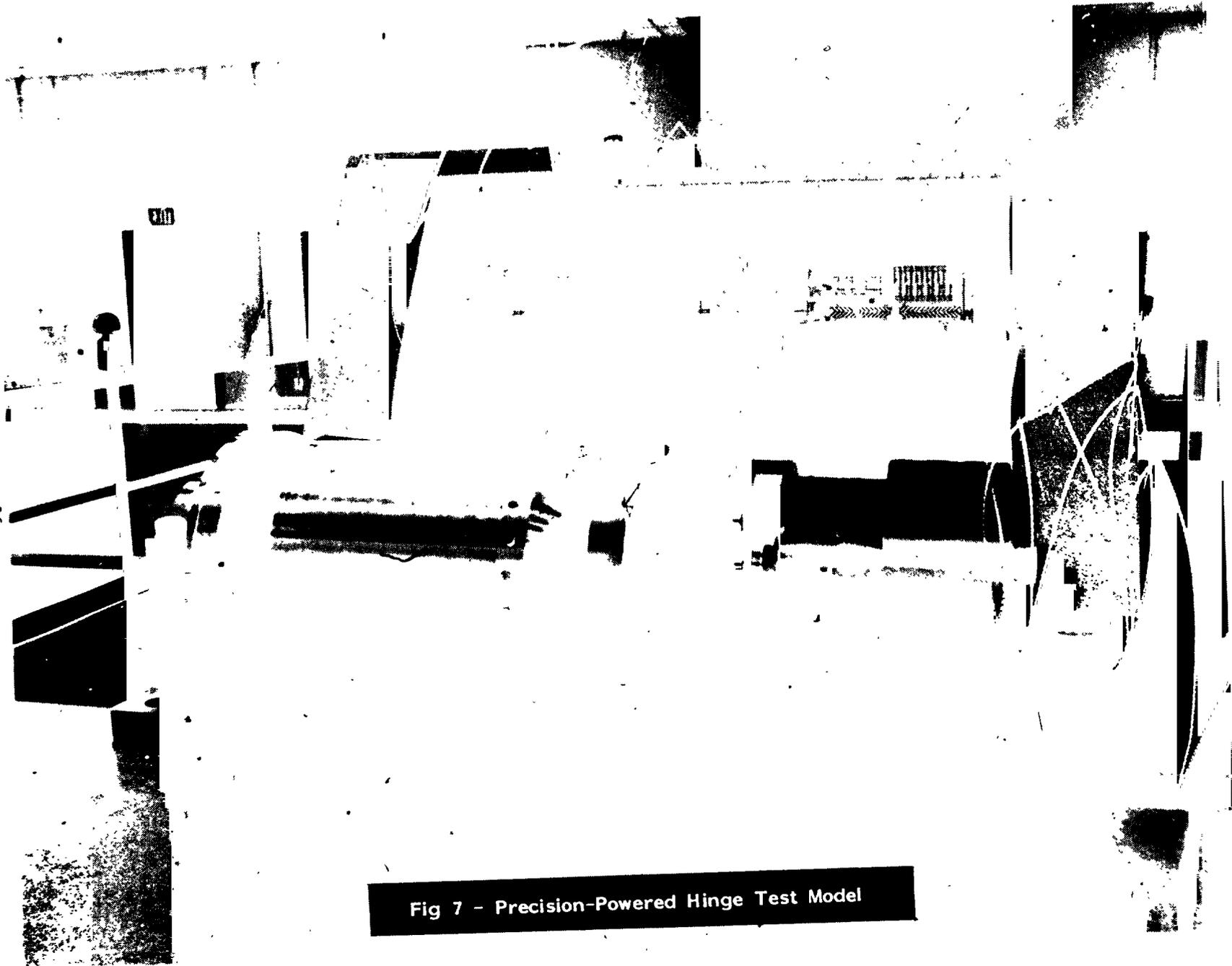
Fig 7 - Precision-Powered Hinge Test Model

86

DESIGN AND DEVELOPMENT OF A
LINEAR THERMAL ACTUATOR

Gerry Bush and Don Osborne[*]

ABSTRACT

The design and development of a Linear Thermal Actuator (LTA) for space applications is described. The actuator is driven by thermal energy and utilizes the property of thermal expansion to do work. Equations to predict performance are developed and used to optimize the design of the Development Model LTA. Design details and test results are presented and discussed.

INTRODUCTION

Concept

An LTA is a device which, when subjected to a change in temperature by the addition or extraction of thermal energy, causes work to be done by the movement of an actuator rod against some external resisting force (Figure 1). The principle of operation through which the actuation is achieved is based on the expansion or contraction of a large number of plates, packaged in such a manner that variations in lengths due to temperature changes are combined.

Applications

The LTA is inherently a high force/low displacement type mechanism, although larger displacements can be obtained by using the LTA with the appropriate linkages. Applications under consideration are:

1. Antenna Pointing Mechanism

   A number of spacecraft require active antenna positioning. Depending on required response time and positioning accuracy the LTA is a viable candidate.

2. Deployment Mechanism

   As a high force mechanism the LTA is well suited for use in deploying structures. It also has a retraction capability which is attractive in light of recent Space Shuttle missions which have demonstrated the capability to retrieve satellites.

3. Thermal Control System

   The LTA can generate sufficient force to make conductive couplings to radiator panels. As spacecraft temperature increases, the LTA actuator moves making conductive couplings to a radiator plate. The result is a simple thermal control system.

[*] Spar Aerospace Limited, Ste. Anne de Bellevue, Quebec, Canada

Objectives

The project goal was to design, manufacture and test a product for space applications based on the above concept. It was to be compact, highly reliable and have desirable performance characteristics. Performance objectives and test results for the Development Model LTA are given in Table 1. Where test results are not yet available, calculated values are presented.

TABLE 1: LTA PERFORMANCE SPECIFICATIONS

CHARACTERISTIC	OBJECTIVE	TEST RESULTS
Displacement Range	8.5 mm	12.0 mm
Maximum Applied Load	± 50 N	± 100N
Repeatability (% of peak to peak displ.)	± 2.5	± 1.0
Non Linearity (% of peak to peak displ.)	Minimize	
Due to Friction		± 2.5
Due to Backlash		± 9.0
Response Time (End to End)		
Heating	5 min	10 min**
Cooling	5 min	180 min**
Power Consumption		
Heating	–	150 W max
Cooling	–	0 W
Position Maintenance	10 W max	10 W max**

**Calculated values – test results not yet available.

88

Configurations

Three configurations were proposed at the start of the project. Two of the arrangements were based on planar components. In the symmetrically loaded planar arrangement, the actuator rod was located in the center of the plate assembly. In the unsymmetrically loaded planar arrangement, the actuator rod was located on one end of the plate assembly as shown in Figure 1. The third arrangement was based on cylindrical elements which assemble one inside the other.

A trade-off analysis was performed to determine which configuration was best. The trade-off study gave high weighting to reliability, a large displacement range against design external loads, repeatable temperature/position actuation with minimum nonlinearity, quick response, compactness, low weight, and minimal power consumption during position maintenance.

The unsymmetrically loaded planar arrangement was chosen because of its ability to be manufactured to analytic predictions for a weight optimal design with no significant penalty to other criteria.

Plate Joining Techniques

A major task in the development of the LTA was to determine a suitable method of joining the ends of the high and low expansion materials. A mechanical joint was selected to avoid high temperature fatigue and strength problems associated with adhesives and solders. Interlocking tabs were developed which are capable of two way operation, do not degrade at elevated temperatures, and can be manufactured to strict tolerances.

Plate Materials

Ideally, a plate material has a high modulus of elasticity, low density, very high or very low coefficient of thermal expansion and a high strength. A high thermal conductivity and low thermal capacitance is desirable for the high expansion plate.

Invar and Graphite Fiber Epoxy Composite (GFEC) were found to be most suitable for use as low expansion materials. Aluminum and Magnesium were found to be best for use as high expansion materials. Invar was selected over GFEC for the low expansion material as it has a much higher shear strength which is required by the interlocking tab joining technique. Aluminum was chosen over magnesium because it behaves more predictably and has a higher yield strength.

DESIGN AND PERFORMANCE EQUATIONS

Displacement

Actuator position was found to be dependent on the following four items, the first being the desired effect.

1. Change in plate length due to thermal expansion when subjected to a change in plate temperature.

2. Change in plate length due to plate clasticity when subjected to a load.

3. Opposition to changes in plate length as a result of the static coefficient of friction and normal forces.

4. Backlash because of clearance at the interlocking tabs and/or clearance between the plate assembly and the casing wall whenever the load is reversed.

The effect of the first two items above can be best illustrated by considering a single plate as shown in Figure 2. It has length l, cross sectional area A, applied load P, and is subject to a temperature change T. The total deflection is equal to:

$$\delta_1 = (\alpha T - \frac{P}{AE})$$

(1)

E = modulus of elasticity
α = coefficient of thermal expansion

Extending this analysis, an equation can be developed to handle the more general case of an LTA with two materials and multiple plate pairs. It is assumed that the cross sectional areas of all plates of the same material are constant and that the total plate length of each material is equal to L. Properties of the high expansion material are designated with the subscript 1, those of the low expansion material with the subscript 2.

$$\delta = L (T (\alpha_1 - \alpha_2) - P(\frac{1}{A_1 E_1} + \frac{1}{A_2 E_2}))$$

(2)

An equation was also developed to predict the effect of static friction on plate actuation which is a function of the static coefficient of friction, assembly preload due to plate warpage, and applied load. For the load range under consideration, its effect on displacement is less than $\pm 2.5\%$.

90

Weight and Volume Minimization

An analysis was performed to determine the values of the design parameters which minimized weight and volume for a given load and displacement. This was accomplished by specifying the weight of the LTA plate assembly as follows; where ρ represents the material density:

$$W_t = A_1 L \rho_1 + A_2 L \rho_2 \qquad (3)$$

Equation (2) can be rearranged to solve for L and substituted into Equation (3). The resulting equation has only two variables A_1 and A_2. Taking derivatives and setting them equal to zero yields equations for the cross sectional areas which minimize weight.

Calculations were also performed to find the plate width and number of plates which minimize LTA volume. The smallest volume occurs when the plate assembly, including space for actuation, takes the shape of a cube. While this shape is not normally ideal, it does provide a useful baseline to which more desireable shapes can be compared.

Response Time

One of the design objectives for the Development Model LTA was to limit power consumptions during position maintenance to a maximum of 10W. To accomplish this it was necessary to isolate the LTA from the environment using multilayer thermal blankets and nonconductive mounting shims. Because the losses are so limited, the LTA can be treated as an isothermal block for the purposes of analysis.

During heating the response time is limited by available spacecraft power or heater capacity and the unit thermal capacitance. During cooling the response time is limited by the ability of the radiator plate to dump power to space and the unit thermal capacitance. The thermal capacitance of the Development Model LTA is calculated to be 491 J/$^\circ$C.

DESIGN AND MANUFACTURING

The Development Model LTA consists of a number of components and assemblies. A sample of each of the components is shown in Figure 3.

Casing

The casing, shown in Figure 3 and Figure 4, is used to hold the plates in position and constrain the motion of the actuator rod. The interior of the casing is coated with dry film lubricant to reduce friction and wear between the plates and the casing. One side of the casing is coated with white paint to act as a radiator plate and dissipate heat to space. Thermistors are mounted on the ends of the casing to monitor temperature. The casing is shown resting on thermal shims which are made of polyimide.

The LTA was covered by the multilayer thermal blanket shown in Figure 3. The large rectangular cutout allows the white painted radiator surface to view space.

Plate Assembly

The plate assembly is made up of 33 aluminum plates and 32 Invar plates. A set of aluminum plates consist of 1 actuator end plate, 10 heater plate assemblies, 18 high expansion plates, 3 thermistor plates and a fixed end plate assembly. One of each of these is shown in Figure 3. The plate in the foreground is a thermistor plate. The remaining aluminum plates are shown in the order mentioned, separated by Invar plates, from left to right. All plates are coated with dry film lubricant.

Details of a high expansion plate and a low expansion plate are shown in Figure 5. The Invar plate has a thickness of .64 mm. The aluminum plate is .94 mm thick and has a pocket .47 mm deep. Both plates have weight optimal cross sectional areas. The slot and the hole in the aluminum plate are used to pass wires for heaters and thermistors through the plate assembly. The tabs on the aluminum plates are 12.5 mm long as compated to 2.5 mm long for the Invar plates. The tabs were lengthened to reduce bending stresses and plate assembly elasticity as a result of any clearance between tabs. It is planned to increase the length of the tabs on the Invar plates for all future LTAs.

Figure 6 shows details of the fixed end plate. The right end of the plate has a single tab on the back which fits into a slot in the casing. A thermistor is mounted in the pocket to monitor plate temperature. The tabs at the left end are similar for all aluminum plates. Figure 7 shows details of the heater plate assembly. It has tabs on both ends and a Kapton film heater bonded into the pocket.

TEST RESULTS

Figures 8 through 15 show test results for the Development Model LTA. The first six curves show actuator displacement as a function of temperature under different loading conditions. The remaining curves give the transient heating and cooling response for two different power inputs. In general, results match theoretical predictions well. Variations occur as a result of backlash and increased elasticity of the plate assembly. Theoretical curves neglect the effect of backlash and friction.

The backlash is apparent only under no load conditions and is of the order of 2.1 mm. It can be viewed in Figure 8. Friction effects can be considered negligible since the normal force is small under these conditions.

Figure 8 also demonstrates the high repeatability of the LTA by actuating through two complete cycles. For both the heating and cooling curve, the actuation follows the same path within $\pm 1\%$.

Figures 9 through 12 demonstrate performance under both compressive and tensile loading. In all cases the effect of plate elasticity is larger than that predicted by theory. This is apparent by the offset between theoretical and experimental results. The nonlinear effect of friction forces is also visible and can be seen to increase with increasing load as expected.

The heating portion of each of the displacement versus temperature curves is shown on one graph in Figure 13. The slope is the same for all curves. The effect of plate elasticity can also be seen by the separation between curves.

Figures 14 and 15 are heating and cooling curves for the Development Model LTA at room temperature and pressure. Under thermal vacuum conditions the heating portion of the curve will be sharper, as losses are limited to a maximum of 10 W. A longer cooling response time is also anticipated.

DEVELOPMENT PROBLEMS AND SOLUTIONS

A number of problems became apparent during testing at different stages. The most obvious are the nonlinearities as a result of backlash and friction.

Backlash was caused primarily by clearance at the tab joints and is seen as a manufacturing problem. It was first noted during breadboard testing where more than .04 mm clearance per joint was evident. With 65 joints in the Development Model LTA even a small clearance is excessive. The proposed solution was to dimension the plates to obtain a light interference fit. This fit was clearly not achieved during manufacturing with the techniques used, however, the solution is still seen as viable.

The static coefficient of friction between the plates coated with dry film lubricant was found to be in the order of 0.35. When first assembled this high coefficient of friction, when combined with preload caused by plate warpage, causes significant binding of the actuator. The problem was reduced by increasing the clearance between the casing and the plate assembly to reduce preload. Decreasing preload by this method resulted in increased backlash and increased plate assembly elasticity.

As noted above, there was more plate elasticity than that predicted by theory. Clearance between the plate assembly and the casing wall allowed the tabs to rotate which induced the plates to assume buckling shapes in the space available. These actions led to increased elasticity. The tabs on the aluminum plates were therefore increased in length to reduce the amount of rotation possible for a given clearance. the ideal solution to this problem is to reduce the static coefficient of friction, which would allow tighter packaging of the plates.

93

CONCLUSIONS

The Development Model LTA has demonstrated the performance characteristics required for the target applications. It has responded in a predictable, repeatable fashion which has been successfully characterized. Both load and displacement obtained by the Development Model LTA have exceeded initial goals.

Future work will be directed towards developing a deployment/retraction mechanism for a flight project.

ACKNOWLEDGEMENT

94
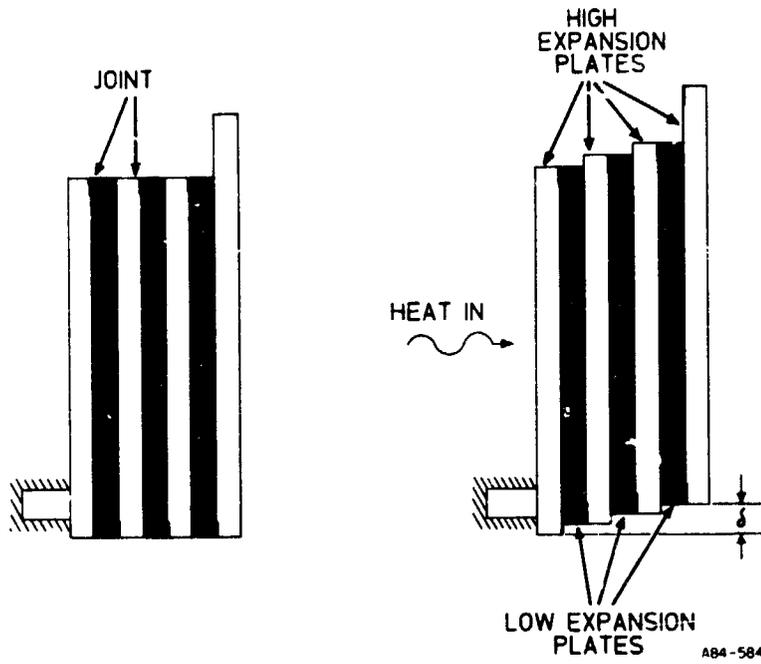
Figure 1.   LTA Concept
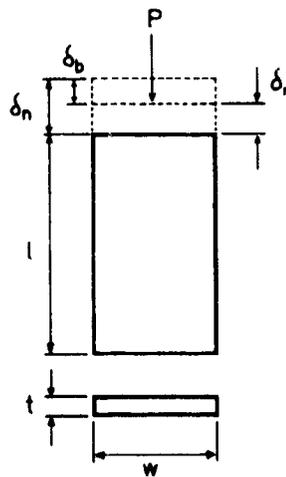
Figure 2.   Displacement of a Single Plate
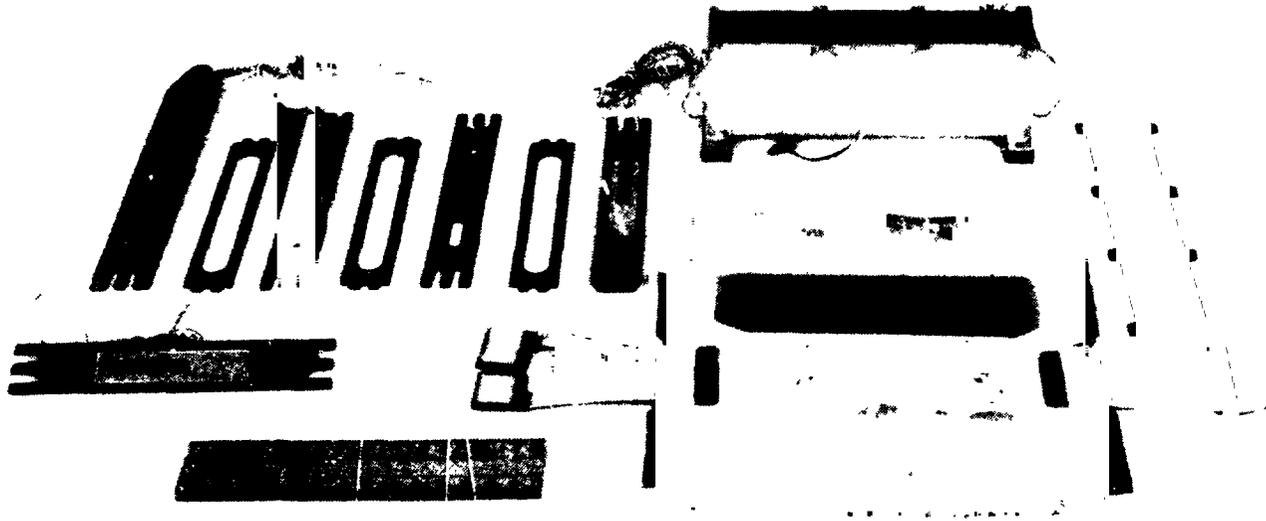
Figure 3.   LTA Piece Parts and Low Level Assemblies
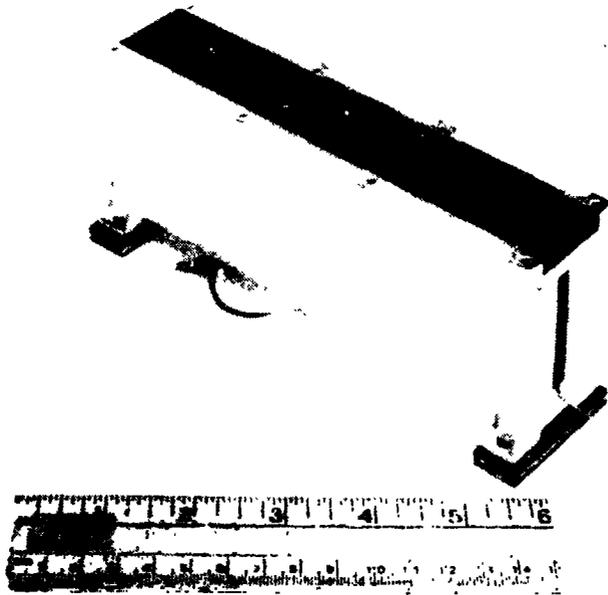
Figure 4.   Casing A embly
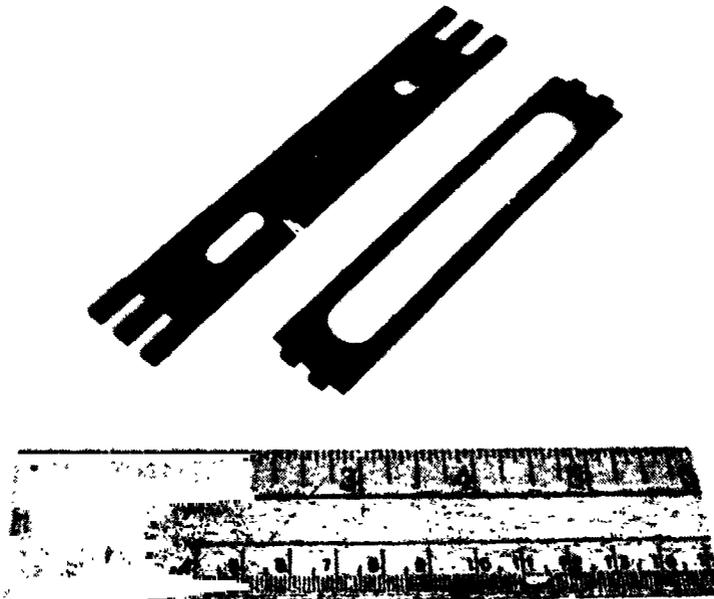
Figure 5.   Sample High & Low Expansion Plate

97

Figure 6.   Fixed End Plate Assembly
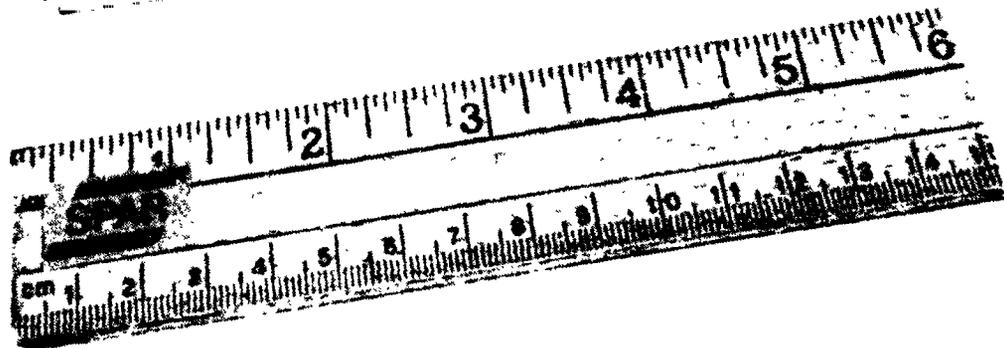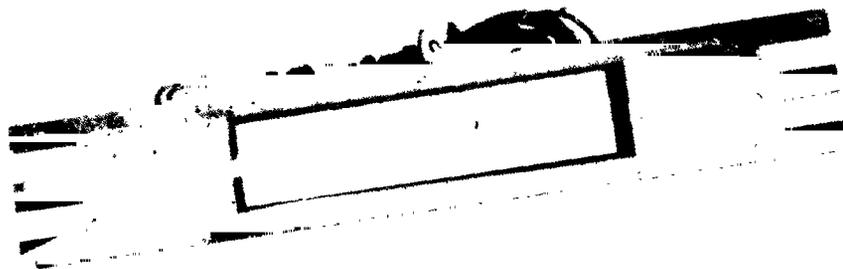
Figure 7.   Heater Plate Assembly

98

DEFLECTION VS TEMPERATURE – NO LOAD

DISPLACEMENT (MM)

12 0

10 0

8 0

6 0

4 0

2 0

0 0

△ HEATING – 1ST CYCLE
✱ COOLING – 1ST CYCLE
□ HEATING – 2ND CYCLE
○ COOLING – 2ND CYCLE
○ THEORETICAL

CHANGE IN TEMPERATURE (°C)

0 0   30 0   60 0   90 0   120 0   150 0
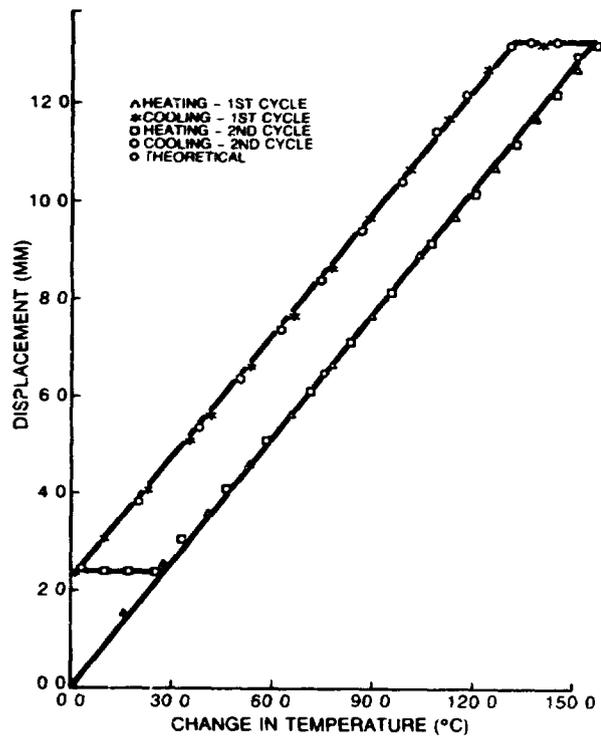
Figure 8. Displacement vs. Temperature
No-Load

**DEFLECTION VS TEMPERATURE –
50 N COMPRESSIVE LOAD**

DISPLACEMENT (MM)

10 0

8 0

6.0

4 0

2 0

0 0

-2 0

△ HEATING – 1ST CYCLE
✱ COOLING – 1ST CYCLE
□ THEORETICAL

CHANGE IN TEMPERATURE (°C)

0 0   30.0   60 0   90 0   120 0   150 0
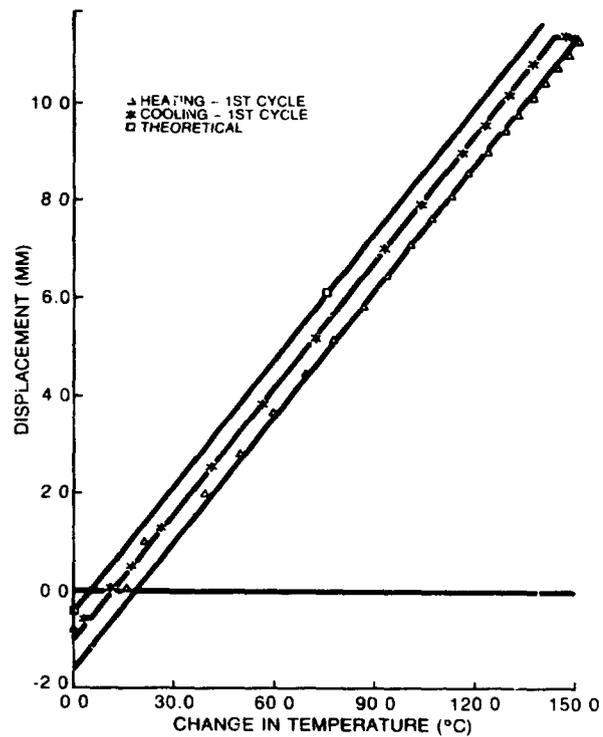
Figure 9. Displacement vs. Temperature
50 N Compression

66
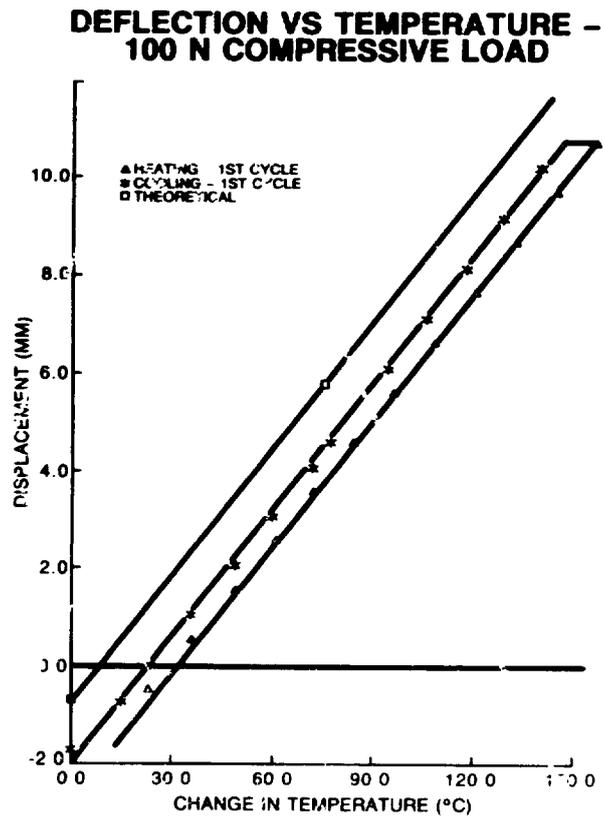
Figure 10. Displacement vs. Temperatur, 100 N compression
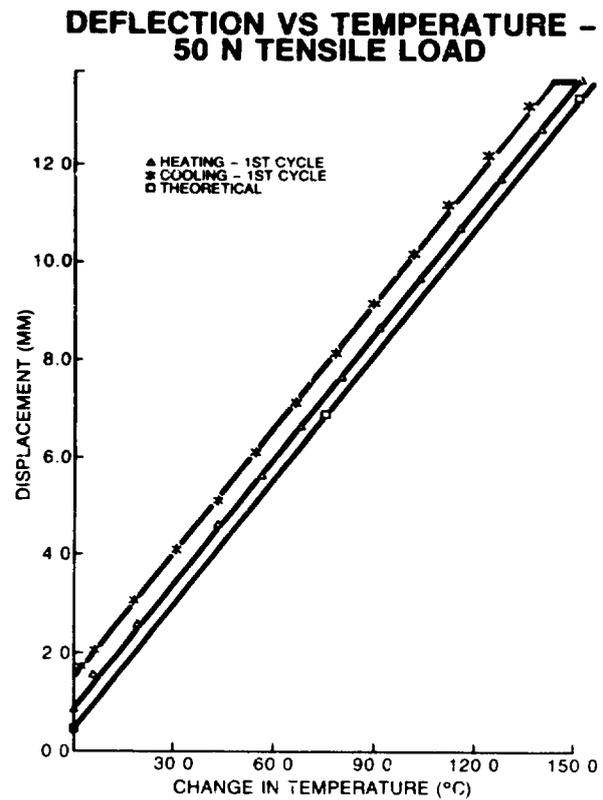
Figure 11. Displacement vs. Temperature 50 N tension

DEFLECTION VS TEMPERATURE – 100 N TENSILE LOAD

△ HEATING – 1ST CYCLE
✕ COOLING – 1ST CYCLE
□ THEORETICAL

DISPLACEMENT (MM)

12 0

10 0

8.0

6 0

4.0

2.0

0 0

30 0   60 0   90.0   120 0   150 0

CHANGE IN TEMPERATURE (°C)

DEFLECTION VS TEMPERATURE – HEATING

△ 10 06 KG COMPRESSION
✳ 5 34 KG COMPRESSION
□ NO LOAD
○ 5 34 KG TENSION
○ 10 06 KG TENSION

DISPLACEMENT (MM)

15 0

12 0

9 0

6 0

3 0

0 0

-3 0

0 0   30 0   60 0   90 0   120 0   150 0

CHANGE IN TEMPERATURE (°C)

Figure 12.   Displacement vs. Temperature
100 N tension

Figure 13.   Displacement vs. Temperature
(Heating Curve Only)

DEFLECTION VS TIME – NO LOAD – 100W

▲ HEATING AND COOLING CYCLE
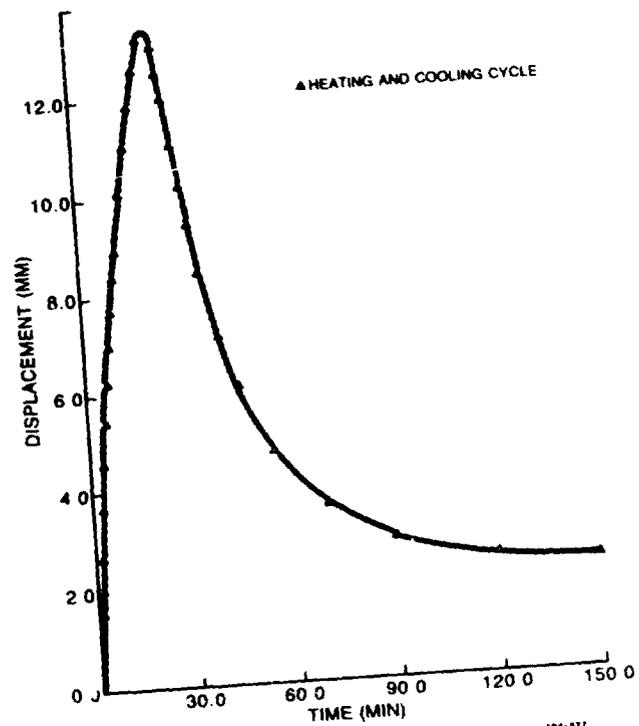
Figure 14. Transient Response
100 W Heating

DEFLECTION VS TIME – NO LOAD – 150W

▲ HEATING AND COOLING CYCLE
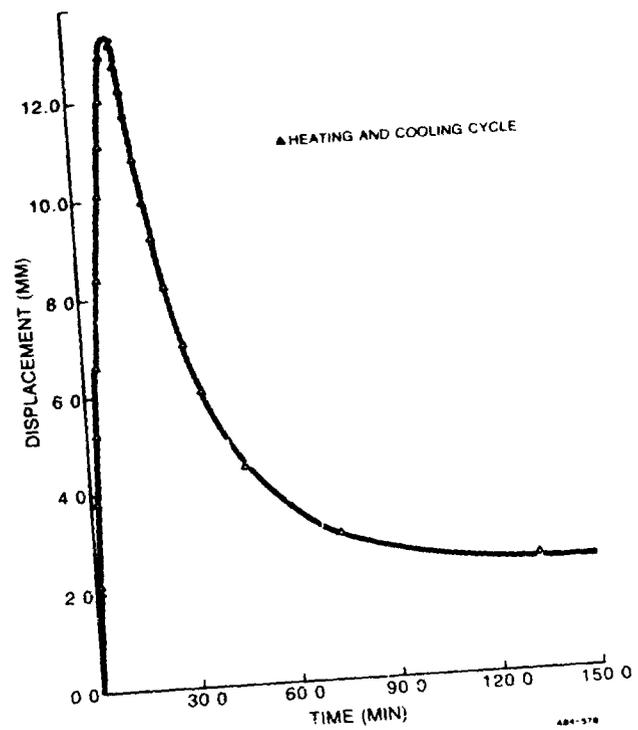
Figure 15. Transient Response
150 W Heating

THE DESIGN AND DEVELOPMENT OF A CONSTANT-SPEED SOLAR ARRAY DRIVE

Howard M. Jones and Neil Roger*

ABSTRACT

This paper describes the design and development of a constant-speed solar array drive system for use in high-power communications satellites. The relationship between continuity of motion in the solar array drive and spacecraft attitude disturbance is investigated. The selection of the system design based on the design requirements including spacecraft disturbance is discussed. The system comprises two main parts: the drive mechanism including small-angle stepper motor and reduction gearing and the control electronics including ministepping drive circuits, such that a very small output step size is achieved. Factors contributing to discontinuities in motion are identified and discussed. Test methods for measurement of very small amplitudes of discontinuity at low rotational rates are described to assist in the testing of similar mechanisms.

INTRODUCTION

The use of sun-pointing deployable solar arrays of increasing power levels on spacecraft for various applications has placed increased emphasis on the design and operational strategies of the solar array drives which maintain the sun-pointing attitude of the solar array while the spacecraft typically remains earth-pointing. As a result of increased solar array size and flexibility the potential to disturb spacecraft has increased dramatically. The use of a constant-speed drive as opposed to the more traditional intermittent or pulsed drive can improve this situation in two ways:

(a) The elimination of discontinuities in angular momentum between the solar array and the spacecraft results in reduced disturbance levels. This permits the use of smaller size or lower power consumption in the reaction or momentum wheels of the spacecraft pitch axis control loop, and/or less frequent momentum-dumping operations of the thrusters.

(b) The reduced energy levels in the dynamic coupling between the solar array and drive system leads to improved operating torque margins and eliminates potential problems of stalling and backdriving due to resonant array dynamics. This phenomenon occurred on-orbit in a large communications satellite recently, resulting in forcible back-stepping of the system while a step forward had been commanded.

However, because the required rate of rotation is very low (i.e., 1 revolution per day for geosynchronous spacecraft), the maintenance of constant speed within limits, expressed as a proportion of the nominal speed, is a difficult proposition. The fundamental problem is therefore one of achieving the necessary continuity of motion in the solar array drive system without leading to excessive mechanical and electrical complexity with the resulting penalties in reliability, cost and mass.

---

*Spar Aerospace Limited, Toronto, Canada

REQUIREMENTS

The continuity of motion requirements for the solar array drive system are derived from analysis of the relationship between speed variations in the drive system and spacecraft disturbance using computer simulations of the drive system, solar array, spacecraft body with flexible appendages and the spacecraft pitch axis control loop.

A typical spacecraft configuration is shown in Figure 1 corresponding to a high-power geosynchronous communications application. Data for the spacecraft, its' flexible appendages and attitude control system parameters are summarized in Table I.

From the computer simulations it was determined that both the amplitude and frequency of speed variations in the solar array drive were important. The approaches used and the continuity of motion achieved are discussed in the Design and Analysis section below.

The spacecraft disturbance and other relevant drive system requirements are presented in Table II.

DESIGN AND ANALYSIS

The design and analysis proceeded in three stages:

(a) Analysis of the relationship between continuity of motion in the solar array drive and spacecraft disturbance using computer simulations of the drive system, solar array, spacecraft body with flexible appendages and the pitch-axis control loop.

(b) Evaluation and trade-off of various drive system concepts to determine which would best achieve the required continuity of motion requirements in terms of reliability, cost and mass.

(c) Further design and analysis of the selected concept.

Drive System Concepts and Trade-off

The concepts considered fell into one of the two main categories:

- Open-loop stepper and synchronous systems.

- Closed-loop brushless DC systems using rate or position sensor feedback (in addition to commutation feedback).

  A variety of gear ratios was also considered for each category.

It was found that because the nominal rotation rate is very low (1 revolution per day) the fluctuations in rate, expressed as a proportion of the nominal, are very small and hence difficult to detect and to control for the closed-loop systems. Therefore the open-loop stepper or synchronous approach was selected due to its simplicity. The system block diagram for the open-loop geared stepper concept is illustrated in Figure 2.

The other major trade-off area involved selection of the optimum combination of techniques for reducing output step size for the stepper or synchronous concepts. The following methods are available:

(a) Motor with small prime step angle.
(b) Electronic step division (mini-stepping).
(c) Reduction gearing.

Gear reductions are selected for other reasons including motor torque amplification (reduces system size and weight) and backdrive characteristics (e.g., low backdrive efficiency reduces susceptibility to solar array dynamic torques). The selected concept uses a conventional 1.8° stepper motor with 64-level mini-stepping and 288:1 reduction gearing to achieve a theoretical output step size of 0.0001°. This step size is so low and the associated stepping frequency of 42 Hz so high, that significant interaction with the solar array and the spacecraft pitch axis control loop are avoided. The lamination shapes for a hybrid stepper motor with 1.8° prime step angle are illustrated in Figure 3, with the associated electrical schematic and sinusoidal ministep drive sequence. The schematic of the ministep electronics is shown in Figure 4. A cutaway illustration of the 288:1 reduction gearing is presented in Figure 5. The second stage of the reduction gearing is a regenerative planetary set which is non-backdriveable. This set functions in a similar fashion to the harmonic drive except that the nutating flexible spline of the later has been replaced by the more robust planet gears, which can withstand much higher backdrive loads. More detailed information on the gears is presented in Table III.

Factors Affecting Continuity of Motion

As described above the selected drive system provides a theoretical output step size of 0.0001° and a stepping frequency of 42 Hz. In practice the drive mechanism will be part of a solar array drive assembly which includes bearings and slip rings mounted on the main shaft. It has been predicted that the achievable continuity of motion at the output is limited by stick-slip effects in the system.

Due to the compliance of the drive train and the slow, synchronous speed of the motor there is a finite rate of drive torque build-up in the main shaft. Therefore when the system is started from zero rate it takes a finite time for the drive torque in the shaft to exceed the static friction due to the slip rings and bearings. Let this time be called T_1. When the breakout torque is exceeded the shaft accelerates to a speed higher than the nominal rate under the action of the "wind-up" torque in the drive train. As the

"wind-up" torque falls below the friction torque the shaft speed decreases until it is caught by static friction. Let this time interval (of relative motion at the slip rings) be called T_2. The process is then repeated and is illustrated in Figure 6A.

The phenomenon could only be completely eliminated by the total elimination of friction or by the addition of viscous or damping friction into the system. However, the problems associated with the stick slip effects can be alleviated by controlling the times T_1 and T_2 and hence the amplitudes of discontinuities in the main shaft rotation. The following parameters were found to affect T_1 and T_2:

(a) Drive system stiffness.
(b) Absolute levels of static and dynamic friction.
(c) Relative levels of static and dynamic friction.
(d) Level of viscous friction in the system.
(e) Solar array dynamics.

The ratio of static to dynamic friction in the slip rings is determined by the properties of the materials used and is not amenable to manipulation. The solar array dynamics are not generally subject to alteration for this purpose while the addition of sufficient viscous friction into the system at these low rates would not be practical. This generally leaves the drive system stiffness and the absolute friction levels under the control of the solar array drive designer. Increasing the drive system stiffness and reducing the slip ring friction levels will decrease the period $(T_1 + T_2)$ and hence the amplitude of the rate discontinuities. A parametric analysis using the computer simulations mentioned earlier was conducted to determine acceptable combinations of stiffness and friction. The predicted effects of various combinations of slip ring friction and drive system stiffness on continuity of motion are illustrated in Figure 6B. This indicates that to maintain an output step size in the same range as the theoretical value, say 0.0003° maximum, the slip ring dynamic friction should be limited to 1.3 Nm and the drive system stiffness at the main shaft should be above 150,000 Nm/radian. While this stiffness is not generally difficult to achieve in a solar array drive mechanism, the limit of 1.3 Nm sliding friction presents a challenge for the larger slip ring assemblies, particularly those of the disc configuration due to the larger diameter of the rings.

TESTING

An engineering model drive system has been built including the ministepping electronics. The test program in progress includes:

(a) Ambient performance tests (torque-speed, etc.).
(b) Environmental testing (vibration and thermal vacuum).
(c) Continuity of motion (systems dynamics).

The ambient performance and environmental testing involve conventional procedures and techniques and need not be discussed further. However, the system dynamics test includes a novel approach for measuring continuity of motion at the output under various operating conditions and is descr ed below.

The purpose of the System Dynamics test is to determine the dynamic characteristics of the Solar Array Drive Assembly (SADA) under various operational conditions. The operational conditions to be represented (or accounted for) are:

(a) Solar array dynamics.
(b) Slip ring friction.
(c) Rotational rates (for sun acquisition and sun-tracking modes).

The system dynamics test rig illustrated in Figure 7 was designed and fabricated to represent the appropriate solar array torsional modes and the slip ring friction. The inertia and stiffness of the simulated solar array and the friction of the simulated slip ring can be adjusted to represent various operational conditions of interest. The drive system can be commanded to run at a variety of rotational rates including those corresponding to typical sun-acquisition and sun-tracking modes for geosynchronous and low-earth orbits.

The main indicator of system performance is the continuity of motion achieved at the SADA output. This parameter readily indicates any problems in the system such as temporary stalling, excessive stick-slip effects or solar array excitation. The relationship between continuity of motion and levels of spacecraft disturbance and solar array excitation was discussed above. Since the predicted discontinuities in the SADA output motion are low, the question of measurement techniques is important.

Dynamics analyses discussed above indicated that the expected discontinuities in rotational rate have amplitudes of 0.0001 to 0.0007 degree and periods of 23 to 170 milliseconds (frequencies of 4-60 Hz approximately).

Two alternatives were considered for determining these discontinuities:

(a) Position or rate sensing.
(b) Acceleration sensing.

Position or Rate Sensing

The predicted amplitudes of the discontinuities are so low that extremely high resolution position sensing is required to measure them to, say, 0.00005 degree. The only feasible techniques identified were either an inductosyn resolver or an optical encoder-resolver, both with digital interpolation electronics. The required resolution is equivalent to a 23-bit encoder. The

sensor generates position versus time data from which the velocity profile of the drive output can be derived.

Several drawbacks were identified with this approach:

o   The sensor is a special, long-lead and expensive device.

o   The sensor would have to be mounted extremely accurately to the SADA/array interface or would require its own precision bearing system with flexible coupling to the SADA shaft.

o   The significant rigid inertia of the sensor rotor would affect the dynamics.

Acceleration Sensing

To overcome the disadvantages associated with the use of the high-resolution position sensor, an alternative approach involving an accelerometer to sense the discontinuities was developed. In this case a high-resolution linear accelerometer is mounted on a stiff, light moment arm attached to the output shaft. The accelerations due to the discontinuities in motion can then be detected and integrated to obtain the velocity profile as shown in Figure. 8.

The limited bandwidth of the accelerometer is predicted to result in some truncation of the acceleration spikes at initiation and termination of each discontinuity when these occur at the higher end of the frequency range identified above, i.e., 20-60 Hz. This, in turn, will result in errors in the velocity profiles derived by integration of the accelerometer output and is illustrated in Figure 8. However, this is not considered serious because:

(a) The errors only become significant at frequencies corresponding to performance considerably better than the continuity of motion requirements derived above.

(b) The velocities can be corrected to some extent by reference to the average orbital rate.

CONCLUSIONS

A constant-speed solar array drive has been developed which offers significant improvements in the levels of spacecraft disturbance and solar array excitation compared with more traditional intermittent and stepper drives. The required continuity of motion has been achieved with an open-loop system using an optimum combination of small prime step angle in the motor, electronic step division, and reduction gearing. This largely preserves the simplicity associated with open-loop stepper drives. The two-stage regenerative planetary gearset is an interesting variation on the harmonic drive conc pt.

An engineering model drive system including the ministepping electronics has been fabricated and is currently undergoing a series of tests. Of particular interest is the method of measuring the achieved continuity of motion at the output under various operating conditions. A novel approach was adopted involving a sensitive linear accelerometer mounted on a stiff, light moment arm attached to the output shaft of the drive system. The accelerometer signal can be processed in a variety of ways to derive the angular velocity profile, frequency spectrum, etc.

The design and test techniques described in this paper are applicable to other low-speed mechanisms such as robot arm joints and pointing drives for large antennae.

ACKNOWLEDGEMENTS

TABLE I SPACECRAFT DATA

A. MASS PROPERTIES		

MASS
Mol - ROLL
   - PITCH
   - YAW
	:
	:
	:
		6,750 kg
		52,000 kgm^2
		32,000 kgm^2
		46,000 kgm^2

B. FREE-FREE MODES OF SPACECRAFT AND ANTENNA		
MODE NO.	AXIS	FREQUENCY
7	ROLL-YAW	0.167 Hz
8	PITCH	0.176 Hz
9	ROLL-YAW	0.243 Hz
C. SOLAR ARRAY FIXED-BASE TORSIONAL · **(PITCH-AXIS) MODES**		
MODE NO.	FREQUENCY	MODAL INERTIA
1	0.0984 Hz	113 Kgm^2
3	0.1487 Hz	80 Kgm^2
D. ACS PITCH AXIS		
POINTING REQUIREMENTS	:	± 0.03°
MOMENTUM CAPACITY	:	± 10 Nms
SATURATION TORQUE	:	0.1 Nm
NATURAL PERIODS	·	13s AND 125s

TABLE II   DRIVE SYSTEM DESIGN REQUIREMENTS

DRIVE TORQUE - (3 cx WORST-CASE RESISTING TORQUES)	16 Nm, MINIMUM
SOLAR ARRAY ORIENTATION - POINTING ACCURACY - DEVIATION BETWEEN NAND S WINGS - SUN-TRACKING RATE - SUN-ACQUISITION RATE	± 2.0° 0.2° 1 REVOLUTION PER DAY 0.27° PER SECOND
INDUCED SPACECRAFT DISTURBANCE (PITCH-AXIS) - POINTING ERROR - REACTION WHEEL TORQUE - REACTION WHEEL MOMENTUM CHANGE	0.03°, MAXIMUM 0.1 Nm, MAXIMUM 1.0 Nms, MAXIMUM*
* 10% OF TOTAL REACTION WHEEL CAPACITY FROM TABLE I	

TABLE III   GEAR DATA

A. FIRST STAGE : EXTERNAL SPUR SET	

NUMBER OF TEETH ON PINION
    NUMBER OF TEETH ON GEAR
    RATIO =200 / 34
	: 34
	: 200
	= 5.88

MODULE (DIAMETIAL PITCH)
    PRESSURE ANGLE
    EFFICIENCY, NOMINAL
	: 1.06 mm (24)
	: 20°
	: 98%

B. SECOND STAGE : REGENERATIVE PLANETARY SET	

NUMBER OF TEETH ON PLANET
    NUMBER OF TEETH ON FIXED RING
    NUMBER OF TEETH ON ROTATING RING
    RATIO = $\dfrac{98 \times 27}{(98 \times 27) - (96 \times 27)}$
	: 27
	: 96
	: 98
	= 49

MODULE (DIAMENTRAL PITCH)
    PRESSURE ANGLE
    EFFICIENCY, NOMINAL
	: 0.94 mm (26.889)
	: 22.5°
	: 30%

FIGURE 1 SPACECRAFT CONFIGURATION
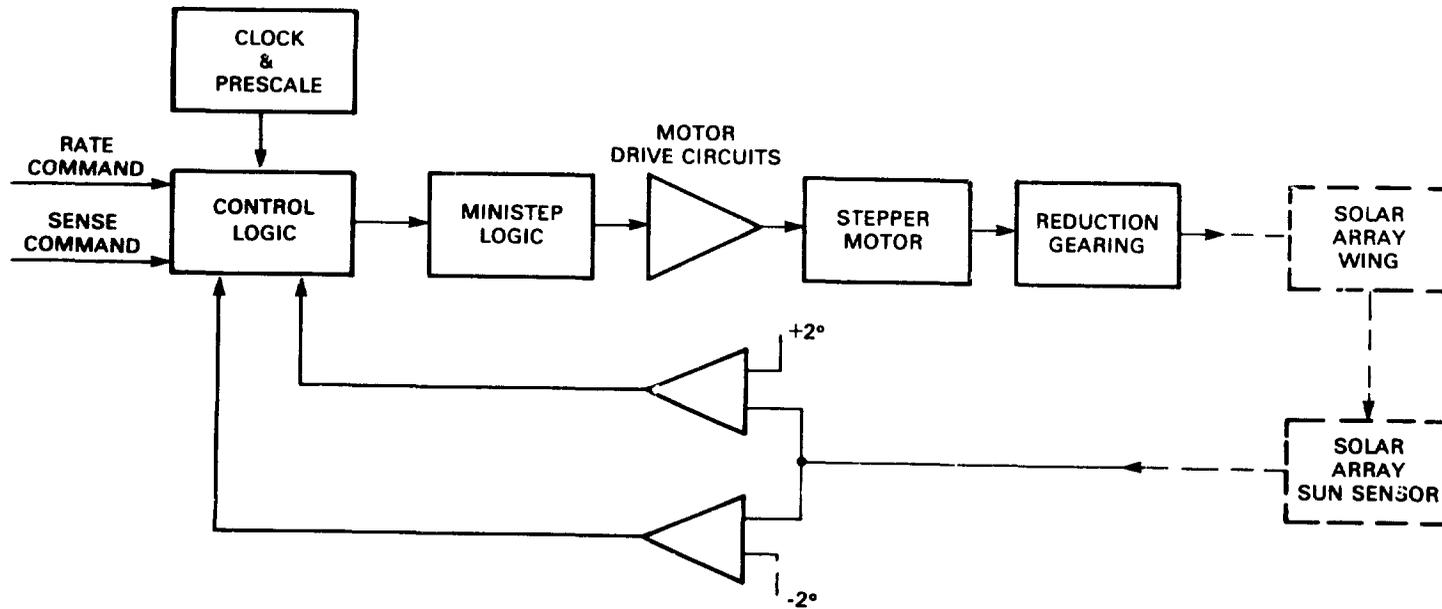
FIGURE 2   DRIVE SYSTEM BLOCK DIAGRAM

113
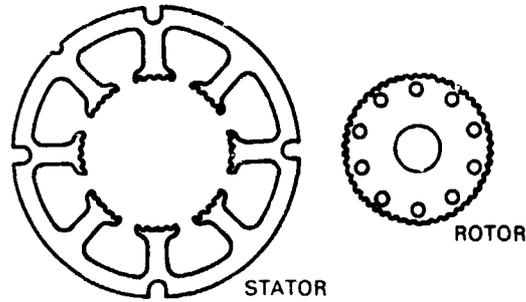
MOTOR LAMINATIONS SHAPES

DRIVE AMPLIFIEΓ (4 PLACES)

MOTOR AND DRIVER SCHEMATIC

WINDING CURRENT

1 PRIME STEP

SINUSOIDAL MINISTEP DRIVE SEQUENCE
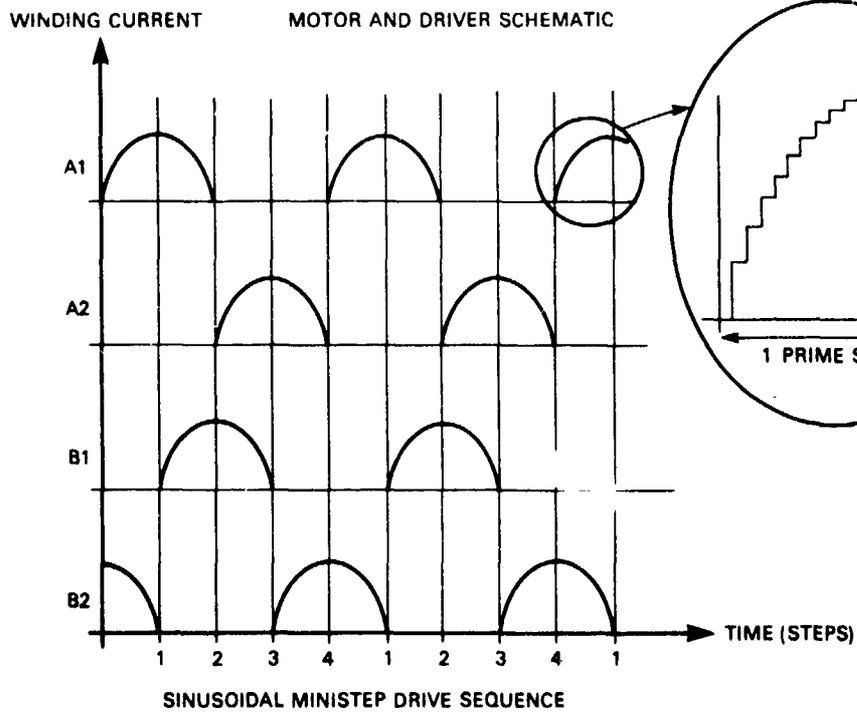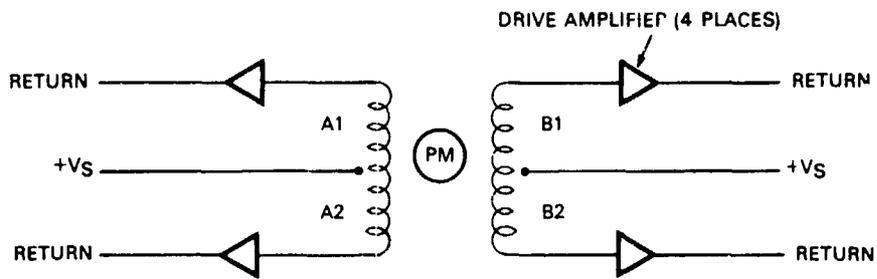
FIGURE 3   MOTOR DETAILS AND DRIVE SEQUENCE
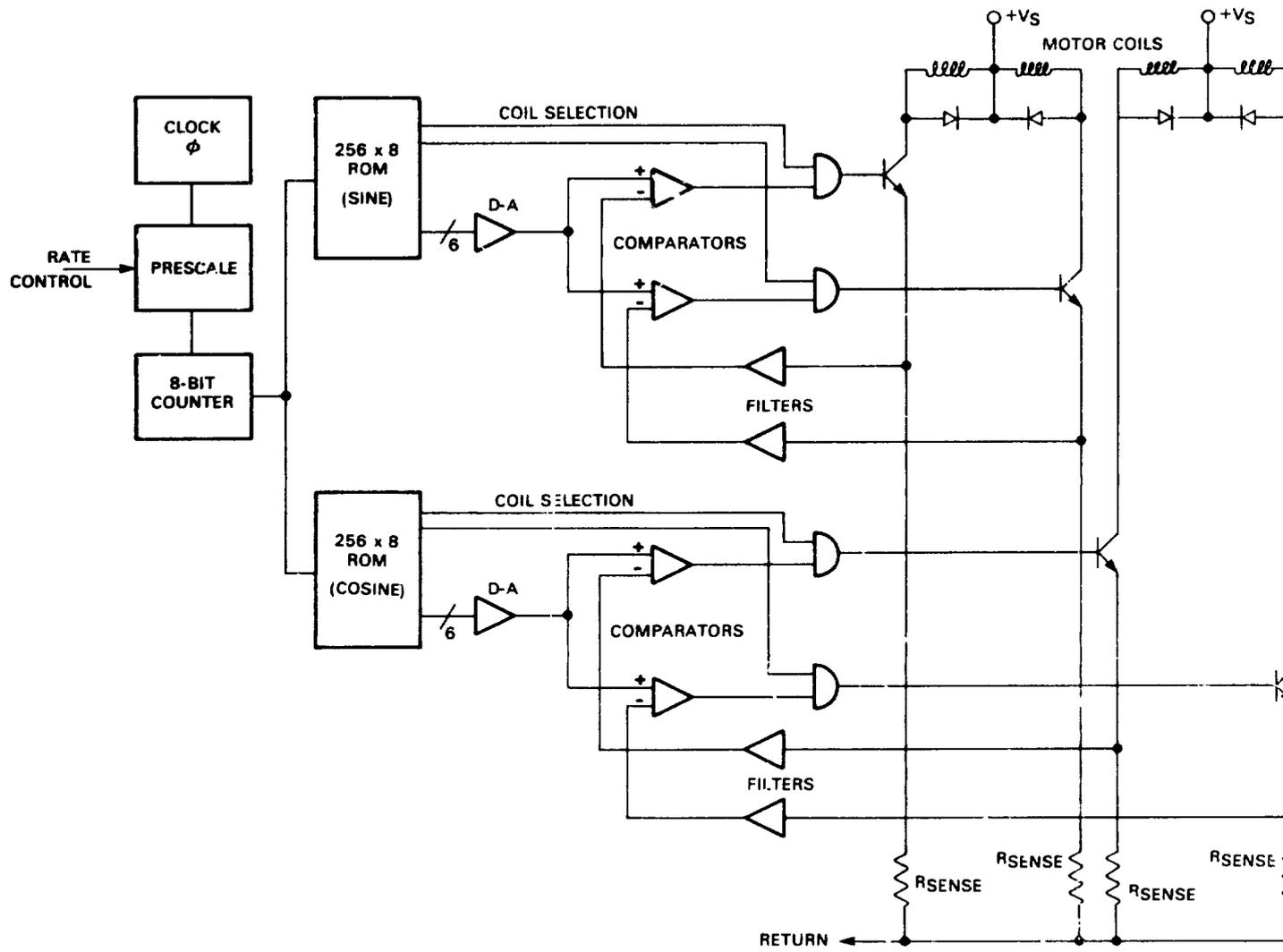
FIGURE 4   SCHEMATIC OF MINISTEPPING ELECTRONICS

MOTOR-ENCODER
(2-PLACES)

1ST STAGE
GEARSET
(5.88:1)

MAIN BEARING
(1 OF 2)

OUTPUT

2ND STAGE
PLANETARY
GEARSET
(49:1)
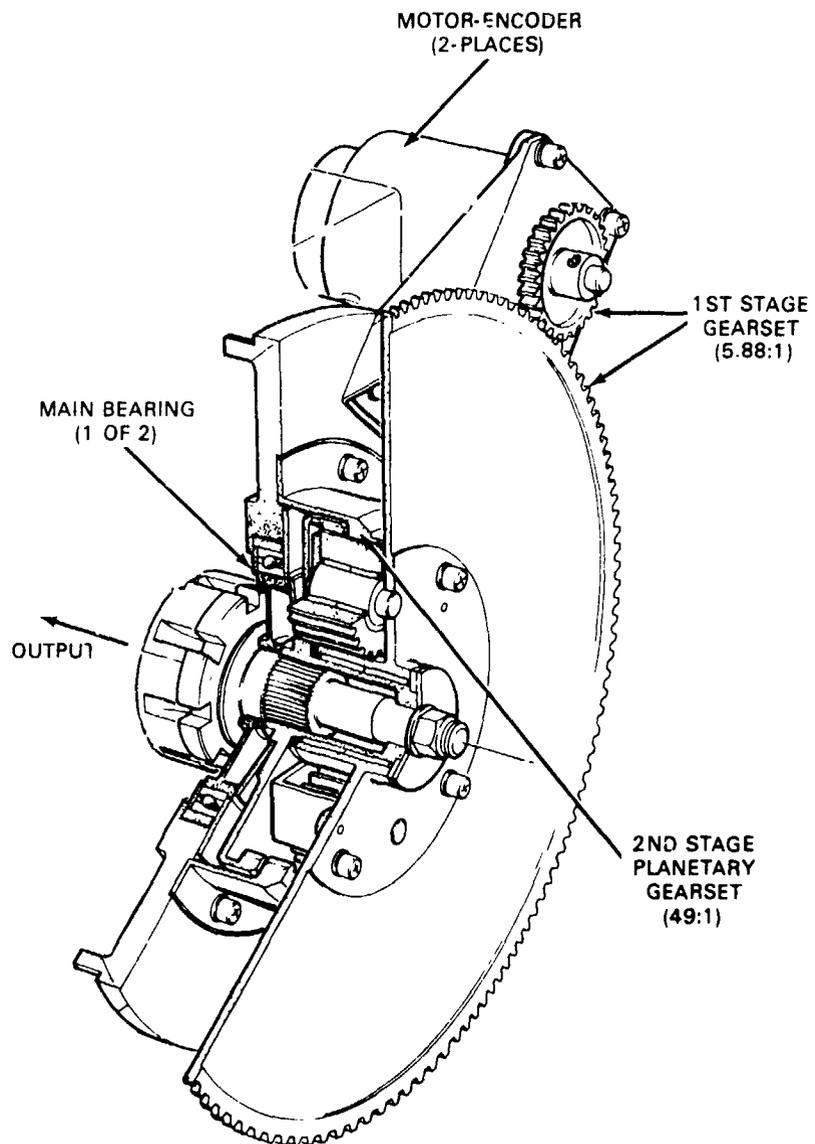
FIGURE 5   CUTAWAY ILLUSTRATION OF REDUCTION GEARING
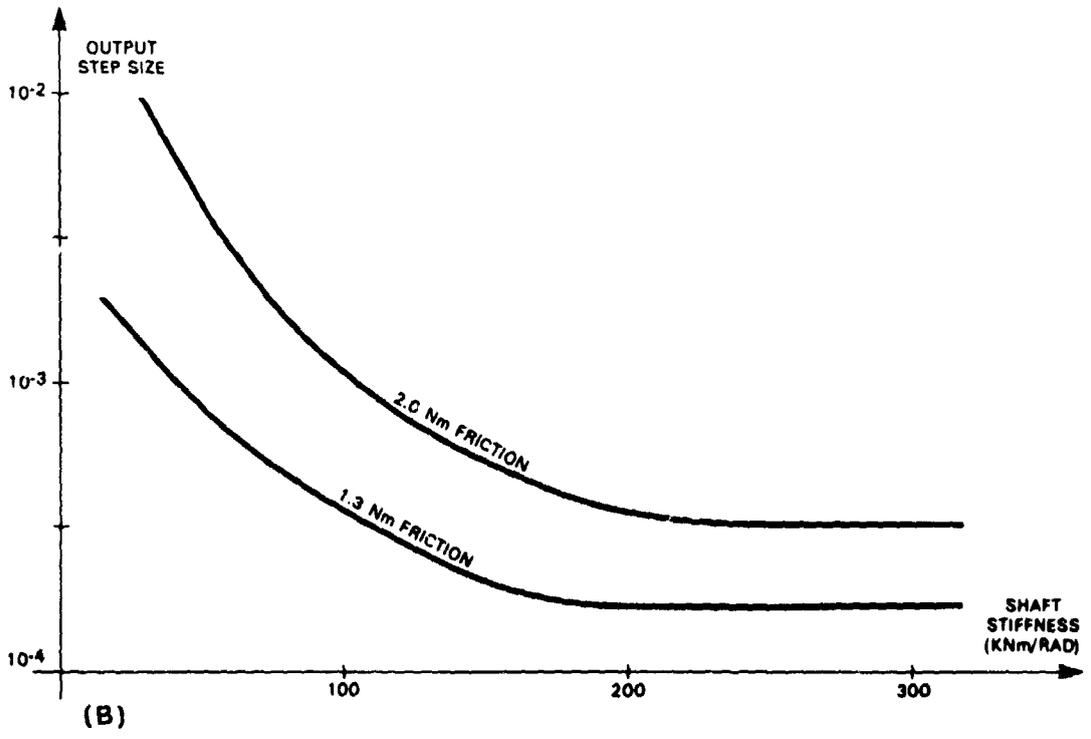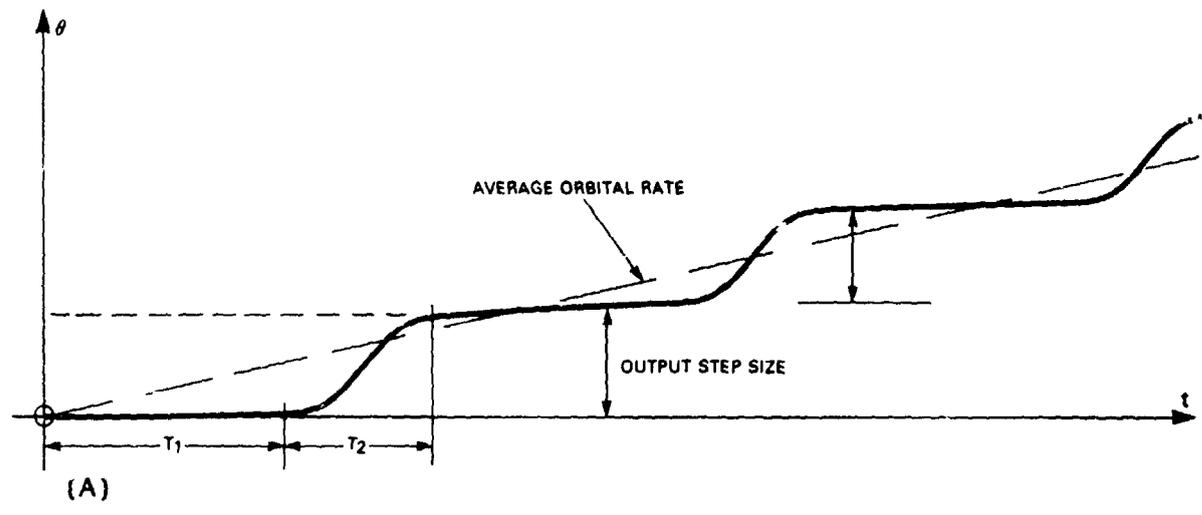
FIGURE 6   STICK-SLIP MOTION AND EFFECTS OF FRICTION AND STIFFNESS

117
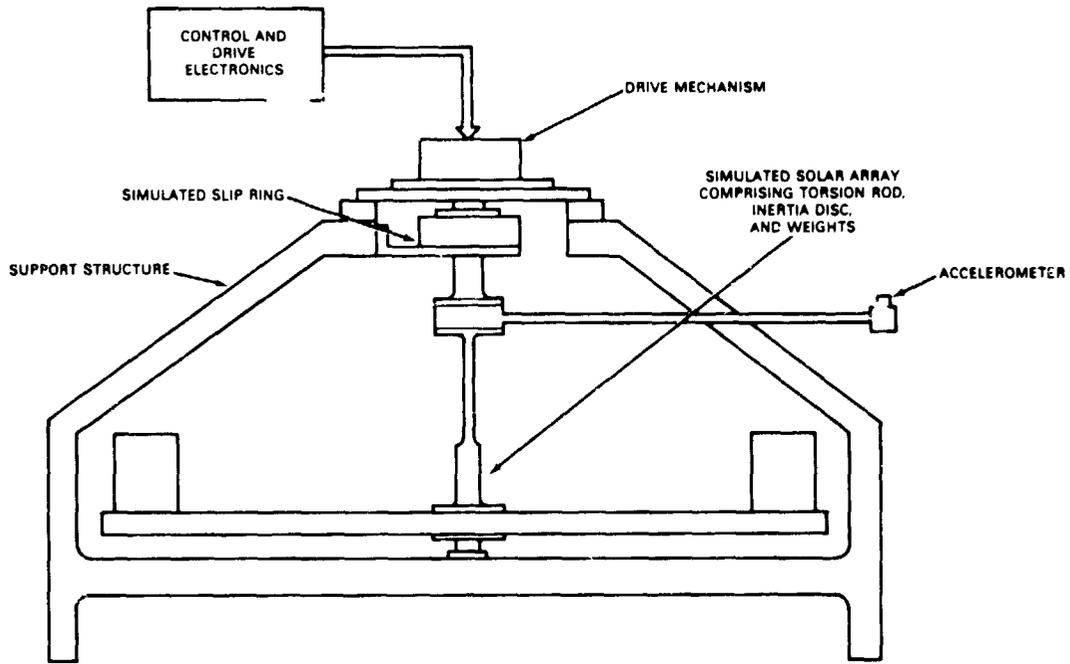
FIGURE 7   SYSTEM DYNAMICS TEST RIG
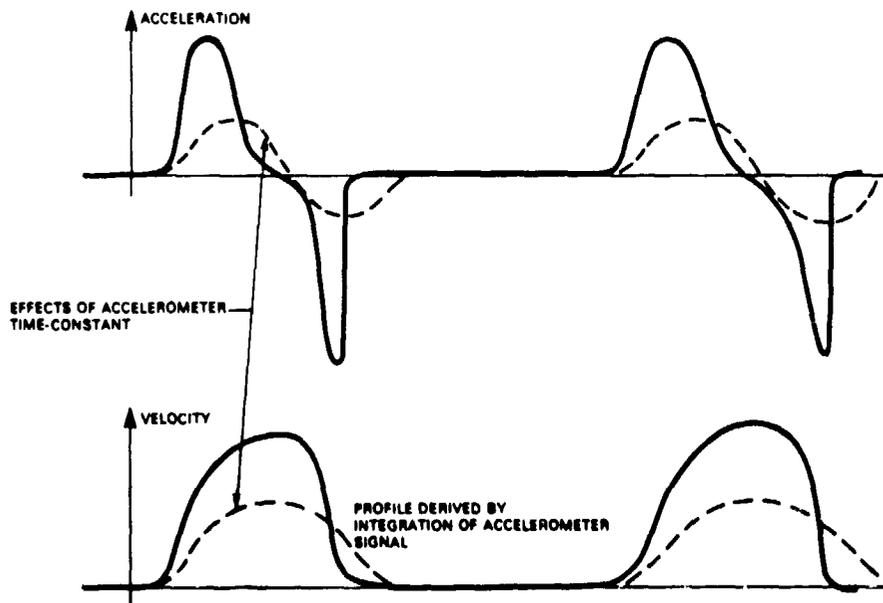
FIGURE 8   DETERMINATION OF CONTINUITY OF MOTION

APPLICATION OF TRACTION DRIVES AS SERVO MECHANISMS

by

Stuart H. Loewenthal, Douglas A. Rohn, and Bruce M. Steinetz*

ABSTRACT

The suitability of traction drives for a wide class of aerospace control mechanisms is examined. Potential applications include antenna or solar array drive positioners, robotic joints, control moment gyro (CMG) actuators and propeller pitch change mechanisms. In these and similar applications the zero backlash, high torsional stiffness, low hysteresis and torque ripple characteristics of traction drives are of particular interest, as is the ability to run without liquid lubrication in certain cases. Wear and fatigue considerations for wet and dry operation are examined along with the tribological performance of several promising self-lubricating polymers for traction contracts. The speed regulation capabilities of variable ratio traction drives are reviewed. A torsional stiffness analysis described in this study suggests that traction contacts are relatively stiff compared to gears and are significantly stiffer than the other structural elements in the prototype CMG traction drive analyzed. Discussion is also given of an advanced turboprop propeller pitch change mechanism that incorporates a traction drive.

INTRODUCTION

An interesting but not particularly well known class of speed changing mechanisms utilize traction as the means to transfer torque. Applications range f.om dry contacts such as the locomotive wheel against the rail and elastomer coated rollers in paper handling equipment to lubricated contacts in industrial adjustable speed traction drives.

As power transmissions, few mechanical drives match their low noise, smooth torque transfer characteristics and speed regulating accuracy. However, their suitability as servo drive mechanisms has not been given wide attention. For some control system applications, their ability to provide a smooth transfer of motion with relatively low hysteresis losses and high torsional stiffness while producing no detectable "backlash" upon direction reversal are obviously beneficial qualities. On the other hand, traction drives are unsuitable for point-to-point (PTP) positioning applications where it is impractical to feedback output position.

The discussion which follows is intended to provide greater insight into some of the performance characteristics of traction drives which may lend themselves to certain servo mechanism applications. A number of examples will be cited, as known to the authors, to help illustrate some of the prior art along with a few applications presently under consideration. Due to the broad

---

*NASA Lewis Research Center, Cleveland, Ohio

nature of this technology and the space limitations set forth here, this review can only hope to touch upon some of the more relevant design considerations. While published information on traction drives is considerably more limited than other types of transmissions, particularly in terms of servo mechanism applications, a significant design data base does exist, as can be found in references 1 to 3.

BACKGROUND

The earliest of speed changing mechanisms used smooth wheels of unequal size in frictional contact. According to his writings, Leonardo Da Vinci devised and experimented with several machines which incorporated frictional wheels. One such machine was for the grinding of lenses or polishing of mirrors where the repetitive toothing errors from gearing would produce imperfect surfaces.

Because of their simplicity and their unique ability to smoothly and continuously regulate speed, friction drives or traction drives, as they are now known, found use in a host of applications. Some early examples include wood working machines (circa 1870) in which the wood feed rate was regulated with friction drive rollers and turn-of-the-century motor cars equipped with continuously variable, friction disk transmissions (ref. 1). More modern examples of feed regulating and loading applications can be found in paper and film handling equipment including printing and copying machines and computer plotting devices. In these applications, the processed material is normally "pinched" between an elastomer-coated drive roller and another that freewheels, such as that used in multicolor printing operations to register the paper. Analogous space vehicle applications include a pinch roller drive mechanism for deploying a spool-wrapped antenna for the Helios B satellite (ref. 4) and one that dispenses and stores a transfer boom for Skylab (ref. 5).

Philosophically, "linear" traction drives include a wide class of vehicles ranging from bicycles to locomotives. This later example of the wheel/rail contact vividly illustrates that traction power transfer need not be limited to trivial load levels. In fact, advanced, light-weight helicopter transmissions (Fig. 1) which incorporate steel traction rollers lubricated with synthetic traction fluids have been tested at the authors' laboratory at power levels to 370 kW (ref. 1).

Although not a mature discipline, design techniques for traction drives have made good progress in recent years. Based on lubrication, fatigue and performance models developed originally for rolling-element bearings, analytical methods are now available to size traction drive contacts for a specified reliability level and to make reasonable estimates of power loss and traction capacity limits. Metallurgical improvements in the fatigue resistance of bearing steels coupled with the commercial introduction of high traction fluids have increased the power capacity of traction drive contacts by several fold. While an extended discussion of these technical advancements is not central to this review, helpful design information can be found from several sources (refs. 1 to 3).

TRACTION DRIVES AS SPEED REGULATORS

Apart from their basic mechanical simpli ity, the most sought after characteristic of traction drives is their ability to provide mechanical stepless speed control over wide ratio ranges, with some units being infinitely variable. In this regard, traction drives have been performing light to medium duty (up to 75 kW) speed matching for industrial machinery for more than 50 years (refs. 1 and 2). Applications range from knitting and fiber-spinning equipment to milling machines and high-speed grinders (ref. 2). There are more than 2 dozen commercial manufacturers of variable ratio traction drives, with some designs dating back to the 1920s. Operating lives of 20 years or more are not uncommon in factory environments.

A sample of commercially available, adjustable speed traction drive geometries appears in Fig. 2. Speed regulation is achieved by altering the rolling radii ratio between input and output member. This is accomplished by either tilting or translating an intermediate transfer element or through direct translation of input or output members. Normally a manual vernier control element is used for this positioning, although feedback control has been used on some aerospace applications. With manual control, output speed regulation and repeatability is often with ±0.1 percent under uniform loading. Under extreme no-load-to-full-load fluctuations, maximum output speed variations are typically 1 to 2 percent. However, with suitable servo controls, accuracy can be restored back to the 0.1 percent level (ref. 6).

TRACTION CURVE

The speed variation between traction rollers due to torque transfer is generally referred to as "creep" (ref. 3). Traction drives are designed to operate along the linear ascending portion of the traction curve (Fig. 3) at some point below the peak. A ball or roller-ramp loading mechanism (Fig. 4) is commonly used to increase the clamping force between roller elements in proportion to the transmitted torque. The angle of the ball ramp is tailored to the lubricant-contact condition. It is selected so that the ratio of the applied tangential to normal force, or traction coefficient, is about 20 to 30 percent less than the maximum available traction coefficient under the least favorable operating condition. This provides some margin against slip. With a torque sensitive loading mechanism, gross slip will not occur, even at torque levels which exceed the elastic limit of the rollers or structural material. This loading action is not unlike the behavior of a roller ramp or sprag-type clutch. Improved part load efficiency and extended service life are additional benefits from modulating the clamping force with the demand load. Maximum efficiencies of adjustable speed traction drives typically range from 85 to 93 percent. However, multiple contact fixed ratio traction drives have efficiencies of about 96 to 97 percent, with single contact systems being as high as 99 percent.

Operating creep rates of traction contacts are relatively small. They range from 0.1 to 0.2 percent for dry contacts or those lubricated with traction fluids at low speeds (Fig. 3), to 3 or 4 percent for lightly loaded, high speed contacts lubricated with mineral oils. This speed difference is

not due to slip between driver and driven roller but is, in fact, the accumulated lost motion due to the tangential stretching and compressing motion or compliance occurring at the roller contact interface. It is well known that a "locked" or "zero slip" region exists at the leading edge of the contact and only at the peak traction point, i.e., point of impending slip, will this region completely disappear. Nevertheless, this lost motion due to creep precludes the use of traction drives for open-looped positioning devices. However, open-looped speed regulation accuracies of +0.5 percent or better are achievable with an automatic loading mechanism over a wide range of speeds and torques based on test data for a 14:1 fixed ratio traction drive reported in reference 7.

It is instructive to note that the creep or slide-to-roll rates associated with traction drives are generally one to two orders of magnitude smaller than those associated with gear teeth as they enter and leave mesh. Under difficult to lubricate conditions, such as those that exist for most space mechanisms, the fundamental rolling nature of a traction contact is a decided benefit in terms of reduced wear and heat generation. This was clearly demonstrated at the authors' laboratory where a 10.8:1 ratio planetary traction drive (Fig. 5) survived 1 hour of repeated full power acceleration (11 kW at 9×10^4 rad/sec^2) tests from 0 to 70,000 rpm while submerged in LOX (ref. 1). Test life was equivalent to 2×10^6 revolutions of the high-speed shaft. Expected gear life under comparable conditions would be a maximum of about 15 or 20 minutes due to excessive wear under this hostile lubrication condition. Furthermore, a similar but 120:1 ratio traction drive was tested fully preloaded for 43 hours at 360,000 rpm without failure using no liquid lubrication whatsoever (ref. 1). Such speeds are, in all likelihood, beyond the realm of even oil lubricated gears.

DURABILITY

Fatigue

The falure modes of traction drive contacts are very similar to those of ball and roller bearings. This is not surprising since the operating stresses, materials (normally hardened bearing steels), contact geometries and surface finishes as well as lubrication conditions are also very similar. As with rolling-element bearings, fatigue or pitting is the likely failure mode when the quality of lubrication is good, that is when the ratio of lubricant film thickness to composite surface roughness or lambda ratio is above about 1.5. Statistical fatigue life can then be predicted from a modified form of the Lundberg and Palmgren theory that is traditionally used to determine service life ratings of commercially available ball and roller bearings. Details of this method can be found in reference 3. In general, fatigue life L is related to size, torque T and available traction coefficient μ as follows:

$$L \propto \text{size}^{8.4} \quad \text{at constant T and } \mu$$

$$L \propto T^{-3} \quad \text{at constant size and } \mu$$

$$L \propto \mu^3 \quad \text{at constant size and T}$$

Thus a 9 percent increase in size or a 26 percent increase in μ will double the fatigue life at constant torque capacity or, in turn, cause a 26 percent increase in torque capacity at constant fatigue life.

Wear

As the quality of lubrication or lambda ratio diminishes, the degree of asperity contact and surface distress increases and the failure mode shifts from predominantly fatigue to one that is predominantely wear. It is this mixed or boundary lubrication regime where most low speed space mechanism contacts must operate.

Solid lubricant films formed from graphite, MOS_2, PTFE or those from soft metals such as lead, gold or silver are potential substitutes for liquid lubricants and greases in the low lambda regime. The general increase in friction coefficient attendant with some dry film lubricants is obviously beneficial for traction drive contacts, allowing some reduction in the required clamping loads. However, the normal concerns of using dry film lubricants still remain, namely their non-renewable nature, the integrity of the film/substrate bond and the detrimental accumulation of wear debris. Also, the somewhat erratic nature of a dry film's friction coefficient may preclude their use for certain torque-sensitive mechanisms. In such cases, low vapor pressure greases, such as the perfluoroether type, are normally preferred provided that potential contamination of optical surfaces are not a factor and evaporation rates are within operational life requirements. hard-faced, ion-sputtered or vapor-deposited coatings such as TiN and TiC avoid some of these problems (ref. 9), but their long-term fatigue resistance still requires better definition.

Polymers/elastomers. - Perhaps the most promising self-lubricating materials for traction drive actuators are some of the polymers and elastomers that have been successfully used for a variety of industrial roller type components. These range from molded polyurethane casters and wheels to polyamide (nylon), acetal and polyamide-imide (Torlon) thermoplastic bearings and gears. Many of these materials can be reinforced with glass fibers for strength and filled with graphite or PTFE for reduced friction. In addition to their self-lubicating abilities, these maintenance-free materials offer significant vibration damping, quietness of operation, low weight and corrosion resistance. The general tribological properties of a large number of these polymers is relatively well defined (ref. 9), but their specific performance as traction drive materials for use in space mechanisms is not as well understood. Specifically, their cold temperature and vacuum, traction and wear characteristics need better definition as does their stress relaxation (cold flow), radiation resistance, and outgassing behavior. Because contamination by liquid lubricants can markedly reduce their traction capability, use of these materials must be restricted to relatively clean environments, not unlike those required for other types of precision mechanisms. Despite these concerns, a surprisingly large class of polymeric materials have been applied successfully as structural, protective, dielectric

and sealing materials on spacecraft (ref. 10). Furthermore, because of their ability to self-lubricate and to resist cold welding even in a hard vacuum, they have also been used in mechanisms at points of sliding. Typical examples include phenolic ball bearing cages impregnated with dry or liquid lubricants and fine-pitched gears made from polyamide or acetal resin.

The load capacity of some commercially available polymers in sliding/rolling contact is surprisingly large. For example, table I lists some of the results of test programs sponsored by the authors' laboratory to define the traction capacity limits of several engineering thermoplastics. In these tests, the rolling failure load limits of six different thermoplastic rollers 50 mm in diameter in contact with equal sized steel rollers were determined in air at ambient temperature and pressure. From the rolling tests, two of these materials, an unfilled polyamide-imide and a cotton fiber phenolic, were selected for torque transfer testing near their peak traction capacity limits. The polyamide-imide resin withstood a remarkable 220 N/mm (1250 lb/in) of unit normal loading at a rolling speed of 10 m/s with 2 percent sliding for 30 minutes of testing without damage. A narrow roller, just 5 mm wide, of this material transmitted 4.8 kW of power continuously for 10 minutes at 20 m/s without failure. While the performance of some of these commercially available thermoplastics clearly exceeds any of those anticipated for servo mechanisms applications, these results do suggest that plastics could be used in place of steel for certain low-cost, moderate power, traction speed regulators.

Polyimides are another class of polymer which offers promise as a low-wear, high-traction material. Polyimide films have excellent UV radiation resistance and vacuum stability, being used extensively on spacecraft for thermal blanket insulation and a variety of external semistructural applications (ref. 10). In addition, some polyimides have unusually high-sliding wear resistance. For example, ambient pin-on-disk experiments with an experimental, partially fluorinated polyimide pin sliding against a steel disk showed it to have an average friction coefficient of 0.8 and an average wear rate of 5×10^{-15} m^3 per meter of sliding at sliding speeds of 2.7 to 3.1 m/s (ref. 11). At this wear rate, it would take 1×10^9 revolutions for a 10 mm wide, relatively heavily loaded traction roller made of this polymer to wear off a 1 m thick layer of material, assuming a relatively high 1 percent slide-to-roll ratio.

Another potentially useful class of materials for traction rollers are vulcanized natural and synthetic rubbers. Some guidelines for the speed/load limits of these elastomers for general traction drive service can be found in reference 3. Polyurethene rubbers are particularly durable, having been used in difficult service conditions such as when molded to forklift truck wheels and subway train tires. Furthermore, polyurethane molded rollers have already been used without failure for one type of traction drive, space qualified, rotary actuator known to the authors. Its traction capacity in a vacuum is high. Sliding friction tests of a molded polyurethane wheel, meeting MIL-R-3065 specifications, exhibited a friction coefficient from 0.7 to 1.3 against an aluminum or magnesium concave slider in a vacuum of 10^{-5} torr at room temperature (ref. 12). Since all elastomers stiffen to some extent at

low temperatures, working traction coefficients would have to be less than this if a temperature controlled environment was impractical.

SERVO MECHANISM APPLICATIONS

While traction drives have had a well established history of use as power transmitting speed changers, their use in servo systems has not been as broad in comparison. This is somewhat unexpected since the typical low power, low speed, low backlash and low starting friction requirements of such applications are particularly well suited to the capabilities of traction drives. In many positioning applicatins such as CMG gimbal drives, the torques may be high but because the speeds are typically low, the buildup of wear or fatigue stress cycles is also low. In addition, the available traction coefficient of a lubricant is greater at low operating speeds. Under these conditions, the traction drive elements can be made relatively small and still provide adequate service life.

Furthermore, smooth rollers in driving contact avoid the meshing errors and torque discontinuities of gear teeth as the load is transferred from one pair of teeth to the next. Since rollers are always in continuous driving contact no matter the direction of tangential loading, backlash is precluded. However, the accumulation of microslip in the contact gives rise to a hysteretic type torque-deflection loop that requires some form of feedback control for high precision positioning systems. As previously discussed, speed regulation accuracies as low as ±0.1 percent can be achieved manually under favorable conditions, although about ±1 percent is probably more representative of a well-designed, open-loop traction drive.

Representative Servo Applications

One prominent example of a traction type aerospace servo mechanism is the Lucas, constant speed drive flying on the AV8-A Harrier VSTOL jet fighter operating in North America and Europe (ref. 1). This toroidal-type roller drive, similar in geometry to that shown in Fig. 4, maintains a constant 400 Hz frequency a.c. generator output within ±1 percent from a variable turbine speed input which ranges from 3250 to 8000 rpm. It delivers 13 kW for driving aircraft generators having output ratings up to 30 kVA. It does so with a power-to-weight ratio that is 10 percent better than comparable equipment with considerably lower maintenance costs. In the 50s, Avco Lycomming offered a similar line of toroidal traction drive type constant speed drives. These flew on several commercial and military aircrafts, including the Lockheed C-121, Douglas A-4E and Grumman S-2D. The servo mechanism performance characteristic of toroidal traction drives were investigated in reference 6. Experimental performance data on a 1 hp prototype model indicated that a velocity control accuracy of ±0.1 percent can be readily obtained with transient-response times varying from 20 to 40 ms depending on signal amplitude and load conditions.

Another example of a speed regulation traction mechanism, but a nonservo type, is a ball type continuously adjustable variable ratio drive which

synchronizes the digital counter readout of a commercially available liquid flow volume meter. The drive couples the positive displacement fluid rotor to the meter's counter. A vernier adjustment screw is used to vary the speed ratio in 0.02 percent increments between the metering rotor and the counter so that accurate readings are obtained when the meter is calibrated against some "master" meter or other liquid volume test standard.

Traction type linear actuators are also commercially available. These units are useful for a wide range of positioning and motion applications particularly where jamming and overload protection are required. In one design, three equally spaced, skewed rollers located on each end of a two piece, spring-loaded, clamping block are loaded against the surface of the smooth, rotating drive shaft. The angle of roller skew relative to the drive shaft axis is directly related to the amount of linear travel of the block per drive shaft revolution or "lead." The thrust capacity at slip can be easily varied by adjusting the screws which vary the spring clamping load. If the linear element would hit its stop or jam, the rollers would automatically slip at the set thrust level and be automatically reset for operation when the jam was relieved.

OPERATING CHARACTERISTICS

In comparison with gear type servo mechanisms, traction drives possess several desirable operating characteristics. These can be summarized as follows:

(1) Zero backlash
(2) High torsional stiffness
(3) Low starting friction or breakaway torque
(4) Low torque ripple
(5) Low velocity errors
(6) High torque density and compactness
(7) Infinite resolution of speed or ratio adjustment

In addition to these features, the roller contact due to its low sliding nature can be designed to operate for extended periods of time without liquid or grease lubrication. As previously discussed, this can be accomplished by either using high traction solid film coatings such as ion-plated gold or silver or using advanced, low-wear polymers such as partially fluorinated polyimides or polyamide-imides. The elimination of a depletable liquid lubrication is a decided benefit for spacecraft mechanism applications.

Furthermore, rollers, unlike gears, have the ability to harmlessly slip at predetermined traction limits. The over torque, release-clutch-tendency can prevent catastrophic damage if jamming should occur at some point in the mechanism drive train.

Finally, in the case of dual fault or multiply redundant servo drive mechanisms, such as those for some spacecraft applications, independent, multiple drive rollers can be readily engaged and disengaged from drive

126

systems with conventional linear actuators wihout the need to stop the system from rotating or the need to provide proper tooth mesh phasing.

Stiffness

To achieve minimum response time for a point-to-point motion control or to increase responsiveness of a servo controller in general, it is necessary to maximize drive system torque-to-inertia ratio and stiffness. In reference 13 a method was presented for analyzing the torsional stiffness and hysteresis effects of a traction drive contact of arbitrary geometry under a wide variety of loading conditions.

Torsional stiffness K_T was found to increase with an increase in normal load N, available traction coefficient , shear modulus of the material G and roller radius R while decreasing with an increase in transmitted torque T. The exact expression for the stiffness of a crowned roller pair of equal size was given as:

$$K_T = \frac{\pi Ga}{\Gamma}\left(1 - \frac{T}{\mu NR}\right)^{1/3} R^2 \qquad (1)$$

where a is the semiwidth of the elliptical contact and   is a contact geometry parameter.

Another finding of the study performed in reference 13 was that the traction contacts themselves are considerably stiffer than the bearings and other structural elements in a complete traction drive system, typically accounting for only several percent of the drive's total compliance.

A comparison of the theoretical stiffness of equally sized gear and traction roller pairs made of steel showed that traction contracts were typically two or three times stiffer than gears under comparable loads. This is illustrated in Fig. 6 where the stiffness of traction contacts relative to comparably sized and loaded gears is plotted as a function of gear tooth size diametral pitch). The method used to analyze gear stiffness considers the local Hertzian normal compliance and tooth beam bending. It also considers standard undercut and fillet bending and shear as well as foundation flexibility (ref. 13).

It is apparent from Fig. 6, that gear mesh stiffness is relatively insensitive to the number of teeth or the torque level and fluctuates between two relatively discrete levels as the load is transferred between single tooth and double tooth contact. Apart from the kinematic (unloaded) errors, this stiffness fluctuation contributes to velocity fluctuations in a loaded gear train. In contrast, the stiffness of a traction drive contact is essentially constant for a given load, although some degradation with increased transmitted torque will occur as shown.

Hysteresis/Backlash

A major advantage of a traction positioning mechanism is the absense of backlash. However, due to the inelastic displacements or microslip that occurs in certain regions of the contact, some hysteretic losses will be present during torque reversals. A comparison of predicted and measured hysteresis and stiffness of a 9.5 mm steel ball against a flat appears in Fig. 7. The experimental data were taken from the investigation appearing in reference 14. For a maximum applied torque value of 100 N-mm, which is 67 percent of the peak slipping torque, the width of the predicted hysteresis loop was 8.2 arc seconds.

In the case of gears, the total lost motion along the displacement axis at zero torque is due to backlash. As a practical matter some backlash allowance is required for all gear sets to prevent meshing interference from gear runout, tooth-to-tooth spacing errors, center distance variations, and thermal and structural deflections. This group of backlash sources is also responsible for the bulk of transmission error (gear train position error). Increasing the quality or precision of the gear set as well as using finer pitched (smaller) gear teeth will help to minimize but not totally eliminate both backlash and transmission error. Philosophically speaking, increasing diametral pitch to the limit, one ends up with a gear having an infinite number of infinitely small teeth, that is, a roller having neither backlash or transmission error.

For servo positioning mechanisms that "hunt," such as most pointing and tracking systems and most gimbal drives, the stiffness and backlash characteristics of the drive train at or near the torque reversal crossing point is of prime importance. At this crossing point, some means must be employed to eliminate the precipitous loss in both stiffness and output position sensitivity as the teeth move freely through the backlash clearance. Otherwise a serious discontinuity in the control system algorithm will be created. The means of eliminating or minimizing backlash take various forms, with spring loaded split gears and preloaded, auxiliary antibacklash gear trains being among the more common.

The traction contact, on the other hand, shows no such backlash discontinuity or "deadband," as illustrated in Fig. 7. In fact, stiffness is not only preserved at the zero torque crossing point but actually reaches a maximum there (Figs. 6 and 7). The noticeable but steadily continuous drop in stiffness at the higher torque levels is usually of lesser importance from a servo viewpoint. However, in some applications it may be desirable to "marry" the best servo drive characteristics of rollers and gears.

Roller-Gear Drives

A novel geometric arrangement that combines traction rollers with gears in parallel was devised by Dr. A. L. Nasvytis in the early 1960s (ref. 15). In the roller-gear drive, as it is termed, the center portion of the roller is replaced with a spur gear. The rollers not only serve to transmit a portion of the torque but also provide a support bearing function since their diameters are equal to the pitch diameter of the gear. Helicopter transmissions of 370, 820, and 2760 kW using a multiple-row roller-gear drive planetary stage have been built and tested. Unusually high efficiencies of up to 99 percent have been recorded due to the nearly ideal positioning of the roller gear elements along the gear tooth's pitch point.

The performance of a 26:1 ratio, 400 ft-lb CMG rotary actuator which incorporated a roller-gear drive (Fig. 8) in combination with a brushless d.c. motor was evaluated in reference 16. The rollers, which share 25 percent of the torque in parallel with the gears, eliminated the effects of backlash and helped to minimize breakaway torque while adding substantial stiffness to the drive system. Static output torsional stiffness values of 680×10^3 N-m/rad (500×10^3 ft-lb/rad) or greater were measured at the zero torque crossing point. Breakaway or starting friction varied from 0.4 to 2.5 percent of rated torque. While no backlash was detected, a small degree of lost motion was measured that ranged from 2.9 to 4.7 arc seconds up to 25 percent of maximum torque. Tests of a similar but smaller 106 N-m (78 ft-lb) torque, 15:1 ratio roller gear/brushless d.c. motor servo drive were conducted in reference 17.

CMG Traction Drive

A 16:1 ratio, 435 N-m (320 ft-lb) output torque, CMG gimbal drive having two rows of stepped planet rollers is being prepared for tests at the NASA Lewis Research Center. This drive, which is shown in Fig. 9, incorporates traction rollers ion-plated with about 3000 angstroms of gold in dry rolling contact. It was designed to provide a minimum output torsional stiffness of 680×10^3 N-m/rad (500×10^3 ft-lb/rad) and to survive 1.6×10^6 operation cycles over a three year operating life. The drive itself is nominally 25 cm in diameter by 11 cm in length and weighs 10 kg. It is equipped with an automatic loading mechanism, similar to that illustrated in Fig. 4, that will be activated above some threshold torque value or initial preload level. The initial preload level can be set anywhere from nearly 0 to 100 percent of the full rated torque. High initial preload values will increase roller normal loads and, in turn, increase the initial torsional stiffness according to equation (1). However, some increase in breakaway torque will also occur. The initial preload setting for optimal response will be selected during system tests.

At the time of this writing, test results are unavailable. However, a breakdown of predicted drive component stiffness and compliance values appears in table II. It can be seen that the planet bearings are the single most torsionally soft element in the drive system, accounting for more than 33 percent of the total drive compliance. By comparison the combined effect of all the traction roller contacts themselves contribute only 14 percent of the drive's compliance.

TRACTION DRIVE PITCH CHANGE MECHANISM

A NASA program was started in the early 1970s to develop technology for an advanced turboprop (ATP) commercial aircraft capable of accommodating up to 150 passengers at a cruise Mach number between 0.7 and 0.8. Fuel savings for an ATP aircraft are projected to be on the order of 20 percent for single rotation (SR) and 30 percent for counter rotation (CR) propeller systems relative to comparable state-of-the-art turbofan engines without a significant compromise in engine noise or emissions. A technology area that has been identified as being critical to the successful development of an ATP aircraft is a highly reliable, efficient gearbox/pitch change mechanism (PCM) propeller drive system (ref. 18).

Due to the unusually high power levels (on the order of 10,000 kW) and large size propellers (on the order of 4 m in diameter) the blade reaction torque which must be carried by the PCM is more than an order magnitude larger than previous turboprop PCM systems. In addition, a goal has been established to increase the operating reliability of the drive system from today's 4000 to 8000 hour mean time between unscheduled removal (MTBUR) to greater than 20,000 hour MTBUR. Furthermore, the propeller blade angle control system must be sufficiently precise to synchrophase the clock position of multiple engine propellers and thus minimize the "beating" noise hitting the fuselage. In view of these new and challenging requirements, PCMs which embody advanced technology features are currently being investigated.

One promising approach being studied is the electromechanical PCM illustrate in Fig. 10. This system incorporates a compact, high-reduction ratio (210:1) hybrid traction drive, powered by an advanced technology, electronically commutated, permanent magnet (PM) synchronous motor. A similarly constructed PM synchronous alternator which is colocated with the motor inside the rotating spinner provides the electrical power. This alternator receives mechanical power across the rotating interface through a power takeoff shaft extending from the main propeller gearbox. Thus, high maintenance, rotating power transfer devices such as electrical slip rings or hydraulic fluid transfer seals, in the case of hydraulic actuators, are eliminated.

The hybrid traction drive (Fig. 11) couples the high-speed servo motor (nominally 20,000 rpm at maximum blade slew rates) to the ball screw. The ball screw, in turn, articulates the individual blades through stiff links, connected at one end to an eccentric pin at the blade root and at the other end to the translating ball screw nut. The motor input to the hybrid drive occurs at the sun roller while the output to the ball screw is taken from the toolhed output ring gear. The planet carrier frame is grounded to the casing while the outer ring roller is allowed to freely rotate, serving as a "containment" ring to react the traction drive rollers' clamping loads.

Blade Angle Control

An autonomous digital electronic control module, located in the nose of the spinner for ease of maintenance, commands blade angle position based on control signal information from the cockpit. This control signal data passes across the rotating interface through a novel fiber optic coupling with superior noise rejection and data bandwidth characteristics. The drive mechanisms is actuated only when a change in blade position is commanded and then only in a low speed, hunting mode to achieve synchrophasing. Since the cruise condition occupies the bulk of the mission, the drive system experiences only intermittent periods of high slew rate when either reverse pitch or emergency feather operations are commanded. However, the drive mechanism carries nearly full torque under practically all operating conditions since it must always react the blades' centrifugal force twisting moment. In the event of PCM failure this twisting moment would back drive the blades toward a flat pitch position which, if left unchecked, could lead to a potentially dangerous overspeed condition. To prevent this situation from occurring, an independently driven pitchlock screw mechanism which tracks the position of the ball screw nut has been incorporated into the system. In the event of any mechanical or electrical component failure downstream of the ball screw, the pitchlock will lock the propeller blades within 1° to 2° of their last position and allow engine operation in a "fixed prop" mode without any danger of overspeeding.

Hybrid Traction Drive

The traction drive was selected for this application for several reasons. Its high ratio capabilities in a compact "pancake" package enables it to be conveniently installed as a module near the nose of the spinner for ease of maintenance and/or replacement with the engine still on the wing. Because of its rolling nature, the roller drive has the ability to handle intermittent bursts of input speeds to 20,000 rpm without the need for liquid lubrication cooling. The unit can be conveniently packed with synthetic "traction" grease (formulated grease with a high coefficient of friction) and then "sealed for life."

The traction drive's low mechanical hysteresis and high torsional stiffness increases blade positioning resolution. While gear type differential speed reducers can be designed to achieve the same 210:1 ratio in a single stage, their expected efficiencies in the neighborhood of 80 percent are decidedly inferior to the mid-90 percent range expected for the hybrid traction drive. With the proposed friction, low inertia mechanism coupled to a high resolution digital controller, blade position accuracies of better than 3 arc min of a degree are projected for the system (ref. 18). Although the level of precision necessary to achieve multiengine synchrophasing has yet to be established, the PCM described here should be significantly more accurate than the current industry standard of about $\pm5^\circ$ on blade clock position.

SUMMARY

Adjustable speed traction drives have been in commercial service for more than 50 years, performing a speed regulation function for a wide range of industrial machinery. Speed regulation accuracies typically range from ± 1 percent with open loop control to about ± 0.1 percent with feedback control or with open loop control when the loads are relatively constant.

Despite their smooth torque transfer characteristics, low rolling friction and undetectable backlash, traction actuators have not been widely applied to aerospace servomechanisms. One notable exception are the constant speed generator drives that have been in service on several commercial and military aircraft. Also "pinched" roller drive systems similar to those commonly used in printing and paper handling machinery have been incorporated in some spacecraft deployment mechanisms.

In this paper, reference is made to the traction-creep characteristics, lubrication principles, material considerations and fatigue life sizing relationships associated with traction drives. The low sliding nature of a traction contact lends itself to the application of solid film lubricants and to the use of soft metal coatings and self-lubricating polymers. Certain classes of thermoplastics, such as polyimides and polyamide-imides have low wear, high traction characteristics and can sustain very high loads without failure. Although several of these polymers have been used as structural and sliding joint materials on spacecraft, their long term tribological performance in a space environment needs greater definition.

The torsional stiffness characteristics of a traction contact were found, from the method presented, to compare favorably with those of gears, particularly at the zero torque crossing point. The typical torque-angular displacement loop of a statically strained traction contacts revealed no backlash, although a small hysteresis displacement, on the order of arc seconds, was observed. High stiffness and the absence of backlash are important to certain "hunting" type positioning mechanisms, such as CMG actuators. In this regard, "roller-gear" CMG drives where traction rollers share the load in parallel with gears have shown excellent performance. A current investigation with a pure traction roller CMG drive suggests that overall system stiffness is primarily dictated by the planet support bearings and structure. The traction contacts themselves have a relatively minor contribution.

Finally, a conceptual design is provided of an electromechanical propeller pitch change mechanism which incorporates a hybrid traction drive. This system, proposed for an advanced turboprop commercial aircraft, contains advanced electric motor and fiber optic control technology. Projected blade positioning accuracies of three arc minutes of a degree should be sufficiently precise to achieve low noise synchrophasing of multiengine propeller blades.

REFERENCES

1. Loewenthal, S. H., Rohn, D. A., and Anderson N. E.: "Advances in Traction Drive Technology." SAE Trans., Vol. 92, sec. 3, 1983.

2. Helich, F. W. and Shube, E. E.: Traction Drives: Selection and Application, Marcel Dekker, Inc., New York, 1983.

3. Loewenthal, S. H. and Zaretsky, E. V.: Traction Drives, Section 34, Mechanical Design and Systems Handbook, H. Rothbart, ed., McGraw Hill Book Co., New York, 1985.

4. Muller, E.J.W.: "The Helios Experiment 5 Antenna Mechanism," NASA TM-33-777, 10th ASM Symposium, July 1, 1976, pp. 133-142.

5. Smith, G. A.: "Metal with a Memory Provides Useful Tool for Skylab Astronauts," NASA TMX-3274, 9th ASM Symposium, Aug. 1975, pp. 81-97.

6. Harned, J. L., Miller, K. M., Szlaga, E. V., and Sudhindranath, P.: "Precise Power Control Utilizing a New Actuator Concept Embodying All-Mechanical Power Flow," ASME Trans., J. of Basic Eng., Vol. 86, No. 1, Mar. 1964, pp. 121-131.

7. Loewenthal, S. H., Anderson, N. E., and Rohn, D. A.: "Evaluation of a High Performance Fixed-Ratio Traction Drive," ASME Trans.. J. of Mech. Des., Vol. 103, No. 23, Apr. 1981, pp. 410-422.

8. Boving H. J., Hintermann, H. E., and Stehle, G.: "TiC-Coated Ball Bearings for Spin-Axis Gyro Application," ASLE Lubr. Eng., Vol. 37, No. 9, Sept. 1981, pp. 534-537.

9. Physiochemical Aspects of Polymer Surfaces, Vol. 1, K. L. Mittal, edit., Am. Chem. Soc., Pro. Int'l. Symp. on Physiochemical Aspects of Polymer Surfaces, Plenum Press, New York, 1983.

10. Rittenhouse, J. B., and Singletary, J. B.: Space Materials Handbook, 3rd edition, NASA SP-3051, 1969.

11. Fusaro, R. L., and Hady, W. F.: "Low Wear Partially Fluorinated Polyimides," NASA TM-83629, Oct. 1984.

12. Engineering Test Report for the Evaluation Test for the Coefficient of Friction of a Urethane Elastomer, LMSC Report No. TA 2388, Apr. 1968.

13. Rohn, D. A. and Loewenthal, S. H.: "An Analysis of Traction Drive Torsional Stiffness," ASME Paper No. 84-DET-100, Oct 1984.

14. Johnson, K. L.: "Surface Interaction Between Elastically Loaded Bodies Under Tangential Forces," Proc. Royal Soc., Ser. A, Vol. 230, 1955, pp. 531-549.

15. Nasvytis, A. L.: "Multiroller Planetary Friction Drives," SAE paper 660763 Oct. 1966.

16. High Torque CMG Rotary Actuator, General Electric Co., Aircraft Equipment Div., Final Rept. ACS10357 for NASA Goddard Space Flight Center, June 1972.

17. Roller-Gear Drive Development, General Electric Co., Avionics Controls Dept., Final Report ACD10104, for NASA Marshall Space Flight Center, Feb. 1971.

18. Steinetz, B. M., Sargisson, D. F., White, G., and Loewenthal, S. H.: "An Advanced Pitch Change Mechanism Incorporating a Hybrid Traction Drive," AIAA Paper number AIAA-84-1383, June 1984.

TABLE I. - EXPERIMENTAL TRACTION CAPACITY LIMITS OF THERMOPLASTIC ROLLERS AGAINST STEEL ROLLERS AT AMBIENT CONDITIONS (50 mm diameter cylindrical rollers from 3 to 20 mm)

Material description	Steady state[a] thermal failure load limit, N/mm		Steady state[b] peak trans mitted power, kW	Typical range of traction coefficient at slip
	Rolling	2 to 3 percent sliding		
Polyamide-imide resin (unfilled Torlon)	215	220	4.8	0.25-0.35
Phenolic w/cotton fibers	115	85	2.2	.3- .5
Polyamide-imide w/graphite and PTFE (filled Torlon)	145	---	---	.15- .25
Extruded Polyamide 6/6 (Nylon 6/6)	39	---	---	.15- .4
Mold-Polymerized Polyamide (Monocast Nylon)	38	---	---	.15- .25
Acetal Copolymer	32	---	---	.1- .2

[a]No failure observed during 30 minute test period at 10 m/s rolling speed. Capacity limits are greater at rolling speeds less than 10 m/s.
[b]Power transmitted by 5 mm wide rollers for a minimum of 10 minutes at 20 m/s rolling speed.

TABLE II. - THEORETICAL STIFFNESS OF A 16:1 RATIO CMG TRACTION
DRIVE AT ZERO TORQUE AND 25 PERCENT INITIAL
PRELOAD - MEASURED AT OUTPUT

Element	Stiffness, 10^6 ft-lb/rad	Compliance, 10^{-6} rad/ft-lb	Percent of total compliance
Planet bearings (cylindrical roller)	2 35	0.426	33
Input shaft, spline, and torque loader	4.52	221	17
Spider cage (guided end condition)	5 12	195	15
All traction contacts ($\mu = 0.1$)	5 44	184	14
Roller support housing (aluminum)	6.54	153	12
Outer housing (aluminum)	10.5	.095	7
Output shaft	29.8	.034	2
Totals	760	1 308	100
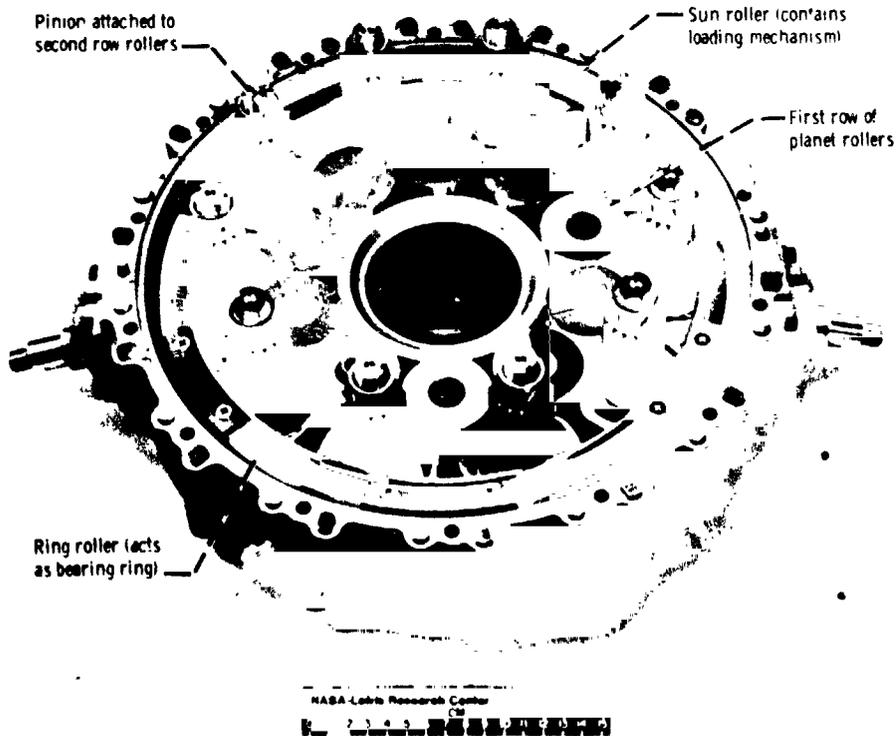
Figure 1. - 500 HP hybrid traction helicopter transmission.
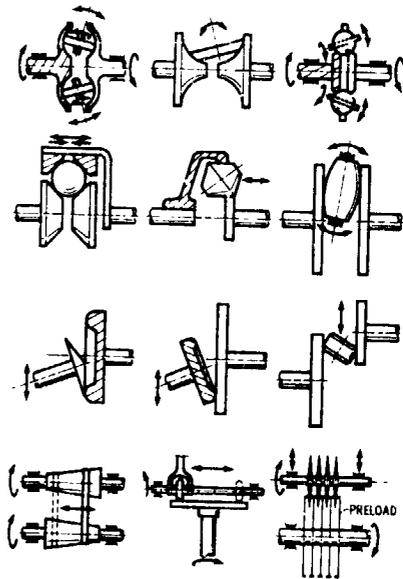
Figure 2. – Typical adjustable speed traction drive geometries.
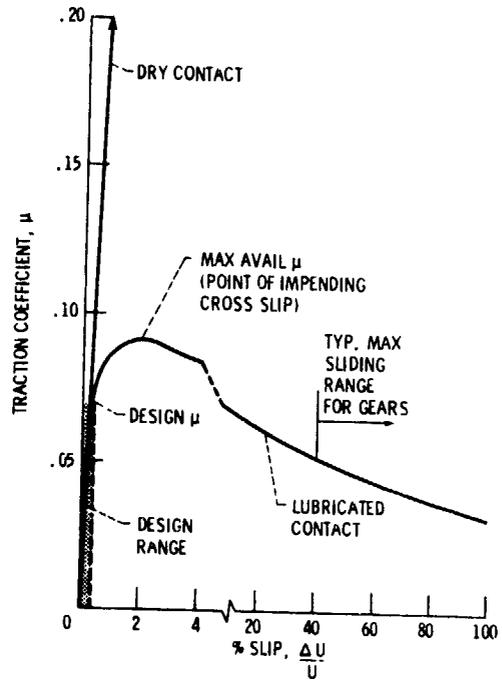
Figure 3. – Typical traction curve showing design range for liquid lubricated and dry traction drive contacts.

SECTION THRU BALL-RAMP

TOROIDAL DRIVE GEOMETRY
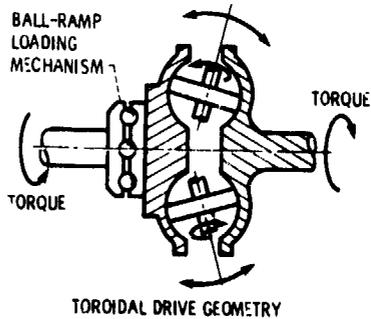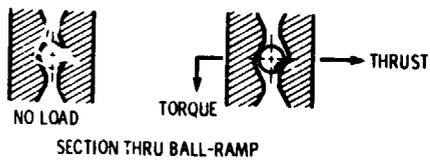
Figure 4. – Typical traction drive torque sensitive loading mechanism.

C-76-4801

Figure 5. – Cryogenic turbopump roller drive.

136
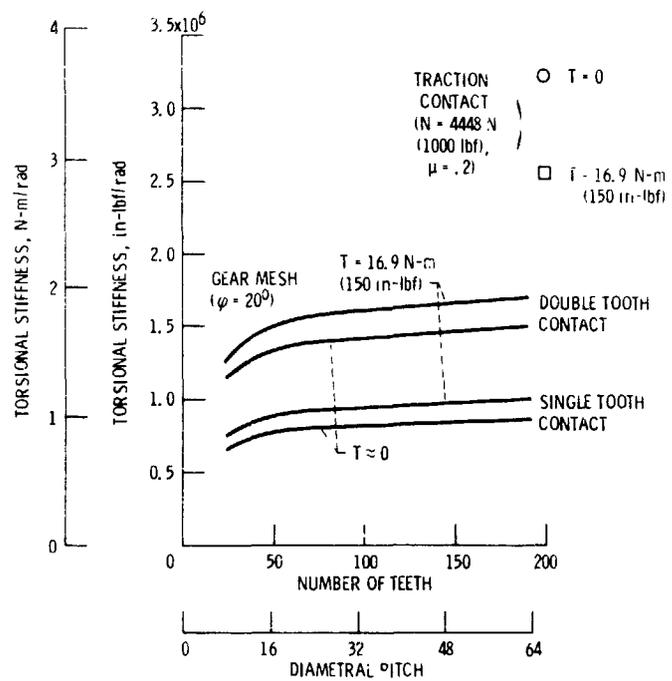
Figure 6 - Theoretical comparison of gear mesh and traction roller contact torsional stiffness at equal diameters, 76.2 mm (3.0 in), widths, 4.57 mm .18 in) and loads.
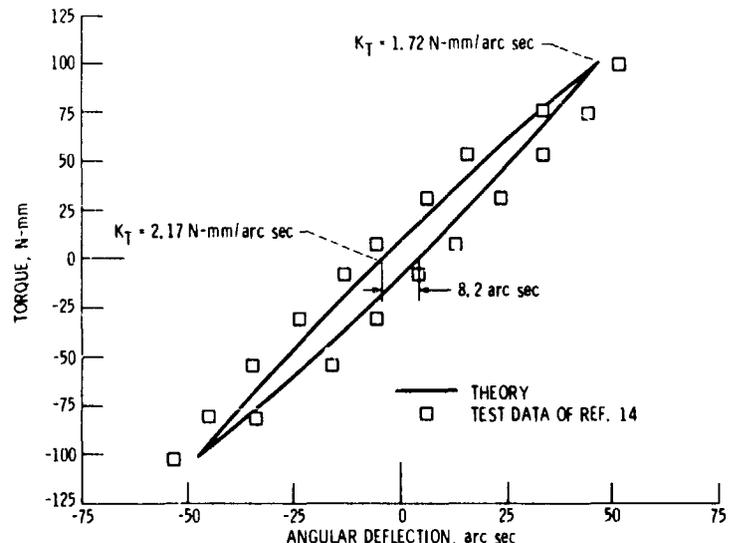
Figure 7. - Comparison of predicted and measured traction contact hysteresis and stiffness of a 9.5 mm steel ball against a flat under a 61.8 N static load from data of ref. 14; μ = .51.
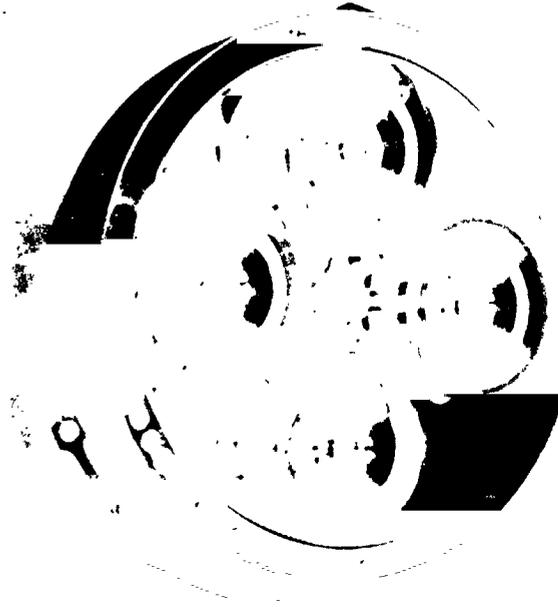
Figure 8. - Control moment gyro roller gear drive.

C-82-7272

Figure 9. - Traction roller control moment gyro drive having ion-plated gold rollers.

HIGH RATIO (210:1)
TRACTION DRIVE

BALL SCREW

ROTATING
ELECTRONIC
CONTROL

MOTOR

PITCHLOCK SCREW

ALTERNATOR

FIBER OPTIC
DATA LINK
(OPTICAL SLIP RING)

INPUT POWER
TAKEOFF SHAFT

CD-84-15096

Figure 10. - Conceptual design of an advanced turboprop propeller pitch change mechanism which incorporates a hybrid traction drive.

OUTER-ROW
ROLLERS

SECOND-ROW
ROLLERS

OUTPUT
TOOTHED
PINIONS AND
RING GEAR

CARRIER
FRAME
STRUCTURE

FIRST-ROW
ROLLERS

INPUT SUN
ROLLER

Figure 11. - 210 to 1 ratio, hybrid traction drive geometry.

139

THE PROPERTIES OF THIN-SECTION, FOUR-POINT-CONTACT
BALL BEARINGS IN SPACE

Robert A. Rowntree*

ABSTRACT

Thin-section, four-point-contact ball bearings are increasingly employed in spacecraft mechanisms because of the potential advantages they offer. However little was previously known of their torque, thermal conductance and stiffness properties at conditions anticipated for their use in space. This paper describes an investigation of these properties.

It has been found that frictional (Coulomb) torque, thermal conductance and stiffness all show marked dependence on the bearing preload, the housing design, the bearing external fit (i.e., free fit or interference) and on the thermal gradient across the races. Optimum bearing performance is achieved only if these properties are well understood. This paper sets out to provide the necessary data.

INTRODUCTION

The ideal of an ideal bearing for any application is usually only a designer's dream. Thin-section, four-point-contact, rolling-element, bearings have been shown to offer a near-ideal solution for some of the novel demands of spacecraft mechanisms. Since one bearing does the work of two, the prime advantages of low weight, small cross section and high stiffness can be utilised to simplify design. With the recognition of these unique properties, thin-section, four-point-contact ball bearings are now employed in many satellite systems and in Europe these include the Olympus and Eurostar series of communication satellites. Brunnen & Bentall (Ref. 1) describe the novel swash plate design of an antenna pointing mechanism (APM) utilizing four-point-contact ball bearings.

To ensure the success of such ball bearings, a knowledge of the bearing properties in space is required. Of major relevan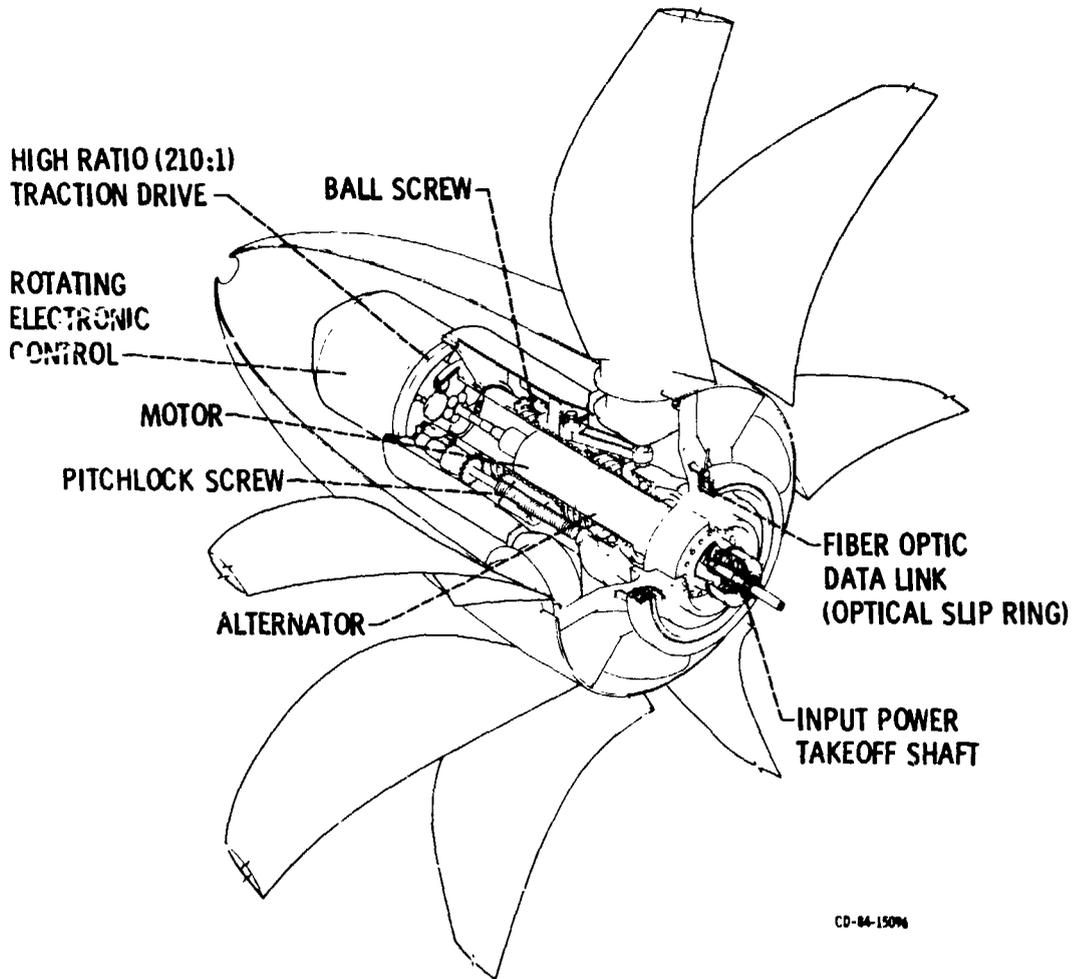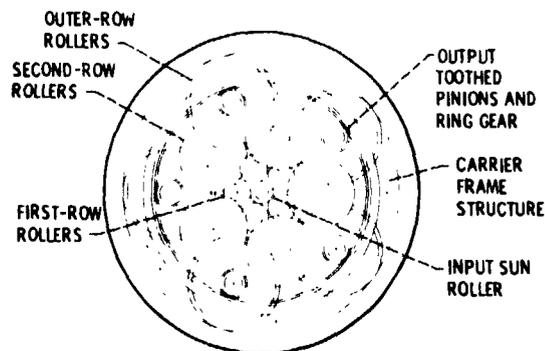ce to mechanism designers is bearing stiffness, frictional (Coulomb) torque and thermal conductance. Experimental and theoretical studies have been performed at the European Space Tribology Laboratory (ESTL) to provide this data (Refs. 2-5). A range of parameters has been examined including the influence of load, preload, fit, thermal gradient, lubricant, and cage type. Studies have concentrated on bearings installed with external diametral clearance and held in-situ with clamp rings, since this permits easy assembly and disassembly in experimental work and also proves to be more convenient than interference fitting in practice.

*European Space Tribology Laboratory, UKAEA, Risley, Warrington, England

BEARING SPECIFICATIONS

Details of the bearings used in these tests are given in Table 1.
Bearing size and range of internal diametral preloads (designated A, K or M)
were chosen to be similar to those used in the Olympus APM (Ref. 1).
Diametral preload is defined as the sum of the interferences in the radial
direction between ball and races (i.e., the sum of the normal Hertzian
approach between ball and races). In this type of bearing, the groove in
each race has two radii whose centres are offset by equal amounts from the
plane of the ball centres. This construction gives the bearing a "Gothic
Arch" configuration making possible four-point contacts between a ball and
the raceways.

Table 1 Bearing details.

Kaydon Bearing No.	KA070XP2
External diameter	190.5mm
Internal diameter	177.8mm
Width	6.35mm
Bearing internal fits (nominal)	0-12.7 m clearance (Brg. A)
" " " "	0-12.7 m preload (Brg. K)
" " " "	12.7-25.4 m preload (Brg. M)
No. of balls	87
Cage	Snap over crown in brass, nylon or spring separators
Contact angle	30 degrees
Bearing steel	AISI 52100
Precision	Class 6 (equivalent to ABEC 7 in run-out tolerances)

MEASUREMENT OF STIFFNESS AT LOW LOADS

Stiffness Rig

The ESTL stiffness rig is illustrated in cross-section in Figure 1. The
bearing was located against a machined shoulder on both the inner and outer
housings and was held in place by clamp rings. The axial clamping force on
the bearing could be varied by the torque imparted to the 24 X M3 clamping
bolts on each clamp ring. Figure 2 shows, in more detail, the configuration
of the clamp rings in relation to the bearing and housings. Bearing
deflections were measured by two, diametrically opposite, contacting
displacement transducer probes which were rigidly clamped via a support arm
to the outer housing. Bending moment was applied using the pulley and weight
system attached to the central rod. Axial load was varied by the addition of
weights to the inner housing.

Structural Deflections in the Rig

From the limited information available, very small axial and moment deflections were to be expected. To ensure any additional deflections did not arise from the stiffness rig itself (despite its massive structure), a solid stainless steel ring of nominally "infinite" stiffness was manufactured and substituted for the bearing. Only minor deflections were measured arising from the rig; where necessary the experimental results have been corrected.

BEARING STIFFNESS RESULTS

Effect of bearing Internal Fit on Moment Compliance (constant axial clamp)

The influence of bending moment on the moment deflections of the three bearings, with differing internal fits (diametral preload), is shown in Figure 3, at a clamp ring bolt torque of 0.8 Nm. This, arbitrarily chosen, bolt torque is equivalent (assuming dry bolt threads and standard cap head bolts) to an axial clamping force per bearing race of approximately 48 N/mm. The bearing movement is such that a moment load in the direction of probe A (see Figure 1) produces a negative deflection at that probe and a positive deflection at probe B. Moment loading towards B produces the reverse deflections. For clarity the results obtained from probe A have been omitted from Figure 3.

The effect of increasing the bearing internal preload is, as expected, to decrease the moment deflection at a given moment load. By imposing higher race deformation (at the four-point contacts) a larger bending moment is required to produce the same moment deflection. The slopes of the lines of Figure 3, defined as the moment compliance with units of Rad/Nm, have been calculated by linear regression and are presented in Table 2. This table is specific to the axial clamping force imparted by a bolt torque of 0.8 Nm. For comparison the moment compliance derived from information in the bearing manufacturer's catalogue (Ref. 10) is included in Table 2. Although the internal preload is not specified in the catalogue, there is good agreement with the values of moment compliance.

Table 2 Moment compliance as a function of original bearing internal fit (clamp ring bolt torque 0.8 Nm).

Bearing	Moment Compliance (Rad/Nm)	
	Experimental	Manufacturer's estimate (internal fit not specified)
A (0-12.5 m clearance)	1.62×10^{-6}	
K (0-12.5 m preload)	1.27×10^{-6}	2×10^{-6}
M (12.5-25 m preload)	0.85×10^{-6}	

The Effect of Axial Clamping Force on Moment Compliance

The pronounced effect of the bolt clamping torque (which is proportional to the axial clamping force) on the moment compliance of the three bearings, is illustrated in Figure 4. Increasing the axial clamping force reduces the moment compliance of the bearings. The range of moment compliance values from all the bearings studied can be encompassed using bearing A (0-12.5 m clearance) solely by adjusting the clamp ring bolt torque. At higher clamp ring bolt torques (2 Nm), it was not possible to differentiate between the moment compliance of the three bearings, as the deflections were so low (0.1 m) that experimental error predominated.

The effect of increasing the axial clamping force is to bend the Gothic-Arched-shaped races and impose additional Hertzian deformation at the four-point contacts. Thus moment compliance will be correspondingly reduced. This result demonstrates the sensitivity of this type of bearing to bending of the rings induced by clamping forces.

A notable feature of Figure 3 is that bearing A (0-12.5 m internal clearance, prior to fitting) responds to moment loads in a similar manner to the internally preloaded bearings; i.e., as the moment load was varied there was no evidence of play or clearance in the resulting moment deflections. Only when the clamp ring bolt torque was reduced to 0.2 Nm was hysteresis and non-linearity, due to ring movement and a highly variable ball complement, exhibited in its moment deflections (Figure 5). The implication of this result is that poor locational accuracy and low stiffness can be avoided by judicious use of axial ring clamping (without the need for interference fitting).

Effect of Bearing Internal Fit on Axial Compliance (constant axial clamp)

Table 3 summarises the effect of the bearing internal fit on the axial compliance of the three bearings studied (at a clamp ring bolt torque of 0.8 Nm). At axial loads of up to 200 N, there was a linear relationship between load and axial deflection; as expected, increasing the bearing preload reduces the bearing axial compliance. Fair correlation is obtained with the axial compliance deduced from the bearing manufacturer's catalogue.

Table 3 Axial compliance as a function of original bearing internal fit (clamp ring bolt torque 0.8 Nm).

Bearing	Axial Compliance (m/N)	
	Experimental	Manufacturer's estimate (internal fit not specified)
A (0-12.5 m clearance)	7.25×10^{-9}	
K (0-12.5 m preload)	5.81×10^{-9}	8×10^{-9}
M (12.5-25 m preload)	4.04×10^{-9}	

Effect of Axial Clamping Force on Axial Compliance

The marked influence of axial clamping force on the axial compliance of bearing A (0-12.5 m clearance) is summarised in Table 4, for three bolt torque settings (0.2, 0.8, and 1.86 Nm). At a given axial clamping force there was a linear relationship between axial deflection and load.

Table 4 Axial compliance as a function of axial clamping force (clamp ring bolt torque). Bearing A (0-12.5 m clearance).

Clamp ring bolt torque	Axial Compliance (m/N)
0.2 Nm	3.0×10^{-8}
0.8 Nm	7.25×10^{-9}
1.86 Nm	1.56×10^{-9}

MEASUREMENT OF TORQUE AND RADIAL THERMAL CONDUCTANCE

Heat Transfer Rig

Figure 6 is a schematic drawing of the rig. Its design was based on an existing bearing heat transfer rig at ESTL (manufactured by the Dutch National Lucht en Ruimtervaart Laboratorium (Ref. 6)). The bearing was mounted between the inner housing and heat flux meter (HFM), locating against shoulders thereon. The bearing housings and seatings were manufactured to ABEC 9 standard. The bearing was held in place by inner and outer clamp ring , whose clamping force could be varied by the torque applied to the M3 clamp ring bolts (24 per clamp ring). The configuration of the clamp rings in relation to the bearing, housing and HFM is as shown in Figure 2. Four radial groups of copper/constantan thermocouples were located at 90-degree intervals around the HFM. Per grouping, two thermocouples measured the inner (T_I) and outer (T_O) bearing race temperatures and two thermocouples measured the temperature difference across the HFM (T_I' and T_O'). The thermocouples measuring T_I and T_O were positioned such that they were in contact with the surfaces of the bearing races. Under isothermal conditions and with a stationary bearing in vacuum, the thermocouples all showed the same reading on a digital voltmeter (DVM) to within 1 V ($1/40^\circ$C). Radiant heat loss from the bearing and HFM was prevented by multiple superinsulation shields. The inner housing, HFM and clamp rings were manufactured from FV 520B, which has the same coefficient of thermal expansion as AISI 52100, thus ensuring tre isoexpansive nature of the rig with respect to the bearing.

The bearing was rotated using an externally controlled motor via a ferrofluidic vacuum feedthrough. Bearing torque was sensed by a strain gauge torque transducer, the output of which was displayed on a potentiometric pen recorder and on a programmable digital voltmeter.

Basis of Method

Heat is made to flow radially across the HFM whose conductance, K, is known. The same heat flows across the test bearing in "series" with the HFM. The inner ring of the bearing and outer circumference of the HFM are held at constant (adjustable) temperatures by thermostatically controlled fluids. Thus, from the average temperatures at the four positions, the measured radial temperature difference across the HFM $(T_0'-T_I')$ signifies a known heat flow rate, and a measure of the temperature across the bearing (T_0-T_I) yields the bearing conductance, C:

$$C = K \, (T_0'-T_I')/(T_0-T_I)$$

Bearing Test Lubricants

Three space-approved lubricants were used in the torque and conductance tests, two oils and one grease. Their descriptions are given in Table 5.

Table 5 Details of Test Lubricants.

Lubricant	Manufacturer	Description	Viscosity at 20°C	Thermal Conductivity
Fomblin Z25	Montedison	Fluorinated oil	240cS	0.084W/m°C
BP110	British Petroleum	Mineral oil Refined to give low vapour pressure	350cS	0.0153W/m°C
Braycote 3L-38RP grease	Brayco Oil Company	Based on Z25 with polymer thickening agent(PTFE)	-	0.084W/m°C

BEARING TORQUE AND CONDUCTANCE RESULTS

Unless otherwise indicated, conductance values were measured with the bearing stationary and the torque was measured at a rotational speed of 1 RPM, i.e., slow enough to make any speed-dependent torque effects negligible. Pressure in the vacuum chamber was maintained at 10^{-3} torr to ensure no convective heat transfer between bearing and environment.

Thermal Gradient

Figure 7 illustrates the marked influence of thermal gradient (T_O-T_I), defined as the temperature diff'ence between the outer and inner bearing race, on the torque and heat t nsfer of bearing A (0-12.5 m clearance). The clamp ring bolts were tightened to 0.8 Nm and this has resulted in preloading the bearing, despite its nominal internal clearance, due to bending of the rings. Conductance is observed to rise linearly with increasing thermal preload (i.e., as T_I is made hotter than T_O) whereas the increase in torque is almost a square law relation.

The results shown in Figure 7 imply that, in this particular case, the outer race needs to be about 10°C warmer than the inner race before the induced preload is apparently relieved, i.e., where the torque and conductance reach their minimum values. However, as will be shown later, other factors can influence the precise determination of this point.

Internal Preload and Devleopment of Internal Clearance

The influence of internal preload on the mean conductance across degreased and unlubricated four-point-contact ball bearings is shown in Figure 8, plotted as a function of thermal gradient. All the bearings have a similar minimum conductance value of 0.08 W/°C; this corresponds to the development of internal clearance in the bearir The effect of increasing the internal preload is to raise the thermal c uctance at a given thermal preload. It may be noted that at ambient conditions $(T_O-T_I=0°C)$ all bearings are internally preloaded at a clamp ring bolt torque of 0.8 Nm.

As the bearings were not rotated without the presence of lubricant (because of the risk of damage), torque measurements on the influence of preload were taken with the addition of 1 1 of Z25 (Figure 9). Increasing the internal preload causes a corresponding increase in the mean bearing torque. Analysis of Figures 8 and 9 reveals that the frictional torque and "dry" conductance reach a minimum (or steady value) at approximately the same thermal gradient.

Axial Clamping Force

Figures 10 and 11 summarise the influence of the axial clamping force on the torque and conductance of bearing A (0-12.5 m clearance). Increasing the axial force and imposing additional Hertzian deformation at the four-point contacts would be expected to raise bearing conductance and torque, a result which is demonstrated in Figures 10 and 11. As in the compliance studies, the effect of increasing the internal preload is to reduce the sensitivity of bearing torque and conductance to the axial clamping force (Ref. 4).

Fomblin Z25 Oil Addition

The influence of Fomblin Z25 lubricant quantity on the torque and conductance of bearing A (0-12.5 m clearance) is illustrated in Figures 12 and 13. There is no effect of lubricant quantity (1 1) on torque at 1 RPM (confirming the absence, under these conditions, of a speed-dependent or viscous torque component). At higher rotational speeds (25 RPM) the viscous torque component becomes predominant and the quantity of lubricant can then influence the torque. Thermal conductance increases in a nonlinear manner with oil quantity. From Figure 13 it may be concluded that 200 l of oil is lubricant quantity. Smaller angular contact bearings exhibit a similar relationship with lubrication quantity (Ref. 7).

Comparison of BP110 Oil With Fomblin Z25

As with Fomblin Z25, the addition of BP110 lubricant had no influence on bearing torque (at 1 RPM) and gave results identical to those for Fomblin Z25. In previous work (Ref. 8) the boundary friction coefficients of BP110 and Fomblin Z25 oils between steel surfaces have been demonstrated to be similar (0.13 and 0.12, respectively).

Table 6 shows, under isothermal conditions, the relative influence of Fomblin Z25 and BP110 lubrication on bearing conductance (BP110 has a thermal conductivity which is approximately twice that of Fomblin Z25). These values have been normalised to indicate the contribution from the oil only (i.e, minus dry component).

Table 6 Influence of oil type on oil conductance component

| Oil Quantity | Normalised conductance (W/°C) | |
	Z25	BP110
Dry	0	0
10 l	0.3	0.35
30 l	0.37	0.51
500 l	0.5	0.97

Inspection of Table 6 reveals that for "flooded" lubrication (500 1) the conductance with BP110 is indeed close to twice that shown with Fomblin Z25. For small additions, however, the extra conductance with BP110 is small. Stevens and Todd (Ref. 7) have shown with smaller angular contact bearings that at low lubricant additions bearing conductance is proportional to the Hertzian contact area, while at large lubricant additions the majority of the heat flows through the oil meniscus at the ball/race contact and thus conductance is related to the oil conductivity. The present results with thin-section bearings are in close agreement.

Grease Lubrication

Figure 14 illustrates the effect of grease lubrication on bearing A (0-12.5 m clearance). The bearing was approximately one-third filled with grease and then rotated for several revolutions to ensure an even distribution. As Braycote 3L-38RP grease is based on Fomblin Z25 oil, bearing torque and conductance may be expected to correspond to the flooded Fomblin Z25 oil values. In fact slightly higher torque and conductance values were obtained for grease lubrication. The small difference in torque is attributable to grease churning losses and the action of the polymer thickening agent, while the increased conductance probably arises from the grease between cage and races, i.e, bridging the conductance path of the ball/race contacts.

Cage Type

The effect of the following cages types was studied:

(i)   Standard brass formed ring, "snap-over" type
(ii)   Nylon segmented "snap-over" type
(iii)   Helical coil springs

Only minor difference in bearing torque were found (Figure 15), where spring separators tended to give higher torques when the bearing was subjected to negative temperature gradients. Whilst the insensitivity of mean torque to cage type implies that, at a rotational speed of 1 RPM no significant cage "hang up" occurs, even with the solid (loose pocketed) brass cage, it should be noted that the precision of the bearing and housings is also crucial. A lower precision of bearing or housing could tend to promote cage "hang-up". Bearing conductance was found to be independent of cage type.

DISCUSSION

It is apparent from the results that the stiffness, radial conductance and frictional (Coulomb) torque of large-diameter, thin-section, four-point-contact ball bearings involve the interaction of several variables and as such a rigorous theoretical analysis is not feasible. However, the relationships between stiffness, torque and conductance with internal preload and thermal gradient, for preloaded bearings. have been shown to be in broad agreement with those predicted with reasonable assumptions from theory (Ref. 9). The chief uncertainty in the theory is in the number of rolling elements effectively loaded. Clearly for such large bearings with thin, deformable rings the effective ball complement will vary greatly with the load applied and with the probability distribution of the ball to race interference. In the absence of such data, theoretical predictions must be rather imprecise.

An important practical consideration for those bearings is in the manner of the installation employed. Provided that the "unfitted" internal preload is accurately known and that one has a precise knowledge of the amount of interference being applied, then it can be argued that interference fitting is desirable (assuming also that a later dismantling is not contemplated). However, in the case of the test bearings, the wide tolerance bands of internal diametral fit (Ref. 10) mean that there would be considerable uncertainty in the start point and, therefore, in the ball load and dry torque after interference fitting. For example, the effect of a 10- m diametral interference on bearing fitting was found to increase the mean torque by a factor of 4. The characteristics of thin-section bearings also change, the bearing becoming more sensitive to thermal gradients, etc. Axial clamping of four-point-contact bearing rings, which are clearance fits, has a similar effect to fitting with interference, but it is possible then to vary the ball load and torque to match the requirements more exactly.

For most uses, the optimum mounting method would combine the use of external diametral clearance for each of bearing fitting (and removal) with allow axial clamp. Such a value of axial clamp would minimise ring bending, but would be sufficient to ensure that the bearing cannot physically move in its housing. Suitable clamp ring design can reduce the dependence of the bearing on the axial clamping force. It is recommended that the bearing torque or deflection be measured after installation, from which the effective internal preload can be inferred.

CONCLUSIONS

Measurements of the frictional (Coulomb) torque, radial thermal conductance and stiffness of thin-section, four-point-contact, ball bearings have shown the following:

a. Internal preload, housing design and external axial clamping force on the bearing rings all have a strong influence upon torque, conductance and stiffness.

b. The thermal conductance of a dry or marginally lubricated bearing depends only upon the thermal strain and varies linearly with radial temperature difference between the rings. Additionally, conductance is a function of type and quantity of lubricant.

c. The Coulomb torque exhibits an almost square law relation with thermal strain.

ACKNOWLEDGEMENTS

REFERENCES

1. Brunnen A J D & Bentall R H 1982, Development of a high stability pointing mechanism for wide application, Proc. 17th Aerospace Mechanisms Symposium, May 1983.

2. Rowntree R A 1982, The axial and moment compliance of thin-section four-point-contact ball bearings, ESTL/TM/33.

3. Rowntree R A 1982, The moment compliance of thin-section four-point-contact ball bearings at light axial clamping forces, ESTL/TM/35.

4. Rowntree R A & Todd M J 1983, Thermal conductance and torque of thin-section four-point-contact ball bearings in vacuum, ESA(ESTL)54.

5. Rowntree R A 1983, The stiffness, torque and thermal conductance of thin-section four-point-contact ball bearings for use in spacecraft mechanisms, Proc First European Space Mechanisms and Tribology Symposium, Neuchatel October 1983, ESA-SP-196.

6. Heemskerk J F et al 1975, A test rig to measure the thermal conductance and frictional torque of bearings in vacuum, Proc First European Space Tribology Symp, Frascati April 1975, ESA SP-111.

7. Stevens K T & Todd M J 1980, Thermal conductance across ball bearings in vacuum, ESA TRIB 1, 15-40.

8. Todd M J 1980, A method for the calculation of torque in dry lubricated ball bearings including the influence of temperature and fit, Proc Second Space Tribology Workshop, Risley October 1980, ESA-SP-158.

9. Todd M J 1983, Computational methods for ball bearings in spacecraft, Proc First European Space Mechanisms and Tribology Symposium, Neuchatel October 1983, ESA-SP-196.

10. Kaydon Corporation, Kaydon bearing division catalogue on "Reali-slim" bearings.

CENTRAL ROD

PROBES

WEIGHTS

SUPPORT ARM

FIG 1
STIFFNESS RIG

B

A

INNER HOUSING

BEARING

OUTER HOUSING

200 mm PCD

168 mm PCD

CLAMP RINGS

INNER
HOUSING

OUTER
HOUSING
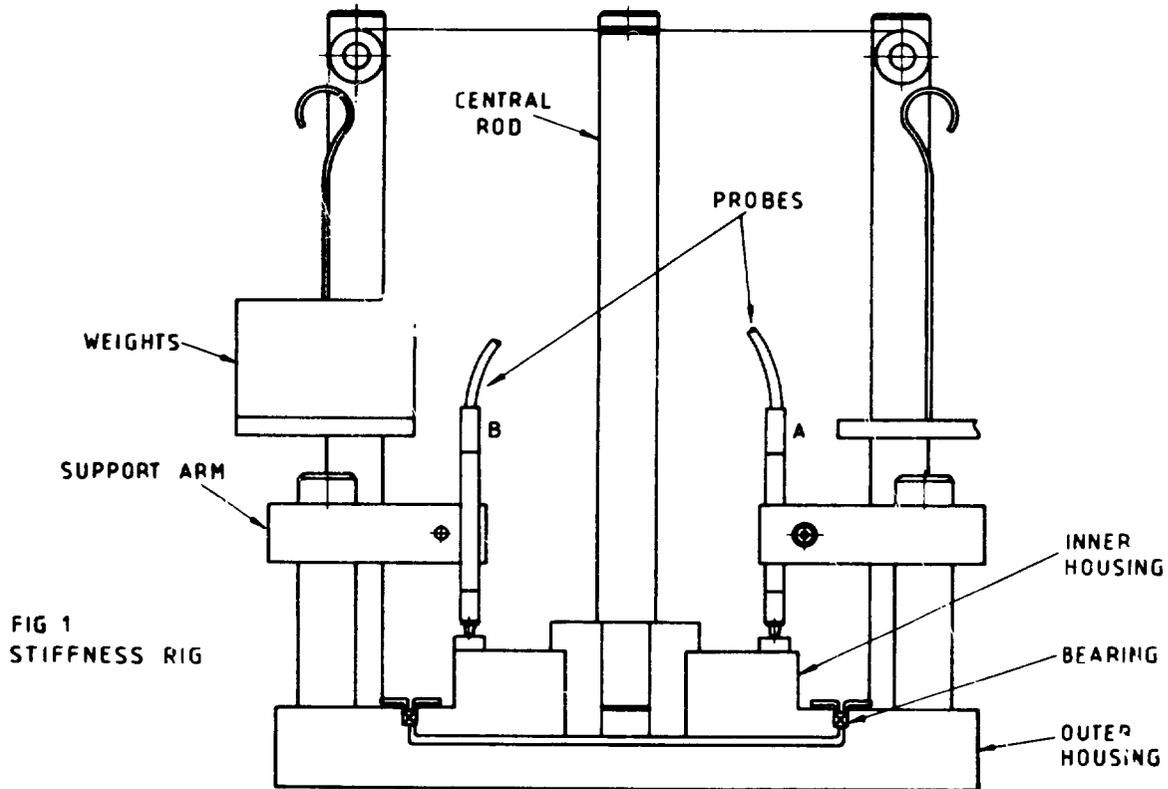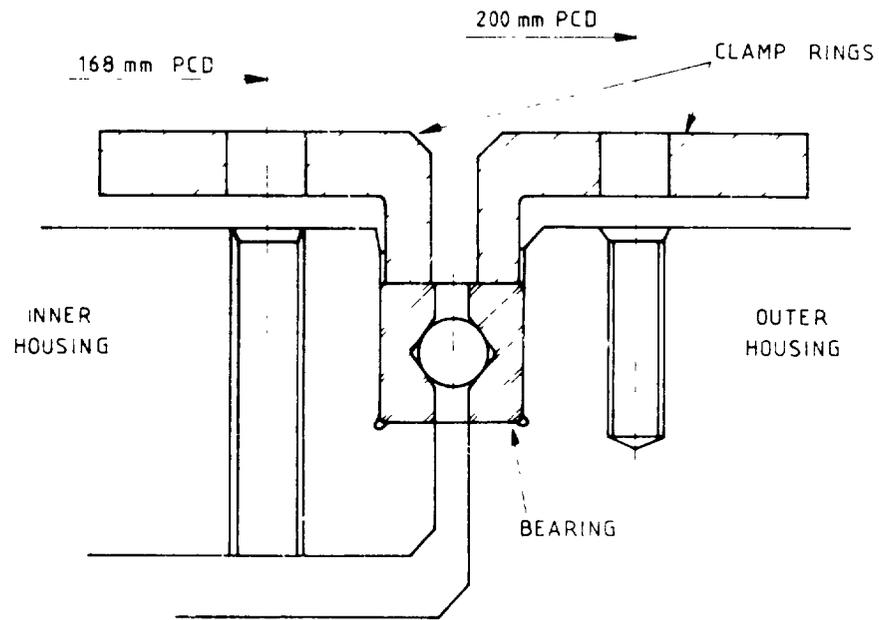
BEARING

FIG 2 SUPPORT CONFIGURATION
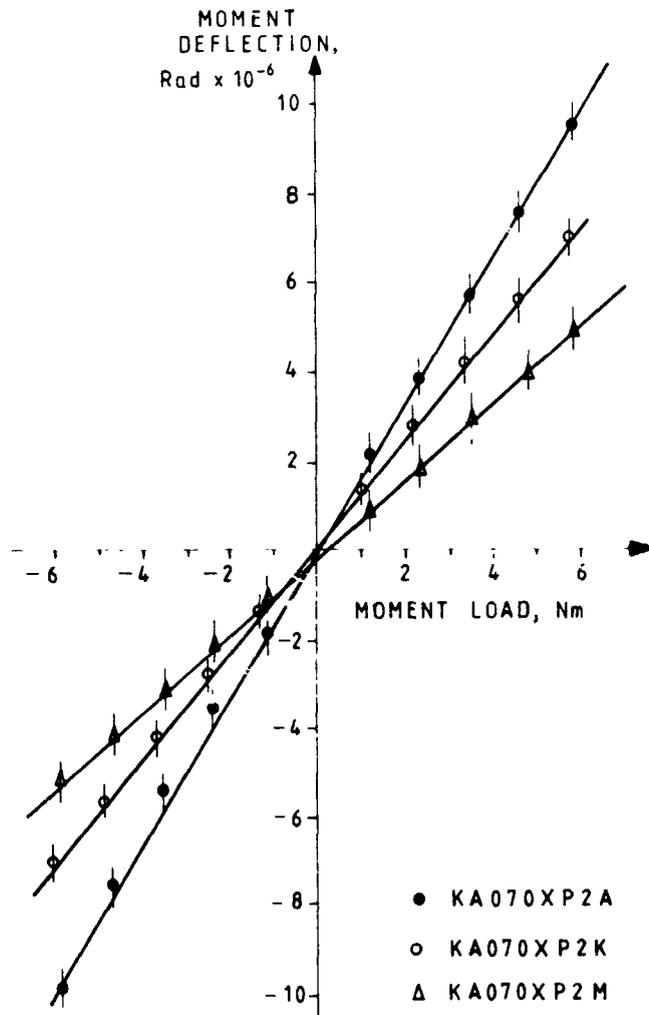
FIG. 3   MOMENT DEFLECTION AS A FUNCTION
OF MOMENT LOAD,   CLAMP RING BOLT
TORQUE 0.8 N m.
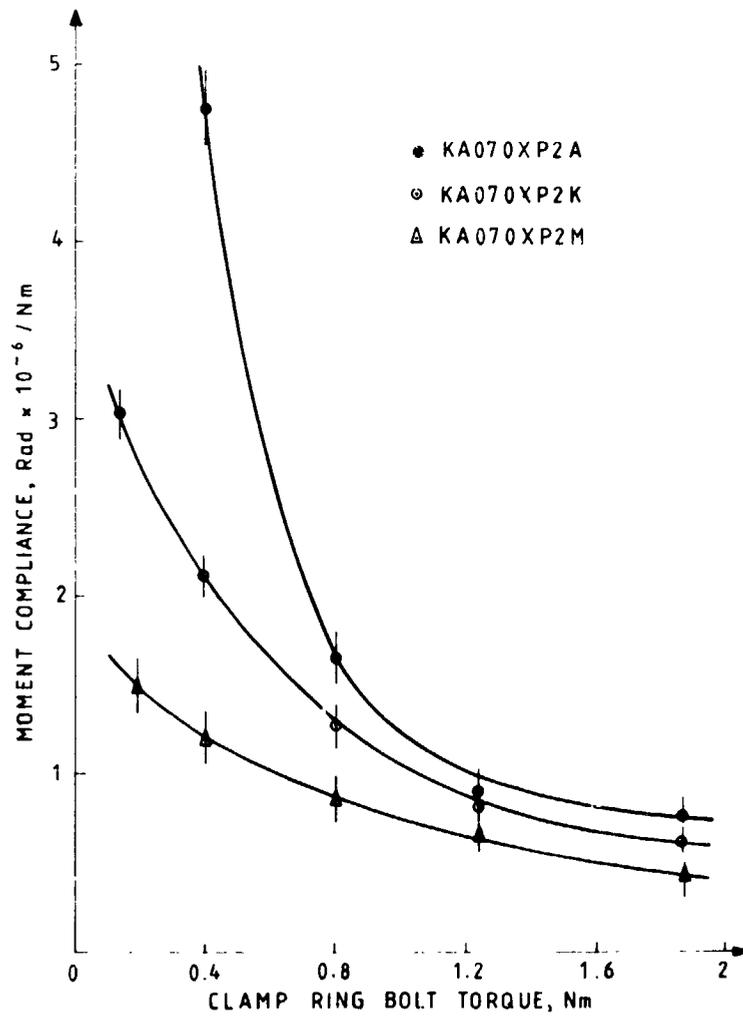
FIG.4 EFFECT OF CLAMP RING BOLT TORQUE ON MOMENT
COMPLIANCE OF THREE KAYDON BEARINGS
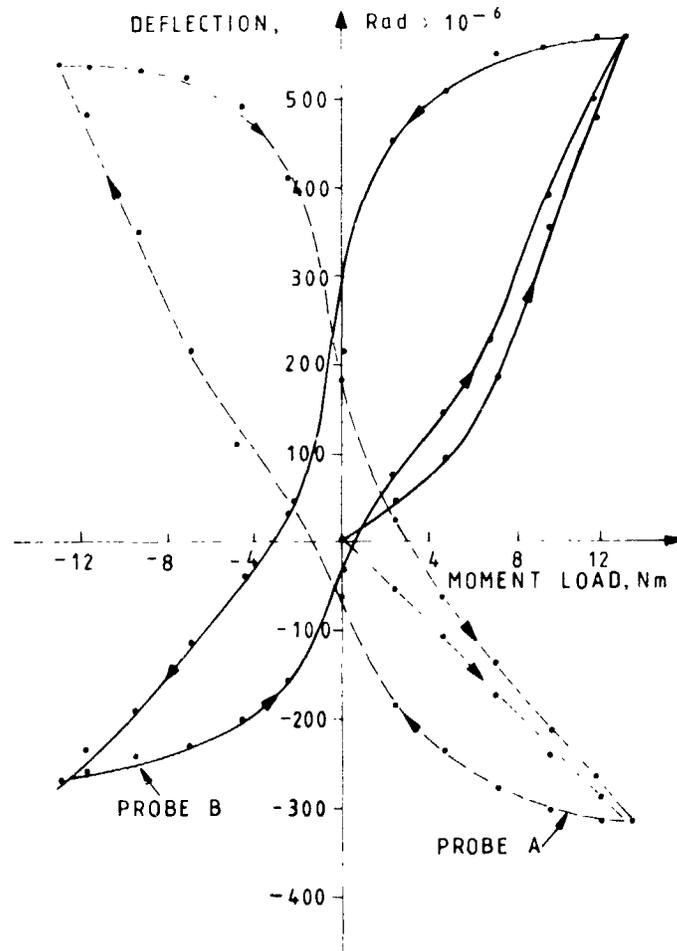
FIG 5   MOMENT   DEFLECTION   Vs. MOMENT LOAD,
BEARING KA070XP2A,   0.2 Nm CLAMP   RING
BOLT   TORQUE
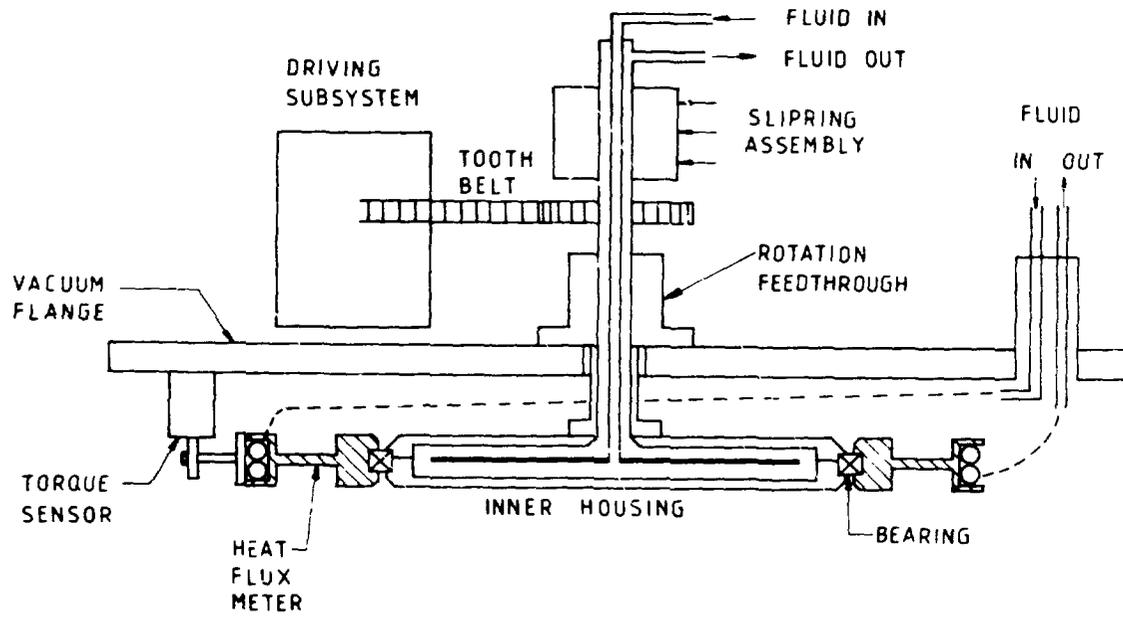
FIG 6 TEST RIG (SCHEMATIC)
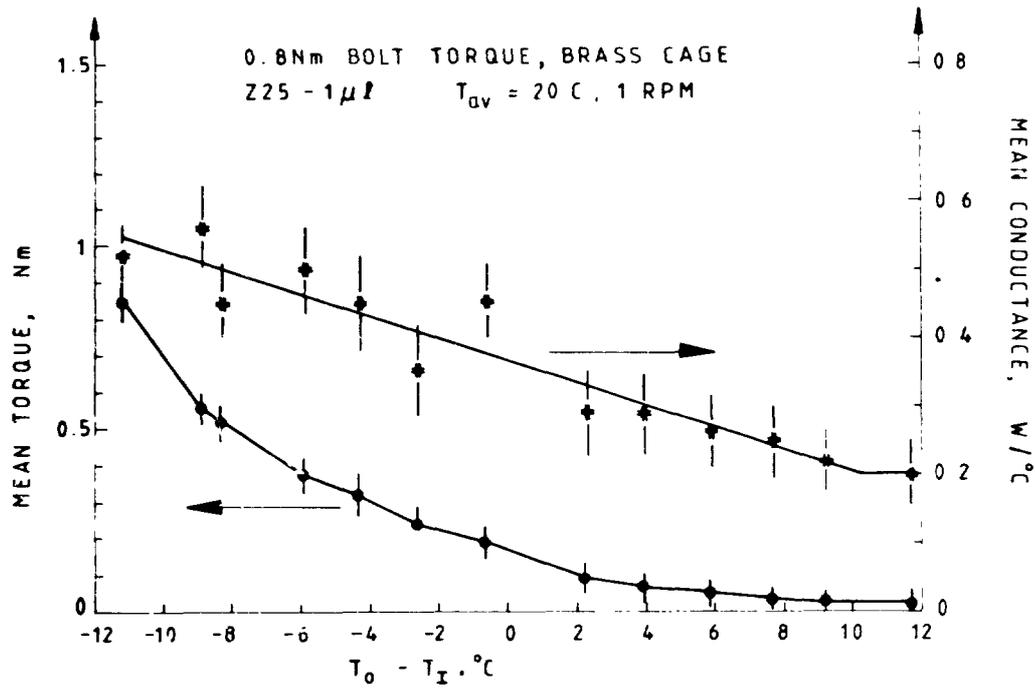
FIG. 7   MEAN BEARING TORQUE & CONDUCTANCE
Vs THERMAL GRADIENT, KA070XP2A
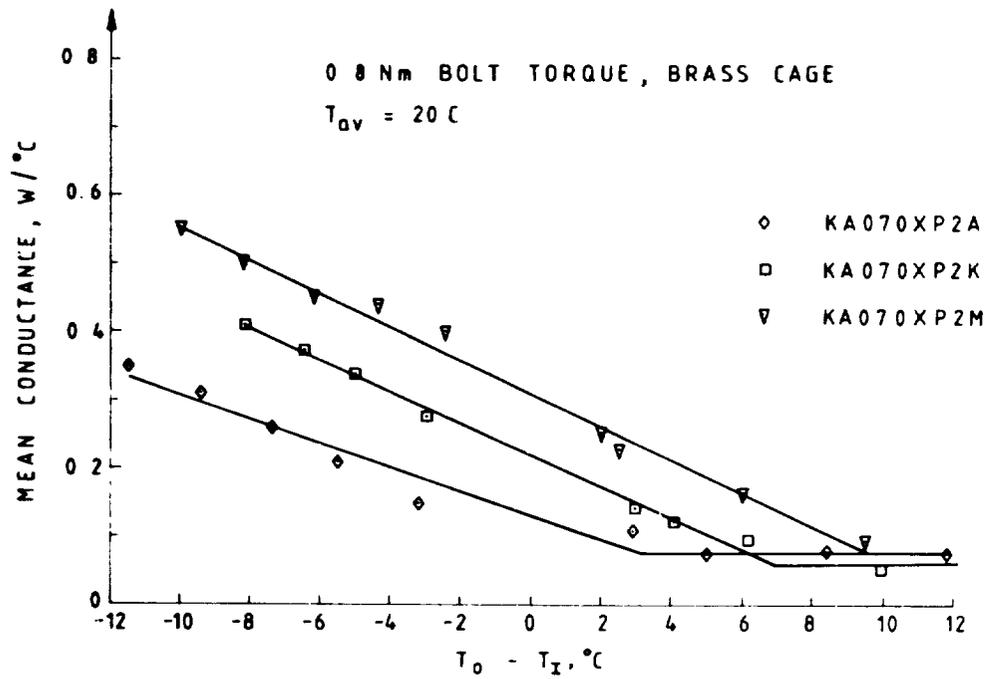
FIG. 8   THERMAL CONDUCTANCE Vs. TEMPERATURE GRADIENT
AS A FUNCTION OF BEARING TYPE (UNLUBRICATED)
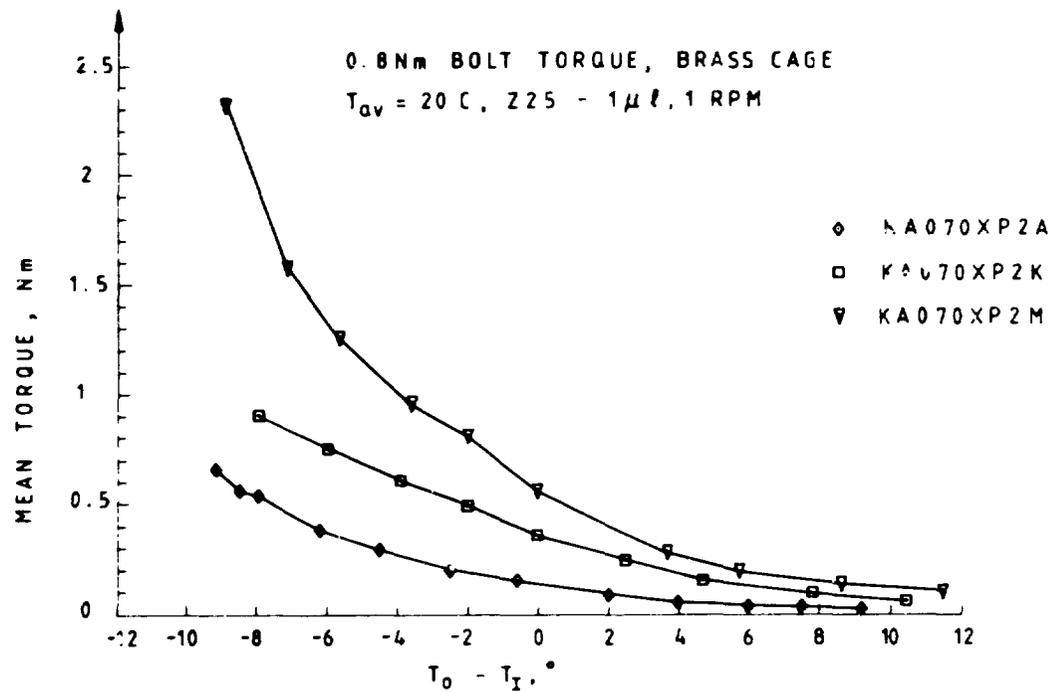
FIG 9   MEAN TORQUE Vs TEMPERATURE GRADIENT AS A
FUNCTION OF BEARING TYPE (LUBRICATED)
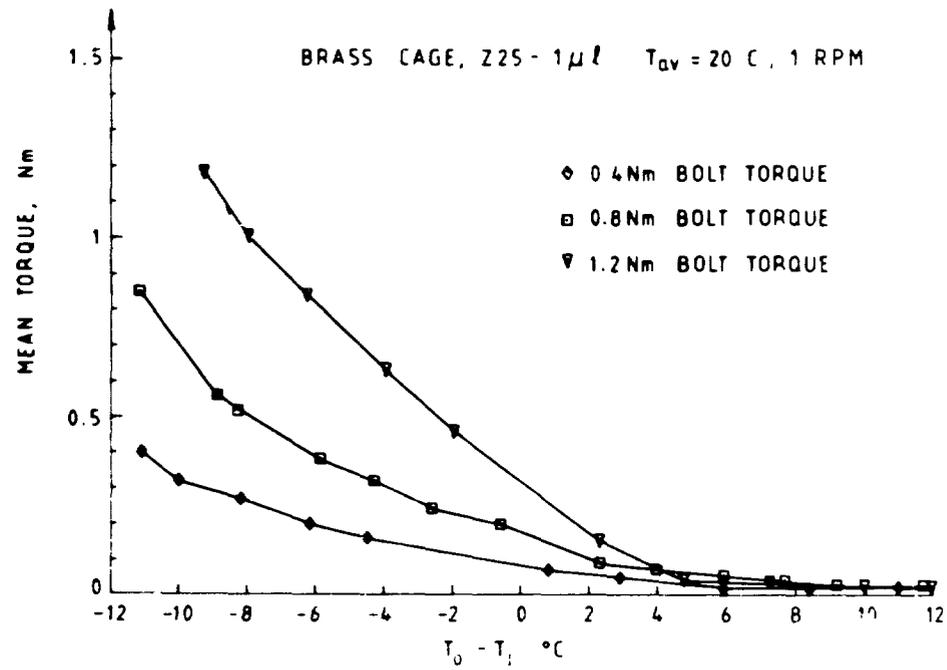
FIG 10 EFFECT OF AXIAL CLAMPING FORCE ON MEAN
BEARING TORQUE, KA070XP2A
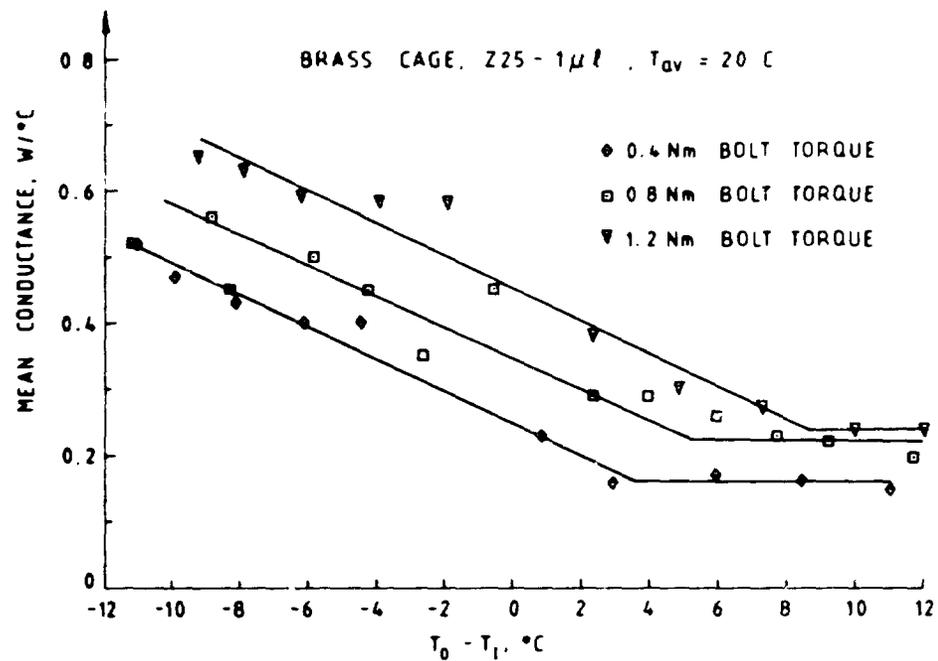
FIG 11 EFFECT OF AXIAL CLAMPING FORCE ON THERMAL CONDUCTANCE, KA070XP2A
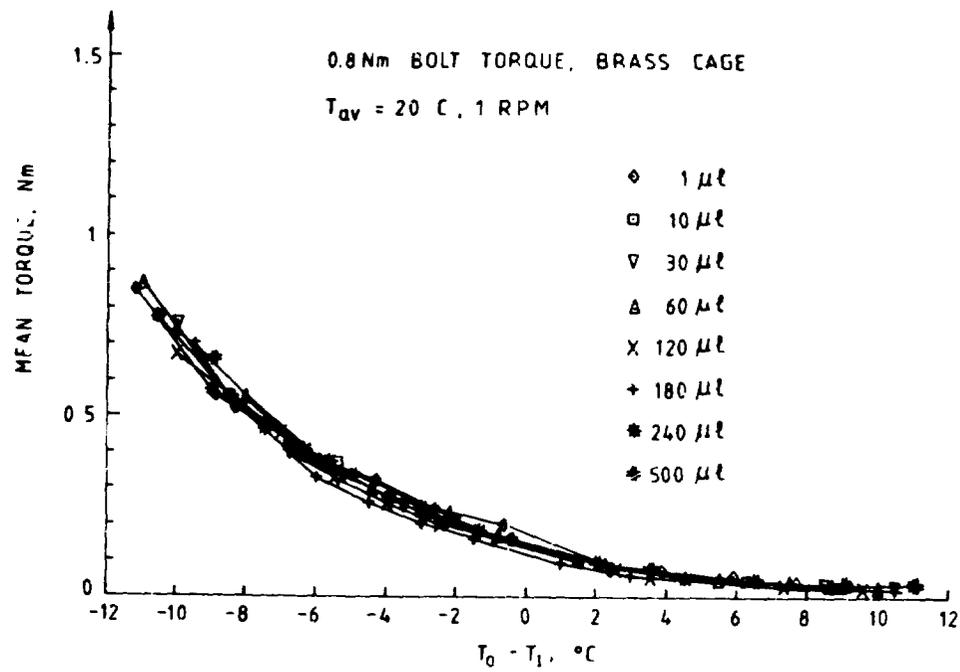
FIG 12 MEAN TORQUE Vs THERMAL GRADIENT AS A FUNCTION OF Z25 OIL QUANTITY, KA070XP2A
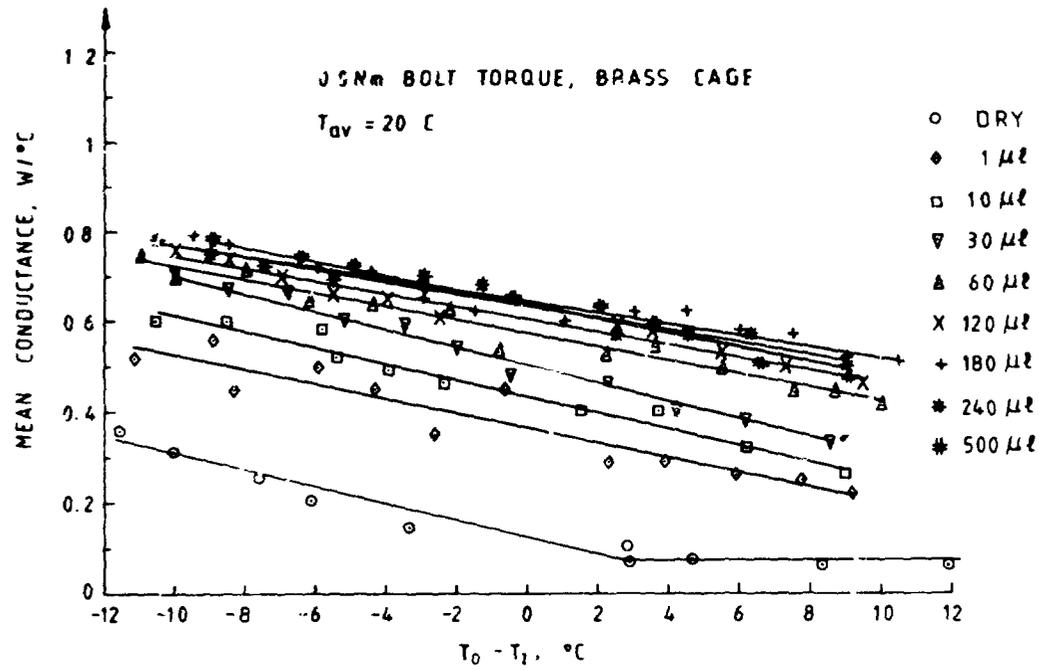
FIG 13 MEAN CONDUCTANCE Vs THERMAL GRADIENT AS A
FUNCTION OF Z25 OIL QUANTITY, KA070XP2A
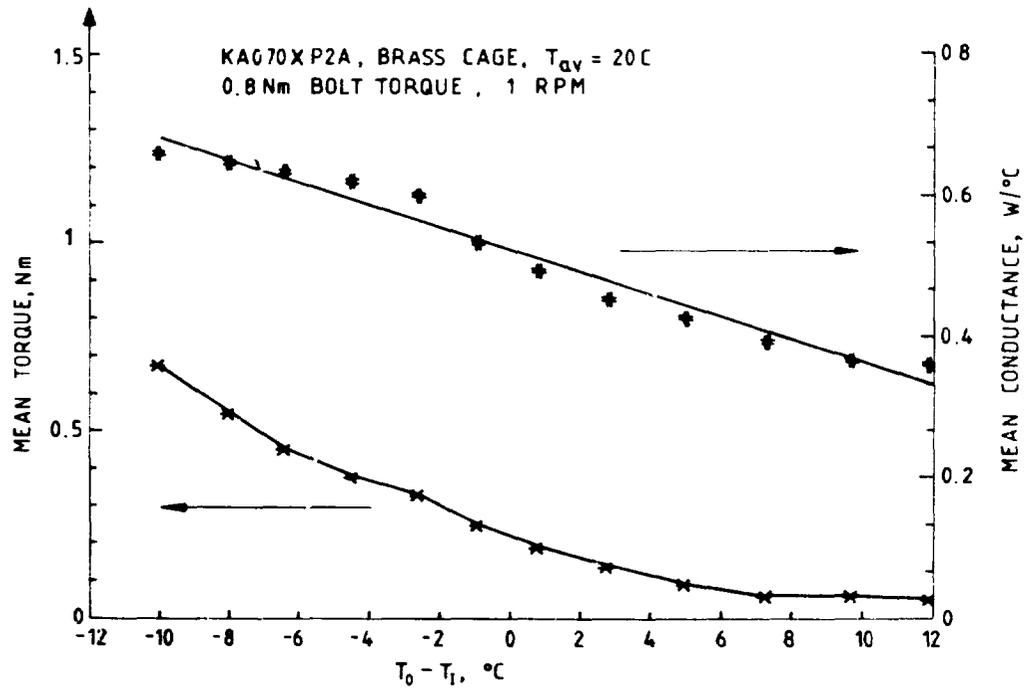
FIG.14 MEAN BEARING TORQUE & COND'JCTANCE Vs. THERMAL GRADIENT,
BRAYCOTE 3L-38 RP GREASE
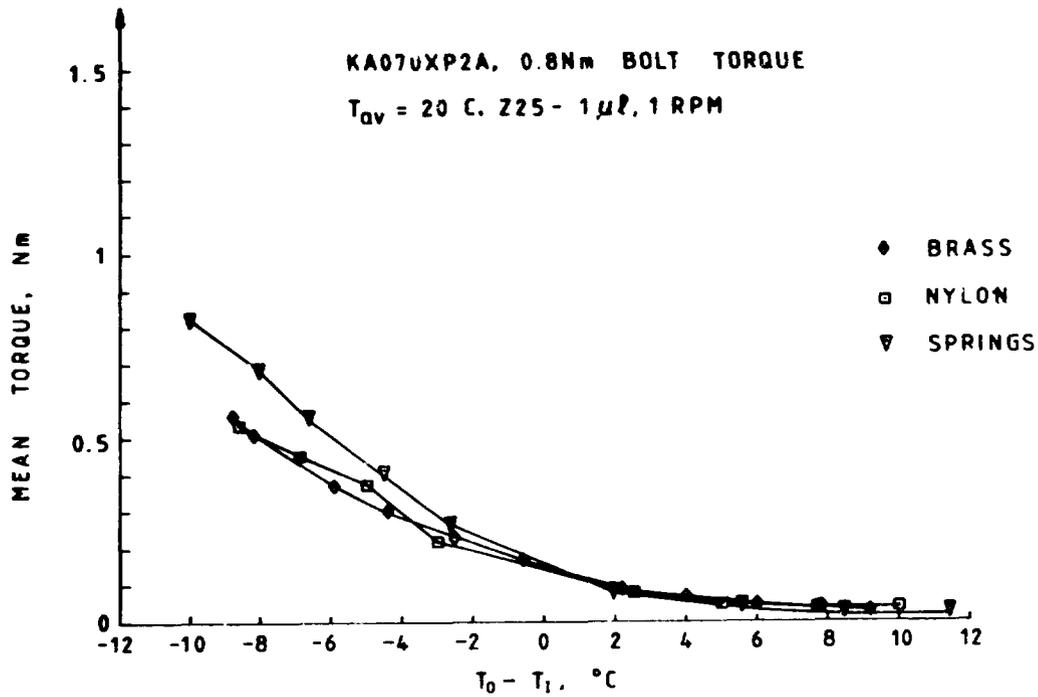
FIG. 15 MEAN BEARING TORQUE Vs. TEMPERATURE
GRADIENT AS A FUNCTION OF CAGE TYPE

THE DESIGN AND DEVELOPMENT OF A SPACECRAFT APPENDAGE TIE DOWN MECHANISM

William D. Nygren and Raymond Head*

ABSTRACT

This paper describes the design and evolution of a spacecraft Appendage Tie Down Mechanism (ATDM), with particular emphasis on the mechanical aspects of using dry lubricants to increase the efficiency of acme threads and worm gearing.

ATDM - DESCRIPTION

The ATDM consists of five major components as shown in Figure 1 and in cross section (Fig. 2). These are (1) a DC torque motor, (2) a worm gear speed reducer, (3) the tension bolt (or T-bolt), (4) nut capture and centering jaws and (5) the capture nut. In addition, there are several minor components such as limit switch assemblies and an anti-backdrive mechanism which couples the drive motor to the worm shaft.

ATDM - OPERATION

The operational sequence is as follows: First the DC torque motor drives the T-bolt through the worm gear speed reducer with a ratio of 58 to 1. The worm gear hub is splined, allowing T-bolt axial advancement while the worm gear rotates. The center section of the T-bolt is a ball screw which advances the T-bolt through its fixed ball nut at a rate of 0.508 cm (0.200 in.) per revolution. The next step is the capture and centering of the nut assembly (see Fig. 4). As the T-bolt advances, it drives the two capture jaws to swing closed. This forces the nut to the proper position to allow the acme threads on the tip of the T-bolt to engage the nut threads.

The capture nut is free to move axially in its housing against two sets of springs. The first is a "soft" stack of wave washers which allows the T-bolt to fully engage the nut under low thread loading. The second stack is made up of Belleville washers which start compressing only after the soft stack spring has completed its stroke. The Belleville springs reach an axial force of 22 678 N (5100 lb) during one revolution of the T-bolt. The mechanism is then shut off by limit switches on the nut housing, which monitor nut spring travel. Figure 3 shows the limit-switch mounting on the nut assembly.

The actual loading or tensioning of the T-bolt by the nut is accomplished by the difference in the leads of the ball screw thread and the acme capture thread on the forward end of the T-bolt. The lead of the ball screw is

---

*Martin Marietta Aerospace, Denver, Colorado

0.508 cm/rev (0.200 in/rev) while that of the 1.905 cm (0.750 in.) double-lead acme screw is 0.846 cm/rev (0.333 in./rev). The T-bolt always advances out of the mechanism at a rate of 0.508 cm/rev (0.200 in./rev); however, after the acme thread engages the capture nut, the nut advances relative to the bolt at a rate of 0.846 cm/rev (0.333 in./rev). Thus the net compression of the nut springs is 0.338 cm (0.133 in.) per revolution of the T-bolt.

DESIGN EVOLUTION

As system requirements were refined, the preload that the ATDM was supposed to develop was substantially increased. The original preload was defined to be 7115 N (1500 lb) maximum. After the first development unit was built, this figure was increased to approximately 13 344 N (3000 lb), and finally to 22 678 N (5100 lb). This tripling of output force required that most attention be focused on mechanical efficiency as the electrical power to drive the mechanism was "fixed" as was the time available for the entire operation to take place. The increased capability of the mechanism was required to take place within the original physical envelope.

To provide this increased capability, the following improvements were made. First, the gear ratio was changed from 50-1 to its present value of 58-1. No further increase was allowable because of gear tooth strength considerations and size and time limitations. The next step was to change from a V-thread to the present ball screw for the driver thread. This was a major improvement; the apparent coefficient of friction dropped from 0.18 to 0.007.

Although this was a major improvement, a 100% torque margin under worst-case conditions of voltage, temperature, and motor K_t torque constant had yet to be demonstrated.

The original development unit had used wet lubricant (Braycote 3L-38RP) for surfaces, and it was calculated during testing that the efficiencies of these two components were around the 30% range because of a coefficient of friction of approximately 0.2 at the mating surfaces. Since the mechanism efficiency was basically the product of the gear box and acme screw efficiencies, the overall mechanism efficiency was only about 10%. A decision was therefore made to switch to a dry lubricant such as molydisulfide for these sliding surfaces of the ATDM the worm/worm gear and the acme capture threads.

The dry lubricant recommended by Materials Engineering was LUBECO 905 as Martin Maretta Co. (MMC) has previously obtained good results with it. After successful application of LUBECO 905, the observed coefficient of friction was .1 or lower at both worm/worm gear interface and at the acme bolt/nut interface in a vacuum environment, this value was seen to futher decrease to the point where efficiencies above 60% were obtained for the individual components, approximately a four-fold increase for the overall mechanism.

DRY-LUBRICANT DIFFICULTIES

When the mechanism was first lubricated with LUBECO 905 and reassembled, it failed almost immediately during testing. This caused carefull reanalysis of the use of dry-film lubricants. Based on the calculated contact stress and wear life required to survive testing, the lubricant should have been successful. However, upon further investigation, the following important facts were learned.

o   No matter how well made and aligned they are, a worm and worm gear must go through a wear-in riod before a true line contact area is established across the face of each gear tooth.

o   In a similar fashion, male and female screw threads must also be mated together by a wear-in period before true area contact is established to support the load.

o   All sharp corners must be removed around each worm and gear tooth, and on all corners of both the male and female acme thread.   In particular this must be done at any partial threads which spiral from minor to major diameters (or vice-versa) such as occurs at the beginning and ending of both the male and the female threads.

o   After the proper contact areas are established, the mating parts should be burnished together, starting with low loads and working up to the full flight loads in gradual steps.

LAPPING

To facilitate a rapid wear-in of the worm/worm gear and T-bolt/nut of the ATDM, the decision was made to lap the mating surfaces together with a grinding compound. Since it is desired to force one surface to conform to the other, both the worm and the T-bolt acme thread were hardened by nitriding prior to starting the lapping process. These surfaces were chosen for the following reasons. It was felt that the T-bolts contour could be more accurately manufactured and dimensionally verified than could its mating nut. The worm was chosen for hardening because it has basically one tooth, which must wear in each tooth of the worm gear to match it exactly. (Thus the worm gets 58 times the wear that any particular worm gear tooth gets during lapping).

After nitriding was completed, the worm/worm gears were serialized along with their housing to be maintained as a matched set. The gear box was then reassembled. The output shaft was attached to a brake which could apply 1.13 N-m (10 in.-lb) of drag. The worm and worm gear were then coated with a 320-grit Clover grinding compound, and the worm was driven at 200 rpm until the desired wear pattern was established across the face of each tooth. Finally, the 320-grit compound was replaced with a 600-grit compound to leave a 16-# to 32-rms surface finish for the application of the LUBECO 905.

In a similar manner, the T-bolt and caging nut were lapped together with the same compounds under a constant axial load of 22-44 N (lb), with the nut fully engaged with the bolt. A special fixture was designed for this purpose (Fig. 5).

BURNISHING

After lapping, the critical parts were relubricated with LUBECO 905. The gear box was then reassembled and reattached to the brake. This time, however, the load was gradually increased in approximately 14 steps to an output torque of 40 N-m (360 in-lb). At this point the input torque was measured to be 0.15 N-m (1.3 in-lb), giving an efficiency of 49.7% under stall conditions. (This would further improve in vacuum conditions.) Likewise, the T-bolt and nut were burnished together at gradually increasing axial load levels to a final load of 17 78 7 N (4000 lb). Here the torque required to rotate the bolt was measured as 33 N-m (291 in-lb), giving an efficiency of 73%. (The bolt required a torque of 12 N-m (105 in-lb) to keep it from over hauling). A coefficient of friction of 0.06 in air can be deduced from these values and the thread geometry.

ANTI-BACK-DRIVE MECHANISM

The success of the dry film lubricant was not completely without a drawback because it led to a futher complication.

At the 22678 N (5100-lb) preload level, it was found that the acme thread would back-drive its low coefficient of friction and large helix angle. This torque was about 17 N-m (150 in-lb) in air and would possibly double under vacuum conditions. The conclusion was that the acme thread could overcome the holding torque produced by the ball nut and so deliver a back-driving torque to the worm gear. Here the low friction coefficient is again harmful as it allows a normally locking gear ratio to back-drive. This potential for back-driving is particularly hazardous during the launch and boost phases of a flight, because the harsh vibration environment increases the likelihood for back-drivirg, at a time when a loss of ATDM preload would be most dangerous.

Of the many possible solutions to this problem, most either caused an unacceptable constant loss of motor torque or required electrical power and control lines which were not available. The solution was to make the coupling between the drive motor and the worm serve as a ratchet which would allow the motor drive the worm in either direction, but not allow the worm to back-drive the motor. The operation of this device is shown in Fig. 6.

The mechanism consists of a detent disk attached to the worm shaft, and a cam disk attached to the motor shaft. These two disks are coupled together by a pin attached to the detent disk, which rides in a slot in the cam disk. This arrangement allow approximately 60° of relative motion between disks. There is also a Vlier-type plunger between the disks (not shown), which locks the disks into the configuration shown in Fig. 6a prior to the start of operations. The final component is the ratchet dog, which in this case has a roller to minimize friction.

The operation is as follows: First, as the motor starts running (see Fig. 6a), the roller rides on the combined outside diameter of the two disks and is held in this configuration by the Vlier pin between them. When the mechanism approaches its desired preload, the transmitted torque becomes large enough to overcome the Vlier pin, the disks shift to the configuration shown in Fig. 6b, and the dog starts ratcheting. Next, if the worm attempts to back off, it can rotate back only until the roller comes against the now "uncovered" detent (Fig. 6c). Finally, when the mechanism, is desired to be uncaged the reversal of the drive motor causes the cam disk to cam the roller out of the detent, and the back-out can commence as shown in Fig. 6d.

PRESENT STATUS

A development model of the ATDM in various configurations has been under test for some time. In its latest version, it has successfully completed thermal vacuum testing, vibration testing, and extended-life testing. Qualification and flight units are scheduled for testing.

FIGURE 1. ATDM

MICRO SWITCH
ASSY

WORM AND
WORM GEAR

TENSION BOLT

DISC SPRINGS

SPLINED
SHAFT

BALL NUT
AND BALL SCREW

FINGER

ACME
NUT

173
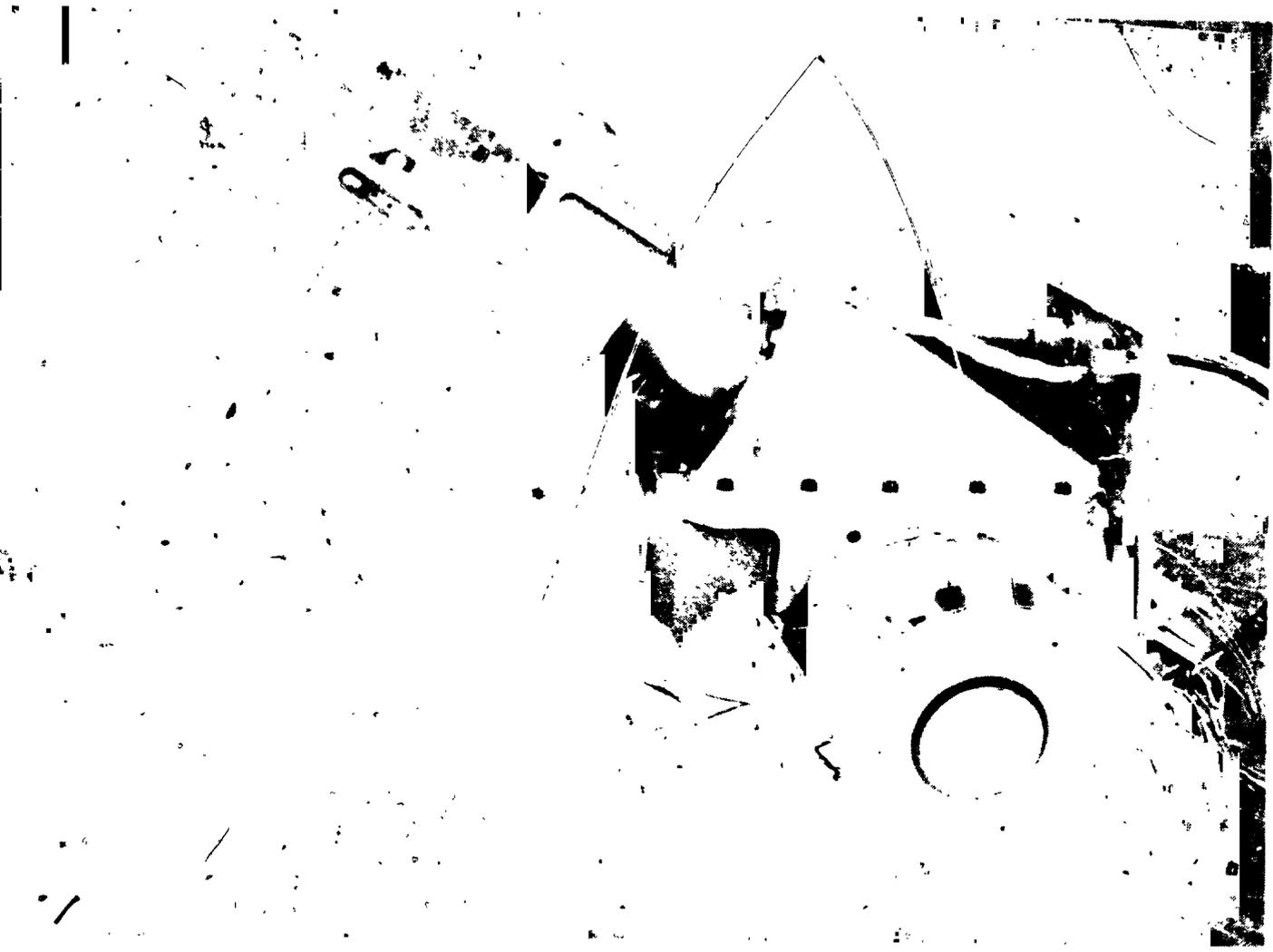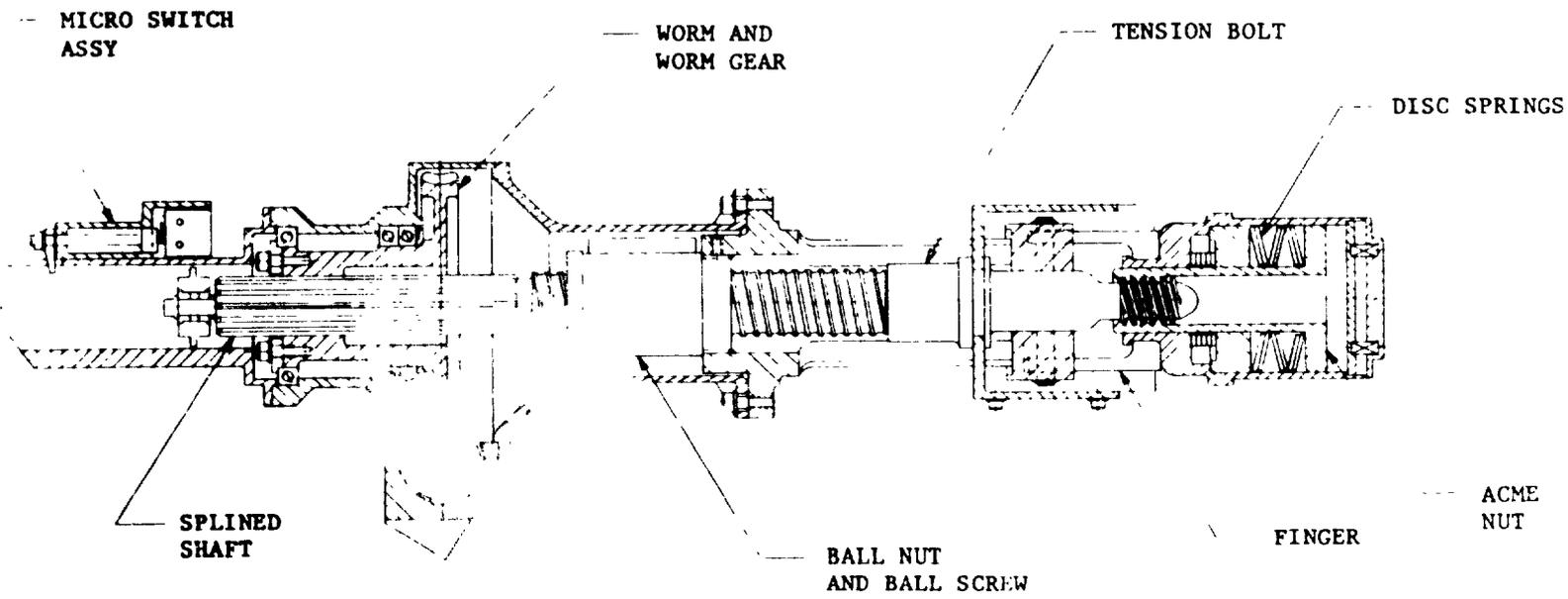
FIGURE 2. MECHANISM CROSS SECTIC..

FIGURE 3. HAND AND FINGER CONFIGURATION

174

UNCAGED   NUT ALIGNMENT   CAGED
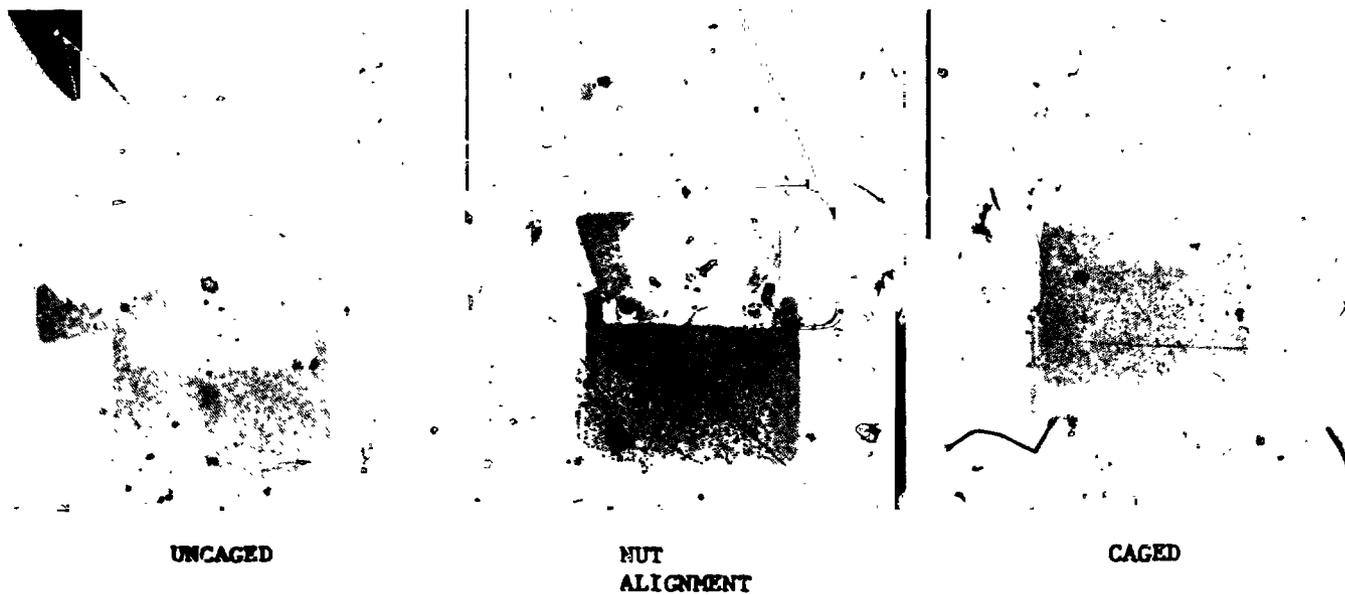
FIGURE 4. CAGING SEQUENCE

FIGURE 5. BOL1 AND NUT LAPPING FIXTURE
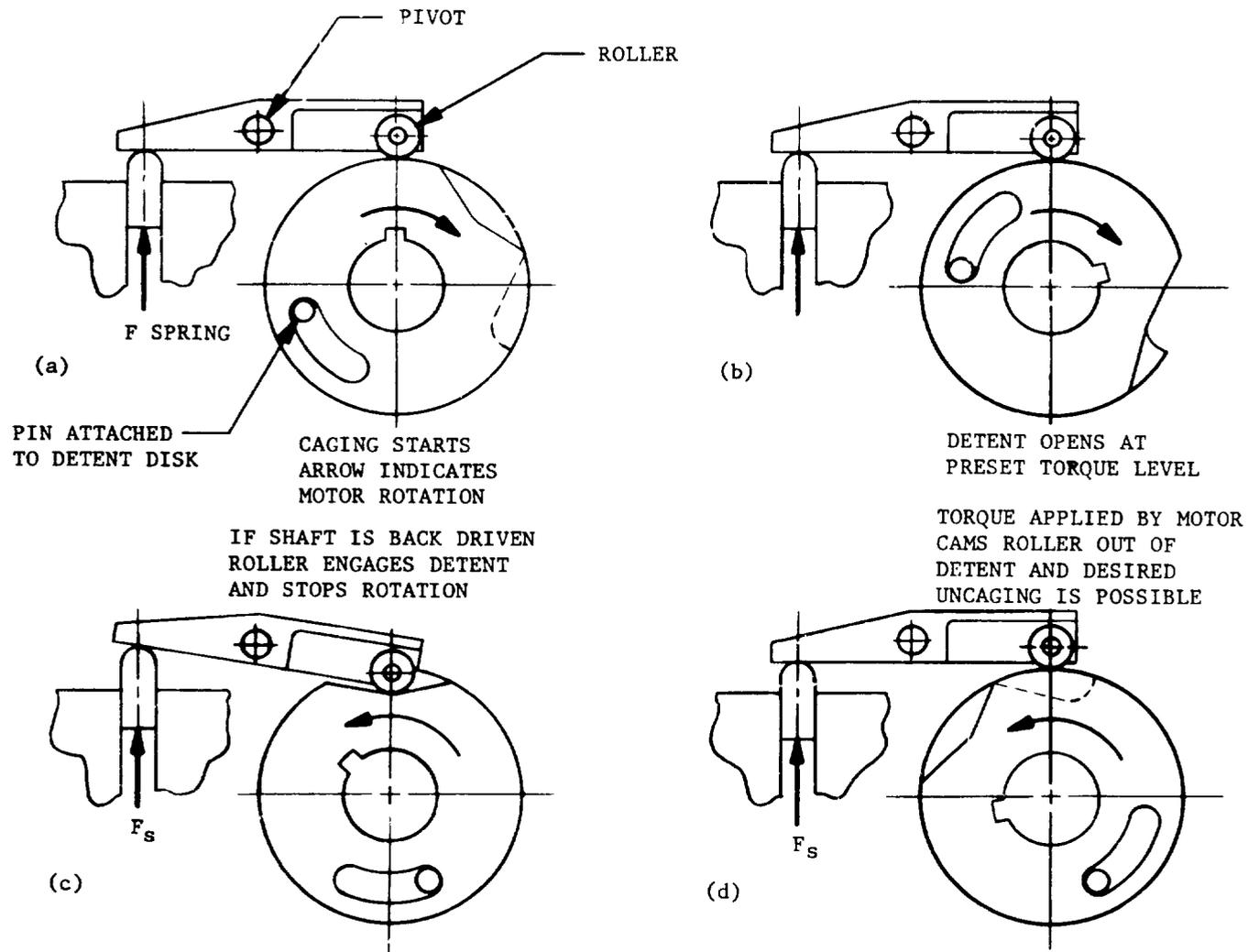
FIGURE 6. ANTI-BACK-DRIVE MECHANISM

THE USE OF PERFLUOROETHER LUBRICANTS
IN UNPROTECTED SPACE ENVIRONMENTS

Bryan H. Baxter*, Barry P. Hall*

ABSTRACT

This paper describes a series of ball bearing tests in simulated space environment to determine durability of perfluoroether lubricants. The results of the examination of the test bearings for each stage are described and experimental techniques designed to overcome lubricant degradation are outlined.

INTRODUCTION

The perfluoroether (PFE) group of lubricants, which is manufactured by a variety of companies around the world, has unique physical properties suggesting that they would be ideal for space applications.

The available range of products in this class of fluids is very large indeed and is complicated by the fact that several different manufacturing routes are used, resulting in different families of product.

To illustrate the physical properties which are relevant to space component lubrication, typical data are presented in Table I for two members of representative series, designated Z and Y.

These properties have encouraged designers to consider the use of such lubricants in space mechanisms, and in order to establish design rules and life data, several research programmes have been initiated.

At the European Space Tribology Laboratory (ESTL) established at the National Centre for Tribology, Risley, England, considerable research effort has been expended on studies of lubrication in the space environment, supported by the European Space Agency (ESA).

Part of this ESTL research programme has involved long term studies of the PFE lubricants, running in test ball bearings under ambient pressures of 10^{-6} torr or less.

At the Materials Science Group, in British Aerospace, Stevenage we have established a small working group which has specialized for several years in studies of lubrication mechanisms. As a result of this specialization we have been pleased to assist ESTL and ESA in the studies of test bearings with the aim of improving the understanding of lubricant degradation studies.

Over the past two to three years, we have been closely associated with a series of studies on the PFE lubricants and this paper describes the sequence of tests involved, the results of examining the test bearings and the conclusions we have drawn from the data.

* British Aerospace plc. Stevenage England

179

LIFE STUDIES WITH Z25 LUBRICATED BALL BEARINGS, RUNNING IN VACUUM

Summary of Tests

In this work, carried out by Mr. K. Stevens at ESTL (1,2), the test bearings were 42 mm o.d. 10 ball angular contact. Raceways and balls were in 440C, and a one-piece fabric reinforced retainer was fitted.

Four bearings were used in this first test, run as preloaded pairs within the vacuum chambers (10^{-6}torr), one at 200 rpm and the other at 1400 rpm, for a total for each pair of 10^8 revolutions.

It was observed during this test that the running torque of both bearing pairs fell steadily, reaching a minimum after 10^6 revolutions. If the tests were stopped for 15 minutes, the torque on restarting was found to be equal to that at the start of the test, but this fell rapidly to the minimum level within a short time.

Bearing noise increased with this fall in running torque, and bearing surface temperature also increased slightly as the minimum torque level was reached.

On completion of the tests it was found that all the bearings were contaminated with brown/black deposits along each ball track and in the ball pockets of the phenolic retainers.

Examination of Bearings

The samples submitted were as follows:

1. An inner race washed free of unchanged oil and contaminant.

2. A sample of contaminant washed free of unchanged oil using trichlorotrifluoroethane (F113).

3. A complete test bearing (1400 rpm) with lubricant and lubricant-degradation products intact.

Preliminary compositional analysis on the contaminant, after washing free of unchanged oil, had been carried out by ESTL, and the results are shown in Table II.

These indicated that the deposits from both the 200 and 1400 rpm bearings were rich in Fe and Cr, both contained a significant level of organic material and that no significant 'foreign' elements were present.

Microscopic examination of the ball track on the raceway of the washed inner bearing (sample 1) showed a well defined wear track with surface pitting. The surface within the wear track carried a very thin, highly adherent film which could not be removed by repeated washing in solvent.

The complete bearing (sample 3) was disassembled and examined microscopically with the lubricant intact on the raceways.

Both inner and outer raceways were heavily contaminated with the black contaminant which had spread on either side of the ball tracks. At higher magnification this contaminant which appeared red/brown in transmitted light was seen to be confined to an immiscible phase separated by clearly visible boundaries from the colourless transparent Z25 film (Figure 1).

Analysis of Deposits

Because of the particular chemical structure of the PFE lubricants, they are totally insoluble in common flushing solvents such as toluene or benzene, chloroform, trichloroethane, etc, and can only be dissolved in fluorinated solvents such as chlorotrifluoroethane (Fl13). Therefore, if a sample of mixed Z25 oil and contaminant was flushed repeatedly with Fl13, it was found that all the free Z25 could be removed, leaving dense dark solid which was completely insoluble in Freon 113.

Micro infra-red spectroscopy was used as a preliminary method of characterization of the sample, and the results showed that the material was free of carbon hydrogen absorption, and had a strong carbon fluorine absorption. This indicated that the contaminant was derived directly from the perfluoroether lubricant and was not a 'foreign' product, such as phenolic polymer constituents of the retainer, or residues of cleaning agents remaining in the bearing.

Since the contaminant was a non-volatile 'polymeric' material it was decided to apply pyrolysis gas chromatography mass spectrometry (PGC MS) both to the sample and the unchanged Z25 oil in an attempt to establish the structure of both and hence the mechanism of formation of the contaminant.

The technique of PGC MS involves the process of rapid heating of a polymeric sample within the carrier gas stream of a gas chromatograph. This heating, typically within the range 700 to 900°C, causes thermal "cracking" of the sample to produce a series of stable compounds of lower molecular weight and hence of much greater volatility than the parent compound. These compounds are formed in the carrier gas stream of the chromatograph and are carried onto the column and separated in the conventional way. By the use of carefully controlled conditions the products of a given polymer are both reproducible and characteristic of the parent polymer and the technique finds widespread use in polymer characterization and identification.

By combining a fast scanning mass spectrometer with the gas chromatograph, it is possible to obtain the mass spectrum of each component of the pyrogram as it leaves the gas chromatograph, and thus a rapid identification of each fragment can be obtained.

The equipment used for this work at B.Ae Stevenage was a Finnigan 4021 GC/MS which is coupled to a Digilab Nova 4 computer. This data processor is used to control the operation of the equipment and also for the identification of compounds separated chromatographically.

In Figure 2 the PGC MS output obtained by the pyrolysis of unused Z25 is shown. It is presented in the form known as the reconstructed ion chromatogram (RIC). This is a plot of the ion current at the mass spectrometer detector as the vertical axis, against the time as the horizontal axis. The form of the RIC shown in Figure 2 is immediately recognizable as a typical gas chromatograph since it is generated by using the mass spectrometer as a GC detector. As each component of the pyrolysis leaves the gas chromatograph and enters the mass spectrometer, the ion current rises, reaching a maximum and then falls as the concentration of the component decays, thus building up the type of output shown in Figure 2.

Despite the apparent simplicity of the output, each pyrogram RIC carries an immense amount of information. Typically, using a mass spectrometer scanning rate of 1 Hz, each RIC contains up to 3000 individual mass spectra, each of which can be recalled from memory, searched against a reference library of some 30,000 standard compounds and identified.

Examination of the output obtained from the pyrolysis of Z25 in Figure 2, shows that it comprises two main parts, a single large component at or near scan number 43, followed by a series of closely spaced, barely resolved peaks numbering some 50 components.

Interpretation of the computer identification of the mass spectrum of the component at scan 43 showed that it was a fluoroalkene, tetrafluoroethene, as shown by the printout in Table III.

When the computer identification was applied to each of the later components from scan 150 to scan 1000, a problem was encountered. Each component when recalled from the computer memory was found to have the same mass spectrum (Figure 3) such that when a computer identification was run each gave exactly the same search. Typical printouts are shown in Table IV from two well separated components, both of which are identified as chloropentafluoroethane.

This apparent anomaly is resolved if the structure of the oil is considered. Since it is a polymer, i.e., a chain of repeating identical units, then the pyrolytic fragments will each be very similar in structure, differing only in their chain length. In the mass spectrum each fragment will ionize to give a relatively small number of ions common to each fragment and independent of the chain length of the fragment.

Thus in the mass spectrum in Figure 3 it is possible to identify the ions CF_2^+ (50), CF_3^+ (69), $C_2F_4^+$ (100), $C_2F_5^+$ (119), C_2F_5O (135) and $C_2F_5.O.CF_2^+$ (185).

The significant information in this series is the pair of ions $C_2F_5^+$ at a.m.u. 119 and $C_2F_5O^+$ a.m.u. 135. This indicates that the repeat unit in the polymer contains two carbons and one oxygen atom, and thus the polymer structure is:
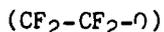
$$(CF_2-CF_2-O)$$

This structure satisfies the pyrolytic fragments obtained, i.e., the first component C_2F_4, followed by a series of fragments of the polymer chain, made up of $CF_2.CF_2.O$ units.

On applying the pyrolytic technique to the washed contaminant, the output shown in Figure 4 was obtained. If this is compared with the pyrogram of the unused oil in Figure 2, it will be seen that only the early compound was obtained; the system of multiple peaks from about scan number 100 to scan number 1000, so characteristic of the Z25 oil was only barely detectable.

Computer searching of the early compound gave an identical output to that obtained from the corresponding component in the Z25 output, namely tetrafluoroethene.

Discussion of Analytical Data

The output obtained from the washed contaminant, namely tetrafluoroethene alone, could only be interpreted as indicating that the "oxygen component" of the polymer had been lost in some way. In simple terms, if the product was a perfluorohydrocarbon, i.e., $CF_2 - CF_2 - CF_2 - CF_2$, then pyrolysis would give the result obtained.

As an example of this, the pyrogram of a sample of polytetrafluoroethylene (Fluon, Teflon, etc.) prepared under identical conditions to those used on the contaminant is shown in Figure 5. This also consisted of a single component searching as tetrafluoroethene.

However, a simple model comprising a perfluorohydrocarbon would not satisfy all the data. For example, the intense color and the very high content could not be satisfactorily explained.

It is proposed therefore that the contaminant consisted of a product formed by interaction between the lubricant and the wearing surface of the bearings. It was further argued that the proposed linear structure of the oil, i.e.,

$$O.CF_2.CF_2.O.CF_2.CF_2$$
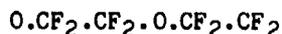
could render the material particularly sensitive to adsorption to a wearing surface, owing to the unprotected nature of the oxygen atoms in the structure. Sufficient work was not done on the product to establish whether this was a true compound, or a complex formed by the adsorption of the lubricant onto wear debris, but it appears likely that pyrolysis of such a

product would result in the release of the tetrafluoroethene, leaving the oxygen component bound firmly to the inorganic residue remaining after pyrolysis.

The formation of such a surface film would help to explain the loss of running torque which developed during the test. This loss of torque could be explained as being due to loss of the viscous drag component of the total running torque of the bearing pair, and the development of a surface film on the ball track could well cause the loss of the oil film due to non-wetting and retraction. On stopping the bearing, slow flow back would occur, allowing the temporary re-establishment of the hydrodynamic condition, before oil retraction recurred and the viscous drag component was lost again.

Thus this initial test suggested that under the conditions used, namely low pressure (zero oxygen, moisture etc.), the Z25 test lubricant was liable to form a surface 'reaction' product which would wear away sacrificially, building up within the bearing as described.

REPEAT OF BEARING TESTS

Introduction

Following the results obtained in the first test, ESTL prepared and ran a second bearing life test, which was identical in all respects to the first run, except that the bearings, to the same specification, were obtained from a different source.

The results were quite different. The torque level remained constant throughout the 10^8 revolutions of the test, and on disassembly of the test rig no trace of the black contaminant could be found in the bearings.

Examination of Test Bearing

As before, a single bearing was submitted for examination and analysis. On disassembly and microscopic examination at low power (Figure 6), the oil film in the raceways was seen to be cloudy. No trace of the black contaminant could be found, and the ball tracks were smooth and free of any of the pitting wear seen previously.

At higher magnification (Figure 7) it was revealed that the cloudiness of the oil film was due to the presence of two immiscible fluids in the bearings, one in the form of a dispersion of droplets in the second fluid, thus causing light scattering and the cloudiness observed.

Analysis of Bearing Lubricants

Without the 'target' of the insoluble contaminant found in the first test bearings, it was obviously necessary to change the method of analysis. Because of the presence of two mutually insoluble fluids, one of which must have been the test oil Z25, it was almost certain that the second fluid would be a nonfluorinated material such as an hydrocarbon or diester oil.

Therefore by flushing down the bearings with Freon 113 in which both components would be soluble, it was possible to concentrate the lubricant in one region of the bearing and obtain a representative sample for PGC MS.

The output obtained is shown in Figure 8. If one compares this output with that from the unused Z25 standard in Figure 2, it can be seen that although the pyrogram starts with a similar early component, identifiable as tetrafluoroethene as before, the later portion was quite different. In contrast to the close spaced components of the Z25 pyrogram, the output obtained showed a different series of well resolved compounds. The computer search data for three typical samples at scan Nos. 138, 600 and 686, are shown in Table V, proving unequivocally that hydrocarbon oil was present. The output in figure 8 also showed the typical pattern of the PFE oil lying beneath the strong output from the hydrocarbon.

(Due to the ease of pyrolysis and lower ionization potential of the hydrocarbon, PGC MS of a mixture of hydrocarbon tends to result in the exaggeration of the level of the hydrocarbon components in the mixture).

Discussion of Data from Second Bearing Life Test

The reason for the difference in bearing performance between the first and second test runs was obvious following the examination of the bearings. The presence of a second hydrocarbon oil would have successfully decoupled the Z25 from the surface and thus prevented any disruption of the PFE lubricant.

Normally when cross contamination of liquid lubricants occurs, the effects are minimized due to the immiscibility of commonly used systems. Because hydrocarbons and PFE systems are so completely insoluble, one with another, each can act independently when present together in a bearing.

Whichever component has the greatest tendency to wet the bearing surface will be the dominant lubricant in the behaviour of the test bearing.

This result did little to resolve the problem of the apparent sensitivity of the Z lubricant to active metal surfaces, and in fact could have been seen as supporting the theory since decoupling by the accidental use of a second lubricant had completely prevented a recurrence of the degradation.

EXPERIMENTAL METHODS TO VERIFY THEORY

Introduction

Two techniques were investigated to overcome the apparent difficulties associated with the use of the Z series oil.

Non-metallic Coating on Test Bearing Surfaces

The first was to decouple the lubricant from the wearing metal surface by the application of non-metallic layers to the bearing surfaces. The system

chosen by Mr. Stevens at ESTL was to use tungsten carbide balls which had been coated with titanium carbide, running against raceways which had been coated with zirconium nitride. In all other respects the bearings were exactly as used in the previous test runs

The results of running the coated bearings in preloaded pairs at 10^{-6} torr as before were excellent. A total bearing life of 10^8 revolutions was achieved without any change in running torque, and on completion of the test, no evidence of oil degradation could be found.

One of the pair of bearings was submitted for analysis as before, and microscopic examination confirmed that no oil degradation resembling the original result could be detected. The zirconium nitride layer had been worn away from the central high load region of bearing raceways, and a low level of solid debris had been generated as a result. The appearance of the nitride layer and the worn track are shown in Figure 9, which shows the junction between the bright, worn ball track and the partially worn nitride layer. The titanium carbide surface of the balls had not been destroyed.

PGC MS of the very low level of Freon residues gave the output shown in Figure 10. Owing to the extremely small sample size, the output was poorly resolved with respect to the PFE fragments which appeared as the ill-defined, broad peak with a maximum near scan number 800.

The information available from this analysis was improved by performing ion specific searches on the data. By this means known or suspected impurities can be identified by feeding in search ions specific to the unknown. This is demonstrated in Figures 11, and 12, in which the search for hydrocarbons, mass numbers 41, 43 and 57, in conjunction with the RIC and a similar search for the PFE fragments, mass numbers 119, 135 and 185, are shown.

This technique showed clearly that the sample was composed of a very low level of Z25 and hydrocarbon oils, at levels insignificant to the result of the bearing test.

Test of an Oil With Different Chemical Structure

The second part of the hypothesis concerning the sensitivity of the Z type of oil to decomposition in ball bearings was that the particular linear structure of the polymer could contribute to the effect.

Other types of perfluoroether lubricant are available, one of which a member of the Y series; YVAC 40/11 is also recommended for instrument bearing use. As shown in the table of comparative physical data in Table I, certain penalties would be incurred in substitution for Z25, such as an increased viscosity, a higher vapour pressure at a given temperature and a higher pour point.

186

The final ESTL bearing test in this series was identical with the first test, except that YVAC 40/11 was substituted for the Z25 lubricant.

As before, the test duration was 10^8 revolutions at 200 and 1400 rpm, and both were completed without change in running torque.

A test bearing (200 rpm) was submitted for study and was found to be in perfect condition. The oil was unchanged and no wear track was visible on either raceway. The precise ball track ꞏ ꞏ only identified on the inner raceway by the use of a surface topography enhancement technique (Nomarski interferometry), which enables very light surface brinells to be detected (Figure 13).

GC MS of the unrun lubricant YVAC 40/11 gave the output shown in figure 14, in which only the polymer fragmentation pattern from scan 300 to about scan 1000 is shown. Comparison of this with the same region in figure 2, the pyrogram of Z25, shows that the YVAC 40/11 gave a more complex pattern.

As before, computer searching of the mass spectra (figure 15) obtained was unsatisfactory due to the uniformity of successive outputs. However a manual interpretation allows the structure of the lubricant to be estimated; e.g., the ions identified were CF_3+ (60, C_2F_3+O (97), C_2F_4+ (100) C_2F_5+ (119), C_3F_5+O (147) and C_3F_7+ (169). The presence of the two ions with three carbons was a very strong indication that the lubricant had the structure.

$$CF - CF_2 - O$$
$$DF_3$$
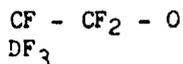
i.e., a branched chain lubricant in contrast to the linear form of the Z series.

DISCUSSION AND CONCLUSIONS

In the in vacuo testing of bearings lubricated with Z25, the evidence of the test results and the post-test examination of bearings point unequivocally to the fact that the lubricant suffered considerable chemical decomposition which had clearly occurred in the contact regions between ball and raceway.

The major difficulty is to explain the cause of the decomposition.

The evidence available at present suggests that the operating bearings in-vacuo, i.e., in "zero" oxygen conditions results in the interaction between the lubricant and the wearing surface. A problem arises in establishing a detailed mechanism for this surface effect since in the first ESTL test, both the 200 rpm test bearing (boundary conditions) and the 1400 rpm test bearing (hydrodynamic) appeared to be equally contaminated, when in fact the boundary condition would be expected to be the most severe with respect to a surface-wear-generated effect. Despite these limitations, each

of the subsequent experiments supported the hypothesis that the lubricant was decomposed by the wearing surfa `, e.g., the accidental contamination of test bearings with a second oil, and the use of nonmetallic surface coatings both resulted in remarkable improvements in lubricant life.

The final experiment using the second, Y series, oil was also consistent with the surface interaction theory, if the stereo chemistry of the lubricant could have the effect proposed, although in this instance the higher viscosity lubricant could have a significant effect on film thickness and stability and could result in improved lubricant life.

Much more investigation will be necessary before a clear understanding is available of the complex mechanisms involved in the tribology of the perfluoroether lubricants. The test described herein were carried out at low pressure (10^{-6} torr) and thus the wearing surface would be low in oxygen and thus chemically active. However other work (not reported) has shown that PFE lubricants can decompose in bearings operating in ambient atmosphere.

This work is also concerned exclusively with PFE lubricants of European origin; other sources, using different synthetic methods of manufacture, could give different results.

At this stage of the work, it appears that bearing surface modification with an inert substance, resulting in "decoupling" of the lubricant from the active wear region of the bearing surfaces, offers the best course to ensure maximum lubricant life.

REFERENCES

1. The performance of Z25 oil in ball bearings operating in vacuum.

    E.S.A. (ESTL) 056 January 1983. European Space Agency.

2. Some observations on the performance of Fomblin Z25 oil and Drayco 3L-38-RP in ball bearings and gearboxes.

    Proceedings of the 1st European Symposium on Space Mechanisms and Tribology.

    Neuchatel 12th -14th October 1983 (E.S.A. SP196, 12/83).

ACKNOWLEDGEMENTS

Table I   Typical Physical Properties for a Z and a Y Type Oil

OIL TYPE	KINEMATIC VISCOSITY Cst 20°C	VISCOSITY INDEX ASTM D2270	VAPOUR PRESSURE mm Hg 20°C	POUR POINT °C	VOLATILITY LOSS % BY WT. 149°C
Z25	233	348	5×10^{-12}	-60	0.1
YVAC 40/11	462		2×10^{-11}	-32	

Table II   Composition of Bearing Contaminant

COMPONENT	200 RPM	1400 RPM
Fe	20 - 30%	90%
Cr	10% of Fe	10% of Fe
Cl	trace	2%
Minor element	trace	trace
Organic	balance	balance

Table III C_2F_4 Computer Library Search

LIBRARY SEARCH   DATA: INNER # 42   BASE M/E: 81
86/11/81 11:26:00 + 0:42   CAL1: C10 # 1   RIC: 434175.
SAMPLE: SAMPLE FROM INNER WASHED SEVERAL TIMES IN FREON 113 (ESTL JOB)
42 - # 32 - # 73 X1.00

25418 SPECTRA IN LIBRARYNB SEARCHED FOR MAXIMUM PURITY
147 MATCHED AT LEAST 4 OF THE 16 LARGEST PEAKS IN THE UNKNOWN

RANK IN NAME
1 1437 1-PROPENE,1,1,2,3,3,3-HEXAFLUORO-
2 1436 ETHENE,TETRAFLUORO-
3 2132 BUTANAL,HEPTAFLUORO-
4 1418 CYCLOBUTANE,OCTAFLUORO-
5 2109 PROPANAL,PENTAFLUORO-
6 2031 OCTANAL,PENTADECAFLUORO-
7 2134 BUTANOICACID,HEPTAFLUORO-
8 2071 BUTANE,DECAFLUORO-
9 2138 CYCLOPENTANE,NONAFLUORO-

RANK	FORMULA	M.WT	B.PK	PURITY	FIT	RFIT
1	C3.F6	150	100	985	840	981
2	C2.F4	100	81	966	834	988
3	C4.H.O.F7	198	100	983	677	825
4	C4.F8	200	100	486	717	512
5	C3.H.C.F5	148	100	458	714	488
6	C8.H.O.F15	398	63	447	612	981
7	C4.H.O2.F7	214	119	394	539	484
8	C4.F10	238	69	362	529	362
9	C5.H.F9	232	60	359	693	372

Table IV Computer Library Search of Two Z25 Pyrolytic Fragments

```
LIBRARY SEARCH          DATA: RES ● 289      BASE M/E:  119
06/05/81 13:50:00 +  4:49   CALI: C10 ●   1   RIC:    25983.
SAMPLE: RESDUE FROM Z25 SAMPLE
  ● 289 - ● 280 - ● 298 x1.00

25410 SPECTRA IN LIBRARYNB SEARCHED FOR MAXIMUM PURITY
   961 MATCHED AT LEAST 2 OF THE 16 LARGEST PEAKS IN THE UNKNOWN

RANK IN NAME
1    332 ETHANE,CHLOROPENTAFLUORO-
2    333 ETHANE,HEXAFLUORO-
3   3175 BUTANE,1,1,1,2,3,3,4,4,4-NONAFLUORO-2-(TRIFLUOROMETHYL)-
4   3822 DISULFIDE,BIS(PENTAFLUOROETHYL)
5  14885 BENZENEPROPANOICACID,.BETA...BETA.-DIMETHYL-,METHYLESTER
6   3821 PENTANE,DODECAFLUORO-
7   2071 BUTANE,DECAFLUORO-
8   2683 BENZAMIDE,2-METHYL-
9  24281 BENZAMIDE,3-METHYL-N-\(PHENYLAMINO)THIOXOMETHYL\-
```

RANK	FORMULA	M.WT	B.PK	PURITY	FIT	RFIT
1	C2.CL.F5	154	119	177	761	160
2	C2.F6	138	119	177	949	181
3	C5.F12	288	119	157	819	189
4	C4.S2.F10	302	119	141	510	182
5	C12.H16.O2	192	119	135	681	165
6	C5.F12	288	119	134	702	90
7	C4.F10	238	69	126	679	72
8	C8.H9.O.N	135	135	121	647	64
9	C15.H14.O.N2.S	270	119	120	631	179

```
LIBRARY SEARCH          DATA: RES ● 318      BASE M/E:  119
06/05/81 13:50:00 + 5:10   CALI: C10 ●   1   RIC:    26847.
SAMPLE: RESDUE FROM Z25 SAMPLE
ENHANCED (S 150 2N 0T)

25410 SPECTRA IN LIBRARYNB SEARCHED FOR MAXIMUM PURITY
   55 MATCHED AT LEAST 3 OF THE 16 LARGEST PEAKS IN THE UNKNOWN

RANK IN NAME
1    332 ETHANE,CHLOROPENTAFLUORO-
2  15372 MOLYBDENUM,TETRACARBONYLBIS(HEXAMETHYLPHOSPHOROUSTRIAMIDE-P)-
3  19633 PYRROLO\1,2-B\\1,2,4\OXADIAZOLE-2(1H)-THIONE,TETRAHYDRO-5,5-DIMETHYL-1
4   4216 PHENOL,2-\1-(4-HYDROXYPHENYL)-1-METHYLETHYL\-
5    599 BENZENEACETAMIDE,.ALPHA.-ETHYL-
6   1733 1,6,10-DODECATRIEN-3-OL,3,7,11-TRIMETHYL-,\S-(Z)\-
7  11006 MOLYBDENUM,PENTACARBONYL(HEXAMETHYLPHOSPHOROUSTRIAMIDE-P)-,(OC-6-22)-
8  19634 PYRROLO\1,2-B\\1,2,4\OXADIAZOLE-2(1H)-THIONE,TETRAHYDRO-5,5,7,7-TETRAM
9   6526 SILANE,(ERGOSTA-5,7,22-TRIEN-3.BETA.-YLOXY)TRIMETHYL-
```

RANK	FORMULA	M.WT	B.PK	PURITY	FIT	RFIT
1	C2.CL.F5	154	119	170	626	266
2	C16.H36.O4.N6.MO.P2	536	119	146	652	206
3	C13.H16.O.N2.S	248	119	146	494	273
4	C15.H16.O2	229	119	132	495	212
5	C10.H13.O.N	163	119	117	474	215
6	C15.H26.O	222	119	99	364	207
7	C11.H10.O5.N3.MO.P	401	119	93	426	219
8	C15.H20.O.N2.S	276	69	85	312	193
9	C31.H52.O.SI	468	69	74	209	197

Table V   Computer LibrarySearch of Three Hydrocarbon Impurities

```
LIBRARY SEARCH              DATA: RISRES2 • 138      BASE M/E:   56
09/07/82 15:25:00 + 2:10    CALI: AGD1 + 3          RIC:     6687.
SAMPLE: RISLEY A OUTER LUB RESIDUE
  • 138 - • 138 - • 150 X1.01

25409 SPECTRA IN LIBRARYNB SEARCHED FOR MAXIMUM PURITY
   87 MATCHED AT LEAST 8 OF THE 16 LARGEST PEAKS IN THE UNKNOWN

RANK IN NAME
1  3131 1-HEXENE
2  1288 CYCLOHEXANE
3  7349 2H-PYRAN-2-ONE,TETRAHYDRO-3,6-DIMETHYL-
4  4011 1-PENTENE,2-METHYL-
5   768 CYCLOPENTANE,METHYL-

RANK  FORMULA                      M.WT B.PK   PURITY   FIT   RFIT
1 C6.H12                            84   41      952    976    978
2 C6.H12                            84   56      913    936    935
3 C7.H12.O2                        128   42      904    937    942
4 C6.H12                            84   56      895    917    920
5 C6.H12                            84   56      895    919    923


LIBRARY SEARCH              DATA: RISRES2 • 600      BASE M/E:   56
09/07/82 15:25:00 + 10:00   CALI: AGD1 • 3          RIC:     8399.
SAMPLE: RISLEY A OUTER LUB RESIDUE
  • 600 - • 592 - • 600 X1.01

25409 SPECTRA IN LIBRARYNB SEARCHED FOR MAXIMUM PURITY
   145 MATCHED AT LEAST 8 OF THE 16 LARGEST PEAKS IN THE UNKNOWN

RANK IN NAME
1  4250 1-DECENE
2  1374 1-DECANOL
3  8192 1-OCTENE,3,7-DIMETHYL-
4  1745 1-NONANOL
5  1389 1-DODECANOL

RANK  FORMULA                      M.WT B.PK   PURITY   FIT   RFIT
1 C10.H20                          140   41      686    996    687
2 C10.H22.O                        158   41      679    961    679
3 C10.H20                          140   43      669    972    675
4 C9.H20.O                         144   56      662    979    666
5 C12.H26.O                        186   41      659    958    671


LIBRARY SEARCH              DATA: RISRES2 • 686      BASE M/E:   43
09/07/82 15:25:00 + 11:26   CALI: AGD1 • 3          RIC:     5119.
SAMPLE: RISLEY A OUTER LUB RESIDUE
  • 686 - • 676 - • 694 X1.01

25409 SPECTRA IN LIBRARYNB SEARCHED FOR MAXIMUM PURITY
   220 MATCHED AT LEAST 8 OF THE 16 LARGEST PEAKS IN THE UNKNOWN

RANK IN NAME
1  4157 1-UNDECENE
2  1383 1-UNDECANOL
3  1374 1-DECANOL
4  1745 1-NONANOL
5  1389 1-DODECANOL

RANK  FORMULA                      M.WT B.PK   PURITY   FIT   RFIT
1 C11.H22                          154   41      847    991    840
2 C11.H24.O                        172   41      835    980    835
3 C10.H22.O                        158   41      828    978    825
4 C9.H20.O                         144   56      818    985    818
5 C12.H26.O                        186   41      807    957    834
```

192

Figure 1. Contaminant Dispersion on Test Bearing x 125

RIC
05/18/91 22:34:00
SAMPLE: STD OF 225
RANGE: G 1.1200 LABEL: N 0. 4.0 QUAN: A 0. 1.0 BASE: U 20. 3

DATA: 225STD 01
CALI: C10 D1

SCANS   1 TO 1268

1142788.

RIC

43

600

210

200
3:20

400
6:40

600
10:00

800
13:20

1000
16.40

1200
20:40

SCAN
TIME
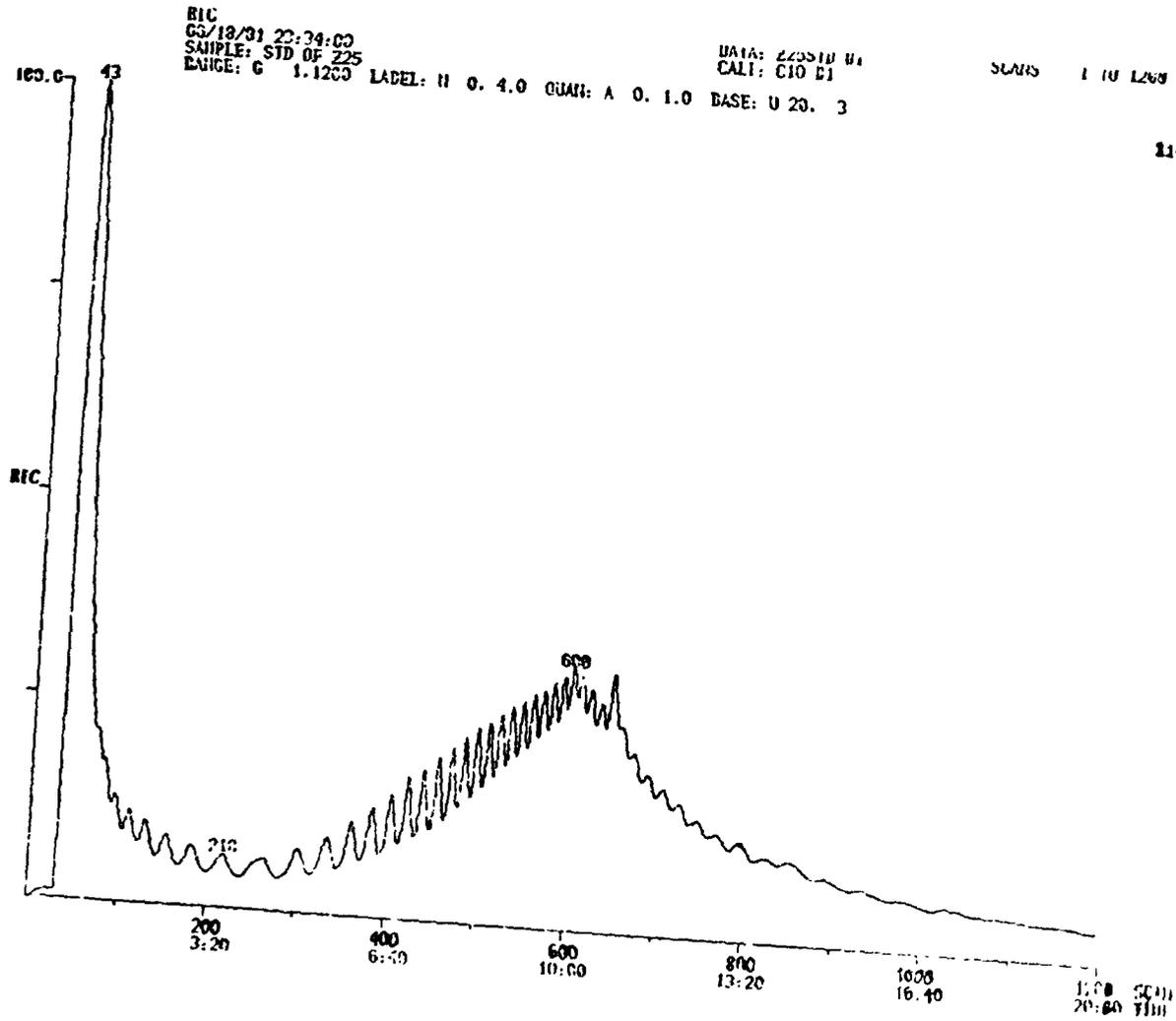
Figure 2.   PGC MS of Fresh 225
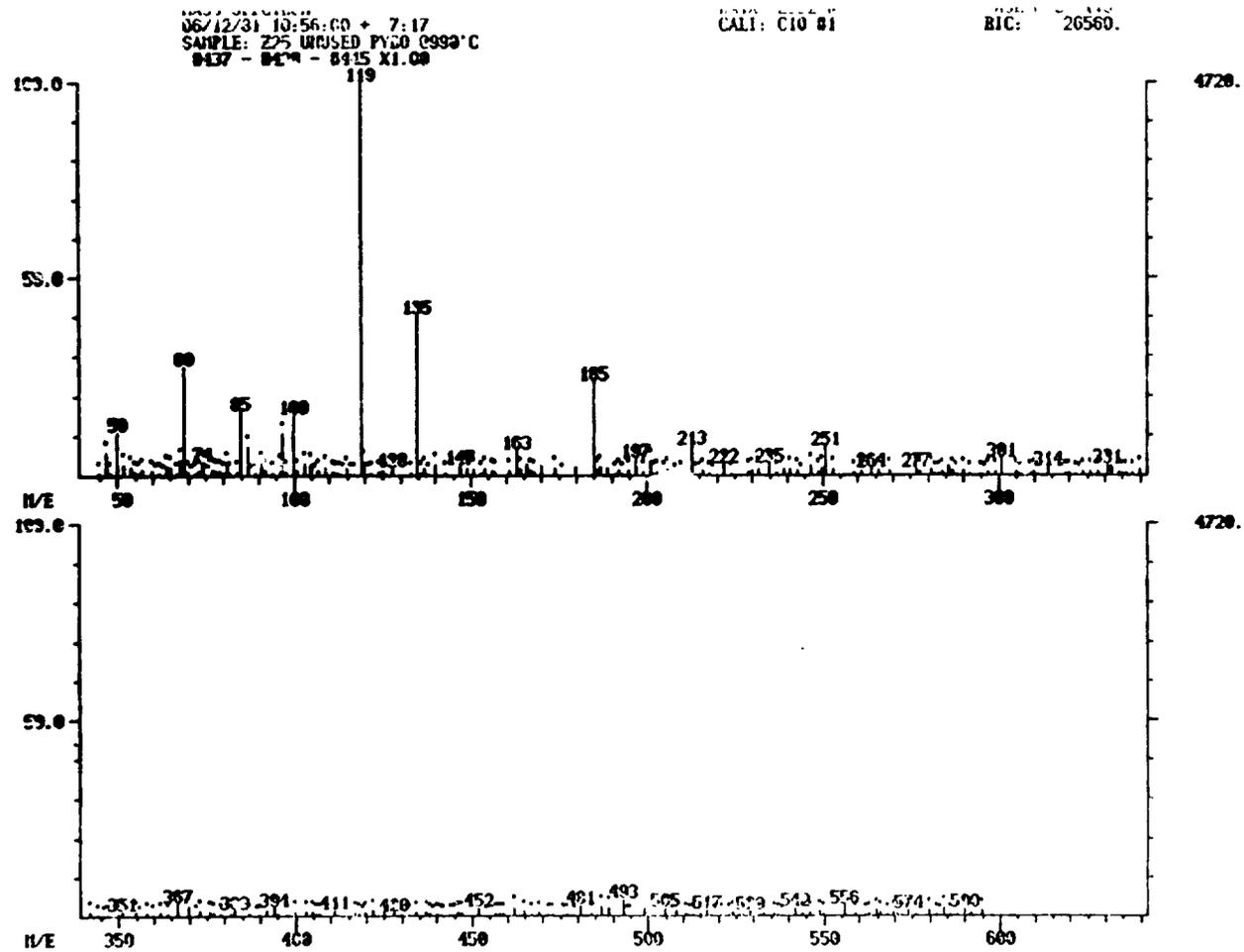
Figure 3. Mass Spectrum of Pyrolytic Fragment (Z25)
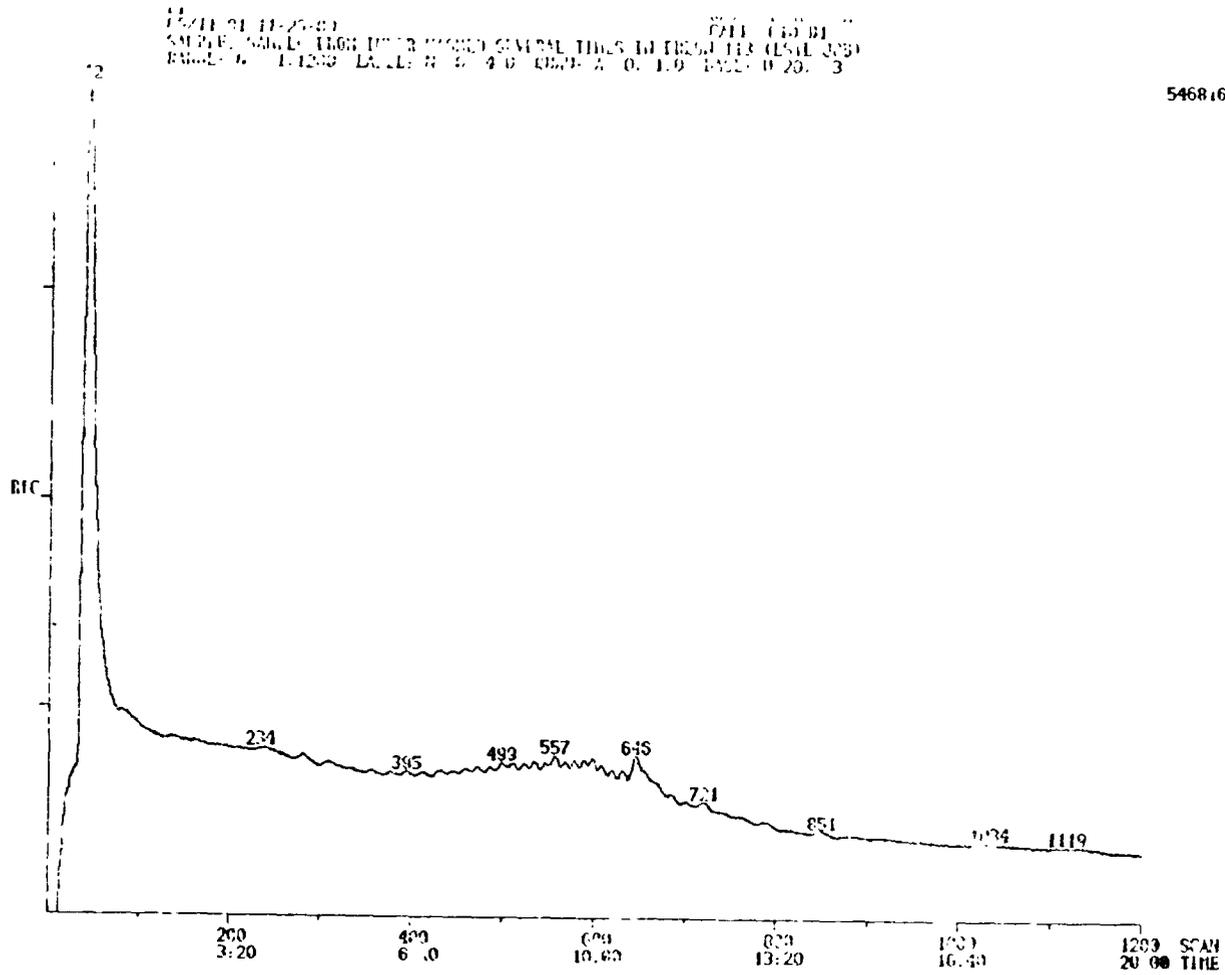
Figure 4.   PGC MS of Freon Insoluble Contaminant
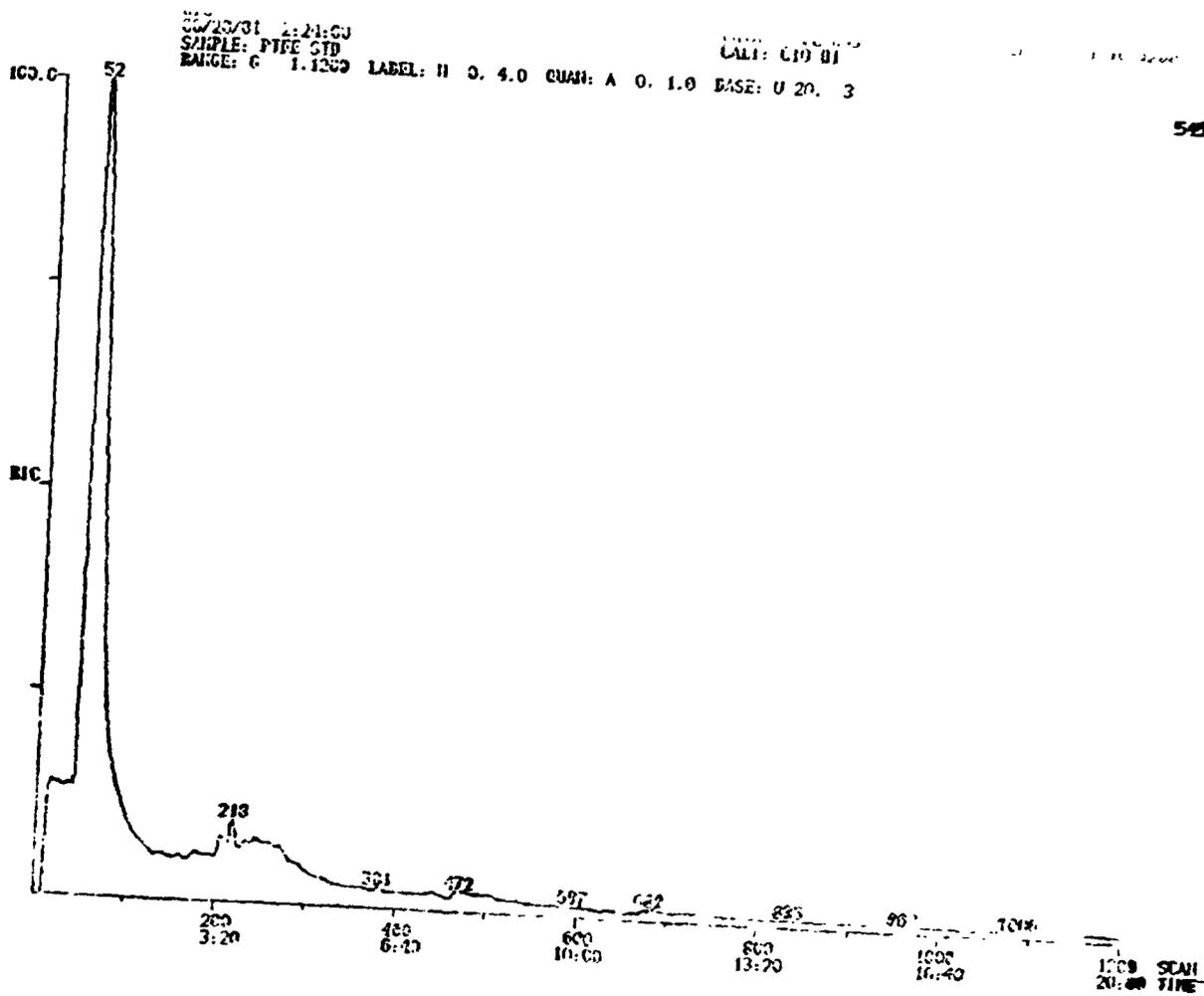
Figure 5. PGC MS of PTFE

Twist Page Figure

Figure 6. Cloudy Oil Film; Re-run Test Bearing x 50
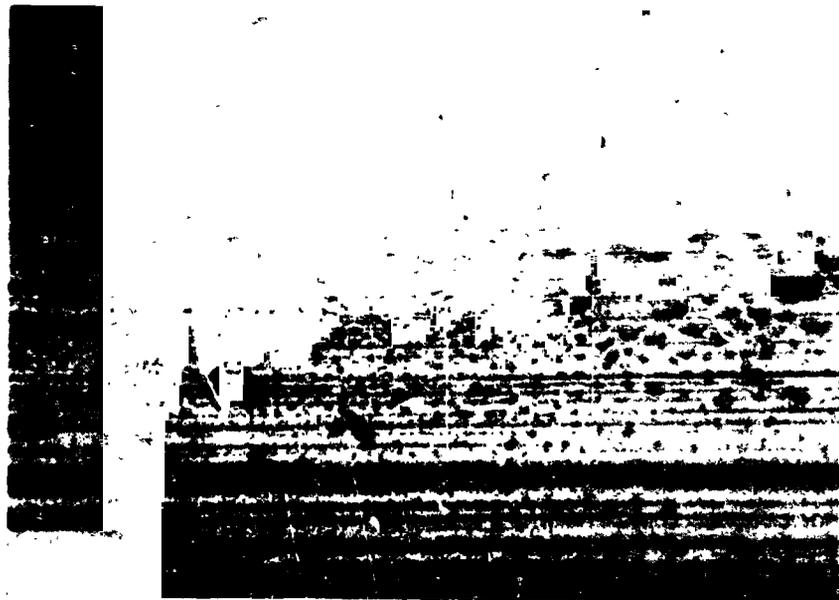
Figure 7.   High Magnification Micrograph of Re-run Test Bearing x 125
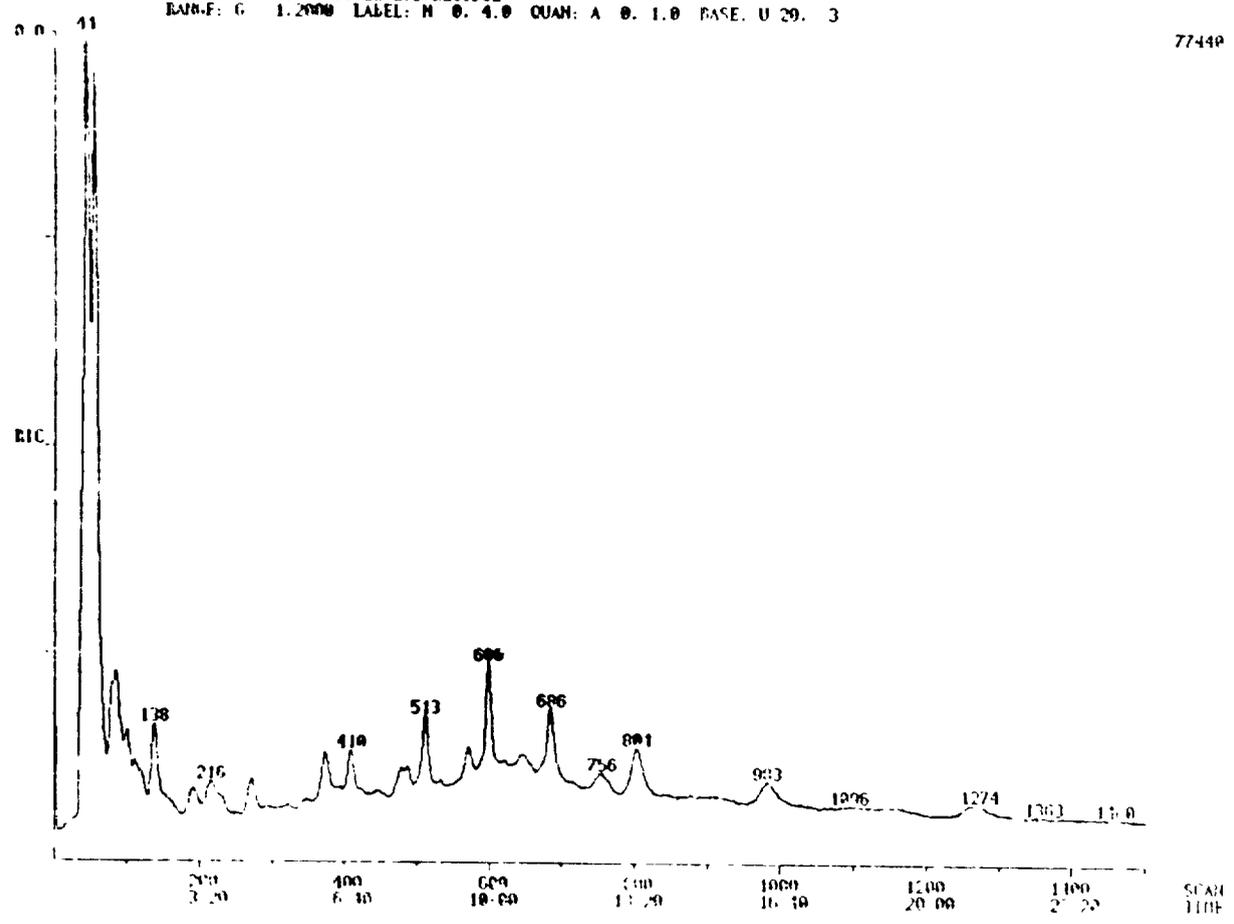
Figure 8. PGC MS of Re-run Test Lubricant (Z25), Hydrocarbon Mix)

Figure 9. Coated Bearing Surface x 125

Figure 10. PGC MS of Freon Insoluble Residue, Coated Bearing Test x 125
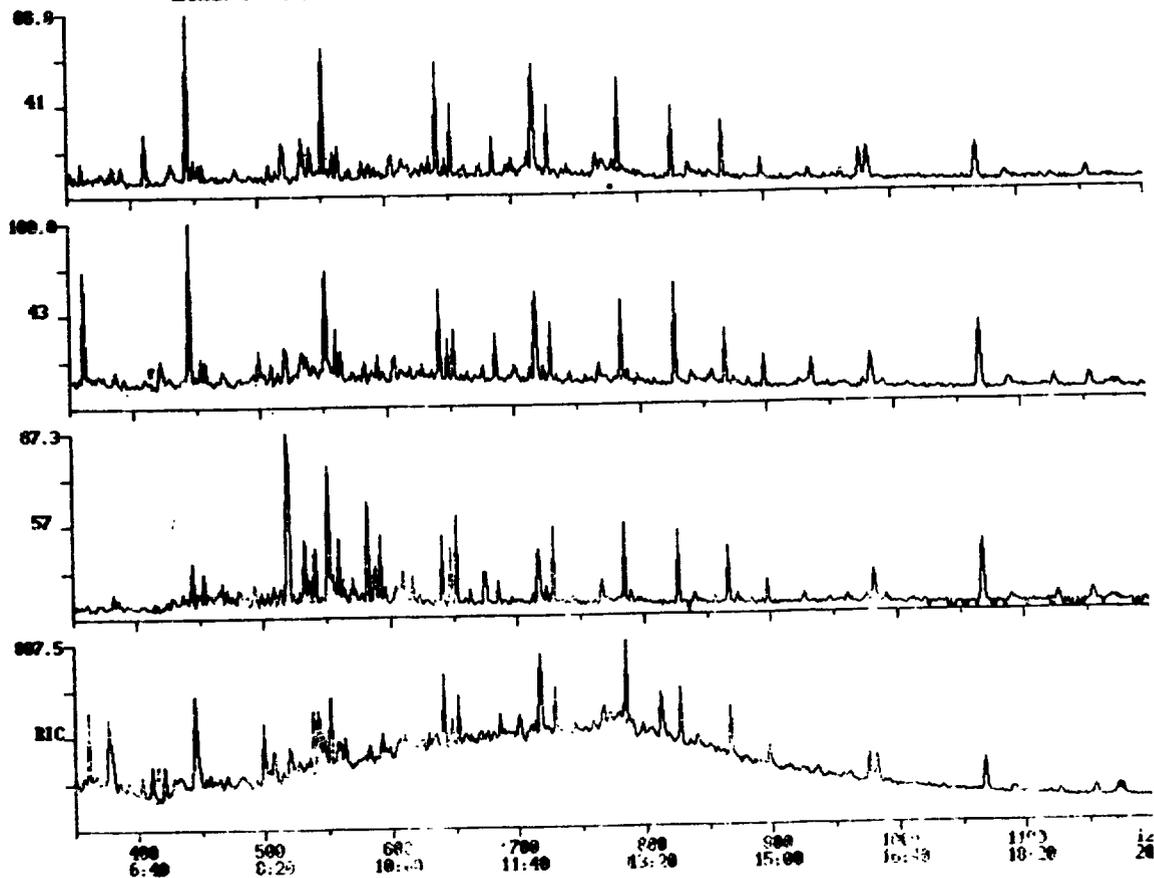
Figure 11. Ion Selective Search, Figure 10 Output (Hydrocarbon)
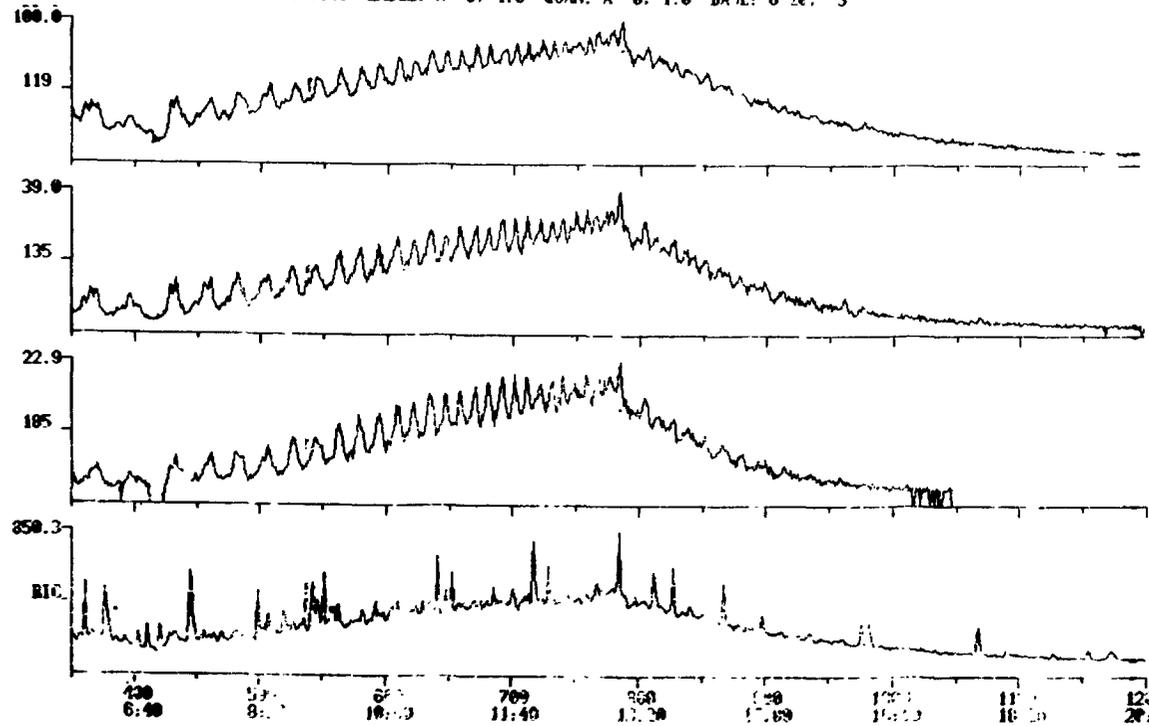
Figure 12. Ion Selective Search, Figure 10 Output (Fluoroether)
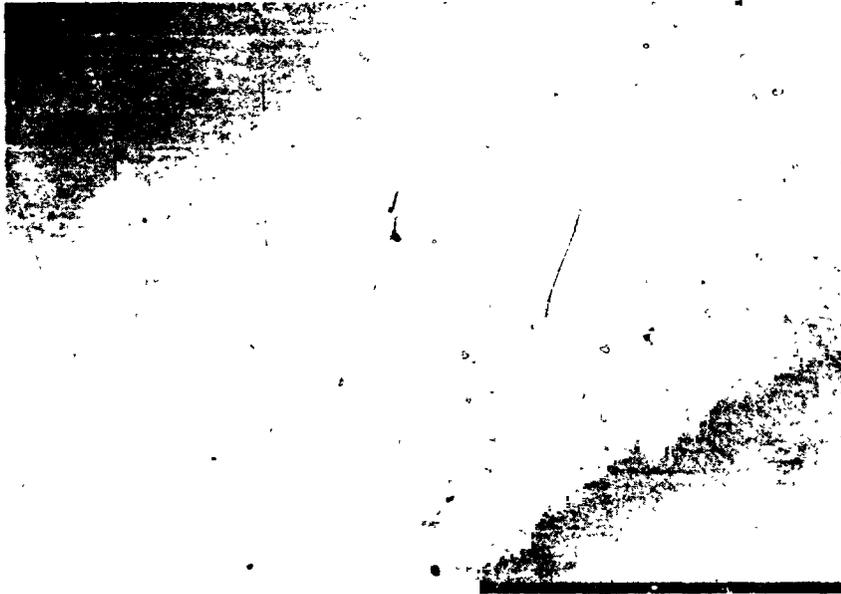
Figure 13. YVAC 40/11; Test Bearing Surface x 125
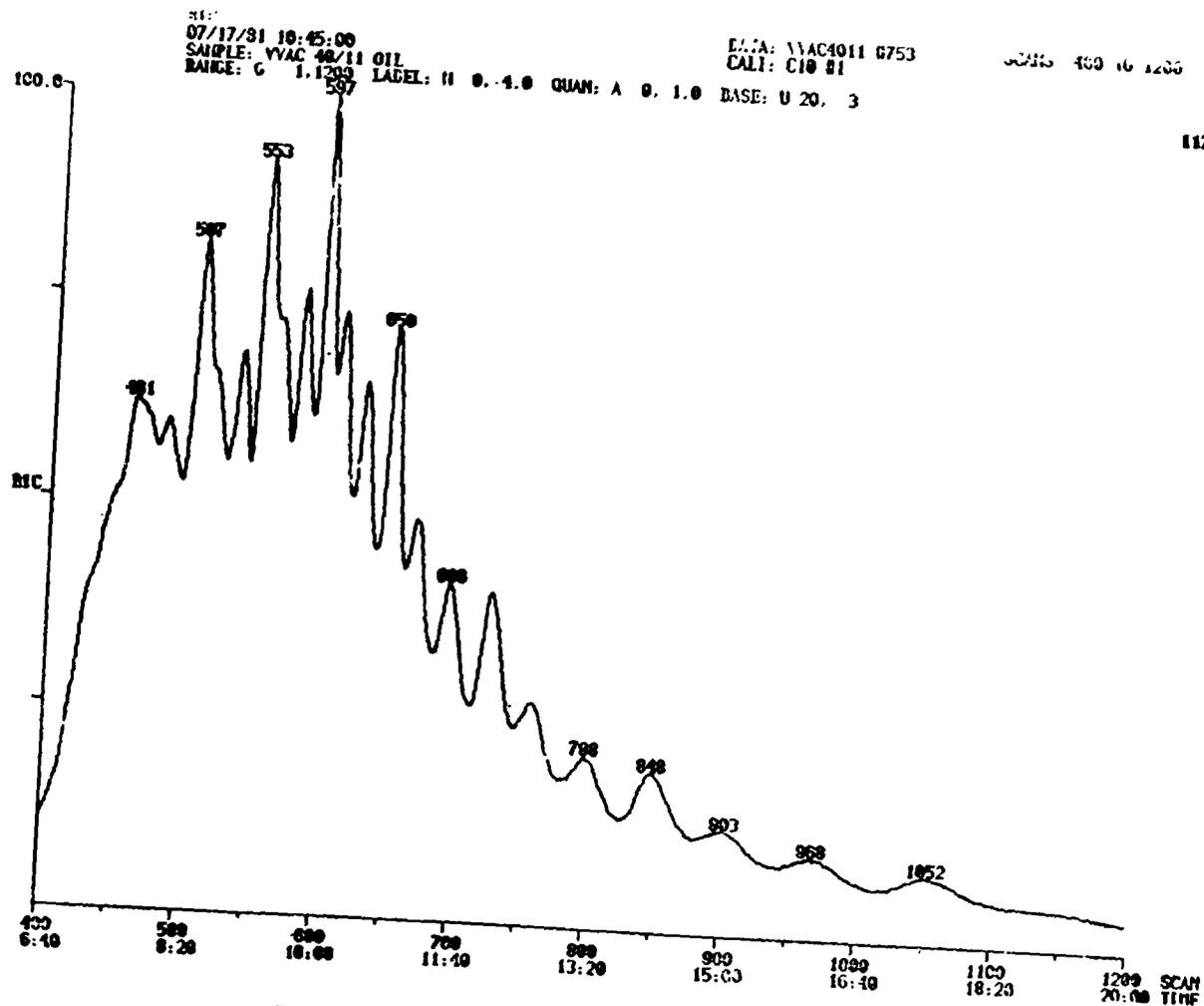
Figure 14.   PGC MS YVAC 40/11 (Unrun)
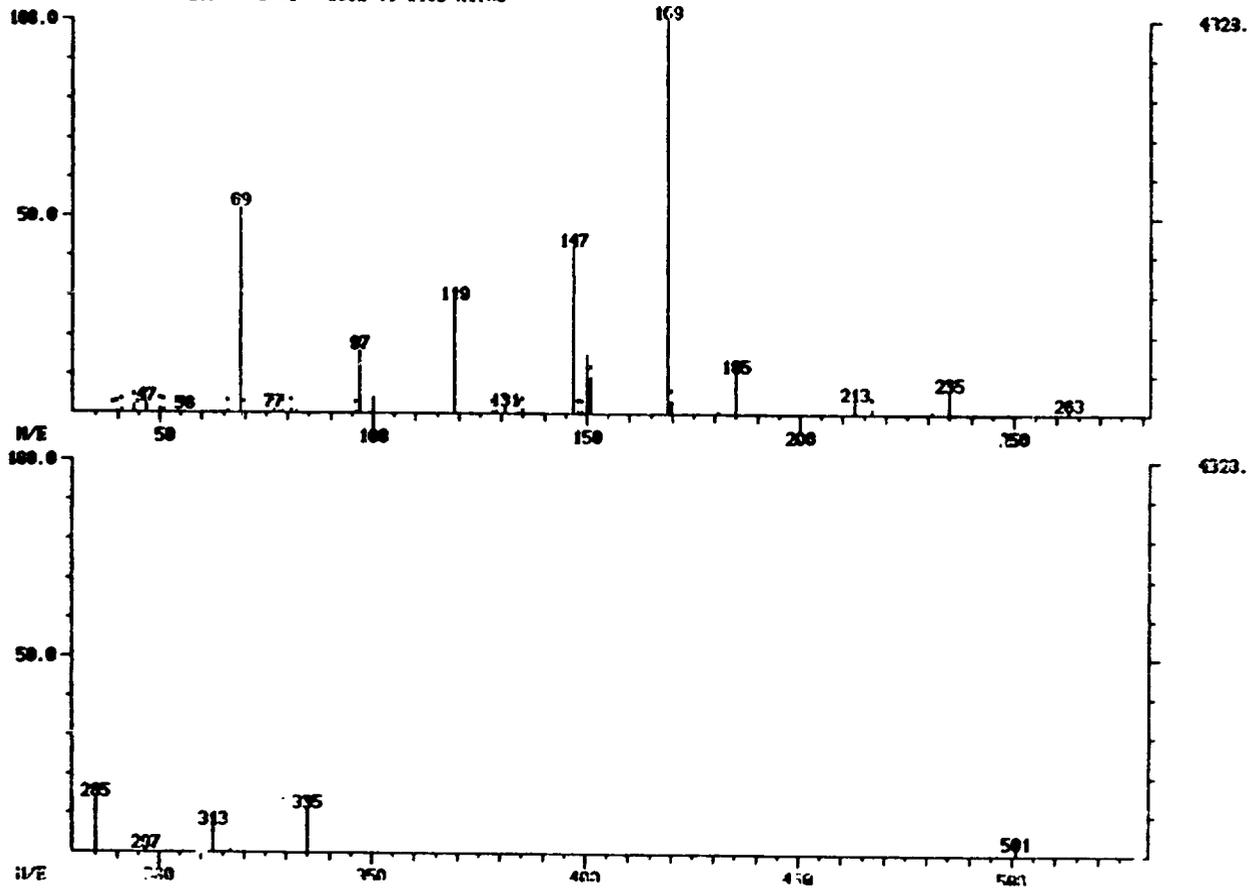
Figure 15.   Mass Spectrum of Pyrolytic Fragment (YVAC 40/11)

ADVANCES IN SPUTTERED AND ION PLATED SOLID FILM LUBRICATION

T. Spalvins[*]

SUMMARY

The glow discharge or ion assisted vacuum deposition techniques, primarily sputtering and ion plating, have rapidly emerged and offer great potential to deposit solid lubricants. The increased energizing of these deposition processes lead to improved adherence and coherence, favorable morphological growth, higher density, and reduced residual stresses in the film. These techniques are of invaluable importance where high precision machines tribo-components require very thin, uniform lubricating films (0.2 m), which do not interface with component tolerances. The performance of sputtered MoS$_2$ films and ion plated Au and Pb films are described in terms of film thickness, coefficient of friction, and wear lives.

INTRODUCTION

To prevent tribological failures of contacting tribo-element surfaces in sliding, rotating, rolling or oscillating motion, friction and wear has to be minimized by application and interposition of lubricating materials. Oils and greases have been found to be inadequate wear preventives under severe environmental conditions. To meet severe operational conditions such as high vacuum, high temperature, nuclear or spacial radiation, extreme loads, and chemically reactive or corrosive environments, it is of great importance to select the proper solid lubricant and a suitable deposition technique. The selected solid lubricant and its application technique will determine the tribological control in terms of friction, wear, and endurance life and is expected to perform over a broad spectrum of these harsh environments. Primarily, the deposition technique selected determines the mode and life of wear or the type of corrosion. In recent years, the glow discharge or ion assisted vacuum deposition techniques, primarily sputtering and ion plating have rapidly emerged and offer a great potential to deposit solid lubricants such as the lamellar solids (MoS$_2$, WS$_2$, NbSe$_2$, etc.); soft metals (Au, Ag, Pb); polymers (PTFE and polyimides); and wear resistant refractor compounds (nitrides, carbides, borides, oxides and silicides).

The sputtering and ion plating techniques are restricte to processes where particle condensation on the substrate is initiated by the ions which transfer energy, momentum, and charge to the substrate and the growing film, and which can be beneficially controlled to affect the nucleation and growth sequence. Consequently, the increased energizing of the deposition process leads to improved adherence and coherence, favorable morphological growth, higher density, and reduced residual stresses in the films. The coating thickness required is generally small, typically 0.2 to 0.6 m thick, and the

---
[*]National Aeronautics and Space Administration, Lewis Research Center, Cleveland, Ohio 44135

highly polished and finished components are coated aʃ the final processing step. All these foregoing coating properties beneficially affect the tribological, mechanical, and corrosive behavior of the contacting surfaces and are described and illustrated in this paper.

SPUTTERING TECHNOLOGY

When energetic ions strike a surface, a number of events can occur, as shown in Fig. 1. First, the incident ion can enter the surface and become trapped. This interaction is referred to as ion implantation. Second, the ion may be reflected from the surface, after being neutralized in the process. Third, as a result of momentum transfer, an atom of the surface can be ejected. This is the mechanism referred to as sputtering.

The sputtering technology offers a great versatility and flexibility in coating deposition, since the sputtered coatings can be tailored in any preferred chemical composition, and the coating morphologies can be modified. Numerous sputtering modes 9direct current-dc, radio frequency-rf, magnetron, reactive, etc.) have emerged and have been widely described in the literature (Refs. 1 to 3). A typical rf diode sputtering apparatus with dc bias capability is shown schematically and photographically in Fig. 2. This sputtering system has been extensively used for sputter-deposition of solid lubricants such as MoS_2, WS_2, PTFE, etc. In rf sputtering, the target (material to be deposited) is energized by the application of rf (13.56 MH_z) power. Before rf sputter deposition, the substrate surface is sputter cleaned and textured by ion bombardment, thus providing excellent adherence.

Performance of Sputtered MoS_2 Films

To achieve effective MoS_2 lubrication, two requirements have to be met: (1) strong film/substrate adherence, and (2) a low crystalline slip during shearing. Sputtered MoS_2 films generally display a strong adherence to most metallic surfaces, with the presently known exceptions being copper and silver and their alloys (Ref. 4). These two metals are highly reactive with the activated free sulphur during the sputtering process, thus forming sulphur compounds which have the tendency to flake off the surface.

Prior to sputter depositing MoS_2, the highly polished surface is cleaned by ion bombardment, thus providing an excellent adherence. Due to the strong adherence, extremely thin films (about 0.2 m) are more effective than thicker films applied by other techniques, as shown in Fig. 3. In thin solid film lubrication, the film thickness has a very pronounced effect on the coefficient of friction. Essentially, the coefficient of friction reaches a minimum value at an effective or critical film thickness, as shown in Fig. 4. The effective film thickness for sputtered MoS_2 films has been experimentally observed to be in the 0.2 m range (Ref. 5). Typical Scanning Electron Micrographs (SEM) in Fig. 5 show that a 1 m thick sputtered MoS_2 film after a single pass sliding has a tendency to break within the columnar region of the film, thus leaving a residual or effective film on the substrate. This effective lubricating film performs the actual lubrication and displays a low coefficient of friction (0.04) under vacuum conditions. The morphological growth zones for MoS_2 films are schematically illustrated

210

after sliding in respect to film fracture in the columnar zone in Fig. 6. This film fracture behavior clearly indicates that the adhesive forces between the substrate and the MoS_2 film are stronger than the cohesive forces in the film itself. It should be remarked that the displaced excess film generates unnecessary wear debris, which has the tendency to increase the torque level and impair the lubrication cycle in precision bearings.

To strengthen the structural integrity of the MoS_2 film in the columnar zone and possibly increase the thickness of the remaining or effective film, gold dispersion was introduced into the sputtered MoS_2 film for densification and strengthening purposes. A compact $Au-MoS_2$ sputtering target prepared by powder metallurgy techniques with 5 to 8 wt % of gold was sputtered to achieve the gold distribution within the MoS_2 films. Similar co-deposited $Ni-MoS_2$ films have been also reported (Ref. 6). These co-sputtered Metallic-MoS_2 films displayed a lower and more stable coefficient of friction and even longer endurance lives than the pure MoS_2 films (Ref. 7).

To insure consistency in performance, precise sputtering quality control is necessary. Film morphology and chemical composition are sensitive to sputtering parameters. The integrity of the sputtered MoS_2 films can be identified by visual appearance prior to and after gentle rubbing or wiping across the surface. An effective lubricating film has a matte-black, sooty surface appearance, whereas an unacceptable film has a highly reflective mirror-type surface. When the matte-black, sooty surface is slightly wiped unidirectionally, the color changes from black to gray and is schematically represented in Fig. 7. The color change reflected from black to gray is due to the reorientation of the crystallites or platelets in the film (Ref. 8).

Sputtered MoS_2 films are particularly indispensable for applications where extremely thin films (0.2 m) are required for tribological control in high precision bearings, where tolerances are close, reliability requirements are high and the minimization of wear debris formation is critical. MoS_2 films are directly sputtered onto bearing components (races, cage, and balls) as shown in Fig. 8. These films have been successfully used in despin bearings for communications satellites, gimbal bearings of reactive motors, bearings for antenna and solar array pointing mechanisms, gears and bearings of spacecraft harmonic drive assemblies, and in numerous other aerospace and earth satellite applications. For instance, in Fig. 9 the adjusting screw which fits into a power nut, is sputter coated with a 0.3 m thick MoS_2 film (Ref. 9). Note, that the left hand bearing diameter is also sputtered to prevent fretting corrosion against the inner face of a ball bearing fit. This assembly is used in the Intelsat V Satellite to position the antennas. The operational requirements are from one to two cycles per day for 16 years.

ION PLATING TECHNOLOGY

The ion plating technique combines the high throwing power of electroplating, the high deposition rates of thermal evaporation, and the high energy impingement of ions and energetic atoms of sputtering and ion implantation processes. The basic difference between sputtering and ion plating is that the sputtered material is generated by impact evaporation and transfer

occur by a momentum transfer process. In ion plating the evaporant is gen-
erated by thermal evaporation. The ion plating process is more energetic
than sputtering, since the process uses a high specimen bias of several
thousand volts to directly accelerate the positively ionized evaporant atoms
into the substrate. The basic ion plating system consists of a dc-diode con-
figuration, where the specimen is made the cathode of the high voltage dc
circuit with an evaporation source as anode shown in Fig. 10. The ion plant-
ing technique and the process parameters are described in the literature
(Refs. 10 to 14).

The interest in ion plating originates from its two unique features:

(1) The high energy flux of ions and energetic neutrals contribute to the
excellent film/substrate adherence and the desirable morphological growth of
the film.

(2) The high throwing power provides for three-dimensional coverage to
coat complex, intricate components such as bearings cages and races without
rotation.

These two features have generated new potentials in coating utilization.
The soft metallic ion plated films such as Au, Ag, and Pb are primarily used
for lubricating spaceborn tribo-element components and ion plated Al films
for corrosion protection of aircraft engine parts and structural components.

Performance of Ion Plated Metallic Films

The excellent film adherence of ion plated films is attributed to the
formation of a graded interface between the film and the substrate, even
where the film/substrate materials are mutually incompatible. This graded
interface not only provides excellent adherence, but also induces surface and
subsurface strengthening effects which favorably affect the mechanical prop-
erties such as yield strength, tensile strength, and fatigue life, as shown
in Figs. 11 and 12. Of the soft metallic films (Ag, Au, and Pb), gold and
lead have found extensive uses in spaceborn bearings of satellite mechanisms
such as solar array drives, despin assemblies, and gimbals. These ion plated
lubricating thin films 0.2 m thick are very effective in increasing the
endurance life, reducing the coefficient of friction, and eliminating instant
or catastrophic failures. The favorable coating behavior is due to the
superior adherence, graded interface, very small, uniform crystallite size
which contributes to high density packing (pore free) and very continuous and
uniform film with a high degree of lattice fit. Due to these favorable coat-
ing formation characteristics, extremely thin films in the 0.2 m range are
far superior to thicker films in terms of the coefficient of friction, as
shown in Fig. 13, for gold and lead (Ref. 14). For instance it has been
shown (Ref. 14) that the Pb film's superior adhesion produced significantly
lower torque noise and the torque behavior was stable over the first million
revolutions.

The high throwing power and the excellent adherence is widely used to ion
plate three-dimensional complex mechanical surfaces, such as internal and
external surfaces of tubing, fasteners, ball bearings, and gear teeth, as

shown in Fig. [?] ... ... hardware components ion plated int[?]ally ... ... thin films. A highly loaded precision ball gear, ... plated with gold (0.12 to 0.2 m) as shown in r[?]. ... ... gear is used in space where it transmits 136 ioules of [?]que, ... film prevents cold welding of the gear pitch line.

In addition to ... ... films for lubrication, in the aircraft industr[?] ... ... on a large-scale production basis to protect aircraft ... ... parts from corrosion. Also, where required, it will be used on all but most critical high strength aluminum and steel structures and on titanium and alloy steel fasteners (Ref. 16). A typical Al ion plated high strength heat treating gear cylinder for corrosion protection is shown ... ... strength aluminum alloy bulkhead for corrosion and fatigue ... ... Fig. 17.

CONCLUSION

The plasma or ion assisted deposition techniques, such as sputtering and ion plating, offer great potential in depositing solid film lubricants and corrosion protective metallic films. The excellent adherence and coherence reduces internal stresses and impedes morphological growth to form dense, cohesive, equiaxed grain structure, all of which have a tendency to lower the coefficient of friction, extend wear life, and increase surface corrosion protection. For consistent performance it is essential that good quality control is maintained during the sputtering and ion plating process.

REFERENCES

1. **Maissel, L.**: Application of Sputtering to the Deposition of Films, Handbook of Thin Film Technology, Ch. 4, L.I. Maissel and R. Glang, eds., McGraw-Hill, New York, pp. 4-1 to 4-44, 1970.
2. **Holland, L.**: A Review of Plasma Process Studies, Surf. Tech. 11, pp. 145-169, 1980.
3. **Bunshah, R.F.**: Deposition Technologies for Films and Coatings, Noyes Public, 1982.
4. **Spalvins, T.**: Influence of Ion on Surface Pretreatments on Adherence of Sputtered Molytdenum Disulfide to Silver, Gold, Copper and Bronze, NASA TND-7169, 1973.
5. **Spalvins, T.**: Characteristic Morphological and Frictional Changes in Sputtered MoS$_2$ Films, ASLE Proceedings - 3rd International Conference on Solid Lubrication 1984. ASLE SP-14 (col-207) Denver Col., 1984.
6. **Stupp, B.C.**: Synergistic Effects of Metals Co-Sputtered with MoS2, Thin Solid Films, 84, (257-760), 1971.
7. **Spalvins, T.**: Frictional and Morphological Properties of Au-MoS$_2$ Films Sputtered From a Compact Target, Thin Solid Films, 118, (375-384), 1984.
8. **Spalvins, T.**: Morphological and Frictional behavior of Sputtered MoS$_2$ Films, Thin Solid Films, 96 (17-24), 1982.
9. **Stupp, B.**: Practical Applications and Uses of Solid Lubricant Films, Tribology in the 80's, NASA CP 2406, vol. II, 681-702, 1984.
10. **Mattox, D.M.**: Fundamentals of Ion Plating, J. Vac. Sci, Technol., vol. 10, no. 1, (47-52), 1973.

11. Spalvins, T.: Survey of Ion Plating Sources, J. Vac. Sci. Technol., vol. 17, no. 1 (315-321), 1980.
12. Spalvins, T.: Ion Plating for the Future, Met. Finish., vol. 80, no. 5, (47-50), May 1982.
13. Mattox, D.M.: Ion Plating Technology, Deposition Technologies for Thin Films, Ch. 6, R.F. Bunshah ed., Noyes Public. 1982.
14. Spalvins, T.: Frictional and Morphological Properties of Ion Plated Soft Metallic Films, Thin Solid Films, 84 (267-272), 1981.
15. Todd, M.J. and Bentall, R.H.: Lead Film Lubrication in Vacuum, ASLE Conference on Solid Lubrication, Denver, ASLE SP-6, 1978.
16. Muehlberger, D.E. and Reilly, J.J.: Improved Equipment Productivity Increases Applications for Ion Vapor Deposition of Aluminum, SAE Reprint P-127, Proc. of the 19th Annual Airline Plating and Metal Finishing Forum, (McDonnel Douglas Corp. Report 830691), 1983.
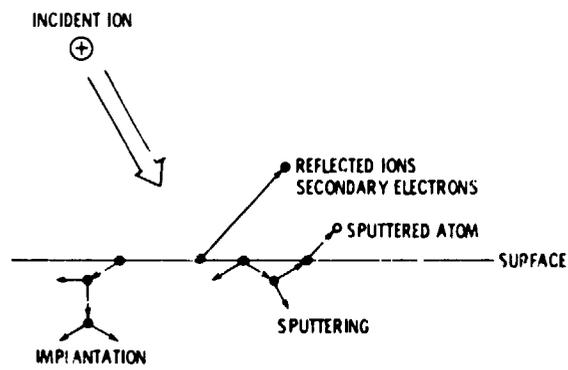
Figure 1. - Ion-surface interactions.
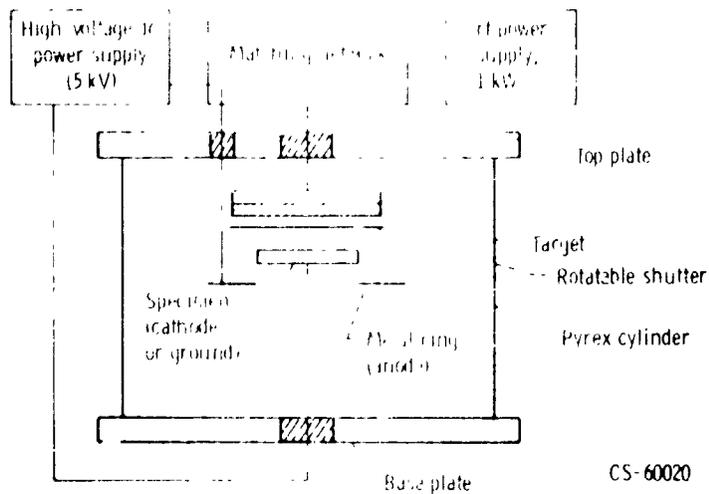
(a) Schematic diagram.

CS-60020

C-73-585
C-71-2537
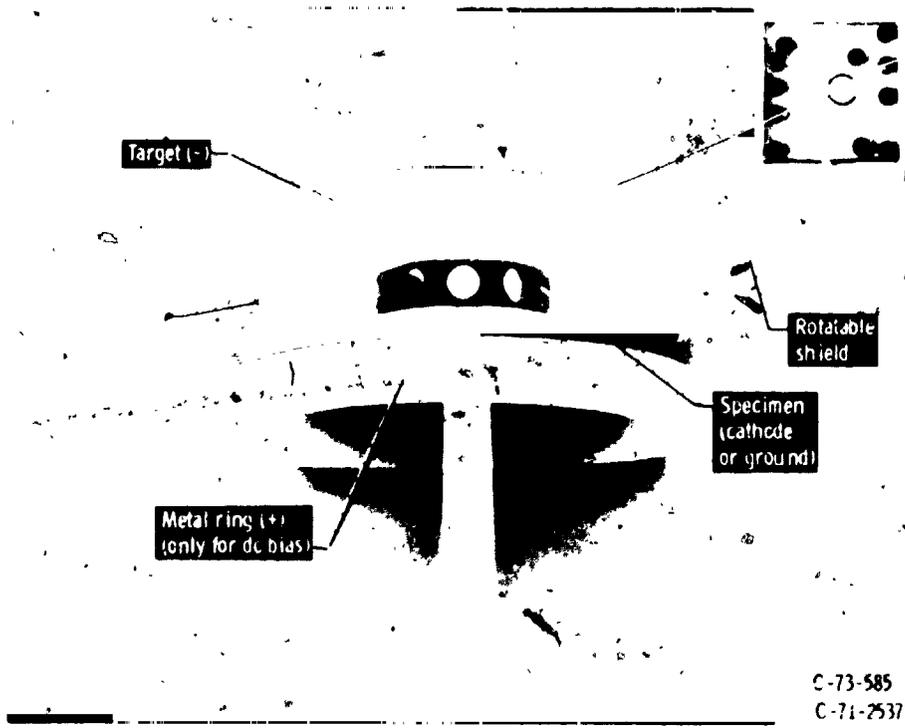
(b) View of apparatus during sputter coating.

Figure 2. - Radiofrequency diode sputtering apparatus with direct-current bias.
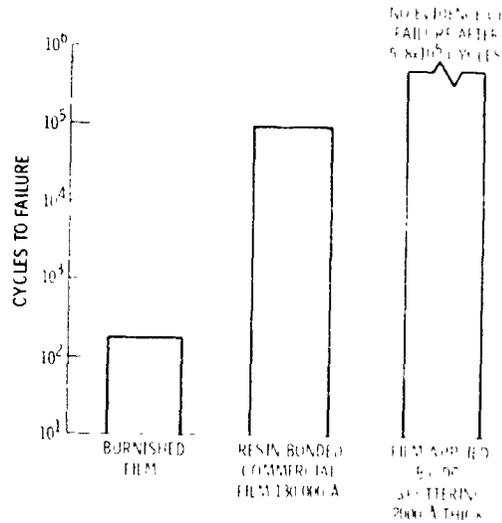
Figure 3. - Endurance lives of MoS$_2$ films applied by various techniques.
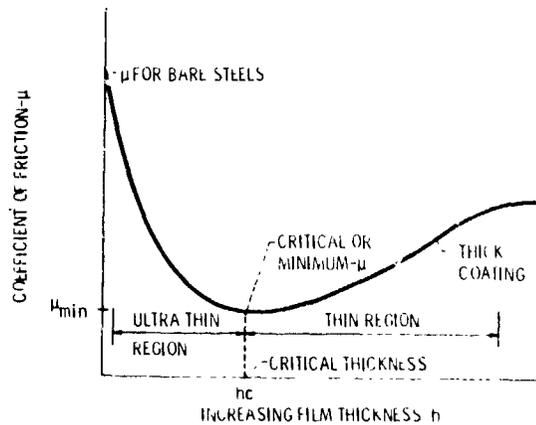
Figure 4. - Schematic representation of the effect of film thickness on the friction coefficient of low shear strength metallic films on steel.

217

(a) On 440C stainless-steel substrate.

(b) On glass substrate.

Figure 5. - Sputtered MoS_2 film after a single-pass sliding.

COLUMNAR
FIBER ZONE

EQUIAXED ZONE

RIDGE
FORMATION

– FRACTURE

EFFECTIVE
THICKNESS
(~2000 A)

SUBSTRATE
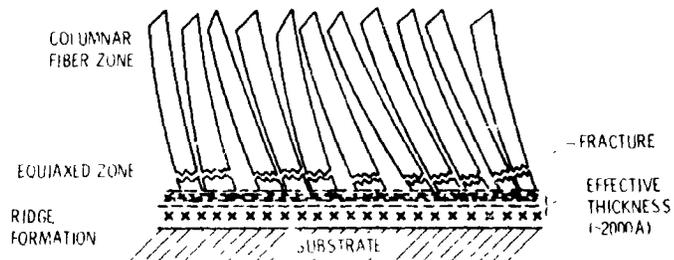
Figure 6 – Fracture during sliding of sputtered MoS_2 film in respect to morphological zones

SLIDING

WIPING
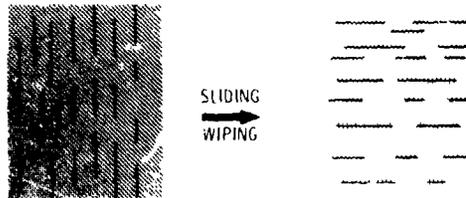
Figure 7. – Reorientation of sputtered MoS_2 platelets.

219
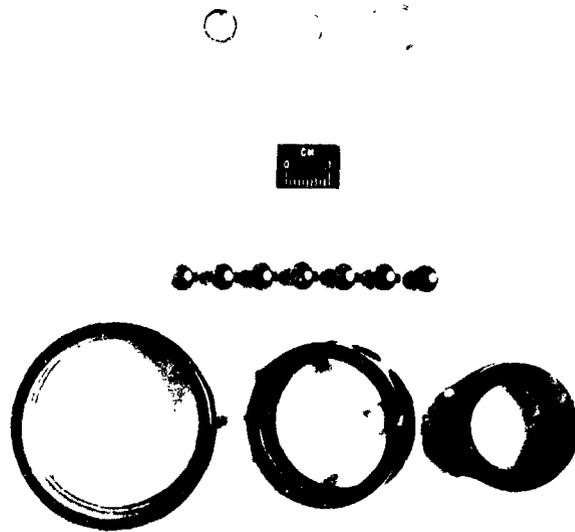
C 81-0331

Figure 8. - Two sets of ball bearing assemblies sputter-coated with MoS_2 films.

Sputtered MoS_2 film.

C 84 5775   Adjusting screw

1 cm

C 84 5776   Power nut

1 cm
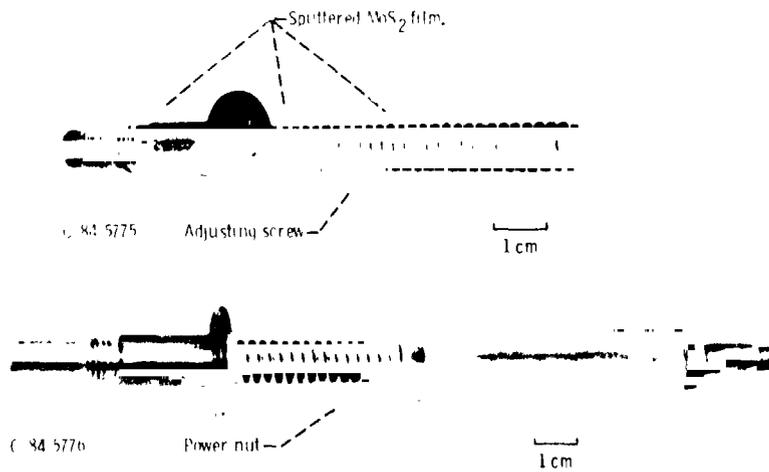
Figure 9.   Power nut and adjusting screw assembly sputter coated with MoS_2

220
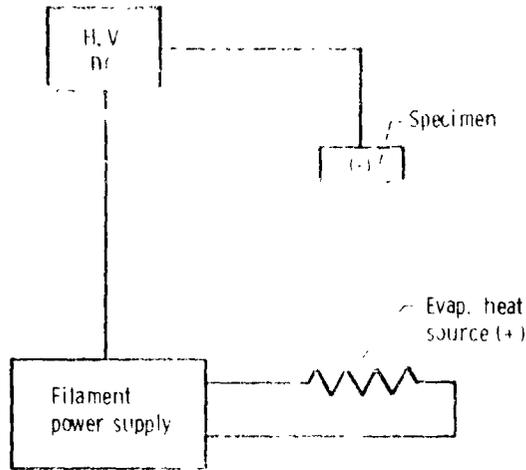
(a) Schematic.
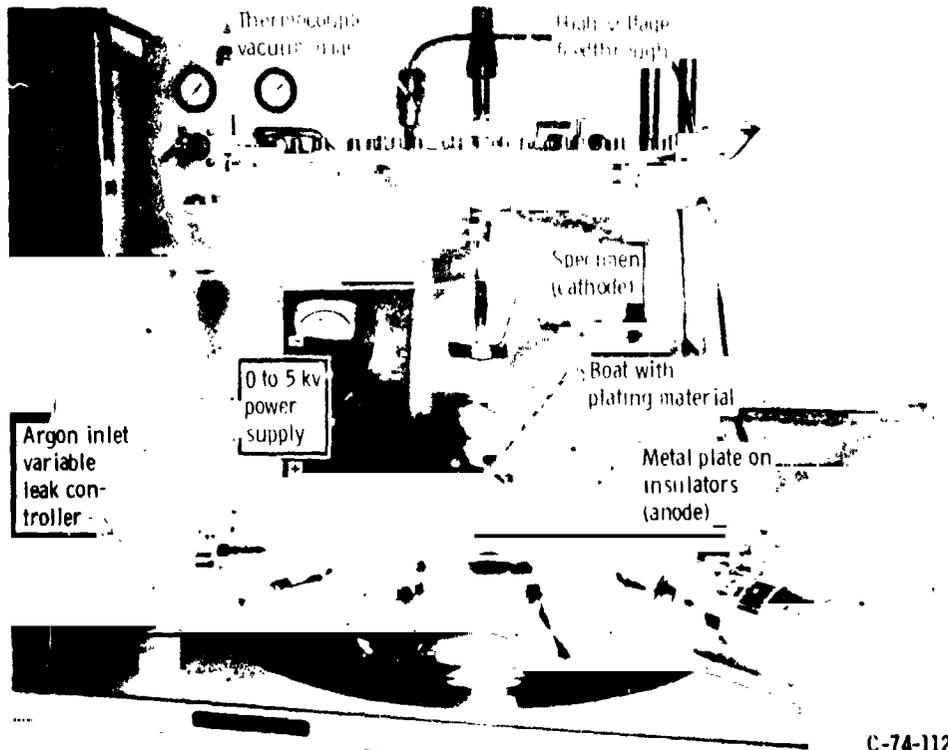
C-74-1121

(b) Ion plating chamber.

Figure 10.   Ion plating system.
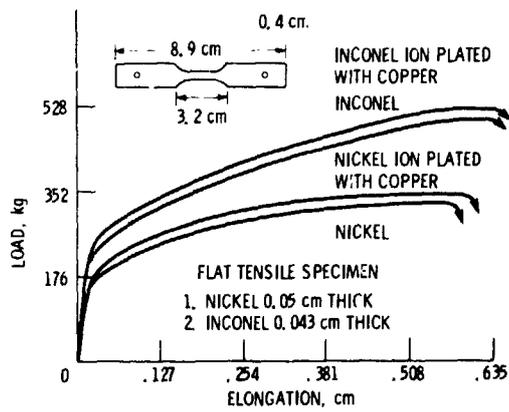
Figure 11. - Load elongation curves during tensile tests.
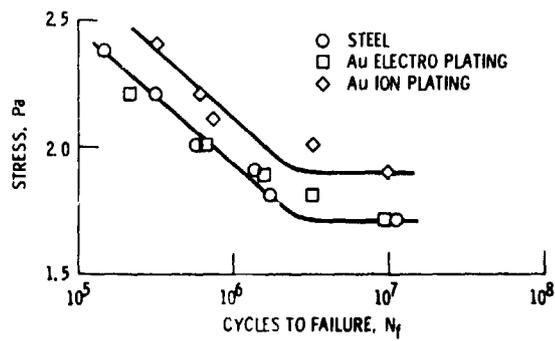
Figure 12. - Effect of ion plating on the fatigue property of low carbon steel.
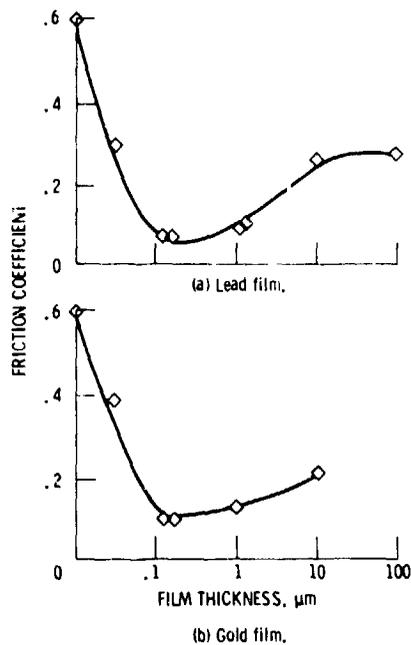
Figure 13. - The variation of friction coefficient with film thickness.

(a) Lead film.

(b) Gold film.

(a) Coated insulators.

(b) Coated internal and external metallic surfaces.
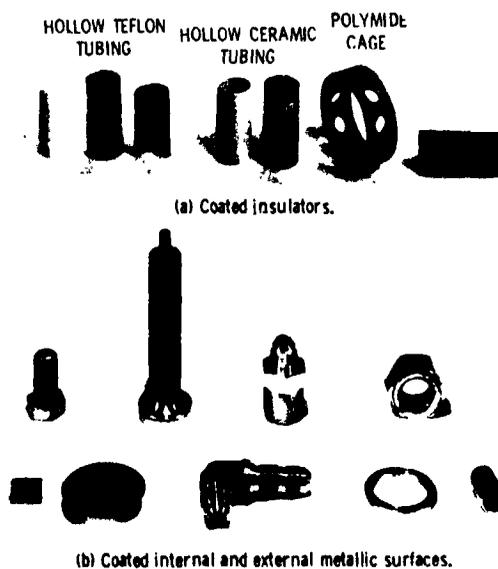
Figure 14. - Ion plated insulators and objects with metallic coating.

CS-79-1272
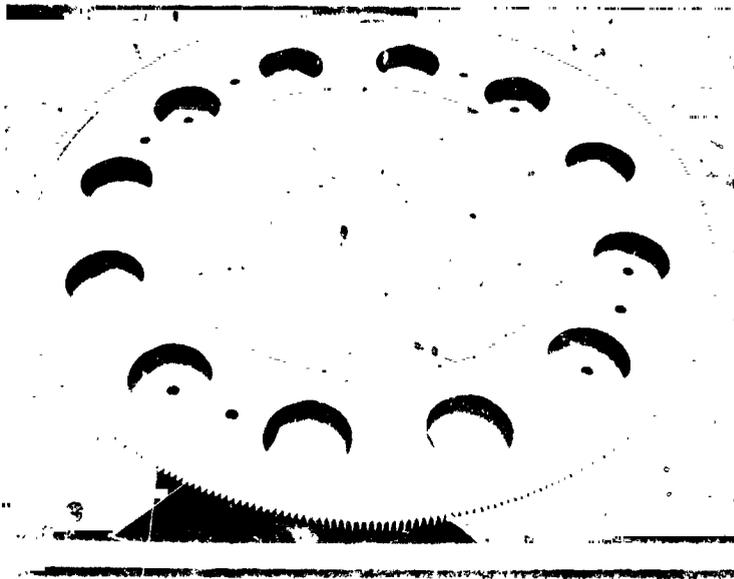
Figure 15. Reflector assembly, ion thruster.   E-84-5780

Figure 16. Manifolding engine cylinder for ion plated with aluminum.

Figure 17. Aluminum ion-plated heat units.

231
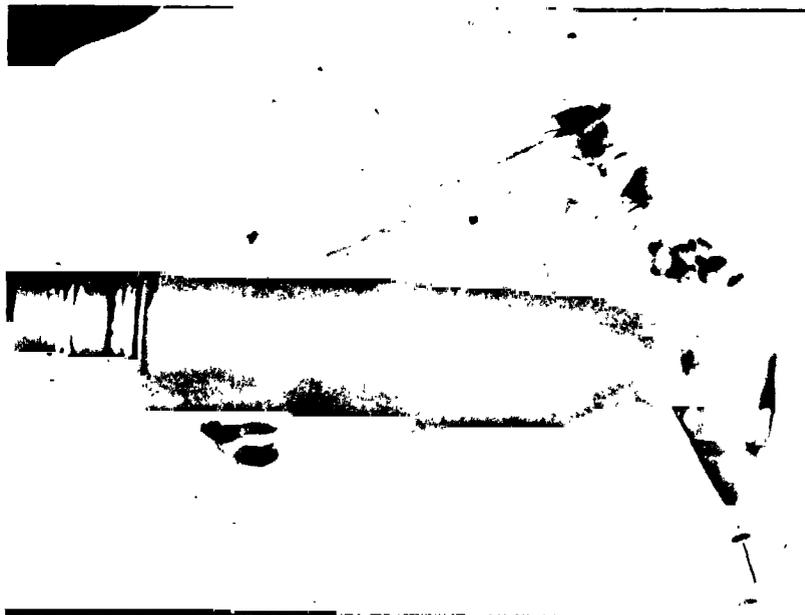
TELEPRESENCE WORK SYSTEM CONCEPTS

Lyle M. Jenkins*

ABSTRACT

Telepresence has been used in the context of space in vita manipulation where the operator is provided with the sensory feedback and control to perform highly dexterous tasks. The concept of a Telepresence Work Station for operation in space is described. System requirements, concepts, and a development approach are discussed. The TWS has the potential for application on the Space Shuttle, on the Orbit Maneuver Vehicle, on an Orbit Transfer Vehicle, and on the Space Station. The TWS function is to perform satellite servicing tasks and construction and assembly operations in the buildup of large spacecraft. The basic concept is a pair of dexterous arms controlled from a remote station by an operator with feedback. It may be evolved through levels of supervisory control to a smart adaptive robotic system.

INTRODUCTION

The term "Telepresence" describes a remote manipulation situation where the operator is provided with the sensory perceptions and control to accomplish intricate tasks requiring great dexterity. An extension of the concept of telepresence is a space flight system that is a combination of teleoperation and robotics called a Telepresence Work System (TWS). The TWS is an evolutionary concept that is intended to provide the operator with the capability to perform tasks in space as though the operator were at the remote site. The basic concept of a TWS is a pair of manipulator arms controlled from a remote station that provides sensory feedback of the work site conditions. Utilization of current technology with the option of including new technology as it develops is a design goal of the concept. The TWS mission and design requirements are pointed toward a general capability rather than specific or unique tasks with limited application. The primary function of the TWS would be the performance of satellite servicing and repair from the Space Shuttle. The TWS can be used for assembly tasks in the buildup of the Space Station. On the operational Space Station, the TWS can aid in the servicing of satellites and in the construction and assembly of new spacecraft.

TWS MISSION AND DESIGN REQUIREMENTS

The Space Shuttle can be expected to increase its role in the servicing, repair, and recovery of operational satellites, such as has been done with Solar Max, WESTAR, and PALAPA (Figure 1). The current and projected EVA (extravehicular activity) capability provides a basis for development of the

* NASA Lyndon B. Johnson Space Center, Houston, Texas

equipment and functions needed for working with satellites. The addition of dexterous functions greater than the current SRMS (Shuttle Remote Manipulator System) can supplement EVA for hazardous, tedious, or repetitious tasks. These dexterous functional requirements can be defined for satellite servicing, assembly and construction, and Orbiter contingency situations in terms of the capability of an EVA astronaut to perform detailed tasks.

Requirements for servicing satellites include the resupply of expendables, the replacement of modules, and the repair of damaged or inoperctive components. The transfer of fluids for a resupply mission involves the attachment of fluid connectors, determination of integrity of the interface, actuation of valves, release of connectors, and verification of lack of system leakage. Resupply by tank replacement also requires the manipulation of fluid connectors as well as the handling tasks inherent in the replacement of equipment modules. Working with modules includes a variety of tasks such as removal of insulation, removal of access panels, fastener disconnection, module handling, fastener insertion, electrical connection, and verification of mechanical and electrical interfaces. Repair tasks are among the most unstructured activities that will be demanded of the TWS. The repair functions require cutting, clamping, soldering, applying adhesives, and other nonstandard operations.

The requirements to perform assembly and construction tasks in the buildup of satellites that are larger than the payload bay of the Orbiter or in the reconfiguration of satellites that are already in orbit will be similar to the operations for satellite servicing. These operations will be better defined and structured with supplemental fixtures and tooling to aid in the assembly of components into the final configuration.

Orbiter contingencies represent another area of operations that will be well structured in some instances and very poorly defined in other cases. The deployment and stowage of payloads involve the actuation of latches or the movement of mechanical appendages that have not functioned properly. With a high degree of dexterity available, the use of kits to repair damaged heat shield tiles becomes practical. The removal of icicles, as occurred on one mission, could be accomplished with ease. A TWS could provide a variety of services to aid the astronaut in EVA operations.

The design of the TWS requires certain subsystems to perform critical functions in the efficient accomplishment of tasks. The work must be stabilized relative to the TWS. The dexterous arms must have sufficient reach and degrees of freedom to place the end effectors in proximity to the work. End effectors need to interface with the equipment being serviced. Vision is an important sense in orienting for remote manipulation. Stereo viewing, while not a requirement, improves the performance of the operator in many circumstances. The interaction of the type of control system with the layout of the control station is fundamental in the case of the Orbiter. For example, the SRMS was driven to a resolved rate system because of the length of the slave arm and the constrained volume of the crew station. Shorter arms on the TWS may allow the option of a master slave controller with the proven force reflection technique to feed back reactions at the end of the manipulator arm.

CONCEPT DESCRIPTIONS

Elements of the TWS are pointed out in Figure 2. The TWS concepts currently under evaluation are composed of the following subsystems: structural base, interface to the carrier, stabilizer arm, dexterous arms, end effectors, closed circuit television, controllers, displays, lighting, communication, and power. There are a number of options in sensors that could be incorporated to enhance the ability of the operator to perform more effectively. Stereo vision, proximity sensing, and tactile and force feedback are probable additions.

Two companies, Grumman (GAC) and Martin-Marietta (MMA), have study contracts with NASA to define concepts for the TWS. A Grumman concept, shown in Figure 3, is based on using one of the dexterous arms as the stabilizing device. The support structure is a simple arrangement for the three dexterous arms and the television camera. The control station is a portable setup in the aft deck of the Orbiter cabin. Another GAC version, illustrated in Figure 4, carries a stabilizer arm and movable cameras to get improved viewing angles. Stowage for end effectors to adapt the manipulators for specific tasks is incorporated in the structure.

A Martin-Marietta concept, as shown in Figure 5, uses 7-degree-of-freedom arms for the dexterous function and an arm with limited articulation for stabilization. Stereo vision simulates the operator eye location with the camera located relative to the two dexterous arms in an anthropomorphic representation. The initial control station concept appears in Figure 6. The controllers shown are 6-degree-of-freedom that input motion to the arms. The controllers are reindexed to keep the controller motion within the available space envelope.

SYSTEM DEVELOPMENT

The concept development will be subject to a number of trade studies. Among the more important trades are: arm length, control by position or rate, stereo or regular TV, number of arms, force reflection vs. displayed force feedback, and stabilizer arm (number, stiffness).

The initial trade results will result in a basic configuration to begin the development. The trades and technology projections are elements in the definition of an evolutionary development plan. An evolutionary program is projected that has objectives beyond the operation on the Orbiter. The OMV (Orbit Maneuver Vehicle) requires a dexterous system to perform tasks on the satellites. Similar requirements are expected for the OTV (Orbit Transfer Vehicle). These operations will be conducted at long distances from the control station. Time delay in excess of about 0.5 second becomes a factor in teleoperation; therefore, development of the TWS should include time delay compensation techniques in the selection of subsystems. Coping with time delay may include predictive graphics, rate control rather than position control, data compression and simplification to reduce communication requirements, and robotic phases in performance of an operation.

227

The ultimate evolutionary objective of the TWS program is the Space Station. The TWS can provide significant assistance in the initial buildup of the Station. It can conduct servicing operations similar to those that it would perform on the Shuttle. Maintenance of the Station offers another opportunity for the TWS to relieve the crew of tedious and time-consuming functions.

With these evolutionary objectives defined, the development and incorporation of technology should be selected for compatibility with the objectives. For instance, the output of a sensor should be adaptable to integration with AI (Aritifical Intelligence) systems as they become available. The crew can monitor and supervise a task. They are available to take over in a teleoperator mode. This suggests a pattern for the development of a smart adaptive robot. The TWS can be configured to do the tasks planned for a robot, including the sensory input needed to establish conditions at the work site. Telepresence provides the operator with the data to monitor the operation and, if necessary, to assume control of all or part of the task in progress.

SUMMARY

The utility of remote systems operating in a remote and hostile environment has been proven in the undersea systems that service offshore oil rigs. The concept of a TWS has the same potential for developing into an invaluable system for performing manipulative tasks in space. The TWS can be evolved into an adaptive robot that can operate autonomously in space. The robot operation can be supervised with an option to take over in a telepresence mode where needed. The TWS concept provides a focus for technology development and flight demonstration leading to operational application on the Space Shuttle and the Space Station.

REFERENCES

(1)   Analysis of Remote Operating Systems for Space-Based Servicing Operations. Contract NAS 9-17066, Grumman Aerospace Corporation.

(2)   Satellite Services System Analysis Study - Final Report, Contract NAS 9-16120, Grumman Aerospace Corporation, August 1981.

(3)   Telepresence Work System Definition Study, NAS 9-17229, Grumman Aerospace Corporation.

(4)   Telepresence Work System Definition Study, NAS 9-17230, Martin-Marietta Aerospace.

(5)   Autonomy and the Human Element in Space, 1983 NASA/ASEE Summer Faculty Workshop.
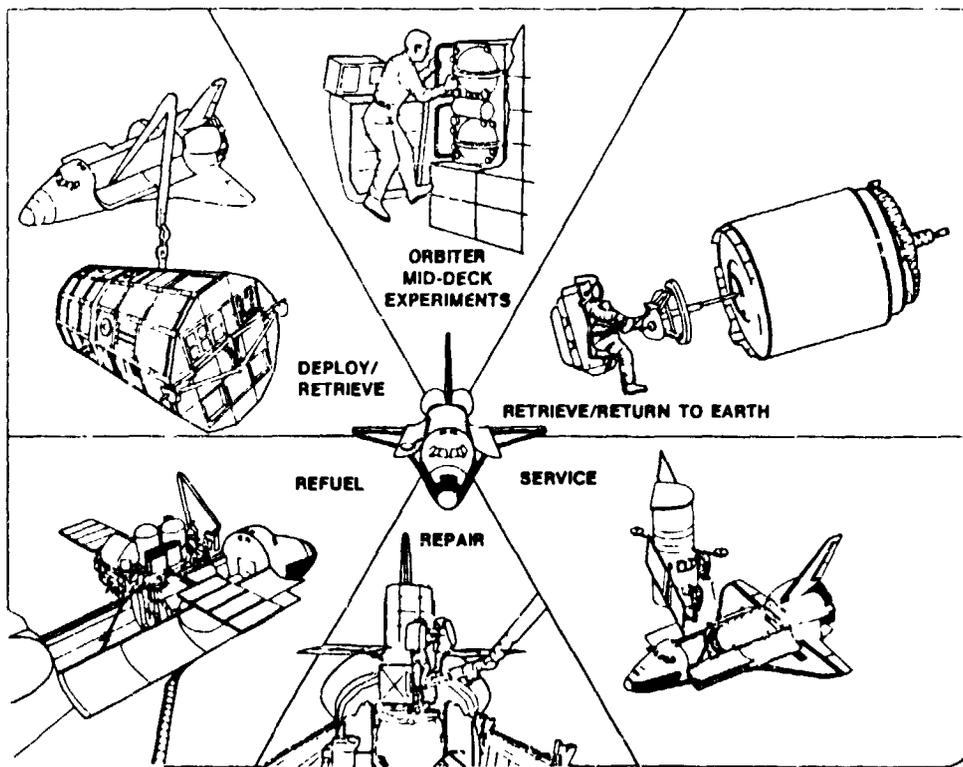
Figure 1.   Shuttle Satellite Servicing Capabilities
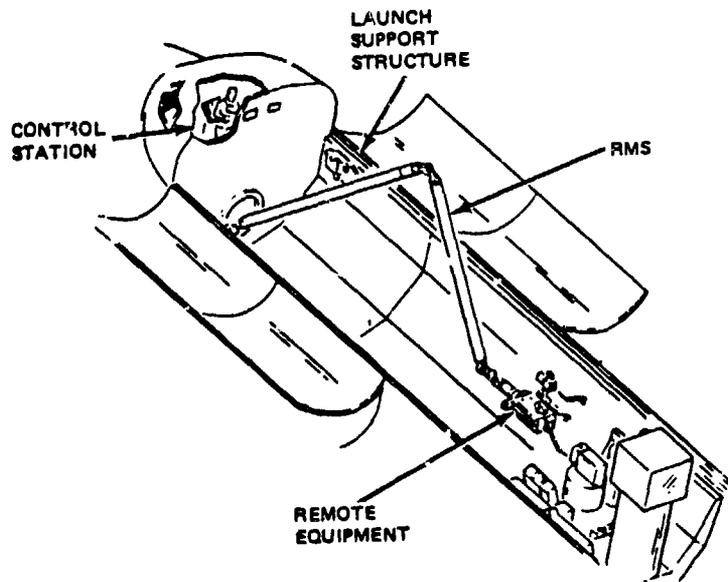
Figure 2. TWS System Elements
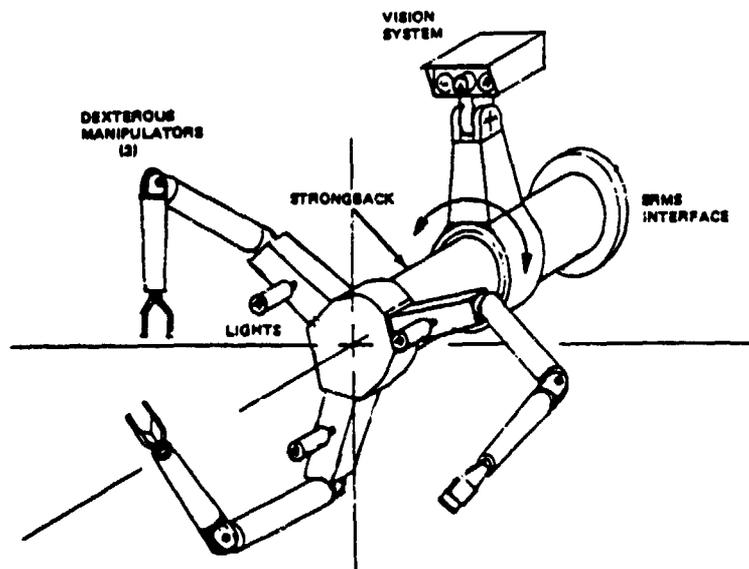
Figure 3. GAC TWS Concepts
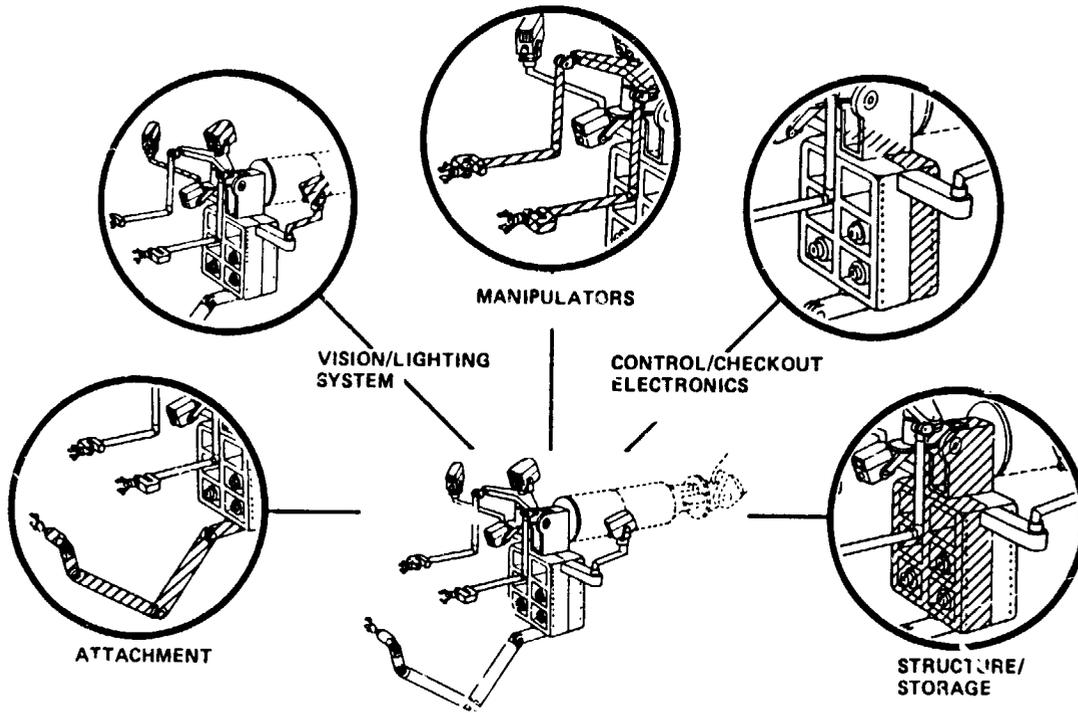
Figure 4.   Alternative GAC TWS Concepts
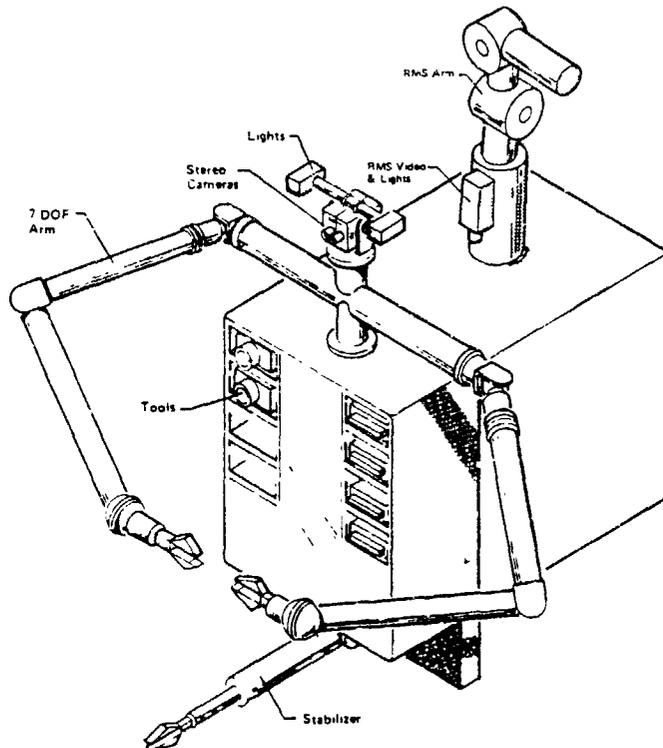
Figure 5. MM TWS Concept
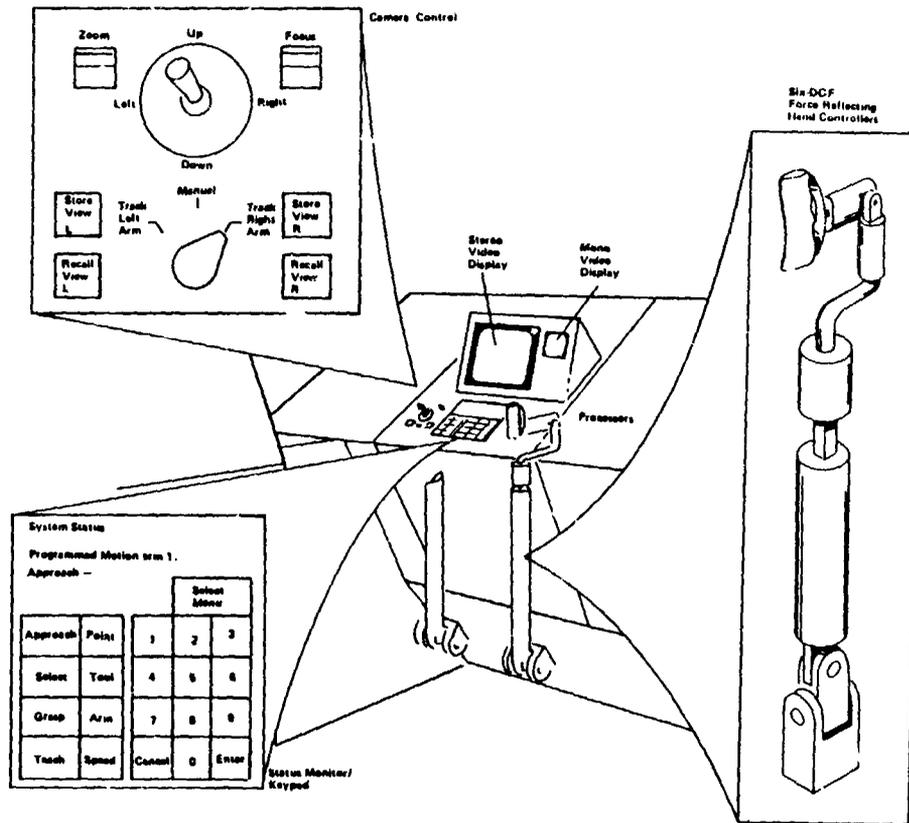
Figure 6.   MM Control Station Concept

233

Consolidated Fuel Reprocessing Program

DUAL ARM MASTER CONTROLLER DEVELOPMENT*

D. P. Kuban** and G. S. Perkins+

ABSTRACT

The advanced servomanipulator (ASM) salve was designed with an anthropomorphic stance gear/torque tube power drives, and modular construction. These features resulted in increased inertia, friction, and backlash relative to tape-driven manipulators. Studies were performed which addressed the human factor design and performance trade-offs associated with the corresponding master controller best suited for the ASM. The results of these studies, as well as the conceptual design of the dual arm master controller, are presented.

INTRODUCTION

The dual arm master controller (master) is the out-of-cell half of the advanced servomanipulator (ASM) teleoperator system. It will be used to operate the ASM slave from the control room, safely behind the biological shielding a shown in Figure 1. It is primarily controlled by inputs from the human operator, with computer augmentation for selected features. The motions of the master are reproduced in the cell by the slave, using bilateral position-position servoloops.[1] The slave was designed to be remotely maintainable in-cell with another ASM slave.[2] This was achieved by designing the ASM slave with remotely replaceable modules and with a gear/torque tube force transmission. These functional requirements increase manipulator inertia, friction, and backlash in comparison to conventional tape-driven servomanipulators. It was also felt that conventional systems needed an improved man/machine interface.

Therefore, the development of the dual arm master controller was intended to optimize both the mechanical design and the human factors asp ts. It was designed to minimize inertia, friction, and backlash to offset the increase of these parameters in the slave. This combination will allow the entire master/slave system to perform comparably to the conventional systems. The human factors of the master were also studied to enhance the man/machine interface. The kinematics, handle type, and joint cross coupling were designed to conform to these results of the studies.

CONTROL SYSTEM FEATURES

In a master/slave (M/S) teleoperator control system, a primary objective is to provide high-quality force-reflection. First of all, the operator must be able to feel the forces he is generating in-cell to operate efficiently. A "high quality" system would accurately reflect the forces being generated in the cell, be highly responsive and stable, and have a low force reflection threshold. The last characteristic is particularly important as it determines the sensitivity of the teleoperator system. Present systems' sensitivities are about 0.5 to 1 kg, but with their different capacities this ranges from 1 to 10% of maximum lift. The goal for this system is 0.5 kg (2%), which has been verified on a single-degree-of-freedom test stand.

Other features of the control system are indexing, force scaling, and position scaling. When indexing, the control system servos the slave about its present position and frees the master. The operator then moves the master to any position desired and restores M/S operations. The system then continues as before, but with the offset between the joints. The force scaling feature allows the operator to select the percentage of the force generated in-cell that is reflected back to him. Presently the ratios available are 1:1, 2:1, 3:1, 4:1, and 8:1. For small delicate tasks 1:1 would be used to maximize sensitivity. For heavy tasks 8:1 would be selected to minimize fatigue. Another useful feature is position scaling. This allows the operator to move the slave only half the distance of the master. This is very useful for delicate tasks and complex motions, such as aligning and inserting a multipin electrical connector. These options are selected from a CRT menu display. The cursor for the menu is controlled from the handle, and once the choice has been selected it is executed by a push-button on the handle.

KINEMATICS

The most basic criterion for designing a manipulator is the kinematic arrangement. The joint relationships and the length of the links can greatly influence the performance and dexterity. These factors were studied in detail,[3] and master kinematics were recommended that were similar to the ASM slave. The kinematics were investigated from a variety of viewpoints, but the overall objective was to maximize the dexterity and transparency to the operator. If this objective is met, it will maximize the operator's performance and efficiency by providing human-like flexibility and by minimizing fatigue and frustration. The master must be capable of motions comparable to a human and should not interfere with the operator's body. Since several kinematic arrangements can achieve this objective, other criteria were established to evaluate these arrangements more closely. One such additional criterion was implementation complexity. Some of the arrangements, though geometrically similar, were not kinematically identical and therefore were difficult to implement. Geometric similarity consists of identical link lengths and joint orientations. Kinematic similarity includes this, but goes further than the structural linkages to include identical force and torque transmission. This also means that the entire manner in which forces are transmitted through the master, including joint interrelations, must be the same as in the slave.

236

The difficulty of implementation that arises when one tries to use a geometrically similarly (not kinematically identical) arrangement is in the type of control loop that must be used. A position-position control loop is currently employed in the ASM control system.[1] This loop is very simple if the master is a kinematic replica of the slave, but becomes very complicated if a nonreplica master is chosen. With identical kinematics, the positions of the individual joints in both the master and the slave are sensed and compared directly. If a position difference (error) exists, a command is derived from the control algorithm and is given to the master/slave pair to eliminate the difference. With nonreplica kinematics the position difference must be derived since the individual joint positions cannot be compared directly. Such a derivation requires motor/joint transformations with significant calculations. Once the position differences are determined, a similar transformation procedure is necessary to obtain the command for each corresponding joint. Since this method is theoretically feasible, an analysis was performed to determine if such a control loop could be closed fast enough to be stable. The analysis indicated that the loop could be implemented, but would require development of complex software. Since the nonreplica kinematic arrangement offered little advantage over the replica arrangement and since the nonreplica option carried with it the need for increased software complexity, a kinematic replica master was chosen.

HANDLES

To properly design the handle for the master, the kinematic arrangement must be considered. Many handle designs were conceptualized.[3] Once the kinematics were chosen, several possibilities were eliminated. Four handle types were evaluated for the replica master kinematics. The criteria for this evaluation were primarily concerned with the human factors that affect the performance of the operator. The handle must be comfortable and nonfatiguing, and must provide the operator with a transparent man/machine interface to the master. From previous studies[4] it was shown that an operator often uses either hand on either handle, so the design must be also be ambidextrous. After a new tong-actuator control concept was selected, the pistol-type handle (Figures 2, 3, and 4) looked most favorable. The initial tong control concept was a backdriveable electromechanical gear train the same as the rest of the joints. However, for this application, it was decided to control the tong with a new concept that employs a trigger with a position sensor (see section on design concept). This control can be easily implemented with the pistol-type handle. This handle also provides a good location for the operator to reach the remaining control switches. A prototype of the chosen handle was built and the human factors were thoroughly studied to design the final version for the master.

CROSS COUPLING

In the slave, all the wrist motors are located above the shoulder on the gear pod, and the forces required for the wrist are transmitted through the elbow, which results in elbow/wrist cross-coupling. A cross-coupled joint is one in which the torque in that joint is a function of the load in that joint

and the load in another joint. For example, the summation of torques about the elbow joint is equal to the torque supplied by the elbow motor, plus an amount proportional to the torques supplied by the wrist motors. Another way to look at it is that the torque required from the elbow motor to support the elbow depends on how the wrist is being loaded. So the force reflected to the operator in the elbow of the master would be changed as the load in the slave wrist changed. The implications of this coupled relationship (as well as the coupling itself) are subtle, but it results in reduced controllability and inaccurate force reflection unless it is properly handled. In the first master design study,[3] a concept was recommended for the master controller. This design was light, with low inertia and almost no backlash, but the wrist motors were located behind the elbow attached to the forearm. This completely eliminated the elbow/wrist cross-coupling in the master. In most manipulator systems, this would be an advantageous feature, but in actuality it was detrimental to the performance of this master/slave system. Since the slave would be coupled but the master would be uncoupled, this unsymmetrical coupling would give the operator of the master a very confusing force and positional response.

The only was to account for this coupled-uncoupled relationship would be to employ motor/joint transformations. This would also require development of the transformation software. Therefore, a new concept was developed based on the knowledge that was gained through the conceptual design efforts on the master and the slave. This new concept is coupled in an identical manner as the slave. The coupling effects will then be reproduced in the opposite direction and cancelled out by the position-position loop. This will give the operator an accurate force and positional response because all the coupling effects have been effectively "eliminated." As electronic advances continue, such motor-joint transformations that are now avoided may be come routine enough to reconsider an uncoupled master. If this transformation option is chosen, then the other kinematic arrangements should also be reconsidered.

MOTORS

The motors used on the master are the same as those used for the slave.[2] These motors have the highest continuous-torque/friction-torque ratio of any available motor. This is their most important feature, since they will obtain the lowest static friction possible for the master. This is very desirable in order to offset the increased friction in the slave. The gear ratio required with these motors ranges from 2:1 to 12:1.

The only disadvantage is that the weight of the motors is approximately 50% of the estimated total master weight. This high weight contribution is because the master is of much lighter construction than the slave. This is an unusually high contribution, but it is warranted by the low overall friction of the motor. A smaller motor (less weight) with a higher gear ratio was considered in order to reduce the high weight contribution. This was not done because friction would actually be increased, since the absolute value of the motor friction torque (42 N.mm) is the same in both the smaller and the larger motor. Also, since the smaller motor has lower continuous torque, it yields a lower continuous-torque/friction-torque ratio, which increases the

static friction and therefore degrades the force reflection. The present slave motor then provides the minimum static friction and, therefore, the minimum force-reflection threshold. In essence, the motor development effort for the slave system identified a nearly optimal servomotor in terms of capacity and friction characteristics. Using this motor on both the slave and the master will assist in producing the best force reflection possible.

FORCE TRANSMISSION

A variety of techniques and hardware are available for transmitting forces from the centralized motors to their respective joints. The most likely possibilities that were considered were metal tapes, cables, and polyurethane cable chains. Cable chains are relatively new compared to the metal tapes or cables. They are available commercially and have been successfully used in many critical applications.[5]

Cable chains were initially selected because they appeared to meet performance requirements and were very inexpensive. Testing is under way to determine how the backdrive friction torque varies with preload. Standard aircraft cable is also being tested for comparison.

DESIGN OBJECTIVES

As stated earlier, the objective of the master design was to provide a system that was best suited for the gear-driven slave. Therefore, the master was designed to minimize friction and inertia with zero backlash while enhancing the man/machine interface. All of these features can be grouped under the single category of improving the operator's performance. Consequently, it also important to achieve a very clean and aesthetically appealing master that is comfortable to operate. In addition, the design options for the master considered simplicity and low cost as high priorities to balance the cost of the slave.

DESIGN CONCEPT

The conceptual design for the dual arm master controller is shown in Figure 5. The master has a capacity of 6 kg, approximately one-fourth the capacity of the ASM slave. It has 7 degrees of freedom and features the anthropomorphic (elbows down) stance to mimic the slave. The master will use an advanced handle developed from rigorous human factors analysis and experimental tests of a prototype handle. The force-reflection threshold has been analytically determined to be about 0.25 kg. A single-degree of freedom test stand that simulates the wrist roll joint has been fabricated to verify these analytical results.

The kinematic arrangement of the joints is identical to that of the slave. All the force transmission, the length of the links, and the location and orientation of the joints are identical, except for the wrist L-housing. Here the distance from the wrist pitch axis to the tong actuator is only 200 mm 50 mm less than the slave) to allow the slave tongs to touch without

the master handles colliding. The master is mechanically counterbalanced to reduce friction. This is accomplished with a 4-bar linkage located inside the support arm tube.

The two upper degrees of freedom are all gear-driven as in the slave. Since the capacity of the master is much less than that of the slave, the gear trains are smaller and simpler. Precision gears, with weight and inertia minimized, and precision bearings are used throughout. This results in a gear train with very low backlash and low inertia.

The elbow is partially gear-driven and ues the 4-bar counterbalance linkage to also transmit the drive forces to the lower arm structure in the elbow joint. This yields a very clean, compact design which is much easier to implement than a bevel gear/drive shaft arrangement.

The three wrist motions (pitch, yaw, and roll) are driven by 1:1 ratio gears to translate and rotate the torque from the motor at the edge of the gear box to the sheave assembly in the center of the gear box. From the sheave assembly to the wrist, the forces are transmitted using commercial aircraft cable. One cable transmits forces from the sheave assembly to the elbow, and a second cable continues the transmission from the elbow to wrist gearing. In the wrist itself, the traditional differential is used to drive pitch and yaw motions, and a partial second differential is nested inside this to drive the roll motion. The roll forces are transmitted from its differential through the L-housing, with a special three-dimensional cable arrangement, to turn the corner and transmit the wrist roll forces to the handle interface.

Another unique featur) is the "unilateral loop" that is used to control the slave tong. Traditionally, the slave tong is controlled similarly to the other joints, with a bilateral force-reflecting drive train. With this method the force-reflection threshold for the tong would be on the order of 1.0 kg. Since this threshold level is so high, a new idea was pursued that was much simpler and more reliable. The new tong actuator is electromechanical, but it is not a backdriveable gear train. Instead, it incorporates a position sensor with a spring to give the operator an artificial force reflection. The slave tong is driven by sensing the position of the tong actuator (trigger) and using this information to calculate a current command to the tong motor. The control system then servos the tong about this resulting force. Since the position of the tong actuator is related (through the spring constant of the actuator spring) to the force applied by the operator to the trigger, this is actually a force-force loop. This control method is very flexible since the gains can be changed in the software to make the tong very sensitive to the tong actuator force for fragile jobs, or insensitive for heavy tasks. The spring in the handle itself can also be changed for various tasks or for individual operators. Overall, this method is deemed very acceptable for the function it is to perform, but it will be thoroughly evaluated during the testing of the master.

PRELIMINARY TEST RESULTS

Much testing of this new teleoperator system has been done with one-degree of freedom test stands: two gear-driven stands (Figure 6), one representing the slave and one representing the master, and one cable-driven stand (Figure 7) representing the master. All of the stands simulate the wrist roll joint, which has the most gear meshes, largest length, and most friction. This joint was chosen because it is obviously the most difficult. Since the most important criterion for the system is force-reflection threshold, the performance of these test stands was quantified by this parameter in Table 1.

SUMMARY

As can be seen from Table 1, the results are very en uraging. The results are well within the predictions and confirm that the present design is quite satisfactory. The dual arm master controller therefore should achieve all of the objectives of a low friction, inertia, and backlash system. Fabrication of the arms is scheduled to be completed in June 1985, and assembly completed in July. Overall, the master represents a significant engineering achievement. It provides a major performance improvement by employing high-achievement. It provides a major performance improvement by employing high-performance commercial components and human factors engineering. This will result in an ASM master/slave system that provides increased performance and capabilities that are competitive with existing servomanipulator systems.

REFERENCES

1. H. L. Martin et al., "Controls and Electronics Subsystem for the Advanced Serve anipulator," this volume.

2. D. P. Kuban and H. L. Martin, "An Advanced Remotely Maintainable Force-Reflecting Servomanipulator Concept," Proc. 1984 Nati al Topical Meeting, American Nuclear Society, April 1984.

3. A. K. Bejczy et al., Advanced Servomanipulator Master Controller Development, JPL D-106 (December 1982).

4. M. M. Clarke et al., "Human Factors in Remote Control Engineering Development Activities," Proc. 31st Conf. Remote Syst. Technol., American Nuclear Society, 1983.

5. Winfred M. Berg, Inc., East Rockaway, L.I., N.Y., Manual Bl.

Results of Force-Reflection Threshold Tests On One-Degree Of Freedom Test Stands.

Table 1

TEST CONDITION	EXPERIMENTAL FORCE-REFLECTION THRESHOLD (kg)	ANALYTICAL FORCE-REFLECTION THRESHOLD (kg)
1. Slave[1] only (open circuit)	1.3	0.9
2. Master[2] only (open circuit)	0.3	0.4
3. Master/slave, no compensation	1.0	1.3
4. Master/slave, with compensation algorithm	0.6	0.9
5. Cable chain master only, no preload (open circuit)	0.2	0.2
6. Cable chain master only, 45-kg preload (open circuit)	1.0	0.3
7. Cable master only, minimum preload	NA	0.2

[1]Slave built with standard gears and bearings, lubricated with grease.

[2]Master built with precision gears and bearings, lubricated with light machine oil.

TRANSPORTER

CELL
WALL

MASTER
CONTROLLER

IN CELL SLAVE
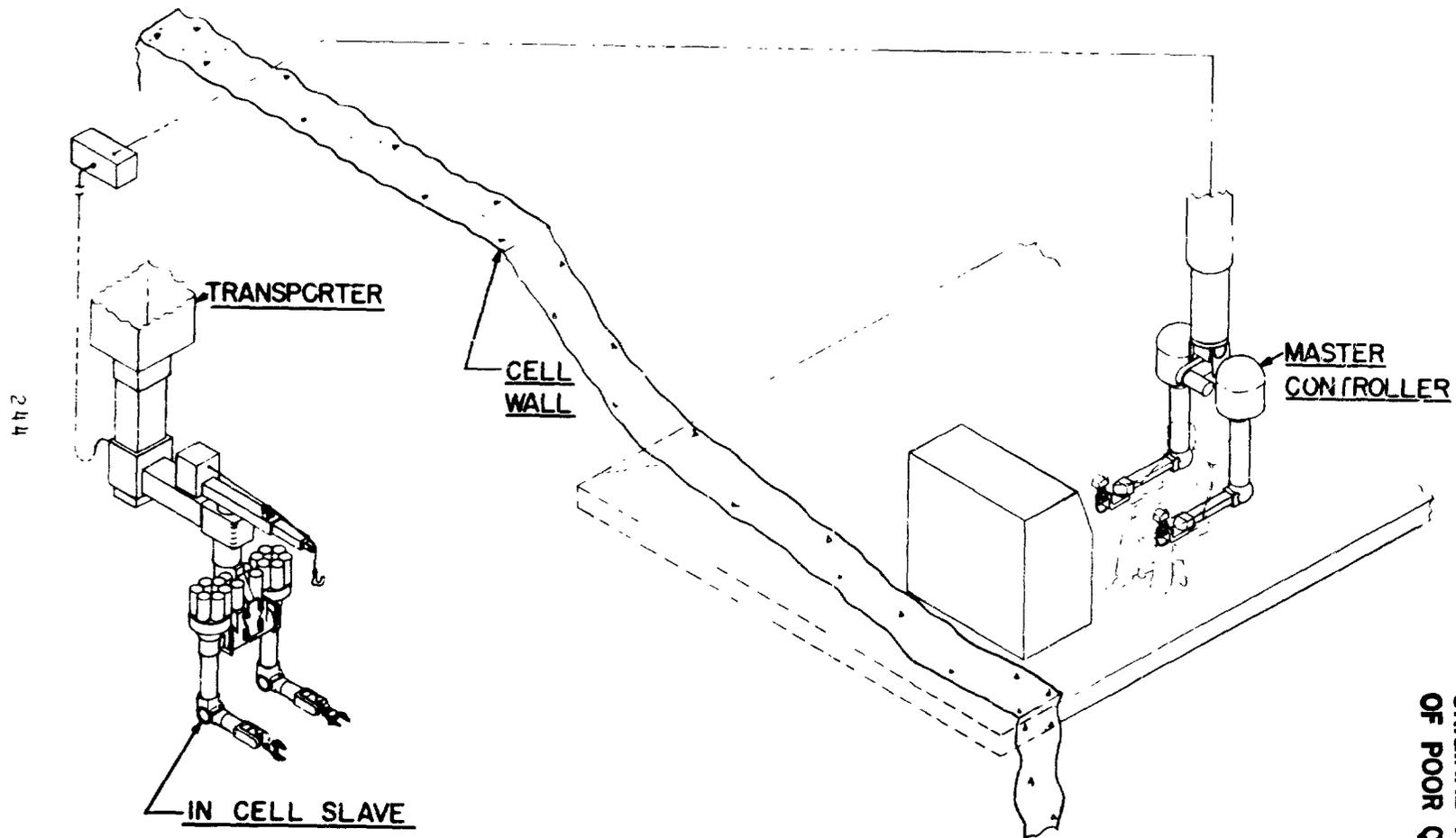
Figure 1.   Master/Slave Teleoperator System
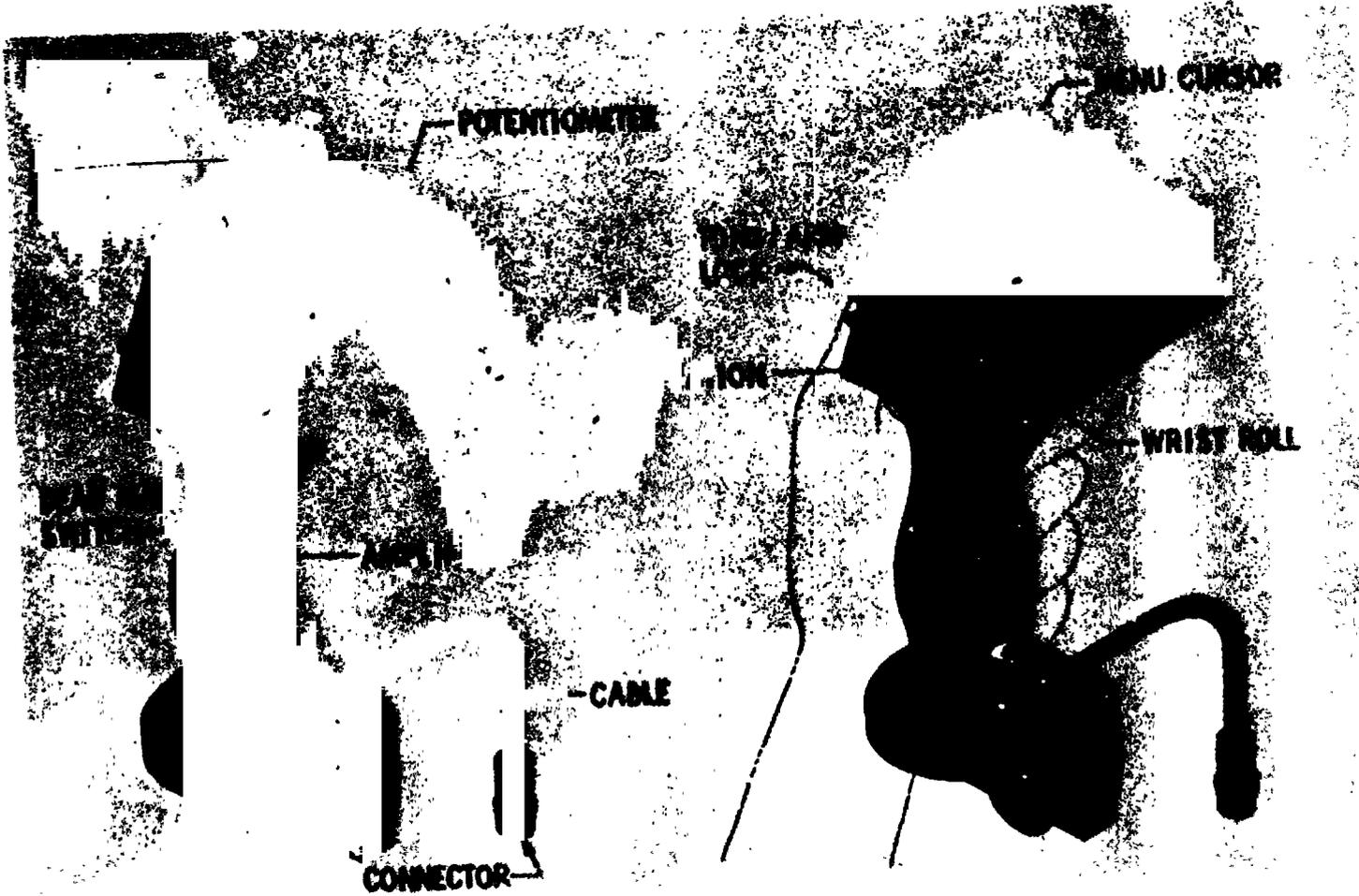
Figure 2. Ambidextrous Master Handle
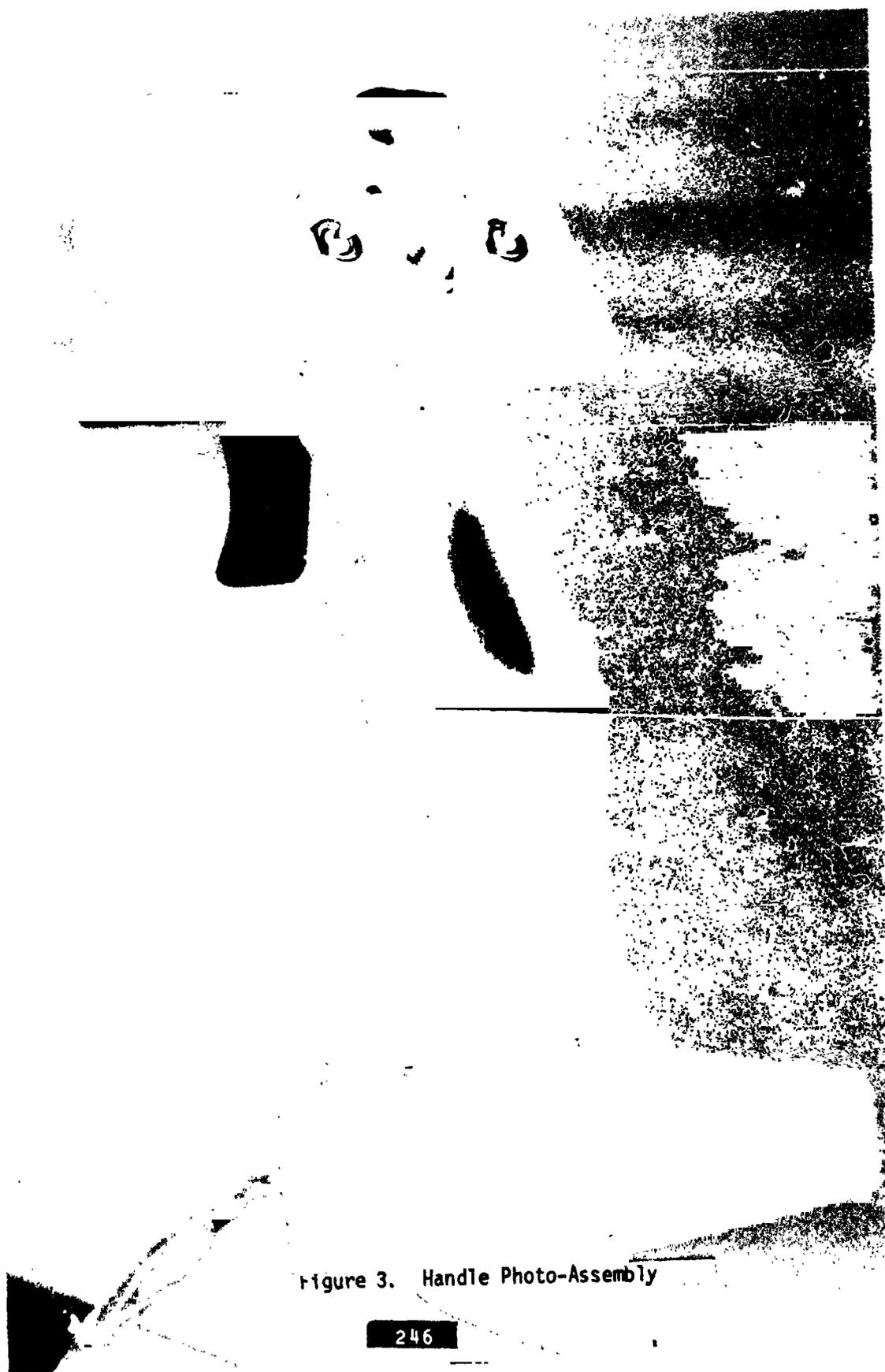
Figure 3. Handle Photo-Assembly

Figure 4. Exploded View of Handle
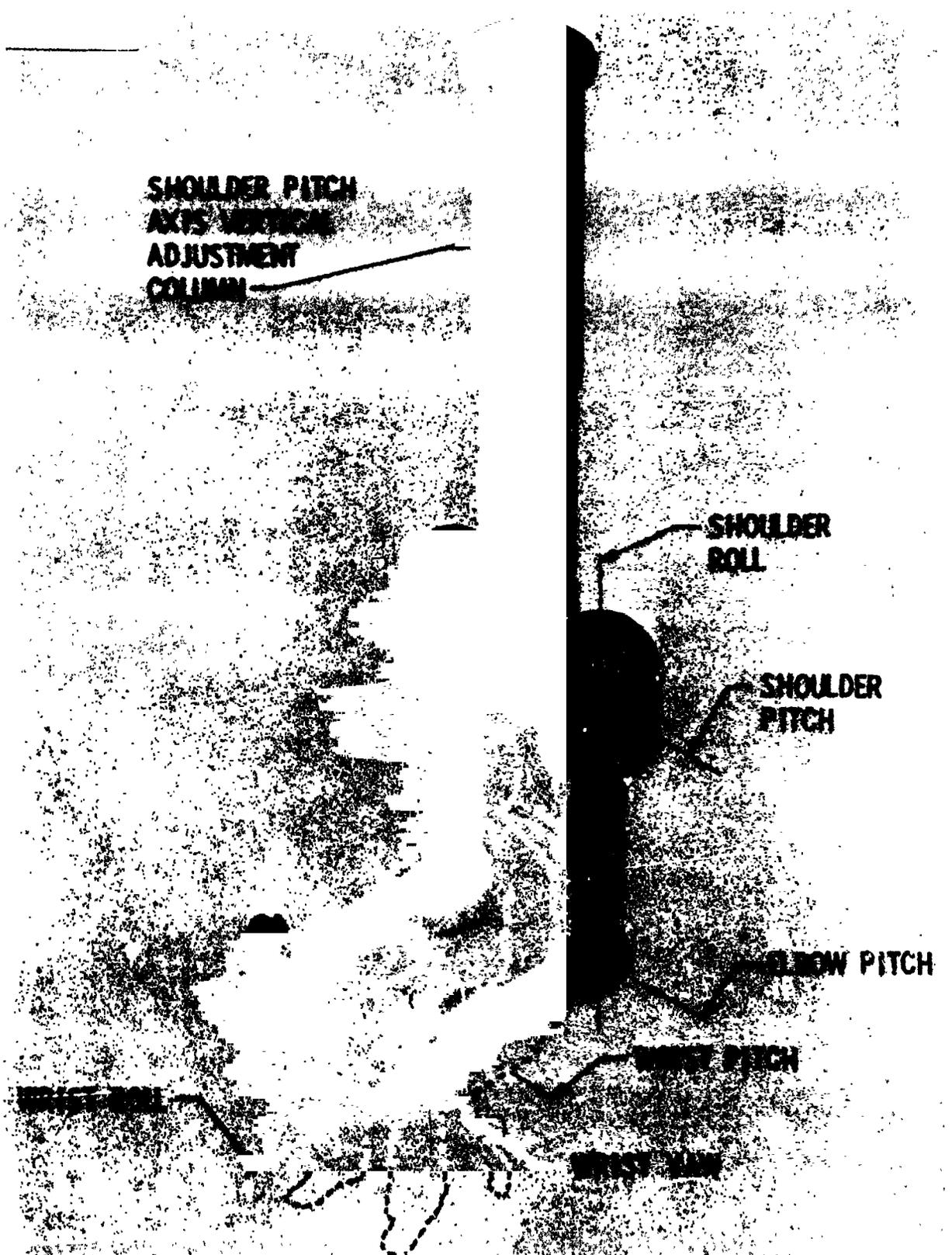
SHOULDER PITCH
AXIS VERTICAL
ADJUSTMENT
COLUMN

SHOULDER
ROLL

SHOULDER
PITCH

ELBOW PITCH

WRIST PITCH

WRIST ROLL

WRIST YAW

Figure 5. Master Controller Assembly
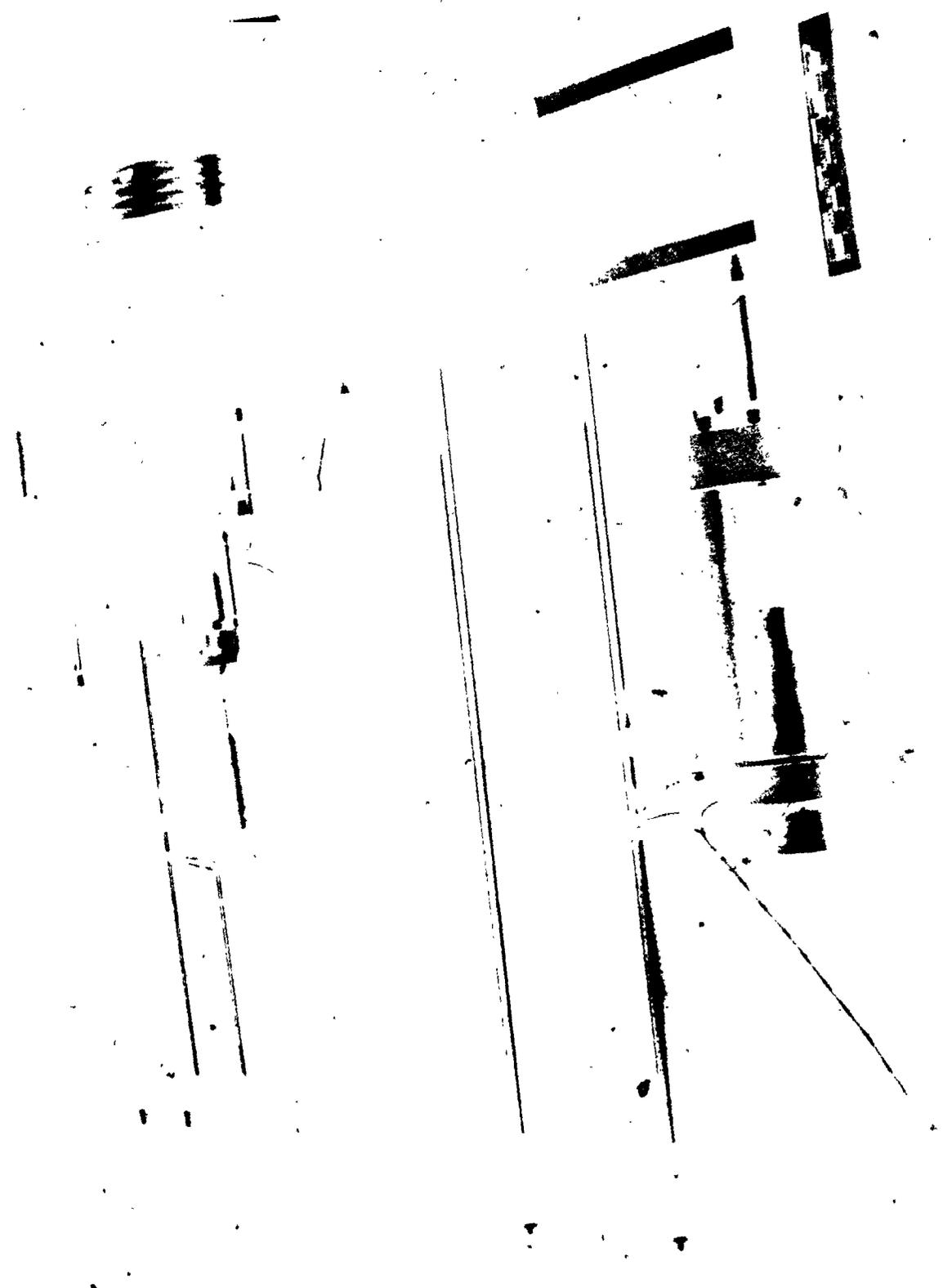
Figure 6. One Degree of Freedom Test Stand: Slave

249
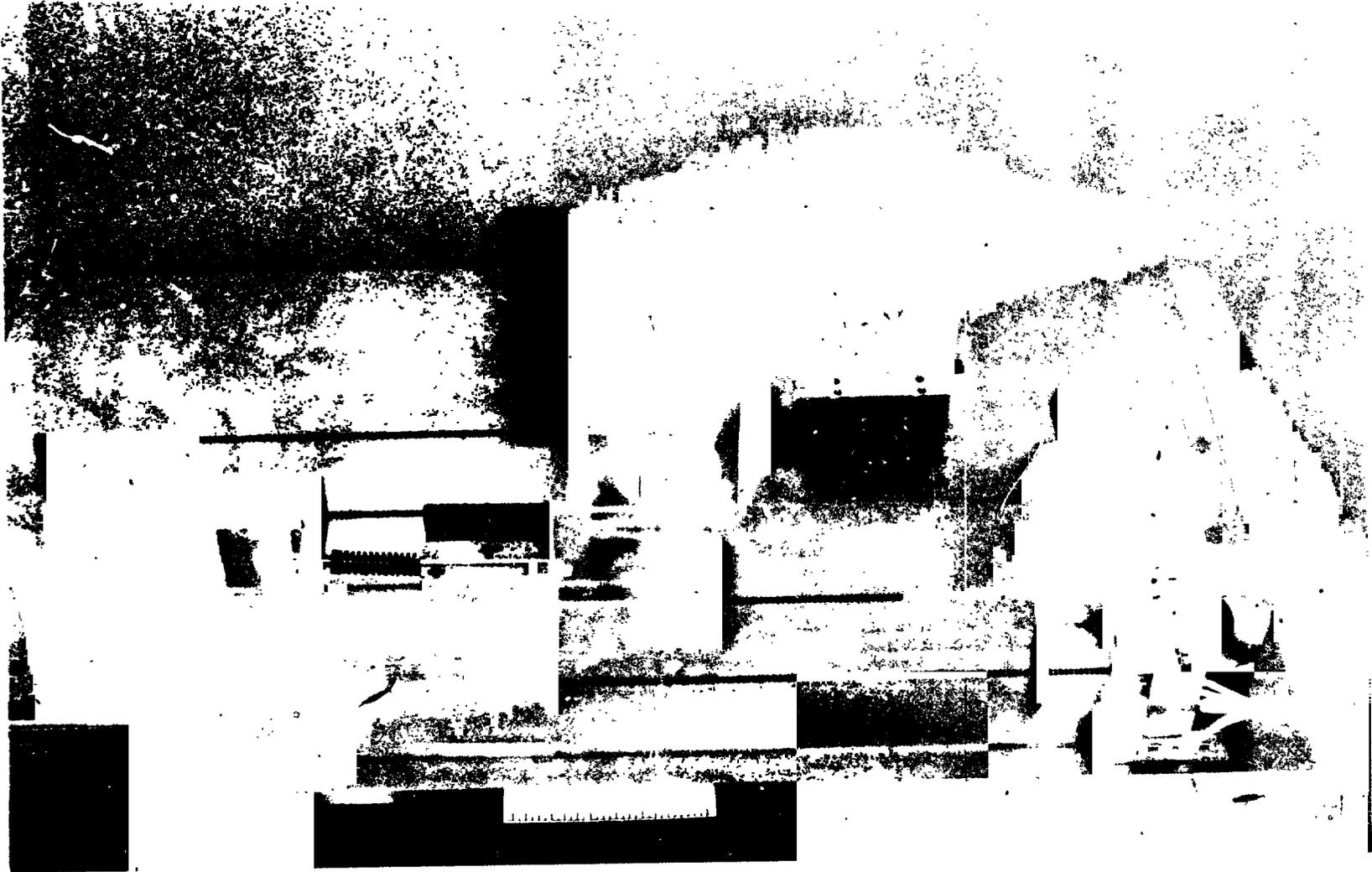
Figure 7. One Degree of Freedom Test Stand: Master

MAN-VEHICLE SYSTEMS RESEARCH FACILITY
ADVANCED AIRCRAFT FLIGHT SIMULATOR THROTTLE MECHANISM

Seth S. Kurasaki* and Wilbur C. Vallotton**

ABSTRACT

This paper describes the conceptual and detail design as well as some preliminary results of an automatic throttle control system for use in an Advanced Aircraft Flight Simulator at the Ames Research Center. The mechanism simulates an aircraft engine throttle system for a future two-engine jet-transport aircraft.

INTRODUCTION

The Man-Vehicle Systems Research Facility Advanced Aircraft Flight Simulator is an important new facility at the Ames Research Center. This new aircraft simulator features a number of innovative aircraft controls and u splays to study advanced cockpit concepts and to investigate pilot-vehicle interactions for the next-generation commercial-transport jet aircraft. The results of human factors research performed on these systems may result in improved safety for future commercial aviation.

Included in these control systems is a dual-throttle, jet-engine control system that can be operated by the Pilot, First Officer, or the aircraft's computer-operated performance-management system. The throttle-control system is located in the Advanced Concepts "Flight Desk" forward of and between the crew seats. The Pilot operates the throttle controls with his right hand and the First Officer operates them with his left hand. The movement of the throttles is conventional with full forward being the maximum thrust condition and full aft being the thrust-reverse condition. A "gate" is used to prevent the accidental movement of the thrust levers into the thrust-reverse condition from the idle position. The simulated aircraft is powered by two advanced, high by pass turbofan engines which contain full-authority electronic engine control both for manual operation and for interface with the aircraft computer-driven performance-management system.

DESIGN REQUIREMENTS

Since existing aircraft simulator throttle systems either could not perform to meet the needed requirements, or be configured for all of the operations necessary for the Advanced Aircraft Flight Simulator, a new throttle control system specific to the simulator was created.

The effort directed to the design of the mechanism was to provide separate engine controls for both pilots within the constraints of the advanced aircraft shell enclosure and crew seating, provide features identified as being critical to aircraft operation, and complete the effort within the project's schedule and cost constraints.

*Research Engineer, NASA Ames Research Center
**Mechanical Engineering Technician, NASA Ames Research Center

In the Advanced Aircraft Simulator, each flightcrew member is 21 inches off the aircraft centerline to provide the correct position for the computer-generated "out-the-window" imagery. The placement of the crew, because of the visual systems and the ergonomic requirements for a 95-percentile pilot, necessitated the installation of dual throttle-control handles so that the pilots could jointly or individually manage the engine-control systems.

The proper arc travels, placements, and heights of the throttle control handles were determined before any design work commenced. The system was configured to conform to the "Flight Desk" Cockpit concept of the Advanced Aircraft.

DESIGN

Various design approaches for the throttle system were considered. Of these, the most promising was a mechanism that combined a mechanical linkage design and separate motor drive systems design. In this manner, separate and simultaneous designs could be worked on without the necessity for constant interfacing to assure that parts would match. The interfacing requirement would be a chain drive where the drive system coupled to the mechanical torque tube. This original design did not work as expected and was replaced later with a mechanical linkage. The new design shown in figure 1 is the system now installed in the simulator.

Figure 1 shows the concept of the throttle system and the relative placement of the components. The system is primarily composed of two sets of four-bar linkages. These four-bar linkages are coupled in sets of two by torque tubes so that operation of one linkage causes the other appropriate linkage to move. In this manner, the throttle system has left and right engine controls that either pilot can operate. All torque tubes are supported on needle bearings, and the pushrods have aircraft spherical rod-ends with both left-and right-hand thread. Alignment of torque tubes and bellcranks with each other during assembly is not critical, and the use of the rod-ends eliminates the requirements for precision tolerances. The thrust levers can be adjusted to reduce free-play and/or increase "binding" in the mechanical system as necessary by twisting the pushrods appropriately. This feature was incorporated into the design to allow the shop fabrication personnel to make a "loose" initial installation and to tighten up the system later to eliminate "slop" by making final adjustments.

Mechanically, the left and right engine controls are independent of each other. However, if it is so desired and because they are motorized, they can be coupled electronically through the simulator computer for any research that may require such configuration. It should be noted that the torque-tube push-rod concept is extendable to three or four engine controls. Each thrust lever, which the pilot operates, has an arc travel limit of 20 degrees. This travel encompases the range of normal operation from idle to the full thrust or the "rated overboost" condition for each engine.

the thrust conditions to instrument displays such as Engine Pressure Ratio, Exhaust Gas Temperature, Revolutions per Minute and fuel flow for each engine.

Two electric switches were incorporated into the handles of the thrust levers. These switches are thumb-operated and represent the "ground spoiler" and "autothrottle disconnect" switches. The switches are located on the left engine handle for the Pilot and on the right engine handle for the First Officer. A separate switch to command the "go-around" mode is located on the throttle panel. All switches are wired into the system computer and function as they would normally in an aircraft. The wires terminate in an electric plug to facilitate ease of removal for any servicing or maintenance.

TESTING AND RESULTS

A chain was originally used to provide power from the motor drive to a sprocket located on the torque tube of each of the two mechanical linkages. An idler wheel was used to take up the slack in the chain to allow the potentiometer to function.

In the initial testing, it became evident that the chain drive system could not provide the accuracy necessary for the potentiometer to resolve the angular position of the thrust levers within the tolerances necessary for correct operations. Consistent repeatability of the thrust lever positions could not be achieved. In addition, friction in the system, due to the idler wheels tensioning the chains, was masking the friction in the magnetic brakes rendering them unusable. The required variable forces could not be achieved if the friction continued. When the chain drive was disconnected, the mechanical linkages freely rotated on their ball bearing rollers and the motor drive mechanism worked properly. The solution to the friction problem, therefore, was to eliminate the chain drive and find an alternative solution to powering the mechanical linkages. This problem was resolved when a direct bell-crank/linkage-arm mechanism was substituted for the chain-drive system. The inherent friction in the chain-drive system disappeared and the brakes could now provide the friction to the thrust levers as originally envisioned without being masked.

Preliminary testing has demonstrated that the drive motors can position the thrust levers to within 0.5 degree of the correct position. The potentiometer feedback system provides sufficient accuracy so that positioning error is negligible. The speed of the thrust levers is approximately 5 - 7 deg/sec. The friction in the system is yet to be measured. The magnetic particle clutches and brakes have been demonstrated to provide variable forces to the thrust levers; however, no accurate measurements have been done on these yet. Because of the demand of the use of the simulator facility to check out other systems, these tests are not planned to be done until after 1985.

The computer that operates the control system is a Digital Equipment Corporation SEL Computer. This computer also operates the B-727 Flight Simulator as well as the rest of the Man-Vehicle Systems Research Facility. Various flight conditions for the Advanced Aircraft Flight Simulator can be

The second four-bar linkage mechanism is "piggy-backed" onto the first mechanism and allows the pilot to engage the thrust reverse of the engines. This part of the thrust lever motion provides an additional 15 degrees of movement aft of the idle position. The engagement of the thrust reverse is accomplished by manually lifting the thrust lever to a different plane before engaging the thrust-reverse features. Figure 2 shows the right engine thrust lever in the full reverse position. When the pilot lifts the thrust lever through the gate to engage the thrust-reverse condition, the second four-bar mechanism mechanically lifts the corresponding thrust lever on the other pilot's side. Movement of the thrust levers in the thrust-reverse condition, however, is still controlled through the first four-bar linkage.

The mechanism provides a cam and follower so that the track of the thrust levers is predetermined. The throttles may be moved through a range from the maximum reverse, through idle, to the rated overboost position. The total arc travel of the thrust levers is, therefore, 35 degrees. Operationally, the computer disengages the drive motors from the system during reverse thrust-operations. Mechanically, whenever the thrust levers are pulled into the reverse condition by either pilot, an electric switch, attached to the thrust lever, is disengaged. When the switch is disengaged, an electrical signal is sent to the systems computer telling it that thrust reverse is to be used and that the drive motors should be disengaged from the mechanism. This is done by deenergizing the magnetic particle clutches. The switch is used since it is very reliable. The potentiometer was not used as it was believed that it would not be a reliable means of detecting the change from normal to thrust-reverse condition.

The motor drive mechanism consists of a globe motor with gear reduction, magnetic particle clutch, and electric brake for each engine. These components are geared to provide the proper angular rotations at the thrust lever handle to the pilot. It also provides proper rotation of a separate shaft connected to a potentiometer. The force at the handle can be varied, by energizing the magnetic clutch and magnetic brake, and hence its friction, from 0 to 7 N (15 lb). The gear-reduction unit of the globe motor, along with the designed gear-reduction system provides some resistance force. The rest of the friction is made up by the brake. The thrust lever forces can, therefore, be configured through software changes by programming the system computer rather than by mechanical design. Although the system does have some mass moment of inertia, the amount is negligible when compared to the friction caused by the brake.

The potentiometer is used to resolve the angular position of the thrust levers and provides the feedback to the system computer to increase or decrease the thrust lever force at various positions. For example, the throttle system requires approximately 3.5 N (7.5 lb) of constant force throughout its normal operating range. In the rated overboost condition at the furthest forward thrust lever position, the system computer, having detected the voltage level from the potentiometer, increases the force required for the maximum thrust condition to 7 N (15 lb) by energizing the magnetic clutch and brake. The pilot operating the thrust levers will then feel the increased force and know that he is operating in this flight condition. The signals from the two potentiometers also are used to supply

simulated including IFR and emergency conditions. All signals sent through the throttle system's two potentiometers are resolved into performance parameters displayed on the flight displays. Similarly, when the aircraft is engaged in the auto throttle mode, the computer provides for correct operation of the throttle system. The system is configured so that, as in a real aircraft, the computer can be overridden by the pilot and the throttle mechanism can be physically overpowered under a simulated emergency condition.

CONCLUSIONS

The Advanced Aircraft Flight Simulator is equipped with a motorized mechanism that simulates a two-engine throttle-control system that can be operated via a computer-driven performance-management system or manually by the pilots. The throttle-control system incorporates features to simulate normal engine operations and thrust reverse and vary the force feel to meet a variety of reserach needs. While additional testing to integrate the mechanism into the facility is required and to verify correct operations, the work required is principally now in software design, since the mechanical aspects function correctly. The mechanism is an important part of the flight-control system and provides the capability to conduct human-factors research of flight crews with advanced aircraft systems under various flight conditions such as go-arounds, coupled IFR approaches, normal and ground operations and emergencies that would or would not normally be experienced in actual flight.

THROTTLE MECHANISM

FIRST OFFICER THRUST LEVERS

PILOT THRUST LEVERS

MAGETIC BRAKE

MAGNETIC CLUTCH

DRIVE MOTORS

FIG. 1

256
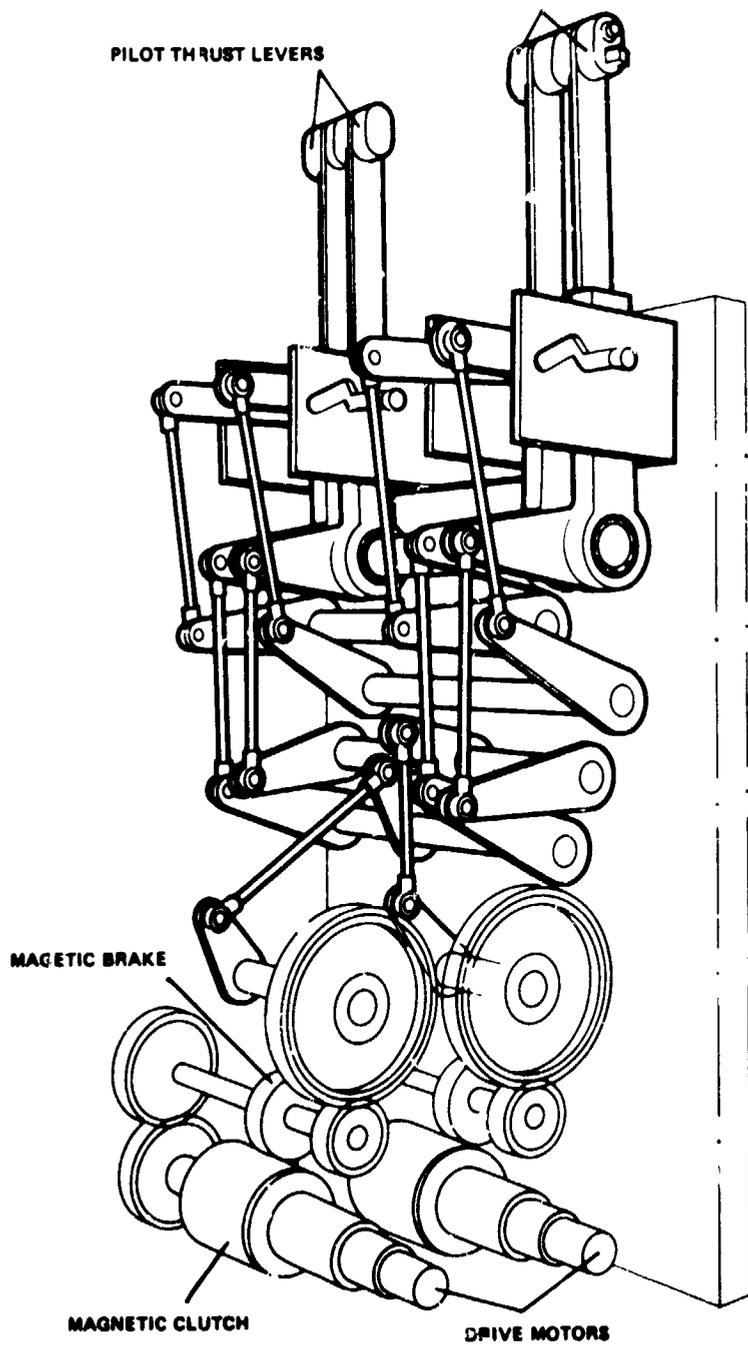
RIGHT ENGINE THRUST LEVER IN FULL REVERSE

TORQUE ROD

MAGNETIC BRAKE

MAGNETIC CLUTCH

DRIVE MOTORS
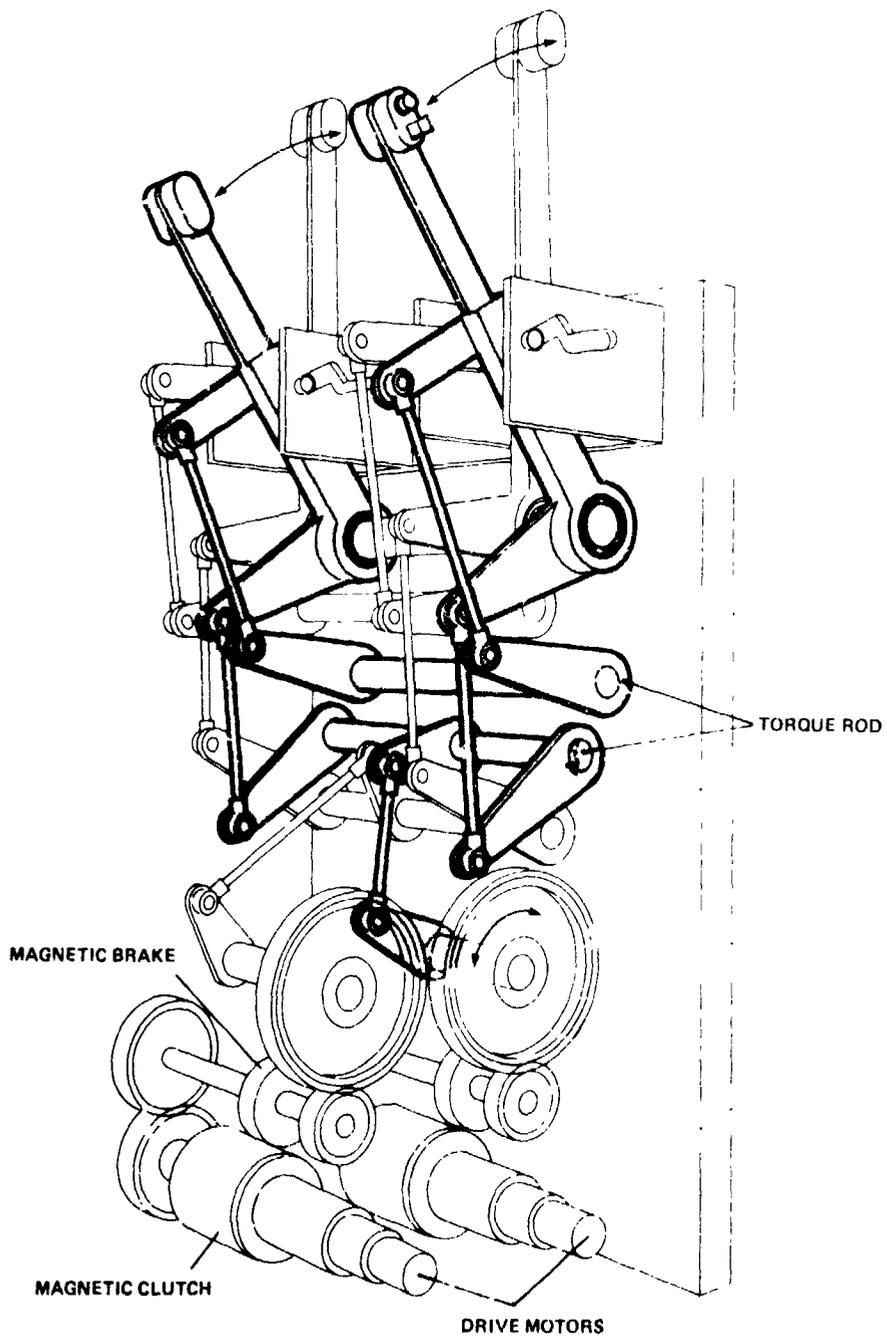
FIG 2

THE DEVELOPMENT OF STAGING MECHANISMS
FOR THE JAPANESE SATELLITE LAUNCHER MU-3SII

Junjiro Onoda*

ABSTRACT

This paper describes the staging mechanisms of the Japanese satellite launch vehicle Mu-3SII involving a unique separation and jettison mechanism for the nose-fairing. The design requirements, the design features and the development problems are presented in this paper together with their solutions.

INTRODUCTION

The Institute of Space and Astronautical Science has developed a solid propellant launch vehicle, the Mu vehicle, for scientific satellites, and has successfully launched 9 scientific satellites and 4 test satellites. A next-generation version, the Mu-3SII, 27.8 m in total length, 1.65 m in maximum diameter and 61 metric tons in total weight, is now in the final stage of development. The development of the staging mechanisms has almost been completed. In this paper, the staging mechanisms of the vehicle are described, stressing the unique separation and jettison system of the nose-fairing and strap-on boosters.

SEPARATION AND JETTISON SYSTEM FOR THE NOSE-FAIRING

The nose-fairing of the Mu-3SII launch vehicle protects the payload, the 3rd stage rocket motor and the optional kick-motor (or 4th stage motor, if it is required for a specific mission), and maintains the desirable aerodynamic configuration during the ascent phase through the atmosphere. The fairing, a hemisphere-cone-cylinder-cone (hammer-head) configuration as shown in Fig. 1, is 6.85 m long and 1.65 m in diameter. The main part of the fairing structure is made of Fiber Reinforced Plastic (FRP) honeycomb sandwich with Graphite Fiber Reinforced Plastic (GFRP) facing covered with a layer for heat protection. The total weight of the fairing involving the separation and jettisoning system is 480 kg.

Requirements

1) The fairing must be capable of jettison without collision, contamination or debris in either a 2nd-stage 5 G acceleration phase with 60 Pa. dynamic pressure or a coasting phase after the burn-out of the 2nd motor.

2) The disturbance caused by the separation and jettison must be less than the counteracting capacity of the actuator of the 2nd stage attitude control system.

---

*The Institute of Space and Astronautical Science, Meguro-Ku, Tokyo, Japan.

3) The fairing structure and the clamp/release mechanism must withstand a loading corresponding to a 4 deg attack-angle with a 0.15 MPa dynamic pressure and a Mach number of 2.6.

4) A payload envelope of 1.4 m diameter must be assured during the ascent phase and separation/jettison phase.

5) The system must function with high reliability.

Selection of the Mechanisms

During the selection of the clamp/release and jettison mechanism for the fairing, the following guidelines were formulated in order to attain high reliability, rigidity and strength for the total fairing system.

1) The halves of the fairing should be clamped to each other continuously or at many points along the split lines.

2) The clamp mechanisms between the halves and between the fairing and the 2nd stage should be released by ignition of a minimum number of pyro initiators.

3) The jettison system should be of the clamshell type.

According to the above-mentioned guidelines, the separation and jettison mechanisms described below were selected. A latch mechanism using balls was also considered. However it was not adopted because of its complexity.

Technical Description

1) The Clamp/Release Mechanism Between the Halves of the Fairing

This mechanism is shown in Fig. 2. The halves of the fairing are provided with many protrusions with wedge-shaped cross sections along the split lines. Figure 2(a) shows the mechanism in the clamped state, where each pair of protrusions are clamped by a clamp-block. The clamp-blocks are linerally linked along the split line, and the bottom end of the train of linked clamp-blocks is retained by the marman bands at the bottom of the fairing. Figure 3 shows the detail of the bottom end of the train. The clamp mechanism can be released by freeing the train of linked clamp-blocks and pulling up the train to the release position. Figure 2(b) shows the released mechanism.

2) The Marman Clamp Between the Fairing and the top ring of the 2nd Stage

The end of the marman clamp bands are fastened to each other by bolts and separation-nuts at the end-blocks. As can be seen in Fig. 3, the marman clamp also retains the train of clamp-blocks by holding the end-ball of the train in the socket between the two end-blocks of the marman band. The marman clamp can be released by the action of the separation-nuts. Each fastening of the marman band is carried out by two separation-nuts, and the action of any one of them can release both the marman clamp and the restriction of the chain of clamp-blocks, providing the system with redundancy.

3) Double-Action Pyro Actuator

The double-action actuator at the top of the nose fairing is shown in Fig. 4. The actuator consists of: two squibs, a gas-generator, piston-A with arms for pulling up the trains of the linked clamp-blocks, piston-B, and two cylinders as shown in the figure. The system has two squibs for the ignition of the gas-generator in order to provide the system with redundancy. The action of piston-A pulls up the freed trains of the linked clamp-blocks to the release position. The port to cylinder-B, which was closed before the action of piston-A, is opened by this action. Piston-B is restrained by the shear-pins until the pressure in cylinder-B increases to 5 MPa. so that piston-B pushes away the other half of the fairing, providing the halves of the fairing with sufficient velocity after the cutting of the shear-pins.

4) Separation-Nut

The above-mentioned separation-nut consists of a nut split into 3 pieces, a nut housing, a piston and a cartridge. Before the release action, the 3 pieces of the split nut are retained in the housing and compose a normal nut. When the cartridge is ignited, the nut-housing is pushed away by the gas-pressure and the pieces of the split nut scatter, releasing the fastening.

The Release and Jettison Sequence

The sequence of events during fairing separation is as follows:

1) Simultaneous ignition of all the squibs of the separation-nuts and the gas-generator by means of an electric current.

2) Within 10 msec, the release action of the separation-nuts followed by release of the marman clamp and the train end-balls of the linked clamp-blocks.

3) Within 30 msec, action of piston-A of the actuator, which pulls up the trains of the linked clamp-blocks to the release position through the levers. After this action, the two halves of the fairing are fastened to each other only by the shear-pin at the top of the fairing. The gas-inlet port to the cyliner-B is opened by this action.

4) Approximately 300 msec - 400 msec after the ignition of the squi , action of piston-B of the actuator, which pushes one of the halves of the fairing away from the other, providing them with necessary separation velocity. This action starts when the pressure inside the cylinder increases sufficiently to enable the shear-pins to be cut.

Development Problems

1) Actuator

During the beginning phase of the development, spring actuators were used to pull up the trains of the linked clamp-blocks and to push away the halves of the fairing with sufficient separation velocity. However, it was found

261

that a relatively large force was occasionally necessary in order to pull up the train of linked clamp-blocks. This occurred because of the spring force of the actuator, which always acts so that the halves separate from each other, and because of the variation of the friction coefficient between the protrusions along the split lines and the clamp-blocks. It proved difficult for the light weight spring actuator to provide the halves with sufficient initial velocity. Therefore, a powerful double-action actuator with a gas-generator was adopted, in spite of the increase of the number of squibs.

2) Initial Separation Velocity of the Halves

As can be seen in Fig. 5, the centers of gravity of the halves move up slightly before the halves fall outward and downward during the jettisoning process. Therefore, the halves must be provided with sufficient velocity to climb this "hill" of potential energy in the acceleration phase of 5 G. It was found from ground tests that the force produced by the pyro actuator does not provide the halves with tanslational velocity efficiently because of the elastic deformation of the halves caused by the actuator force. This problem was overcome by an increase in the operational pressure of the actuator and an increase in the stroke length of piston-B.

3) Deformation of the Fairing

The main structure of the unseparated fairing deforms under external ascent loads. The trains of the linked clamp-blocks must follow this deformation. As a result, the trains are sometimes subjected to a relatively large load. The load on the trains is especially high in the bottom area, where the deformation of the main structure is large, because of the high bending load and because of the tapered configuration in this area. This problem has been overcome by reinforcing the main structure and by introducing buffer devices with preloaded springs as shown in Fig. 3, which permit some deformation.

Tests

1) Functional test

During the process of developing the fairing, separation and jettison tests were performed 8 times. The last 4 tests were qualification tests utilizing the final configuration.

All the separation and jettison tests were carried out under ground conditions. The performance under flight conditions during both the acceleration phase and the coasting phase -- was estimated by means of analytical simulation based on the measured data of the ground tests. The effects of air, especially the negative pressure inside the fairing caused by the separation action, was conspicuous, although the test adapter was provided with relatively large holes. The effect of elastic deformation on the initial separation velocity of the halves was also significant. All these effects were taken into account, based on the measured pressure inside the fairing and the measured vibration. The results of the numerical simulation indicated normal functional performance in both the acceleration phase and the coasting phase.

2) Load Test

The fairing was subjected to a load equivalent to an attack angle of 4 deg with dynamic pressure of 0.15 MPa. The maximum bending moment at the bottom end of the fairing was 0.32 MN-m. The main structure was fractured by 98 percent of the above-mentioned load in the third test, after twice withstanding the 100 percent load.

THE SEPARATION AND JETTISON MECHANISM OF THE STRAP-On BOOSTER

The first-stage rocket motor of the Mu-3SII vehicle is accompanied by two strap-on boosters which must be jettisoned after burn-out. The boosters are 9.1 m long and 0.735 m in nominal diameter. A strap-on booster weights 5.1 metric tons before ignition and 1.1 tons after burn-out.

Requirements

1) The joint between the strap-on booster and the core motor must withstand the longitudinal load caused by the 0.35 MN thrust of each strap-on booster and the lateral inertial force due to the lateral bending vibration of the vehicle.

2) The sub-boosters must be separated from the core motor and must be jettisoned without collision, excessive shock or disturbance on the core motor. The acceleration just before the separation is nominally 3.8G. The nominal dynamic pressure at that time is 95 KPa. with a Mach number of 3.2 and a roll rate of less than 0.3 rps.

In the selection of the separation and jettison mechanism, the following guidelines were adhered to:

1) The separation mechanism should be designed and adjusted to provide the strap-on boosters with both the initial attitude and the initial translational and angular velocity for a collison-free jettison action.

2) Separation and jettison should be perfu med with a minimum number of pyro initiators.

Following the above guidelines, the separation and jettison mechanism shown in Fig. 6 was selected. A feature of this mechanism is that the front and rear braces push the strap-on boosters away from the core-motor when the boosters travel rearward, and therefore the initial attitude and velocity of boosters can be easily adjusted by selection of the length of the braces and their attach points.

The trajectories of the strap-on boosters after the separation were numerically calculated taking account of the aerodynamic force and the effect of the plume of the core-motor exhaust jet. This analysis was used to determine the attach points and lengths of the braces. No assist-rocket-motors for separation were adopted because of the possibility of damaging the core motor casing and because of the increase in the required number of pyro initiators.

Technical Description

Figure 6 shows the separation and jettison mechanism for the strap-on boosters. Figure 6(a) shows the mechanism before the separation. The thrusts of the strap-on boosters are carried to the core motor mainly by the thrust-tubes. The bottom part of each booster is supported by the thrust-tubes, rear braces and a rear attach-fitting. The top part of each booster is supported by the front attach-fitting, which restricts the relative movement of the booster in the radial and circumferential directions, and the stabilizers, which restrict the rotation of the booster around the front attach-fitting. The front brace can be shortene telescopically and is preloaded by a compression-spring installed inside. Therefore, the relative movement in the axial direction is not restricted at this station.

Separation and jettison is initiated by action of the separation-nuts installed in the thrust-tubes, disconnecting the tubes. Subsequently, the strap-on boosters are pushed rearward by the aerodynamic drag and the inertial force due to the acceleration caused by the thrust of core motor. As a result, the front portion of the booster moves axially rearward and the front braces are shortened. After a certain amount of rearward travel of the top part of the booster, the front attach-fitting is freed and subsequently the front braces push the booster away from the core-motor when the braces have been shortened to the limit. The rear portion of the booster is pushed away from the core motor by the rear braces from the beginning of the jettison action. After a certain amount of rotation of the braces, the compressive loads on the braces decrease, and finally the braces are pulled away from the core-motor as shown in Fig. 6(b). The rear braces are fixed to both the core-motor and the booster in the state shown in Fig. 6(a), and can carry both tensile and compressive loads. However, the core-motor-side ends of the rear braces are freed by a certain amount of rotation of rear-braces. Therefore, the braces, stabilizers and most of the thrust-tubes are jettisoned, together with the boosters, as shown in Fig. 6(b).

A Development Problem

As has been mentioned, the front-braces are shortened in the initial phase of separation. After a certain amount of shortening, they impact the stroke-ends and they begin to function as rigid rods. As a result of these impacts, the braces and the adjacent structure are subjected to a shock load. It is difficult to use powerful buffers to reduce the shock, not only because the space for installation is limited, but also because too powerful buffers may prevent the braces from being shortened to the expected length when conditions, such as thrust and dynamic pressure, vary, and may in the worst case result in a failure of the release of the front attach-fitting. Therefore, a certain level of shock is unavoidable in the separation action.

The estimation of the shock level during the early phase of design was somewhat difficult because the shock level depends on the effective flexibility of the structures, which is sometimes governed not only by the longitudinal stiffness of the braces but also by the local dynamic deformations of the joint structures, core-motor and boosters. The shock load was estimated by a law of similarity based on the results of sub-scale

(1/2-scale) ground tests as well as the numerical simulation in the final step of development based on the measured stiffness data of prototype structural components.

Tests

As a first step in the development tests, the 1/2-scale ground tests were carried out seven times. Three of them were in the zero-spin condition and the others were with a spin of 0.3 rps. The functional performance was confirmed and the loads during separation were measured.

In order to confirm the functional performance, loads at separation and the motion of the strap-on boosters subsequent to the separation in nearly actual conditions, a separation test was carried out under flight conditions with an approximately 1/2-scale vehicle. It was observed by means of an on-board TV camera, ground telescope cameras and telemetry data, that the separation action and the subsequent motion of the boosters were normal.

Full-scale structural components were subjected to a load of 100 to 150 percent of the design load and it was confirmed that they withstood the loads. No separation tests using the full-scale mechanism have been performed.

INTER-STAGE SEPARATION SYSTEMS

The Mu-3SII-1, the first vehicle of the Mu-3SII series, has four interstage joints as listed in Table 1, because an optional kick-motor has been installed for an interplanetary mission. However a detailed description of the joint between the kick motor and the payloads is omitted in this paper because it is an ordinary marman clamp joint.

The Interstage Separation System Between the 1st and 2nd Stages

The interstage structure between the 1st and 2nd stages joins the Y-rings of the motor casings of each stage. The nozzle of the 2nd stage rocket motor, thrust vector control equipment, side-jet equipment and hemispherical end-plates of the motor casings are installed inside the interstage joint. Therefore, an open-petal joint was adopted as shown in Fig. 7, because of the large diameter of the nozzle of the 2nd stage installed in the joint, and to reduce the inert mass of the joint to be left on the 2nd stage after the separation. A truss structure was selected for the joint, which has the advantage of ease of access to the equipment installed around the nozzle. As can be seen in Fig. 7(a), in the clamped state the top nodes of the triangular trusses are fastened to the upper-stage structure directly by bolts and separation-nuts. Two separation-nuts are used for each fastening point, and action of any one of them releases the fastening, providing redundancy. This system is used because the load on the joint was estimated to be relatively large. Figure 7(b) shows the joint in released state. The relative velocity of 0.8 m/s is provided by 12 separation springs installed at the fastening points. The petals of truss are opened by the torsion spring installed at the hinges.

Functional separation tests were carried out under ground conditions by using a full-scale proto-model, and normal functioning was confirmed. The load tests were also carried out wqith a maximum combined load of 1.3 GN-m bending, 0.99 GN compression and 0.27 GN shear. The equivalent bending stiffness of the joint was measured in the static load test as shown in Table 1.

The Inter-Stage Separation System Between the 2nd and 3rd Stages

An open-petal joint was also selected for the 2nd and 3rd inter-stage joint for the same reasons as mentioned above. However, as can be seen in Fig. 8, a marman clamp is used instead of the direct fastening by separation-nuts, for the following reasons.

1) The 3rd stage motor casing is nearly spherical. Therefore, it is not provided with a Y-ring. Furthermore, the thickness of the titanium casing is very small (2.5 mm). As a result, a concentrated load on the 3rd motor casing is not permissible.

2) The inert mass of the 3rd stage should be decreased as much as possible.

3) The load on the joint is not as great as it is on the above-mentioned joint.

As can be seen in Fig. 8 (b), only the V-ring of the marman clamp is left in the 3rd stage as the inert mass of the joint. The relative separation velocity of 0.9m/s is provided by separation springs. The petals are opened by the torsion springs at the hinge and the centrifugal force due to the spin of 2rps.

Separation tests were carried out on a spin table under a 2rps spin. Normal function was confirmed. It has been estimated from the observed motion of the upper stage that the disturbance due to the separation action causes only 0.4 deg. nutation of the 3rd stage of the actual vehicle in the worst case. It has also been confirmed that the joint withstands up to a maximum combined load of 0.53GN-m bending, 0.24GN compression and 0.23GN shear.

The Inter-Stage Separation Systems Between the 3rd Motor and the Kick-Motor

As shown in Fig. 9 and Table 1, an ordinary marman-clamp joint with a lightweight, lattice, cylindrical structure made of carbon fiber reinforced plastic was selected for the inter-stage separation system between the 3rd motor and kick-motor. This system was selected in order to decrease the inert mass of the upper stages. This joint is not an open-petal-type. However, it was confirmed that a collision-free separation can be performed based on the measured data of the dynamic unbalance of the 3rd motor after static firing tests, and the estimated unbalance of the 3rd motor after static firing tests, and the estimated inevitable unbalance of the upper stage as well as the measured motion at the separation ground test.

CONCLUDING REMARKS

Staging systems for the Mu-3SII : tellite launcher, including the unique separation and jettison systems for the strap-on boosters and nose-fairing, have been developed. Normal performance of the sytems is expected based on functional tests, load tests and numerical simultions utilizing test data, and will be confirmed in the first launch of the vehicle in January 1985.

ACKNOWLEDGMENTS

Table 1   INTER-STAGE JOINTS FOR Mu-3SII-1

Location	1st and 2nd	2nd and 3rd	3rd and KM[a]	KM and PL[b]
Length	2.0 m	1.36 m	0.86 m	0.17 m
Maximum Diameter	1.65 m	1.42 m	0.82 m	0.50 m
Type	Open-Petal Direct Fastening by Separation Nuts	Open-Petal, Merman Clamp	Marman Clamp	Marman Clamp
Structure	Truss	Truss and Panel	Lattice made of CFRP	Cylindrical Shell
Equivalent Bending Stiffness	$3 \times 10^8 Nm^2$	$8 \times 10^7 Nm^2$	$6 \times 10^6 Nm^2$	$1 \times 10^6 Nm^2$
Relative Separation Velocity	0.8 m/s	0.9 m/s	2.1 m/s	2.2 m/s

(a) KM = Kick Motor,
(b) PL = Payload
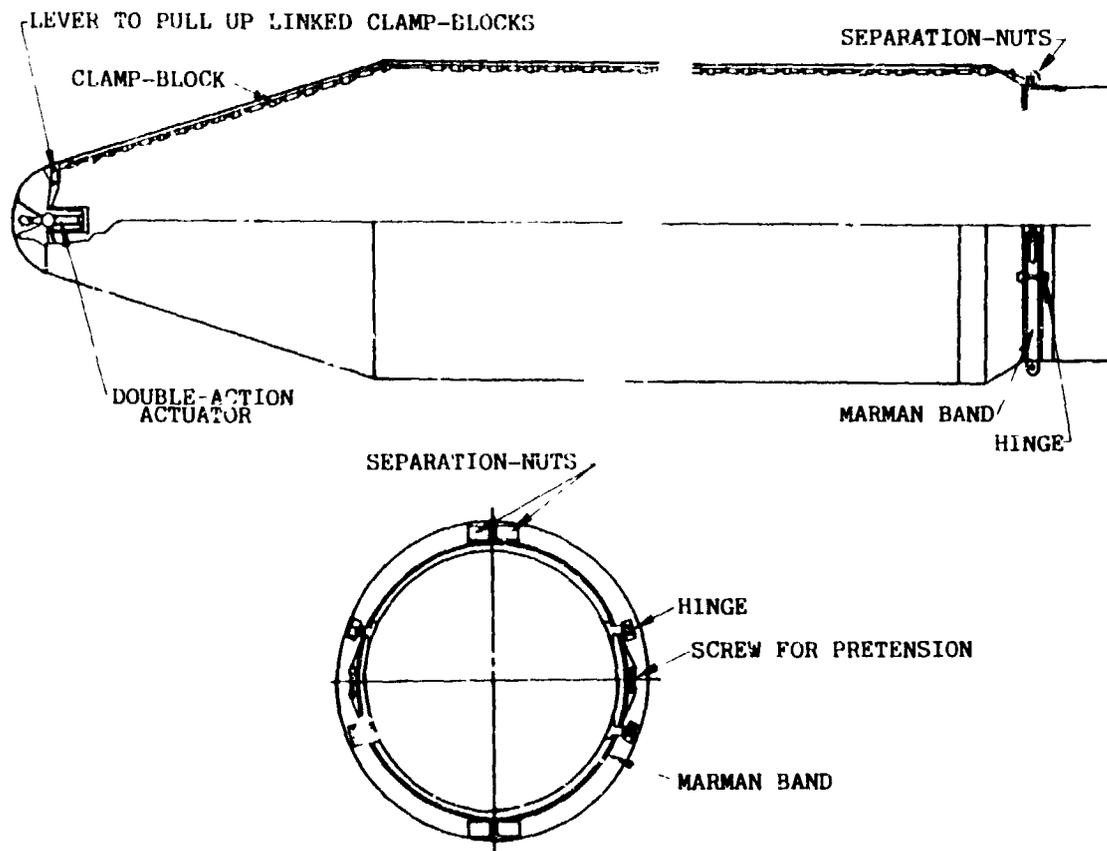
Figure 1. Nose-Fairing Separation and Jettison System

(a) CLAMPED STATE

(b) RELEASED STATE
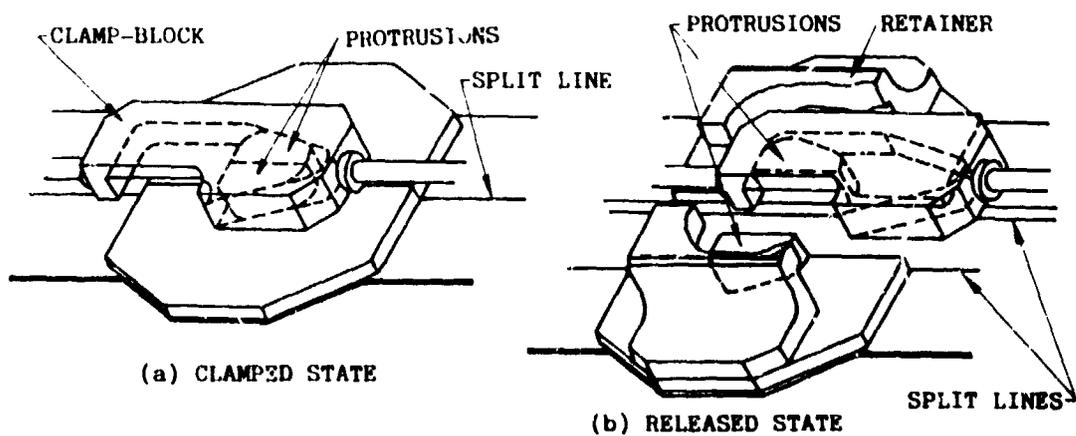
Figure 2. Clamp Mechanism Along Split Line
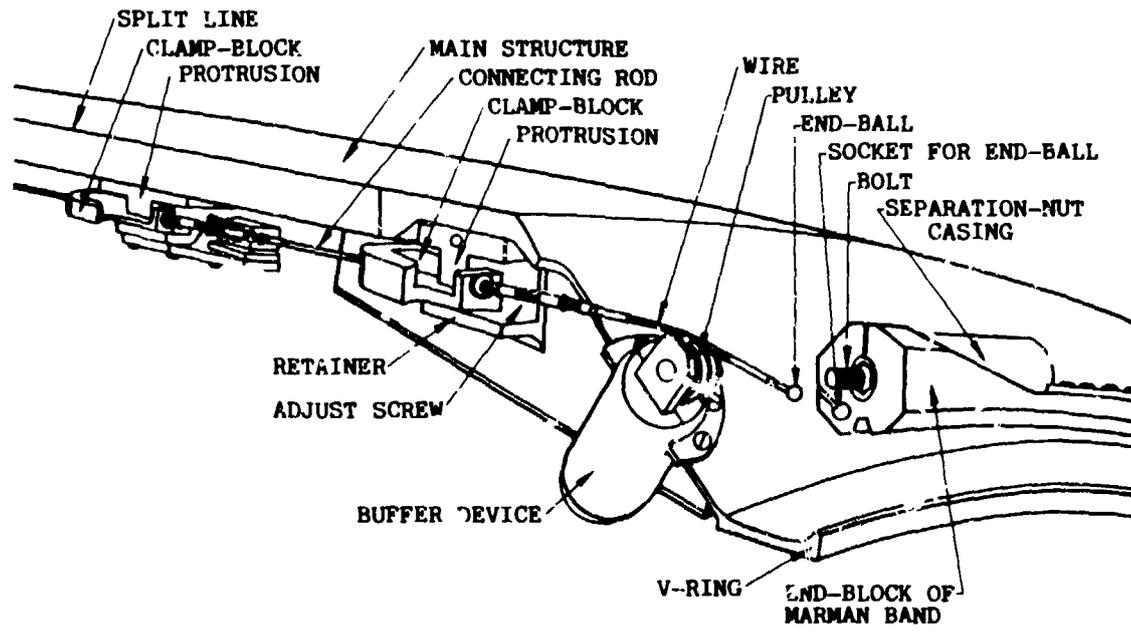
Figure 3. Detail of Bottom End of Split Fairing
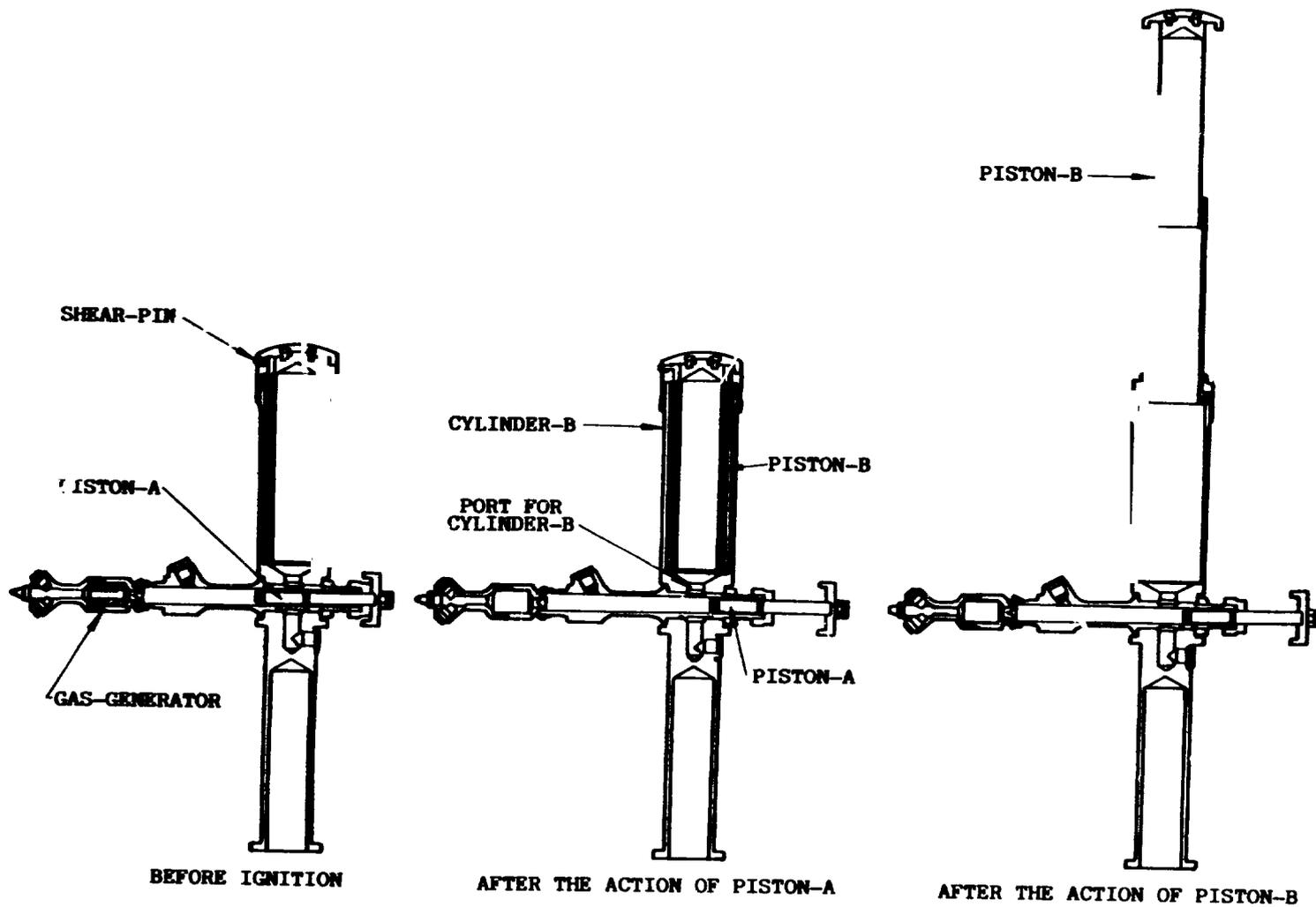
Figure 4. Double-Action Pyro Actuator
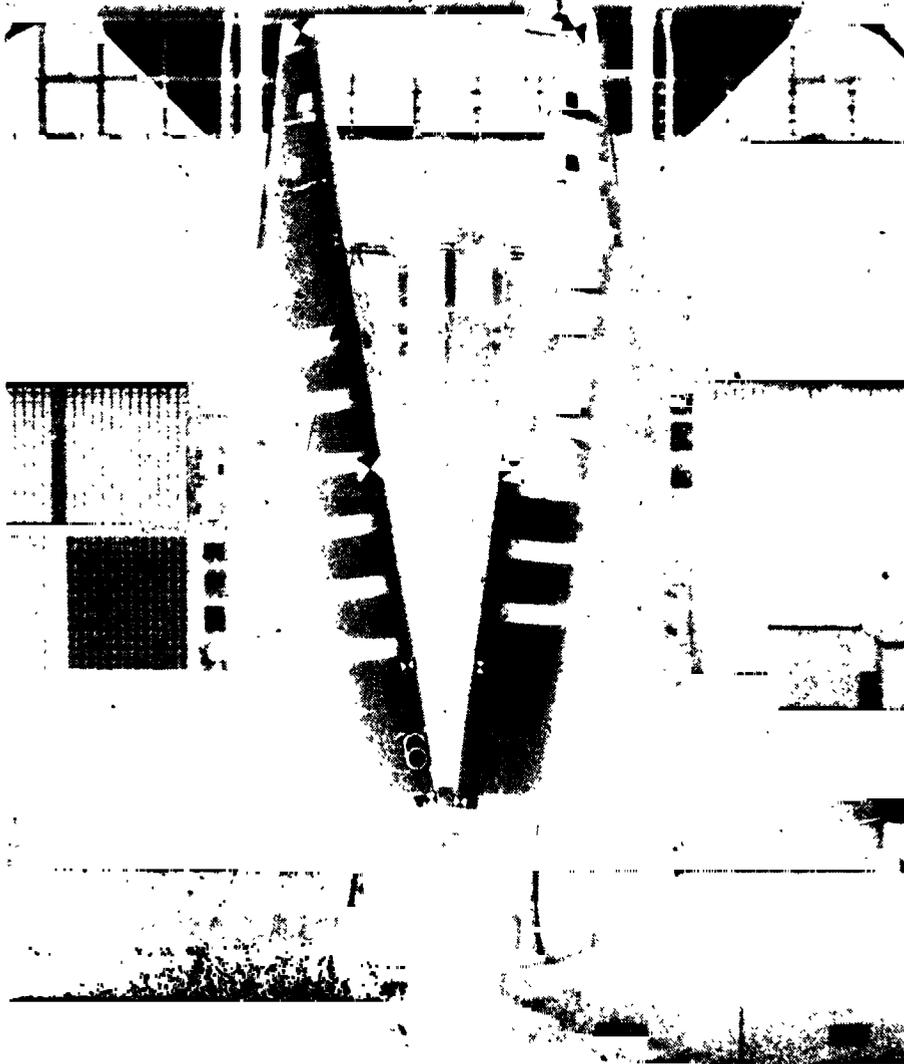
Figure 5. Nose-Fairing Separation and Jettison Test

FRONT
BRACE

STABILIZER

FRONT
ATTACH-FITTING

REAR
BRACE

THRUST-TUBE

REAR
ATTACH-FITTING

STRAP-ON BOOSTER

FRONT BRACE

STABILIZER

SEPARATION-NUTS

THRUST-TUBE

REAR ATTACH-FITTING

REAR BRACE
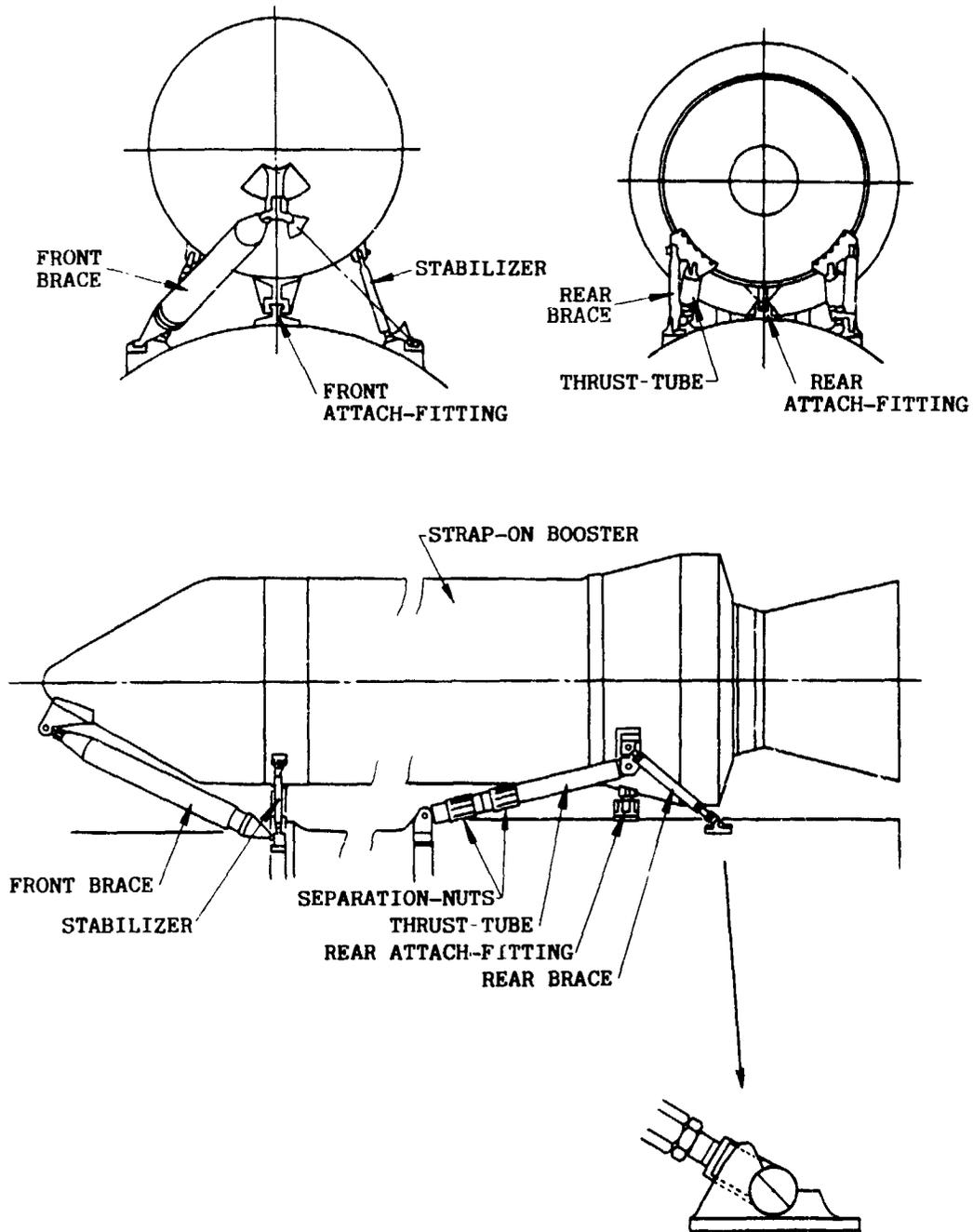
Figure 6 (a) Strap-on Booster Separation and Jettison System
(Before Separation)

273
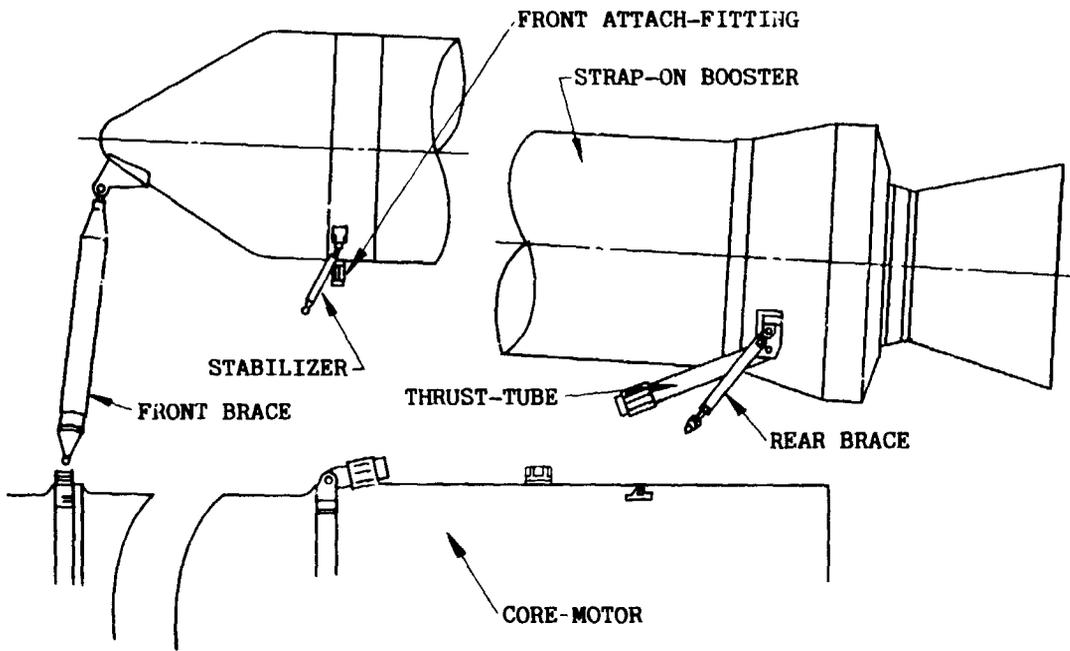
Figure 6 (b). Strap-on Booster Separation System
(After Separation)
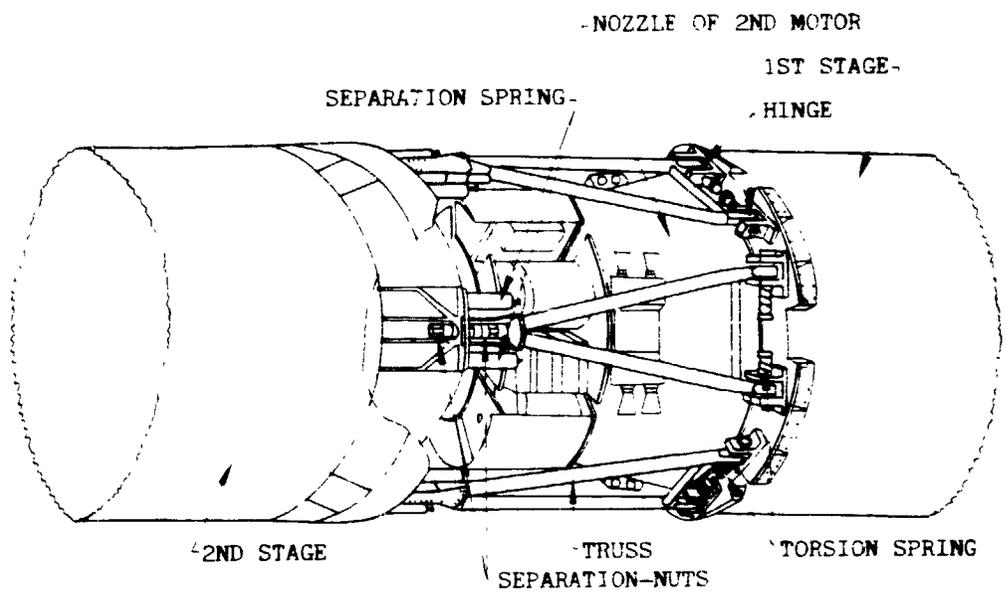
(a) Before Separation
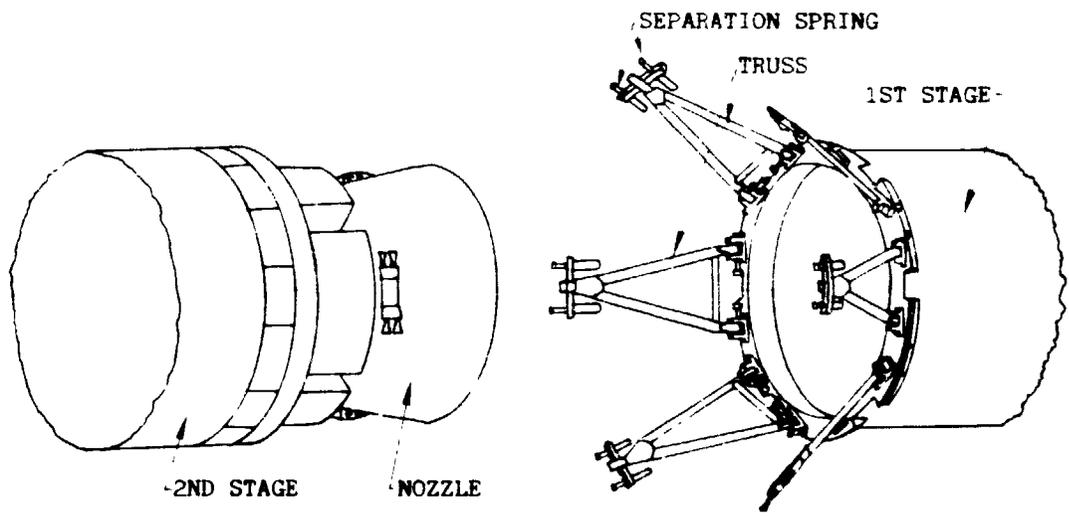
(b) After Separation

Figure 7. Inter-Stage Joint Between 1st and 2nd Stages

Figure 8.
Inter-Stage Joint
Between 2nd and 3rd stages

(a) Before Separation

(b) After Separation
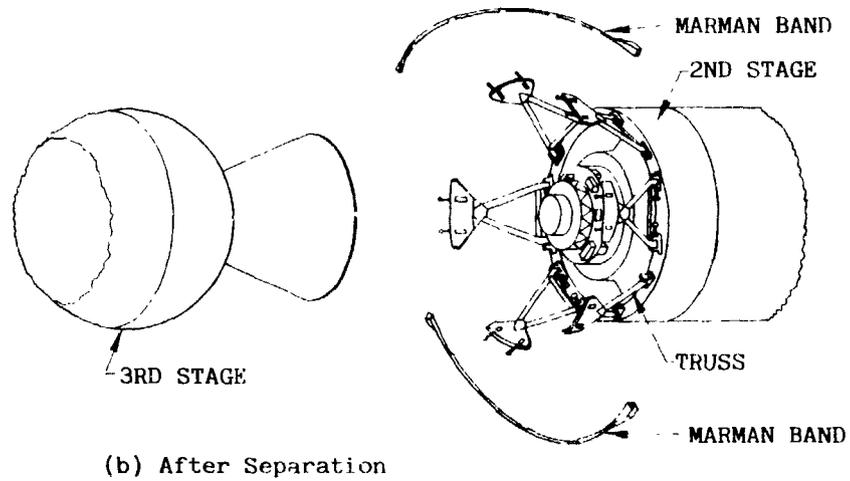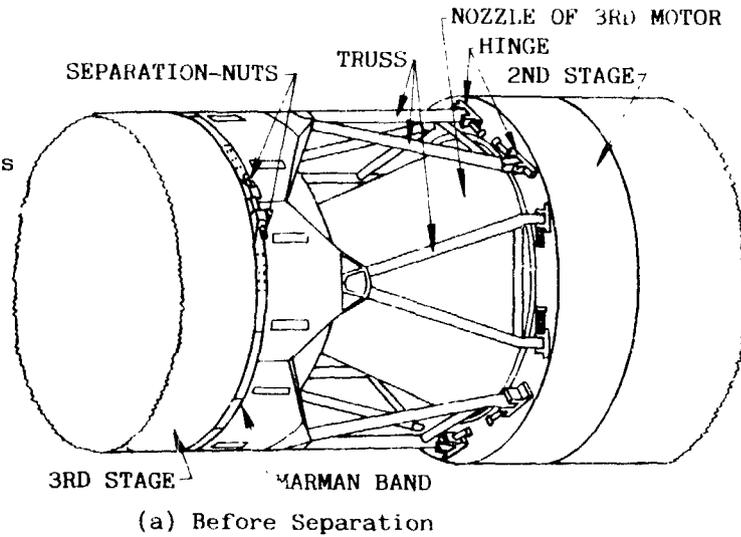
Figure 9.
Inter-Stage Joint Between
Kick Motor and 3rd Stages

276
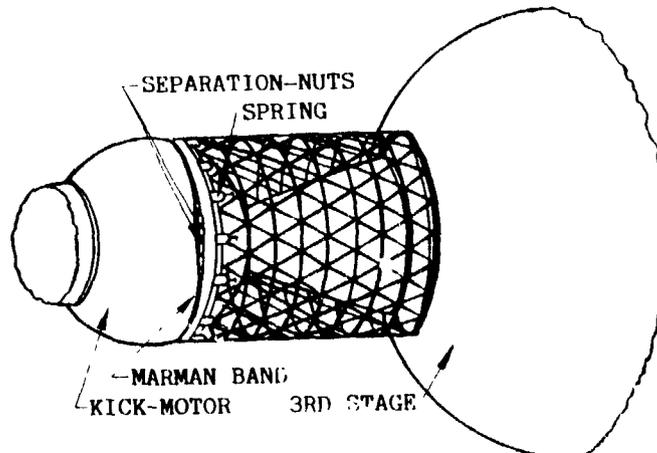
A ROTATING ELECTRICAL TRANSFER DEVICE

Ryan S. Porter*

ABSTRACT

This paper describes the design, development, and performance characteristics of two roll-ring configurations - a roll ring being a device use in transferring electrical energy across a continuously rotating or oscillating interface through one or more flexible rolling contacts, or flexures. Emphasis is placed on the design problems and solutions encountered during development in the areas of flexure fatigue, contact electroplating, electrical noise, and control of interface geometry. Also, the present status of each configuration is summarized.

INTRODUCTION

A roll ring consists of one or more flexures captured by their own spring force in the annular space between two concentric conductors, or contact rings. Figure 1 shows a photograph of each configuration. These inner and outer contact rings are rigidly mounted to the rotating and fixed sides of the rotating axis.

Two basic roll-ring configurations are presently under continuous research: the single flexure, 0- to 15-amp configuration and the multiflexure, 0- to 200-amp, high-power design.

The single circuit shown in Figure 1A is typical of over 400 circuits with a cumulative test history of approximately 600,000 circuit-hours, tested under several parameter-controlled conditions in an effort to optimize operational performance.
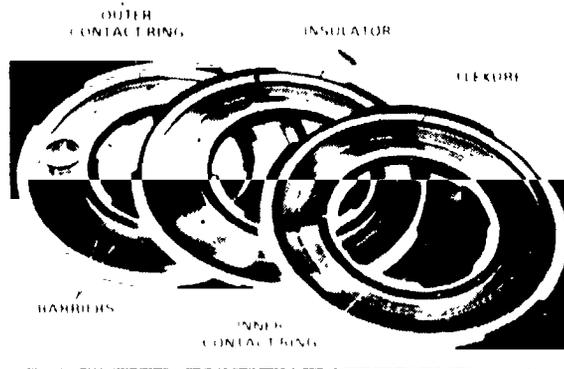
Figure 1A. Single-Flexure, 15-Amp Roll-Ring Circuits

*Sperry Corporation, Aerospace & Marine Group, Space Systems Division, Phoenix, AZ

At present four high-current designs have been fabricated and at least partially evaluated. Figure 1B is a plan view of one circuit in an 8-circuit module that was designed and fabricated.
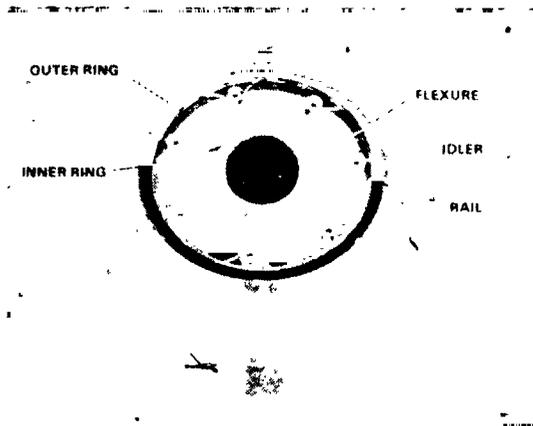
Figure 1B. Multiflexure High-Current Configuration

DEVELOPMENT OF 15-AMP DESIGN

Very little information was available when research and development began on this rolling-contact interface. The bulk of available literature dealt with sliding contacts (as in slip rings) or with make/break devices (as in switches). It was, therefore, necessary to empirically determine the design sensitivities of this new technology.

Flexure Fatigue

Early in the development of the 15-amp flexure, a fatigue failure at 30 million reverse bending cycles indicated that either the stress model or the allowable stress limit was incorrect. After the stress model was carefully scrutinized and exonerated, the material properties were investigated.

Flexures are machined from beryllium copper alloy 172 and subsequently precipitation-hardened for optimized mechanical properties. The published fatigue stress data used in designing the flexure deflection limits were derived from Berylco's strip stock results and ASTM rotating beam testing. Their respective S/N curves are shown in Figure 2. The cold-rolled processing gives the strip and rod stock a preferred grain orientation. This preferred grain orientation enhances the fatigue properties of the material when stressed along the grains (Ref 1). During operation, a flexure is stressed across the grain, its weakest axis (as summarized in Figure 3). Therefore, an S/N curve for beryllium copper in an operating flexure's stress orientation was needed to select an acceptable fatigue stress for a long-life flexure design.

278
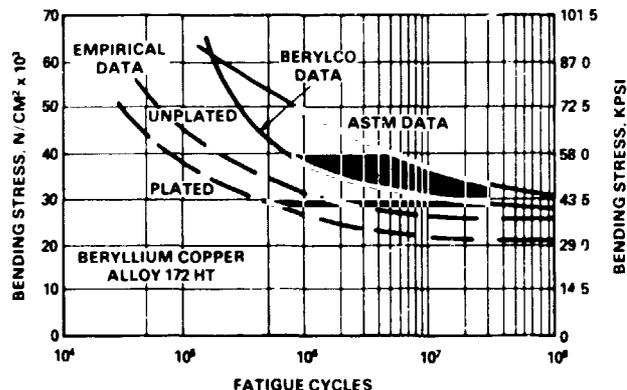
Figure 2. Fatigue Curves for Various Testing Configurations
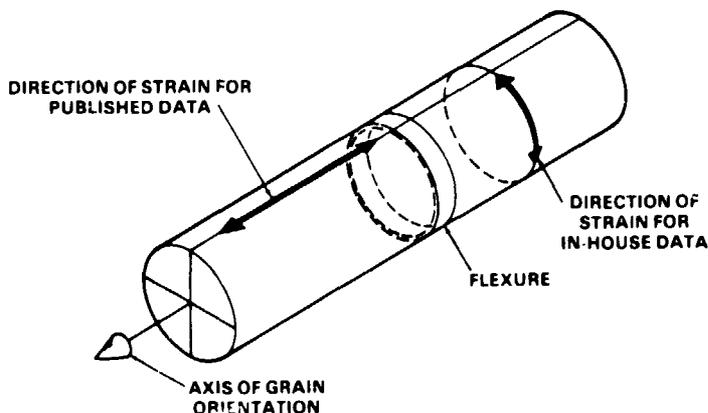
Figure 3. Strain Axes of Cold-Rolled Flexure Material

This curve was established by subjecting nearly 60 specimens to reverse bending in proper stress orientation at various stress levels until a predetermined number of cycles was achieved or fracture occurred. To accelerate the testing, an oscillating driver was used for cycle accumulation, with a quartz load cell and accelerometer used to determine load and displacement. The test setup is shown in Figure 4. Some development was required to arrive at a satisfactory means of holding the specimen so as not introduce uncharacteristic end restraints on the test specimens. Mechanical schematics of the initial and final test configurations are shown in Figure 5. The initial configuration introduced a nonrepeatable clamping arrangement, making data correlation impossible. The final configuration schematic (in Figure 5) shows how the test specimens were ultimately configured to compensate for fixture deficiencies. By removing a portion of the flexure, its stiffness was reduced by an order of magnitude, permitting higher induced stresses at a lower amplitudes and higher frequencies, permitting collection of a greater number of data points in a given amount of time.

279
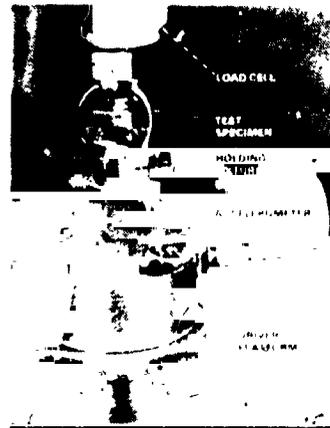
Figure 4. Fatigue Test Setup
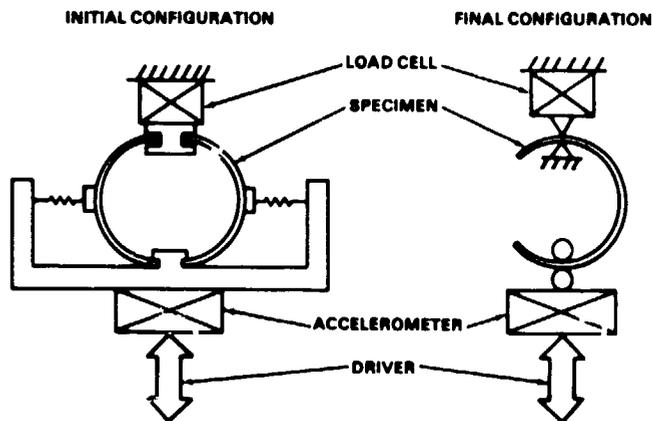
Figure 5. Fatigue Test Mechanical Schematic

Once the fixturization had been established, an S/N plot was generated. The specimens were subjected to various heat-treat schedules and plating-thickness matrices. The results are shown in Figure 2. To date, not one in over 400 properly designed flexures has experienced a fatigue failure, even though some have undergone more than 35 million reverse bending cycles.

In addition to preferential grain orientation, cold-rolled stock has properties that vary with distance from the surface; i.e., the percentage of grain area reduction (or cold working) decreases with the distance from the surface (Ref 1). Since mechanical properties improve with the amount of cold work, the nearer the material is to the surface, the higher are its mechanical properties. Therefore, flexures are made from rod stock that is nearest the finished diameter of the flexure.

Interface Geometry and Fabrication

The roll-ring design must assure dynamic stability of the flexure(s) while running in, and captured by, the ring grooves. The stability of the flexure relates to its inherent ability to remain aligned in the grooves during rotation. In general, the stability diminishes as the annulus width (R_0-R_I) approaches the sum of the ring contact groove radii (R_G), as shown in Figure 6, or:

$$\frac{2\,R_G}{(R_0 - R_I)} < 1$$
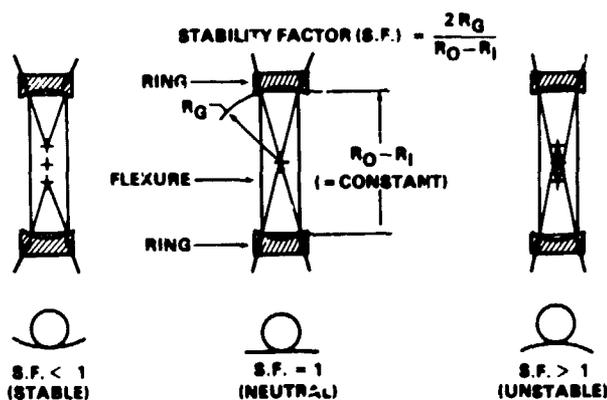
Figure 6. Stability Factor of Flexure/Ring Interface

Today's test units have a stability factor of approximately 0.22, which provides excellent operational stability.

The conformity of the interface is a definition of the degree to which the radiussed edges of the flexure (r_f) nest in the ring groove radius (R_G). This geometry is similar to a ball bearing. It is important for the roll ring, not only for its effect on contact stress, but for its influence on contact resistance as well. As r_f approaches R_G, the conformity approaches 100 percent, at which the contact stress is a minimum because of maximized contact area. This also yields minimum contact resistance.

The flexure began as a pure rectangular section. However, the resultant excessive contact stresses promoted premature wear-through of the gold-plated interface. The second generation incorporated chamfered corners which, although easy to fabricate, resulted in inconsistent interfaces. At this point, radii were applied to the flexure corners with close tolerance controls on their center locations.

Initial efforts to apply the radius on a lathe were unsuccessful because it was difficult to locate the radius centers by hand. Therefore, blanks with rectangular sections were made and the radii added in a different setup with a form tool. Special tooling had to be developed that could hold the blank without runout or distortion. This process proved acceptable, but tended to be operator-sensitive and could only provide parts with the surface finish and accuracy of the form tool. Also, because of tolerance sensitivity, the conformity could be reliably maintained at about only 50 percent.

The final solution, in standard practice today, was to manufacture the flexures on a numerically controlled lathe with very low feed rates, large cutter diameters, and empirically determined cutting sequences – resulting in surface finishes of less than 0.2 micrometer. The accuracy and repeatability of numerically controlled machinery provide a reliable means of producing, in today's designs, conformities in excess of 90 percent.

Conductor Plating

Several different plating materials and combinations of materials on contact rings and flexures have been evaluated from the standpoint of electrical noise and wear.

Most of the plating configurations studied are variations on a nickel and gold matrix on both contact rings and flexures. In almost all cases a copper flash is plated onto the substrate (brass for rings and beryllium copper for flexures) for adhesion purposes. This is then overplated with 2.5 to 4.0 microns (100 to 150 microinches) of a sulfamate nickel as a copper migration barrier and as a hard underlayment for the gold to follow. The nickel is then overplated with the same thickness of either a hard alloy gold or a soft pure gold. Gold was selected for its excellent electrical properties and corrosion resistance.

Ion plated and electroplated rhodium configurations were also evaluated with very little success. Rhodium is a strong catalyst for the formation of polymers in the presence of organics. Since it is difficult to eliminate all sources of organic contamination, particularly in a vacuum environment, it was concluded that rhodium was an inherently poor choice as a roll ring conductive overplate. This was demonstrated by exceptionally poor electrical performance, although wear resistance was excellent because of its exceptional hardness.

It was thought that by plating very thick (25 microns or 1000 micro-inches) layers of gold onto the rings and the flexures, the contact area could be maximized by allowing the flexure and rings to mold themselves into each other. The gold used (Sel-Rex BDT-200) turned out to be too hard to permit adequate mating, and the excessive thickness resulted in unacceptably high flexure bending stresses.

One source of flexure fatigue in early testing was thought to be residual stresses in the nickel layer. Some flexures were, therefore, plated without nickel. This theory proved incorrect. However, without the nickel as a migration barrier, the circuits developed excessive electrical noise, thought to be due to metal oxides on the surface.

Thick copper plating beneath the nickel was tried in an attempt to improve the "imbedibility" of random contact anomalies. No disposition was arrived at, but difficulties in plating such thick layers of copper prompted abandoning that approach.

Nominal plating thicknesses of pure soft gold on both flexures and rings seemed suitable to provide low noise, but wear was marginal for long-life applications (one million revolutions) because of the high ductility of pure gold. The gold in the contact zones of the rings and flexures would be partially displaced, and some of these gold extrusions would sometimes break loose, forming conductive debris. Although some debris was generated, it amounted to 2 or 3 orders of magnitude less volume than that found in a slip ring assembly with even a fraction of the travel. As flexure fabrication techniques and conformity improved, the tendency for extrusion was reduced - particularly with the lower stress, lower preload flexure designs. Today's configurations generate virtu lly no debris, even for very-long-life applications.

A noise mechanism was hypothesized that correlated high friction to electrical noise. It was also reported that increased hardness reduces friction (Ref 2). Therefore a matrix using hard-gold-plated rings and soft-gold-plated flexures was tried. This configuration resulted in improved wear because of less extruding, but no significant noise improvement was detected.

The last and most recent configuration under study is hard-gold flexures on hard-gold rings. The wear is practically nonexistent, but the contact resistance tends to be somewhat higher because of the reduced contact area and higher resistivity of the hard-gold alloy.

The present status indicates that several of the nickel-plus-gold configurations may be adequate for most applications if appropriate preloads and conformities, which are now routine, can be maintained. The configurations to avoid are those that create high bending stresses in the flexure (plating thickness in excess of 25 microns (1000 microinches)), those that use catalytic materials for polymer formation (rhodium, platinum, palladium, etc.), and those that allow metal oxides to form (plating that is too thin to prevent wear-through, is subject to porosity, or has a migration barrier eliminated).

The question arose of cold-welding of a gold-on-gold interface. Since the friction coefficients of most metallics increase in vacuum, the frictional forces of sliding members also increase to the point that friction-welding can occur under certain conditions (Ref 3). Another welding phenomenon is associated with the molecular adhesion of ultraclean, highly stressed interfaces under very special laboratory conditions (Ref 4).

283

Thousands of hours of vacuum tests of the roll ring under simulated application configurations for static, dynamic, and dither modes of operation have not shown any tendencies toward cold-welding. This fact is attributed to the mainly rolling interface, the gold contact materials, the contact stress level, and the nonsputter-cleaned surfaces. This determination is made on the basis of both visual and elemental evaluations of post-test items using SEM/EDXA procedures.

DEVELOPMENT OF 200-AMP DESIGN

In 1979 an application requiring a 60-amp capability for a single circuit launched the development of the high-current/high-power design presently under intense investigation. This configuration incorporates a full complement of flexures in the annulus space of a single circuit to handle the increased current loads. It contains a unique idler system for maintaining angular spacing between adjacent flexures.

Multiflexure Spacing

When a high-current design was first approached, several flexures were evenly spaced in the same ring set to distribute the current load among them, the number of flexures governed by the current capacity requirements. During rotation, however, tolerance variations allowed the flexures to move circumferentially with respect to one another so that two or more flexures eventually came into contact, resulting in unmitigated sliding at the line of contact. Flexure damage occurred as a result of the high sliding friction coefficient.

The idler concept emerged as the means to maintain circumferential spacing without sliding. These idlers are guided by the flexures, and roll on a set of rails that are mechanically attached to the inner ring assembly. A unique set of roller diameters exists for every set of flexure and ring diameters. These are analytically determined by matching instantaneous velocity vectors of the flexures and rollers at points of mutual contact. Figure 7 identifies the graphic representation of these various velocity vectors.

Mechanical and Electrical Isolation

Although a high degree of mechanical isolation exists in the 15-amp design due to the insulator geometry (shown in Figure 1A), the mechanical isolation is taken a step further for the multiflexure, high-current designs. These are also being designed to withstand voltage potentials near 500 volts in order to obtain power transfer capacities on the order of 100 kilowatts. This is accomplished by selecting appropriate materials and geometry, as well as preventing line of sight between conductive surfaces or materials.
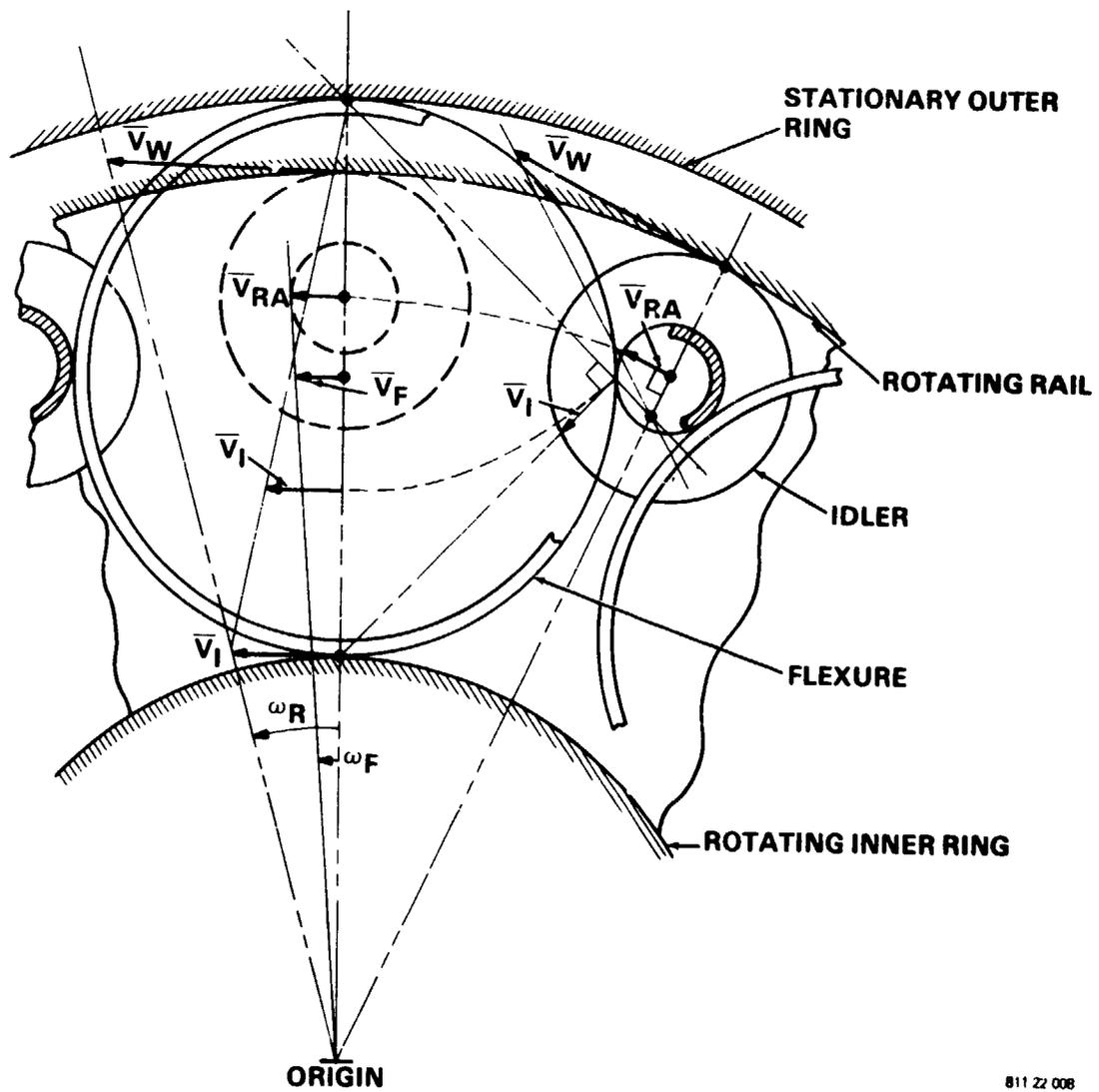
Figure 7. Vector Definition for Flexure/Idler Velocity Match

285

The primary concern when designing high-voltage systems is electrical breakdown, which manifests itself as corona or arcing. Although 500 volts, by most power standards, is not considered particularly high voltage, it is still above the minimum spark voltage of 240 volts RMS and requires special attention.

Corona is not a critical concern since all applications studied to date operate in a vacuum environment, and a gaseous ambient is required to support corona. Therefore, by providing adequate ventilation of the module, the internal pressure can be maintained below the regime required to sustain corona - especially if system voltages are kept down to 500 volts or lower.

However, since some ground testing invariably occurs at atmospheric pressure, the use of overlapping barriers to prevent line of sight provides labyrinths that result in relatively large air gaps. These labyrinths are included primarily to inhibit arcing (by providing a torturous path for an arc), as well as to keep out external debris.

To inhibit arc susceptibility, a dual insulator system is used between adjacent conductors. The primary insulation consists of a glass-filled resin that has a high dielectric strength (15.6 V/ m, 400 V/mil). This is used for axial as well as radial insulation. The secondary insulation is provided by teflon-impregnated, hard anodized aluminum. The teflon impregnation tends to fill the pores typically present in a hard anodized coating, resulting in a very reliable insulator.

The teflon-filled coating (designated Hardtuf by the supplier, Tiodize Co, Inc.) produces a very low friction surface for structural parts, which permits smoother assembly of close-fitting components.

Thermal Considerations

When transferring high power (10 to 100 kilowatts), a prominent operating parameter of the system is transfer efficiency. The transfer efficiency (e_T) is defined as the percentage of power transferred through the rotating interface without thermal loss and is given by

$$e_T = \frac{EI - I^2R}{EI} = \frac{E - IR}{E}$$

where   E = source voltage, volts
        I = system current, amps
        R = circuit resistance, ohms

Given a circuit with fixed current and supply voltage, the designer may maximize the transfer efficiency by minimizing the circuit resistance. In the case of a roll ring, this is accomplished by increasing the number of parallel contacts, or flexures, in a given circuit. The measured circuit resistance of the most recent, 10-flexure configuration is approximately 0.38 milliohm under current load. The circuit resistance is about 20 percent higher during a low-current, four-wire measurement because of film effects. Therefore, the transfer efficiency under 500-volt, 200-amp condition is

$$e_T = \frac{500 - 200 \times .00038}{500} \times 100\% = 99.985\%$$

However, even with transfer efficiencies this high, thermal losses are generated because of the finite circuit resistance. At maximum current, the development module generates approximately 15 watts per circuit; so that, being an 8-circuit assembly, it converts 120 watts of power to thermal energy which must be managed.

Since this device operates in a vacuum, the primary modes of heat transfer are conduction and radiation. Therefore, geometries were selected to maximize the contact area of adjacent components, and materials with high heat-transfer coefficients were used for fabrication.

Besides providing secondary insulation, the hard anodized aluminum rails provide an axial heat conduction path for the thermal energy in the rings as well as a radial path for the roller/rail heat-transfer interface. The roller, in turn, is acting as a partial sink for the flexures.

Although the test setup was not configured to model the radiation mode of heat transfer seen in flight operation, the hard anodized housings provide high-emissivity surfaces to act as radiators should a receiver be present.

In an effort to predict the temperature profile of a unit in operation, a thermal model is being developed and the thermal resistances are being determined empirically. Several interface resistances must be determined empirically because very little literature exists on the interface characteristics of various material combinations. Because of the symmetric nature of the plan view of a multiflexure circuit, a lumped analytical approach is used (i.e., the characteristics of all 10 flexures can be thermally equated to a single flexure with appropriate coefficients).

In the model, only the current-carrying components are considered active, heat-generating components: those consisting of the contact rings, connecting bolts, flexures, and their contacts. Since the contact resistance of this particular gold-on-gold interface can be directly measured and the materials used are well documented, the Q (rate of heat generation) and K (thermal conductivity) terms can easily be determined. However, hundreds of empirical measurements are necessary to determine the remaining terms. At the writing of this paper, this work is still in progress.

287

ELECTRICAL NOISE

Electrical noise is defined as resistance transients of the electrical interface that occur during operation. This is distinguished from steady state resistance, which is a function of the material properties and remains constant. Several applications, however, can tolerate various levels of electrical noise - characterized by amplitude, duration, wave shape, and frequency of occurrence.

During the course of several years of investigation, a variety of mechanisms that may or may not cause electrical noise have been theorized and proven or disproven. Several of these studies and conclusions are included here for the benefit of the reader. It should be pointed out that, although these mechanisms may behave as described herein for a roll ring - which uses conformal rolling interfaces - they may behave differently when applied to conceptually different devices.

Organic Films

It is believed that, for a roll ring, the presence of an organic film does not cause electrical noise under most conditions. Indeed, the presence of a large quantity, as in an oil film, actually benefits the electrical performance for signal current levels. Though organics are by nature primarily nonconductive, their viscous properties permit a flexure with sufficient mechanical preload to make electrical contact-either by complete displacement of the film or by partial displacement to a thickness that will permit conduction by tunneling.

There are exceptions, however. In the presence of large quantities of a viscous organic, experience has shown that currents exceeding 3 amps may cause breakdown of the organic into less viscous insulators that will not permit efficient conduction. Also, viscous films result in hydroplaning of the contact at elevated rotational rates. The speed at which transition occurs is a function of both flexure preload and film viscosity. These results were compiled during testing of contacts intentionally lubricated with a variety of lubricants.

Stick Slip

It was suggested that the high friction coefficient of gold-on-gold in vacuum was permitting the flexure to edge up the ring groove until some surface anomaly initiated a "skid" back into the bottom of the ring groove. During the "skid" the contact surfaces were thought to separate elastohydrodynamically. After much study and investigation, it is felt that this is a very improbable mechanism.

First, a stick-slip mechanism implies a fairly random nature with unpredictable periods. However, whenever a roll-ring circuit is experiencing resistance transients, it can almost always be traced to the defect period of an outer ring, inner ring, flexure, or combination thereof.

Second, stick slip is a dynamic condition that can occur only during actual rotation or oscillation. However, it is sometimes possible to "park" on an area of increased resistance.

Third, there has been no visible physical evidence of such an action. Gold, being exceptionally malleable, would leave some sort of a ransverse scratch in the gold that has never been seen. The only noncircumferential markings that have been observed on the rings are epicyclic swirls associated witn the entry and exit paths cf the flexure contact across the footprint's finite width.

Fourth, stick slip is by nature a very rapid event that would have a distinct repeatable time-history wave shape. Roll-ring noise tends to be randomly shaped and of various durations despite its often periodic nature.

Preload

Experience has shown that there is very little correlation between flexure preload and electrical noise. Preloads as low as 0.09 newton (0.02 lbf) and as high as 2.0 newtons (0.45 lbf) have yielded low noise performance. The preload does have a small effect on dc contact resistance, which is to be expected since a higher preload establishes a larger footprint and hence lower resistance. Finite deflection and therefore finite preload is necessary, however, to ensure running stability. Typical 15-amp flexures today have preloads of 0.22 to 0.36 newton (0.05 to 0.08 lbf) and deflections around 0.6 mm (0.025 in.).

Polymers

As mentioned earlier, the only instances that nonconductive polymers were encountered were when rhodium was used as part of the plating matrix. It was discovered during testing that rhodium is a very good catalyst for polymer formation for a roll ring in the presence of organic films or vapors. Since organic vapors are habitually present in vacuum systems because of the outgassing of several materials, polymers did form on the roll ring and poor electrical performance resulted. However, to date, no indications of polymers have been detected when a gold-on-gold system has been used.

Silicon

A high correlation was found between the presence of silicon in the system and resultant electrical noise. Although the exact form of the nonconductive film containing silicon was never identified, several sources of silicon contamination were eliminated from the test system, resulting in greatly improved electrical performance. The primary source of silicon contamination was the result of operating fixture drive motors with silicon-grease-lubricated gear-heads in the vacuum chamber with the circuits under test.

Metallic Oxides

Recently, a correlation between electrical noise and codeposited copper in the gold has been established. Copper is a very active metal that oxidizes readily and has a tendency to migrate (Ref 5). That is why a nickel migration barrier is generally included in most gold-plating matrices.

Most gold-plated electrical contacts can tolerate a small level of copper in the gold because they quite often have wiping actions that scrape away any oxide layers before making contact. This may explain why small amounts of active metal contamination would not alarm a plating vendor. However, the roll ring does not have an aggressive wiping action and is therefore more sensitive to the presence of oxide films on the contact surface. Once this is known by the plater, it is a relatively simple matter to control the active metal contaminants and so reduce or eliminate the presence of metallic oxide films.

Surface analysis techniques have been, and are, invaluable tools for investigating resistive films. The Scanning Electron Microscope (SEM) has provided a great deal of visual support and some help in identifying bulk materials on the contact surface through Energy Dispersive X-ray Analysis (EDXA). However, the electron beam has a finite penetration that does not permit analysis of very thin surface films. To examine very thin surface films (0 to 100 Angstroms), Electron Spectroscopy for Chemical Analysis (ESCA) is used. ESCA is the only surface analytical technique that provides direct information on the chemical (as well as elemental) nature of the atoms in an unknown sample (Ref 6). For three-dimensional mapping of various elements in a sample, Auger Electron Spectroscopy (AES)N is used in conjunction with sputter etching. ESCA demonstrated the presence of copper on the surface, while AES determined that it was codeposited with the gold rather than a result of migration or a surface condition only.

SUMMARY

A great deal of development has been completed, and is in progress, relative to a rolling electrical contact device that is uniquely suited for signal/power transfer in present and future space applications. Several technology areas had to be enlarged, resulting in new knowledge in a variety of areas. This virgin technology has provided two configurations of the roll-ring mechanism that demonstrate not only a very low torque capability but reduced resistivity and a high voltage capability as well.

A design and performance summary of the two configurations is given in the listing below:

ROLL-RING DESIGN SUMMARY

Parameter	Single Flexure	Multiflexure
Current Capacity	15 amp	200 amp
DC Circuit Resistance	10 milliohms	0.4 to 0.5 milliohm
Peak Electrical Noise	50 milliohm goal[a]	3 milliohms
Life	10^7 revs (proven)	10^7 revs (theoretical)
Torque per Circuit	1.4×10^{-4} N-M	3.5×10^{-3} N-M (10 flexures)
Weight per Circuit	35 grams	900 grams
Transfer Efficiency	99.50% (15 A, 30 V)	99.985% (200 A, 500 V)

REFERENCES

1. Spotts, M. F. 1971. Design of Machine Elements, 4th ed. Englewood Cliffs, NJ: Prentice-Hall, Inc.

2. Antler, M. March 1974. Wear of Gold Plate: Effect of Surface Films and Polymer Codeposits. Trans IEEE, Vol PHP-10, No. 1.

3. Cuthrell, R. E., and D. W. Tipping. May 1973. Factors That Affect the Solid-Phase Bonding of Gold Wire Electrical Leads. Sandia Laboratories Report SLA-73-0535.

4. Cuthrell, R. E., and D. W. Tipping. December 1972. Electric Contacts: Equipment and Mechanics of Closure for Gold Contacts. Sandia Laboratories Research Report No. SC-RR-72-0783.

5. Antler, M. March 1973. Tribological Properties of Gold for Electric Contacts. Trans IEEE, Vol PHP-9, No. 1.

6. Evans, Charles A., Jr., and Richard J. Blattner. 1978. Modern Experimental Methods for Surface and Thin-Film Chemical Analysis. Annual Reviews Inc, p. 199.

7. Patent No. 4,372,633. 8 February 1983. High Current Transfer Roll Ring Assembly.

---

[a]Development in this area, although converging rapidly, is not yet complete. Therefore, a definitive value for peak electrical noise is difficult to reference.

A DUAL, FAULT-TOLERANT AEROSPACE ACTUATOR

Clete J. Siebert*

ABSTRACT

The requirements for mechanisms used in the Space Transportation System (STS) are to provide dual fault tolerance, and if the payload equipment violates the Shuttle bay door envelope, these deployment/restow mechanisms must have independent primary and backup features. This paper describes the research and development of an electromechanical actuator that meets these requirements and will be used on the Transfer Orbit Stage (TOS) program.

INTRODUCTION

This deployment/restow mechanism will be used to perform three separate functions on the TOS program:

o   Provide power to latch and unlatch the upper half of the forward Airborne Support Equipment (ASE) cradle.

o   Provide power to open and close the upper half of the forward ASE cradle.

o   Tilt the TOS/spacecraft (TOS/SC) combination for separation from the Shuttle and restow the aft ASE cradle for landing.

The Shuttle/TOS on-orbit configuration is illustrated in Figure 1.

REQUIREMENTS

The requirements imposed on the actuator mechanism to perform the required functions are summarized as follows:

Safety Requirements (in accordance with NHB 1700.7A)

o   Independent primary and backup actuator functions are mandatory.

o   Combination of primary and backup methods must be two-failure tolerant.

*Martin Marietta Aerospace, Denver, Colorado

Operational Requirements

o   Provide power to latch and unlatch the forward cradle halves.

o   Provide power to open and close the upper half of the forward cradle 112° ±5°.

o   Erect the TOS/SC combination 45° ±5° for separation.

o   Provide erection capability under active Vernier Reaction Control System (VRCS) or free-drift conditions the Primary Reaction Control System, (PRCS) and Orbiter Maneuvering System (OMS) are inhibited during rotation.

o   Provide capability to react VRCS and PRCS when TOS/SC is in the erected position.

o   Provide multiple erection/restow cycle capability for each mission; restow capability for an abortive mission is mandatory.

o   Provide performance for 80 orbiter missions over 10 years.

System Requirments

o   Unlatch or latch forward cradle in less than 4 minutes.

o   Raise or lower forward cradle half 112° in less than 2 minutes.

o   Erect or restow TOS/SC 45° in less than 2 minutes.

o   Withstand all deployment and landing loads (each actuator). These loads to be reacted through the actuator structure and lock gears.

o   Not to exceed 310 N (70 lb) per actuator.

o   Operate at temperatures from -28°C to +59°C (-15°F to +140°F).

o   Provide redundant limit switches, solenoids, DC power and avionics.

o   Provide (one motor/clutch combination) sufficient torque under worst-case conditions to perform required function.

o   Provide force margins of 100% at worst-case conditions for all actuators.

CONCEPT DEVELOPMENT

During the design trade-off phase, several priorities were established as design goals. These were

o   Satisfy all safety requirements of NHB 1700-7A without any waiver requests.

o   Use minimal design complexity and manufacturing simplicity.

o   Use previously qualified space hardware and components.

o   Provide a common design capable of a broad range of torque output forces with minimal configuration changes.

o   Combine additional mechanism functions within the actuator to eliminate additional separate mechanisms.

HARDWARE CONFIGURATION

Each actuator, as illustrated in Figure 2 consists of the following major components:

o   Structural housing containing the ball screw and nut assembly, reduction gear train, and attachment clevis ends.

o   Redundant DC gearhead motors.

o   Redundant DC solenoid-type, positive-engagement clutches.

o   Spring-loaded drive-engagement pin and pyrotechnic disengage.

o   Redundant position-indication potentiometers.

o   Redundant solenoid-powered lock gears.

o   Redundant microswitches for lock-gear and actuator-engagement-pin indication.

ACTUATOR FEATURES

Most actuator systems presently being used on the STS are physically separated from the structure in the event of primary actuator failure, thus allowing the backup actuator to be used. These systems require separate swingaway, catch, and latch mechanisms. The Martin Marietta actuator is self-contained in the event of primary actuator disengagement. This is possible since the actuator selector drive pin with its pyro release is contained within the actuator. The disengaged primary actuator simply becomes a free-sliding, telescoping tube assembly.

Additionally, the actuator has been designed to withstand the orbiter launch and landing loads, the TOS/SC deployment loads, and the orbiter maneuvering loads. This design feature eliminated the requirement for a separate landing lock mechanism and a deployment lock mechanism.

Rate control is normally used with actuators to control the output speed and prevent excessive slew rates to the payload being raised for deployment. This closed-loop, complex electronic control is required on rotary actuator systems and some existing screw-drive systems to prevent a possible runaway condition.

In the Martin Marietta actuator, this rate controller can be eliminated because drive motor gearhead reduction limits the maximum RPM. Maximum screw extension/retraction rates cannot exceed the free running speed of the drive motor as reduced through the reduction gear train and drive nut.

The maximum impact force when erecting the TOS/SC is less than 33.9 N-m (25 lb ft.). This low impact force allows the use of a simple structural hard stop, rather than a viscous damper.

The actuator motor shutoff is accomplished by use of a redundant motor current limiting circuit. The structure being deployed, or stowed, contacts a structural hard stop, thus increasing motor current demand, and motor shutoff occurs.

This method allows the required 100% force margin at worst-case conditions, while preventing structural overloads under best-case conditions. Additionally, the clutch assembly can be adjusted to slip at a predetermined torque, also preventing an accidental overload condition. Position indication to the crew is accomplished by the use of redundant rotary potentiometers that provide actuator extension/retraction data.

Since the actuator mechanism is a back-driveable device, a locking mechanism must be incorporated. A redundant, solenoid-operated, dual-gear, mesh lock has been selected for this design. A similar design has previously been used on the Inertial Upper Stage (IUS) program.

DISCUSSION

This actuator mechanism meets all the STS safety requirements as defined in NHB 1700.7A, and also meets the structural, life, and TOS mission requirements for the following reasons:

o   The orbiter crew can use the Standard Switch Panel (SSP) at any point in the actuation cycle to stop, restart, and disengage the primary actuator, and engage the backup actuator. This allows for complete restow of the TOS/SC in case of a mission abort.

o   Force margins are at least 100% greater than the required torques at worst-case conditions (Figures 3A, B and C).

o   Each pair of actuators, primary and backup, has triple electrical
    redundancy and complete mechanical redundancy.

o   All rolling-element bearings are sized to exceed the L10 life by a
    minimum factor of 17.

o   Each actuator is capable of greater than 1000 duty cycles during its
    operating life, which far exceeds the 80 mission requirement.

o   Clutches are designed for positive power-off disengagement using
    redundant, captive compression springs.

o   The structural ultimate factor of safety is 1.4 minimum. Gear
    stress levels are less than one-fourth of the material ultimate
    stresses.

o   Lubrication is a combination of wet and dry lubricants. All sliding
    surfaces are treated with space-qualified dry lubricants; however,
    they are designed to function without lubrication. All bearings,
    gears, and ball screw are lubricated with Bray Oil 3L-38RP, a
    qualified vacuum-stable grease.

o   The static load capability of the actuator is 8000 lb.

o   The actuator design can be easily modified to meet a variety of
    force and extension/retraction rate requirements (Table 1).

CONCLUSION

The actuator design selected for use on the TOS program meets the
requirements for STS safety requirements. This design has successfully
passed the NASA Phase I Safety Review without receiving any mechanical Review
Item Discrepancies, nor were any safety waivers required. The design studies
and tradeoff analysis resulted in a multifunction, simple mechanism that is
easily adaptable to various output torque requirements and
extension/retraction cycle times.

SHUTTLE/TOS CONFIGURATION

FIGURE 1

ELECTROMECHANICAL DRIVE ACTUATOR
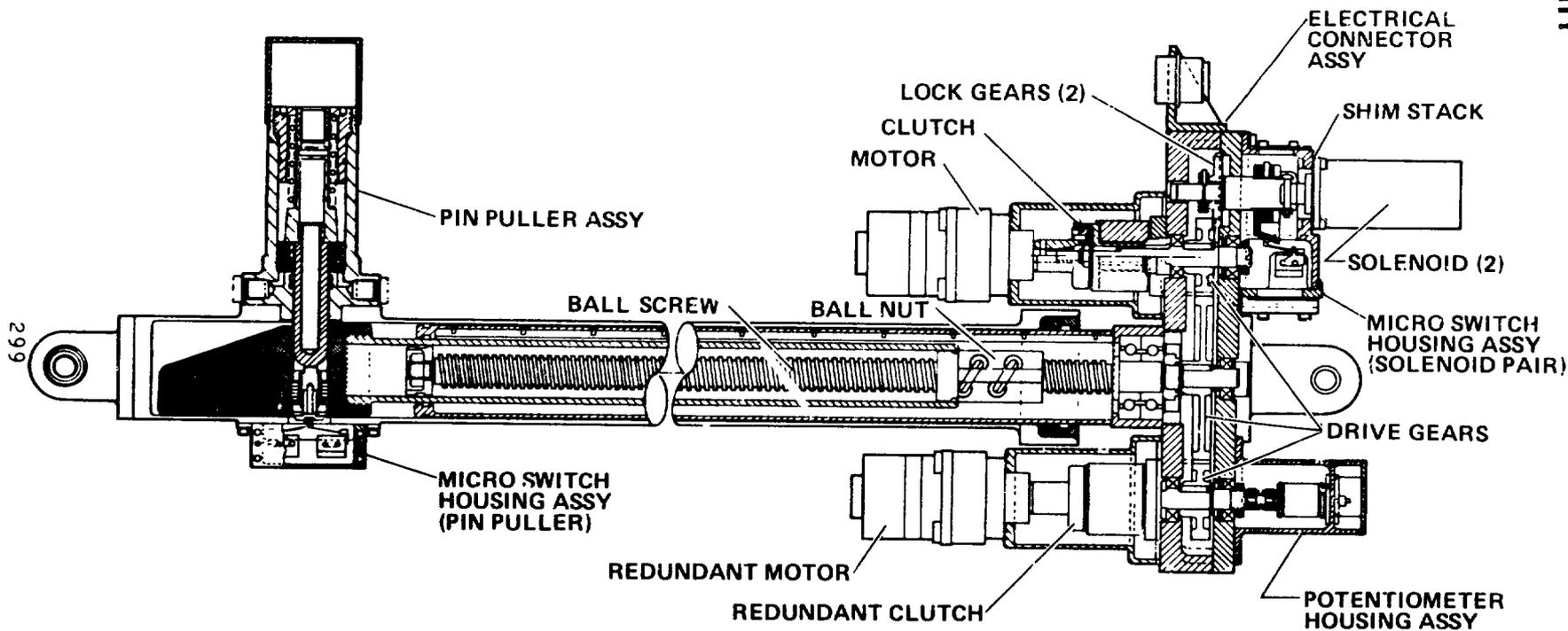
FIGURE 2

FIGURE 3A

UPPER FORWARD CRADLE HINGE TORQUE MARGINS
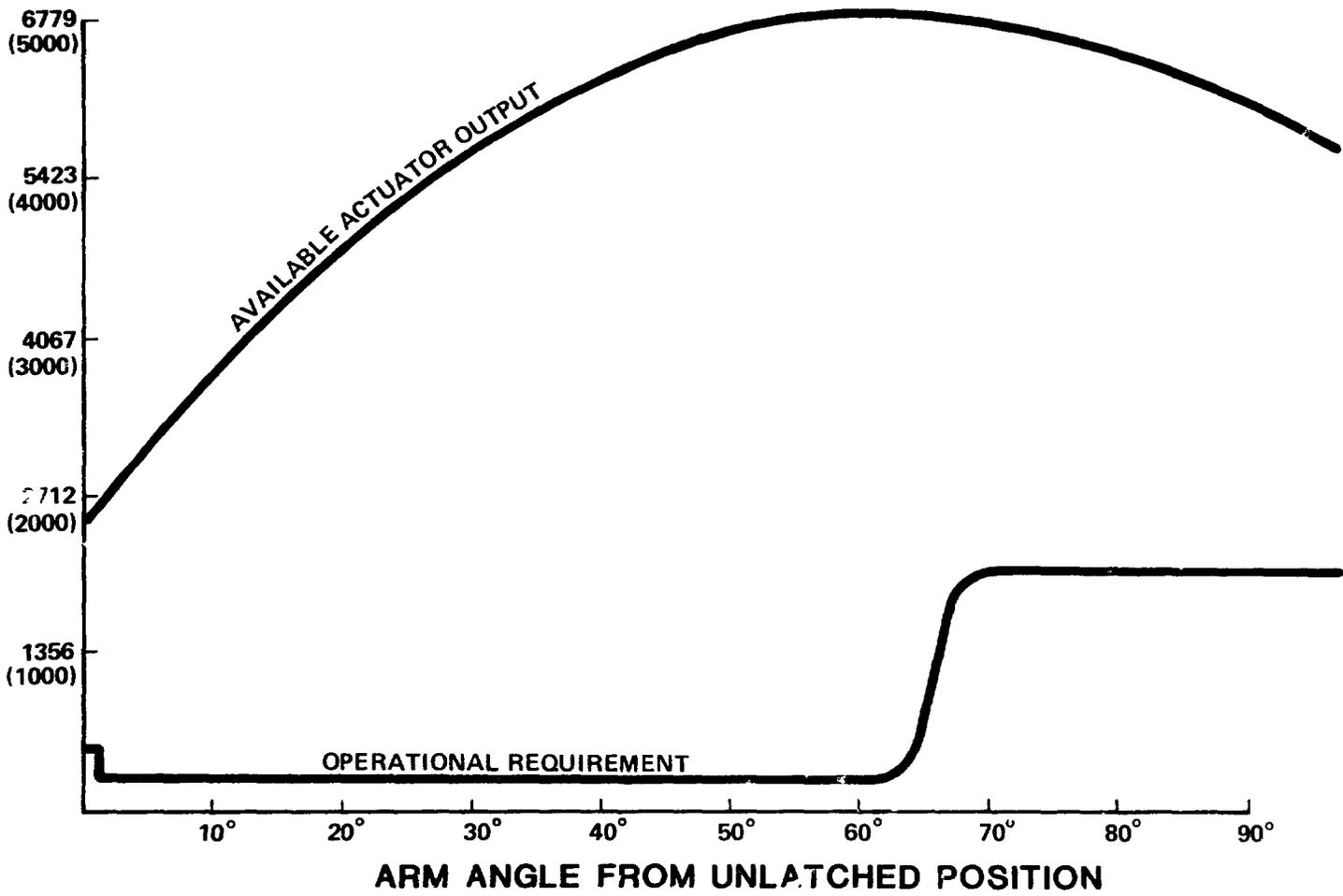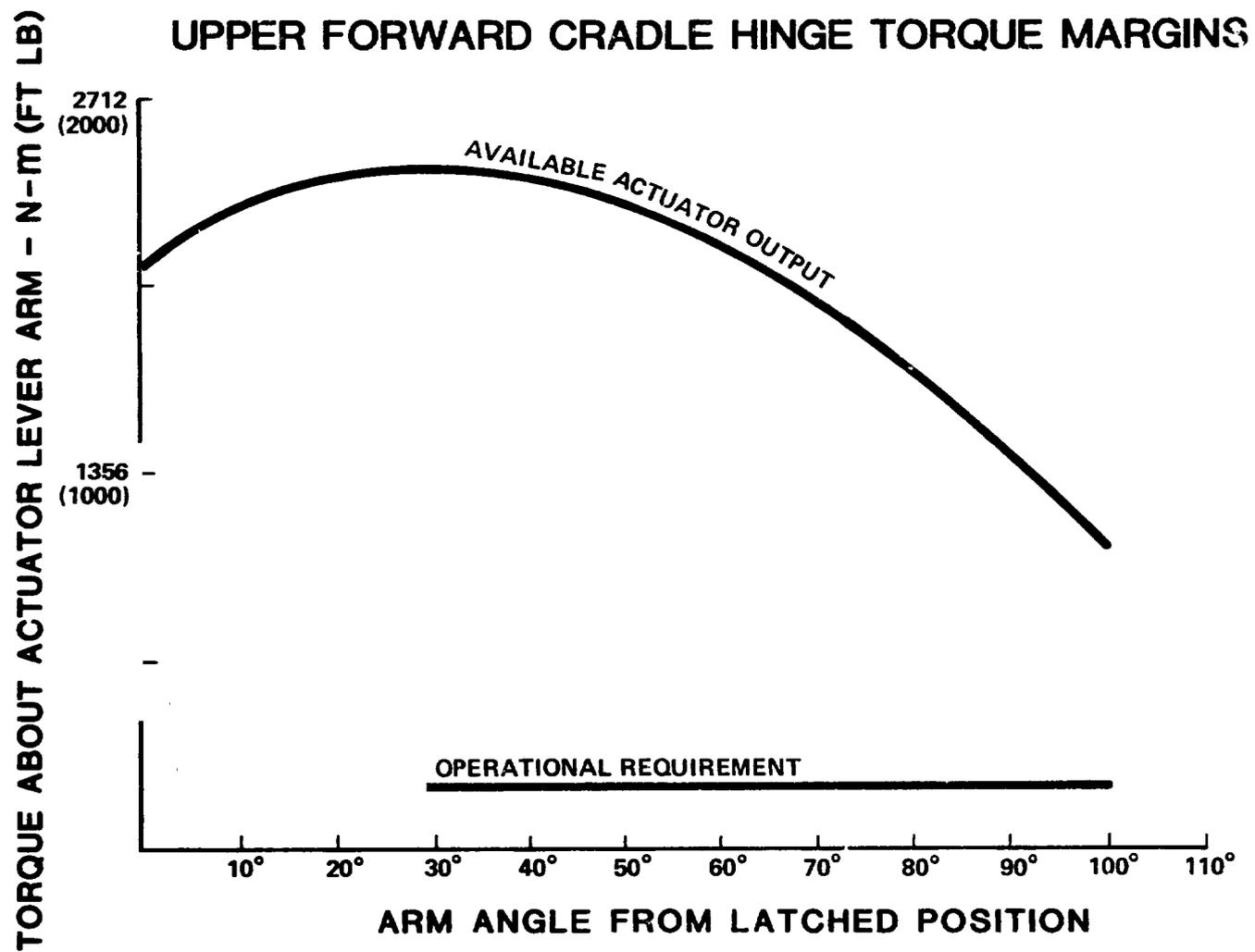
FIGURE 3B
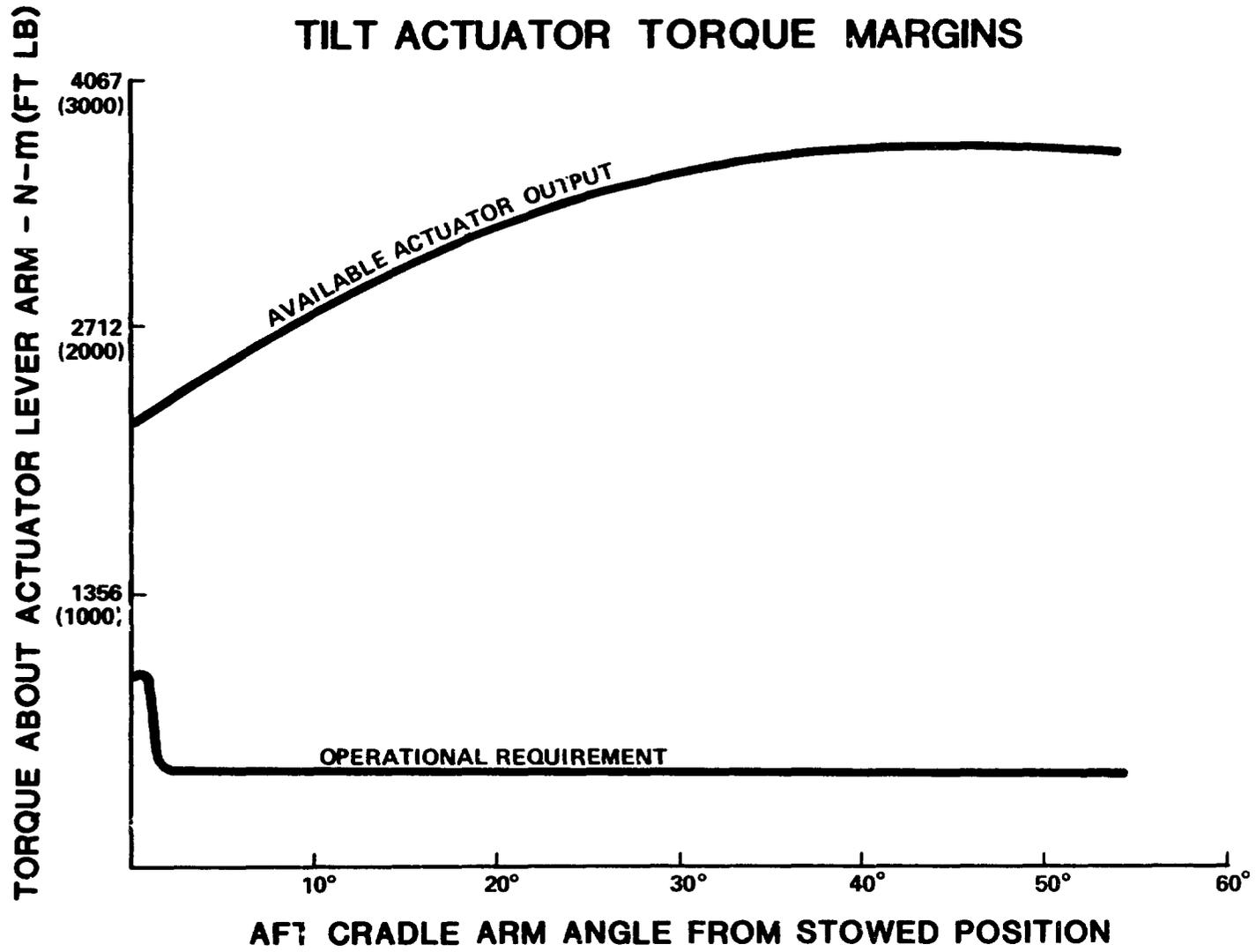
FIGURE 3C

TABLE 1

ACTUATOR CAPABILITIES

	LATCH ACTUATOR	TILT ACTUATORS
MAXIMUM FORCE BEFORE STALL	48930 N (11,000 LBF)	15569 N (3,500 LBF)
AVAILABLE FORCE (CURRENT LIMITED)	17793 N (4,000 LBF)	10053 N (2,262 LBF)
MAXIMUM EXTENSION/RETRACTION RATE. NO LOAD	2.54 mm/SEC (0.10 IN. /SEC)	3.8 mm/SEC (0.15 IN.SEC)
AVAILABLE STROKE	432 mm (17 IN.)	432 mm (17 IN.)
STATIC LOAD CAPABILITY	35586 N (8,000 LBS)	35586 N (8,000 LBS)

DESIGN OF A DUAL FAULT TOLERANT
SPACE SHUTTLE PAYLOAD DEPLOYMENT ACTUATOR

DUANE R. TESKE*

ABSTRACT

As the Shuttle Transportation System (STS) becomes operational, the number and variety of payloads will increase. The need to deploy these cargo elements will require a variety of unique actuator designs, all of which will have to conform with STS safety policy.

For those missions where payload operations extend beyond the payload bay door envelope, this policy deems the prevention of door closure as a catastrophic hazard. As such, it must be controlled by independent, primary and back-up methods. The combination of these methods must be two-fault tolerant.

This paper describes the design of such an actuator. The device consists of a single linear ballscrew with two ballnuts, each ballnut forming an independent actuator using the common ballscrew. The design requirements, concept development, hardware configuration, and fault tolerance rationale are highlighted.

INTRODUCTION

An Orbiter based satellite delivery system is presently under development. Comprising an upper stage and associated airborne support structure, this system is carried "lying down" within the Orbiter bay and raised from the bay for deployment, Figure 1. As the raised element extends beyond the payload bay door envelope, failure could impede door closure and prevent safe return of the Orbiter. The actuator system thus can cause a catastrophic hazard, requiring control by independent primary and backup methods, the combination of which must be two-failure tolerant.[1]

PAYLOAD & SUPPORT STRUCTURE
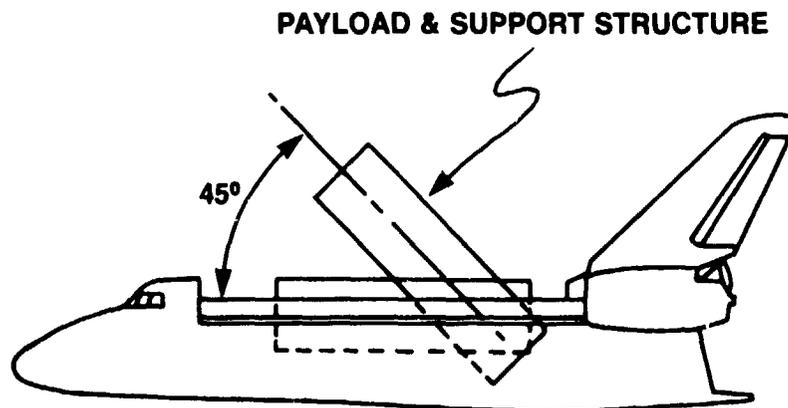
Figure 1 Payload Deployment Schematic

*Sundstrand Energy Systems, Rockford, Illinois

CONCEPT DEVELOPMENT

A survey of existing deployment systems was made to determine if any were adaptable to this application. In general, dual fault tolerant capability is achieved by using two actuators.

The shortcoming of this approach, however, is the ability of a failed actuator to lock the entire drive train, defeating the backup unit. Either extra vehicular activity (EVA) or a disconnect mechanism, such as a pyrotechnic device,pin puller or clutch is, therefore, required. However, each device adds its reliability factor to the system and increases complexity. In addition, to prevent inadvertent disconnection of the healthy unit, either a method of discriminating the failed actuator must be devised,or a mechanism which allows reliable reconnection must be conceived. Similarly, a retention/stowage device for the disconnected unit is often required.

Existing systems solve this problem in various ways, but with considerable proliferation of parts. Further, such solutions usually result in a number of items or functions which cannot be allowed to fail. These "noncredible" failure items are always the subject of debate and generally increase the precision of manufacture required.

Nevertheless, in an attempt to improve existing designs, several dual actuator design studies were made. All the resulting concepts, however, offered only marginal improvement. As a result, a single actuator system which would possess the necessary fault tolerance was sought.

DESIGN DESCRIPTION

The single actuator design concept which evolved is illustrated in Figure 2. The mechanism consists of a linear ballscrew upon which are mounted two independent ballnuts. Each ballnut is enclosed in its own housing, forming, in essence, an independent actuator free to transit a portion of the ballscrew. The mounting arrangement of the actuator, Figure 3, is such that retracting the actuator raises the payload and extending the actuator lowers it.
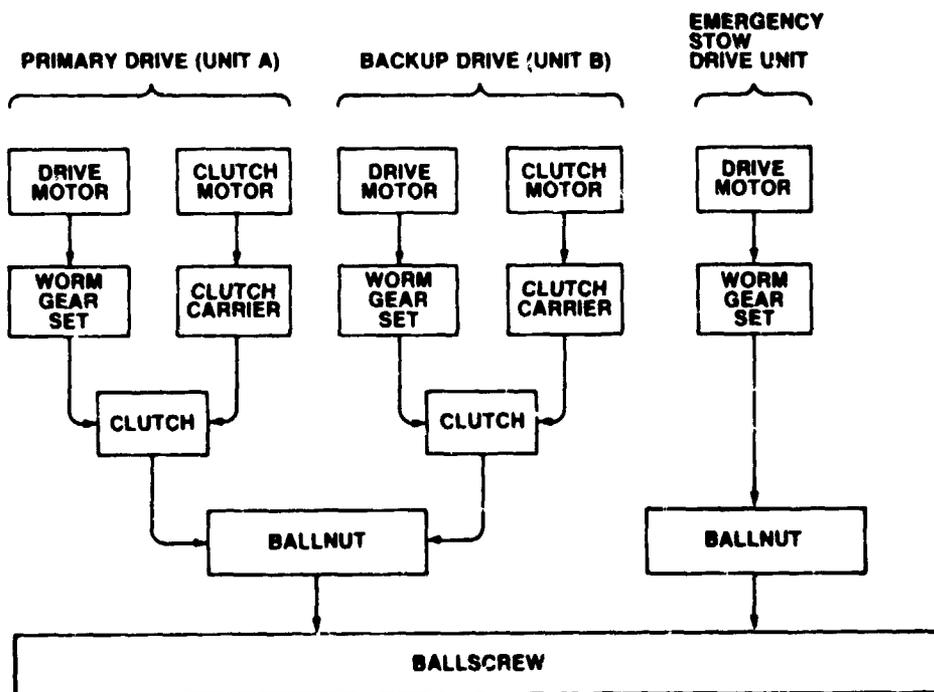
Figure 2 Actuator Block Diagram

306
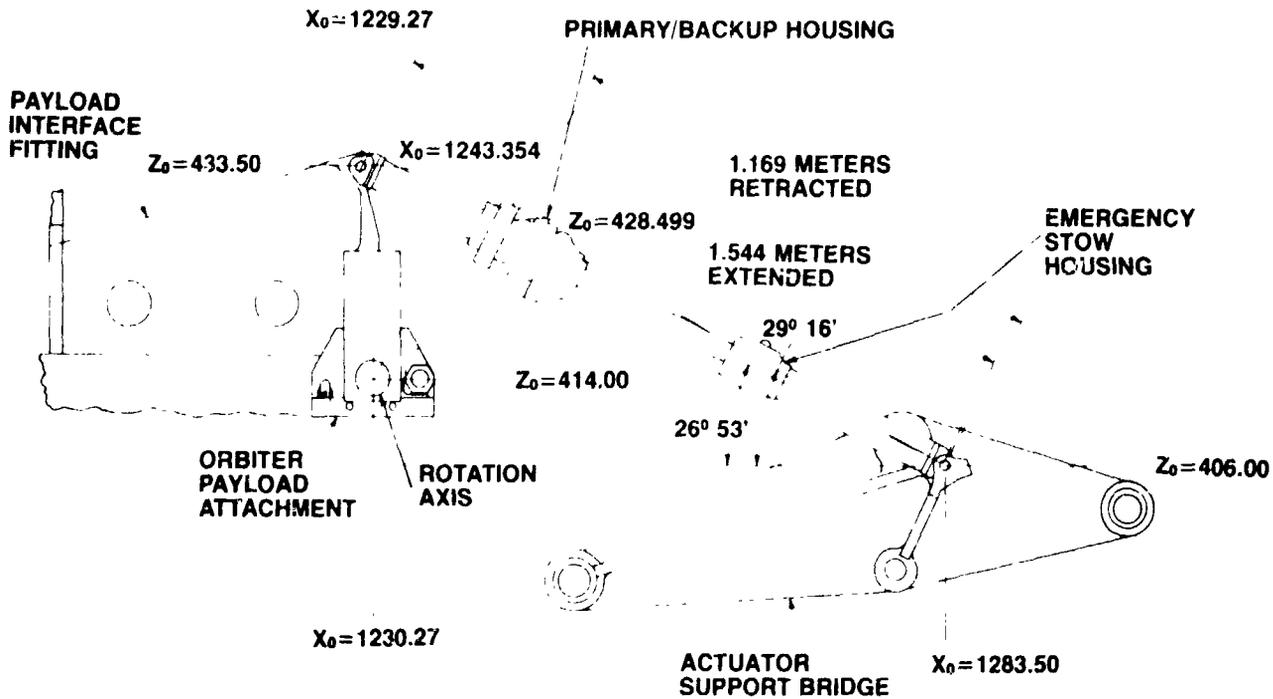
Figure 3 Actuator Installation

DuaHault tolerance is achieved by providing each actuator half with the full stroke necessary for the application. For normal operation, one ballnut is used to extend or retract the actuator, Figure 4. Two independent methods of driving this ballnut are provided, permitting full mission performance even with one failure.

PAYLOAD STOWED

PAYLOAD DEPLOYED
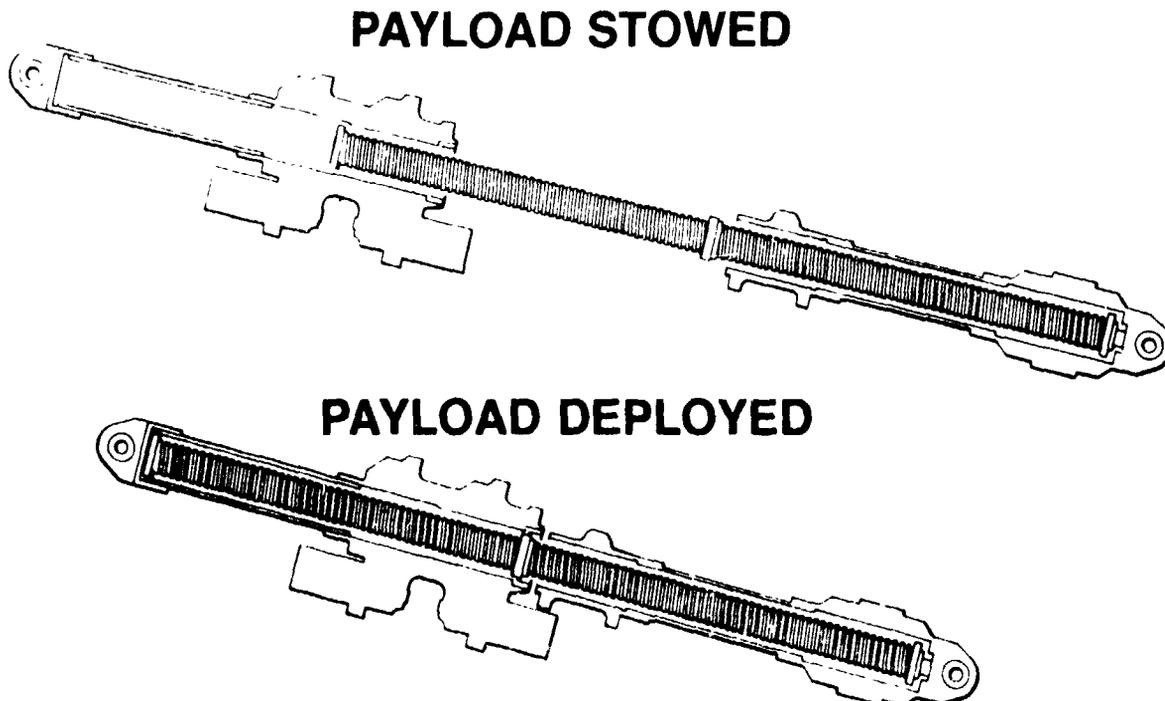
Figure 4 Normal Operating Sequence

If a combination of two failures immobilizes this primary and backup system, the second ballnut is activated. This portion of the actuator serves as an emergency stowing unit by paying out the additional stroke length which is stored within its housing Combinations of failures which have resulted in either failed fixed or failed free situations in the primary backup unit can be handled equally, Figure 5. The emergency unit is also geared higher than the primary backup to provide additional force capability in emergency situations. This arrangement thus possesses single fault tolerance with respect to fulfilling mission performance and dual fault tolerance in controlling the catastrophic hazard.

FAILED FREE CASE

FAILED FIXED CASE
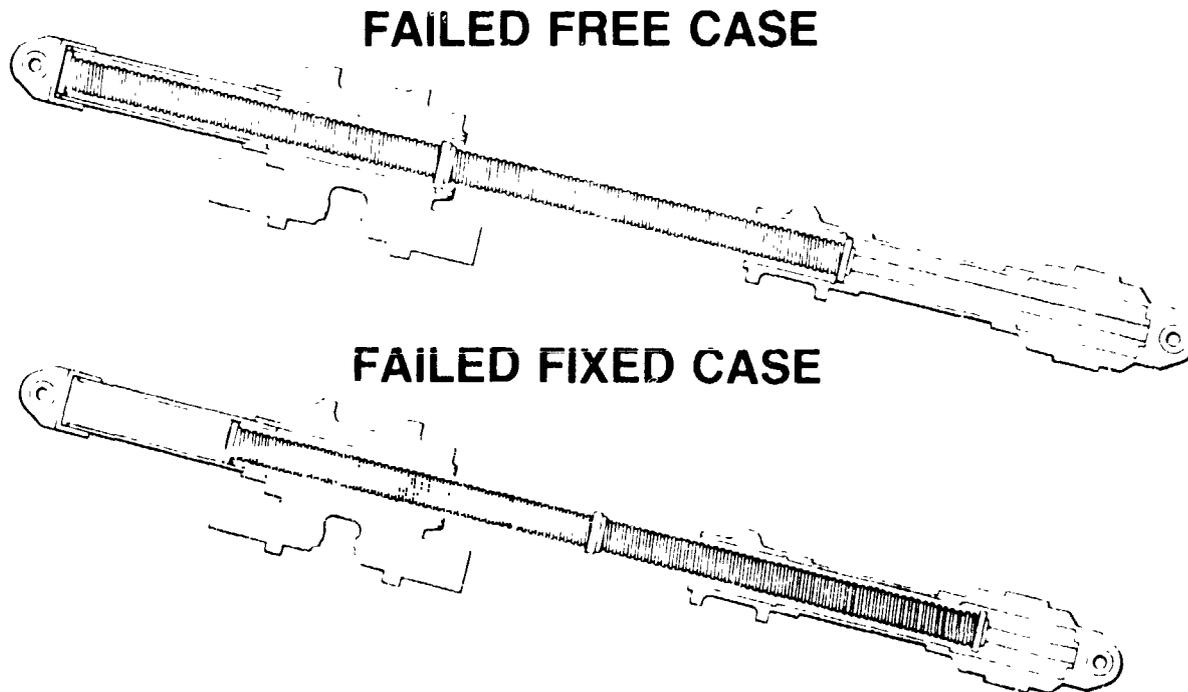
Figure 5 Emergency Stow Operation

In addition, the number of single point failure items which need "noncredible" status has been greatly reduced. Most are controlled in a straightforward fashion. Single load path items, using methodology similar to that for the vehicle structure, are designed for generous safety margins and subjected to fracture analysis and control. Critical rotating interfaces are provided with two independent rotating surfaces. Single fastener attachments have two independent methods of retention.

Inspection of the block diagram in Figure 2, however, will reveal that jamming of both ballnuts (two failures) will render the mechanism inoperative, defeating the two fault tolerant philosophy. Design features employed to render this a noncredible failure mode include two independent ball circuits in each nut; fits, finishes, lubrication, and materials which provide a calculated life well above the intended use; non-jamming wipers on ballnut external interfaces, plus adherence to a contamination control plan for manufacture, assembly, and test. Small parts internal to the actuator's housings are also retained or captured to prevent their loosening and migrating to the ballnut interface. Based on over 21,000,000 hours of operation on similar Sundstrand ballscrew actuators, these controls permit a ballnut/ballscrew assembly to be considered an intrinsic single-failure tolerant device.

The resulting actuator is illustrated in Figure 6. Actual weight of an engineering prototype is 15% less than that calculated for a comparable dual actuator system.

SINGLE BALLSCREW

**PRIMARY BALLNUT
(DUAL BALL CIRCUITS)**

ANTI-ROTATION SPLINE

CLUTCH CARRIER

**EMERGENCY
BALLNUT
(DUAL BALL CIRCUITS)**

**PRELOADED
BELLEVILLE
SPRINGS**

LENGTH:
  EXTEND   1.54 M
  RETRACT   1.17 M
  STROKE   0.37 M

WEIGHT: 43 KG
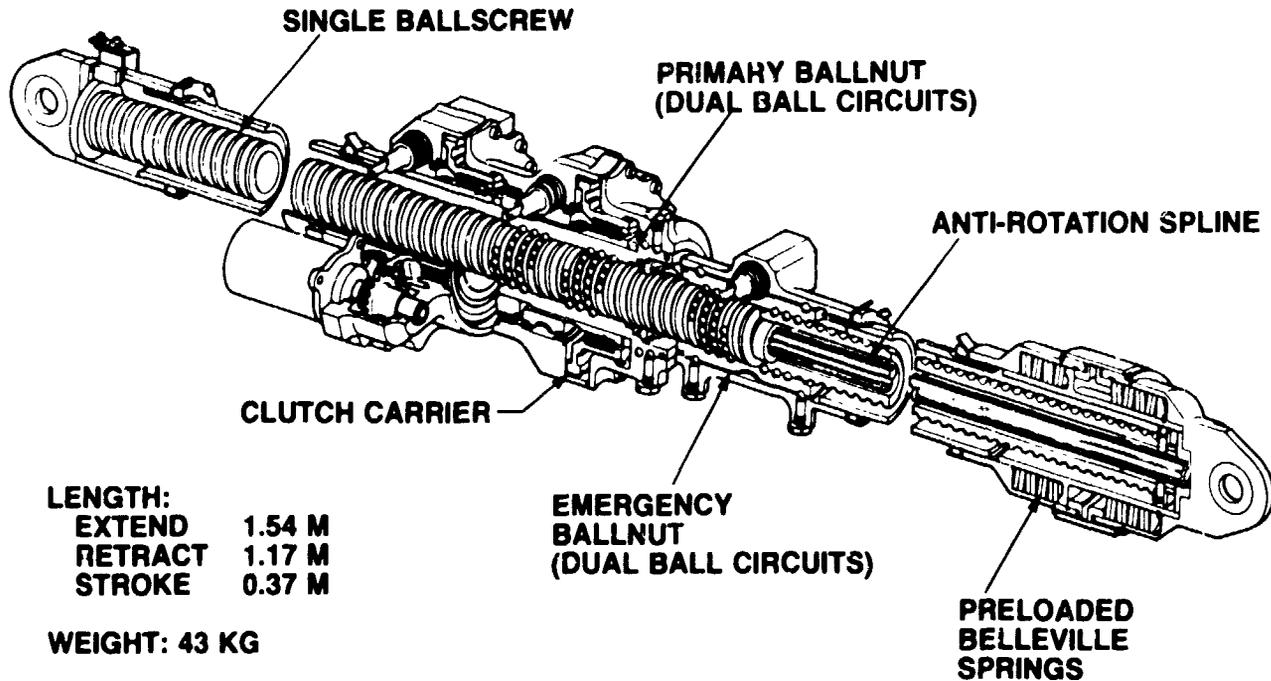
Figure 6 Actuator Cutaway

DESIGN CONSIDERATIONS

In addition to the fault tolerance requirements, other performance issues impose design constraints, many often conflicting, Figure 7. For example, stability in launching the spacecraft is necessary to avoid collision with the airborne support structure. This dictates a low backlash, high stiffness actuator to prevent pitch oscillations as the spacecraft pushes off and exits the cargo bay. High stiffness is also desired to prevent dynamic coupling of the cargo element with the Orbiter thrusters during payload erection and stow.

Safety

- Independent Primary and Backup Actuation Methods
- Combination of Primary and Backup Methods Must Be Two-Failure Tolerant

Operational

- Erect the Payload to Any Angle From 0^0 to 45^0 in Less Than 10 Minutes
- Maintain High Stiffness/Low Backlash to React Upper Stage Separation at Any Angle
- Prevent Backdriving Under Load
- Maintain a Minimum Force Capability of 5340 Newtons Over the Operating Environment
- Provide an Emergency Force Capability of 15,570 Newtons
- Limit the Maximum Force From Combined Impact Loads and Actuator Output to a Level Compatible With Orbiter Structure
- React Orbiter Vernier and Primary Reaction Control Loads
- Minimize Dynamic Coupling Between the Orbiter and the Payload
- Minimize Telemetry and Monitoring Requirements to Permit Minimal Crew Involvement
- Provide 10 Mission Life

Figure 7 Requirements

However, during Orbiter launch and landing, the vehicle will be subjected to structural deflections and vibration environments that cause relative motion between the two actuator mounting points. A stiff actuator in this situation can potentially impart undesirable loads to the supporting structure.

The initial design solution was to accommodate the motion through free-wheeling of the unclutched primary/backup ballnut. However, there was a degree of uncertainty as to the ability of the ballnut to respond rapidly enough to attentuate loads at higher frequencies. In addition, a clutch-engaged failure occurring during deployment can defeat this feature for the subsequent landing.

For these reasons, a load relief device was conceived, Figure 8. Consisting of preloaded bellville springs, the device presents a stiff actuator up to 26,690 newtons (6,000 lb) axial load, either compressive or tensile. Above 26,690 newtons, deflection of the device accommodates the relative motion of the mounts without overloading the structure, Figure 9.
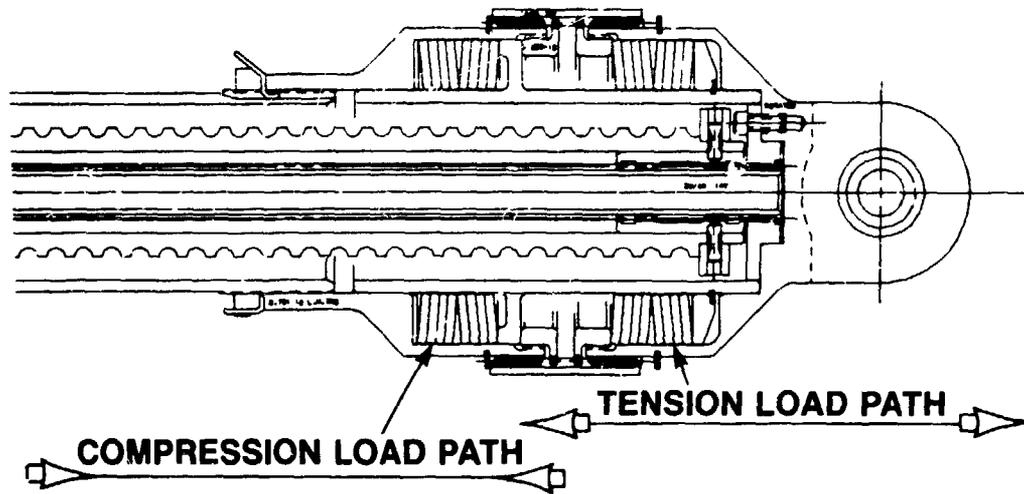
Preload = 26,690 Newtons
Travel = 1.57 MM @ 37,810 Newtons

Figure 8 Load Relief Device
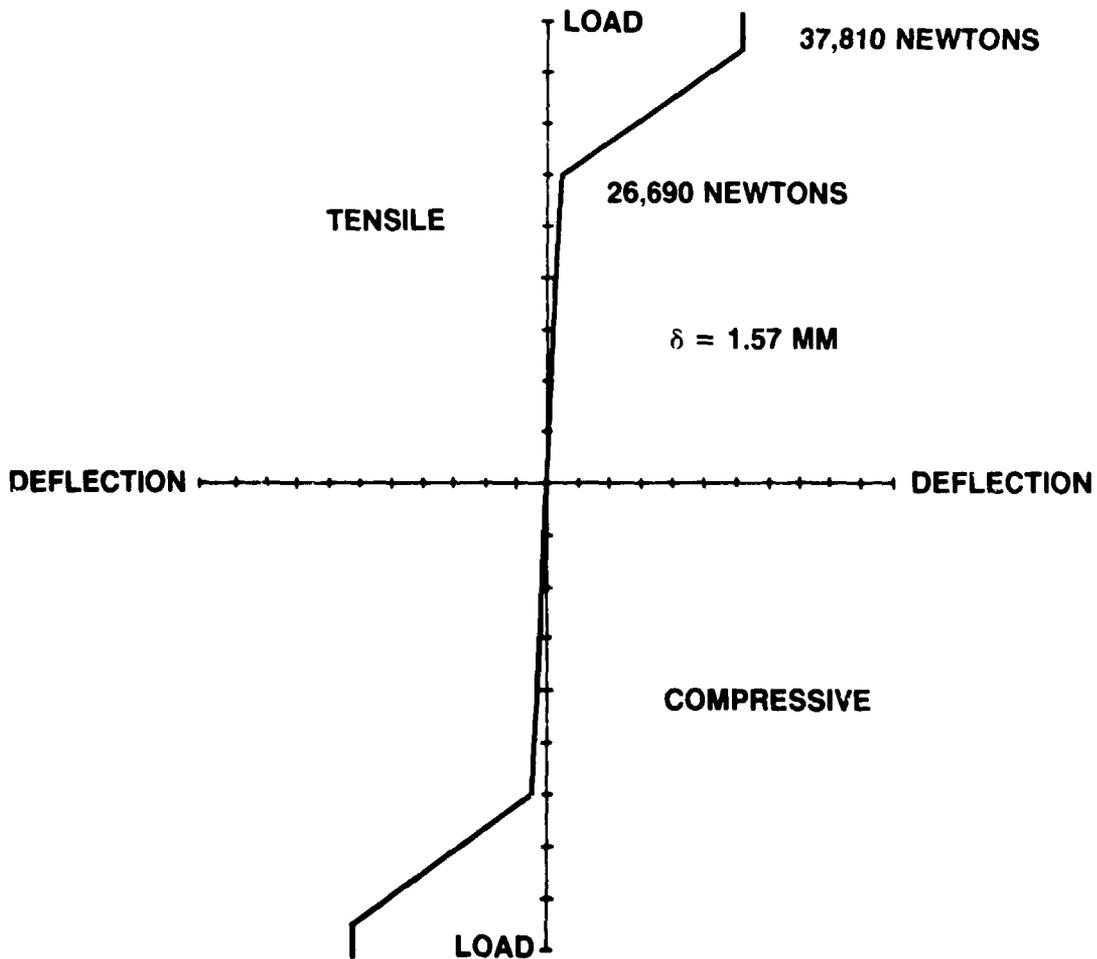
Figure 9 Load Vs. Deflection for Load Relief Device

311

Fault tolerance considerations extended to the design of the load relief device. Springs were sized such that adequate preload would remain after two spring failures.

The need for load relief is predicated on two factors, the ascent/descent vibration induced deflections and the strength limitations of the mounting structure. Both of these areas incompletely defined at the time the actuator was designed. For that reason, the load relief device was designed to be modular, permitting its easy removal if subsequent tests and analyses should indicate it to be unnecessary.

Competing requirements also arose in establishing the force vs. speed characteristics of the actuator. In service, the actuator can be subjected to a variety of loads as illustrated in Figure 10. Because the dynamics of the interaction between the cargo element and the Orbiter are complex, the precision with which these loads could be defined was uncertain. In addition, the loads are bi-directional, capable of either aiding or opposing actuator motion. Yet the actuator has to provide sufficient force capability to perform at all credible load combinations. Operating force requirements of 0 to 1600 newtons (360 lb), which excursions to 15,520 newtons (3,500 lb), were specified.

• Operating   (On-Orbit)

— Vernier Reaction Control System

— Primary Reaction Control System

— Dynamic

— Stop Impact at 45°

— Spacecraft Upper Stage Separation

• Nonoperating   (Ascent/Descent)

— Random Vibration

— Shock

— Structural Deflections

Figure 10 In-Service Loads

In providing sufficient force capability to satisfy these requirements, it was necessary, however, to limit the maximum force potential of the actuator so that the mechanism's output would not exceed the strength of surrounding structure. This consideration limited the maximum actuator output to 37,810 newtons (8,500 lb).

In a similar manner, establishing the actuation speed required balancing the desire to deploy in a reasonable time with the maximum insertion speed of the Orbiter's payload retention latch assemblies. The combination of these speed and force requirements served to define an acceptable operating envelope as shown in Figure 11. The actuator design had to satisfy this envelope under all combinations of supply voltages, environments, and manufacturing tolerances.
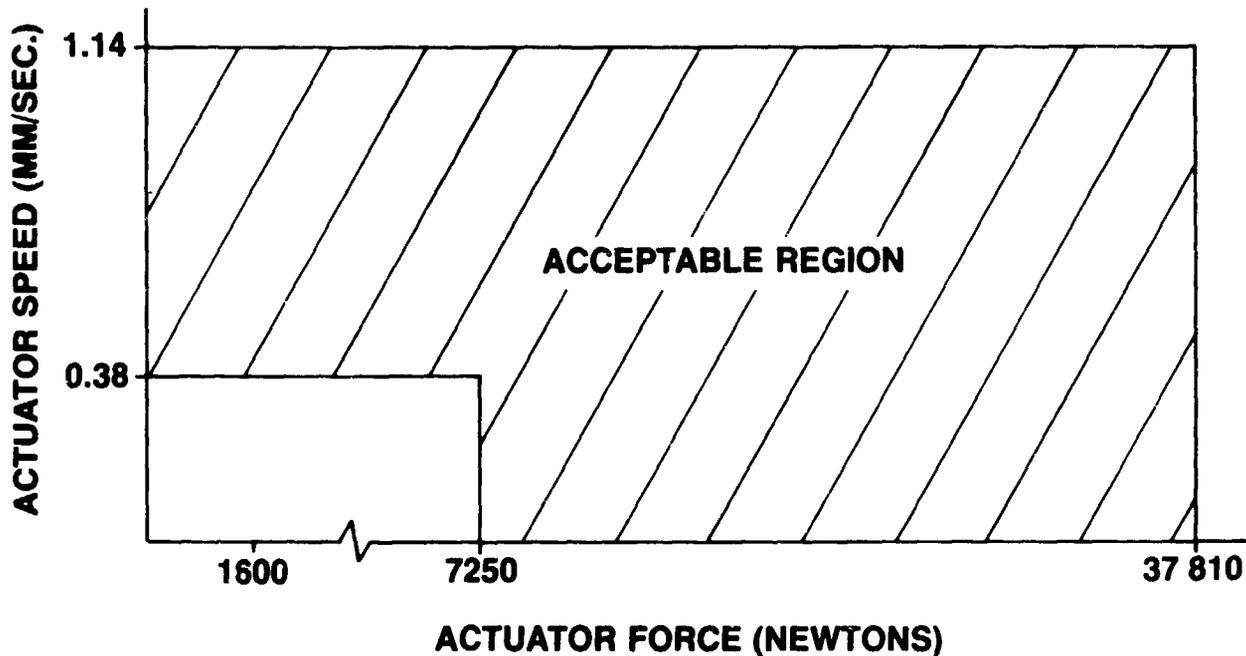
Figure 11 Design Operating Envelope

STATUS AND CONCLUSION

An engineering prototype is presently (November 1984) undergoing performance testing. As noted, this unit is 15% lighter than the calculated weight for the comparable dual actuator system.

More significantly, the actuator design has passed a preliminary NASA Safety Review, a step necessary for acceptance as a Shuttle cargo. This Safety Review has historically resulted in design changes for dual actuator systems.[2] The relative simplicity of the single actuator design and the minimum number of noncredible failure situations facilitated this acceptance.

Although this design has the drawback of requiring the room to accommodate a long mechanism, the approach to fault tolerance is an advantage. It offers a simpler, lighter system with considerable performance versatility.

REFERENCES

1. "Safety Policy and Requirements for Payloads Using the Space Transportation System", NHB 1700.7A, December 1980, P. 2-4.

2. Hornyak, Stephen, "Inherent Problems in Designing Two Fault Tolerant Electromechanical Actuators", Proceedings 18th Aerospace Mechanism Symposium, May 1984, NASA Conference Publication 2311.

FEATURES OF THE SOLAR ARRAY DRIVE MECHANISM
FOR THE SPACE TELESCOPE

Raimund G. Hostenkamp[*]

ABSTRACT

The Solar Array Drive Mechanism for the Space Telescope embodies several features not customarily found on Solar Array Drives. Power and signal transfer is achieved by means of a flexible wire harness for which the chosen solution, consisting of 168 standard wires, is described. The torque performance data of the harness over its temperature range are presented. The off-load system which protects the bearings from the launch loads is released by a trigger made from Nitinol, the memory alloy. The benefits of memory alloy and the caveats for the design are briefly discussed. The design of the off-load system is described and test experience is reported.

INTRODUCTION

The solar array is part of the equipment contributed to NASA's Space Telescope (ST) by the European Space Agency. Figure 10 shows an overall view of the ST Solar Array (SA). The Solar Array Drive Mechanism (SADM) and its electronics are a subassembly of the SA. The rotational range of the wings is limited to some 340 degrees because of vehicle pointing constraints which prevent the sunlight from getting into the ST aperture. Under these circumstances a flexible wire harness is an obvious choice for the transfer of a large number of electrical channels.

In the launch configuration the SAs are stowed along the ST body and fixed by clamps. Since the loads induced into the SADM through the primary deployment mechanism exceed the load-carrying capability of the bearings, it was necessary to provide an off-load system in order to protect them. Because pyrotechnic devices were banned from use in the SADM, memory alloy elements were chosen to trigger the release of the bearing off-load device.

[*] Dornier System GmbH, Friedrichshafen, Federal Republic of Germany

FLEXIBLE WIRE HARNESS

Each SA wing provides 10 solar cell modules with a nominal current of 7.5 A each. These modules were wired independently from each other and the wiring had to be redundant. This resulted in a minimum of 40 lines of AWG 16 for 50 percent derating.

In addition to these SA power lines, 20 wires with a maximum capacity of 3 A were required for the redundant motors of the primary and secondary deployment mechanisms, the redundant resolvers of the solar array drive itself and for bonding.

Finally, 68 housekeeping data lines were needed with a current capacity of up to 250 mA. These data lines had to be separated from the power lines by a screen.

Since a high wind-up torque was anticipated from the American Wire Gauge (AWG) 16 wires needed for the SA power, it was necessary to find an alternative which met the redundancy approach which aimed to avoid single point failures for vital functions. The chosen approach utilized 80 cables AWG 22, of which 20 cables are for redundancy purposes.

Four options of flexible wire harnesses were studied by breadboarding and analysis. The trade-off is presented in Table 1.

Though torque, torque noise and hysteresis of the flexible wire harness played an important role in the design of the SADM control system, the printed circuit, which is best in these respects, was not selected. The printed conductors for power transfer would have had to be very wide in order to achieve the necessary cross section. In addition to serious difficulties at the Printed Circuit (PC)/connector interface, this design would have exceeded the given envelope, even with a double-layer arrangement of the PC belts and a reduced derating. In fact the criterion of compatibility with the given volume rendered the option with the single wires the only feasible solution.

The principle of the chosen solution is shown in Figure 1. The axial degree of freedom required for one cable end of this twisted wire configuration was provided by performing the cables in a half circle from their shaft location towards their fixation points at the stator. Twisting and shielding of cable pairs within the flexible wire harness was discarded because it impaired cable flexibility. The required shielding between the signal lines and the power lines is achieved by a screening tube. The signal lines (68 off AWG 24) pass through the screening tube and the power lines (100 off AWG 22) are arranged in the annulus between the tube and the hollow shaft. The length of the flexible wires amounts to some 580 mm. Although the wires are neither fixed nor tied together over that length, both a centrifuge test, giving up to 4.5 g's, and vibration tests showed that the wires would suffer no permanent deformation as a result of the launch mechanical environment.

The torque at the boundaries of the rotational range is adjusted to about the same level by suitable pre-orientation of the power and signal leads during assembly. A breadboard model (see Fig. 5) was built in order to determine the spring constant, torque noise and hysteresis characteristics of the harness. The wires were short-circuited outside the flexlead compartment. This allowed the routing of current through the leads and the determination of their performance at elevated temperatures. Low-temperature tests down to -25°C were carried out in a large temperature chamber. The results met expectations and, with a margin of 2, were taken into account for the design of the control circuit.

Following testing of the Qualification Model SADM in a dynamic test rig, to verify pointing accuracy and interactive torque between the ST and the wings, it was demonstrated that the torque characteristics of the flexible wire harness had an unexpectedly large impact on the system performance. Both maximum torque and hysteresis of the flight-configured qualification model exceeded the corresponding values of the breadboard model by a factor of 3, even though the flexleads inside were identical. The difference was attributed to the harness located outside the flexlead section. In contrast to the short-circuit looms of the breadboard model, the cables of the Qualification Model harness outside the mechanism were twisted, shielded, bundled and fixed as required to form the conventional harness between the SA panel and the diode box (see Fig. 6). These measures had resulted in a deterioration of the torque and hysteresis characteristics to an unexpected extent. By corrective actions, e.g., deletion of most of the spare lines and provision of slight slack at those tie-down points where the bundles emerge from the housing, it was possible to recover the original harness performance.

The harness torque and hysteresis characteristics of the flight model mechanisms are summarized in Figures 2, 3 and 4.

Figure 2 shows the basic shape of the torque/hysteresis loop for the full angular range. Torque rises linearily as the shaft is rotated in one direction. Upon reversal there is a steep (1°) decay of torque followed by a steady transition (10°) towards the linear wind-back behavior. The area between wind-up and wind-back torque is due to hysteresis. As a result of the deletion of spare lines, which were mainly in the signal section, the hysteresis is not constant over the whole angular range. The mechanical properties of the wire insulation are changed by temperature fluctuations of the harness. This affects the whole torque envelope, i.e.,the slopes and resulting maximum torques as well as the hysteresis.

Figures 3 and 4 show the maximum torque values at the ends of the angular range and the corresponding hystereses as functions of temperature. The data for a specific temperature give the corners of the torque envelope "trapezoid".

OFF-LOAD SYSTEM

Discussion of Memory Alloy

Nitinol Memory Alloy Elements (MAE) are used as release triggers for the
off-load system. The choice of this actuator type was encouraged by some
experience from a joint test programmer with the manufacturer and from
in-house development studies.

The memory effect is based on a reversible maternistic transformation of
the crystal lattice of the nickle-titanium alloy. The effect is imparted by
plastic deformation of the element at low (ambient) temperature. When
subsequently heated above the transformation temperature, the element returns
almost completely to its initial shape. All kinds of motion can be
achieved: bending or torsion, expansion or contraction. During motion, the
element is capable of exerting a force (or torque). Both force and stroke
are controlled by the dimensions of the element. The trigger temperature can
be adjusted by the manufacturer rather accurately by controlling the
percentage of the alloy constituents. If an "educating force" is applied
during cooling, the effect can repeat many times.

These characteristics suggest a very simple design for all kinds of
mechanisms which have to lock or release an item. However there are some
constraints which limit the use of memory alloy:

- machining is very difficult because the alloy is susceptible to heat,
  developed by most machining processes, and to work-hardening.
  Therefore the shape of the element should be simple, commensurate with
  the still-growing experience of the manufacturer.

- together with the desired stroke there is a minute change of the other
  dimensions of the element resulting from the alteration of the crystal
  structure.

- when the element cools, after having produced the memory effect, it
  may, to a certain extent, return to its deflected shape.

- the efficiency of mechanical energy output to heating energy input is
  very low compared to other systems.

If these constraints are taken into account with the design, memory alloy
can be a suitable material for relatively cheap actuator elements.

Description of the System

The SADM is equipped with two separable, thin-section, angular-contact ball
bearings in a back-to-back mounting. The outer race of one bearing is fixed
to the housing through a diaphragm which controls the axial preload. This
arrangement allows a slight axial displacement of the shaft, with the result
that the bearing in the diaphragm experiences small increased axial load

318

corresponding to the additional deflection of the diaphragm, and the other bearing becomes completely unloaded.

This method is utilized by the off-load device of the SADM. Figure 7 shows two orthogonal views of the off-load device.

Four supports are mounted on the outboard front face of the mechanism housing, and extend two tabs each over a collar at shaft. "L"-shaped rocking levers are hinged in the supports (see Fig. 7). Under a radial force the levers press against the collar from underneath, lifting the shaft and clamping it against the tabs of the supports. The radial force is applied to the rocking levers by a cable through intermediate levers which are hinged between the side walls of the rocking levers. The cable is routed over pulley segments mounted on the intermediate levers. Rotation of the intermediate levers is prevented by locking elements. In two places the locking elements are bolts, and in the other two places there are latches. The latch position is secured by a pin made of Nitinol protruding through an eye in the latch. The pin is fixed by a bracket which is bolted to the housing. The shaft is released as one of the locking elements (bolt or latch) is disengaged from the corresponding intermediate lever.

Automatic release is performed by one of the MAEs. The MAEs are mounted to the mechanism in a bent form. A tubular heater encloses each element. When heated up to the threshold temperature the element becomes straight and lifts the latch. Under the pre-tension of the cable, the intermediate lever rotates outwards. The cable is then disengaged from the pulleys and secured by four soft springs on a sheet metal tray which is located underneath the off-load system (see Fig. 8). Since only one locking element has been removed, the other intermediate levers move inwards together with their main rocking levers under the action of springs. The shaft is then pulled back into its operational position by the diaphragm.

In an emergency, when the off-load device cannot be released, even by one of the redundant MAEs, an astronaut can unlock one of the other intermediate levers by actuating one of the bolts. This bolt is accessible through a hole in the thermal shield. Release is verified by redundant micro-switch circuits.

This rather complex configuration evolved from a series of breadboard tests. Initially the MAE was clamped in a slot between the main rocking lever and the intermediate lever (see Fig. 9). When heated to the trigger temperature, the MAE deformed into a flat "S"-shape rather than becoming straight, because friction could not be controlled effectively. The problem was solved by the introduction of the latch. The force required to lift the latch is less than 50 percent of the capability of the MAE. However it was necessary to add a spring to prevent the intermediate lever from swinging back to its original position since, during cooling down after release, the MAE could deform back and reengage the latch, thereby jamming the shaft again.

The MAEs for the SADM off-load system have a diameter of 10 mm, a length of 56 mm and a force capability of more than 450 N over the full stroke of 6 mm. The trigger temperature amounts to 115°C which is well above the hot survival temperature of 85°C stipulated for the SADM. After use, MAEs can be "recharged" by the manufacturer (which involves a heat-treatment) to achieve the same certified performance.

For development tests, however, it is sufficient to rebend the MAE at ambient temperature to restore the memory. More than 10 consecutive reuse cycles have been achieved, this being a notable economic advantage over the use of pyrotechnics. Only a gradual decrease of the trigger temperature has been observed in this series.

The heaters consist of a heating wire embedded in silicone rubber. At the nominal power output of 40 Watts, the trigger temperature is reached after about 100 seconds when starting from ambient conditions and about 180 seconds when starting from -60°C thermal vacuum conditions.

Thirty-five of the procured lot of 60 MAEs have been subjected to date to formal qualification and acceptance tests. The first 25 elements were used for lot qualification. This qualification included verification of the dimensions prior and after subjection to hot and cold survival temperatures and subsequent function tests in order to demonstrate strength and stroke capability at the trigger temperature. The other 10 elements were used to release the off-load devices of the individual SADM models during the course of the program. The tests demonstrated the Nitinol elements can be a reliable replacement for pyrotechnics.

CONCLUSIONS

Based on the experience with the SADM harness, similar flexible wire harnesses have been implemented in further space mechanisms, e.g., the gimbal drives of the Instrument Pointing System (IPS) for the Spacelab.

The utilization of memory alloy elements for other space applications has not yet progressed beyond breadboarding. At the present time the prime impetus in MAE development comes from terrestrial applications ranging from Nitinol motors to medical applications, and there is considerable progress being made in the manufacturing techniques applied to these useful alloys.

320

Flexible Wire Harness Type				
Cable Design	Standard Belts	Standard Belts	PC Special Design	Standard Wires
Qty. of Power Segments Signal	2 / 2	1	1 / 1	1 / 1
Cable Arrangement in Segments	Multi-Layer	Multi-Layer	Double Layer	Separate Wires
Connector	Conventional	Conventional	Special Design	Conventional
Shielding Between Power & Signal	Easy	Difficult	Easy	Easy
Rel. Cable Length	1.5	1	0.3 - 0.4	1
Rel. Power Dissipat.	1.5	1	1.8 - 2.4	1
Heat Radiation	Poor	Poor	Poor	Fair
Torque & Torque Characteristic	Low; Constant	Low; Spring	Very Low; Const.	Low; Spring
Torque Noise	High (Multi-Layer)	High (Multi-Layer)	Very Low	Low
Hysteresis	Large	Large	Very Small	Large
Growth Flexibility	Margin by Design	Moderate	Poor	Good
Assembly	Fair	Difficult	Easy	Easy
Compatibil. with Given Volume	No	No	No	Yes
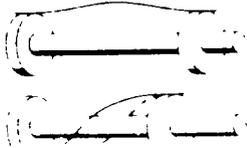
Table 1   Flexible Wire Harness Trade-off
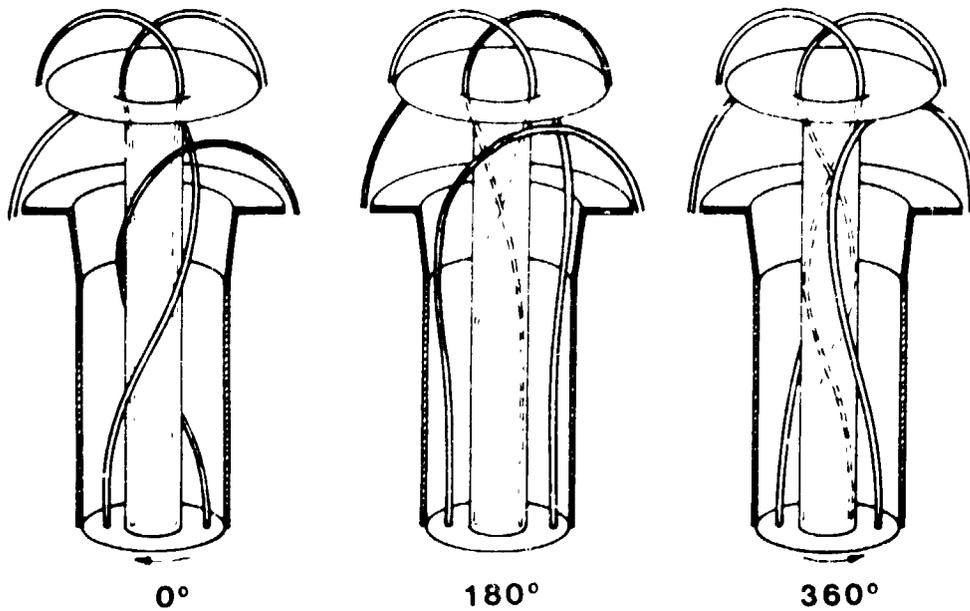
Fig. 1   Flexible Wire Harness - Schematic
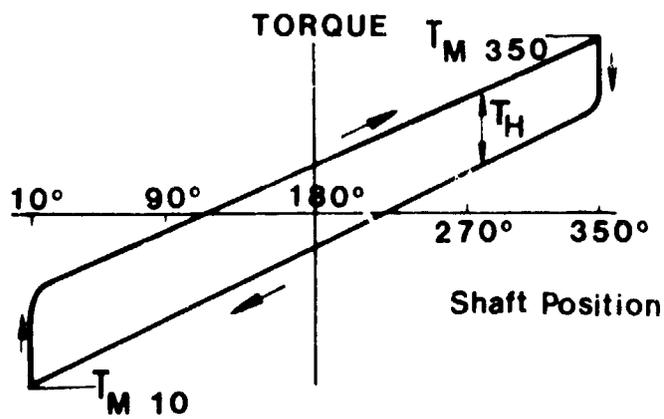
Fig. 2   Flexible Wire Harness Torque Envelope
as Function of Shaft Position

MAXIMUM HARNESS TORQUES AND HYSTERESES
(AT THE BOUNDARIES OF SAD ROTATIONAL RANGE)
AS FUNCTIONS OF TEMPERATURE
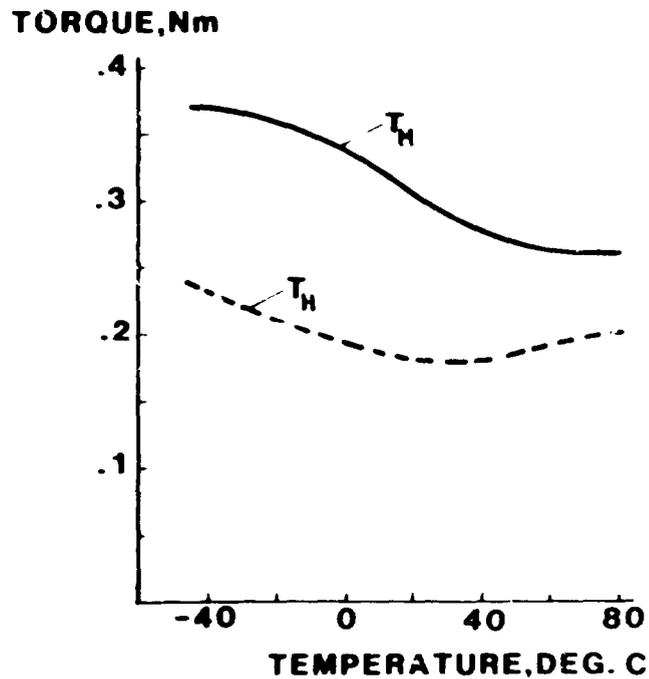
TORQUE,Nm

TORQUE,Nm

Fig. 3   Maximum Torque T_M and
Hysteresis T_H at Position 10°
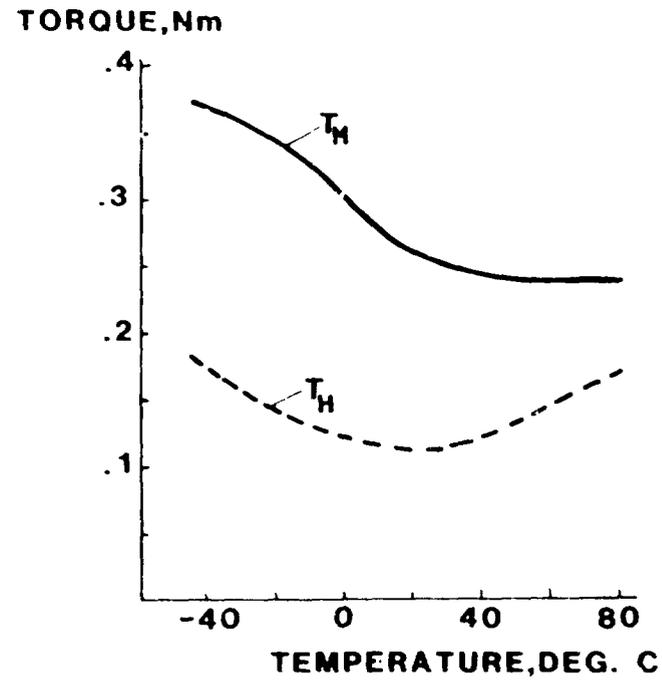
Fig. 4   Maximum Torque T_M and
Hysteresis T_H at Position 350°

Fig. 5 Flexible Wire Harness
Breadboard Model

Fig. 6 Harness Configuration
Qualification Model

324
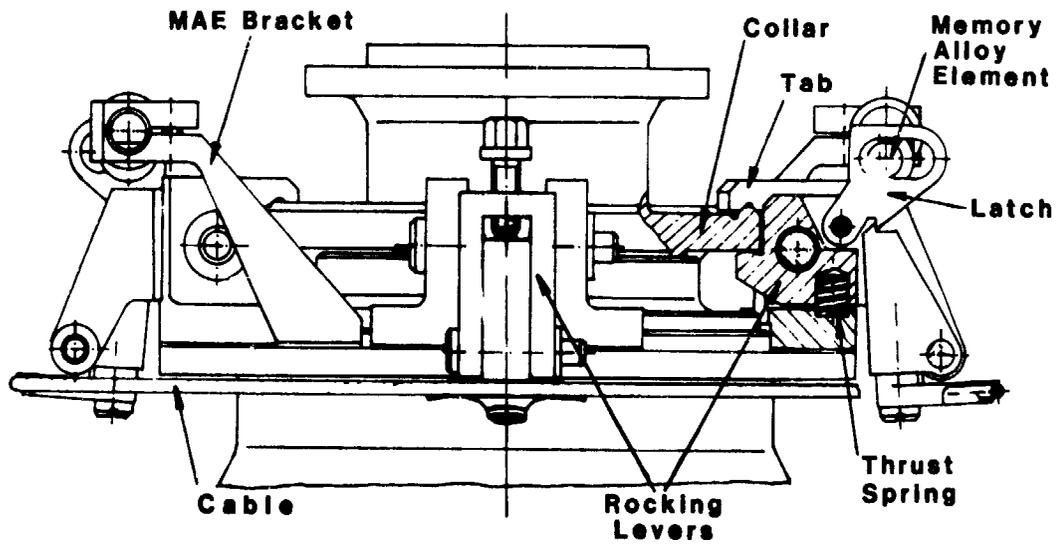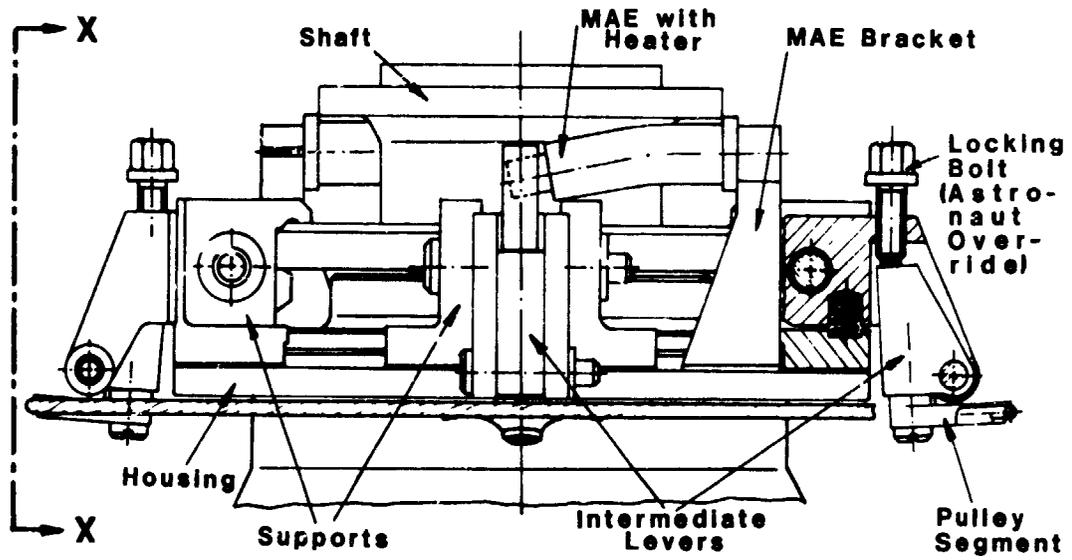
View X -X

Fig. 7 Off-Load Device

325

Fig. 8   Off-Load Device
Qualification Model

Fig. 9   Off-Load Device
Breadboard Model

Solar
Array
Drive
Mechanism

Primary
Deployment
Mechanism

Secondary
Deployment
Mechanism

Blanket
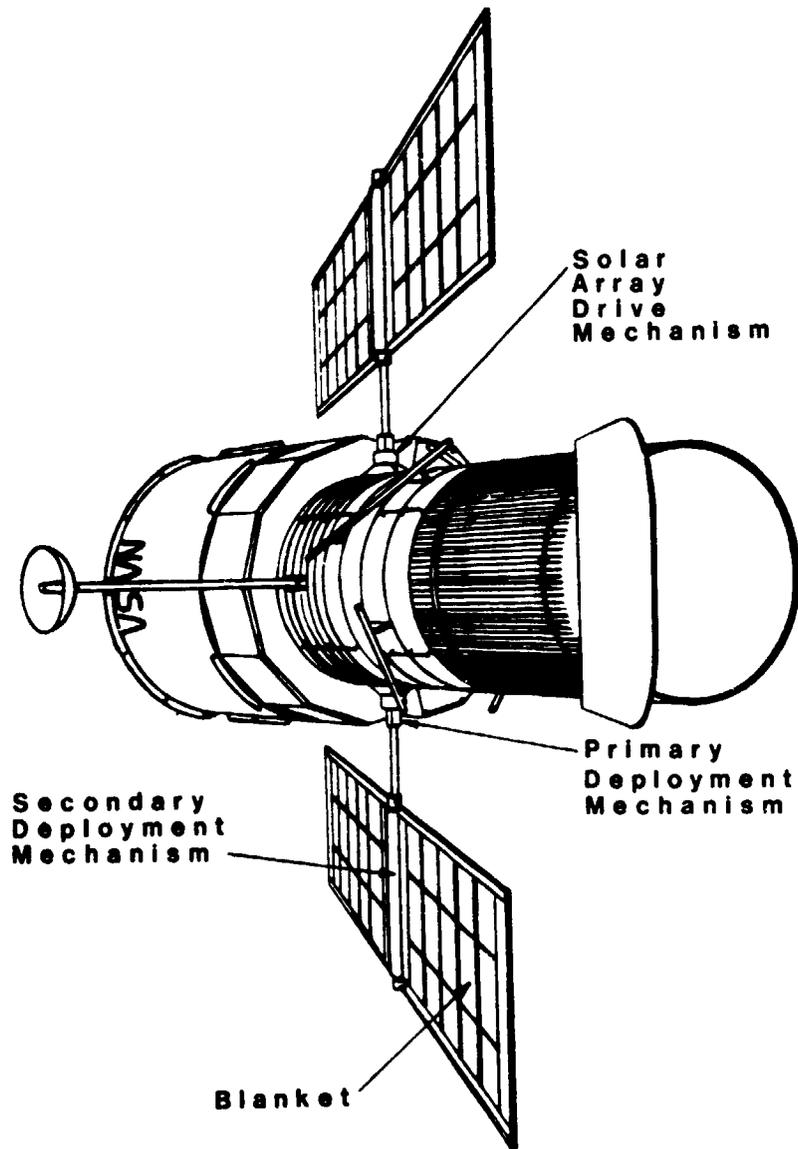
Fig. 10   ST - SA Orientation &
          Deployment Mechanisms

APPENDAGE DEPLOYMENT MECHANISM
FOR THE HUBBLE SPACE TELESCOPE PROGRAM

Herbert T. Greenfield*

ABSTRACT

This paper presents the key requirements, a design overview, development testing (qualification levels), and two problems and their solutions resolved during the mechanism development testing phase. The mechanism described herein has demonstrated its capability to deploy/restow two large Hubble Space Telescope deployable appendages in a varying but controlled manner.

INTRODUCTION

As part of the NASA Hubble Space Telescope (ST), a Shuttle-launched spacecraft, three appendages are deployed/stowed by an electromechanical hinge mechanism: two antennas and an aperture door. One use of the mechanism is for the deployment/stowing of the two high gain antennas (HGA) used to transmit scientific data to the ground station. The second use is to open/close the large aperture door (AD) located at the end of the telescope aperture, which must close to preclude the sun from shining in on the telescope primary mirror. Figure 1 shows the deployed telescope. The deployment mechanisms are shown in Figure 2.

DESIGN REQUIREMENTS

The deployment mechanism, a limited-angle hinge device, was designed to deploy/stow two spacecraft appendages with the following specific requirements:

o   The deployment mechanism must be capable of surviving five Shuttle launches, four returns to Earth, and eight in-orbit docking operations with appendages stowed and locked.

o   The deployment mechanism must be redundant so that no single component failure will jeopardize recovery of the spacecraft or result in hazards to personnel.

o   The deployable appendages must be capable of manual operation and jettison by an Extra Vehicular Activity (EVA) crewmember to ensure deployment, restowage, and safe return of the ST spacecraft to Earth.

o   The aperture door deployment mechanism must be capable of closing within one minute after a command from the sun sensor, precluding irreversible damage to the telescope optics if the spacecraft points the aperture toward the sun.

---

*Lockheed Missiles & Space Company, Inc., Sunnyvale, California
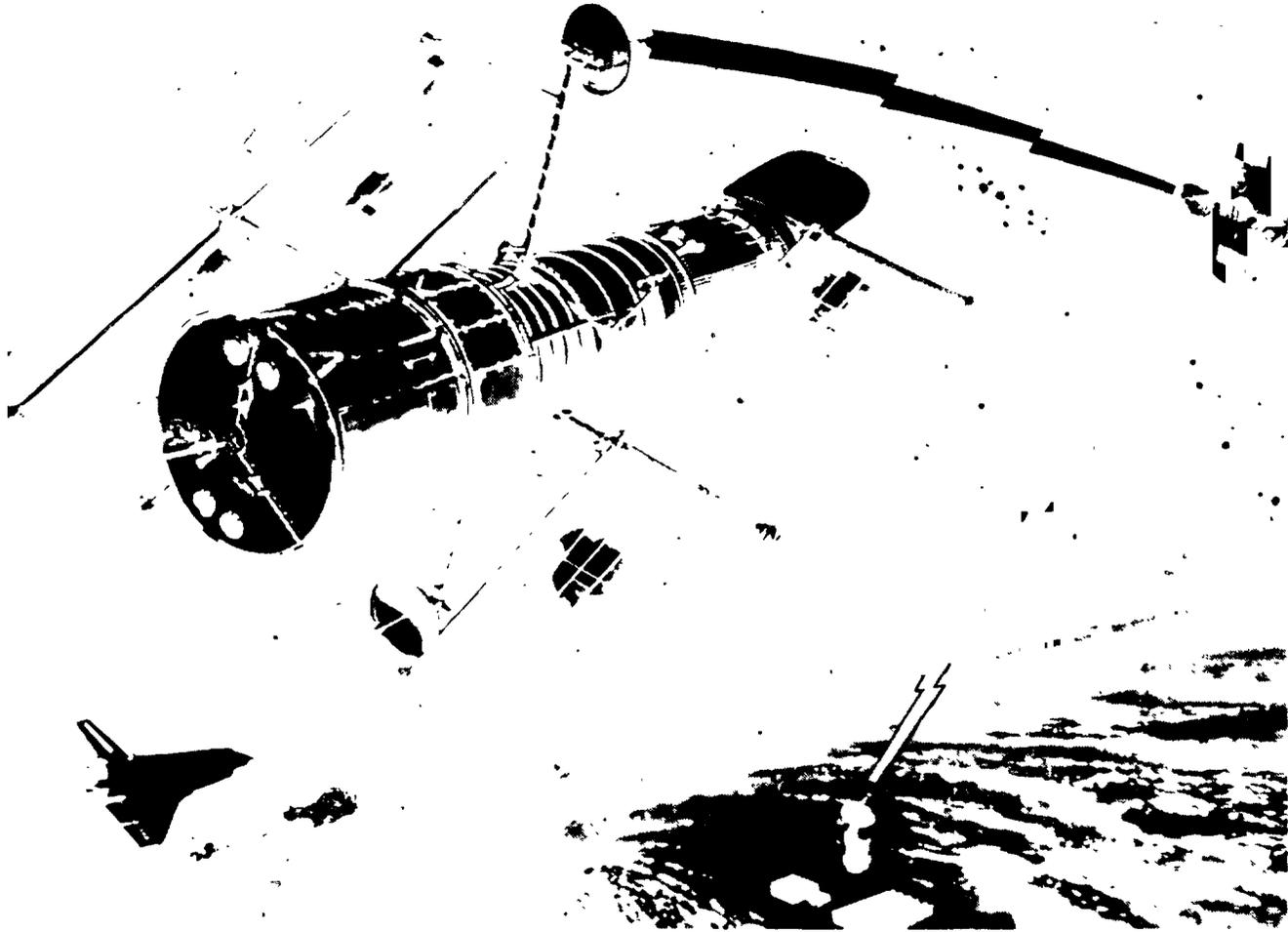
Figure 1   On-Orbit ST Deployed and Transmitting to Ground Station.

HIGH GAIN ANTENNA

TWO AXIS GIMBAL

ANTENNA

GRAPHITE/ALUMINUM
MAST

FWD

PASSIVE HINGE

ACTIVE HINGE
(ACTUATOR DRIVEN)

SPACE
TELESCOPE

APERTURE DOOR

ACTIVE HINGE
(ACTUATOR
DRIVEN)

PASSIVE HINGE

Figure 2   Stowed ST, Close-up of Two Deployed Appendages.

o   The deployment mechanism must operate in an Earth-orbiting pressure environment and at heater-controlled temperatures from -62.2°C (-80°F) to +43.3°C (+110°F).

o   The hinge mechanism deployed stiffness must meet a first mode natural frequency of less than 1.0 Hz.

MECHANISM DESCRIPTION

The deployment mechanism consists of an active hinge (dc rotary drive actuator powered) and a passive support hinge. Detailed design features may be identified in Figs. 3 and 4.
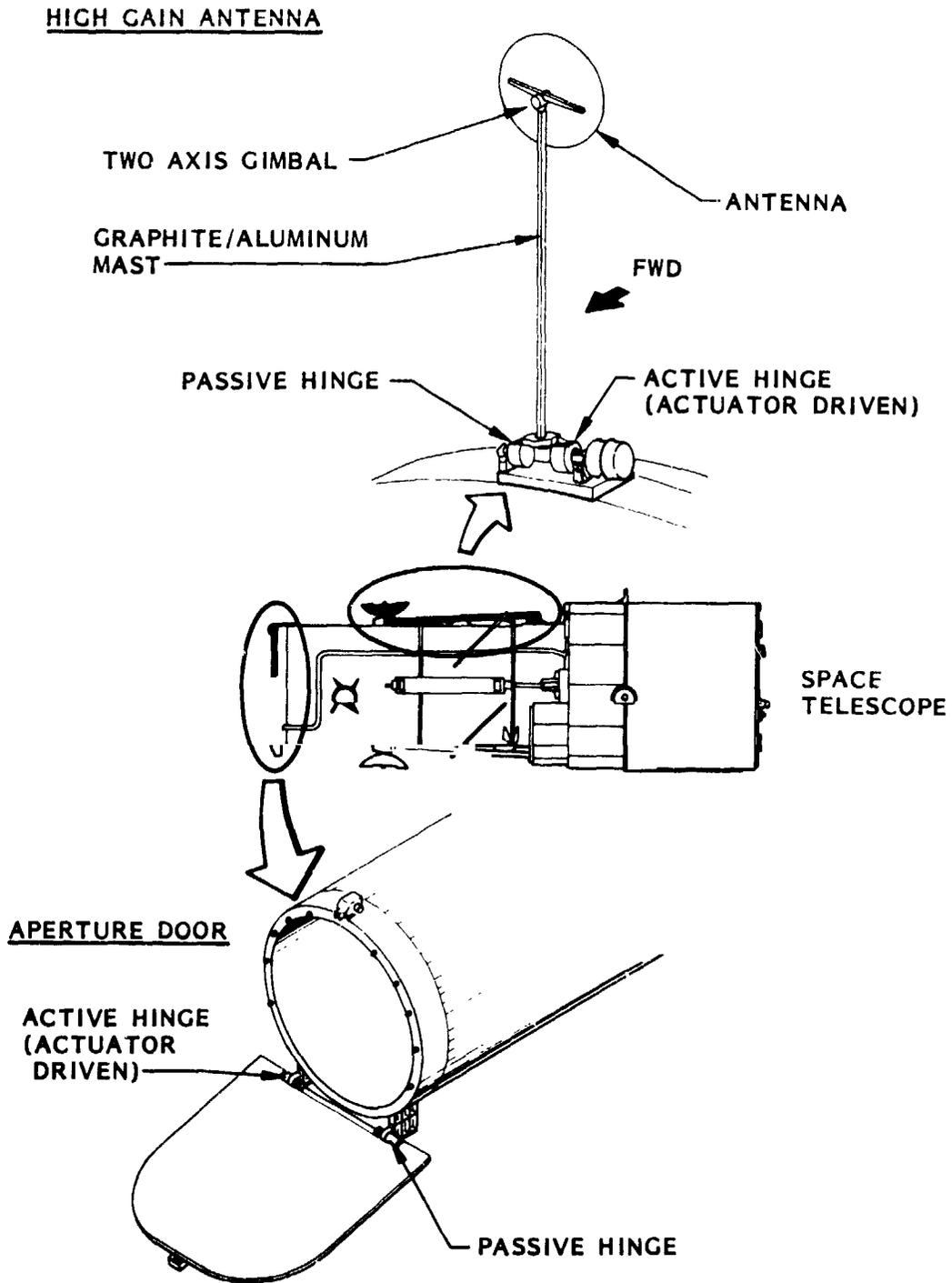
The large-diameter, angular-contact, output-support bearings and the self-aligning spherical bearing are identical in each active and passive hinge assembly. The self-aligning feature permits some angular misalignment between the active and passive assemblies since, in the aperture door hinge installation, they are approximately 147.3 cm (58 in.) apart.

The active hinge mechanism, Fig. 3, is driven by a Schaeffer Magnetics, Inc., three-phase, six-state, "wye" connected, 1.5° permanent magnet dc stepper motor driving through a 200:1 Harmonic Drive speed reducer. The bidirectional rotary actuator drives a torsion rod via a splined shaft which is keyed to the domed end cover. The torsion rod permits the actuator, with its inherent powered detent torque, to move larger inertias than if direct coupled. This is the point where the AD or HGA is attached. The spring-loaded friction plugs of Delrin AF rub constantly against the end cover to provide damping during movement of the mechanism. Just prior to the fully deployed position, the adjustable intermediate stops located in the domed cover contact the intermediate torsion tube and the torsion tube, both compliant members, although with different spring rates, which reduce the end-of-travel dynamic loads and contribute to the overall deployed mechanism stiffness; the intermediate torsion tube also has coulomb damping in the form of annular Delrin AF friction segments.

A manual wrenching point to rotate the active hinge is provided at the end of the torsion rod opposite the rotary drive actuator. The wrenching point accepts the standard EVA hexagonal 10.9-mm (7/16-in.) socket.

As noted in the mechanical schematic, Fig. 5, the rotary drive actuator drives into an adjustable stop just after preloading the torsion rod and the other two compliant members at the deployed position.

If an appendage is manually deployed by a crew member, the active hinge must be manually preloaded by imparting a small angle of travel to the output shaft of the rotary drive actuator; the crew member does this by inserting the standard socket with a long extension attached through a hole in the rotary drive actuator adapter housing and levering the actuator into its stop (Fig. 6).

End-of-travel telemetry (TLM) switches are provided to indicate when the deployment mechanism is near either the stowed or deployed position. In addition, the aperture door mechanism includes a rotary potentiometer to provide full mechanism travel-position readout.
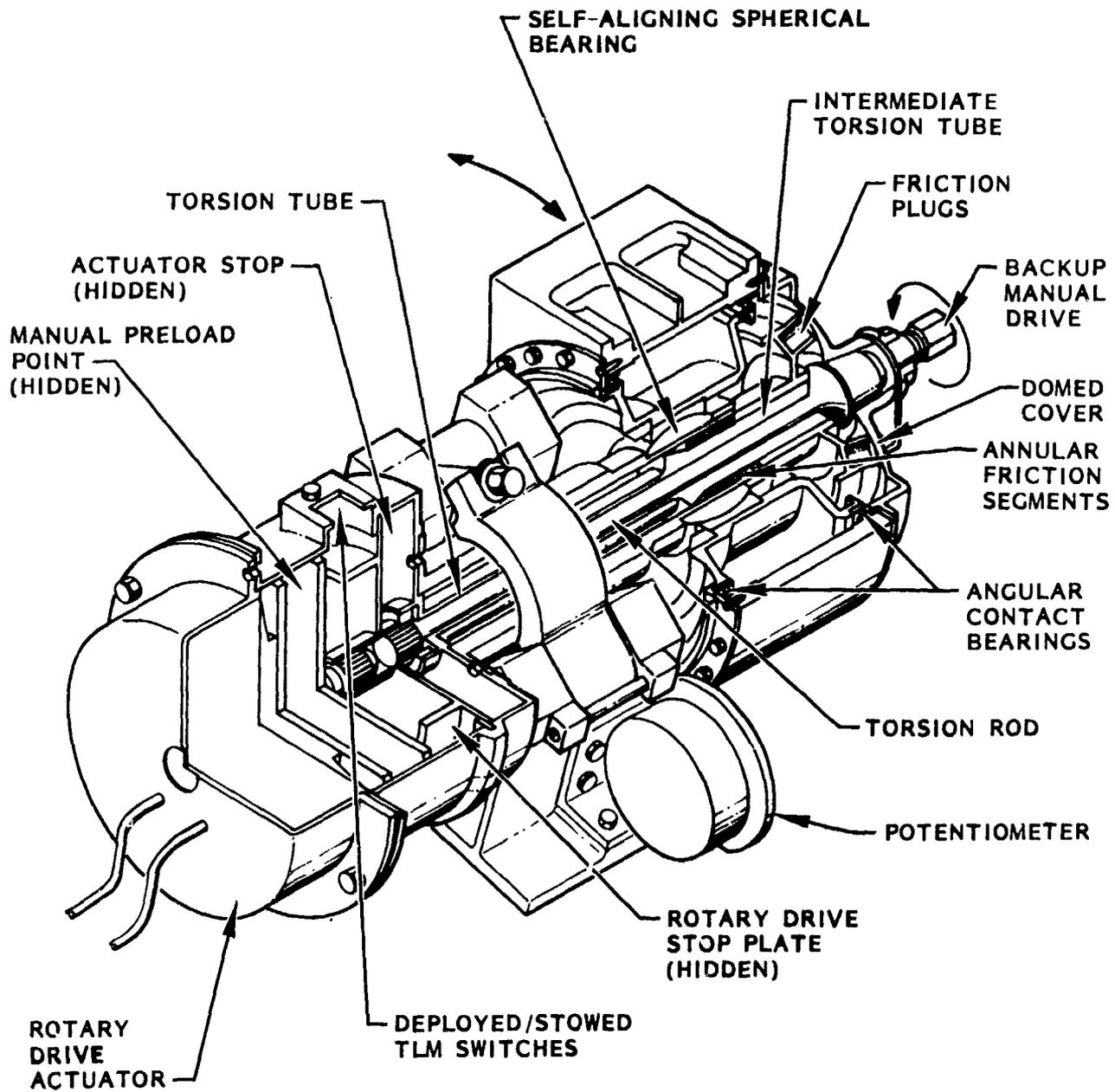
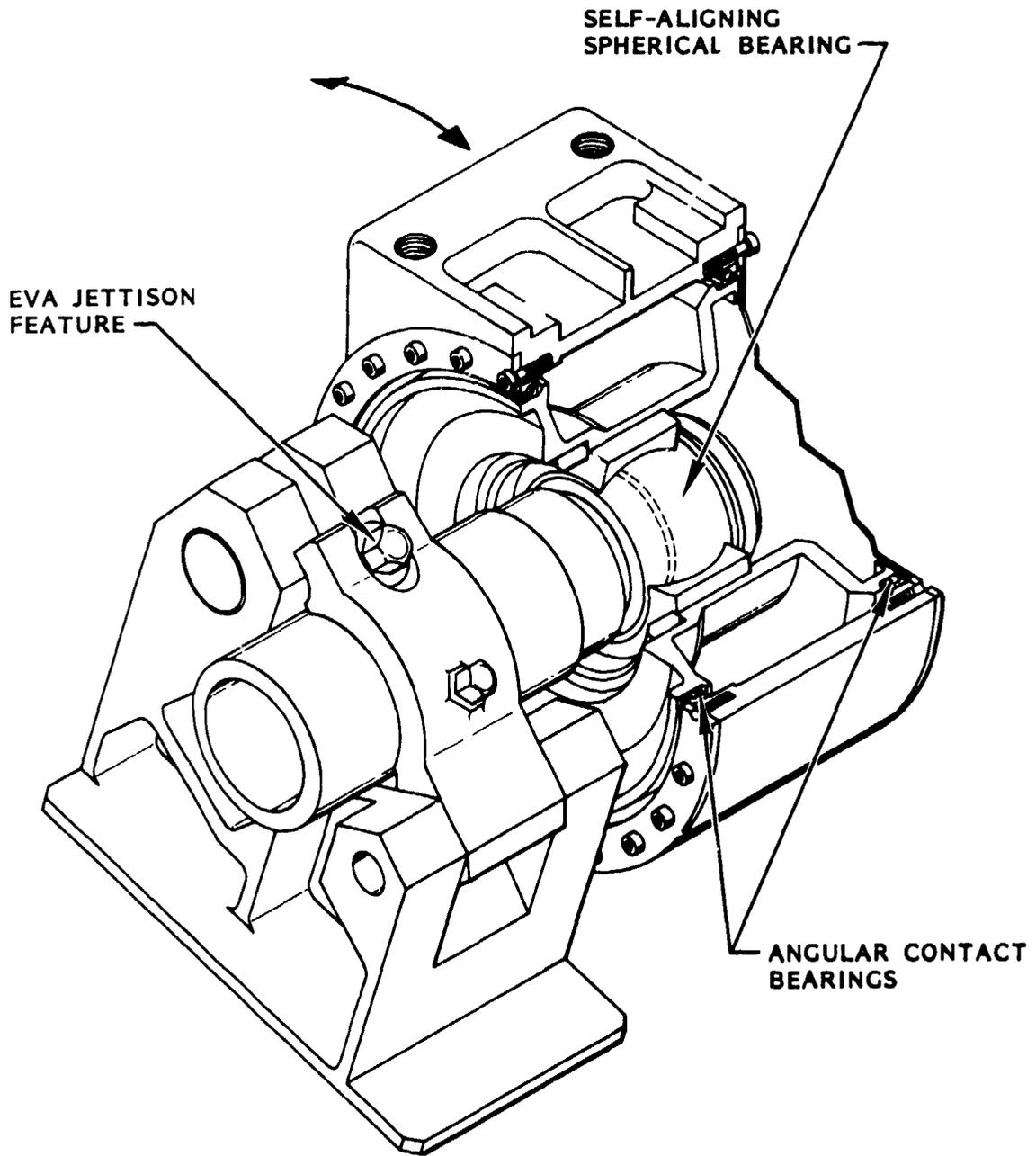Figure 3. Active Hinge Assembly.

333

Figure 4. Passive Hinge Assembly.

The self-aligning bearing not only provides mechanism misalignment correction capability, but also acts as a redundant rotational bearing to the two angular contact bearings. Note that the angular contact bearing inner races are supported on a "zee" section spring diaphragm support. This provides some compliance between the inner and outer components as the mechanism goes to orbital temperatures where different material coefficients of thermal expansion (contraction) could cause additional bearing loads. The zee shape deflects sufficiently to maintain only a slight increase in bearing preload at the coldest orbital temperatures.

Bray Oil Co. wet lubricants, Brayco Micronic 815Z oil as well as their Braycote 3L-38RP (Braycote 601) grease are used to lubricate vital components within the mechanism, including the rotary drive actuator as well as the potentionmeter. The large angular contact bearings are lubricated with a solvent-thinned solution of the Braycote 3L-38RP grease (grease plating), then vacuum-baked, leaving a thin, evenly distributed film of the lubricant.

The passive hinge, Fig. 4, uses the same rotational bearing support, except for one additional feature: the 15-5 PH stainless steel stub shaft is permitted to slide along the axis of rotation of the inner race of the stainless steel spherical bearing. A groove is cut into the shaft, providing a reservoir for Braycote 3L-38RP grease. The sliding feature is important for the AD use of the mechanism since the active and passive hinges are approximately 147.3 cm (58 in.) apart and small temperature gradients between the large aluminum honeycomb door and the 3.05-m (10-ft)-diameter spacecraft structure change the width between the two hinge assemblies. The slip feature then accommodates this dimensional change.

Both active and passive hinge assemblies carry radial loads via the bearings; however, only the active hinge resists thrust bearing loads (parallel to hinge line), and they are carried out through a conical pin installed in the hinge support bracket and seated in the outer support tube of the mechanism.

HINGE MECHANISM OPERATION

The rotary drive actuator is a current-controlled device which also has its step rate (pulses per second), rotational angular travel (total steps), and direction of travel controlled. For the two deployment mechanisms described here, the actuator is driven at two rates, either 30 pulses per second (0.23 deg/sec), or 300 pulses per second (2.25 deg/sec), or a sequential combination of the two. The total travel angle in either use is less than one revolution; 92.7° to deploy/stow the HGA or 105.3° to open/close the AD. The electronic control unit commands the travel angle to the stepper motor via a predetermined number of steps which includes approximately 1000 more steps than are actually needed to reach the commanded position. This assures more than sufficient steps for any contingency.

The deployment sequence is initiated by driving the actuator at the desired stepping rate, which relieves a slight stowed preload in the torsion rod. With the preload relieved, the actuator begins winding up the torsion rod, which
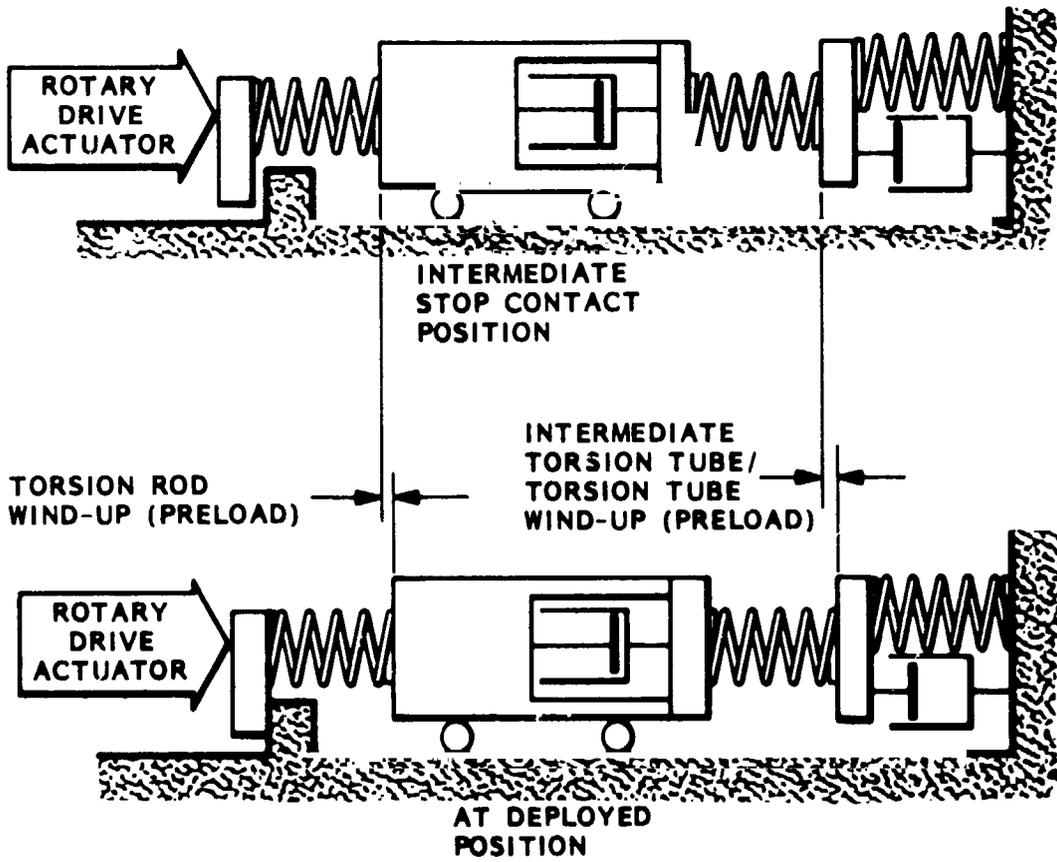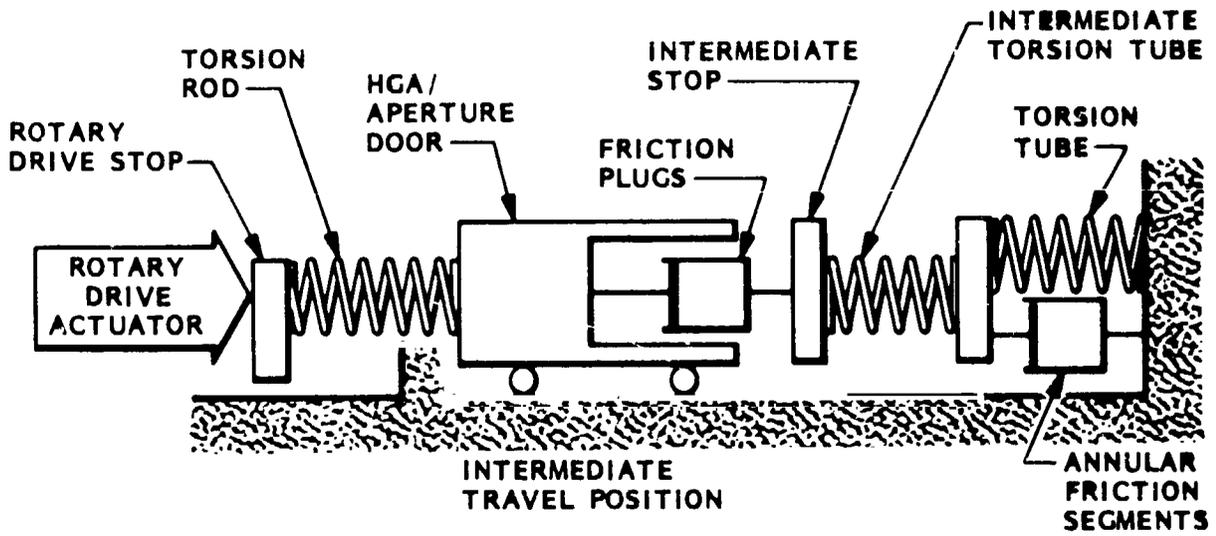
Figure 5. Mechanical Schematic.

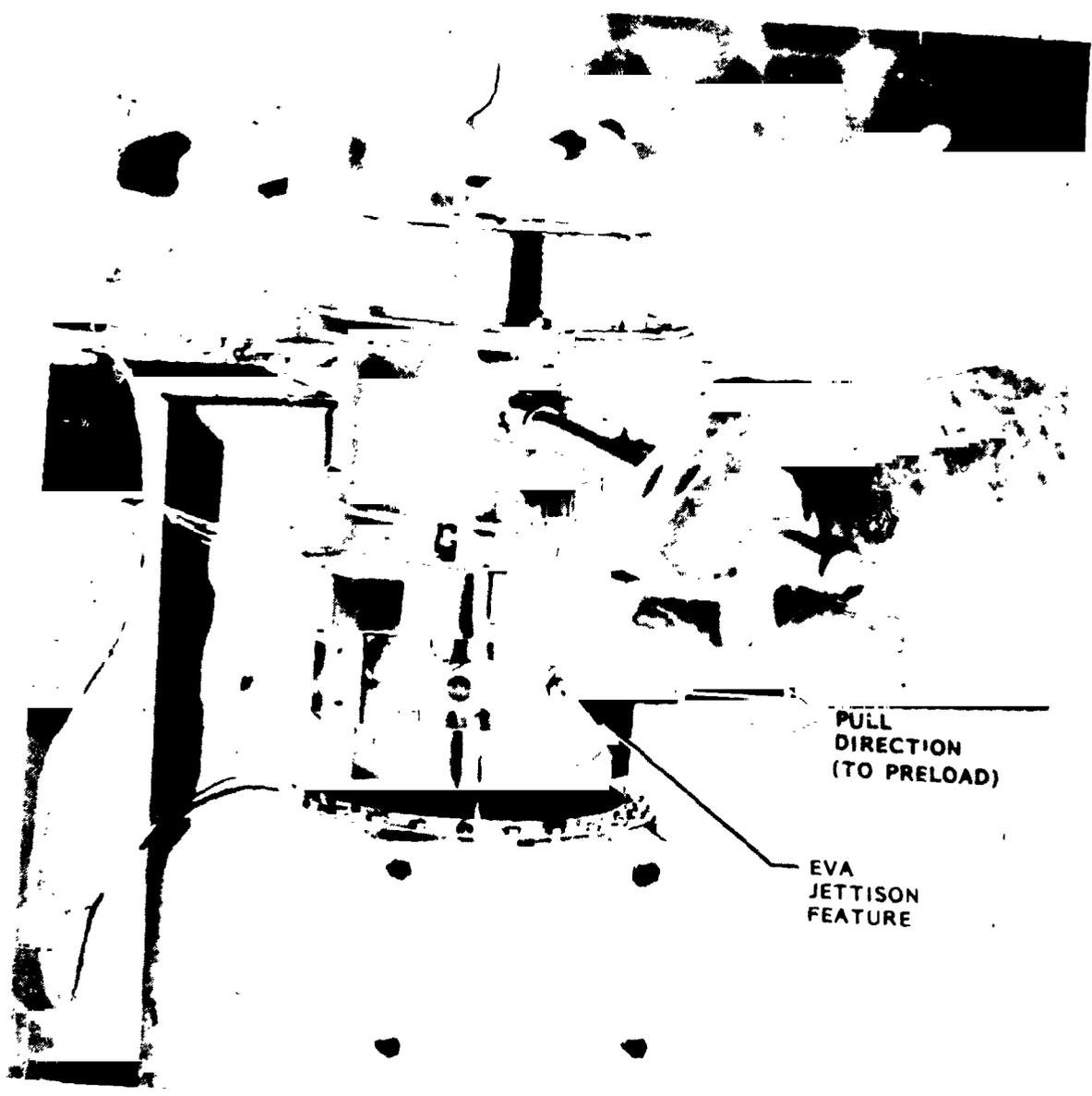PULL
DIRECTION
(TO PRELOAD)

EVA
JETTISON
FEATURE

Figure 6. Manually Preloading Mechanism.

337

soon overcomes bearing viscous friction and coulomb friction from the Delrin plugs and moves the outer bearing housing, which is connected to the appendage. During deployment, only viscous friction provides damping while coulomb damping is only effective when the mechanism is at or near its end-of-travel when motion direction may reverse. This occurs during the AD speed change and at intermediate stop contact.

Approximately 3 deg before the final open position in the AD deployment sequence only, the control electronics changes the actuator step rate from 2.25 deg/sec to 0.23 deg/sec. Motion continues until less than 1 deg from end-of-travel, when the stops on the moving domed cover contact the intermediate torsion rod and the torsion tube. The rotary drive actuator continues to drive, increasing the wind-up (load) in the torsion rod, intermediate torsion tube and the torsion tube until the adjustable actuator stop is contacted. The actuator stalls against the stop for the final 1000 steps.

This preload, amounting to 9.04 N·m (80 in.-lbs), ensures that the appendage stays in the deployed position despite small spacecraft maneuvers. The deployed position is depicted in the mechanical schematic, Fig. 5, which shows the appendage ultimately positioned between the small angular wind-up of the torsion rod and torsion tube. Unpowered magnetic detent of the rotary drive actuator provides greater than 22.6 N·m (200 in.-lbs) of resistive torque to maintain the preloaded position. The detent torque is developed by the permanent magnet 1.5 deg stepper motors within the actuator, and the torque is amplified by the 200:1 Harmonic Drive gearhead.

The stowing operation is the reverse of deployment, the primary difference being the absence of the domed cover stops, thus only the torsion rod winds up as the securing latches are contacted.

APPENDAGE SYSTEM OPERATION

Aperture Door

To protect the optics, the door must close within 60 seconds, it is moved at the higher step rate of 300 pulses per second (2.25 deg/sec). The sequence is to drive the 1164-N·m-sec^2 (97 slug-ft^2) door inertia through 102 deg of its 105.3 deg of total travel in approximately 47 secs, at which time the step rate is reduced to 30 pulses per second (0.23 deg/sec). At the point of speed change, the door has effectively blocked direct sunlight from shining down the optical aperture and may then close at the slower rate, reducing the end-of-travel impact dynamics. For system convenience, the AD is opened using the same operation used for closing the door - this means that only the direction of travel of the rotary drive actuator has to be changed.

High Gain Antenna

This appendage consists cf a 132-cm (52-in.)-diameter parabolic reflector which is pointed at a relay satellite by a two-axis gimbal subsystem. Thus in turn is attached to a 358-cm (141-in.)-long mast/rf waveguide support. The mast is then bolted directly to an adapter connecting both the active and passive ninge mechanisms, which are close to each other (Fig. 2). With the exception of the angle of travel, these are the identical components used in the AD deployment mechanism. Here the mechanism is deploying 2532 N·m-sec^2 (211 slug-ft^2) through an angle of 92.7 deg of total travel.

Because the two gimbals are low-output torque devices and are subject to disturbing torques (i.e., coming into or out of the stow position), they are powered to hold their zero position during appendage deployment or restowage. The slowest deploy/restow rate of 30 pulses per second (0.23 deg/sec) is used for the full travel of this mechanism, requiring over 7 min to deploy or restow the appendage.

DEVELOPMENT TESTING

Scope

All in-house development testing is now complete. Thermal testing consisted of testing to qualification levels of at least 16.6°C (30°F) lower and higher than wrst se predicted orbital temperatures. To validate the structural analysis, static and dynamic proof load tests were performed to 140% of design limit loads.

It should be noted that the bidirectional rotary drive actuator was the subject of thorough prototype, development and flight acceptance testing as part of the purchase subcontract. The testing by the supplier Schaeffer Magnetics, Inc., included thermal vacuum testing by driving an inertia simulator, at all step rates, through compliant elements simulating the torsion rod spring rate used in the mechanism. Although the actuator is thermostatically heater-controlled to operate at -34.4°C (-30°F) or above, it was operated successfully to as low as -73.3°C (-100°F).

The wire-wound potentiometer was also tested by its supplier, Spectrol Electronics Corp, to test levels well beyond its expected orbital requirements.

The in-house testing was conducted in three phases:

Phase I - Mechanism Characterization

o   Thermal vacuum testing of lubricated angular contact bearings and coulomb friction elements.

o   Thermal testing of the self-lubricated (low friction liner) spherical bearing and determination of parasitic torque characteristics of the electrical cable and rf coax. The cables are required to bend as the HGA mechanism rotates.

Phase II - Hinge Mechanism Operation

o   Thermal testing of the mechanism with an inertia simulator driven
    through full travel at the two deploy/stow rates, 2.25 deg/sec and
    0.23 deg/sec.

o   Static proof load testing (1.4 times design limit load) simultaneously
    applied normal and parallel to the mechanism rotation axis.

o   Dynamic inertia proof load testing (1.4 times the design limit load).

o   Random vibration of the mechanism in three axes for 1 min in each axis.

o   Deployed mechanism natural frequency verification.

Phase III - Subsystem Testing

o   Subsystem operation at ambient conditions - approaching and leaving
    securing latches and preloading at the deployed position.

o   Flightcrew member interface verification; manual operation of
    mechanism, including appendage jettison features.

o   Compatibility verification of mechanism and flight bre;dboard
    electronics.

o   Evaluation, using flight two-axis gimbals, of the solution to a
    line-of-sight jitter problem with the pointing and control of the HGA.

o   Demonstrate at least 77 mechanism operations to verify the life
    requirement.

TESTING RESULTS - PROBLEMS IDENTIFIED

Phase I - Mechanism Characterization

Key testing in this phase involved nonpowered motion study of the principal
mechanism elements at vacuum and cold temperatures. The friction damping
elements used to decrease oscillations during speed changes or change of
direction proved to be within 5-10% of the desired damping range.

Problem 1: The spacecraft's thermal control system was based on biasing
temperatures toward the colder regimes to reduce thermal gradients. Because of
this, initial predicted AD mechanism temperatures could be well below -87.2°C
(-125°F). This proved to be a problem for the grease plating of Braycote
3L-38RP on the angular contact bearings. The solidification temperature of
this lubricant is near -84.4°C (-120°F). The resulting "stiffness" of the
lubricant caused unacceptably high bearing torques even though the mechanism
would operate to as low as -107°C (-160°F). Because the Braycote lubricant has
low outgassing characteristics (a particularly attractive feature for an
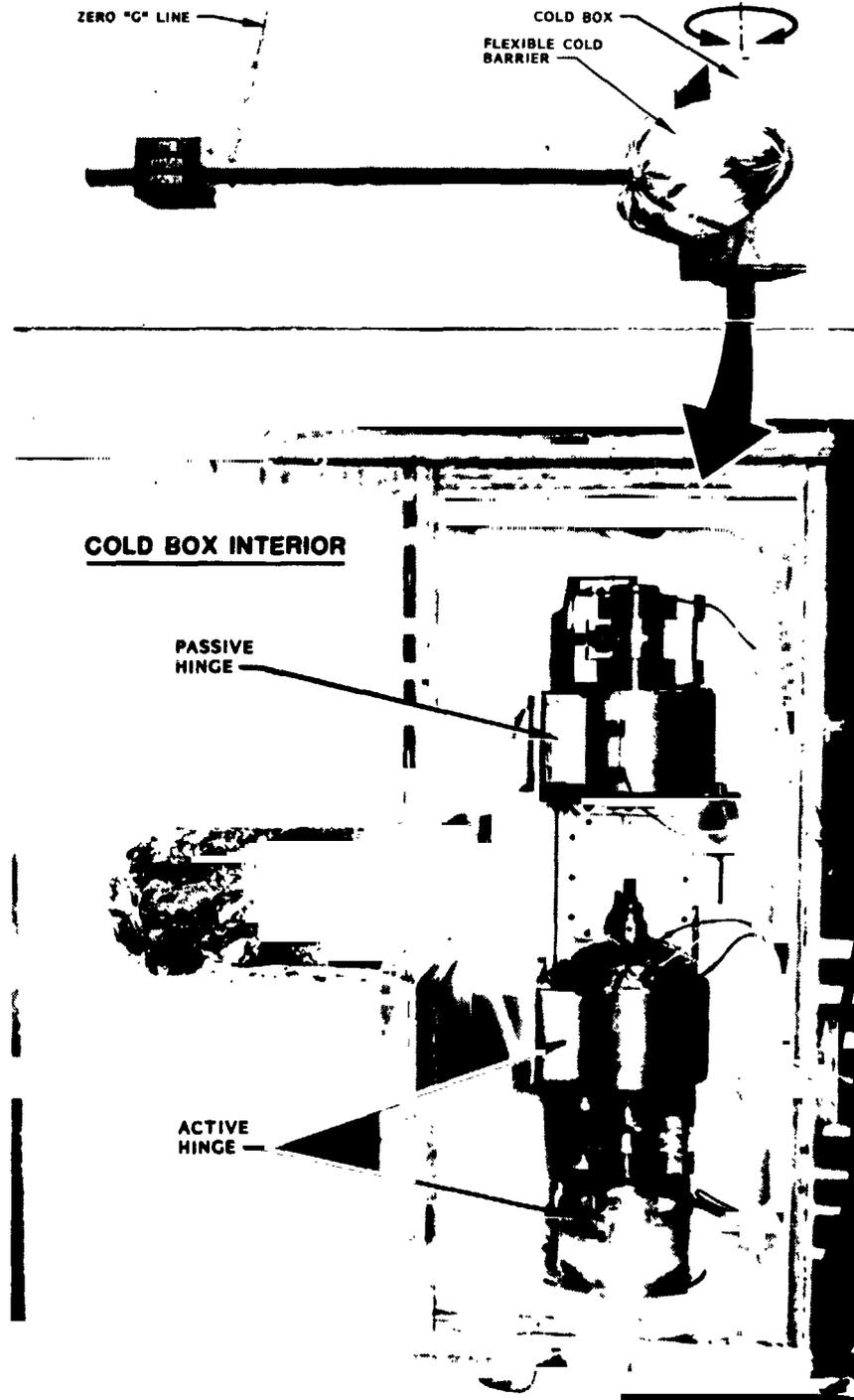
340

Figure 7. Hinge Operation with Cold Box.

341

ANTENNA MASS SIMULATOR ——

GIMBAL MASS SIMULATOR

STOWED
SECURING
LATCHES

DEPLOYMENT
HINGE
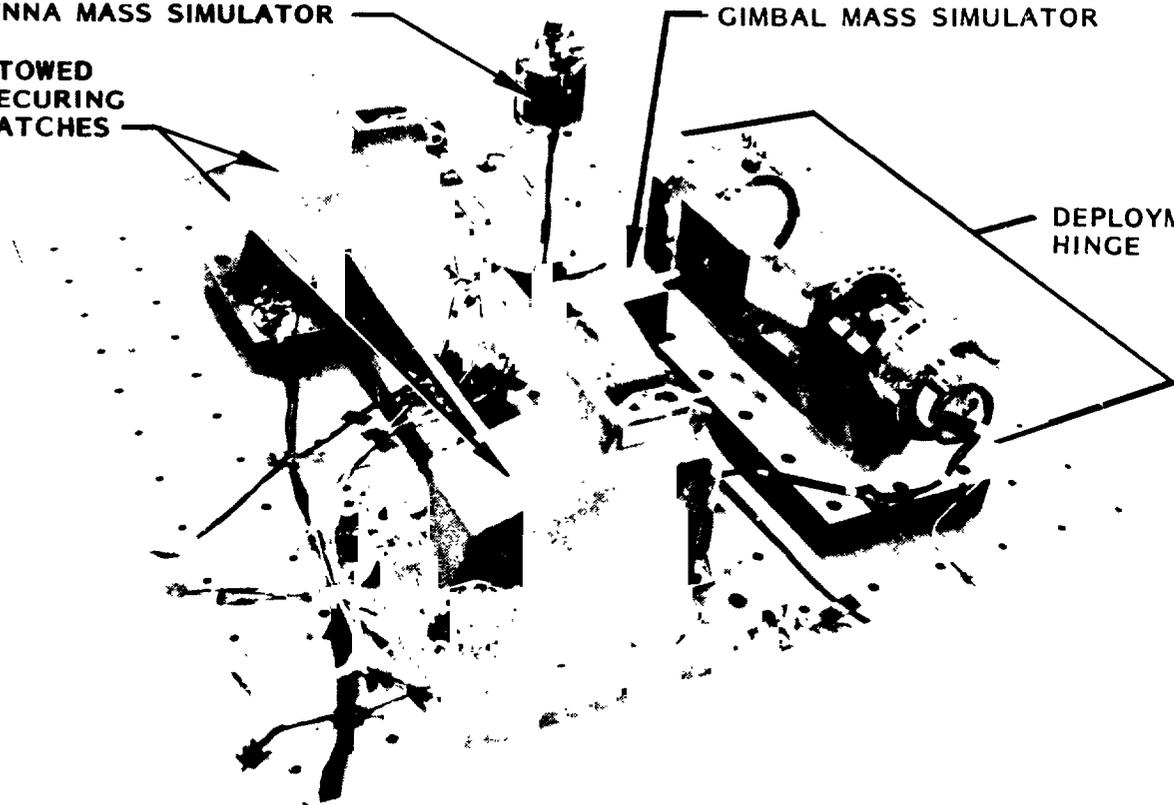
342

Figure 8.   Vibration Test Setup.

ANTENNA DISH
SIMULATOR

ZERO "G" LINE

DEPLOYMENT
HINGE

WAVE GUIDE
MAST

TWO AXIS
GIMBAL
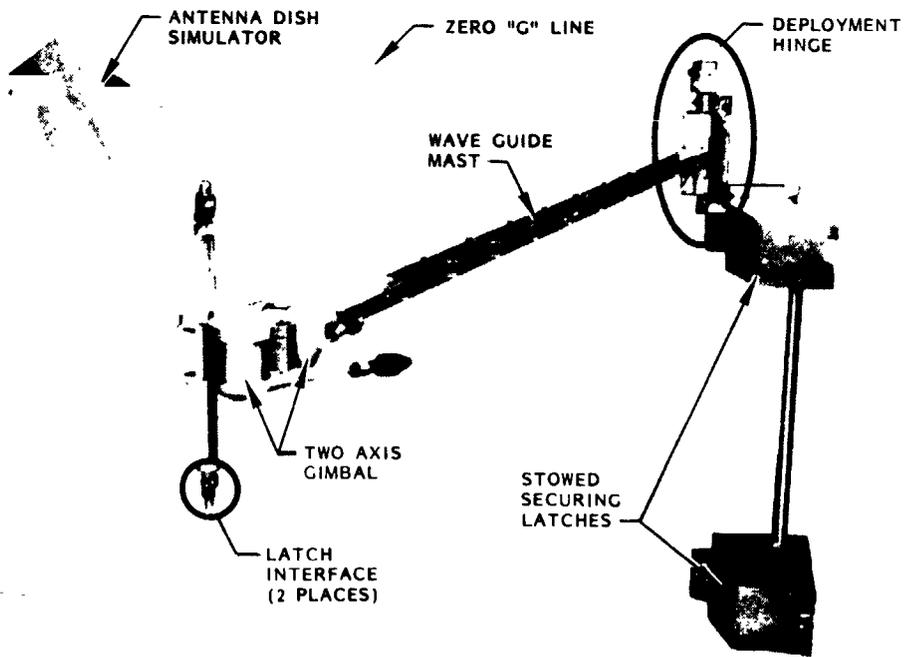
STOWED
SECURING
LATCHES

LATCH
INTERFACE
(2 PLACES)

Figure 9.   HGA Appendage Test Setup.

343

optical system) and because of a desire to avoid a lengthy lubrication
development program, heaters capable of keeping the mechanism at a temperature
of -62.2°C (-80°F) or above were installed to solve the problem. The addition
of heaters to both the active and passive hinge mechanisms for the AD assured
consistent operation for this important appendage. The HGA mechanism is not
fitted with heaters (other than the one on the rotary drive actuator) since
predicted cold operation is -47.2°C (-53°F) or above.

Thermal testing of the self-aligning spherical bearing was needed since
(1) it is the redundant rotational feature to the angular contact bearings and
(2) no cold-test data were available from the supplier. The cold-testing
results were acceptable and the bearing torque contribution was factored into
the overall mechanism torque margin.

Likewise, a cold test of the HGA power and TLM data cable, routed across
the mechanism along with the rf coax from the mast/waveguide, showed
acceptable parasitic torque contributions. This series of tests sensed the
torque contribution of the cable routing, as a function of temperature, over
the full angular travel range of the mechanism.

Phase II - Hinge Mechanism Operation

This series of tests involved mechanism operation over the full range of travel
at hot and cold temperatures and with the test specimen connected to inertia
simulators representing both the HGA and the AD. The mechanism rotational axis
was mounted vertically and the additional weight was supported by a zero "G"
line pivoting in line with the mechanism rotational centerline. A cold box was
constructed around the mechanism (Fig. 7); the rotary drive actuator was kept
outside the test environment so the mechanism operation contributors could be
identified directly.

This test phase permitted verification of the analytical model as well as
providing a test bed for a two-axis, static-proof test and a deploy-direction,
dynamic-proof test. These tests at ambient temperature were preceded and
followed by functional operation and no anomalies were identified.

The deployed and preloaded natural-mode frequency of the mechanism was
verified during this test phase to be 0.875 Hz, below the 1.0-Hz maximum.

The deployed or open position of the mechanism was also verified during
this test phase and was shown to be repeatable within 0.033 deg, well within
the AD position accuracy needed of $\pm$0.25 deg.

The final phase of this test series centered on a three-axis vibration test
using the mechanism configured for the HGA usage (Fig. 8). The mechanism was
connected via a short tube to a pivoted mass simulating one of the two-axis

gimbals. The assembly was then secured by flight-like development latches. The antenna dish was also represented by a mass simulator. The rotary drive actuator was monitored during the test to sense unacceptable mechanism motion and none was detected during all three orientations of the vibration test. An ambient functional test, performed after each axis was tested, revealed no damage to the mechanism.

Phase III - Subsystem Testing

This test phase addressed, in particular, the HGA configuration and its deployment and restow. Figure 9 shows this setup which included the preproduction mast/waveguide, a foam-core simulation of the antenna dish, and the pair of securing latches. The configuration was initially fitted with nonpowered gimbal simulators; these were later replaced with flight gimbals for the last segment of this test phase.

Problem 2: The first portion of this test sequence was plagued by a problem that was finally diagnosed as "lost motion", which resulted in variable performance at the stow position. As the mechanism drives into the stow position, it must be positioned correctly for the latches to "capture" and secure the appendage. This involves also tripping four telemetry switches which indicate to the ground station when the latches may be closed, a separate operation. Although always within latch "capture" range, the inconsistant performance needed correcting.

"Play" in the keyway tying the torsion rod to the domed aluminum cover was determined to be the cause, and once corrected by small shims in the keyway, consistent and reliable results were demonstrated. A redesign, however, was initiated to effect a long-term solution to compression yielding of the aluminum portion of the cover interface brought on by numerous manual deployments and stowings. The solution selected was to provide a conical or tapered fit-up of the 15-5 Ph stainless steel torsion rod to the aluminum domed housing. The tight friction fit in conjunction with the keyway assures a "no-lash" joint. (See Reference 1 for an in-depth discussion of this design feature.)

Because the Hubble Space Telescope is designed to be compatible with the Shuttle crew members, it was important to demonstrate and verify crew member interfaces, including manual deployment and resto/ of the appendages. Two crew member foot restraints are located to permit lifting or pulling on the long mast/waveguide for manual deployment or stowage. If a jettison of the appendage should be required, one crew member must first disconnect the wing tab electrical harness connectors, then back off the two bolts securing the jettison clamp-halves, while another crew member pushes the appendage away from the spacecraft. All of these interfaces were verified and were shown to function satisfactorily.

345

During this test, the flight breadboard mechanism drive electronics became available and this interface was also successfully validated. A specifically built drive electronics panel is normally used for development testing and has faithfully represented the interface as confirmed by the breadboard check.

The final portion of testing was to fit a flight pair of gimbals to the HGA appendage to validate a solution to a control problem in pointing the antennas at the relay satellite. Testing with fullypowered and computer-controlled gimbals did confirm the design solution which involved counterbalancing the offset mass of the antenna dish about the outboard gimbal rotation axis (Fig. 9). Additionally, with the fully powered gimbals, it was feasible to demonstrate a simulated on-orbit deployment and restowage.

One final note to the total tests completed in the various environments: a 70% life margin was demonstrated for the mechanism and, other than the problems noted, partial disassembly has revealed no areas of concern.

TESTING STATUS

All development testing to qualification temperature and load levels has been successfully completed. Acceptance testing of the three flight hinge mechanisms is scheduled for the first quarter of 1985. Detail fabrication and assembly is complete.

Future system-level testing, will include functional demonstrations before and after an acoustic test and during a month-long thermal vacuum test.

CONCLUSIONS

A deployment mechanism has been designed, tested and has demonstrated its versatility to move two large appendages, one twice the inertia of the other and one deployed at an angular rate 10 times that of the other, with a common design utilizing a single rotary drive actuator. Two significant design problems have been overcome with minimum disruption to the program in terms of cost and schedule.

ACKNOWLEDGEMENT

REFERENCE

1. Angle, Thomas L., "Analyzing Taper Fits", Machine Design, February 24, 1983, Vol. 55, No. 4.

SIX MECHANISMS USED ON THE SSM/I RADIOMETER

Howard R. Ludwig[*]

ABSTRACT

Future USAF Block 5D Defense Meteorological Satellites will carry a scanning microwave radiometer sensor known as SSM/I. SSM.I senses the emission of microwave energy and returns to earth data used to determine weather conditions, such as rainfall rates, soil moisture, and oceanic wind speed.

The overall design of the SSM/I radiometer was largely influenced by the mechanisms. The radiometer was designed to be stowed in a cavity on the existing spacecraft. The deployment of the sensor is complex due to the constraint of this cavity and the need for precision in the deployment. The radiometer will continuously rotate, instead of oscillate, creating the need for a bearing and power transfer assembly (BAPTA) and a momentum compensation device. The six mechanisms developed for this program are described in this paper.

1. INTRODUCTION

Future spacecraft of the USAF Defense Meteorological Satellite Program (DMSP) will carry a passive microwave radiometric system known as the special sensor microwave/imager (SSM/I). It is a seven channel, four frequency, linearly polarized, passive system. The SSM/I measures ocean, atmospheric, and land surface brightness temperatures. The Air Force Air Weather Service and the Naval Oceanography Command will process these data to obtain precipitation maps, oceanic wind speed, sea ice morphology, and soil moisture percentage. Figure 1 illustrates the SSM/I integrated into the DMSP satellite.

2. SSM/I OVERALL MECHANICAL DESIGN

The existing DMSP Block 5 spacecraft had only two possible locations to stow the sensor. Potential designs were made to use these locations. For each of these designs, mechanisms were selected. The final selection was based on an efficient, low-risk system. Figure 2 illustrates the selected sensor in stowed and deployed configurations. The mechanisms had a major influence in the overall design of the sensor. These account for approximately 30 percent of the weight of the SSM/I. The stowed volume is approximately 20 percent of the deployed on-orbit swept volume.

One of the major decisions was in the manner of scanning. It was decided to continuously rotate the sensor at 31.6 rpm to provide 103° of uninterrupted earth scan. As the sensor rotates beyond this range, the sensor passes a hot load and a cold space reflector that calibrate the sensor. This method is more efficient and accurate than a back and forth or oscillating reflector. Continuous rotation of the sensor adds uncompensated momentum to the

[*] Hughes Aircraft Company, El Segundo, California

spacecraft. Previous studies (Ref. 1) suggested use of gear or belt driven counterrotating masses to compensate for sensor momentum. A trade-off study for providing compensating momentum determined that an existing momentum wheel would be more reliable and efficient than the previously proposed devices. Developing a geared or belted system for a 3-4 year life was felt to be too risky. The momentum wheel could be located in a separate compartment of the spacecraft to help its balance and not take up volume in the location chosen for the sensor.

Deployment of the SSM/I is unique. First, the whole sensor is deployed from the spacecraft. The reflector is then released and rotated 170° by the reflector deployment mechanism. At that point a four-bar linkage is engaged which translates the reflector into its final location (Figure 3). This sequence does not interfere with the view of the DMSP's other sensors. Six mechanisms are used on the SSM/I: bearing and power transfer assembly, momentum wheel, three deployment mechanisms, and pyrotechnic devices.

3. MECHANISMS

3.1 Tribological Design

In the design of mechanisms there are two general philosophies (usually unstated) on the tribological aspects. One is to perform the electrical and mechanical designs and to then add the lubrication method. The other approach, and the one used on the SSM/I mechanisms, is to consider the tribological aspects of the design from inception. The general type of lubrication is chosen early in the design, and compatible materials are selected. The final lubricant is based on requirements such as temperature, load, and speed.

3.2 Bearing and Power Transfer Assembly

Continuous rotation of the SSM/I sensor is provided by the BAPTA (Figure 4). The BAPTA developed for this program has some unique features, but it was based on existing technologies. The BAPTA provides rotating mechanical and electrical interfaces between the spinning and stationary sections of the sensor. The physical characteristics are shown in Table 1.

The tribological design of the SSM/I BAPTA uses state of the art technology. A pair of CEVM 440C angular contact bearings with patented nitrileacrylic copolymer retainers (Refs. 2-3), in an open cell configuration, are used. Stainless steel sideplates provide the required mechanical stiffness and strength. The copolymer material has a large capacity for oil storage (Figure 5).

Each bearing is lubricated with HMS 20-1727 oil, which is a highly refined, low vapor pressure, mineral oil with a 5 percent lead naphthanate extreme pressure additive. The nitrile-acrylic copolymer with this oil is now at the 9 year mark in a continuing life test and has been successfully flown on the Pioneer Venus, GMS II, and GOES programs.

348

The electrical power and signal transfers are through slip rings made of silver and brushes of a self-lubricating material made of 85 percent silver, 3 percent graphite, and 12 percent molybdenum disulfide. Based on the wear rate from a 10 year life test, these brushes will last more than 100 years.

3.3 Deployment Mechanisms

3.3.1 General Design Philosophy.

There are two general approaches to the design of spring-driven deployment mechanisms for delicate appendages or devices that have to point precisely. One method is to use a deployment spring that is only slightly stronger than the resistive torque. This is done to avoid shock damage at the end of stroke. A great deal of testing and adjustments are usually associated with this approach. The second approach is to employ very large torque margins and to rate-limit the deployment. This is accomplished by viscous or eddy current damping. The bottom line of the trade-off study indicates that the high torque margin rate limited method is more reliable and easier to test at the expense of weight. Although the simple spring mechanism is less costly as a unit, the overall cost is usually higher due to the complexity of testing and need for exotic offloaders for system level testing.

The use of the high torque margin was chose for SSM/I so that there would be no risk of a failure to deploy. Additionally, all tests were performed in 1G without offloaders. This was accomplished by mounting the sensor with the deployment hinge in line with the gravity vector for each deployment.

3.3.2 Viscous Damping.

The deployment mechanisms for SSM/I are multispeed. There was a system requirement that all deployments be made in a 10 minute period and also a self-imposed rate requirement to keep the precision and repeatability. The two were not compatible with a single speed device. In order to make the mechanism multispeed, the damping gap is varied. The radiometer deployment mechanism (RDM) has two speeds and the antenna deployment mechanism (ADM) has four speeds (two fast and two slow) to meet the time requirement at cold condition.

The two main deployment mechanisms for SSM/I are rotary viscous damped. These devices combined the features of the pivot hinge and bearings, deployment springs, viscous damper, and hard stops into one unit. The mechanisms are powered by redundant laminated spring sets. They feature redundant spring-loaded tapered latch pins to provide a positive lock at latch-up and adjustable hard stops to ensure positioning accuracy. These actuator designs have evolved from the basic JPL concept originally developed for Mariner '71 and Viking Orbiter to their current compact third generation design (Ref. 4).

The actuator mechanism consists of a housing, two end plates containing O-ring seals, and a stator shaft with integral damping paddles. These are all made of aluminum. A take-up reel is provided for the deployment springs. The dimethyl silicone fluid of 0.1 m^2/s kinematic viscosity provides damping. A reservoir compensates for the change of fluid volume with temperature. Figure 6 is a cutaway view of an actuator.

Double paddle wheels are used for deployment angles less than 130° and a single paddle is used for angles greater than 130°. The nousing rotates about the slator shaft. Torque is supplied by the constant torque deployment springs. Damping is provided by flow of the damper fluid from the high pressure side of each paddle, through the gaps between each paddle and the housing, into the low pressure side. The majority of the damping comes from the flow of fluid through these orifices (the gap between each paddle and the housing), while the remainder is due to viscous shear.

The main pivot ball bearings are selected to provide proper stiffness and strength. Lubrication of the deployment devices is a combination of wet and dry. The main bearings are in the silicone fluid. The laminated springs, take-up reel bearings, and latch pins are lubricated with sputtered MoS_2 (Ref. 5). The tips of the latch pins are made of a self-lubricating plastic material.

3.3.3 Radiometer Deployment Mechanism. Deployment of the SSM/I radiometer from the stowed position is accomplished by the RDM. The pyrotechnic devices at the base plate are fired, releasing the radiometer. The RDM rotates the sensor 90° about the deployment axis, bringing the BAPTA spin axis parallel to the local vertical. Tapered latch pins drop into place to brace the radiometer in the deployed position. Completion of the deployment is indicated by a normally closed microswitch which opens as the latch pin drops into place. Adjustable hard stops control the deployment angle and repeatability of the deployment angle. Figure 7 shows the RDM. As can be seen, the mounting base for the radiometer was made integral with the RDM. Table 2 provides test results for the engineering, qualification, and the first flight models. Figure 8 shows a typical deployment angle versus time plot for the RDM. As can be seen, the first (70°) is at a rate of 0.4 rad/s and the last (20°) at a rate of 0.04 rad/s.

3.3.4 Antenna Deployment Mechanism. After the radiometer has been deployed from the spacecraft, the antenna is released by firing another set of pyrotechnic devices. The antenna is then driven 170° about the first antenna deployment axis by the deployment springs. As the antenna reaches this fully extended position, a four-bar linkage is engaged. The antenna is then translated into the operating position. Again, tapered latch pins are engaged and microswitches are closed to indicate latch-up (Figure 3). The deployment scheme is a result of a customer imposed requirement that other sensors on the spacecraft not have their fields of view obscured by SSM/I during its deployment. Table 3 summarizes the test results.

3.3.5 Bias Momentum Wheel Assembly. The specification for the SSM/I radiometer required no unbiased momentum from the radiometer system. The choice of using a continuously rotating antenna, together with the unbiased momentum specification, led to incorporating a bias momentum wheel into the design.

The momentum compensation system, an independent open loom momentum wheel and a continuously rotating radiometer, was compared with mechanically coupled momentum wheels through gear or belt drives. These alternatives were eliminated as a result of radiometer jitter caused by the coupling system, dry lubricant life limitations, and volume constraints. Gear or belt drive linking the radiometer to the compensation wheel would feed back any jitter to the radiometer spin control loop inducing rate errors. It would also result in an excessive weight penalty (for gear ratios near unity) or excessive number of revolutions of the compensation wheel (for gear ratios of 50 or more). Dry film gear lubricant is not compatible with a 3-4 year life requirement. Wet lubrication could be employed, but would require an additional sealed housing, adding complexity and weight. Other self-lubricating gear materials would require extensive development and life testing. Belt drives similar to those used on JPL designed radiometers were considered, but again additional development/life testing would be necessary to meet reliability requirements. Discussions with other aerospace company personnel have indicated the critical nature of belt drive details to reliability. It was unlikely that a belt drive system development program could be satisfactorily accomplished during the 14 month SSM/I development period.

The momentum required to compensate for the SSM/I in nominally 3.0 N · m. There were several commercial momentum wheels in this size range. The final momentum specified can be adjusted over the range of 2.75 to 4.25 N · m in 205 increments by final adjustment of the drive electronics. The desired speed of the momentum wheel is programmed by using 10 jumpers on a programming connector plug. This system allows final selection and momentum adjustments to match the momentum of the radiometer as the two are integrated. Table 4 indicates the characteristics of the momentum wheel, and Figure 9 shows the momentum wheel with its drive electronics.

3.4 Simple Deployments

When precision pointing or end of stroke shock are not important, simple undamped deployments are ample. The fact that a deployment is without rate control does not mean that the details of design and lubrication are not important. The materials should be selected with lubrication in mind and the drive springs should be redundant. In the case of SSM/I, there are two such deployments.

3.4.1 Lubrication Aspects. The general lubrication technique used on simple deployment mechanisms is to choose shaft and bushing or pivot materials that will not gall. For example, a hard stainless steel pin and a hard anodized aluminum bearing have to be used on most of the SSM/I pivot joints. All rubbing surfaces and springs are then sputtered with MOS_2 to give a low coefficient of friction. This combination of materials and lubricants has been reliable and trouble-free throughout the development and hardware programs.

3.4.2 Launch Support Bracket Deployment. The SSM/I antenna is held in the stowed position with a pyrotechnic device. The launch support bracket is a swing-away structural member. The loads from the antenna are passed through this bracket into the radiometer structure. Upon firing the pin pullers, the launch support bracket pivots 135° and is held in place by the redundant deployment springs. The springs and part of the bracket can be seen in Figure 10.

3.4.3 Cold Sky Reflector Deployment. The SSM/I radiometer is calibrated each revolution. An ambient hot load and reflected cold space are viewed by the sensor each revolution. The cold sky reflector can be seen in Figure 10. It is the small reflector on the top surface of the sensor body. During launch it is stowed under the larger antenna. It is kept from deploying by a strip of self-lubricating plastic material attached to the back of the main reflector. As the main reflector deploys approximately 45°, the cold sky reflector is no longer restrained and rapidly rotates to its deployed position.

3.5 Pyrotechnic Release Devices

The selection of pyrotechnic release device types is dictated by locations and mass properties of the items to be released and the amount of preloading required. For SSM/I an additional requirement of pyrotechnic redundance was specified.

The SSM/I is secured to its base plate by two independent redundant pyro lock systems, and is preloaded against four posts attached to the spacecraft interface mounting plate (Figure 11). Launch locking in this fashion provides two distinct advantages. First, pulling down the spinning portion of the sensor against the base provides rigid nesting without carrying undue loads through the radiometer deployment mechanism bearings of the BAPTA bearings. Second, the launch loads, spread over a large area of the spacecraft panel, place no local moment loading on this panel.

The two pyro systems with redundancy provisions have been fully qualified and flown on the NASA Pioneer Venus program. The same hardware was used. Redundant pint pullers tie down a "whiffle tree" fitting so that retraction of either pin will release the load. The pins are in double shear. With this dual system, retraction of either pin in each of the two circuits will deploy the radiometer.

The antenna lock system uses the same hardware as the has lock system, except that two whiffle trees are in the double shear clevis to effect a dual element release. The antenna support arm is locked to the support arm as shown in Figure 10. Both of these elements are independently preloaded to achieve an overall rigid system.

There were two structural failures during development test in the launch restraint devices. The whiffle tree pivots failed structurally under the 454 kg load. The whiffle tree material was then changed from aluminum to stainless steel. The second failure occurred when the bracket holding the pin pullers on the antenna support arm broke off as the pin pullers were fired. It was theorized that the shock load caused by the pistons in the pin pullers pulled the bonded-on bracket loose. This bracket was redesigned to be a bolted-on bracket. After these two redesigns were made, no further failures occurred.

4. CONCLUSION

Six mechanisms were successfully designed, developed, and qualified for the SSM/I radiometer. The major accomplishment was in the successful development of high precision, repeatable, multispeed deployment mechanisms.

5. REFERENCES

1. NASA-CR-144853, "Scanning Mechanism Study for Multi-Frequency Microwave Radiometers," General Electric Company.

2. Christy, R. I., "Evaluation of a Nitrile Acrylic Copolymer As A Ball Bearing Retainer," ASLE preprint 74 AM5A-1, 1974.

3. U.S. Patent 4,226,484 (1980), Bearing Retainer.

4. JPL Drawing Package, Deploy/Damper/Latch Assembly Solar Panel 10040060, Rev D, 1972.

5. Christy, R.I. and Ludwig, H.R., "RF Sputtered MoS_2 Parameter Effect on Wear Life" Thin Solid Films, 64 (1979) 223-229.

Table 1. BAPTA Characteristics

Weight	9.1 kg
Dimensions	19.4 cm max OD x 27.5 cm length
Bearings	
Type	Angular contact
Size	60 mm bore
Class	ABEC Class 9
Material	CRES type 440C CEVM
Lubricant	HMS 20-1727
Retainer	Nitrile-acrylic copolymer
Slip Rings	
Power rings	4 ea
Power circuits	2 ea
Circuit capacity	1.5 A
Brushes per power ring	4 ea
Current density	$700 \ A/m^2$ (2 brush contact)
Signal rings	36 ea
Brushes per signal ring	2 ea
Ring material	Silver
Brush material	85% Ag, 3% C, 12% MoS_2
Lubricant	MoS_2 in brushes
Pulse Generators	
Master	1 pulse per revolution
Encoder	45 pulses per revolution
Motor	
Type	Brushless dc resolver commutated
Torque constant	0.1100 Mkg/A
Winding resistance	15Ω
Back EMF	0.983 V/rad/sec

354

Table 2. RDM Test Results

Parameter	Requirement	Model		
		Engineering	Qualification	Flight
Repeatability, °	±0.05	+0.0003 -0.00015	+0.001 -0.000	+0.003 -0.000
Spring torque, N · m	11 to 12	11.08	11.0	11.8
Torque margin, %	400	433	636	585
Deployment time, s	4 to 80			
22°C		15.7	9.2	8.0
-34°C		50.0	42	17.0 at -11°C
71°C		7.1	4.1	5.6 at 41°C

Table 3. ADM Test Results

Parameter	Requirement	Model	
		Qualification	Flight
Repeatability, °	±0.04	+0.00 -0.02	+0.00 -0.01
Spring torque, N · m	3	3.6	4.3
Torque margin, %	200	329	215
Deployment time, s	<161		
22°C		17.8	29.0
-32°C		89.0	118.5
69°C		10.0	16.8
Deployment rate into stop, °/s	<10	3.3	4.9

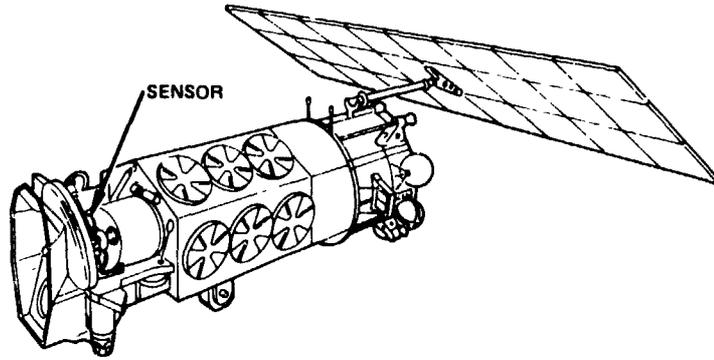Table 4. SSM/I Momentum Wheel Design Data

Unit angular momentum	3.0 N · m at 1300 rpm
Unit weight	5.5 kg without electronics
Rotor inertia	0.022 kg · m^2
Rotating weight	3.64 kg
Rotor diameter	18 cm
Envelope dimensions	20 cm dia by 28.5 cm high excluding mounting feet and connector
Spin motor type	AC squirrel cage induction
Synchronous speed	2400 rpm (theoretical) at 400 Hz
Unit internal atmosphere	98% HE, 2% O$_2$, 50% ATM
Friction and windage torque	58 gm · cm at 1400 rpm
Bearing type	Deep groove R8, double shielded
Lubrication type and quantity	MIL-L-6085A, +5% TCP, 20 to 25 mg
Tachometer type	Permanent magnet pulse Generator - 12 pulses/rev

356

Figure 1. DMSP satellite with SSM/I

SENSOR

a) Stowed
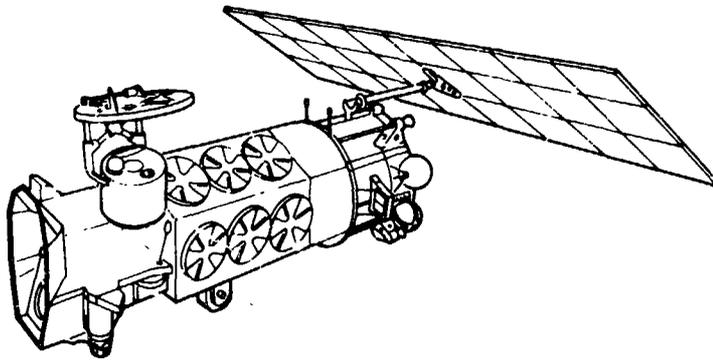
b) Deployed

Figure 2. Sensor location

a) Instrument pivoting   b) Antenna reflector rotation   c) Antenna reflector translation
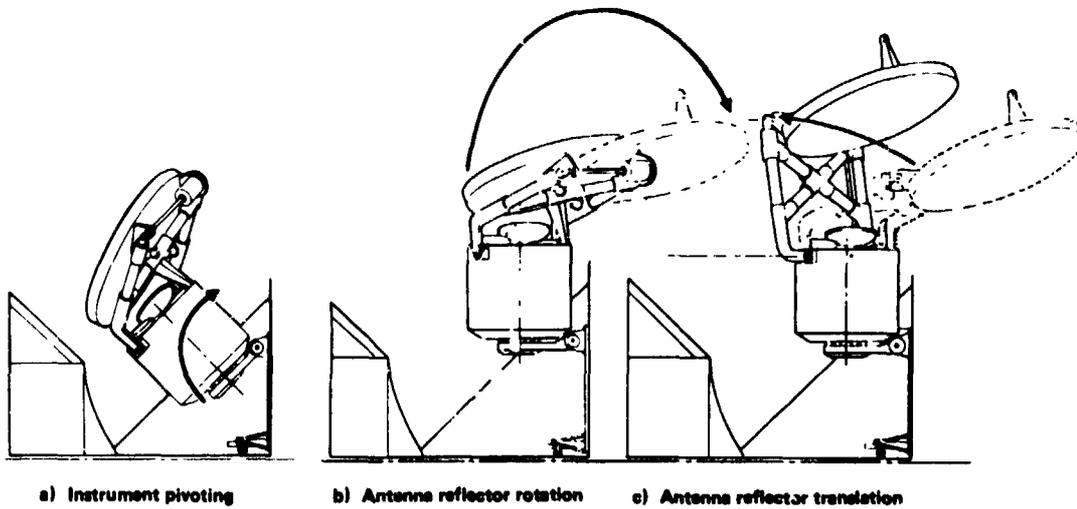
Figure 3. Deployment sequence

358
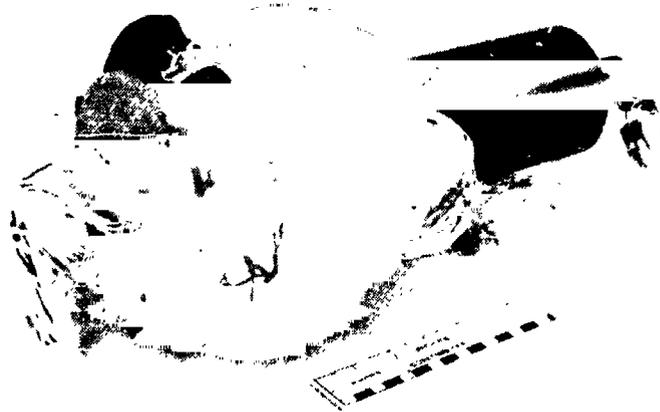
Figure 4. SSM/I BAPTA

Figure 5. Retainer lubricant capacity

CONTROLLED GAP   HOUSING

CAVITY FILLED WITH
0.1 m²/s
VISCOSITY CIL
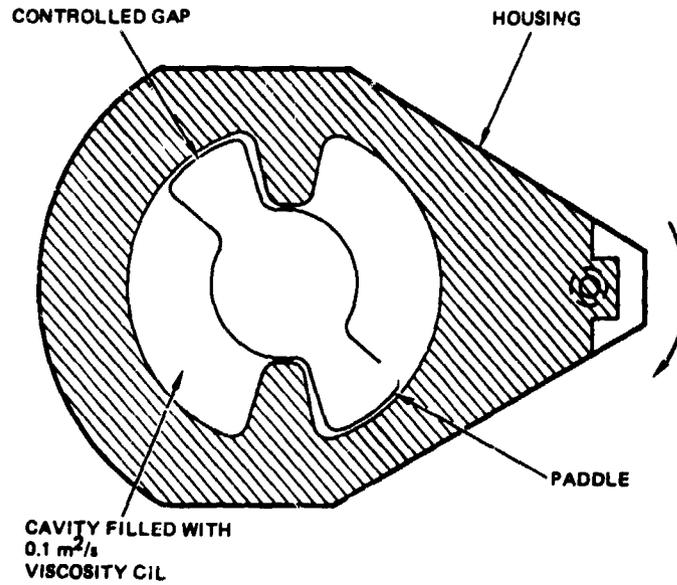
PADDLE

- PADDLE IS PINNED TO SUPPORT STRUCTURE
- HOUSING ROTATES WITH RESPECT TO PADDLE
- FLUID IS FORCED THROUGH CONTROLLED GAPS

Figure 6. Deployment mechanism cross section

Figure 7. Radiometer deployment mechanism

360
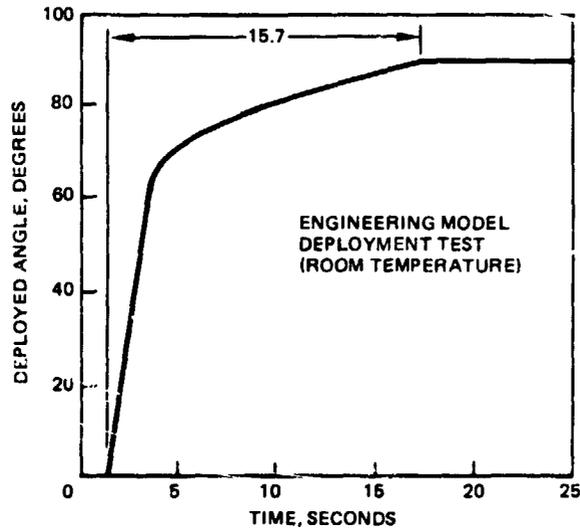
Figure 8. RDM deployment angle versus time

Figure 9. Momemtum wheel assembly and drive electronics
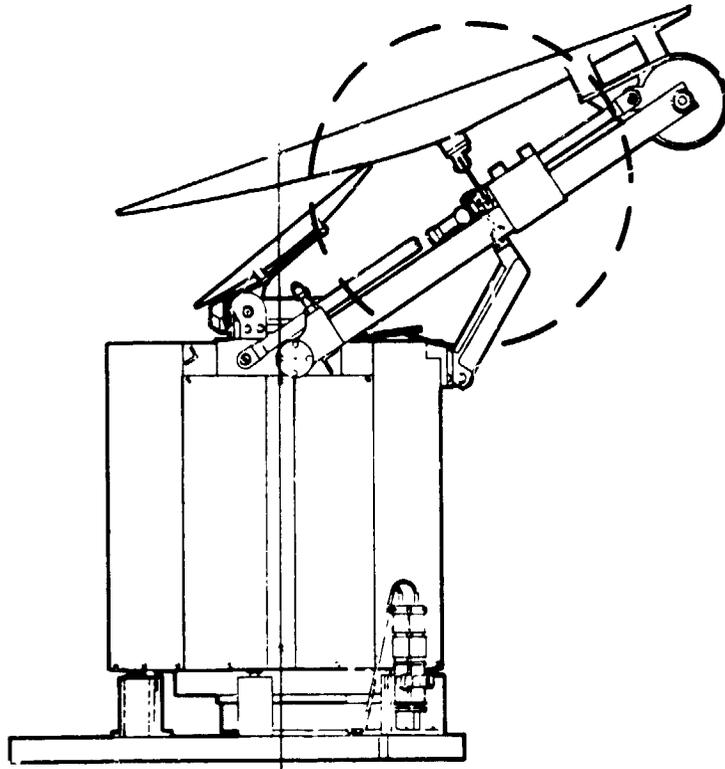
Figure 10. Launch support bracket deployment

Figure 11. Base launch lock system

362

CIRCULATION CONTROL LIFT GENERATION EXPERIMENT:
HARDWARE DEVELOPMENT

Tina L. Panontin*

ABSTRACT

A circulation control airfoil and its accompanying hardware have been developed to allow the investigation of lift generation that is independent of airfoil angle of attack and relative flow velocity. The test equipment, designed for use in a water tunnel, includes the blown airfoil, the support systems for both flow visualization and airfoil load measurement, and the fluid-control system, which utilizes hydr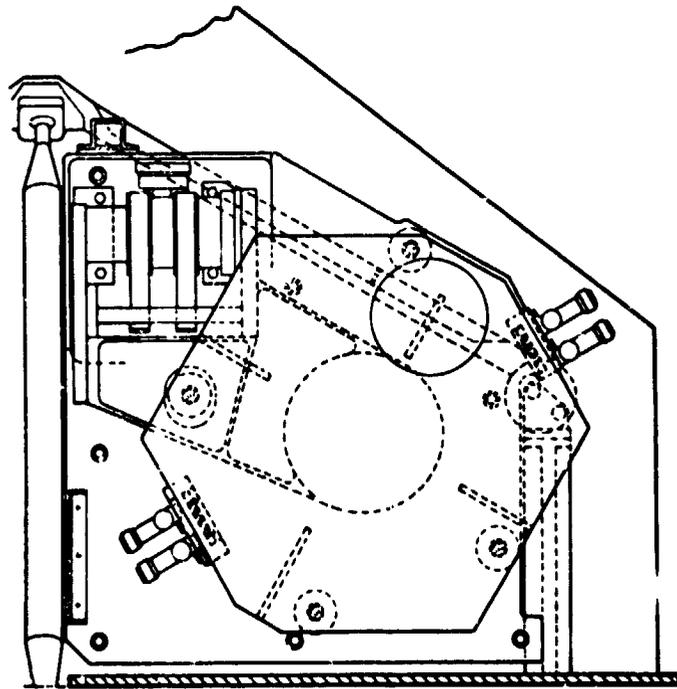aulic technology. This paper describes the primary design tasks, the selected solutions, and the unforseen problems involved in the development of these individual components of hardware.

INTRODUCTION

Inherent in current lift generation methods are the constraints imposed by their dependence on free-stream velocity and angle of attack. For fixed wing aircraft to perform low-speed landings and takeoffs, complex flap systems must be used to increase the effective area of the wings to compensate for the decrease in airstream velocity. More severe limitations are demonstrated by standard rotor blade designs; here, lift generation is inhibited by the reversed relative flow experienced by retreating blades and by the eventuality, as angle of attack is increased, of dynamic stall. As a consequence of these constraints, conventional rotorcraft have been unable to achieve desired increases in forward flight speed.

The method of circulation control lift generation may remove these types of constraints. Utilized with a blunt airfoil, circulation control refers to the discharge of a jet blown tangentially over the surface of the airfoil's rounded trailing edge. The jet, by adhering to the airfoil contour, moves the stagnation point further toward the lower surface to increase the circulation, which, in turn, increases the lift generated (see Fig. 1). Hence, circulation control can provide high lift coefficients as a function of jet blowing alone, unhampered by the problems attributed to free-stream velocity and angle-of-attack dependence.

In applications to fixed wing aircraft, circulation control would negate the need for flap systems and allow for even lower landing and takeoff speeds. Application of circulation control to rotorcraft would see rotor blade sections, symmetric about midchord and possessing upper surface leading and trailing edge jets, developing high lift coefficients irrespective of relative

*Research Engineer, NASA Ames Research Center

velocity direction and without angle-of-attack stall. Control of the aircraft in both cases would be accomplished through modulation of the jet(s) blowing.

Although the potential of circulation control as a viable alternative to current high-lift generation methods is attractive, its exploitation is hindered by an insufficient understanding of the flow field surrounding the blown airfoil. Without this knowledge, accurate prediction methods for the airfoil's performance cannot be formulated. Moreover, in proposed implementatic _ of this technology, aircraft lift control would be achieved through the periodic and transient blowing of the jets, and yet little experimental information exists concerning unsteady leading edge or transient trailing edge jet blowing.

NASA scientists have devised an experiment to obtain experimental data concerning the aerodynamics developed by a circulation control airfoil under various blowing conditions. Its primary objective is to visually define the fluid mechanical structure of the flow field for steady/unsteady leading and trailing edge blowing. To this end, water is to be used as the test medium; visualization of the flow field is facilitated by the use of dye injection or hydrogen bubble tracers, and is made more discernable because of increased time scales (one order of magnitude greater in water than in air). Also to be examined in this study is the influence of unsteady blowing on airfoil performance (forces and moments) and the influence of unsteady blowing on the movement of the leading and trailing edge stagnation-point locations. This latter complication poses a major obstacle in the development of a theoretical model.

To realize the objectives described above, NASA engineers have developed several major pieces of hardware. First, a model has been designed to capture, on a reduced scale, the characteristics of circulation control lift generation as utilized in applications to rotorcraft. Second, modifications to an existing water tunnel have been made to accommodate the model during flow-visualization studies and to provide uncontaminated airfoil load measurements. And finally, a fluid-control system has been designed to supply the model with the specified periodic and transient blowing conditions demanded in the experiment.

This paper describes the development of the hardware listed above. The details of each component design are given below individually, each preceded by the pertinent design requirements. The problems encountered during the manufacture and testing of the hardware are described collectively in the section titled PROJECT STATUS.

DESIGN

Model Design

The model is a two-dimensional representation of the circulation control methodology proposed for rotorcraft application. Designed for use in a water tunnel, the model, as shown in Figure 2, simulates rotor blade operation by

blowing jets of water from the leading and trailing edge slots of a symmetrical (about midchord) airfoil. The specifics of the circulation control airfoil geometry and flow generation were defined by the Principal Researcher and are as follows:

o Shape and Size Constraints

- the airfoil cross section must be elliptical, with circular arc leading and trailing edges and a 10.16-cm (4.0-in.) chord.
- the jet slots must be situated on the upper surface of the leading and trailing edges over the entire 21.08-cm (8.3-in.) length of the model.
- the slot exit height, the narrowest point of the jet construction, must be .015 + .0013 cm (.006 + .0005 in.).

o Flow Generation Contraints

- the jet plenum chambers must be isolated from each other.
- the velocity of the water leaving the jets should be 100 times faster than the velocity of the water in the plenum chambers.

o Structural Constraints

- the model must withstand 2.07×10^5 Pa (30 psi) internal pressure, 133.2 N (30 lb) lift load, 22.2 N (5 lb) drag load, and 3.38 N-m (30 in-lb) pitching moment.
- the height of each slot cannot deflect more than .00254 cm (.001 in.) under load (i.e., the applied plenum chamber pressure).

    The primary design task consisted of finding the configuration that would fulfill the geometrical contraints and yet maintain the structural integrity and desired flow characteristics of the model.

    In terms of the severity of the given requirements, the jet slot proved to be the most difficult design area. Deflection of the jet slot by the pressure developed in the plenum chamber had to be minimized without drastically changing the internal features of the model. The plenum chamber height, which controls the velocity of the jet discharge, and the slot entrance area, which determines the flow field uniformity, were especially sensitive to alteration.

    This design was further complicated by the positioning of the slot lip along the airfoil chord. The slot lip had to be located on the upper surface of the airfoil so that the jet discharge would exit through the minimum throat (slot) height. Adherence to design requirements necessitated that the slot lip be located along the chord at 4.708 cm (1.8537 in.) and cut to a thickness of .010 cm (.004 in.).

    A specific effort also had to be directed toward assuring the integrity of the model as a pressure vessel. Material was trimmed from the model interior

C-5

365

to enlarge the plenum chambers and establish a minimum flow velocity ("dead water") in the plenums. The structure of the model was further reduced to allow space to divert the water, support the wing, and isolate the plenum chambers. Hence, a maximum internal pressure of 2.07×10^5 Pa had to be contained with a minimum of structure.

Supplying isolated plenum chambers with independent sources of water was a difficult design task as well. Water had to flow into the plenum chambers with sufficiently slow velocity so that it would not be forced directly out the slots. However, the model size constraints would not permit increasing the diameter of the tubes bringing the water to the chambers. And decreasing the wall thickness of the tubes was undesirable since the tubes would act as the structural members supporting the model against the airfoil forces described above.

The model's final design is shown in Figure 3. Manufactured in several pieces, the model consists of two main body halves, two end pieces, a solid spar support, and two water injection pipes. The main body was sectioned so that the jet slot lip is part of the top half, while the circular arc leading and trailing edges are part of the bottom half. This allowed the jet slot area and the model interior to be easily accessed during fabrication.

The plenum chambers are isolated from each other by the solid center section of the wing halves and are supplied with water by separate water injection pipes. The large cutouts in the pipes allow the water to fill the chambers slowly. Lateral movement of the pipes is prevented by pins slotted into the bottom wing half. Plugs (not shown) welded into the ends of the pipes prevent the pipes from being ejected from the model by the pressure force.

Six support posts are evenly distributed along the length of each jet slot to prevent the deflection of the slot lip. Screws are threaded through these posts to provide increased resistance to the internal pressure. The slot lip, therefore, is constrained rather than cantilevered and the deflection of the slot lip edge is reduced; NASTRAN analysis shows this deflection to be .0023 cm (.0009 in.). In addition, the support posts allow for the adjustment of the slot height, using shims or a file, should the height deviate from .015 cm (.006 in.) for any reason. Although the posts do produce some obstruction to the flow through the slot entrance area, they are contoured into the surrounding internal geometry as much as possible to reduce this effect.

As mentioned above, the support posts aid in containing the internal pressure. The 12 screws through the posts, along with the four through the solid center section, hold the body of the wing together, while the end pieces, which slip over the solid spar and the water injection pipes, bolt into the main body to complete the pressure-vessel construction. The assembled wing is supported in the tunnel by the solid spar on the one side and the water injection pipes on the other.

Control of the slot lip deflection allowed the plenum chamber height to be maximized as a function of geometry alone. At the final design, the height measured 1.02 cm (.4 in.), 70 times the jet slot height. As a consequence, the flow through the jet slot is blown out of the airfoil at 70 times the velocity with which it enters the plenum chamber, achieving 70% of the design requirement.

Support System Design

The support system for the circulation control airfoil is the means by which the model is held in the water tunnel during the flow studies. The success of the experiment, namely how well the flow field is defined and the airfoil forces measured, depends on how well the support system fulfills the requirements listed below.

The support system must

o provide an unobstructed view of the model during flow-visualization tests;

o allow the adjustment (static) of the angle of attack prior to testing;

o contain pressurized water within the tunnel (1.03 x 10^5 Pa or 15 psi max.);

o conform to existing load cell and tunnel frame apparatuses;

o isolate the load path from the model to the load cells;

o comply with model movement to allow measurement of airfoil forces.

At the onset of the support system design, a decision was made to separate the flow-visualization and load-measurement phases of the experiment; the configuration of the water injection pipes made it impossible to fulfill the requirements for measuring the loads without obstructing the view of the model. Hence, two support systems were designed, one permitting flow visualization and documentation and the other permitting airfoil load measurement. In addition, a decision was made to orient the model in the test section so that it could be observed from the solid spar end. In order to supply water to the model through the water injection pipes, the fluid-control system needs to be adjacent to the model, close to the tunnel window. Consequently, the solid spar side of the model was deemed to be the "viewing side."

The subsystem designed for flow visualization consists simply of two transparent polycarbonate windows which mount into the existing test section. Cut into the water injection side window is a circular plug that may be rotated, by loosening the wing nuts holding it in place, to adjust the model's angle-of-attack. The water injection pipes extend through two holes in the

367

plug and are sealed by O-rings to contain the water. The plug itself utilizes a gasket to prevent leaking. On the solid spar side, the window has a hole cut in it for the spar, which is sealed by an O-ring. As the circular plug and the water injection pipes rotate to bring the model to a new angle-of-attack, the solid spar need only slide in its O-ring seal. The model is held against lift, drag, and pitching moment by the 2.54-cm-thick (1-in.-thick) transparent polycarbonate windows. The water injection side window is painted black to provide a better background for laser-lighted photography.

The airfoil load-measurement support subsystem was of necessity made more sophisticated. The load cells that had been used to measure lift and drag loads in previous water tunnel tests were to be used again. Consequently, the main design effort for this subsystem was directed toward determining a method which could isolate the load path (from the model to the load cells) from the tunnel structure and windows, contain the pressurized tunnel water, and be compliant to model displacements, all within the constraints imposed by the existing structure.

The method selected for the final design, shown in Figure 4, utilizes welded metal bellows. The bellows are used as flexible connections through which the spar and water injection pipes are brought to the load cells. Able to withstand an internal pressure of 2.07×10^5 Pa (30 psi), the stainless steel bellows are sufficiently compliant in the axial and cantilevered directions to transfer airfoil displacements to the load cells without absorbing any load themselves. Also, the windows are cut so that the pipes and spar do not make contact with any structure on their way to the rigid load cell connections. Thus, the measurements obtained by the system are virtually uncontaiminated.

The load cell connections are designed to be completely rigid to support the model in the lift and drag directions. The bellows are torsionally very stiff and can prevent the model from rolling with the pitching moment. The pitching moment is measured by strain gages placed on the water injection pipes.

The angle-of-attack of the airfoil may be adjusted by rotating the circular plug and the attached bellows assembly on the water injection side. The solid spar is again allowed to slide in its O-ring seal so no rotation of its bellows assembly is required.

Fluid-Control System Design

The fluid-control system must develop the blowing conditions through the model that a circulation control airfoil experiences in a rotorcraft-type application. Because control of the lift developed by the model is accomplished by the modulation of the jet discharge, the blowing conditions, set by the experimenter with the fluid-control system, provide the means for correlating the data obtained during the flow-visualization and load-measurement phases of the experiment. To ensure that the information gained through this correlation be meaningful, the fluid-control system must be extremely accurate in constructing the specified test conditions.

The fluid-control system must not only be accurate, but versatile as well. The discharge of the two jets must be independently adjustable, whether the jets are blowing individually or simultaneously. The main parameter to be controlled by the system is the individual plenum pressure, which is expressable as:

$$p_i = p_i + (p_i - p_a) f(t); \quad i = 1,2$$

where
p_i = mean plenum pressure
p_a = tunnel pressure ('atmospheric')
$f(t)$ = pressure variation with time

As apparent from the above expression, the fluid-control system must maintain for each jet a mean plenum pressure and a pressure variation with time. Periodic blowing conditions are to be obtained by forcing the plenum pressure to vary sinusoidally, so that $f(t) = A \sin(wt + \phi)$. The additional parameters, frequency and phase angle, must be independently adjustable for each plenum. Transient blowing conditions are to be simulated by forcing the plenum pressure to follow a ramp function, or $f(t) = C_1 t + C_2$, which again requires that an additional paramater, the time constant for total response, be adjustable for each jet. Setting $f(t) = 0$ will provide steady blowing test conditions.

From known relations between plenum pressure, p_j, jet velocity, V_j, tunnel pressure, p_a, and free-stream velocity, V_∞, and from consideration of the operational constraints of the tunnel, $V_\infty = 3$ m/s and $p_a = .01$ MPa, the following limits were placed on the test conditions to be be provided by the fluid-control system:

In general, the system must

o conserve the mass of the water used;
o provide a maximum plenum pressure of 1.38×10^5 PA (20 psi);
o deliver a maximum flow rate of .44 lps (7 gpm) to each plenum chamber (to produce the pressure given above).

For periodic blowing, the system must

o maintain a sinusoidal pressure variation in each plenum for frequencies up to 10 Hz;
o maintain a phase shift between plenum pressure variations of as much as 180°.

For transient blowing, the system must

o be capable of following a ramp (pressure variation) that reaches full amplitude in 1/40 sec.

The primary tasks involved in the design of the fluid-control system were creating a constant mass system, isolating the control of the water supplied

to each plenum chamber, and determining a method or mechanism capable of accurately constructing the required pressure variations.

Creating a constant mass system and isolating the control of the fluid diverted to each plenum were simple to do in concept but difficult to implement. The conservation of mass required that the water to be blown through the model be drawn directly from the tunnel. Any excess water not supplied to the model (i.e., the test conditions demand less than the maximum flow rate) would have to be returned to the tunnel. The requirement that individual plenum pressures be adjustable could easily be fulfilled by the construction of separate water supplies for each jet. However, constructing the "closed circuit" for conservation of mass and the separate supply routes for independent fluid control proved difficult because the tunnel structure could not be modified.

The most critical design task was the determination of the means which could produce the sinusoidal and linear pressure variations accurately. Because controllability and quickness of response are necessary to such a method or mechanism, ordinary water-handling components were judged to be inadequate. Such components (i.e, check valves) were too slow or too unmanageable to meet the requirements listed above.

While the possibilty of designing a mechanism specifically for application to this system was considered, it was decided instead to adapt a readily available hydraulic component to control the water. This component, the servovalve, is capable of providing sufficiently quick response and of handling the required range of flow rates (0 to .44 lps). Operation of the valve is regulated by the amount of electric current applied to the valve; a spool inside the valve moves in proportion to the signal it receives to close or open ports which control the flow of fluid.

The servovalve provides an attractive solution to the design task described above for it permits the flow through the model to be varied according to any time function by the application of an appropriate signal. Furthermore, the valve flow follows the input signal very accurately if it is operated within a closed feedback loop; the flow through the valve is continually monitored to ensure it matches the desired flow.

However, adaptation of the servovalve to a system run with water to the extremes demanded of the fluid-control system requires that several important issues be addressed. First, flow rate is not the paramater that is controlled for the experiment as it is for the servovalves. The model plenum pressure must be modulated, and so the feedback system must be designed to measure and compare pressures. Second, the valve is designed to operate with hydraulic fluid. For use in water, the moving parts contained inside the servovalve must be protected from corrosion and excessive wear. A final consideration is the high pressure required by the valves for maximum responsiveness. A pressure of 6.9 MPa (1000 psi) should be supplied to the valves, but the model (supplied by the valves) can only withstand a pressure of .21 MPa (30 psi). Some type of protection against such extreme pressure, then, must be devised for the model.

A schematic of the fluid-control system's final design is shown in Figure 5. A constant displacement pump delivers 1.64 lps (26 gpm) at 6.9 MPa (1000 psi) to two servovalves, one to supply each plenum chamber. The regulator, located just after the accumulator used to dampen the pressure fluctuations developed by the pump, is set at 6.9 MPa; if the test conditions are such that less than 1.64 lps are allowed through the valves, pressure will build in the supply line and cause the regulator to respond to divert the excess water away from the valves. Should the regulator fail to operate, a relief valve set to blow at 8.3 MPa (1200 psi) is included in the system to prevent the pressure in the supply line from building to dangerous levels.

The accumulator situated behind the servovalves is used to dampen the pressure surges generated by the opening and closing of the valves. Contamination of airfoil load measurements from these same pressure fluctuations is prevented by utilizing flexible hose to connect the valves to the water injection pipes. Hard lines containing rupture discs are constructed in parallel to these soft lines. The discs are set to rupture at 2.07×10^5 Pa (30 psi) to provide protection for the model against all pressures greater than the design pressure.

The internal parts of the servovalves are protected from wear and corrosion by a microsealing process; the spool is impregnated with carbon to lubricate its movement through the sleeve. In addition, special seals were installed to replace those used for hydraulic fluid service. The water sent through the valve must remain extremely clean since a particle the size of $3 \mu m$ can destroy the precise valve operation. Two hydraulic filters, one $15 \mu m$ and the other $3 \mu m$, are placed upstream of the servovalves to prevent their contamination.

As apparent from the schematic (Figure 5), the fluid-control system is indeed a constant mass system. Water, however, cannot be drawn directly from the tunnel for the pump requires a larger intake line than can be accommodated by the tunnel. Instead, a tank is used to hold water for the pump intake. The water blown off by the regulator and the overflow from the tunnel (water blown through the model) are diverted back to this tank.

The schematic in Figure 6 depicts the control loop of one of the servovalves. The desired pressure variation for each plenum is constructed by a signal generator and sent to the servovalve electronics in the form of a voltage. There, the voltage signal is converted to a current, which is then applied to the servovalve to initiate the corresponding flow rate. The flow characteristics of the model are such that the plenum pressure is directly proportional to the square of the flow rate through the plenum chamber. In a sense, then, the model converts the valve flow to plenum pressure. A pressure transducer, mounted in the model plenum, measures the pressure and feeds this voltage back to the valve electronics. By comparing this signal to the signal representing the desired pressure, an error signal is produced to correct the valve flow, which in turn, corrects the plenum pressure.

371

PROJECT STATUS

The circulation control airfoil entered the shop for fabrication in October 1983 and was completed in February 1984. Since that time, the model has been run in the tunnel, using the flow-visualization supports, so that its flow characteristics could be verified. It has subsequently been returned to the shop for installation of the pressure tranducers.

Few difficulties arose during the fabrication of the model. One problem that did occur, though, was that the two model halves would shift relative to one another during the contouring of the model ends. The dowel pins placed along the centerline of the model that were to hold the halves during machining did not control this problem; the slippage occured at the jet slot support interfaces and was caused by play in the screw threads. To correct this, cylindrical inserts were pressed into the support posts on one model half so that upon assembly, they fit into corresponding counterbores cut around the threads of the other half. The play in the screw threads was thus contained.

The flow-visualization support system was submitted for fabrication shortly after the model. While no difficulties were encountered during the system's manufacture, a problem did arise during its implementation when the model's angle-of-attack was to be changed. The seal developed by the gasket used to prevent water from leaking around the circular plug could not be broken easily. As a consequence, it was difficult to rotate the plug to set a new angle-of-attack. The problem was remedied in this design by fixing two pins in the plug to assist the operator in breaking the seal. All subsequent designs in which plugs are required utilize O-rings instead gaskets to avoid the problem entirely.

Fabrication of the load-measurement supports began in July 1984. The pieces have been machined and assembled (welded). The estimated installation date is May 1985.

The fluid-control system has been constructed and is being qualified for operation. Problems with the performance of the regulator have been discovered; its response to an increase in pressure in the supply line is too slow and too harsh. One solution that is to be attempted is to pump less water (.95 lps instead of 1.64 lps) through the regulator by slowing the speed of the pump. The regulator, not having to work as hard, should respond less harshly. Several more weeks of making adjustments to the fluid-control system are foreseen.
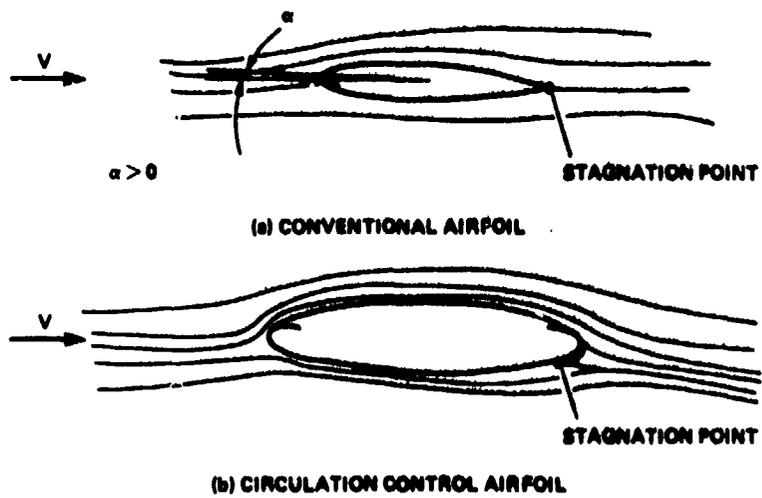
Figure 1.   Lift Generation
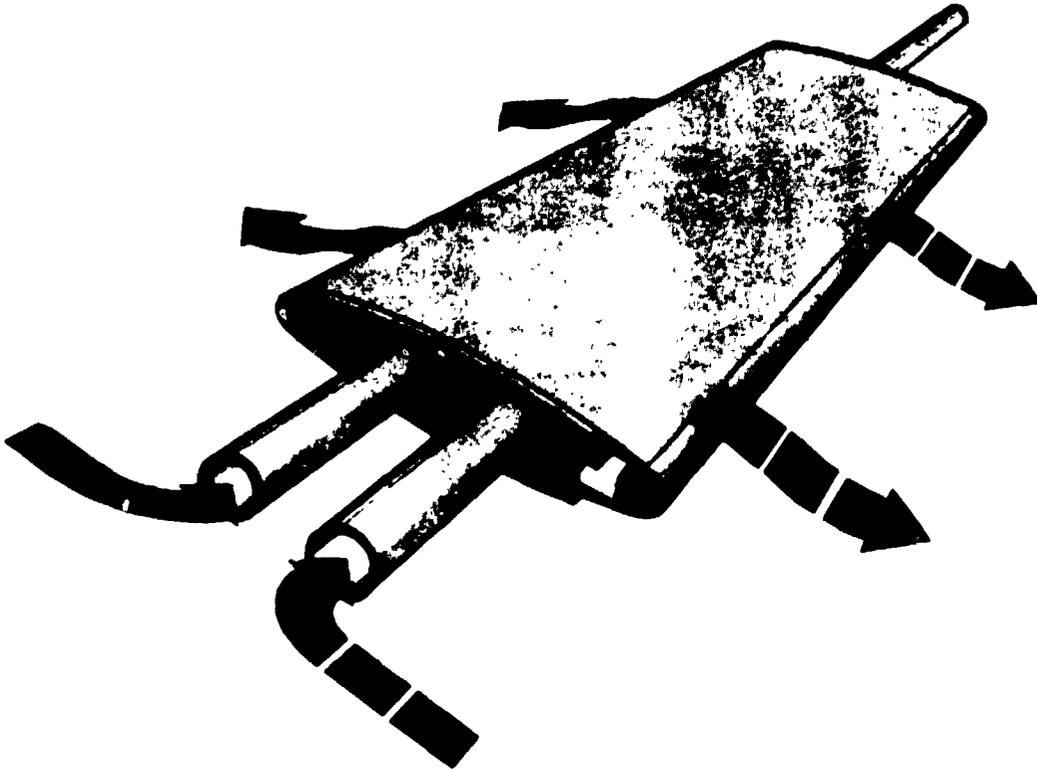
Figure 2.   Circulation Control Airfoil
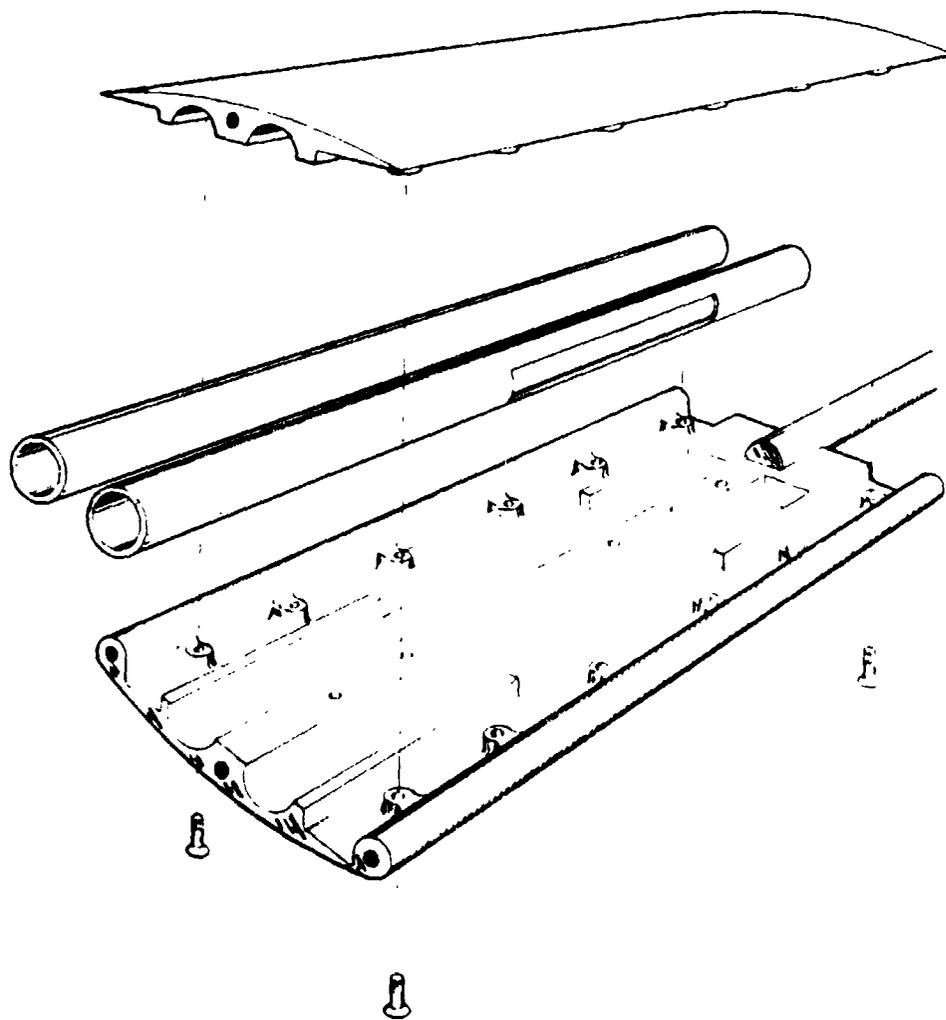
Figure 3. Airfoil Assembly
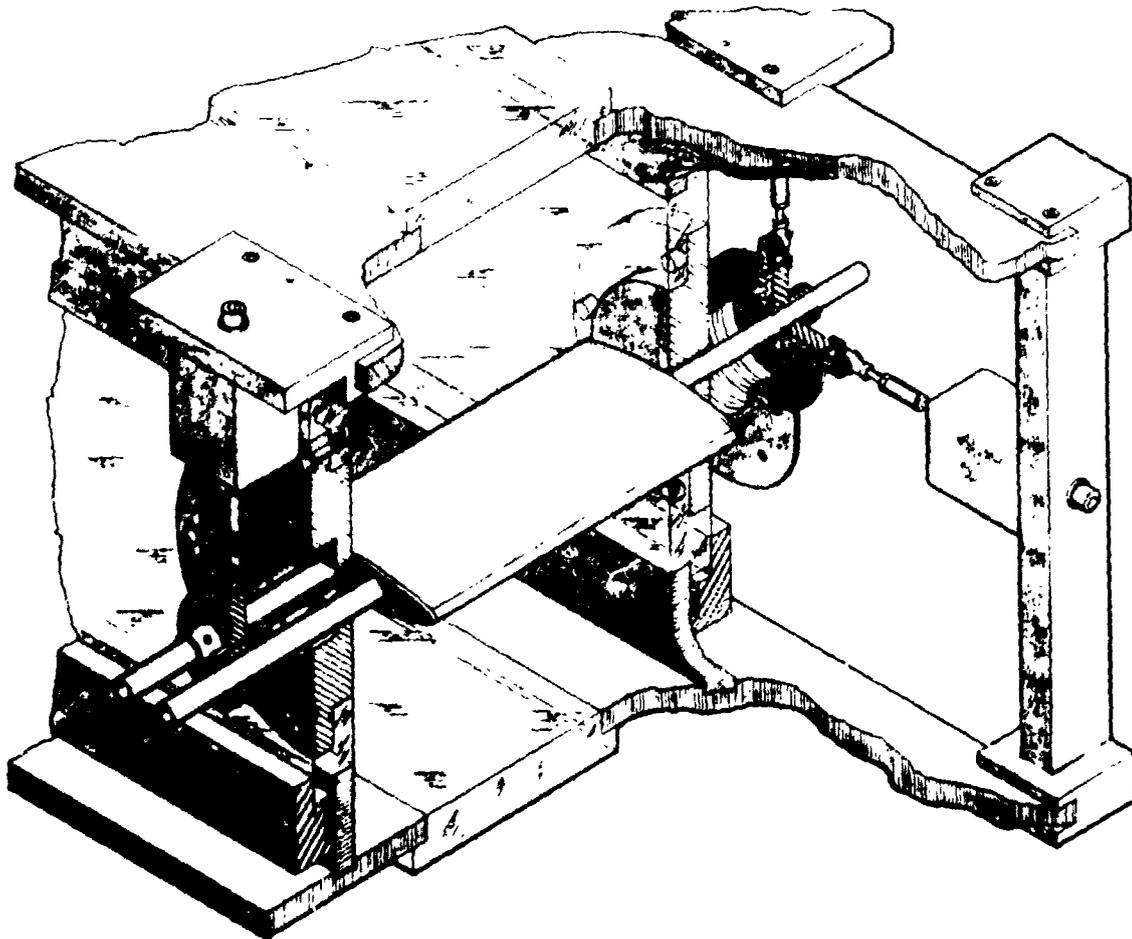
Figure 4. Load Measurement Support System
(Test Configuration)
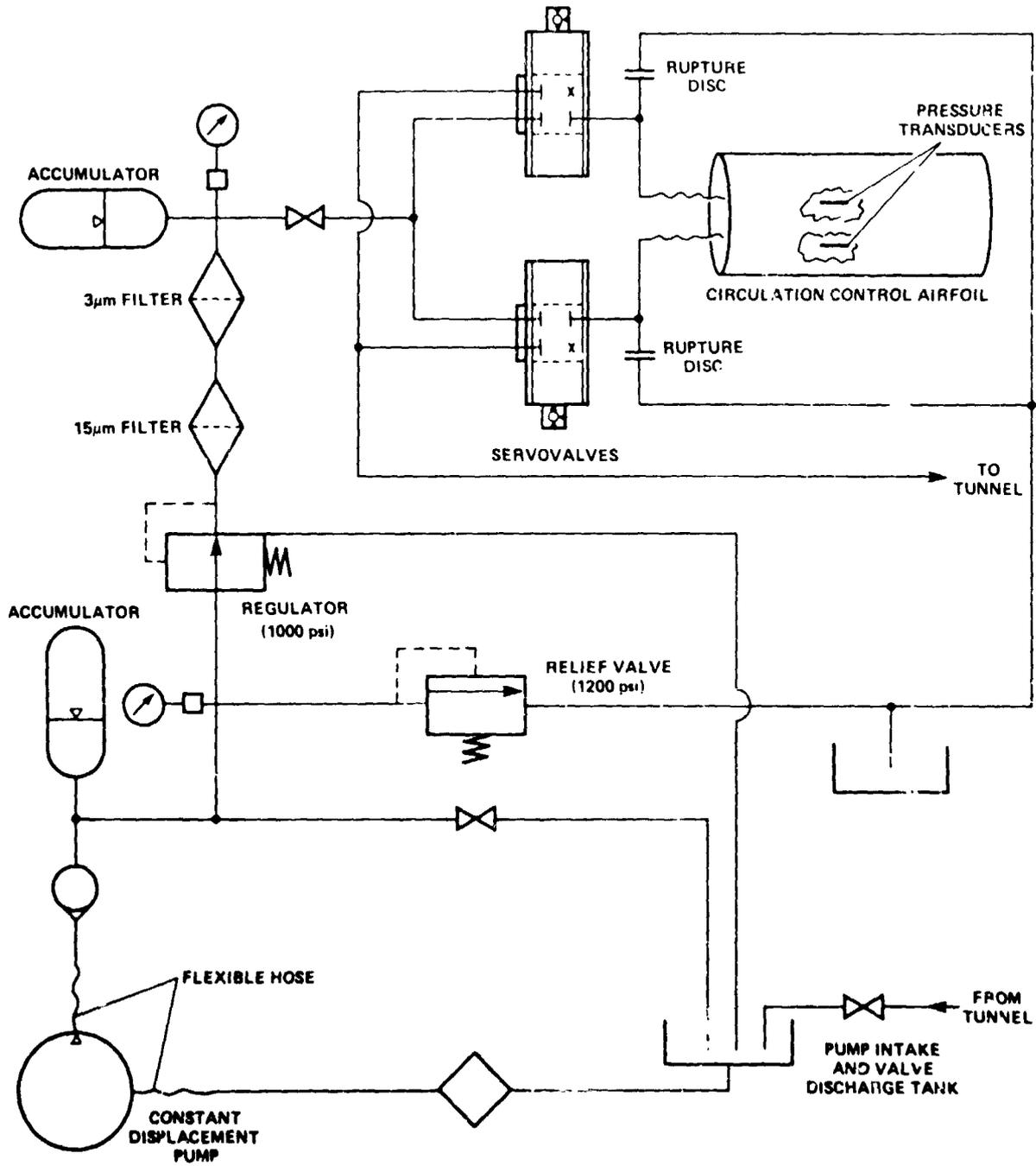
Figure 5. Schematic Fluid-Control System

AIRFOIL

PRESSURE TRANSDUCER

SERVOVALVE

FROM PUMP

RETURN

FEEDBACK

SERVOVALVE ELECTRONICS

COMMAND

SIGNAL GENERATOR

(a) PICTORIALLY

| SIGNAL GENERATOR | | VOLTAGE | SERVO-VALVE ELECTRONICS | CURRENT | SERVO-VALVE POSITION | FLOW RATE | AIRFOIL PLENUM CHAMBER | PLENUM PRESSURE |

VOLTAGE

PLENUM PRESSURE SENSOR
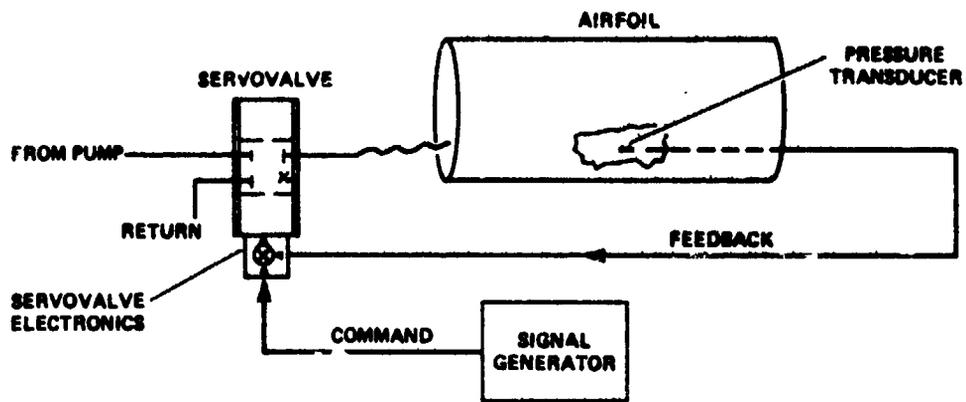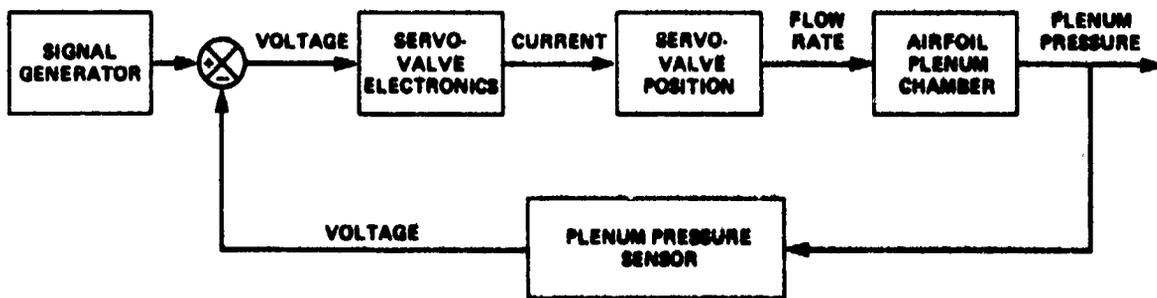
(b) SCHEMATICALLY

Figure 6. Servovalve Feedback Control

TWO-PLANE BALANCE
AND
SLIP-RING DESIGN

Phil M. Luna *

ABSTRACT

A 3.25-cm (1.28-in.) two-plane balance and eight-channel slip-ring assembly has been designed to measure and transmit the thrust (667-N;150-lb) and torque (135-N-m;100-lb-ft) components produced by wind-tunnel model turboprops and drive motors operating at 300 Hz.

INTRODUCTION

An Advanced Turboprop Program is currently under development at Ames Research Center. The purpose of the program is to investigate and develop the use of large-diameter, high-solidity propellers (turboprops) as an economical and efficient means of aircraft propulsion. The possible fuel savings that could be attained from using turboprops can be as high as 15%. This is especially important to commercial airlines sinc the cost of fuel is about 50% of their operating expenditure.

The program will feature a fully powered, .084-scale, wind tunnel model of a modified Douglas DC-9 transport aircraft.

Some of the model's versatile characteristics include:

o wing-mounted power plants
o plyon-mounted power plants secured to the tail
o interchangeable wings which may be mounted in
   three different locations along the fuselage
o interchangeable horizontal tails with adjustable
   angle of attack settings

Each power plant consists of eight .304-m-diam (1-ft) graphite composite propeller blades driven at 300 Hz.(18,000 rpm) by a small, 149- KW (200-hp) air motor. The air motor requires air at 3.46 MPa (500 psi) and 1.36 kg/s (3 lb/s).

In order to measure the thrust and torque components produced by the propeller blades, a two-plane balance and slip-ring assembly will be used. As shown in figure 1, the inner sleeve of the balance will be pinned to the forward end of the air motor shaft, and the slip-ring assembly will be secured to the aft end of the air motor shaft. The central portion of the balance

*Research Engineer, NASA Ames Research Center

outer sleeve will then be pinned to a hub which secures the propeller blades. Instrumentation wires from strain gages on the balance will be routed to the slip-ring assembly through the center of the hollow air motor shaft.

The sizes of the balance and slip-ring assembly were defined by the anticipated thrust and torque loads, and the geometrical contraints imposed by the size of the air motor nacelle. This paper will describe the design of the balance and slip-ring assembly.

Two-Plane Balance Design

The two-plane balance, developed at Ames Research Center several years ago, is shown in figure 2. It consists of an outer sleeve attached at its extremities to an inner, hollow sleeve by a brazing/heat treatment-process. Nicoro braze wire (.127-cm-diam) is wrapped around the inner sleeve grooves (two at each end) prior to the outer sleeve/inner sleeve assemblage. The gap between the two sleeves is equalized by setscrews located at each end of the outer sleeve. An inert gas vacuum furnace is used to braze the two sleeves together while the balance is supported in a vertical position. The brazing cycle also serves as the condition A heat treatment. Afterwards, the balance is cooled to room temperature and then reheated to attain the precipitation-hardening phase of the heat treatment.

The outer sleeve has eight identical flexures, four at each end, arranged symmetrically in two parallel planes, perpendicular to the longitudinal axis. The flexures are instrumented with strain gages and can detect loads along any of the three axes in addition to moments about the three axes. A load along the longitudinal axis (thrust load) will be equally distributed among the eight flexures and will produce a bending stress in each flexure. The torsional load will also be equally distributed among the eight flexures, but it will produce a column-type (compression/tension) stress in each flexure. For a further description of a two-plane balance, refer to NASA Technical Memorandum X-1278.

By adapting this basic design to suit the needs of this program, a two-plane balance was designed specifically to

o measure a 667-N (150-lb) maximum thrust load
o measure a 135-N-m (100-lb-ft) maximum torsional load
o have a 3.25-cm (1.28-in.) outside diameter
o have a 1.91-cm (0.75-in.) inside diameter
o withstand an out-of-balance radial load of 8.9 KN (2000-lb) caused by an accidental loss of four of the eight propeller blades
o utilize flexures with natural frequencies about and along all axes greater than 900 Hz (three times the exitation frequency) to prevent dynamic excitation

380

The size of each flexure, shown in figure 3, is determined by the
following factors:

o sensitivity (strain level) to each design load
o interactions between design loads
o adequate surface area to bond miniature strain gages
o geometrical constraints

The geometry of the balance is such that the length (L) and width (B,C) of
each flexure are inversely related to each other, while the thickness (H) is
an independent variable. Consequently, each flexure may be either long and
narrow, or short and wide, and may have any thickness.

Additionally, the length and width are futher defined by the inner and
outer diameter of the outer sleeve. Since the outer diameter is fixed
(3.25-cm), the inner diameter (to some extent) is a variable. It is bounded
by the size of the inner sleeve.

The maximum bending stress produced by the thrust load (P) occurs at the
flexure base. This stress is $\phi = 3PL/8CH^2$, where L is the flexure length, H is
the thickness, and C is the base width. In order to produce an adequate
strain level, the flexure should be thin and long (and consequently narrow)
because of the moderate thrust load.

The column-type stress produced by the torsional load (T) on each flexure
is $\phi = T/4HBD$, where D is the outer sleeve mean diameter, and B is the width.
The large torsional load coupled with the small diameter requires a flexure
with a large cross-sectional area (HB) to prevent the flexure from being
overstressed.

The above parameters demonstrated that designing to the torsional load
required a flexure with a large width or thickness. However, the thrust load
required a flexure with a large length (i.e., a small width) and small
thickness. Consequently, the design of the flexures and of the related outer
sleeve inner diameter was an iterative process.

The final size of the flexures and strain levels produced by the design
loads are as follows:

o length (L) = 9.12-mm (.359-in.)
o thickness (H) = 2.28-mm (.090-in.)
o width (B) = 1.78-mm (.070-in.)
o base width (C) = 3.45-mm (.136-in.)
o 610 microstrain for the 667-N thrust load
o 1440 microsrain for the 135-N-m torsional load

Some other features of the 3.25-cm, two-plane balance include
the following:

o a stop nut to prevent the propeller blade hub from separating from the
  nacelle in case the balance/hub shear pins fail

381

o a stop nut to prevent the balance and propeller blade hub from
   separating from the nacelle in case the balance/air motor shaft
   shear pins fail

o soldering pins embedded through the forward end of the balance to ease
   and improve the strain-gage wire-soldering procedure

o a phenolic cover on the forward end of the balance which protects the
   instrumentation wires

o a spiral groove on the exterior surface of the outer sleeve to ease
   balance/propeller hub installation and removal by providing a cavity
   for dirt particles since the gap between the balance and the propeller
   hub is only .003-mm

Slip Ring Assembly Design

A slip ring assembly was designed to transmit the electrical signals from
the balance strain-gages to a data-acquisition system while operating at 300
Hz. The constraints governing the design were that the slip-ring assembly had
to interface with the existing air motor shaft, fit within an exit guide vane
set located at the aft end of the air motor, and provide a means for
delivering an air/freon mixture for cleaning and cooling the contacts.

The slip ring assembly, shown in figure 4, is secured to the aft end of
the air motor shaft and consists of the following major items:

o a hollow kevlar shaft
o coin silver contact discs
o silver, graphite, molybdenum-disulfide brushes
o phenolic brush housing and sleeve
o exit guide vane set
o stainless steel retaining and adapter nuts

The contact discs are positioned over the kevlar shaft and sandwiched
between phenolic spacers to orient them with respect to the shaft's
longitudinal axis. Instrumentation wires are soldered to the contact discs
and routed through the hollow kevlar shaft to its aft end. Before the kevlar
shaft is inserted into the hollow air motor shaft, the lead wires from the
balance strain-gages are routed through the center of the hollow air motor
shaft and connected to the lead wires from the contact discs.

The kevlar shaft, which has a key on the surface of its flange, is
inserted into the air motor shaft so that the key fits into a slot in an
adapter nut at the end of the air motor shaft. The kevlar shaft is retained
by a nut which fits over the flange and threads onto the adapter nut. The
retaining nut and key prevent the kevlar shaft from slipping. The kevlar
shaft must always rotate at the same speed as the air motor shaft so that the
instrumentation wires are not damaged.

382

The phenolic brush housing is then placed over the kevlar shaft/disc assembly. An alignment screw is threaded into the closed end of the brush housing and slides into the hollow kevlar shaft. This screw helps hold the brush housing concentric to the kevlar shaft while the brushes are bei.g inserted and fastened to the brush housing.

Instrumentation wires are connected to ea͏ brush leg and run along the brush housing to soldering pins located at the closed end of the brush housing. Once the connections are complete, a phenolic sleeve is slid over the brush housing. This sleeve covers the holes in the brush housing through which the brushes are inserted and protects the instrumentation wires.

An exit guide vane set (which contains a nacelle supported by a stator) is fitted over the phenolic sleeve and into the aft end of the air motor. The geometry of the nacelle creates a plenum chamber around the sleeve. The air/freon mixture (which will be delivered through an air line in the stator) will pressurize the nacelle to .69-MPa (100-psi). This mixture will be directed to the areas where the brushes contact the discs via eight 1.067-mm-diam (.042 in.) orifices through the brush housing and sleeve. The instrumentation wires at the soldering pins will be routed out of the nacelle through another ..le in the stator.

Once the exit guide vane set encases the brush housing, the concentricity between the kevlar shaft and the brush housing is maintained by the nacelle. Thus the alignment screw (which is through the brush housing and kevlar shaft) is no longer needed. This alignment screw must be removed because the kevlar shaft rotates while the brush housing remains stationary. Removing a threaded cap on the end of the nacelle provides enough room to remove the alignment screw. The threaded cap is then replaced and a retention screw is installed through the cap and brush housing. The retention screw prevents the brush housing from moving forward with respect to the nacelle and prevents an excessive amount of the air/freon mixture from leaking into the aft end of the nacelle.

Previous testing has shown that this brush/contact disc system works well. Since each contact disc has opposing brushes, any vibrational displacement that lifts one brush leaves the other brush in contact. Thus, a "clean" signal is consistently provided.

SUMMARY

Although the two-plane balance and slip-ring assembly are small parts of the whole wind tunnel model that will be used in the Advanced Turboprop Program, they play an important role in the program. They will measure the turboprop loads and transmit the electrical signals which will eventually aid in determining the effectiveness of using large-diameter, jet-driven propeller blades to propel an aircraft.
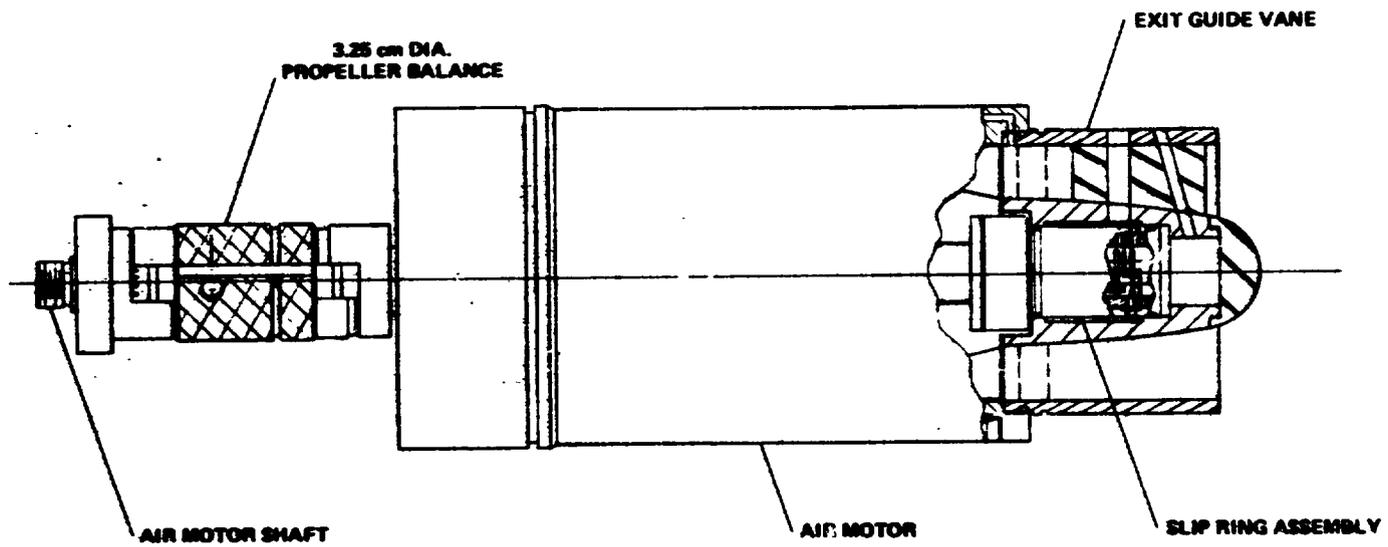
3.25 cm DIA.
PROPELLER BALANCE

EXIT GUIDE VANE

AIR MOTOR SHAFT

AIR MOTOR

SLIP RING ASSEMBLY

Figure 1.   Balance/Motor/Slip-Ring

SECTION B-B

STOP NUT

OUTER SLEEVE

INNER SLEEVE

SECTION A-A

Figure 2. Two-Plane Balance

385

Figure 3. Flexure
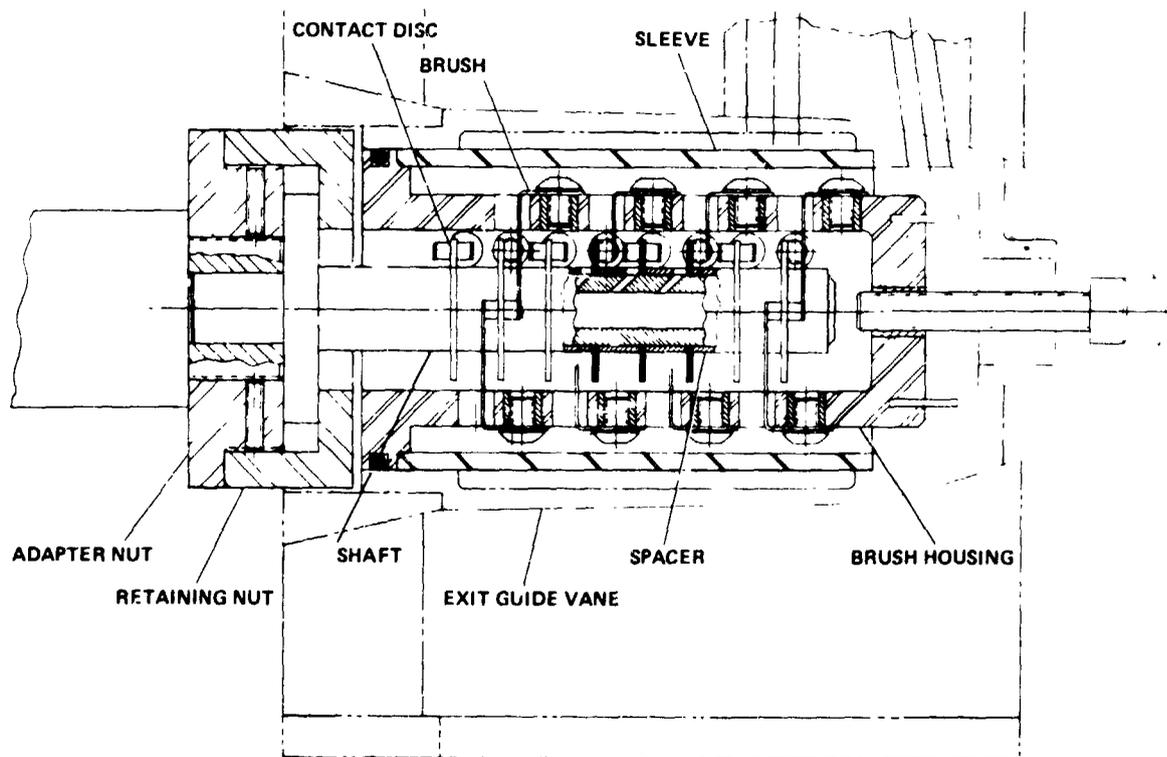
Figure 4.   Slip-Ring Assembly

1. Report No NASA CP-2371	2. Government Accession No.	3. Recipient's Catalog No
4. Title and Subtitle 19th AEROSPACE MECHANISMS SYMPOSIUM		5. Report Date **August 1985**
		6. Performing Organization Code
7. Author(s)		8. Performing Organization Report No 85181
9. Performing Organization Name and Address NASA Ames Research Center Moffett Field, CA 94035		10. Work Unit No
		11. Contract or Grant No
12. Sponsoring Agency Name and Address National Aeronautics and Space Administration, Washington, D.C. 20546; California Institute of Technology, Pasadena, CA 91109; and Lockheed Missiles & Space Company, Inc., Sunnyvale, CA 94088		13. Type of Report and Period Covered Conference Publication
		14. Sponsoring Agency Code

15. Supplementary Notes

16. Abstract

The proceedings of the 19th Aerospace Mechanisms Symposium held at the NASA Ames Research Center at Moffett Field, California, on May 1-3, 1985, are reported. Technological areas covered include space lubrication, bearings, aerodynamic devices, spacecraft/Shuttle latches, deployment, positioning, and pointing. Devices for spacecraft docking and manipulator and teleoperator mechanisms are also described.

17. Key Words (Suggested by Author(s)) Docking devices Staging mechanisms Actuators Space lubricants Circulation-control lift Thin-section bearings	Teleoperation Manipulator arm Thermal actuators Deployment devices Traction drives Energy-absorbing seat Positioning mechanisms	18. Distribution Statement Unclassified – Unlimited Subject Category 39	
19. Security Classif (of this report) Unclassified	20. Security Classif (of this page) Unclassified	21. No of Pages 402	22. Price* A18